Flow Boiling of HFE-7200 in Multi-Microchannel Heat Sinks for High-Heat Flux Applications

by

Vivian Lee Yue Sze

Department of Mechanical and Aerospace Engineering

College of Engineering, Design and Physical Sciences

Supervisor: **Professor Tassos G. Karayiannis**

Thesis submitted for the degree of Doctor of Philosophy in Mechanical Engineering

September 2020

Abstract

The thermal management of high power-density electronics due to miniaturisation is a key bottleneck in the continued enhancement of processing power and device functionality in compact packing assemblies. With air cooling generally limited to heat fluxes below 1 MW/m^2 and single-phase liquid cooling exhibiting high pressure drop and temperature gradients across the heat sink, flow boiling in microchannels, offering high heat transfer rates with enhanced temperature uniformity on low coolant charge, is an emerging solution to manage heat fluxes in modern electronics projected to reach 10 MW/m^2 with hotspots of 6 to 8 times the background heat flux. However, poor understanding of fundamental issues in flow boiling and lack of design tools to optimise two-phase cooling have hindered the implementation of the technique in industry. Additionally, whilst heat fluxes up to 7 MW/m^2 have been demonstrated using microchannel flow boiling, high coolant subcooling is typically employed, which may not be attainable in integrated two-phase cooling systems for compact electronics packages.

Accordingly, the objectives of the present experimental study is to (i) clarify and understand the fundamental aspects and basic mechanisms of flow boiling in multi-microchannels, (ii) investigate the effect of operating parameters, including heat flux, mass flux, system pressure and degree of subcooling, on microchannel two-phase flow patterns, flow instabilities, heat transfer and pressure drop, (iii) evaluate existing flow regimes maps, heat transfer and pressure drop correlations in literature, (iv) explore the use of a surface coating to enhance heat transfer rates in a parallel microchannel heat sink and (v) propose a conceptual design of a small-scale, integrated two-phase pumped cooling system for multiple heat sources within a compact electronics enclosure, including estimations of the power consumption of the system based on experimental data.

Flow boiling experiments were conducted in a plain and coated copper microchannel heat sink with a square footprint area of 400 mm^2 and 44 parallel channels of nominal width, height and length of 360 μm, 700 μm and 20 mm respectively. The hydraulic diameter of the plain channels was 475 μm. A dielectric working fluid, HFE-7200, with a boiling point of 76 °C at 1 atm was employed, as it is suitable for the cooling of electronics (typical junction temperatures of +85 °C to +125 °C) and is able to reject waste heat at low pressures from the

condenser to high ambient environments of up to +70 °C. The experimental range investigated was between inlet pressures of 1 – 2 bar, mass fluxes of 200 – 400 kg/m^2 s, subcooling degree of 5 – 20 K for exit vapour qualities of up to 1, corresponding to wall and base heat fluxes 24.8 – 234.3 kW/m^2 and 93.7 – 896.3 kW/m^2 respectively. High-speed flow visualisation was conducted along the microchannels at each condition to monitor flow pattern developments in the heat sink.

Flow patterns developed from bubbly to slug, churn and annular flow with increasing heat flux along the channel. Nucleating bubbles were observed on the channel side walls and were periodically suppressed with liquid film thinning in the slug and annular flow regime. Similar but earlier flow pattern evolutions were observed in the coated channels due to higher bubble generation frequency on the coated surface. Increasing mass flux and decreasing the degree of inlet subcooling generally accelerated flow regime transitions in the microchannels. Increasing system pressure delayed flow pattern development in the plain channels while the opposite was observed in the coated channels. Saturation pressure, degree of inlet subcooling and the surface coating were found to have an effect on flow boiling instabilities in the microchannel heat sink. The flow pattern transition boundaries were compared with predictions in literature.

Both the local and averaged flow boiling heat transfer coefficients increased with increasing heat flux. A peak in local heat transfer coefficient was generally observed near the onset of boiling and depreciated with increasing vapour quality corresponding to nucleate boiling suppression. Heat transfer enhancement of up to 50 % was achieved using the surface coating. Nevertheless, in some instances, excessive bubble nucleation activity in the coated channels led to prolonged wall dryout and the premature occurrence of critical heat flux. Increasing saturation pressure enhanced two-phase heat transfer in the microchannels while varying the degree of subcooling had only a marginal effect on average flow boiling heat transfer. The mass flux effect was only notable at high heat fluxes where annular flow was dominant, corresponding to the increasing contribution of the convective boiling mechanism to two-phase heat transfer. The heat transfer results were compared with correlations reported in literature.

Two-phase pressure drop increased with increasing heat flux, exit vapour quality and mass flux in the channels. Flow boiling pressure drop was generally higher in the coated channels, where

the penalty may be as much as 83 %. There appears to be an interdependence between the magnitude of pressure drop, wall dryout and two-phase flow oscillations in the microchannels. Increasing system pressure lowered channel pressure drop due to significant changes in the thermophysical properties of the fluid while increasing subcooling degree reduced pressure drop due to delayed flow pattern development in the channels. The pressure drop results were compared with past correlations with varying success. All correlations assessed did not capture the effect of inlet subcooling on flow boiling pressure drop.

A maximum cooling capacity of 800 kW/m^2 was demonstrated with uniform heat sink wall temperatures below typical allowable junction limits. The surface coating enhanced temperature uniformity and further lowered wall temperatures on the heat sink without significant compromise in the pump power consumption of the system. The power consumption of the heat sink is only a small fraction of the power consumption of the system due to the complex experimental circuit. Based on experimental data, the proposed design of a small-scale pumped two-phase cooling loop for a multiple heat source high heat flux electronics package was projected to be less than 10 % of the device power input. A prototype of an integrated cooling loop should be investigated, with a focus on flow boiling behaviour when subject to dynamic and non-uniform heat dissipation profiles.

Declaration

I, Vivian Lee Yue Sze, hereby declare that the present study is my original and independent work except where otherwise specified, or where acknowledgements are made by references to published literature. This research was conducted at the Department of Mechanical and Aerospace Engineering, Brunel University London, under the supervision of Professor Tassos G. Karayiannis and Dr. Jun Xia.

This work has not been submitted for another degree or award to any other institution.

VIVIAN LEE YUE SZE 25th September 2020

Signed: ……..... Date: …….....

Acknowledgements

I am forever grateful to my supervisor, Professor T.G. Karayiannis, who emphasised good research practices within the group and nurtured my development and growth as a researcher. Your comments and engaging discussions have done a great deal in improving the quality of this work. The support of Mr. Costas Xanthos in the commissioning of the experimental facility is greatly appreciated. I would also like to thank Dr. Mohamed Mahmoud for his guidance in the early stages of this project. The generous assistance of the staff at the Experimental Techniques Centre as well as manufacturing technicians are gratefully acknowledged.

I would like to express my gratitude to TMD Technologies Ltd. for sponsoring this work, in particular, Gary Henderson and Tracey Ledwell, both of whom have provided invaluable and constructive input throughout the course of the project.

Special thanks to my friends, most of whom understood that I was a better version of myself when on a full stomach – your company and support encouraged me during the production of this work – even when the rice was not quite up to standard.

To my family, the values you have instilled in me continue to hold up the pillars of my moral compass each day.

Above all, to my mother - this work is dedicated to you, in honour of your grit, patience and resilience. Words cannot express my gratitude for your unconditional support.

To my fellow countrymen and women, Malaysia Boleh!

Table of Contents

List of Figures

List of Tables

Nomenclature

AR	channel aspect ratio, [-], AR = W_{ch} / H_{ch}
c_p	specific heat capacity, [J/kg K]
C^+	dimensionless constant in Eq. (3.21), [-]
C_c	coefficient in Eq. (3.11), [-]
D	diameter, [m]
D_h	hydraulic diameter, [m], $(2 H_{ch}W_{ch}) / (H_{ch} + W_{ch})$
E	enhancement percentage
f	friction factor, [-]
$(fRe)_{fd}$	fully-developed Poiseuille number in Eq. (3.21), [-]
G, G_{ch}	mass flux in the channels, [kg/m^2 s], $G = \dot{m} / (N W_{ch}H_{ch})$
G_{fl}	mass flux in the fluid line, [kg/m^2 s], $G_{fl} = \dot{m} / (\pi R_{fl}^2)$
G_p	mass flux in the plenum, [kg/m^2 s], $G_p = \dot{m} / (0.5 \pi R_p^2)$
H	height, [m]
h	heat transfer coefficient, [W/m^2 K]
$\bar{h}$	average heat transfer coefficient, [W/m^2 K]
i	specific enthalpy, [J/kg]
i_{fg}	latent heat of vapourisation, [J/kg]
J_g	gas superficial velocity, [m/s]
J_l	liquid superficial velocity, [m/s]
Ja	Jakob number, [-], $Ja = [\rho_l c_{p,l} (T_w - T_{sat})] / [\rho_g i_{fg}]$
K	loss coefficient, [-]
k	thermal conductivity, [W/m K]

$K(\infty)$	dimensionless constant in Eq. (3.21), [-]
L	length, [m]
L^+	dimensionless length in Eq. (3.21), [-]
m	fin parameter, [-]
$\dot{m}$	mass flow rate, [kg/s]
N	number of channels, [-]
Nu	Nusselt number, [-], $Nu = (h\ D_h) / k_f$
$\overline{Nu}$	average Nusselt number, [-]
P	pressure, [bar]
P_r	reduced pressure, [-], $P_r = P / P_{sat}$
q''	heat flux, [W/m^2]
r_b	bubble radius, [m]
r_c	cavity radius, [m]
R	radius, [m]
Ra	average surface roughness, [μm]
Rp	roughness parameter in Eq. (4.15), [μm]
Re	Reynolds number in the channels, [-], $Re = (G_{ch}\ D_h) / \mu_f$
T	temperature, [K]
t	time, [s]
v	specific volume, [m^3/kg]
V_{ch}	velocity in the channels, [m/s], $V_{ch} = G_{ch} / \rho_f$
V_{fl}	velocity in the fluid line, [m/s], $V_{fl} = G_{fl} / \rho_f$
V_p	velocity in the plenum, [m/s], $V_p = G_p / \rho_f$

W	width, [m]
x	vapour quality, [-]
X	Martinelli parameter
X_M	parameter in Eq. (4.7)
Y	vertical distance between thermocouples, [m]
z	axial location along channel, [m]
ΔP	pressure drop, [Pa]
ΔT_{sub}	degree of inlet subcooling, [K], $\Delta T_{sub} = T_{sat,P_{in}} - T_{in}$

Greek symbols

α_f	liquid thermal diffusivity, [m^2/s]
α_p	plenum area ratio, [-], $\alpha_p = \left(0.5\,\pi\,R_p^{\,2}\right) / \left(\pi\,R_{fl}^{\,2}\right)$
β	area ratio, [-], $\beta = (N\,W_{ch}H_{ch}) / (H_{ch}W)$
δ_t	thermal boundary layer thickness
σ	surface tension, [N/m]
η	fin efficiency, [-]
ρ	density, [kg/m^3]
ν	kinematic viscosity, [m^2/s]

Subscripts

3	three-sided wall heating condition in a rectangular channel
4	four-sided wall heating condition in a rectangular channel
30	thirty percent error band
avg	average

b	base
bub	bubble
c	contraction
ch	channel
cor	correlation
cu	copper
day1	experimental dataset from day 1
day2	experimental dataset from day 2
e	exit
f	fluid
fin	fin
fl	fluid line
fo	fluid only
g	gas
go	gas only
h	hydraulic
i, in	inlet
ip	inlet plenum
k	liquid or vapour phase
op	outlet plenum
out	outlet
p	plenum
pen	penalty
pred	predicted

sat	saturated
sc	sudden contraction
se	sudden expansion
sp	single-phase
sub	subcooled
tc	thermocouple
tp	two-phase
v	vapour
w	wall

Abbreviations

A	annular
B	bubbly
C	churn
CB	coalescing bubble
CHF	critical heat flux
CNC	computer numerical control
DAQ	data acquisition system
DLC	diamond-like carbon
EES	Engineering Equation Solver
GaN	gallium nitride
GWP	global warming potential
HTC	heat transfer coefficient
IB	isolated bubble

ODP	ozone depleting potential
S	slug
SEM	scanning electron microscope
SiC	silicon carbide
SiOC	carbon-doped silicon oxide
SiOx	silicon oxide
SP	single-phase
Ti	titanium
TP	two-phase
VC	vapour compression

Dimensionless Numbers

	Parameter	Definition	Expression
Bd	Bond number	$\frac{\text{Gravitational force}}{\text{Surface tension force}}$	$\frac{\Delta\rho\, g\, D_h^{\,2}}{\sigma}$
Bo	Boiling number	$\frac{\text{Heat flux}}{\text{Latent heat and mass velocity}}$	$\frac{q_w''}{G\, i_{fg}}$
Co	Confinement number	$\frac{\text{Surface tension force}}{\text{Gravitational force}}$	$\frac{(\sigma/\Delta\rho\, g)^{0.5}}{D_h}$
Cv	Convection number	Density ratio and vapour quality	$\left(\frac{\rho_g}{\rho_f}\right)^{0.5}\left(\frac{1-x}{x}\right)^{0.8}$
Fa	Fang number	$\frac{\text{Buoyancy force}}{\text{Gravitational force}} \times \frac{\text{Surface tension force}}{\text{Inertia force}}$	$\frac{\Delta\rho\,\sigma}{D_h\, G^2}$
Fr	Froude number	$\frac{\text{Inertia force}}{\text{Gravitational force}}$	$\frac{\nu^2\, G^2}{g\ D_h}$
Nu	Nusselt number	$\frac{\text{Convection resistance}}{\text{Conduction resistance}}$	$\frac{h\, D_h}{k}$
Pr	Prandtl number	$\frac{\text{Momentum diffusivity}}{\text{Thermal diffusivity}}$	$\frac{c_p\, \mu}{k}$
Re	Reynolds number	$\frac{\text{Inertia force}}{\text{Viscous force}}$	$\frac{G\, D_h}{\mu}$
We	Weber number	$\frac{\text{Inertia force}}{\text{Surface tension force}}$	$\frac{D_h\, \nu\, G^2}{\sigma}$
X	Martinelli parameter	$\frac{\text{Liquid frictional pressure gradient}}{\text{Vapour frictional pressure gradient}}$	$\sqrt{\frac{\left(\frac{dP}{dz}\right)_f}{\left(\frac{dP}{dz}\right)_g}}$
Ja	Jakob number	$\frac{\text{Sensible heat}}{\text{Latent heat}}$	$\frac{c_p\,(T_w - T_{sat})}{i_{fg}}$

When life itself seems lunatic, who knows where madness lies?

– Miguel de Cervantes, *Don Quixote*

1 Introduction

1.1 Motivation

Since the invention of integrated circuits in 1958, the number of transistors in electronic chips have increased exponentially, from just over 2,000 transistors in 1971, to 21.1 billion transistors per microprocessor in 2017 [1], [2]. The trend of miniaturisation in electronics enabled higher processing speeds in smaller electronics packages and made significant impacts in the commercial, military and aerospace sector. However, the exponential growth of system-on-chip devices, as predicted by Moore's law [3], is rapidly converging toward critical bottlenecks in recent years, due to major challenges in thermal management amid strict performance, size, weight and cost requirements.

Increase in transistor density on shrinking feature sizes increase the power dissipation and power density of a chip. To give an example, the revolutionary Intel 4004 microprocessor released in 1971 had a die size of 12 mm^2 with a thermal power dissipation of 1 W, giving a heat flux value of 83 kW/m^2 [4]. In contrast, heat fluxes reach up to 370 kW/m^2 in the Nvidia GV100 Volta released in late-2017, which has a feature size of 815 mm^2 and thermal power dissipation of 300 W [5]. Power density is predicted to reach 4.5 MW/m^2 in computing systems by 2026 while heat flux requirements in *current* military avionics and IGBT modules already extend up to 10 MW/m^2 and 50 MW/m^2 respectively [6], [7]. Furthermore, uneven processing workload distribution, high packing densities and 3D chip architectures in modern integrated circuits create spatiotemporal non-uniformity in die power dissipation. Localised regions with very high heat fluxes, typically referred to as hotspots, may be between 6 to 10 times the background heat flux of a processor [8] and result in large temperature gradients across a die if not mitigated with an appropriate cooling solution. Note that overcooling regions around the hotspot, which are at lower heat flux levels, will exacerbate temperature non-uniformity on the die. Temperature variations induce thermal stresses and interfacial delamination due to mismatched thermal expansion, thus jeopardising the functionality and reliability of a device.
Efficient thermal management is essential to maintain operating temperatures below the junction limit of a device – typically ranging from +85 °C in consumer electronics to +175 °C in SiC and GaN-based modules [9]. The difficulty in thermal management design for high heat flux devices is further exacerbated by small packaging volume, which pose space and weight

constraints on the thermal subsystem, as well as harsh operating environments, particularly in aerospace applications. For instance, avionics equipment have to operate reliably whilst subjected to a wide range conditions depending on mission profile, where ambient temperature change from -15 °C to +55 °C and variations in cooling air density with altitude could occur in very short instances [10]. In fact, military grade electronics are routinely tested to operating temperature ranges between –55 °C to +125 °C [11]. Inadequate thermal management limits device operation and capability in fear of compromising junction temperature, reliability and service life of the equipment. For example, axial flux motors, a key component in aircraft electric actuation, can only continuously operate at 188 kW, 43 % less than the peak power output of 440 W. This means that peak operation is limited to a mere window of 20 s due to thermal concerns, even with water/glycol liquid cooling, which generally outperforms conventionally adopted air cooling solutions in the market [12]. Evidently, traditional thermal management strategies are unable to sustain the disproportionate rise in chip power density of embedded systems.

Although air cooling is a popular thermal management technique in many of the aforementioned industries due to ease of application, air cooling assemblies have generally been reported to be inadequate for heat fluxes above 1 – 1.5 MW/m^2 as they begin to approach their volumetric footprint and acoustic limits as well as being difficult to integrate on multi-core boards [13]–[15]. Novel techniques using porous surfaces [16], vortex generators [17] or hybrid systems integrating air-cooling with phase-change materials and heat pipes [18], [19] have been demonstrated to improve the efficiency and temperature uniformity of air-cooled modules. Nonetheless, air is ultimately a poor heat transfer fluid and thus adapting air cooling techniques to manage high heat fluxes generally results in excessive increase in fan noise, bulky packaging size and overall weight of the cooling system. Liquid cooling technologies benefit from the superior thermophysical properties compared to air and have been employed from as early as the 1960s in space applications [20] and later in computing platforms [21] as well as liquid-flow through modules for avionics cooling [6], [22], [23]. Commercial-off-the-shelf liquid cooling systems are widely available for avionics modules, data centre servers and is increasingly being adopted in gaming PCs to support overclocked processors.

Microchannel liquid cooling was first introduced by Tuckerman and Pease [24] in the early 1980s and has since been extensively studied for the cooling of miniaturised technologies. The water-cooled silicon microchannel heat sinks in [24], of base area of 1 x 1 cm^2, achieved a

maximum heat flux of 7.9 MW/m^2, albeit at a relatively large pressure drop of 204 kPa. The temperature rise of the substrate was 71 K with a water inlet temperature of 23 °C, resulting in chip temperatures of around 94 °C. Escher et al. [25] optimised the manifold design in their silicon-based microchannel heat sinks to reduce the pressure penalty and dissipated more than 7 MW/m^2 at a fraction of the pressure drop value, 22 kPa. This was achieved at a water flow rate of 17 g/s and a temperature rise between the chip and the water inlet of 65 K. At a heat flux of 1 MW/m^2, the authors reported a temperature gradient of 0.5 K, which was found to increase to 5 K at lower flow rates due to fluid maldistribution and coolant temperature gain along the flow direction. Large temperature gradients along the flow direction at higher heat fluxes approaching 7 MW/m^2 is likely to increase temperature non-uniformity on the substrate to beyond 5 K. Mixing effects induced flow disruptions using pin-fin arrays have been shown to improve single-phase heat transfer coefficients and temperature uniformity [26]–[28]. Nevertheless, single-phase cooling for hotspots typically requires complex design of the liquid flow path and variable-density fin clusters at the hotspot locations in order to obtain more even temperature profiles on chips with non-uniform heat flux dissipation [29]–[31]. Many studies have employed single-phase jet impingement [32], [33] and hybrid microchannel/jet impingement modules for hotspot targeted cooling [34], [35]. However, surface erosion due to impinging flow at high velocities [36] and integration of the jet nozzles in small package volumes are practical concerns regarding this technique.

1.2 Flow Boiling for High Heat Flux Devices

By exploiting the latent heat of vapourisation of a fluid, heat transfer coefficients up to two orders of magnitude higher than forced liquid convection may be attained, achieving significantly higher heat dissipation capability at a given coolant flow rate [6], [37]. A maximum heat flux of 7 MW/m^2 was achieved using microchannel heat sinks of base area 5 mm x 10 mm in Lee and Mudawar [38] whilst Drummond et al. [39] managed heat fluxes up to 9.1 MW/m^2 by employing a hierarchical manifold design with dedicated fluid delivery to each microchannel heat sink in a 3 x 3 square array. Flow boiling in microchannel heat sinks can potentially moderate temperature non-uniformities associated with sensible heat rise in single-phase microchannels, since the vapourisation process occurs isothermally. Additionally, two-phase microchannel cooling could be more efficient in alleviating hotspots due to self-optimising heat transfer coefficients in response to heat flux, especially in the nucleate boiling regime [7]. The simple and compact system architecture of a two-phase microchannel heat sinks is more suitable for embedded cooling applications compared to that of jet impingement and spray cooling nozzle modules, which have also been studied in boiling mode for high heat flux thermal management, as reviewed recently by Gao et al. [40].

Microchannel evaporators may be integrated in a two-phase pumped loop. The low coolant flow rates required for a given heat flux and lower pumping power directly translates to small pump size and simpler piping infrastructure. The microchannel heat sinks may be optimised based on the footprint area of the chip and can easily be integrated on multichip boards with cores at various locations within an electronics package. Working fluid boils in the microchannel evaporator and exits as two-phase liquid and vapour flow. The mixture is conveyed to a condensing unit, which rejects waste heat to the ultimate heat sink, which in aerospace applications may be conditioned air provided by the aircraft environmental control system or aviation fuel. Condensed liquid coolant is then collected in a reservoir before being recirculated to the heat sinks in order to sustain the two-phase cooling loop. The condenser module may be located remotely, i.e. external to the package, to maximise packaging density in the electronics enclosure. Importantly, the condenser should interface well with the global cooling solution and reject waste heat efficiently at a system level as well as being optimised for appropriate SWaP-C requirements. Alternatively, two-phase evaporative cooling may also be employed in the form of vapour compression (VC) refrigeration cycles, generally in applications where sub-ambient coolant temperatures are required. Applications of miniature

vapour compression cycles are thoroughly reviewed in [41] and have been demonstrated for electronics as well as avionics cooling [42]–[47] using small scale compressors. Vapour compression systems typically yield coefficient of performance (COP) values between 1.5 to 9.1, largely dependent on cooling load, compression parameters and refrigerant charge. Not surprisingly, the performance of the compressor is a critical factor in VC systems. However, several studies have highlighted the reliability of miniature compressors at low compression ratios, noise and vibration levels at high frequency operation including compressor power consumption as limitations of this technique [7], [48]–[51]. For these reasons, pumped two-phase loops remain an attractive option for compact evaporative cooling due to equipment reliability and reasonable system power consumption for above-ambient cooling applications.

Despite many potential merits and proven high heat dissipation capability, flow boiling based evaporative cooling systems with microscale heat sinks have limited commercial availability and industry trends remain slow in adopting two-phase microchannel cooling compared to its single-phase counterpart. Technological implementation of the technique has largely been hindered by poor understanding of fundamental issues relating to flow boiling as well as the lack of established design tools to reliably predict and optimise the performance of two-phase thermal management systems [7]. Challenges and the corresponding research needs to advance the application of flow boiling are summarised in Karayiannis and Mahmoud [7], Kandlikar [52], Cheng and Xia [53] and most recently in Kuznetsov [54]. These include: (i) large scatter in flow boiling results, attributed to the influence of surface characteristics, channel geometry and fluid properties etc. [7], [55], [56]. By extension, (ii) disagreements in heat transfer mechanisms, i.e. dominance of nucleate or convective boiling. (iii) the lack of generally accepted prediction methods for two-phase flow patterns, heat transfer, pressure drop and critical heat flux. Prediction of flow boiling trends using correlations in literature yielded a mean average deviation (MAE) between 13.84 % – 397.6 % for heat transfer and 18.7 % – 157.58 % for pressure drop results in a recent paper by Al-Zaidi et al. [57]. This is in part due to (iv) unclear dependence on operational conditions (i.e. effects of heat flux, mass flux, system pressure and inlet subcooling), working fluid, channel characteristics and manifold design. This includes their effects on flow instabilities and critical heat flux in flow boiling systems. Lastly, (v) the difficulty in triggering boiling for some surfaces, leading to flow instabilities, high wall superheat at boiling incipience and excessively high wall temperatures with increase in heat flux [56], [58].

Evidently, a clear understanding of fundamental phenomena is important to resolve disagreements in literature in order to validate and develop reliable analytical and numerical tools for two-phase thermal system design. Additionally, operational as well as design recommendations to avoid unwanted system instabilities, excessive device temperatures and critical heat flux are required to optimise thermal devices within a specified safe range of operation [59].

Accordingly, the current work employs high speed flow visualisation along with intricate temperature and pressure measurements to obtain a better understanding of bubble growth, flow pattern development as well as two-phase heat transfer mechanisms a microchannel heat sink. The use of a porous surface coating was explored to enhance boiling incipience superheat and flow boiling heat transfer. Surface enhancement by means of a surface coating was selected in consideration of cost and ease of implementation on flow boiling modules. Extensive surface analysis was conducted to correlate surface characteristics in the microchannel to flow boiling behaviour. Additionally, the dependence of flow boiling trends on operational conditions including heat flux, mass flux, system pressure and degree of inlet subcooling were analysed. The is believed to be able to contribute greatly to advance the community's knowledge on flow boiling phenomena and associated enhancement methods.

Detailed analysis and evaluation of prediction methods in two-phase flow patterns, heat transfer and pressure drop would promote the development of design and optimisation tools for two-phase pumped loops in commercial applications. Furthermore, design guidelines for the thermal design of two-phase systems adopting flow boiling technology are proposed for the stringent requirements in aerospace applications with an emphasis on system intergration. For instance, in the present study a low degree of inlet subcooling (i.e. 5 K to 20 K) was selected to best represent conditions during application. Although critical heat fluxes of up to 6.9 MW/m^2 have been demonstrated in the study of Lee and Mudawar [38], [130], the two-stage cascade refrigeration system was used to control coolant temperatures at the inlet of the heat sink. Such systems are unsuitable for compact thermal management systems to be integrated for avionics applications where energy consumption as well as size and weight constraints are more restrictive. Additionally, the current experimental facility employs a liquid-to-air heat exchanger, which is more relevant in aviation applications where the ultimate heat sink is generally air.

The working fluid, 3M™ Novec™ HFE-7200, was selected for its high dielectric strength (minimises damage in the case of coolant leakage), low ozone depletion potential (ODP) and low global warming potential (GWP). Most importantly, the boiling point of the fluid is + 76 °C at atmospheric conditions, which is appropriate for ambient air cooling and the thermal management of electronics devices with junction temperatures of +125 °C at low system pressures. The fluid has a low freezing point of –138 °C and a wide operating temperature range of – 110 °C to + 60 °C (recommended for pumped single-phase cooling) [60], which is suitable for harsh environment avionics applications where ambient temperatures could plummet down to – 40 °C and reach up to + 55 °C. Whilst the fluid has been the subject of several investigations for the case of single-phase and two-phase cooling in micro pin-fin arrays [61]–[63] as well as pool boiling [64]–[67] for high heat flux cooling applications, there is a lack of data available for the flow boiling of HFE-7200 in straight microchannel heat sinks.

1.3 Research Objectives

The objectives of the current experimental study are summarised as follows:

i. Investigate the fundamental issues and clarify the basic mechanisms in microchannel flow boiling using high-speed flow visualisation and local heat transfer measurements in a parallel microchannel heat sink.

ii. Examine the effect of operating parameters including the effect of heat flux, mass flux, saturation pressure and subcooling degree on microscale two-phase flow patterns, flow reversal, heat transfer and pressure drop trends.

iii. Evaluate the accuracy of prediction methods in literature for two-phase flow patterns, flow boiling heat transfer and pressure drop in microchannels based on the current experimental data in plain channels. Analyse the parameters and assumptions adopted in prediction correlations.

iv. Explore surface modification of microchannel surfaces by means of a surface coating to enhance two-phase heat transfer rates in a similar microchannel configuration to the plain microchannel heat sink. Assess the flow pattern development, enhancement effect and pressure drop penalty resulting from the coating with baseline results obtained from the plain microchannels.

v. Assess the viability of a pumped two-phase cooling loop adopting microchannel flow boiling technology in terms of cooling performance and capacity, as well as pump power consumption of the system.

vi. Propose a conceptual design and provide design recommendations for a small-scale, integrated two-phase thermal management system, specifically for compact, multiple high-power density heat source electronic assemblies in aerospace applications.

1.4 Thesis Structure

The outline of the thesis is presented as follows:

Chapter 1 – Introduction – This chapter briefly reviews the current thermal bottleneck in the electronics cooling industry, existing as well as emerging thermal management techniques to manage high power density devices.

Chapter 2 – Literature Review – A detailed literature review on flow boiling phenomenon, including the effect of operating parameters on flow patterns, flow instability, heat transfer and pressure drop is presented in this chapter. Prediction methods available in literature are also discussed. The chapter also explores heat transfer enhancement using surface modification techniques.

Chapter 3 – Experimental Methodology – In this chapter, details of the experimental facility and microchannel test sections are presented. The experimental procedure, data reduction and uncertainty analysis methods are also detailed. Single-phase validation results and repeatability of the data are discussed.

Chapter 4 – Flow Boiling in Plain Microchannels – Flow boiling results, including flow visualisation, obtained in the plain microchannels are extensively discussed in this chapter. The discussion includes the effect of heat flux, mass flux, saturation pressure and degree of inlet subcooling on flow patterns, heat transfer and pressure drop in the microchannels.

Chapter 5 – Comparison with Flow Pattern Maps – Several flow pattern maps are assessed based on the flow pattern data obtained in the plain microchannel test section. The prediction capability as well as sensitivity to operating parameters of the flow regime maps are evaluated.

Chapter 6 – Comparison with Heat Transfer Correlations – Flow boiling heat transfer correlations are evaluated in this chapter against flow boiling results obtained in the plain microchannel heat sink for HFE-7200. A sensitivity study of the fluid properties and dimensionless parameters considered in the heat transfer correlations is presented. Analyses of the models and assumptions adopted in the heat transfer correlations are performed based on the prediction results.

Chapter 7 – Comparison with Pressure Drop Correlations – Two-phase pressure drop correlations are evaluated in this chapter using flow boiling pressure drop results obtained in the plain microchannel heat sink for HFE-7200. Both the prediction capability of macroscale and microscale pressure drop correlations are assessed.

Chapter 8 – Flow Boiling in Coated Microchannels – In this chapter, flow boiling results obtained in the coated microchannel heat sink is presented. A detailed discussion into flow pattern, heat transfer and pressure drop characteristic in the coated channels is included. The effect of the coating on flow instabilities, heat transfer enhancement effect and pressure drop penalty are assessed.

Chapter 9 – Small-Scale Integrated Two-Phase Thermal Management System – The power consumption of the experimental two-phase loop and the microchannel heat sinks are discussed in this chapter. A design of an integrated, small-scale thermal management system is proposed for an electronics package with multiple high-power density heat sources. Design recommendations are made specifically for avionics cooling.

Chapter 10 – Conclusions and Recommendations – The key findings drawn from the current study are summarised. Recommendations for further investigations are also proposed.

2 Literature Review

2.1 Introduction

This chapter presents the fundamental aspects of flow boiling behaviour, including boiling incipience, critical heat flux, heat transfer, pressure drop and flow instabilities in microchannels. Sections 2.2 to 2.5 discusses the effect of heat flux, system pressure, mass flux and inlet subcooling on microchannel flow boiling characteristics. Sections 2.6 to 2.8 presents a detailed review of two-phase flow regime maps, heat transfer and pressure drop correlations in literature. In Section 2.9, the employment and optimisation of surface modification techniques, in particular, surface coating technology, to enhance two-phase heat transfer performance is discussed. Lastly, a concluding summary of all sections is given in Section 2.10.

2.2 Effect of Heat Flux

Increasing heat flux affects the development of two-phase flow patterns, heat transfer as well as pressure drop behaviour in flow boiling systems. Flow boiling heat transfer coefficients are also highly influenced by flow patterns in microchannels, as the occurrence of wall dryout in certain flow regimes, for instance, could affect the local heat transfer trend and subsequently depreciate overall microchannel heat transfer performance. Conflicting heat transfer trends with respect to heat flux increment and its effect on the local as well as average heat transfer coefficient have been reported in literature.

2.2.1 Effect on Heat Transfer Rates

A number of studies have found that an increase in heat flux led to either an increase in average heat transfer coefficient, or an increase in the heat transfer coefficient monitored at a fixed location on multichannel heat sinks [57], [68]–[70]. The location of interest is normally selected to be at the centre or at the most downstream location of the heat sink, typically the latter, in order to represent the highest extent of saturated boiling in the channels. The increase in heat transfer coefficients with regards to heat flux was attributed to the dominance of nucleate boiling, and the increase in the number of active nucleation sites in the channels at higher heat fluxes [57], [70]. A similar heat flux effect was also reported for micro-pin fin

evaporators [71], [72] (for DI water only in Reeser et al. [72]) as well as for enhanced microchannel configurations [73]. Interestingly, when HFE-7200 was employed in the same heat sink, heat transfer coefficient exhibited a different trend in response to heat flux increase in Reeser et al. [72]. This highlights the distinguished influence of fluid properties on flow boiling heat transfer behaviour.

On the other hand, Markal et al. [74] reported a consistent decline in the heat transfer coefficient, assessed near the channel exit, with respect to heat flux from a maxima near the onset of boiling. From their flow visualisation, the authors noted that higher heat fluxes aggravated flow reversal, which suppressed nucleate boiling in the channels. Li et al. [75], [76] also found a decreasing heat transfer trend in their comparative study of regular microchannels and triangular cavity enhanced microchannel heat sink, along with Zeng et al. [77] and Deng et al. [78], the latter specifically at high subcooling and low mass flux conditions in the heat sink. Lu and Pan [79] and Deng et al. [80] used DI water as the working fluid and found that heat transfer coefficients decreased rapidly with increase in heat flux after the onset of boiling but stabilised with further increase in heat flux, without a sudden drop in heat transfer coefficient toward the high heat flux range of their respective studies. This could be due to the high latent heat of vapourisation of water, which allowed high heat fluxes to be achieved under relatively small increase in vapour quality.

The effect of heat flux may also become negligible at high heat fluxes. Lee and Garimella [81] and Jones and Garimella [82] found that boiling heat transfer coefficient increased with increase in heat flux, however, heat transfer coefficient trend became insensitive to further increase in heat flux level beyond the region where convective boiling was assumed to dominate in the channels. Costa-Patry et al. [83] also reported a similar effect and cited the competing effects between increased evaporation rate at higher heat fluxes, increasing overall heat transfer coefficient (calculated based on local wall heat flux on the heat sink), and partial cyclical dryout, the frequency of which increases with heat flux and reduces heat transfer coefficient.

Contrastingly, a rapid decline in heat transfer coefficient at high heat fluxes were found in some conventional and unconventional microchannel configurations [73], [84]–[86], albeit with differences in the effect of heat flux leading up to the drop in heat transfer coefficient. Increasing heat flux initially resulted in increasing heat transfer coefficient in Harirchian and

Garimella [84], [85] and Yin et al. [73]. The drop in heat transfer coefficient was attributed to partial wall-dryout in the channels at excessive heat fluxes. In one study, Agostini et al. [87] identified three heat transfer trends in their microchannel flow boiling study using R236fa and R245fa as working fluids. For R245fa at high mass flux but low heat flux, heat transfer coefficients decreased with increase in heat flux. On the other hand, the heat transfer behaviour of R236fa was not affected by heat flux in the low heat flux region. For both fluids, heat transfer coefficients increased with heat flux at medium heat flux levels. Further increment in heat flux in the high heat flux region produced a reduction in heat transfer coefficient instead. This further illustrates the effect of fluid properties on flow boiling behaviour as highlighted previous for the results reported by Reeser et al. [72].

Although a decreasing trend in heat transfer coefficient at high heat fluxes was observed, a group of studies found a range of intermediate heat flux levels where average heat transfer coefficients stabilised with respect to wall heat flux. As mentioned above, the flow boiling heat transfer coefficient of HFE-7200 was markedly distinct compared to DI water in Reeser et al. [72], which decreased following a peak after the initiation of nucleate boiling, stabilised for a range of heat fluxes and then decreased again toward high heat fluxes. The same trend was also noted in Fu et al. [88] as well as under certain operating conditions in Chen et al. [89] and Deng et al. [80]. In the study by Chen et al. [89], the heat transfer coefficient dropped rapidly from the boiling incipience heat flux but remained largely independent of heat flux with further increase in heat flux level. At the lowest mass flux condition, a sharp drop in local heat transfer coefficient was observed at high heat fluxes. Based on these observations, the paper concluded that nucleate boiling was the dominant heat transfer mechanism in the early stages of boiling. The authors reasoned that with the formation of elongated bubbles, nucleation behaviour is gradually suppressed and subsequently caused a drop in heat transfer coefficient at high heat fluxes. This was also observed in the comparative study of Deng et al. [80], in regular microchannels and microchannels with micro-pin fins on the bottom channel wall using DI water and ethanol. The decline in heat transfer coefficient at high heat fluxes was less severe in the pin-fin enhanced microchannels.

Local heat transfer trends, that is, local heat transfer coefficients measured at several axial locations along the streamwise direction have also been presented as a function of local vapour quality in selected works. Local heat transfer coefficients have been found to peak at very low vapour qualities and near the incipience of boiling. Al-Zaidi et al. [57] emphasised that local

heat transfer coefficients decreased along the channel following a maximum near the location of boiling incipience. Similarly, Qu and Mudawar [90] also reported a peak in heat transfer coefficients where the local thermodynamic vapour quality was near zero. Bertsch et al. [69] reported that for R134a, at low heat and mass flux levels, local heat transfer coefficients were relatively stable between vapour qualities between 0 to 0.5, after which a rapid drop in heat transfer coefficient was recorded. At higher heat and mass fluxes, heat transfer coefficients decreased immediately from the onset of boiling. The authors reported that the trends observed were mainly for the slug and intermittent flow regime in their study.

Another group of researchers have identified a characteristic U-shape or V-shape trend in local heat transfer coefficients. Costa-Patry et al. [83] reported a distinct V-shape trend in their local heat transfer data with respect to vapour quality. A peak in heat transfer coefficient, associated the onset of boiling at low vapour qualities, dropped to a minimum with increase in vapour quality, corresponding to the formation local dry patches in the channels. Heat transfer coefficients increased again with increase in vapour quality, characteristic of the heat transfer trend in the annular flow regime. This is analogous to the U-shape trend found in Agostini et al. [87] as well as in the dataset of Balasubramanian et al. [91] and Huang and Thome [92], [93]. Agostini et al. [87] noted that for fluid R245fa at low heat fluxes, heat transfer coefficients dropped from a maxima following the incipience of boiling and increased again with further increase in vapour quality. It is interesting to note that average heat transfer coefficients decreased with increase in heat flux in this region. At medium heat flux levels, local heat transfer coefficients were largely independent of vapour quality. The local heat transfer trend depreciated with vapour quality in the high heat flux region.

Agostini and Thome [94] reviewed 13 flow boiling heat transfer studies and concluded that the majority of heat transfer data were represented by several key trends. (i) At vapour qualities below 0.05, heat transfer coefficient increases with vapour quality, or is independent of vapour quality, but increases with heat flux. (ii) In the vapour quality range between 0.05 and 0.5, heat transfer coefficient decreases or remains relatively stable with increase in vapour quality. Heat transfer coefficient also increases with heat flux in this region. (iii) At vapour qualities larger than 0.5, there is a significant depreciation in heat transfer coefficient with respect to vapour quality, but exhibit no dependency on heat flux or mass flux of the system. Reduction in heat transfer coefficient with increase in vapour quality was postulated to be due to cyclical dryout on the channel walls [95]. The authors further noted that in general, increasing heat flux

increases heat transfer rates in flow boiling, however at very high heat fluxes, this may result in a reduction in heat transfer. This may be due to dryout phenomenon as the system approaches its critical heat flux limit at a particular operating condition.

2.2.2 Effect on Two-Phase Pressure Drop

Generally, flow boiling pressure drop increases with increasing heat flux or vapour quality in microchannel heat sinks using various working fluids including DI water, R245fa, HFE-7100 and HFE-7200 [57], [74], [99], [81], [82], [85], [90], [92], [96]–[98]. The increase in two-phase pressure drop with vapour quality is typically attributed to the increase in flow resistance due to bubble generation in the channels, with increasing heat flux and vapour quality in the saturated boiling region. Two-phase pressure drop in microchannel heat sinks is intrinsically related to the flow patterns occurring in the channels. As a general rule, pressure drop increased with increase in heat flux and vapour quality in straight microchannel heat sinks, and where the reported predominant flow regimes were slug, elongated bubble or annular flow [57], [74], [85], [87], [90], [92], [96]–[99]. Amongst these studies, Costa-Patry et al. [96] found that the pressure drop increase with respect to vapour quality was steeper in R245fa compared to R236fa, and attributed this to the higher vapour volume and thus higher shear produced using R245fa.

In addition to that, Falsetti et al. [71] studied the flow boiling of R236fa while Reeser et al. [72] investigated the flow boiling behaviour of DI water as well as HFE-7200 in micro-pin fin evaporators. They concluded that two-phase pressure drop increased with heat flux and vapour quality in the heat sink. The inline pin-fin array produced a much lower pressure drop in both fluids compared to the staggered fin array configuration [72]. Similarly, an increase in pressure drop with respect to heat flux and vapour quality increase was reported by Deng et al. [78], who evaluated flow boiling behaviour in pin-fin interconnected re-entrant microchannels using DI water and ethanol as the working fluids. The pressure drop of ethanol was slightly higher compared to DI water. Balasubramanian et al. [91] investigated two heat sink configurations, featuring straight and expanding microchannels using DI water and also found that pressure drop increased with wall heat flux. The expanding channel configuration decreased two-phase pressure drop, particularly at high heat fluxes. This was attributed to the wider downstream channel width, which decelerated the vapour flow and thus pressure drop in the channels. Chen et al. [89] investigated the flow boiling of DI water in an interconnected porous microchannel

heat sink and also found that pressure drop increased with increase in heat flux. Li et al. [75], [76] and Zeng et al. [77] compared the performance of regular microchannel heat sinks with microchannel configurations populated with cavities using pure acetone and DI water respectively. Both studies reported that the cavities alleviated flow reversal in the heat sink and two-phase pressure drop increased with increasing heat flux. While the mitigation of flow instabilities in Li et al. [75], [76] also resulted in a reduction in flow boiling pressure drop, the micro-groove cavities employed in Zeng et al. [77] gave rise to pressure drop penalties in the heat sink, associated with the additional frictional losses due to flow resistance and liquid retention by the grooves.

On the other hand, Yin et al. [73] studied an open microchannel heat sink, i.e. with a gap on the top of microchannel fins, employing DI water as the working fluid in an attempt to mitigate flow boiling instabilities, which have been previously reported to adversely affect heat transfer performance in microchannel heat sinks. Along with the bubbly and slug flow regime, the authors identified two-types of stratified flow in their open microchannel configuration. Two-phase pressure drop initially increased with increase in heat flux and vapour quality, where flow patterns evolved from bubbly to slug flow in the channels. After the onset of stratified flow, however, pressure drop in the channels decreased with increase in heat flux and vapour quality. This was attributed to the reduction in frictional forces between the liquid and gas phase following phase stratification in the channels at sufficiently high heat fluxes. Kim et al. [47] conducted experiments using FC-72 in a regular rectangular fin heat sink and observed that although pressure drop along the channel increased with respect to vapour quality, it was relatively independent of heat flux. The authors concluded that the acceleration pressure loss component was negligible in comparison to the frictional pressure drop in the heat sink.

2.3 Effect of Saturation Pressure

Key fluid thermophysical properties such as surface tension, viscosity, specific heat and latent heat are typically sensitive to changes in system pressure, and thus could have significant impacts on flow pattern development and flow boiling behaviour in microchannels. Based on two-phase flow theory, frictional and momentum pressure drop components, as well as void fraction are proportional to fluid properties such as liquid viscosity and liquid-vapour density ratio [100]. Accordingly, a reduction in two-phase pressure drop in microchannels at higher operating pressures have been reported in Kuo and Peles [101], Saisorn et al. [102] and Dário et al. [97]. System pressure has also been experimentally and analytically shown to affect nucleation criteria, bubble growth and departure dynamics in microchannels [56], [103]–[106].

2.3.1 Effect on Bubble Nucleation

Some studies have found that bubble departure frequency increases with increasing saturation pressure. Euh et al. [103] conducted a flow visualisation study on subcooled flow boiling of water in a 19.1 mm diameter tube at system pressures of 1.67 bar – 3.46 bar, mass fluxes of 214 – 1869 kg/m^2 s, heat flux between 61 – 238 kW/m^2 and subcooled conditions ranging from 7.5 – 23.4 K. Although the tube diameter investigated may be more relevant to macroscale flow boiling, the fundamental findings on the dependency of bubble nucleation behaviour on saturation pressure at the macroscale level are still useful in the understanding of microscale boiling behaviour. Euh et al. [103] attributed the enhanced bubble generation frequency at higher pressures to the increase in vapour density corresponding to pressure increase. Considering the mechanical equilibrium of a vapour nucleus [100], the authors reasoned that higher vapour density resulted in lower required wall superheat for bubble nucleation, which reduced waiting time between consecutive bubble ebullition cycles and thus increased bubble generation frequency. Bubble departure frequency was also reported to increase along with pressure in the work of Murshed et al. [105].

Smaller bubble departure sizes were also noted by Euh et al. [103] at higher saturation pressures. Referring to the force balance models developed by Situ et al. [107] and Klausner et al. [108], it was noted that the higher vapour density at higher pressures also significantly lowered the drag force acting on bubbles, which reduced bubble departure diameter and bubble growth time. Flow visualisation also revealed smaller bubble diameters in Kuo and Peles [101], Prodanovic et al. [106] and Yuan et al. [104]. The latter used the liquid-vapour density ratio to

correlate the pressure effect on bubble diameters. Similarly, applying the force balance model by Klausner et al. [108] and comparing bubble growth and departure time of water, ethanol, R134a and R245fa, Mahmoud and Karayiannis [56] showed that bubble growth rate exhibited a strong dependence on liquid-vapour density, surface tension and viscosity ratio of a fluid.

Furthermore, the range of active nucleation sites may also increase under higher pressure conditions. Mahmoud and Karayiannis [56] highlighted the importance of surface conditions, namely the size range of active nucleation sites for bubble nucleation and boiling incipience wall superheat on heated surfaces. The authors predicted this range using the model proposed by Hsu [109], which is a function of wall superheat condition as well as fluid properties including surface tension, vapour density and latent heat of vapourisation. The analysis revealed that the required wall superheat for nucleation in certain fluids, for instance, water, decreased drastically when system pressure was increased.

Consequently, fabricating cavities of appropriate sizes based on nucleation theory on boiling surfaces as well as modifying system pressure to reduce the required wall superheat for nucleation could potentially mitigate flow instabilities related to explosive boiling as well as delay the occurrence of critical heat flux (CHF) in two-phase systems. Kuo and Peles [101], [110] investigated the use of re-entrant cavities to supress flow instabilities and delay flow instability-induced premature CHF by promoting controlled bubble growth in the channels. Cavities 7.5 μm wide were etched on the sidewalls of the 223 μm hydraulic diameter silicon microchannels. The experimental study was conducted with water as the working fluid at base heat fluxes up to 2.5 MW/m^2, mass fluxes between 86 – 520 kg/m^2 s and exit pressures ranging from 50 – 205 kPa. High wall superheat at the inception of boiling caused vigorous flow oscillations in the channels at low operating pressures and led to early transition to the CHF condition in the system. At higher system pressures, a stable boiling regime was established after boiling incipience and lower pressure gradient in the channels resulted in an increase in CHF. It was not explicitly stated if the degree of inlet subcooling was kept constant in the study. For subcooled flow boiling of water in tubes of diameter between 0.406 mm – 2.54 mm, Mudawar and Bowers [111] reported an increase in CHF with increase in pressure from 2.5 bar to 30 bar. CHF did not vary significantly following further increase in pressure but fell as pressures approach the critical point. Nonetheless, the degree of inlet subcooling, which could affect both wall superheat required for bubble nucleation (as noted in Mahmoud and Karayiannis [56]) and the development of CHF condition was not kept constant in their study

of pressure effect in Mudawar and Bowers [111]. On the other hand, it was not explicitly stated whether the degree of inlet subcooling was kept constant in Kuo and Peles [101].

2.3.2 Effect on Heat Transfer Rates

In accordance with the findings of enhanced bubble departure frequencies above, many studies have found that increasing system pressure improved flow boiling heat transfer performance [87], [112]–[117]. Amongst these, the influence of saturation pressure on the latent heat of vapourisation [114], density ratio and surface tension [115], [118] were highlighted as plausible reasons to heat transfer enhancement. Despite concluding an insignificant effect of saturation pressure on average heat transfer coefficient in their microchannel evaporator at low mass flux in an earlier paper by Bertsch et al. [68], a slight increase in heat transfer coefficient with increase in saturation pressure was reported at a higher mass flux condition in a later study by Bertsch et al. [69]. Agostini et al. [87] reported a significant increase in local heat transfer coefficients with increase in saturation pressure for refrigerant R236fa, but found a negligible pressure effect on heat transfer coefficients for R245fa. The authors suggested that the less obvious saturation pressure effect observed for R245fa could be due to the high experimental uncertainties as the experiments involving the fluid was conducted under relatively low heat fluxes. Thiangtham et al. [117] also found a slight increase in heat transfer coefficients and attributed this to higher bubble generation at higher saturation pressures in the channels.

On the other hand, the effect of pressure has also been found to be insignificant at vapour quality regions where nucleate boiling might not be the dominant mode of heat transfer. Wen et al. [119] studied the flow boiling of R134a in serrated fin minichannels and found that increasing the system pressure from 2.9 bar to 4.5 bar improved heat transfer coefficients at low to moderate vapour qualities (vapour quality around 0.5), while the pressure effect was negligible in the high vapour quality region where convective boiling was assumed to dominate. The authors reasoned that higher bubble generation activity at higher saturation pressures in the low vapour quality region is a result of a reduction in latent heat of vapourisation following system pressure increase. Similar enhancement effect, i.e. limited to low vapour qualities were also reported for the flow boiling of R134a in microtubes [55], [120]. Karayiannis et al. [55] reported an increase in heat transfer coefficients in a 1.1 mm diameter tube at vapour quality less than 0.3, corresponding to an increase in pressure from 6 bar to 10 bar, but found no enhancement in heat transfer coefficients at higher vapour qualities with the

same increment in system pressure. The higher heat transfer coefficients in the low vapour quality region was attributed to the reduction of surface tension with increase in system pressure, which induced smaller bubble departure diameters in the nucleate boiling dominant region. In and Jeong [120] studied the effect of saturation pressure (1.58 bar and 2.08 bar) on fluid R123 in a 0.19 mm diameter tube and found no heat transfer enhancement at the higher pressure condition in the high vapour quality region, where convective boiling reportedly dominated. Note that the work did not include flow visualisation, even though the authors inferred based on similar studies that elongated bubbly flow dominated at high vapour qualities. The paper also found stronger effects of mass flux and heat flux on heat transfer coefficients at lower saturation pressures. It was suggested that due to the lower vapour density of R123 at lower pressures, the elongated bubbles travel at a higher velocity, causing the thickness of the surrounding liquid film to be thinner, which resulted in a higher dependence of heat transfer on mass flux and heat flux at lower pressures.

Contrastingly, Saisorn et al. [102] reported a significant decrease in heat transfer coefficients of R134a in a 1.75 mm diameter tube when system pressure increased from 8 bar to 10 bar and theorised that smaller latent heat of vapourisation and lower liquid viscosity at higher pressures formed thinner liquid film on the tube walls, which could have a higher tendency to rupture compared to thicker liquid films.

2.4 Effect of Mass Flux

Phase-change processes such as boiling incipience heat flux, bubble formation as well as flow pattern development are also dependent on fluid flow rate in the channels. Increasing channel mass flux generally delays boiling incipience heat flux [69], [84] and induce a lower degree of wall superheat for a given heat flux condition. Euh et al. [103] showed experimentally that bubble departure frequency of water in a heated glass tube decreased with increasing mass flux.

Alam et al. [121] analysed the forces acting on the liquid-vapour interface and concluded that whilst some acting forces, such as buoyancy and surface tension are not sensitive to mass flux, inertia and shear force rise significantly with mass flux. As a result, increasing system mass flux could also affect the development of flow patterns in microchannels. Huang et al. [92] reported that increasing mass flux brought about earlier flow pattern transition to annular flow in their silicon microchannels, as did Costa-Patry et al. [83]. On the other hand, Harirchian and Garimella [84] and Al-Zaidi et al. [57] both noted delayed flow pattern transitions at higher channel mass fluxes. The former also found smaller bubble diameters in the bubbly flow regime at higher mass flux conditions. Additionally, the liquid film thickness in the annular flow regime appeared to become thinner and takes on a wavy form as mass flux increases, which was attributed to the higher vapour velocity at higher mass fluxes.

The influence of mass flux on flow regime evolution subsequently determines the dominant heat transfer mechanisms as well as heat transfer performance in microchannel heat sinks. The nucleate boiling mechanism is generally insensitive to changes in mass flux, while the convective boiling mechanism is enhanced at higher mass fluxes [56]. However in their review of heat transfer trends from numerous flow boiling studies as covered in Section 2.2, Agostini and Thome [94] highlighted that the effect of mass velocity on flow boiling heat transfer coefficient varied with vapour quality range. Namely, two-phase heat transfer may be observed to increase or decrease with increasing mass flux at low to medium vapour qualities, but generally had little influence on heat transfer rates at high vapour qualities.

2.4.1 Effect on Heat Transfer Rates

A large number of flow boiling studies on conventional microchannel and micro-pin fin heat sinks [72], [85], [92], [117], [122], [123] as well as enhanced microstructure heat sinks [77],

[124] have found no mass flux dependence typically at low heat fluxes, but significant improvement in heat transfer coefficient with increase in mass velocity at high heat fluxes, or where convective boiling dominant flow regimes are observed in the channels.

Harirchian and Garimella [85] conducted experiments using FC-77 at mass fluxes between 250 – 1600 kg/m^2 s and found that heat transfer coefficients were independent of mass flux after the onset of nucleate boiling. At heat fluxes corresponding to bubble nucleation suppression at the channel walls (observed in flow visualisation), higher heat transfer coefficients were measured at higher mass flux conditions. Studying the flow boiling characteristics of R1233zd(E) in a silicon microchannel heat sink at mass fluxes between 500 to 2750 kg/m^2 s, Huang et al. [92] reported transition to annular flow at very low vapour qualities (which was further lowered with increasing mass velocity), and subsequently a strong mass flux effect on heat transfer coefficients in this region. Thiangtham et al. [117] also found similar enhancement in the annular flow regime. While Li and Jia [123] did not include an independent flow visualisation study, they used the flow pattern map proposed by Chen and Garimella [125] to predict flow pattern boundaries in their microchannels. A strong mass flux effect was observed in churn and annular flow, in other words, convective boiling may be dominant in the channels.

In most cases where water is employed as the working fluid, heat transfer coefficients increased significantly with increase in mass velocity, as reported in Markal et al. [126] in microchannel heat sinks and Krishnamurthy and Peles [127] in micro-pin fin evaporators. In the former, this is possibly due to the high bubble generation rate associated with water, which induced transition to annular flow even at relatively low heat fluxes. In the latter, thin-film evaporation is likely the predominant heat transfer mechanism due to the trapping of vapour slugs in the pin-fin array at low and moderate heat fluxes which developed to annular flow at high heat fluxes. A similar mass flux effect was also observed with DI water as the working fluid in Chen et al. [89] for a porous-wall, interconnected channel array. Li et al. [75], [76] employed pure acetone in their comparative study using microchannels with triangular cavities and reported the dominance of confined annular flow and elongated bubble flow in the plain microchannels and the triangular cavity configuration respectively. Increasing mass velocities in the range of 83 – 442 kg/m^2 s suppressed flow boiling instabilities and thus enhanced heat transfer coefficients for a given heat flux. The authors reasoned that at higher mass fluxes, bubble

departure frequency increased and hindered bubble coagulation in the channels, which delayed dryout on the channel surface. This is however in contradiction with the findings of Euh et al. [103], who reported a decrease in bubble generation frequency at higher mass fluxes. Costa-Patry [83] also noted a higher rate of bubble coalescence at higher mass velocities.

Some studies employing straight microchannel heat sinks have found a weak dependence of heat transfer coefficient on mass flux in their respective investigated operating ranges [57], [69], [70], [122], [128]. Al-Zaidi et al. [57] studied the flow boiling heat transfer of HFE-7100 in a multi-microchannel heat sink for wall heat fluxes and mass fluxes ranging from 25.1 – 191.6 kW/m^2 and 50 to 250 kg/m^2 s respectively. While the effect of mass flux was generally negligible in the two-phase region, slightly higher heat transfer coefficients were observed for decreasing mass fluxes in the low heat flux region, as was observed in the studies by Bertsch et al. [69] and Harirchian and Garimella [85]. This was attributed to the effect of mass flux on exit vapour quality in the channels. Similarly, Fayyadh et al. [70] highlighted the effect of mass flux on vapour quality in the channels and importantly, when assessing the mass flux dependence of heat transfer coefficients in order to infer the dominant heat transfer mechanism in flow boiling systems.

An increase in mass flux may also result in a depreciation of heat transfer rates in microchannels. Costa-Patry et al. [83] reported a drop in heat transfer coefficients with increase in mass velocities between 594 – 1051 kg/m^2 s at low vapour qualities, due to earlier bubble coalescence and more intermittent dryout in the coalescing bubble regime.

The effect of mass flux may also be dependent on the heat flux range and flow patterns in the channel. In particular, Agostini et al. [87] found that the effect of mass flux manifested at medium and high heat fluxes for R245fa while it was only noticeable at high heat fluxes for R236fa. The authors suggested that this could be due to the differences in the dynamics of the elongated bubbly flow owing to the difference in fluid properties. Nonetheless, flow visualisation was not reported in the study. Heat transfer trends in microchannel heat sinks featuring re-entrant cavities by Deng et al. [124] and Zeng et al. [77] also exhibited mass flux dependence toward high heat fluxes where annular flow was observed. Yin et al. [73] observed

a stronger dependency on mass flux in the stratified flow regime in open microchannel heat sink configurations.

Similarly, Alam et al. [121] found that average heat transfer coefficients increased to a maxima with mass flux increase of up to 400 kg/m^2 s but dropped considerably with further increase in mass flux at a given heat flux condition in their silicon nanowire microchannel array. However, the authors did not clarify the effect of mass flux on boiling incipience heat flux and subcooled length in the channels. Furthermore, the study included analysis of forces affecting two-phase flow regime development in microchannels and concluded that surface tension force dominated in the channels at low mass velocities, while at mass velocities beyond 400 kg/m^2 s, inertia force overcame surface tension force in their system. The authors reasoned that because flow boiling instabilities were prevalent in the region where surface tension force dominated in the channels, increasing mass flux strengthened inertia force and reduced bubble departure diameters, which prevented flow reversal in the system. Flow boiling mitigation contributed to heat transfer enhancement with increase in channel mass flux. In the region where inertia force is larger than surface tension forces, heat transfer coefficients deteriorated with increase in mass flux. This was attributed to the suppression of annular flow development with increase in channel mass flux due to small bubble departure diameters, and therefore the nucleate boiling mechanism, rather than thin-film evaporation was dominant in the channels. Nevertheless, the nucleate boiling regime is largely believed to be independent of mass flux based on the conventional criterion [56].

2.4.2 Effect on Critical Heat Flux

Increasing system mass flux typically extended the critical heat flux limit in microchannels. Mudawar and Bowers [111] found that the critical heat flux of water increased steadily with increasing mass flux, from 5000 to 134000 kg/m^2 s, at a fixed inlet temperature of 25 °C in a 0.406 mm and a 0.902 mm diameter tube. The authors found that critical heat flux can be correlated to mass flux by $G^{0.446}$ in their study. For parallel microchannels, Qu and Mudawar [129] found increasing critical heat flux values of water with increasing mass velocities at a fixed inlet temperature. Similarly, for other working fluids, higher critical heat flux limits for the flow boiling of HFE-7100, R134a and R245fa were also reported in [69], [88], [130], [131] for multi-microchannel heat sink configurations.

The enhancement in critical heat flux may be attributed to the higher potential to suppress flow boiling instabilities as well as channel wall dryout in two-phase systems at higher mass fluxes, as reported by Lee and Mudawar [38]. From flow visualisation, the authors noted that premature critical heat flux occurred at low mass fluxes due to early development of annular flow and subsequently flow reversal and dryout phenomenon in their microchannel heat sink with HFE-7100 as the working fluid. Increasing the mass flux in the system increased the momentum of the incoming liquid and mitigated vapour backflow in the heat sink. A delay in the occurrence of wall dryout (i.e. sudden drop in heat transfer coefficient observed) to higher heat fluxes with increasing mass flux, were also observed by Chen and Garimella [122] and Harirchian and Garimella [85] for the flow boiling of FC-77 in parallel microchannel evaporators.

2.4.3 Effect on Two-Phase Pressure Drop

As mentioned above, increasing mass flux affects flow pattern development as well as the dominance of different forces in microchannel flows at a given heat flux and vapour quality condition. Accordingly, two-phase pressure drop increases with increase in mass velocity. This is because at higher flow rates, wall shear stress as well as energy loss due to fluid acceleration increase, thereby increasing the frictional pressure drop and acceleration pressure loss components of the system. The effect of mass flux on pressure drop is well-reported in flow boiling studies – higher heat sink pressure drop corresponding to mass flux increase has been observed for conventional parallel microchannels [85], [92], [96], [97], [99], [132], [133], micro-pin fin arrays [71], [72] as well as enhanced microscale heat sinks [73], [77] respectively. Generally, the pressure drop gradient with respect to vapour quality is steeper at higher mass fluxes, due to the proportionality of both the frictional and acceleration pressure drop components to the square of mass velocity. This is evident in Huang et al. [92] for R1233zd(E), where the pressure drop profile at mass fluxes above 1500 kg/m^2 s was significantly steeper than at lower mass fluxes. The same trend was similarly highlighted in the works of Dário et al. [97] and Madhour et al. [99] for fluid R134a.

Harirchian and Garimella [85] found a steady increase in both the single-phase and two-phase pressure drop of FC-77 with increase in mass flux in their silicon microchannel heat sinks. Preserving a base area of 12.7 mm x 12.7 mm, the authors varied the number and dimensions of the channels in their study. The maximum pressure drop measured in the heat sink configuration with 24 channels of width 400 μm was roughly 11 kPa, which rose to nearly 24 kPa as microchannel width was reduced down to 100 μm. In a related study and employing DI water as the working fluid, Holcomb et al. [133] reported a similar pressure drop trend with regards to mass flux. The relatively low pressure drop values reported in the former could be related to fluid properties while the large channel width could have resulted in low pressure drop values even at high mass flux and heat flux conditions. Agostini et al. [132] measured the pressure drop across their multi-microchannel heat sink and found maximum pressure drop magnitudes of over 110 kPa for R236fa and 120 kPa for R245fa respectively, but noted that these were incomparable due to the different manifold configurations between the heat sinks. The authors confirmed using the homogenous model that the two-phase pressure drop is lower for R235fa due to the lower vapour density of the fluid. Costa-Patry et al. [96] also reported similar results for the two fluids for mass velocities and base heat fluxes between 499 – 1100 kg/m^2 s and 130 – 1400 kW/m^2 respectively.

Falsetti et al. [71] evaluated the effect of mass flux on total pressure drop in a micro-pin fin evaporator between 750 – 2500 kg/m^2 s for R236fa while Reeser et al. [72] presented the two-phase pressure drop of DI water and HFE-7200 in an in-line and staggered pin-fin array. Both studies agree with the observations reported for conventional microchannel heat sinks, as did Zeng et al. [77] in micro-grooved channels coupled with re-entrant cavities. Arranging the pin-fins in a staggered configuration increased the pressure penalty in the heat sink in Reeser et al. [72]. Although Yin et al. [73] found a non-conventional pressure drop trend with respect to heat flux, as mentioned in Section 2.2, increasing system mass velocity still increased overall pressure drop in their open microchannels.

Deng et al. [124] assessed the pressure drop results in their re-entrant porous microchannels with respect to heat flux and found that at a given heat flux, pressure drop decreased with increase in mass flux. This was attributed to a reduction in vapour quality condition at higher mass fluxes, which shortened the flow boiling length in the channels at a similar heat flux level.

Plotting the pressure drop trend against vapour quality, the authors concluded that pressure drop increased with increasing mass flux. Similar observations of pressure drop variation with respect to heat flux were reported by Balasubramanian et al. [91], Chen et al. [89] and Li et al. [75].

Interestingly, Chen and Garimella [122] investigated the flow boiling of FC-77 at a constant inlet subcooling of 26 K and found that pressure drop was insensitive to changes in mass flow rate in their silicon microchannel heat sink. The authors suggested that this could be due to the counteracting effects of frictional pressure loss and acceleration pressure loss. While increasing mass flux causes frictional pressure loss to rise, the lower vapour qualities in the channels at higher mass velocities are also effective in decreasing acceleration pressure drop in the system.

On the other hand, total pressure drop initially decreased as a function of mass flux, but increased at higher mass fluxes in Markal et al. [126]. They explained that stronger inertia forces at higher mass flow rates easily overcame flow resistances in the upstream direction of the channels (generated by evaporative momentum force following bubble nucleation) compared to lower mass flux conditions and reduced pressure drop even with higher frictional losses at higher mass velocities, at least in the mass flux range where a reduction a pressure drop was observed with increase in flow rate.

2.5 Effect of Inlet Subcooling

In spite of the fact that inlet conditions of the working fluid could significantly influence flow boiling in microchannels, there is generally a lack of literature addressing the effect on inlet subcooling on the performance of microchannel heat sinks. The size range of effective cavities, based on the classical model by Hsu [109], is a function of subcooling degree. Similarly, Kandlikar [134] showed a high dependency of flow boiling nucleation criteria, as well as flow boiling stability on bulk liquid subcooling. Accordingly, bubble growth and departure dynamics have been shown to vary with liquid subcooling, as discussed thoroughly in Euh et al. [103] and Goel et al. [135]. Even though these studies were primarily concerned with flow boiling at the macroscale level, the findings still indicate a potential influence of liquid subcooling on the nucleation characteristics in microscale flows. Bubble departure diameter and frequency were generally found to decrease with increase in subcooling degree (i.e. lower bulk fluid temperature). Lower bubble departure frequencies are caused by the longer waiting time between successive bubble ebullition cycles, as lower bulk liquid temperatures require a longer period in order to re-establish a certain degree of superheat at the wall for nucleation after bubble departure.

2.5.1 Effect on the Onset of Boiling

For microchannels, a delay in the onset of boiling from 1184 kW/m^2 to 1897 kW/m^2 was reported with increasing subcooling degree at a given flow rate in Lee and Mudawar [136] using HFE-7100 as the working fluid. Ong and Thome [137] investigated the influence of inlet subcooling, between 2 K to 9 K, on the flow boiling of refrigerant R134a, R245fa and R236fa in circular tubes covering the microscale range and reached the same conclusion, i.e. delayed onset of boiling with increasing subcooling. Additionally, Chen et al. [89] and Zhang et al. [138] both demonstrated a slightly higher boiling incipience wall superheat by around 2 K at higher inlet subcooling in a similar interconnected microchannel configuration using deionised water at subcooling conditions of 10, 40 and 70 K. Boiling incipience heat flux increased with subcooling in Deng et al. [124] in a re-entrant porous microchannel array, while Deng et al. [78] noted higher degrees of wall superheat, of around 4 K at boiling initiation at high subcooling conditions for the flow boiling of water and ethanol in an interconnected pin-fin heat sink. Zeng et al. [77] found that the wall superheat condition at the onset of nucleate boiling increased from 0.3 K to 4.9 K corresponding to an increase in inlet liquid subcooling from 10 K to 40 K for flow boiling of DI water in micro-grooved channels with secondary

grooves as re-entrant cavities. From the above, it is clear that the degree of subcooling influences both the degree of superheat and the wall heat flux required for boiling incipience, although the work presented so far is not detailed or enough to quantify these changes.

2.5.2 Effect on Flow Instability

A number of researchers studied the effect of degree of subcooling on flow instabilities in microchannels. Prajapati and Bhandari [139] cited flow reversal and parallel channel interaction, for large inlet subcooling conditions, as major causes of flow instabilities in microchannels. However, past researchers gave contradictory statements on the dependence of flow instability on the degree of subcooling. Lee et al. [140] found with R134a that increasing inlet subcooling mitigated pressure drop oscillations in microchannels. The authors reasoned that low liquid inlet temperatures had a higher damping effect on vapour backflow into the inlet plenum. Pressure drop oscillations intensified intermittent dryout, which occurred predominantly in annular flow and degraded heat transfer coefficients appreciably in this region. Chen et al. [89] also reported lower two-phase oscillations including the inlet pressure and inlet temperature at higher inlet subcooling. This was attributed to the delayed transition to annular flow, a regime where flow reversal was typically observed in their heat sink.

On the contrary, high inlet liquid subcooling produced significant flow oscillations in [80], [141], [142]. Bogojevic et al. [141] studied the flow boiling of water in silicon microchannels at two inlet subcooling conditions (inlet temperatures 25 °C and 71 °C at an approximate inlet pressure of 1 bar) and found that the magnitude of temperature oscillations as well as temperature non-uniformity resulting from vapour backflow from the channel array to the inlet plenum were significantly amplified at higher liquid subcooling conditions. Similarly, more severe pressure and temperature fluctuations were recorded at lower water inlet temperatures in the study by Deng et al. [80] in both their plain microchannel and micro-pin fin structured microchannel heat sink . They compared results for inlet subcooling degrees of 10 K and 40 K using water and ethanol as the working fluid. Kingston et al. [142] studied the flow boiling of fluid HFE-7100 in a parallel microchannel heat sink and found high amplitude temperature oscillations at higher degrees of inlet subcooling. The instabilities were associated to rapid bubble growth in the channels.

The effect of inlet subcooling on flow instabilities is also dependent on fluid properties of the working fluid. Deng et al. [78] reported different subcooling effects using water and ethanol as working fluids in the same pin-fin re-entrant microchannel heat sink. Flow instabilities were aggravated using water with increase in inlet subcooling degree, whilst in ethanol higher inlet subcooling suppressed two-phase flow oscillations in the test section. The authors also noted that the amplitude of oscillations of ethanol were generally larger than that recorded using water. No justification was provided for the disparity between the two fluids. In summary, there are conflicting reports on the effect of the degree of inlet subcooling on flow instabilities in microchannels. Furthermore, the effect of fluid properties on the magnitude of the effect of the degree of subcooling is not clear.

2.5.3 Effect on Heat Transfer Rates

Some past reports indicate an insignificant effect of subcooling on heat transfer coefficients, particularly in the saturated boiling region [87], [137], [143]. Agostini et al. [87] concluded that increasing inlet subcooling did not significantly affect heat transfer coefficients in the saturated region for subcooling conditions of 0.6 K to 18.3 K and from 0 K up to 19 K for refrigerant R245fa and R236fa respectively. The authors emphasised however, that in the subcooled region, increasing inlet subcooling resulted in a reduction in the heat transfer coefficients for both fluids. Similarly, a small effect of subcooling on local heat transfer coefficients at vapour qualities $x < 0.1$, influenced by the location of boiling incipience, as covered above, was also observed in Ong and Thome [137], [143]. The same group, Huang and Thome [93], monitored the local heat transfer coefficient at a fixed location along their multi-microchannel heat sink and reported lower local heat transfer coefficients in the subcooled and saturated boiling region at higher inlet subcooling due to a corresponding extension of the subcooled region for refrigerants R245fa and R236fa.

Contrary to the above, research in enhanced or structured microchannel heat sinks typically concluded a positive effect of subcooling on heat transfer coefficients [73], [80], [89], [124]. In an open microchannel configuration (i.e. cover plate does not completely seal on the top of the fins), Yin et al. [73] reported that increasing inlet subcooling delayed the occurrence of stratified flow, a flow regime prone to local wall dryout, and hence increased the local two-phase heat transfer coefficient assessed near the channel outlet. Chen et al. [89] sintered a porous copper layer on a microchannel heat sinks with square re-entrant cavities and found that

increasing inlet subcooling delayed the development of annular flow, and thus liquid film dryout in the channels. When they presented the local two-phase heat transfer results at the most downstream location on the heat sink, an improvement in heat transfer with increase in inlet subcooling was demonstrated. Deng et al. [124] and Deng et al. [80] separately reported an increase in downstream (i.e. nearest to channel exit) heat transfer coefficients at higher subcooling.

Zeng et al. [77] recommended selecting an optimum liquid subcooling may also be used to control flow pattern development in the channels to benefit heat transfer performance. They studied a range of degree of subcooling at 10, 25 and 40 K for water. The highest two-phase heat transfer coefficient at the channel outlet was obtained at a medium inlet subcooling of 25 K, due to the persistence of stable annular flow in their grooved microchannel array. The authors explained that at low inlet subcooling (at 10 K inlet subcooling), slug and annular flow developed early in the channels. A longer dryout period, which was assumed to be the cause of heat transfer deterioration, was observed downstream in the channels. Flow visualisation revealed that the dryout period persisted for 25 ms longer at 10 K compared to when subcooling was set to 25 K.

2.5.4 Effect on Critical Heat Flux

Increasing inlet subcooling may also delay the occurrence of critical heat flux in microchannels, although this might only be relevant at very high degrees of subcooling. Furthermore, the occurrence of critical heat flux is typically related to flow instabilities and flow reversal in multi-microchannels, which has been covered above. Lee and Mudawar [130], [136] reported that the critical heat flux limit was extended at higher degree of subcooling for the subcooled flow boiling of HFE-7100 in a microchannel heat sink. Revellin and Thome [144] demonstrated a slight increase in critical heat flux with subcooling due to an increase in the channel saturated length. Nonetheless, the authors noted that the effect of subcooling is limited at low values of inlet subcooling. The study by Lee and Mudawar [130], [136] employed very high inlet subcooling degrees of over 60 K and even 90 K. Agostini et al. [132], for instance, found that the critical heat flux in their microchannel heat sink using R236fa was unaltered at subcooling degrees in the range of 0.4 K to 15.3 K. This agrees with the observation in Ong and Thome [137]. Even though Qu and Mudawar [129] investigated relatively high degrees of subcooling in their paper, the effect of inlet subcooling appeared to be negated by

vapour backflow in the channels. Deng et al. [124] studied the flow boiling of ethanol and water at subcooling degrees of 10 K and 40 K and also attained a much larger critical heat flux value at 40 K at a given mass flux condition.

2.5.5 Effect on Two-Phase Pressure Drop

Two-phase pressure drop generally decreased with increase in inlet subcooling [89], [124]. Chen et al. [89], using water as the working fluid with an inlet pressure of approximately 1 bar, reported a reduction in flow boiling pressure drop from 5.5 kPa to 1.5 kPa when the inlet subcooling was increased from 10 K to 70 K. This was attributed to lower void fraction in the channels at higher subcooling. Deng et al. [124] reasoned that pressure drop in the two-phase region was lower due to the smaller two-phase region in the heat sink at higher subcooling conditions. Huang and Thome [92] investigated the effect of inlet subcooling of R245fa and R236fa at subcooling degrees of 5.5, 10 and 15 K, and demonstrated that there was a notable reduction of total pressure drop in the heat sink when the subcooling degree was increased from 5.5 K to 10 K, but did not vary with further increase in subcooling to 15 K. On the other hand, the pressure drop in the channel array, that is, the total pressure drop corrected for inlet and outlet restriction pressure losses, increased with increase in subcooling at low vapour qualities, i.e. vapour quality less than 0.15 at the exit. This was attributed to the dominance of single-phase liquid pressure drop in the channels at low vapour qualities. The liquid viscosity decreases at higher inlet temperatures, resulting in a higher single-phase pressure drop component and consequently higher channel pressure drop. Whilst the authors did not comment on the weak subcooling effect at higher vapour qualities, this is of course not expected at high exit qualities where the two-phase pressure drop component dominates.

On the contrary, Yin et al. [73] found a notable effect of subcooling on two-phase pressure drop only at low heat fluxes where bubbly and slug flow dominated in the channels. The authors reasoned that this is because decreasing inlet subcooling promoted nucleate boiling, which resulted in an increase in the frictional pressure drop in the channels. A combination of the shorter subcooled length and dominance of stratified flow at higher heat flux conditions resulted in an insignificant subcooling effect in this region. Additionally, Zeng et al. [77] attributed higher heat sink pressure drop to more severe flow boiling instabilities when operating at higher inlet subcooling degrees. In summary, and as mentioned in the opening statement of this part on the effect of subcooling on two-phase pressure drop, there is evidence

that the two-phase pressure drop decreases with increasing inlet subcooling. However, there are some reports to the contrary and this requires some further work.

Overall, the effects of inlet subcooling on flow boiling behaviour needs to be clarified and in general, there is a lack of literature on the effect of inlet subcooling on the flow boiling characteristics of HFE fluids. Moreover, very high degree of subcooling was employed in several studies such as in Chen et al. [89], where the subcooling degree was 70 K, as well as in Lee and Mudawar [38], [130], where HFE-7100 at sub-atmospheric inlet temperatures of -30 °C was conveyed to the microchannel heat sink. Such low coolant temperatures may not be suitable for some compact and integrated cooling systems with limited space and energy consumption allocation to the integrated thermal unit. A two-stage cascade refrigeration system was used to condition coolant temperatures in the study of Lee and Mudawar [38], [130]. Although CHF was enhanced up to 6.9 MW/m^2, the resultant thermal management solution would likely exceed size and weight constraints typically imposed the majority of cooling applications. In addition, most studies did not assess the effect of inlet subcooling on temperature uniformity on the heat sink, which was reported to worsen in Bogojevic et al. [141], and is also important in view of minimising thermal stresses on the chip die.

2.6 Flow Pattern Maps

The mechanics of heat and mass transfer in flow boiling intrinsically interrelate with two-phase flow phenomenon. In other words, flow boiling heat transfer and pressure drop characteristics, and the development of two-phase flow regimes are coupled to each other [145]. For example, higher bubble nucleation activity (i.e. larger heat and mass transfer rate) may trigger instabilities in two-phase systems and induce flow pattern transition, while certain flow regimes have a higher tendency to suppress nucleation activity. Visual inspections of flow patterns occurring during flow boiling are typically conducted using high speed imaging techniques. Commonly observed two-phase flow patterns in microchannels are bubbly, slug, churn, annular and mist flow, as presented by Thome and Cioncolini [146]. From a more practical stance point, the development of flow regimes exhibits different degrees of parametric dependence due to the effects of heat flux, mass flux and operating pressure etc. on nucleation behaviour and bubble dynamics in two-phase systems. As such, two-phase flow pattern evolution are also affected by fluid properties, flow boiling instabilities as well as manifold design in microchannel heat sinks [147]–[149].

Despite the widespread agreement that microchannel heat transfer trends are flow pattern-dependent, there is a scarcity of flow regime-based models in literature compared to empirically correlated heat transfer prediction methods [146], [147], even though some of these correlations were proposed based on large databanks covering multiple working fluids and channel sizes, such as in Shah [150]. Thome et al. [151] first proposed the three-zone model based on the cyclic passage of slugs in a channel, which was later modified by Costa-Patry and Thome [152] and most recently in Magnini and Thome [153]. On the other hand, Qu and Mudawar [154], Kim and Mudawar [155] and Thome and Cioncolini [156] separately developed heat transfer models specific to annular flow boiling. Harirchian and Garimella [157] first presented a flow regime map based on a comprehensive experimental database including several working fluids and microchannel geometries. The authors later developed a flow regime-based heat transfer model in Harirchian and Garimella [158]. A new correlation for confined annular flow was proposed while the classical pool boiling correlation by Cooper [159] and a modified three-zone model by Thome et al. [151] were recommended for the bubbly and slug flow regime respectively.

Even though numerous flow pattern maps have been proposed for both adiabatic and diabatic macroscale two-phase flows in literature, few comprehensive flow regime maps specifically for multi-microchannel flow boiling is available. Flow transition boundaries are generally predicted based on the fluid properties of the working fluid, channel geometry, confinement effects and operational conditions etc. [157], [160]–[164]. The maps are commonly presented on coordinate systems of superficial velocity, mass flux, vapour quality, as well as using dimensionless groups such as Weber number, Boiling number, Bond number and Reynolds number etc. As different transition boundaries may be governed by different sets of fluid properties, they typically require representation by different flow parameters and dimensionless groups [145]. Chen [165] plotted their flow pattern data, obtained for the flow boiling of fluid R134a in microtubes between diameters 1.1 mm – 4.26 mm, against several coordinate systems and noted that maps based on dimensionless groups are more effective, since they are able to contain the effects of multiple parameters, but commented that a combination of different dimensionless groups were required to capture different parametric effects on two-phase flow patterns.

Broadly speaking, due to the effect of heat flux on flow pattern transitions in diabatic flows, adiabatic flow pattern maps generally have poor applicability to flow boiling phenomenon in microchannels [146], [147]. Furthermore, direct extrapolation of macroscale flow pattern maps to predict microscale flow pattern data is not recommended [146], [166], since the effect of confinement and surface tension become relevant in microscale flows [167]. Flow maps produced from singular channel studies may also be inaccurate for parallel channel configurations due to flow interaction between channels and the plenum [167]. In line with the scope of this study, only diabatic flow pattern maps for microscale flows are reviewed in this section.

Revellin and Thome [160] conducted flow boiling experiments in glass tubes of 0.51 mm and 0.79 mm diameter using R134a and R245fa at heat fluxes and mass fluxes ranging from 3.1 – 597 kW/m^2 and 200 – 2000 kg/m^2 s respectively. Bubble generation frequency was measured in the experiments and the effect of saturation pressure (from 6.7 bar to 8.9 bar) was also investigated for R134a. The authors categorised flow patterns into three distinct zones, namely the isolated bubble regime (IB), the coalescing bubble regime (CB) and the annular flow regime (A). In particular, the IB regime includes bubbly flow, where bubble generation frequency increases with increasing heat flux. On the other hand, the CB regime refers to slug flow, where

the rate of bubble generation decreases with increasing heat flux. Churn flow was designated as a transitional regime between slug and annular flow. The flow pattern map by Revellin and Thome [160] was presented with respect to mass flux and vapour quality, with proposed relations of the transition vapour qualities as follows:

$$x_{IB/CB} = 0.763 \left(\frac{Re_{fo}\, Bo}{We_{go}} \right)^{0.41} \tag{2.1}$$

$$x_{CB/A} = 0.00014\, Re_{fo}^{1.47}\, We_{fo}^{-1.23} \tag{2.2}$$

In their study, the authors observed that increasing mass flux resulted in earlier flow pattern transitions because of increased rates of bubble coalescence, while inlet subcooling had no effect on the transition boundaries. Increasing heat flux and saturation pressure shifted the IB/CB transition to higher vapour qualities, due to an increase in the bubble nucleation frequency and smaller bubble sizes in the channel respectively. Accordingly, the effect heat flux and pressure are taken in account through the boiling number, Bo and liquid-only Weber number, We_{fo}, while the effect of mass flux and liquid viscosity is represented by Re_{fo}. Since the authors concluded no heat flux effect in this region, in $x_{CB/A}$, the dimensionless terms are representative of the ratio of surface tension force to kinematic viscosity, i.e. $\sigma/(\mu_f\, \rho_f^{-1})$. The applicability range of the map is as follows:

- Bo = 0.00003 – 0.00632
- Re_{fo} = 640 – 8855
- We_{fo} = 4 – 34970
- We_{go} = 125 – 12525

Ong and Thome [161] investigated flow pattern transition covering macro-to-microscale circular channels between diameters 0.50 mm – 3.04 mm using refrigerant R134a, R236fa and R245fa. Extending the work of Revellin and Thome [160] to both macroscale and microscale flows, the authors proposed updated flow map incorporating the effects of channel diameter and bubble confinement (through the confinement number, Co) as well as viscous, surface tension and shear forces in the channels. Macro to microscale transition was suggested to be between Co ~ 0.3 – 0.4.

$$x_{IB/CB} = 0.36\, Co^{0.2} \left(\frac{\mu_g}{\mu_f} \right)^{0.65} \left(\frac{\rho_g}{\rho_f} \right)^{0.9} Re_{go}^{0.75}\, Bo^{0.25}\, We_{fo}^{-0.91} \tag{2.3}$$

$$x_{CB/A} = 0.047\, Co^{0.05} \left(\frac{\mu_g}{\mu_f} \right)^{0.7} \left(\frac{\rho_g}{\rho_f} \right)^{0.6} Re_{go}^{0.8}\, We_{fo}^{-0.91} \tag{2.4}$$

The range of dimensionless numbers covered in the study are listed below:

- $Co = 0.27 – 1.67$
- $Re_{fo} = 1567 – 31387$
- $Re_{go} = 8519 – 452600$
- $We_{fo} = 0.58 – 1247$

The authors observed earlier flow regime transitions at higher mass velocities. Fluids with higher surface tension also resulted in lower transition vapour qualities at a given saturation temperature. Additionally, increasing saturation temperature and pressure also induced a shift in transition boundaries to larger vapour qualities, which was attributed to changes in fluid surface tension, density and fluid viscosity corresponding to saturation conditions. As was concluded by Revellin and Thome [160], the CB/A flow transition boundary was also not a function of heat flux in the map by Ong and Thome [161].

Costa-Patry et al. [168] investigated the flow boiling of R134a, R1234ze(E) and R245fa in a copper microchannel heat sink with local heaters to measure local heat transfer coefficient on the underside of the heat sink, including flow visualisation. The heat sink had fifty-two parallel microchannels of hydraulic diameter 246 μm. Additional tests were also conducted in a silicon evaporator with 135 channels of hydraulic diameter 148 μm using R236fa and R245fa [83]. Assessing the flow map of Ong and Thome [161], the authors also included their own data in order to adapt the flow map, developed for single channels, to multichannel heat sink configurations. The combined database covered a mass flux range of 100 – 1100 kg/m^2 s, wall heat fluxes between 8 – 260 kW/m^2 and hydraulic diameters from 0.15 – 3.04 mm. The authors reported that local heat transfer coefficients exhibited a V-shape trend and corresponded the minima in heat transfer coefficients to annular flow transition in the channels. Based on this, they also found that transition to annular flow occurred at larger vapour qualities at higher heat fluxes. On the other hand, at a given wall heat flux condition, increasing mass flux accelerated annular flow transition in the channels [83]. The original Ong and Thome [161] correlation was recommended to predict IB/CB transition, while a new correlation for CB/A transition that incorporates the observed effect of heat flux, mass flux and channel diameter was proposed:

$$x_{CB/A} = 425 \left(\frac{\rho_g}{\rho_f}\right)^{0.1} \left(\frac{Bo^{1.1}}{Co^{0.5}}\right) \tag{2.5}$$

Harirchian and Garimella [157] conducted flow boiling experiments using FC-77 in twelve silicon parallel microchannel heat sinks with hydraulic diameters ranging from 96 – 707 μm for mass fluxes from 224 kg/m^2 s – 1461 kg/m^2 s. The authors identified bubbly, slug, churn, wispy-annular and annular flow in the channels [84]. The authors argued that flow confinement does not solely depend on channel diameter, but is also a function of mass flux, due to the effect of mass velocity on bubble diameters in channels. Based on a curve fit to their experimental data, a new flow confinement criterion using the Bond number and liquid-only Reynolds number, the latter to address the mass flux effect on bubble confinement in microchannels.

$$Bd^{0.5}\ Re_{fo} = 160 \tag{2.6}$$

The flow is unconfined when $Bd^{0.5}\ Re_{fo} > 160$, where bubbly flow is observed. The flow map developed utilised the convective-confinement number, $Bd^{0.5}\ Re$, on the vertical axis and a dimensionless heat flux parameter, Bo Re, on the horizontal axis. The transition from slug to churn and annular flow is given below:

$$Bo\ Re_{fo} = 0.017 \left(Bd^{0.5}\ Re_{fo} \right)^{0.7} \tag{2.7}$$

Additionally, the authors also compared the flow regime map with several other experimental studies, including singular and parallel microchannels, and cited good agreement with the flow pattern data [157].

Choi et al. [163] investigated the flow boiling behaviour of FC-72 in copper multi-microchannels between mass fluxes 100 kg/m^2 s – 458 kg/m^2 s and heat fluxes 3.2 kW/m^2 – 49 kW/m^2. The authors proposed a heat transfer prediction model using the Churchill and Usagi [169] method. The authors obtained a curve fit using the liquid-only Weber number and vapour quality, in order to identify the transition between the nucleate boiling dominant regimes, i.e. bubbly and slug flow, to the convective boiling dominant regime, i.e. annular flow. Accelerated transition from bubbly/slug to annular flow was observed at higher mass fluxes.

$$We_{fo} = 0.021\ x^{-2.458} \tag{2.8}$$

Based on the previous work of Chen [165], Mahmoud and Karayiannis [162] combined their flow pattern data, obtained using R245fa at a pressure of 1.85 bar, heat fluxes 3 – 25 kW/m^2 and mass fluxes between 100 – 400 kg/m^2 s in a 1.1 mm diameter tube and modified the

prediction model for the transition boundary between bubbly and slug flow. Although the flow map, based on the liquid and vapour superficial velocity, has been developed for single tubes, each transition mechanisms are considered thoroughly and modelled accordingly [162], [165] (see Eq. (9) – (14)). For instance, slug-churn transition was proposed to occur through three mechanisms, (i) distortion of slugs after reaching a critical bubble length, (ii) deformation of the slug tips in the presence of a chaotic flow field, typically at intermediate liquid superficial velocities, and (iii) distortion of slugs due to dominance of turbulence over surface tension force at high liquid superficial velocities. Full notations and definitions are available in Mahmoud and Karayiannis [162].

Bubbly to slug:

$$We_r = \frac{\rho_f U_r D_h}{\sigma} = 4 \tag{2.9}$$

Slug to churn:

$$u_h = 2.75 \sqrt{\frac{\sigma}{\rho_f f_l D_h}} \tag{2.10}$$

$$u_{gs} = 587.1 \left(\frac{\mu_f}{\rho_g D_h}\right)^{1.447} \left(\frac{\rho_g D_h}{\sigma}\right)^{0.937} \tag{2.11}$$

$$Re_{ls} = 81.08\ We_{gs}^{1.447}\ Fr^*_{gs}{}^{-0.267} \tag{2.12}$$

Churn to annular:

$$Fr_{gs}\ Re_{ls} = 3.119 \times 10^5 \tag{2.13}$$

$$We_{ls} = 1.567 \times 10^{-17} \left(Fr_{gs}\ Re_{ls}\right)^{3.41} \tag{2.14}$$

Overall, an effective flow regime map should predict flow pattern boundaries based on the general classification of flow regimes in microchannels for ease of comparison between studies. Thome et al. [170] urged the community to report flow patterns in their respective studies based on four primary classifications (namely bubbly, slug, annular and mist flow), with the use of sub-regimes to describe transition zones between the four principle flow patterns (for e.g. churn flow between slug and annular flow) in order to streamline the comparison of flow pattern data between independent studies. Additionally, a comprehensive flow map should also exhibit an appropriate degree of sensitivity to operating parameters, most importantly the effects of heat flux and mass flux, including any possible effects of saturation

pressure, degree of subcooling as well as bubble confinement on flow pattern evolution in microchannels.

Nevertheless, there is no universal agreement between flow pattern maps, even if developed for similar experimental configurations and working fluids in literature, as highlighted in Cheng et al. [147]. Although Ribatski [167] noted satisfactory agreement for single-channel flow pattern data, the authors commented that maps developed for singular microchannels might not be as appropriate for multichannel flow configurations, particularly when subject to flow instabilities [167]. More recently, Al-Zaidi et al. [57] compared several flow pattern maps, including those proposed based on parallel channel studies, with their experimental data using HFE-7100 in a multi-microchannel heat sink and found poor predictions for most flow regimes. The authors noted, however, that annular flow was generally predicted to a reasonable accuracy. Still, a good prediction of the bubbly and slug flow regime is relatively important to establish the nucleate boiling dominant region in the operating range of microchannel heat sinks. Cheng et al. [147] attributed the lack of agreement to subjectivity during flow pattern identification and visualisation techniques employed in individual studies. Additionally, this could also be due to different threshold methods used as the criterion for macro-micro scale transition, as cited in several works including Thome and Cioncolini [146] and Mahmoud and Karayiannis [7].

2.7 Two-Phase Heat Transfer Correlations

As covered in Section 1.1, the trend of miniaturisation in electronics enabled higher processing speeds in smaller electronics packages and made significant impacts in the commercial, military and aerospace sector. However, modern integrated circuits are rapidly converging toward critical bottlenecks in recent years, due to major challenges in thermal management amid strict performance, size, weight and cost requirements [6], [7]. Power density is predicted to reach 4.5 MW/m^2 in computing systems by 2026 while heat flux requirements in *current* military avionics and IGBT modules already extend up to 10 MW/m^2 and 50 MW/m^2 respectively. Flow boiling heat transfer at the microscale level, offering high heat transfer rates with compact volume ratios on low coolant inventories as well as improved temperature uniformity on chip dies, is a promising thermal management solution to miniaturised electronic systems. Consequently, prediction methods and design tools, including the prediction of flow boiling heat transfer performance, pressure drop penalty and critical operational limits are duly required by thermal engineers to optimise and implement two-phase cooling to their respective applications.

In fact, such correlations are widely available in literature. Over 60 correlations have been proposed for the prediction of flow boiling heat transfer coefficients alone since the 1990s, as reviewed in Fang et al. [171], including those recommended for macroscale flow boiling. The types of correlations include (i) enhancement-factor models [117], [172]–[175], (ii) nucleate boiling models [176]–[179], (iii) superposition models [180]–[182], (iv) asymptotic models [81], [163], [183], [184], (v) predominant mechanism models [150], [185]–[188] and (vi) criterion-based models [123], [189]–[192]. Many macroscale correlations are adapted for microscale applications to account for the effects of flow confinement and surface tension forces in microscale two-phase flows, for instance in Shah [150] and Mahmoud and Karayiannis [182]. More recently, Qiu et al. [193] trained and developed a heat transfer correlation based on an artificial neural network model saturated microchannel flow boiling heat transfer data based on 50 different sources. The model performed relatively well even for experimental results outside of the training database, but highlighted that poor predictions were obtained for working fluids not included in the initial training dataset.

2.7.1 Nucleate Boiling Mechanism

Tran et al. [177], Yu et al. [178] and Sun and Mishima [176] proposed correlations to predict two-phase heat transfer in nucleate boiling dominant regimes (see Table 6.7). Dimensionless numbers Bo, We_{fo} and (ρ_f/ρ_g) were correlated in all three prediction models, which were modified from the work of Lazarek and Black [179] based on the flow boiling of R113 in a 3 mm diameter tube. Lazarek and Black [179] found a strong dependence of heat transfer coefficient with heat flux but a negligible influence of vapour quality. Hence Bo, a non-dimensional form of heat flux was used to represent the effect of heat flux on flow boiling heat transfer. The liquid Reynolds number considers viscous effects in the flow and channel diameter. Citing the importance of surface tension on microscale heat transfer in their flow boiling data using fluid R12 and R113, Tran et al. [177] replaced the Reynolds number term in the Lazarek and Black [179] correlation with the liquid-only Weber number, which quantifies the ratio of fluid inertia to surface tension. Furthermore, the variation in fluid properties with operating conditions are captured by the liquid-to-vapour density ratio. Yu et al. [178] modified the constants and exponents of the Tran et al. [177] correlation to correlate flow boiling heat transfer results of water. Based on a database of 2505 data points involving 11 fluids for channel diameters down to 0.21 mm, Sun and Mishima [176] found that heat transfer coefficients varied weakly with vapour quality but exhibited a strong dependence on liquid-only Weber number. The proposed model retained the liquid Reynolds number in the Lazarek and Black [179] correlation and incorporated the liquid-to-vapour density ratio and liquid-only Weber number from Tran et al. [177] to further account for the effect of surface tension.

Another popular nucleate boiling heat transfer correlation is the Cooper correlation [159] developed for pool boiling applications.

$$h_{nb} = 55\, P_r^{0.12 - 0.434 \ln Rp} (-\log P_r)^{-0.55}\, M^{-0.5}\, q_w''^{\,0.67} \tag{2.1}$$

This has been adopted by several correlations including the Bertsch et al. [181], Mahmoud and Karayiannis [182], Eraghubi et al. [194] and Liu and Winterton [183]. Note that the roughness parameter used in Cooper's correlation, R_p, is the root mean square roughness of the surface, which is related to the average surface roughness by $R_a = 0.4\, R_p$ [195]. A nucleate boiling suppression factor is typically applied to the nucleate boiling heat transfer component to account for the suppression of active nucleation sites in the channel with increasing void fraction in the channels (see Section 4.2.2).

The reduced pressure ratio is formulated in Cooper's correlation to correlate system pressure. The average surface roughness, R_p, as well as the molecular weight of the working fluid, MW, are also employed in Cooper's nucleate boiling equation. The former accounts for the surface characteristics of the boiling surface, which has been shown to significantly influence heat transfer behaviour in microchannels [56] while the latter considers the working fluid in the boiling system. Docoulombier et al. [188], on the other hand, adopts a modified Cooper's nucleate boiling correlation proposed by Cheng et al. [196] for the flow boiling of CO_2.

Based on a large database of 10,805 data points for 18 working fluids, Kim and Mudawar [184] developed a asymptotic model to predict flow boiling heat transfer and proposed their own nucleate boiling relation partially based on P_r, the heated-wetted perimeter ratio and the single-phase liquid heat transfer coefficient. The reduced pressure term and the density ratio deals with different thermophysical properties of working fluids and difference in operating conditions. Additionally, the authors included the ratio of the heated perimeter to wetted perimeter, P_H/P_F, to adapt the prediction method for three-sided heating. Note that most methods use the Nu_3/Nu_4 multiplier in their models to account for different heating configurations. The term $(1 - x_e)$ simulates the suppression of nucleate boiling with increasing vapour quality, indicated by a drop in heat transfer coefficient with increasing vapour quality.

Choi et al. [163] correlated the nucleate boiling component with the boiling number, liquid Reynolds number and a modified Weber number. Weber number accounts for the influence of surface tension in microchannel flows. On the contrary, Kandlikar and Balasubramaniam [187] calculated the nucleate boiling component as a factor of the single-phase liquid heat transfer coefficient using the convection number, boiling number and a fluid-dependent parameter. Shah [150] also used the boiling number, convection number, along with the liquid-only Froude number to estimate nucleate boiling heat transfer.

Based on flow boiling experiments with fluid N_2, Qi et al. [192] found that the dominant heat transfer mechanism is nucleate boiling at vapour qualities below 0.3. Accordingly, a relation containing the boiling number, liquid-only Weber number, turbulent-turbulent Martinelli parameter and confinement number was proposed to predict heat transfer coefficients in this region. A dimensionless pressure parameter, K_p, was introduced to reflect the effect of system

pressure on heat transfer coefficients (heat transfer coefficients increased with increasing pressure).

2.7.2 Suppression Factor

A nucleate boiling suppression factor is normally applied to the nucleate boiling component in superposition models and asymptotic models, as noted in the Kim and Mudawar [184] correlation, where the suppression of nucleate boiling was directly related to the exit vapour quality, i.e. $(1 - x_e)$. Mahmoud and Karayiannis [182], Eraghubi et al. [194] and Liu and Winterton [183] proposed their respective suppression factors based on the work of Chen [180]. The Liu and Winterton suppression factor is given below as an example:

$$S = \frac{1}{1 + 0.055\, F^{0.1} Re_f^{0.16}} \tag{2.2}$$

The partial or total suppression of active nucleation sites is related to the liquid Reynolds number and dominance of the forced convection heat transfer mechanism, represented by the forced convection enhancement factor, F. The formulation of the enhancement factor is discussed in detail in Section 2.7.4. The suppression factor tends to zero, indicating total suppression of nucleate boiling at high mass flow rates and defaults to unity, i.e. pool boiling conditions at zero flow rate.

Shah [150] applies a suppression factor:

$$S = 1.8\, J^{-0.8} \tag{2.3}$$

where J is determined based on the liquid-only Froude number and convection number. The convection number is a modified from of the Martinelli parameter and includes the vapour quality and vapour-to-liquid density ratio.

2.7.3 Convective Boiling Mechanism

The convective boiling mechanism in flow boiling is typically estimated based on the single-phase liquid heat transfer coefficient [150], [181]–[183], [187], [188], [190], [197]. An enhancement factor, to account for the enhancement in two-phase convective boiling compared to single-phase liquid flow is generally employed. The correlations generally express the two-phase heat transfer coefficient in the form of the Nusselt number. This will be discussed separately in Section 2.7.4. A number of models, namely the Kandlikar and Balasubramaniam [187], Kim and Mudawar [197] and Shah [150] also estimates the nucleate boiling heat transfer component as a function of the single-phase liquid heat transfer coefficient.

Amongst these, the Dittus-Boelter single-phase liquid heat transfer coefficient relation is typically adopted.

$$h_{sp,f} = 0.023\ Re_f^{0.8} Pr_f^{0.4} \left(\frac{k_f}{D_h}\right) \tag{2.4}$$

Generally speaking, the liquid regime is in laminar flow conditions in microchannels due to the small channel diameter. Kandlikar and Balasubramaniam [187] determines flows at $Re_{fo} < 1600$ to be in the laminar condition while Mahmoud and Karayiannis [182] recommends $Re_{fo} < 2000$ for the determination of laminar flow. Nonetheless, as the flow velocity of the liquid regime in two-phase flow is typically enhanced due to channel confinement in microchannels, the Dittus-Boelter equation is used with reservation in most models.

Kandlikar and Balasubramaniam [187] and Lee and Mudawar [190] recommends calculating the single-phase heat transfer coefficient based on the all liquid laminar Nusselt number for three-sided heating.

$$h_{sp,f} = Nu_3 \left(\frac{k_f}{D_h}\right) \tag{2.5}$$

The correlation of Mahmoud and Karayiannis [182] that was developed solely for circular tubes (i.e. all sides heated) adopted Nu = 4.36 to calculate single-phase liquid flow heat transfer.

Bertsch et al. [181] cited low Reynolds numbers along with short channel lengths usually encountered in microscale two-phase flows and used the Hausen correlation [198] for developing laminar flows.

$$h_{sp,f} = \left(\frac{k_f}{D_h}\right)\left[3.66 + \frac{0.0668\left(\frac{D_h}{L_{ch}}\right)Re_{fo}Pr_f}{1+0.04\left[\left(\frac{D_h}{L_{ch}}\right)Re_{fo}Pr_f\right]^{2/3}}\right] \quad (2.6)$$

Some heat transfer correlations developed their own methods to directly estimate the two-phase convective boiling component. Choi et al. [163] proposed a correlation for FC-72 based on the liquid Reynolds number, modified liquid Weber number and confinement number. Similarly, Qi et al. [192] formulated a relation to estimate convective boiling heat transfer coefficient for vapour qualities above 0.3 for the flow boiling of N_2.

2.7.4 Enhancement Factor

The convective boiling mechanism is generally believed to be enhanced in two-phase flows due to the higher flow velocity in microchannels in comparison to single-phase liquid-only flow in the channels.

Chen [180] correlated the enhancement factor to the Martinelli parameter, which includes the viscosity ratio, density ratio and exit vapour quality. Note that the turbulent-turbulent Martinelli parameter was employed in the model. The Chen model was adopted by Eraghubi et al. [194]. Liu and Winterton [183] proposed an enhancement factor using the liquid Prandtl number, which represents the ratio of thermal and momentum transfer in a system.

$$F = \left[1 + x_e \, Pr_f \left(\frac{\rho_f}{\rho_g} - 1\right)\right]^{0.35} \tag{2.7}$$

The authors reasoned that the liquid Prandtl number is enhanced in two-phase flows due to the steeper temperature gradient between the saturated fluid and the wall temperature compared to single-phase flows. The effect of vapour quality and liquid-to-vapour density ratio were also included, derived from the two-phase multiplier based on the assumption of homogenous flow [100].

Mahmoud and Karayiannis [182] used the Martinelli parameter and the confinement number to express their enhancement factor.

$$F = \left(1 + \frac{2.812 \, Co^{-0.408}}{X_M}\right)^{0.64} \tag{2.8}$$

The enhancement factor decreases as the confinement number increases (i.e. smaller diameter) due to the damping of turbulence in the channel. The authors noted that the Martinelli parameter should be calculated based on actual flow conditions in the channel.

Similarly, Bertsch et al. [181] also concluded that higher channel confinement result in a smaller enhancement of the convective boiling mechanism. The vapour quality effect is correlated in a polynomial relation in the model and captures the increase in heat transfer

coefficient during the period of transition to annular flow, as well as the depreciation of heat transfer following the onset of dryout in the channels.

$$F = 1 + 80(x_e^2 - x_e^6) \text{ EXP } (-0.6 \text{ Co}) \quad (2.9)$$

Kim and Mudawar [197] expressed the convective boiling enhancement factor partly based on the turbulent-turbulent Martinelli parameter, vapour-to-liquid density ratio and the liquid-only Weber number. The latter accounts for the increased surface tension effect in microchannel flows. Similarly, Docoulombier et al. [188] calculated the enhancement factor for CO_2 based on the boiling number and turbulent-turbulent Martinelli parameter. Shah [150] and Kandlikar and Balasubramaniam [187] expressed their respective enhancement factors using the boiling number and convection number. The latter also included a fluid-dependent parameter to correlate the enhancement effect in convective boiling for different working fluids.

2.7.5 Two-Phase Enhancement-Factor Models

Enhancement-type models assume the two-phase heat transfer coefficient solely to be a factor of the single-phase liquid heat transfer coefficient, without differentiating between the nucleate and convective boiling mechanism. The empirical correlations are also generally expressed in the form of the Nusselt number. Enhancement factor correlations are also adopted in hybrid models [190]–[192].

Based on a large database of R134a flow boiling data with hydraulic diameters ranging from 0.19 to 8 mm, Fang [173] developed a two-phase heat transfer correlation based on the boiling number, liquid Reynolds number and liquid Prandtl number. The Fang number, Fa, which relates the interaction between the buoyancy, gravitational, surface tension and inertial forces during bubble departure was also included. Additionally, the authors used a liquid viscosity ratio, (μ_{lf}/μ_{lw}) evaluated at the fluid bulk temperature and wall temperature respectively, to correlate heat transfer data. A modified convection number, F, which considers the vapour quality and liquid-vapour density ratio was also employed.

Fang et al. [174] introduced a fluid dependent parameter and the molecular weight of the working fluid into their correlation to cope with the range of working fluids collected in their database. The Boiling number, Bond number and liquid-only Froude number were also correlated. The liquid-only Froude number was included to account for flow direction (horizontal or vertical). The liquid-vapour density ratio and reduced pressure ratio, which is able to capture the effect of system pressure, was also included.

Although Thiangtham et al. [117] found a dominance of nucleate boiling at low heat flux and an increased dominance of the convective boiling component at high heat fluxes, the authors proposed a correlation based on the nucleate boiling model of Tran et al. [177]. Li and Wu [191] established a criterion to classify macro and microscale heat transfer phenomenon based on the Bond number and liquid Reynolds number, $BdRe_f^{0.5}$. The Boiling number along with the liquid-only Reynolds number was accounted for in the macroscale correlation while the Bond number and liquid Reynolds number was considered in the microscale correlation.

Lee and Mudawar [190] identified three heat transfer regions: (i) bubble nucleation dominant region of x_e up to 0.05, (ii) bubbly/slug flow dominant region when $0.05 < x_e < 0.55$ and (iii) a liquid deficient heat transfer region when $0.55 < x_e < 1$. The heat transfer coefficient in the bubble nucleation region was correlated to the Martinelli parameter and single-phase liquid heat transfer coefficient based on three-sided heating (see Section 2.7.3). The boiling number and liquid-only Weber number were further introduced to predict the heat transfer coefficient in the bubbly and slug flow dominant region. As dryout was assumed in the liquid deficient region, the convective boiling to pure vapour was also considered alongside two-phase heat transfer coefficients in the annular flow regime prior to the incipience of dryout.

In conclusion, the Boiling number, liquid Reynolds number, Martinelli parameter, liquid-only Weber number and the liquid Prandtl number are popular parameters considered in two-phase heat transfer correlations. Additionally, the liquid-vapour density ratio and the reduced pressure ratio are also typically correlated. Incidentally, the nucleate boiling models [176]–[178] generally incorporates the Boiling number, liquid-only Reynolds number, liquid-only Weber number and liquid-vapour density ratio. Cooper's nucleate boiling model, adopted by several correlations [181]–[183], [194] to predict the nucleate boiling heat transfer coefficient, further considers the surface characteristics of the boiling substrate through the roughness parameter and the molecular weight of the fluid. The molecular weight of the fluid is also considered in the enhancement-factor model of Fang et al. [174]. The correlation, along with the Kandlikar and Balasubramaniam [187] also fitted experimental data for different working fluids and recommended fluid-dependent parameters in their models. The fluid dependent parameter was not specified for fluid HFE-7200 in both correlations.

2.8 Two-Phase Pressure Drop Correlations

Accurate prediction methods for flow boiling pressure drop in microchannels is an important design variable in pumped two-phase cooling loops. A good approximation of the pressure losses across the microchannel heat sink, along with the pressure penalty in the remainder of the circuit, allow for proper pump sizing and power consumption optimisation of the cooling system. Furthermore, two-phase pressure drop prediction models, alongside heat transfer prediction methods, that are able to capture experimental trends corresponding to changes in operating conditions are also crucial in establishing a safe range of operation where coolant delivery and the effectiveness of the thermal system are not compromised. Table 7.1 summarises the pressure drop correlations discussed in this section.

Pressure drop in horizontal two-phase flow configurations is made up of the frictional pressure loss and acceleration pressure loss components.

$$\Delta P_{tp} = \Delta P_{fric} + \Delta P_{acc} \tag{2.1}$$

Two main approaches are generally employed to predict two-phase pressure drop. These are the homogenous model and the separated flow model. The main differences between the two models are related to the determination of the friction factor and void fraction definitions adopted.

2.8.1 Homogeneous Flow Model

The homogenous flow model assumes that the liquid and vapour phases are sufficiently mixed and travel at the same velocity through a channel, i.e. slip ratio = 1. The model is generally an appropriate assumption applicable for flows in the bubbly flow regime, where the velocities of the dispersed vapour phase and liquid phase do not differ greatly. The frictional pressure drop is expressed in terms of a two-phase flow friction factor, f_{tp}, where f_{tp} is evaluated based on the two-phase Reynolds number, Re_{tp}, and is dependent on the mixture viscosity, μ_{tp}.

$$\Delta P_{fric} = \frac{2\, f_{tp}\, L_{sat}\, G^2\, v_f}{D_h} \left[1 + \left(\frac{x_e}{2}\right)\left(\frac{v_{fg}}{v_f}\right)\right] \tag{2.2}$$

$$Re_{tp} = \frac{G\, D_h}{\mu_{tp}} \tag{2.3}$$

Several definitions of two-phase viscosity are available in literature and affect the prediction of frictional pressure gradient greatly. Li and Hibiki [199] evaluated the performance of nine different mixture viscosity models, including the more widely accepted forms proposed by McAdams et al. [200] and Cicchitti et al. [201], in the homogeneous flow model for the prediction of 1029 frictional pressure drop datapoints collected from 8 working fluids. The assessment found large deviations, i.e. MAE ranging from ±1.2 to ±104 %, in the prediction accuracy of the homogenous flow model based on the definition of two-phase viscosity. Qu and Mudawar recommended $f_{tp} = 0.003$ in their investigation of water flow boiling in multi-microchannels.

Acceleration pressure drop based on the assumption of homogenous flows is expressed in terms of the homogeneous void fraction (see Eq. 2.4 and 2.5) [100]:

$$\alpha_v = \left[1 + \left(\frac{1 - x_e}{x_e}\right)\left(\frac{\rho_g}{\rho_f}\right)\right]^{-1} \tag{2.4}$$

$$\Delta P_{acc} = G^2 \nu_f \left[\frac{x_e^2}{\alpha_v}\frac{\rho_f}{\rho_g} + \frac{(1 - x_e)^2}{(1 - \alpha_v)} - 1\right] \tag{2.5}$$

Evidently, the prediction of pressure losses due to acceleration is dependent on the definition of void fraction. The homogeneous void fraction neglects the effect of interfacial shear and have been reported to overpredict acceleration pressure drop in comparison to other void fraction models adopted by separated flow models [202].

2.8.2 Separated Flow Model

Contrary to the homogeneous flow model, the separated flow model assumes that the liquid and vapour phase travel with different velocities through the channel and considers the flow properties in each phase individually, i.e. slip ratio ≠ 1.

Lockhart-Martinelli Based Correlations

Two-phase frictional pressure drop is expressed as a function of the single-phase liquid pressure drop and a two-phase multiplier, see Eq. (2.6).

$$\Delta P_{fric} = \frac{L_{sat}}{x_e} \left[\int_{x=0}^{x=x_e} \frac{2\, f_f\, G^2\, (1 - x_e)^2\, v_f}{D_h}\, \varphi_f^{\,2}\, dx \right] \tag{2.6}$$

Lockhart-Martinelli [203] first proposed the use of a two-phase frictional multiplier to estimate frictional pressure drop component in macroscale flows based on the assumption of separated model:

$$\varphi_f^{\,2} = \frac{\left(\frac{dP}{dz}\right)_{fric,tp}}{\left(\frac{dP}{dz}\right)_{fric,f}} \tag{2.7}$$

where φ_f^2 is ratio of the frictional pressure gradients of the two-phase and liquid phases. Chisholm [204] later proposed a theoretical basis for the two-phase multiplier based on the flow conditions of each individual phase, giving φ_f^2 as:

$$\varphi_f^{\,2} = 1 + \frac{C}{X} + \frac{1}{X^2} \tag{2.8}$$

where the value of C ranges from 5 to 20 depending on the laminar or turbulent regimes of the liquid and gas phase (see Table 7.1). X is the Martinelli-parameter:

$$X^2 = \frac{\left(\frac{dP}{dz}\right)_f}{\left(\frac{dP}{dz}\right)_g} \tag{2.9}$$

which is defined as the ratio of the pressure gradient of the liquid and gas phase respectively, that is, the liquid and vapour phase exist simultaneously and are assumed to flow alone in the channel.

Many of the presently existing correlations are based on the work of Lockhart-Martinelli and modification of Chisholm's empirical correlation of the C parameter for the prediction of microscale two-phase pressure drop [81], [199], [202], [205]–[209]. Mishima and Hibiki [205] included the effect of hydraulic diameter in the expression of C.

$$C = 21 \left[1 - e^{(-319\, D_h)} \right] \tag{2.10}$$

Based on the work of Mishima and Hibiki [205], Qu and Mudawar [206] and Lee and Garimella [81] further correlated the C parameter to mass flux. Dimensionless parameters such as the liquid-only Reynolds number is also a popular parameter used to correlate Chisholm's

parameter. Kim and Mudawar [202] noted a significant difference between the pressure drop trends of boiling and non-boiling microchannel flows, especially with regards to droplet entrainment in annular flows. The authors proposed C as a function of dimensionless parameters including the liquid-only Weber number, liquid-only Reynolds number, Boiling number and the gas-only Suratman number to account for the different flow structures based on a consolidated database of 9 working fluids in boiling and non-boiling mode (see Table 7.1). Keepaiboon et al. [207] studied the flow boiling pressure drop of R134a in single rectangular microchannel and modified C based on the liquid-only Reynolds number, confinement number and Martinelli parameter. Huang and Thome [208] produced empirical fits for the Chisholm parameter based on the liquid-only Reynolds number and gas Reynolds number. Markal et al. [209] considered the additional effects of aspect ratio and the saturated length in their C correlation. Li and Hibiki [199] applied the definition of two-phase viscosity given by McAdams et al. [200] to calculate Re_{tp} and proposed a correlation for the Chisholm parameter based on vapour quality and their own two-phase viscosity number, $N_{\mu tp}$. $N_{\mu tp}$ considers the effect of fluid density, surface tension and mixture viscosity. The authors suggested that non-uniform flow distribution tended to increase frictional pressure loss in multichannel arrays and proposed their C parameter specifically for the prediction of frictional pressure gradient in multichannel configurations. The abovementioned correlations are summarised in Table 7.1.

Chisholm's B-Coefficient Correlations

Based on the work of Baroczy [210], Chisholm [211] proposed a B-coefficient method, where the two-phase frictional pressure gradient is expressed as a function of the single-phase all-liquid pressure gradient and the all-liquid two-phase multiplier. This gives the two-phase frictional pressure loss as:

$$\Delta P_{fric} = \frac{L_{sat}}{x_e} \left[\int_{x=0}^{x=x_e} \frac{2\, f_{fo}\, G^2\, v_f}{D_h}\, \varphi_{fo}{}^2\, dx \right] \tag{2.11}$$

In Eq. (2.11), f_{fo} is the friction factor based on all-liquid flow, that is, as if the whole mixture flows as liquid, and the all-liquid multiplier, $\varphi_{fo}{}^2$, is defined as follows:

$$\varphi_{fo}{}^2 = 1 + \left(\Gamma^2 - 1\right) \left[B\, x_e{}^{0.875} (1 - x_e)^{0.875} + x_e{}^{1.75} \right] \tag{2.12}$$

B is a coefficient dependent on the mass flux and the value of Γ (see Table 7.1). Γ is the physical property coefficient defined by the authors as the ratio of the pressure gradients as a result of all-liquid and all-gas flow.

$$\Gamma^2 = \frac{\left(\frac{dP}{dz}\right)_{fo}}{\left(\frac{dP}{dz}\right)_{go}} \tag{2.13}$$

Tran et al. [212] found that Chisholm's B-coefficient method closely predicted their pressure drop data trend, obtained for the flow boiling of three refrigerants (R134a, R12 and R113) in 2.46 mm – 2.92 mm diameter tubes. To further improve the prediction of two-phase frictional pressure drop, the authors introduced a constant and recommended the replacement of B with the confinement number:

$$\varphi_{fo}{}^2 = 1 + \left(4.3\Gamma^2 - 1\right)\left[\, Co\, x_e{}^{0.875}\,(1 - x_e)^{0.875} + x_e{}^{1.75}\,\right] \tag{2.14}$$

Amongst the existing correlations, the pressure drop correlation proposed by Mishima and Hibiki [205] is regularly cited as one of the top performing models in the prediction of frictional pressure loss for microscale two-phase flows [57], [81], [206], [213]. Kim and Mudawar [202], who assessed a large database of 2378 pressure drop data points from various sources, noted that the Mishima and Hibiki [205] correlation was relatively successful in predicting a portion of data in the pressure drop database. Frictional pressure gradients above 10 kPa/m were found to be generally underpredicted while data points below 10 kPa/m were overpredicted by the correlation. In a more recent study, Huang and Thome [208] also concluded that the Mishima and Hibiki [205] model, alongside the Kim and Mudawar [202] and Lee and Garimella [81] correlations, had a tendency to underpredict the pressure drop data of R1233zd(E), R245fa and R236fa in a multichannel evaporator above 15 kPa. The macroscale Lockhart-Martinelli correlation has been found to overpredict two-phase pressure drop results in [57], [81], [202], [209].

As shown in Eq. (2.5), the void fraction is an important parameter for the prediction of the acceleration component in two-phase pressure drop. Channel void fraction is flow regime dependent, although transition effects between macroscale and microscale flows remains unclear. On one side, Kawahara et al. [214] concluded from their study of air-water flow in a 0.1 mm diameter tube that the slip ratio in microchannels could be several magnitudes higher than in channels with diameters greater than 1 mm. The dominant flow regime observed in the study was intermittent and semi-annular flow. Hence it would appear that the homogeneous flow assumption is inappropriate for channels smaller than 0.1 mm. On the other hand, Shedd [215] suggested that the void fraction behaviour approaches that of the homogeneous theory

with decreasing channel diameter. Based on this study, Cioncolini and Thome [216] further suggested that during the bubbly and slug flow regimes, reducing channel diameter could prevent slippage between the liquid and gas phase. This appears to agree with Triplett et al. [217], who found that the void fraction predicted using the homogeneous flow model matched the experimental measurements in the bubbly and slug flow regime well. In the churn and annular flow regime, the model generally overpredicted the experimental void fraction. On the contrary, Saisorn and Wongwises [218] studied the void fraction of air-water two-phase flow in a 0.53 mm tube, where the observed flow regimes were slug, churn and annular flow, and concluded that the homogeneous void fraction predicted the experimental data well.

Empirical void fraction correlations typically adopted by two-phase pressure drop correlations include the Lockhart-Martinelli [203], Zivi [219] and Chisholm [220] models. Whilst the abovementioned correlations are proposed for channels in the macroscale range, as indicated above, there is a lack of reliable void fraction correlations in the mini and microscale range and hence are typically adopted by microchannel pressure drop correlations [81]. Zivi's void fraction correlation is adopted by a large majority of correlations to predict acceleration pressure drop [81], [177], [202], [207]–[209], [221].

Despite the disagreement in void fraction behaviour in microscale two-phase flows, the choice of void fraction model may not be as critical in the prediction of two-phase pressure drop. As mentioned above, Kim and Mudawar [202] found that the void fraction correlation derived based on the homogeneous flow theory (see Eq. (2.4)) tended to overpredict acceleration pressure drop. However, other than the homogenous void fraction, the authors found a weak influence of void faction models on the prediction of acceleration pressure loss. The evaluation was based on 495 pressure drop datapoints and included void fraction correlations proposed by Lockhart-Martinelli [203], Zivi [219] and Rouhani and Axelsson [222]. The homogeneous void fraction resulted in a mean absolute error of almost ±50 %, while the void fraction correlations considering the separated flow model (i.e. slip ratio ≠ 1) produced fairly similar errors between ±15.1 to ±16.3 %.

Lockhart-Martinelli [203] proposed a void fraction correlation using the Martinelli parameter for turbulent liquid and turbulent gas flow, X_{tt} (see Table 7.1), mainly for the annular regime [100]:

$$\alpha_v = \frac{1}{1 + 0.28\ X_{tt}^{0.71}} \tag{2.15}$$

Zivi's void fraction correlation [219] is based on the principles of minimum entropy generation for an annular flow configuration under the conditions of zero wall friction and zero liquid entrainment:

$$\alpha_v = \frac{1}{1 + \left(\frac{1 - x_e}{x_e} \right) \left(\frac{v_f}{v_g} \right)^{2/3}} \tag{2.16}$$

Chisholm [220] developed his void fraction correlation based on void fraction measurements of steam-water two-phase flow:

$$\alpha_v = 1 + \left(\frac{1 - x_e}{x_e} \right) \left(\frac{\rho_g}{\rho_f} \right) \sqrt{(1 - x_e) \left(1 - \frac{\rho_f}{\rho_g} \right)} \tag{2.17}$$

2.9 Heat Transfer Enhancement using Surface Modifications

As covered in Section 1.2, main issues hindering the adoption of flow boiling in microscale heat sinks for high heat flux thermal management include flow instability, high boiling incipience temperatures, wall dryout and low critical heat flux limits. Yen et al. [58] demonstrated that the boiling incipience superheat could be up to 70 K using fluids R123 and FC-72 in stainless steel microtubes of diameters 0.19 mm – 0.51 mm. As an example, in a two-phase system using water, surface temperatures on the heat sink could overshoot to up to 170 °C before two-phase cooling commences, which exceeds the junction temperature of military electronics (up to 125 °C). As a matter of fact, water is not a suitable working fluid for the two-phase cooling of commercial electronics (where junction temperatures are typically 85 °C) due to its high boiling temperature (i.e. 100 °C at atmospheric pressure). Employing water below atmospheric pressure increases the boiling wall superheat further, as demonstrated in [56]. Furthermore, rapid bubble growth in the highly superheated liquid could trigger explosive boiling in the channels, leading to large pressure and temperature oscillations in the heat sink which may affect heat transfer performance [7], [128]. For the flow boiling of water in parallel silicon microchannels, Hetsroni et al. [128] found that the onset of boiling was followed closely with a periodic cycle of rapid bubble expansion, flow reversal, wall dryout and rewetting in the channels. As expected, dryout phenomenon typically has a detrimental effect on flow boiling heat transfer coefficients.

Some of these issues relate directly to bubble nucleation dynamics, surface characteristics and fluid wettability of the channel substrate. Through fundamental studies, mostly in pool boiling, it is widely accepted that surface defects and imperfections are favourable sites for bubble nucleation due to vapour entrapment [56]. As such, surface modification techniques such as altering surface roughness using sandpaper treatment, fabrication of artificial cavities and surface coatings have been employed to produce surface topologies with nucleation sites that may help to lower boiling incipient superheat, augment heat transfer and improve the critical heat flux limit in two-phase microchannel systems. This was briefly covered in Section 2.3.1. Surface modification techniques to improve two-phase heat transfer performance are thoroughly reviewed for both pool and flow boiling in Shojaeian and Kosar [223] and more recently for flow boiling, covering both macro and microscale, in Liang and Mudawar [224]. Khan et al. [225] also presented a critical review of micro and nanoscale surface coatings for

heat transfer enhancement in the nucleate boiling regime, which was focused more on pool boiling.

In all, the authors concluded that modified surfaces have the potential to lower boiling incipient wall superheat, suppress flow instabilities, enhance heat transfer performance (especially in the nucleate boiling region), and extend the critical heat flux limit of boiling systems. These may be achieved through (i) the integration of microscale features or artificial nucleation sites on the boiling surface, (ii) an increase in nucleation site density as well as (iii) altered surface wettability on modified surfaces compared to smooth surfaces. Enhanced capillary wicking also contributed to delaying critical heat flux phenomenon. Additionally, the lower degree of wall superheat at the onset of boiling on modified surfaces, including secondary microstructures in microchannels, could help suppress two-phase flow instabilities in multi-microchannel heat sinks, as reviewed in Prajapati and Bhandari [139]. The use of inlet restrictors have also been demonstrated to mitigate flow boiling instabilities and improve critical heat flux limit, although at a significant cost of pressure drop [226] and even decreased heat transfer performance in microchannel heat sinks [227].

The use of artificial cavities may provide stable nucleation sites that are triggered at low wall superheats and sustain stable flow regimes in the heat sink. Li et al. [75], [76] and Zeng et al. [77] both found significant enhancements in heat transfer and critical heat flux performance using artificial cavities compared to regular microchannel configurations. Boiling incipience wall superheat were also lowered significantly using artificial cavities. Li et al. [75], [76] reported a 300 % enhancement in heat transfer coefficient due to the promotion of bubble nucleation and detachment using triangular cavities on the channel side walls. Wall superheat at the onset of boiling in the enhanced heat sink was up to 17 K lower compared to the straight channels. Furthermore, flow reversal typically observed in confined annular flow, which resulted in large fluctuations in wall temperature, and two-phase pressure drop was lowered by as much as 50 % due to flow area enlargement as well as stable bubbly/slug flow using the cavities. Similarly, Zeng et al. [77] fabricated re-entrant cavities on the side walls of V-shaped channels using a specially designed tool. Boiling incipience wall superheat was reduced slightly by 1 K, i.e. from 3.1 K to 2.1 K in the channels with re-entrant cavities. Heat transfer coefficients at the outlet of the heat sink was improved significantly compared to the plain V-shaped channels at high vapour qualities, as the re-entrant cavities sustained annular flow without dryout for a larger range of vapour qualities. Contrary to [75], the pressure drop penalty

was up to 78.1 % due to liquid retention in the cavities and additional friction losses in the enhanced channels. Interestingly, the authors reported that flow reversal was retarded by the sharp corners of the re-entrant cavities on the side walls. Accordingly, oscillations in pressure and temperature was lower in the heat sink with the re-entrant cavity array.

Deng et al. [78] employed several stages of micro-milling at different angles to fabricate a pin-fin interconnected re-entrant microchannel heat sink. The authors obtained an enhancement in heat transfer coefficient of between 39 % to 284 % for water and 29 % to 220 % for ethanol. This was attributed to the break-up of long slugs by the diamond pin-fins, which would otherwise suppress further bubble nucleation in the channels. Wall superheats were relatively low in the re-entrant microchannels, between 0.4 K to 3 K in both water and ethanol tests. Integrating micro pin-fins on the bottom walls of microchannels, Deng et al. [80] obtained enhancements of between 10 % to 105 % using water and between 90 % to 175 % using ethanol as the working fluid. The authors noted that the cavities induced capillary forces and introduced wicking effects which helped rewetting and prevented dryout on the channel walls, thus enhancing heat transfer coefficients even at high heat fluxes and vapour qualities. Flow instabilities were mitigated using with the micro pin-fin structure on the channel bottom and were attributed to stable nucleation and reduced occurrence of wall dryout.

Whilst artificial cavities and re-entrant cavities have shown promising results in improving two-phase heat transfer characteristics, they are complex and time consuming to fabricate by conventional micro-machining techniques. As mentioned above, Deng et al. [78] machined re-entrant cavities using different milling angles while Zeng et al. [77] designed a bespoke tool to fabricate their re-entrant cavities. On the other hand, surface coatings are easier to apply to conventionally-machined microchannel heat sinks but could provide similar benefits in terms of increased nucleation site density and promotion of stable flow regimes that may enhance heat transfer performance as well as delay the occurrence of critical heat flux. These methods include sintering, spray pyrolysis, chemical etching, chemical vapour deposition, nanofluid boiling etc., which are more versatile and quicker to implement in existing systems. Khan et al. [225] concluded that surface coatings are a promising heat transfer enhancement technique, with sintered copper particle coatings yielding between 4.5 to 5 times the pool boiling critical heat flux of unmodified surfaces. Critical heat flux enhancements of other porous coatings including of zinc oxide, diamond and alumina particles ranged between 1.3 to 3.5 times. Pool boiling heat transfer coefficients were up to 4.5 times the value obtained on bare surfaces.

Liang and Mudawar [224] also noted that micro-porous coatings were successful in improving flow boiling heat transfer as well as critical heat flux behaviour in macroscale and microscale channels. Sun et al. [228] recorded a 178 % increase in the subcooled flow boiling heat transfer coefficients of water using a porous copper particle coating in microtubes while Yang et al. [229] demonstrated an improvement of over 300 % in the critical heat flux of water in parallel microchannels using a silicon nanowire coating. Not surprisingly, modifications to the surface topology of channels could induce higher pressure losses especially in microchannels due to higher shear stress on the coated channel walls, as found in [230], [231]. Nevertheless, reductions in pressure drop, owing to stabilised bubble growth and liquid films, have equally been reported in [232], [233]. An efficient heat transfer coating should induce reasonable pressure drop penalty in proportion to the yield in heat transfer enhancement.

Importantly, heat transfer coatings must be able to withstand the test of time as well as durability in a wide range of operating conditions. Khan et al. [225] urged future investigations into cost improvement and importantly, the durability of heat transfer coatings, which would hinder the practical implementation of the enhancement technique. Reliability concerns, especially of nanoscale heat transfer coatings were also highlighted in Liang and Mudawar [224], in their review of surface modifications for flow boiling enhancement. Particularly for the case of flow boiling, deformation of carbon nanotubes [234], [235] and gradual detachment of nanoparticle coatings [236], [237] have been reported at high mass fluxes as well as following the occurrence of critical heat flux. It would appear that microscale enhancement techniques, i.e. features ranging between 1 μm to 1000 μm, including micro-fins, artificial cavities and micro-porous coatings appear to have higher long-term reliability compared to nanoscale surface modifications. As mentioned above, micro-fins and artificial cavities require much more complex manufacturing techniques and may inflate cost and manufacturing lead times considerably.

Furthermore, surface coatings may be used to alter surface wettability in order to influence boiling behaviour. However, there appears to be contradictory reports on the effects of surface wettability (i.e. hydrophobic or hydrophilic) on flow boiling heat transfer [224], [238]. For instance, Choi et al. [239] found that for the flow boiling of water in a 0.5 mm diameter tube at low mass flux (i.e. 25 kg/m^2 s) and for vapour qualities below 0.2, the hydrophilic surface exhibited higher heat transfer coefficients compared to the hydrophobic surface studied. Elongated bubble flow developed quickly in the hydrophilic channel, whilst a larger number

of isolated bubbles were observed in the hydrophobic channel. The lower heat transfer coefficients were attributed to dry patches beneath bubbles, whose departure was hindered due to the hydrophobicity of the surface. On the other hand, the opposite trend is observed at vapour qualities beyond 0.2, i.e. heat transfer coefficient obtained on hydrophobic surface is higher than the hydrophilic surface. The authors observed that at higher vapour qualities, the elongated bubble regime in the hydrophobic surface was characterised with an unstable liquid film. Heat transfer enhancement was associated with the unstable motion of the liquid film, which was also believed to have delayed the occurrence of wall dryout in the hydrophobic channel. However, at higher mass flux conditions in the study, i.e. 75 kg/m^2 s, the hydrophobic surface outperformed the hydrophilic surface across the range of vapour quality investigated (i.e. between 0 to 0.3). The nucleation density on the hydrophobic surface was, as before, comparatively higher in relation to the hydrophilic surface. Moreover, flow visualisation showed that the nucleation activity in the hydrophobic channel was somewhat lower at the higher mass flux condition compared to the low mass flux condition. Bubbles departed more easily due to the higher mass flux in the hydrophobic channel. Evidently, there is an interplay between surface wettability and operating conditions such as mass flux and vapour quality on bubble growth and flow pattern development, which in turn have significant impacts on flow boiling heat transfer.

The majority of fundamental studies published about wettability effects on bubble nucleation behaviour have been studied in pool boiling mode. Whilst pool boiling studies do not consider the effect of wettability on flow patterns that may be critical to flow boiling heat transfer behaviour, these studies nevertheless provide insights to the basic processes of bubble formation as well as nucleate boiling dynamics in flow boiling systems. For the case of pool boiling, hydrophilicity generally improves nucleate boiling heat transfer coefficients by encouraging rapid bubble detachment and enhanced rewetting mechanism post bubble departure. However, hydrophilic surfaces tend to flood surface cavities, leading to high wall superheats at the inception of boiling. On the contrary, hydrophobic surfaces induce the onset of boiling at relatively low wall superheats as trapped vapour pockets are easily formed on surface cavities, albeit at the expense of low critical heat flux due to the bubble coalescence and the subsequent formation of a vapour blanket above the boiling substrate.

In terms of bubble growth and nucleation activity, Phan et al. [240] found a strong influence of surface wettability on bubble departure as well as bubble generation frequency.

Additionally, pool boiling heat transfer coefficients of water peaked at specific contact angles (i.e. at a contact angle of 0° or 90°). In their review of wettability effects on two-phase heat transfer, Choi and Kim [238] concluded that in pool boiling, high wettability tended to decrease the number of active nucleation sites as well as bubble departure frequency. Accordingly, hydrophobic surfaces resulted in higher heat transfer coefficients in the nucleate boiling region. On the other hand, near the critical heat flux condition, hydrophilic surfaces encouraged liquid rewetting and helped extend the critical heat flux limit. As such, biphilic surfaces, i.e. surfaces with distinctive hydrophilic and hydrophobic regions, have been investigated to enhance critical heat flux in pool boiling by delaying the formation of a vapour blanket on the surface [241], [242].

A flow boiling study conducted by Kim et al. [243] involved the use of biphilic surfaces for the flow boiling of water in a 7.5 mm diameter channel, i.e. macrochannel. The authors employed a series of hydrophobic coating patterns of variant configurations in width and orientation to manipulate bubble confinement and merging behaviour, and obtained varying degrees of enhancement in flow boiling heat transfer as well as critical heat flux using the different patterns through the encouragement of the break-up of merged bubbles. Biphilic surfaces could combine the advantages of both hydrophobic and hydrophilic surfaces, yielding low boiling inception wall superheat as well as delaying the occurrence of critical heat flux. Such surfaces would be beneficial to microchannel flow boiling where, due to manufacturing processes, channel surfaces may be quite smooth, without adversely affecting the critical heat flux value and narrowing the range of operation of the microchannel device.

In summary, porous coatings is an easy method to alter surface characteristics in order to influence bubble nucleation and flow boiling heat transfer behaviour, firstly through the increase in nucleation site density and secondly through the modification of surface wettability. With regards to the former, the size of pores may be optimised based on nucleation theory, for e.g. Hsu's model [109], which is dependent on various fluid properties such as vapour density, surface tension, as well as operating parameters including saturation temperature, bulk liquid subcooling degree and degree of wall superheat. Designing re-entrant cavities based on Hsu's effective cavity range for water, Kuo and Peles [101] suppressed flow instabilities related to rapid bubble growth (found to be triggered by high boiling incipience wall superheat) in their silicon microchannel array. This indicate that particle sizes and porous structures of heat

transfer coatings may be optimised to result in favourable cavities within the active nucleation range for specified working fluids and operating conditions in microchannels.

In terms of the effect of surface wettability on bubble nucleation, fundamental studies in pool boiling suggest that hydrophobic surfaces trigger early onset of boiling due to entrapped vapour pockets in cavities but have low critical heat flux due to dryout phenomenon. On the contrary, hydrophilic surfaces typically exhibit higher boiling incipience wall superheat as cavities are easily flooded, but also higher critical heat flux values due to channel rewetting mechanism. In flow boiling, the effect of surface wettability on heat transfer behaviour is more complex owing to the influence of flow patterns and channel mass flux, as shown in the results reported by Choi et al. [239]. Biphilic surfaces incorporating the benefit of both hydrophobic and hydrophilic surfaces on bubble nucleation behaviour have been demonstrated for the flow boiling of water in macrochannels by Kim et al. [243]. The effect of surface modifications, particularly with the use of porous coatings, on microchannel flow boiling behaviour at different operating conditions, as well as the influence of various parameters of the coating structure, including coating thickness and particle diameter, are discussed in detail in Sections 2.9.1 to 2.9.3.

2.9.1 Effect on the Onset of Boiling

It is widely accepted that bubble nucleation is initiated, with sufficient wall superheat, on surface cavities with pre-existing trapped gases. In fact, such surface cavities may be optimised based on nucleation models, such as the theoretical model proposed for pool boiling by Hsu [109], which were modified for flow boiling in Davis and Anderson [244] and Kandlikar [245].

In the model developed by Hsu [109], the authors assumed that bubble nucleation may be sustained from a particular cavity if the temperature of the surrounding liquid, more specifically at the height of the bubble, is at least the temperature of vapour inside the bubble. The bubble temperature was determined based on the Clausius-Clapeyron and Young-Laplace equation. It is a function of fluid parameters including the vapour density, surface tension, saturation temperature and latent heat of vapourisation, as well as the vapour pressure inside the bubble and radius of the bubble. The height of the bubble was assumed to be 1.6 times the cavity radius, which gives a corresponding contact angle of 53.1°. Based on the assumptions above, the range of active nucleation sites may be predicted as follows:

$$r_{c\,(max,min)} = \frac{\delta_t}{4} \frac{\Delta T_{sup}}{(\Delta T_{sup} + \Delta T_{sub})} \left[1 \pm \sqrt{1 - \frac{12.8\,\sigma\,T_{sat}\,(\Delta T_{sup} + \Delta T_{sub})}{\delta_t\,\rho_g\,i_{fg}\,\Delta T_{sup}^{\,2}}} \right] \tag{2.15}$$

where δ_t is the thickness of the thermal boundary layer, ΔT_{sub} is the degree of subcooling and ΔT_{sup} is the degree of wall superheat. The thermal boundary layer thickness was obtained using transient conduction equations in the original work of Hsu [109] , but may also be estimated based on the liquid thermal conductivity and single-phase liquid heat transfer coefficient calculated from fully-developed laminar flow (Nu = 4.36) [56].

From Eq. (2.15), the finite range of active nucleation sites is a function of fluid properties including surface tension, σ, latent heat of vapourisation, h_{fg}, and vapour density, ρ_g, as well as the system subcooling, wall superheat and the thermal boundary layer thickness. The model is applied for HFE-7200 and water in Figure 2.1 for wall superheat degrees of up to 30 K, for a saturation temperature of 75 °C with zero degree system subcooling. The channel hydraulic diameter was taken as 475 µm. The corresponding saturation pressures of HFE-7200 and water at this temperature are 1 bar and 0.39 bar respectively.

The point at the tip of the curve may be interpreted as the cavity size and minimum wall superheat for the onset of nucleate boiling in a given system. The main conclusions are as follows: (i) superheat is required before a cavity may be activated and (ii) for a given range of wall superheat, only a finite range of cavities may become active nucleation sites. Importantly, the nucleation cavity range is also a strong function of fluid properties, as shown by the large difference in nucleation range between water and HFE-7200. Water typically nucleates in cavities larger than 1 µm while HFE-7200 will nucleate from cavities one magnitude smaller in the channel (less than 0.1 µm). Thermophysical properties of different working fluids in turn exhibit different degrees of sensitivity to changes in the saturation temperature of a system.

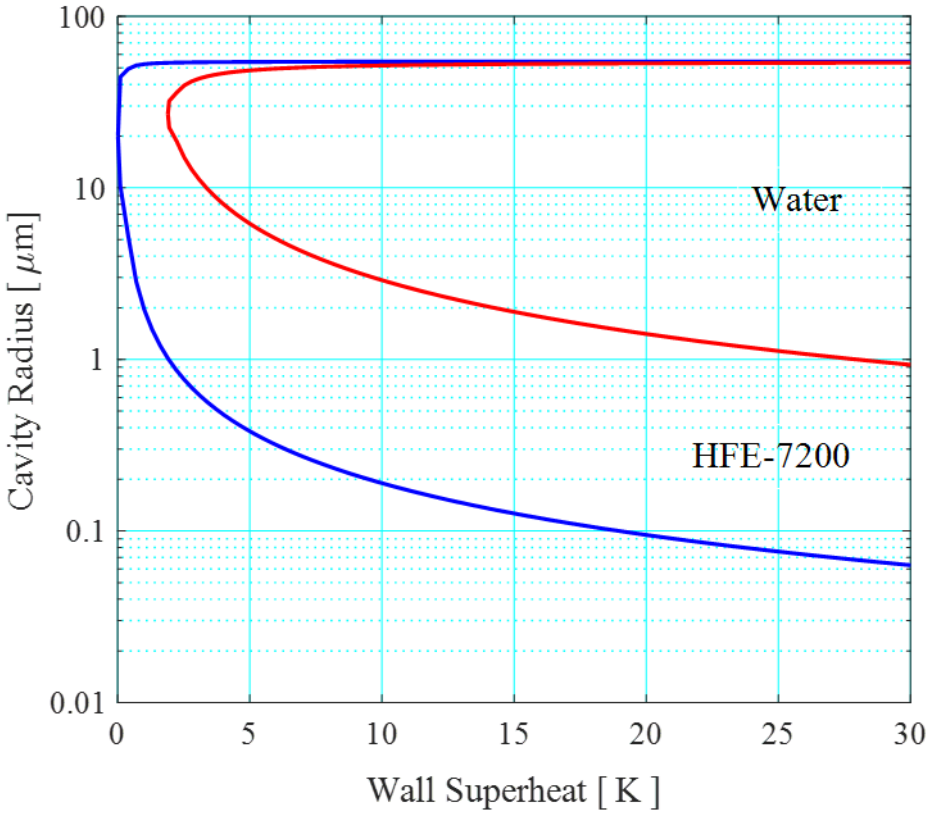

Figure 2.1: Active nucleation range of water and HFE-7200 in a 475 µm hydraulic diameter channel at a saturation temperature of 75 °C with zero degree system subcooling for wall superheat degree up to 30 K.

Additionally, in flow boiling systems, changing the operational mass flux will also affect the thermal boundary layer thickness [246]. Increasing the system mass flow rate reduces the thermal boundary layer thickness, which delays the onset of nucleate boiling, thus narrowing the range of active nucleation sites [245], [247]. Liu et al. [247] studied the flow boiling of

water through a microchannel with a width and depth of 275 μm and 636 μm respectively using high speed imaging and found higher boiling incipience wall heat fluxes at higher flow velocities. Increasing system subcooling was also found to result in a delay in the onset of boiling and hence narrowed the active cavity range. Kandlikar et al. [245] also found that the range of active nucleation sites shrink considerably and is eventually suppressed with increasing flow rate. From their experimental investigations, Liu et al. [247] proposed an analytical model for boiling incipience heat flux, which included the effects of contact angle and channel diameter. The boiling incipience heat flux and range of nucleation sites were marginally affected by changes in the contact angle, but exhibited dependency on the channel diameter. Decreasing the channel diameter triggers boiling incipience at lower wall heat fluxes and resulted in a larger active cavity range. However the effect of channel dimension may diminish with increasing channel width [85], [246].

Kandlikar [134] compared several nucleation models, including the pool boiling model of Hsu [109] and flow boiling models [109], [134], [244], [248], with the flow boiling nucleation data for water in a 1 mm x 40 mm minichannel. Notably, the model of Kandlikar et al. [134] is based on the receding contact angle and the static contact angle is introduced as a variable (rather than a constant of 53.1° as in Hsu's model) in the model proposed by Davis and Anderson [244]. The assessment showed that all models predicted a similar range of cavities for the flow boiling of water, including the pool boiling model of Hsu [109], and showed only some deviation at low wall superheat and cavity radius above 4 μm for water at 80 °C. This implies that the nucleation range is not very sensitive to changes in contact angle. Liu et al. [247] also reported low sensitivity to contact angle in their study. As such, many flow boiling studies adopt the nucleation theory of Hsu [109] to explain flow boiling phenomena [56], [101], [249].

Nevertheless, contact angle still plays an important role in nucleation dynamics on heated surfaces. Hydrophobic surfaces are generally more likely to trap vapour pockets within cavities, leading to lower degree of superheat at the onset of boiling, while cavities in hydrophilic surfaces tend to be flooded more easily and thus have higher boiling incipience wall superheat. Note that the critical heat flux limit is also typically lower on hydrophobic surfaces, due to wall dryout. It is thus not surprising that surface modifications to enhance the onset of flow boiling are more effective in cases where the mechanism of bubble ebullition is dominated by surface cavities. In certain cases, modifying the topography of the boiling surface

may not have a significant influence on boiling incipience wall superheat. This was the case in Yang et al. [250], where relatively small degrees of boiling incipience wall superheat of around 1 K to 3 K was measured in their silicon microchannel array. Incorporating a silicon nanowire coating did not appear to reduce the degree of wall superheat any further, since bubble generation was controlled by cavitation rather than cavity nucleation.

Phan et al. [251] investigated the effect of surface wettability on the flow boiling of water at atmospheric pressure in single microchannels with characteristic widths and heights of 5 mm and 0.5 mm respectively. The surface wettability was altered by depositing a layer of (i) silicone oxide (SiOx), (ii) titanium (Ti), (iii) diamond-like carbon (DLC) and (iv) carbon-doped silicon oxide (SiOC) on a Pyrex wafer base. The static contact angles of water, measured at room temperature, on the above-mentioned surfaces are 26°, 49°, 63° and 104° respectively (i.e. coated surfaces are in the order of decreasing wettability). The study found that boiling incipience wall superheat decreased with increasing contact angle. In other words, low wettability is favoured for the onset of nucleate boiling due to vapour entrapment from cavities on hydrophobic surfaces. This agrees with the majority of pool boiling studies on wettability effects. However, due to rapid bubble coagulation in the channels after the onset of boiling on hydrophobic surfaces, the authors recommended the use of heterogeneous surfaces (i.e. high wettability surface with artificial hydrophobic nucleation sites) to sustain low wall superheat at boiling incipience and promotes bubble detachment from cavities. As a matter of fact, surfaces with heterogeneous wettability have been investigated in Betz et al. [241] for pool boiling and Kim et al. [243] for flow boiling in macrochannels with promising results in heat transfer enhancement.

Accordingly, wall superheat at the onset of boiling may be reduced on modified surfaces by between 6 K to 8 K, as reported in [228], [230], [252] for various working fluids. Bai et al. [230] sintered copper particles (particle diameters ranging from 30 μm to 90 μm) on the bottom surface of copper channels (0.54 mm hydraulic diameter) and obtained a reduction in boiling incipience wall superheat of around 8 K (from nearly 55 K) with the coating. The lowest wall superheat at the onset of boiling was observed on the 55 μm diameter coating and the working fluid employed was ethanol. For the flow boiling of water in Sun et al. [228], the wall superheat at the onset of boiling was reduced from 9.5 K on the polished surface to 3.5 K compared to the surface with a 120 μm particle size coating applied, i.e. by 62 %. A 51 % and 59 % reduction in wall superheat was obtained on with the 35 μm and 240 μm particle coatings respectively.

Similarly, comparing the flow boiling of FC-72 on polished and coated channels at a nominal mass flux of 700 kg/m^2 s, Sun et al. [252] found a reduction of boiling incipience wall superheat by 4.7 K – 7.4 K from 10.6 K on the polished surface using 20 µm, 50 µm and 120 µm particle diameter coatings. The smallest wall superheat was measured on the 50 µm coated surface. The lowered wall superheat degrees were directly attributed to the increase in nucleation site density on the boiling surface.

Importantly, the studies above also highlight the influence of particle diameter and the resulting cavity size on surfaces on triggering the onset of boiling in different working fluids. With water, the optimum particle size was found to be 120 µm [228] while for FC-72 and ethanol, the optimum particle size was comparatively smaller at around 50 µm [230], [252]. This shows that the surface topography and porous structure of coatings should be considered carefully when modifying surfaces for boiling.

For instance, Morshed et al. [236] reported a delay in the boiling initiation of water on a nanoparticle deposited surface. In the study, nanoparticles were deposited on a 0.36 mm x 5 mm channel through the pool boiling of ethanol-based alumina nanofluid (Al_2O_3) on a copper surface. The contact angle of water reportedly reduced from 97° on the bare copper surface to 57° on the coated surface (i.e. increased wettability). The authors noted that the nanoparticles clogged the existing cavities on the bare copper surface, which in effect reduced the nucleation site density on the boiling surface. Khan et al. [225] also noted that nanoparticle deposition is more difficult to control with the nanofluid boiling method. Furthermore, due to high shear forces in the elongated bubble regime, the nanoparticle layer detached gradually with fluid flow. This raises concern over the reproducibility of heat transfer enhancement after prolonged operation. In a recent review of surface modification techniques by Liang and Mudawar [224], concerns over the consistency of heat transfer performance using surface treatments by means of nanoparticle deposition were also raised for similar reasons.

2.9.2 Effect on Heat Transfer Performance

Varying degrees of flow boiling heat transfer enhancement has been achieved with the use of porous coatings in mini- and microchannels. Studies have found that the enhancement effect could be influenced by channel dimensions, coating particle diameter, coating thickness and the operating parameters such as working fluid, mass flux, heat flux and vapour quality. These will be discussed in further detail in Sections 2.9.2.1 – 2.9.2.6.

2.9.2.1 Effect of Wettability

As indicated above, heat transfer phenomenon have been demonstrated to be strongly related to the wettability of a fluid on the boiling substrate, especially in microscale flows where surface tension and viscous forces are more dominant compared to inertial forces. Cubaud et al. [253] conducted a fundamental study into the effects of surface wettability on microscale two-phase flow patterns in 0.53 mm square channels and concluded that two-phase flow morphologies in microchannels are significantly influenced by surface modifications. In hydrophilic flows, gas bubbles were dispersed in the liquid phase while in hydrophobic flows, they were trapped in the channel corners. Slug and annular flow were more common in hydrophilic flows while plug flow prevailed in hydrophobic flows. Note that the wettability of a surface is classified such that the surface is (i) hydrophilic if the contact angle of a liquid on a solid substrate is less than 90°, (ii) superhydrophilic if the contact angle is around 0°, (iii) hydrophobic if the contact angle of a liquid on a solid substrate is between 90° and 150° and (iii) superhydrophobic if the contact angle is more than 150° [254].

Authors in [235], [251], [255] found that hydrophobic porous surfaces were more favourable towards nucleate boiling phenomenon due to vapour entrapment in the cavities. However, high rates of bubble coalescence following more active nucleation activity may also be detrimental, as they induce wall dryout and deteriorate heat transfer coefficients [251]. On the other hand, studies in [232], [233], [250], [256]–[258] reported enhanced flow boiling heat transfer performance with hydrophilic surfaces. The improved heat transfer performances were attributed to higher bubble generation activity from the porous surfaces, leading to the formation of capillary-induced annular flow in [233], [250], as well as enhanced rewetting mechanisms, which prevent wall dryout in [232], [256]–[258].

Choi et al. [239] studied the effect of wettability on the flow boiling of water in a 0.5 mm hydraulic diameter channel. The measured contact angle of water on bare photosensitive glass was 25°, i.e. hydrophobic, while the contact angle measured on an octadethyltrichrolosilane (OTS) coated glass surface was increased 105°, i.e. hydrophilic. The investigation concluded that at a fixed mass flux condition, the hydrophilic surface triggered local dryout at lower vapour qualities compared to a hydrophobic surface. Heat transfer coefficients dropped dramatically after dryout. Elongated bubbly flow was predominant in the hydrophilic channel while annular flow prevailed in the hydrophobic channel. Furthermore, flow visualisation showed that the annular liquid film was unstable and bubble nucleation was observed in the film, leading to higher heat transfer coefficients in the hydrophobic channel.

As covered previously, Phan et al. [251] investigated the effect of surface wettability on the flow boiling of water using SiOx, Ti, DLC and SiOC coatings, in the order of increasing wettability. Local heat transfer coefficients peaked in the bubbly and slug flow regime, and depreciated sharply with flow pattern transition to semi-annular flow with increasing vapour quality due to intermittent wall dryout in the Ti, DLC and SiOC coated channels. However, local heat transfer coefficients did not appear to vary significantly with increasing vapour quality in channel with the SiOx coating and resulted in lowest heat transfer coefficients in relation to the other coatings. The SiOx surface exhibited the highest wettability property in the study. Furthermore, the hydrophobic SiOC surface triggered subcooled boiling in the channels due to the high amount of trapped vapour in the cavities. However, as mentioned above, the high bubble generation activity resulted in rapid bubble coalescence which quickly induced wall dryout, leading to deterioration in heat transfer coefficients in the channel.

Sujith-Kumar et al. [258] investigated spray pyrolyzed iron-doped aluminium oxide and titanium oxide (Fe-Al_2O_3-TiO_2) composite coatings with different concentrations of iron to vary the surface wettability of a copper minichannel (30 mm in length, 20 mm in width and 0.4 mm in height). The thickness of the coatings were around 20 μm. The contact angle of water on the sand-blasted copper surface was 75.5° and decreased with increasing Fe concentration to 40.1° at 7.2 % concentration (i.e. more hydrophilic). Accordingly, porosity increased from 45 % to 72 % corresponding to 0 % and 7.2 % Fe concentration. All of the enhanced surfaces resulted in higher heat transfer coefficients at a given mass flux condition. The largest percentage enhancement in the heat transfer coefficient of water was 44.1 % at boiling incipience for a mass flux of 88 kg/m^2 s. This was directly linked to the higher density of

nucleation sites as well as enhanced liquid rewetting on the 7.2 % Fe-doped surface, which exhibited the highest porosity and highest wettability from the surfaces investigated.

Combining both properties, Nedaei et al. [259] used two coatings, namely pHEMA (hydrophilic) and pPFDA (hydrophobic) coatings, in 0.5 mm diameter stainless steel microtubes and accessed its effects on the flow boiling of water. One microtube was coated with pHEMA at the inlet and pPFDA at the outlet, i.e. hydrophilic inlet/hydrophobic outlet. The other microtube had the opposite configuration, i.e. hydrophobic inlet/hydrophilic outlet. Both configurations resulted in enhanced heat transfer coefficients compared to the plain stainless-steel tube, with the hydrophobic inlet/hydrophilic outlet resulting in a higher enhancement effect. Bubble nucleation was encouraged and occurred at a more upstream location in the hydrophobic inlet/hydrophilic outlet tube. The hydrophilic nature at the outlet end of the tube, on the other hand, promoted rewetting and mitigated wall dryout, which the authors believed was prone to occur near the outlet due to high surface temperatures. The authors also found that both coating configurations performed better compared to their previous work in Kaya et al. [256], solely with the pHEMA coating.

2.9.2.2 Effect of Vapour Quality

In certain cases, heat transfer enhancement using porous coatings may only be effective over a certain vapour quality range, as reported in [230], [250], [252]. Sun et al. [252] observed an increase in outlet flow boiling heat transfer coefficients by up to 692 % using a sintered copper coating layer with a mean particle diameter of 50 µm on the bottom surface of a 0.9 mm hydraulic diameter channel and fluid FC-72. The highest augmentation was obtained at low vapour qualities just after the onset of boiling, i.e. $x \sim 0.1$, and depreciated steeply with increasing vapour quality. The decrease in heat transfer coefficients with vapour quality in the coated section was attributed to bubble confinement, which suppressed nucleate boiling and induced local dryout in the channel.

Similarly, Bai et al. [230] observed an increase of around 81 % in the local flow boiling heat transfer coefficients of ethanol with a sintered copper coating with a characteristic particle diameter of 55 µm on the bottom surfaces of a parallel channel array (0.54 mm hydraulic diameter), in relation to bare copper channels at very low vapour qualities of around 0.02. In contrast to the plain copper channels, where heat transfer coefficients remained relatively constant with vapour quality, heat transfer coefficients in the coated channels decreased significantly with increasing vapour quality, hence reducing the enhancement effect. Whilst no flow pattern results were presented, the authors argued that this was due to the change in heat transfer mechanism corresponding to flow regime development in the channels. Experiments were only conducted for low vapour qualities up to 0.3.

On the other hand, Yang et al. [250] etched silicon nanowires with an average height of 5 µm on parallel silicon microchannels with a height of 0.25 mm and a width of 0.22 mm. The working fluid employed was HFE-7000. The experiments were only limited to low vapour quality ranges (up to vapour quality of around 0.4). Heat transfer enhancement ratios generally increased with increasing vapour quality, although a sharp drop in local heat transfer coefficients, indicating critical heat flux, at $x = 0.25$ in the coated channels is evident at the mass flux of 1867 kg/m^2 s. The largest enhancement factor of 344 % was observed at the lowest mass flux condition investigated in the study, i.e. 1108 kg/m^2 s where capillary-induced annular flow was dominant in the channels. The hydrophilicity of the coated surface maintained the thin-liquid film in annular flow and reduced liquid entrainment to the vapour core, thereby reducing wall dryout in the channels. In an earlier study using water as the working fluid, Yang

et al. [260] also found heat transfer enhancement of up to 326 % using a silicon nanowire coating on plain silicon microchannels. The highest enhancement was obtained at a relatively low vapour quality of 0.07. The authors similarly attributed the enhancement to enhanced nucleate boiling, thin film evaporation and enhanced liquid rewetting (owing to the superhydrophillic nature of the silicon nanowires) in the annular flow regime.

2.9.2.3 Effect of Heat Flux and Mass Flux

As implied above, heat transfer enhancement is strongly dependent on the flow pattern development in mini- and microchannels. Accordingly, the effectiveness of heat transfer enhancement using porous coatings may also be dependent on heat flux and mass flux condition. Several studies have found a notable depreciation in heat transfer enhancement at high heat fluxes, as well as different enhancement behaviours at different operating mass fluxes.

As covered above, Nedaei et al. [259] modified the wettability along the longitudinal direction 0.5 mm stainless steel microtubes with pHEMA (hydrophilic) and pPFDA (hydrophobic) coatings. The hydrophobic inlet/hydrophilic outlet configuration produced the largest enhancement out of the two coating configurations. Heat transfer enhancement increased with heat flux until approximately 8000 kW/m^2 and drops sharply with further heat flux increase. However, no reason was given for the difference in heat transfer enhancement behaviour at different heat fluxes.

In a later study using stainless steel microtubes of inner diameter 0.9 mm coated with polyperfluorodecylacrylate (pPFDA), Nedaei et al. [255] found that heat transfer enhancement ratio was relatively constant at a nominal mass flux condition but increased with increasing mass flux. However, in a smaller microtube of 0.6 mm with the same coating applied, the enhancement ratio behaved differently with heat flux and mass flux, varying between 1.1 to 1.5 times the subcooled boiling heat transfer coefficient of water in a plain stainless-steel tube. At the lowest mass flux condition of 6000 kg/m^2 s, enhancement ratio decreased with increasing heat flux, while the opposite was observed at higher mass fluxes. Enhanced heat transfer performance in the coated tubes were attributed to the higher availability of nucleation sites on the porous structure and also to the increase of heat transfer area on the porous surface. Justifications for the different enhancement behaviour observed at different mass fluxes and heat fluxes were not provided. In addition to that, the observations above also imply an effect of channel diameter, which will be discussed further in Section 2.9.2.4.

Sujith-Kumar et al. [235] investigated the effect of carbon nanotube-coated and diamond-coated copper substrate on the flow boiling heat transfer performance of a sand-blasted copper surface. The substrate was 25 mm in length and 20 mm in width, with a height of 0.4 mm.

Experiments were conducted with water at mass fluxes ranging from 283 kg/m^2 s to 427 kg/m^2 s for heat fluxes up to 500 kW/m^2. The contact angle of water on uncoated surface was 54.9° while the contact angles on the carbon-nanotube and diamond coated surfaces were 135.5° and 89.9° respectively. In other words, the wettability of the sand-blasted surface is decreased with the coatings and the coated surfaces are more hydrophobic. At the lowest mass flux condition, heat transfer coefficients of the carbon-nanotube coated surface were only noticeably higher compared to the sand-blasted surface toward high heat fluxes. At higher mass fluxes, heat transfer enhancement appear to peak at moderate heat fluxes and dropped as the critical heat flux limit is approached. The higher heat transfer coefficients were attributed to an increase in bubble nucleation and an increase in heat transfer area on the coated surfaces. The drop in heat transfer augmentation at high heat fluxes was related to large bubbles generated on the copper surface. The difference in heat transfer enhancement ratios at different mass fluxes were attributed to the bending of the carbon nanotubes at high flow rates. This was also observed in Khanikar et al. [234]. Furthermore, the diamond-coated surface resulted in little to no augmentation in heat transfer coefficients. This shows that the feature size of the coatings may also play a part in heat transfer enhancement, which will be discussed further in Section 2.9.2.6.

Wang et al. [232] etched silicon nanowires on the side and bottom walls of a parallel silicon channel array with nominal widths and depths of 0.25 mm. The degree of wall superheat at a given heat flux and mass flux condition was reduced by around 15 K from 75 K to just over 60 K in the silicon nanowire-coated channels. The flow boiling heat transfer enhancement of water was relatively unchanged with heat flux at a mass flux of 250 kg/m^2 s and increased slightly at high heat fluxes. This is due to the prevention of wall dryout with capillary-assisted rewetting provided by the nanowires. At a higher mass flux of 500 kg/m^2 s, a peak enhancement effect of around 134 % is recorded at a base heat flux of around 1000 kW/m^2 but decreases notably to just over 105 % approaching the critical heat flux limit. The smaller enhancement effect at the higher mass flux condition was suspected to be due to contamination-related degradation of surface wettability of the coated surface during experiments.

Similarly, Li et al. [233] also found higher heat transfer enhancement phenomenon at higher mass fluxes. The authors used silicon nanowires to improve the surface wettability on the bottom surface of their silicon microchannel array, consisting of 14 channels with nominal width and height of 0.25 mm and 0.2 mm respectively. The silicon nanowires were found to agglomerate and formed cavities in the order of several micrometres wide, which were

projected to serve as favourable boiling nucleation sites. The flow boiling characteristics of water at mass fluxes ranging from 119 kg/m^2 s to 571 kg/m^2 s were investigated in a plain silicon and nanowire-coated channel array. Heat transfer coefficients in the coated channels after boiling incipience were actually lower compared to the plain channel array at a mass flux of 119 kg/m^2 s. Nonetheless, at mass fluxes between 238 kg/m^2 s and 571 kg/m^2 s, heat transfer coefficients in the nanowire-coated channels were typically higher compared to the plain channels. This disparity was attributed to dryout phenomenon in the channels during annular flow. Due to higher bubble generation activity in the coated channels, annular flow was induced earlier in the nanowire-coated array. At a given heat flux, higher mass fluxes are able to replenish the annular liquid film, thus preventing dryout on the channel walls. However, at low mass fluxes, the earlier transition to annular flow and the lower ability to replenish the liquid film on the channel walls induced dryout, thereby reducing heat transfer coefficients in the coated channels compared to the plain channels. The integrity of the silicon nanowire coating was verified after flow boiling experiments, indicating long term heat transfer enhancement using silicon nanowires.

2.9.2.4 Effect of Channel Diameter

Heat transfer enhancement using porous coatings may also be dependent on the channel diameter. Kaya et al. [256] used an initiated chemical deposition technique to apply a porous coating, polyhydroxyethylmethacrylate (pHEMA), of an approximate thickness of 30 nm on stainless steel tubes with inner diameters ranging from 0.25 mm to 1 mm. The coating increased the wettability of the tube surface. The contact angle of water on the plain and coated stainless steel surface were 75° and 45° respectively. For a nominal heat flux and mass flux condition, flow boiling heat transfer coefficients of water were up to 109 % higher in the 0.25 mm diameter coated tube compared to the uncoated stainless-steel tube. This was attributed to an increase in the nucleation site density with the porous coating, which resulted in an increase in the bubble generation frequency of water. The maximum heat transfer enhancements obtained in the 0.51 mm and 1 mm tube were significantly lower, at 26 % and 22 % accordingly, compared to the smallest tube. Justification for the different enhancement factors at different tube diameters was not provided in the paper.

As discussed at above, Nedaei et al. [255] found that subcooled flow boiling heat transfer coefficients of water were enhanced with a layer of pPFDA coating by between 1.2 to 1.6 times in their larger tube of 0.9 mm diameter. Heat transfer enhancement appeared to increase with increasing mass flux and heat flux. However, in the 0.6 mm tube, heat transfer enhancement varied with mass flux and heat flux between 1.1 and 1.5. This could be because different heat flux ranges were studied in the two tubes. This was also the case in Cikim et al. [257] with pHEMA coatings in 0.25 mm, 0.51 mm and 1 mm diameter tubes. At a given heat flux and mass flux condition, the highest heat transfer enhancement of up to 97.4 % was obtained in the smallest tube. The coatings produced maximum enhancements of 85 % and 77.1 % in the larger tubes.

2.9.2.5 Effect of Coating Thickness

Cikim et al. [257] investigated the effect of coating thickness on heat transfer enhancement using crosslinked pHEMA coatings on microtubes with inner diameters ranging from 0.25 mm to 0.91 mm. The heat transfer enhancement effect was found to increase with increasing coating thickness, which was varied from 50 nm, 100 nm to 150 nm. The authors highlighted that surface wettability increased with increasing coating thickness. Two-phase heat transfer coefficients of water was enhanced by up to 126 % in the smallest tube with the largest coating thickness of 150 nm at a mass flux of 20,000 kg/m^2 s. The largest enhancement ratios in the 0.51 mm and 0.91 mm tube were 90.1 % and 86.4 % respectively, also obtained at the largest coating thickness configuration. Interestingly, the flow boiling heat transfer enhancement ratios are only moderately lower in the larger tubes, in comparison to a related study by Kaya et al. [256], where heat transfer augmentation dropped from 109 % in the smallest tube to around 20 % in the larger coated tubes.

Nedaei et al. [255] applied a polyperfluorodecylacrylate (pPFDA) coating layer of thickness 50 nm and 160 nm in stainless steel microtubes of inner diameter 0.6 mm and 0.9 mm. The contact angle of water on the plain surface (Si wafer) and surface with a 50 nm coating layer were 61° and 121° respectively (i.e. lower wettability, higher hydrophobicity). Increasing the coating thickness from 50 nm to 160 nm decreased the contact angle of water slightly to 106°. For the subcooled flow boiling of water, the enhancement ratios for two-phase heat transfer coefficients ranged from 1.1 to 1.6 at different mass flux and heat flux conditions compared to the plain tubes, with the 160 nm thick coated tubes consistently outperforming the 50 nm thick coated tubes. The highest enhancement of 1.6 was observed at the highest mass flux in the study, i.e. 8000 kg/m^2 s, in the larger tube with the thicker applied coating, i.e. 160 nm. The authors reasoned that the porous coating increased the density of nucleation sites on the surface, hence increasing boiling heat transfer coefficients. Additionally, the mitigation of dry patches, believed to be generated near the tube exit, was more effective in the tube with the 160 nm pPFDA coating due to the higher surface wettability, thus sustaining higher flow boiling heat transfer coefficients compared to the plain and 50 nm coated tubes.

However, the thickness of coating layers should be optimised and thicker coatings may not always result in higher enhancement effects in microchannels. On the one hand, Sun et al. [228] found that varying the thickness of their sintered microporous coating on the bottom surface of

a microchannel (hydraulic diameter 2.3 mm) only weakly influenced water subcooled flow boiling heat transfer enhancement. Subcooled flow boiling heat transfer coefficients were enhanced by up to 178 % using the microporous surface in relation to the polished surface. The authors found similar degrees of enhancement with coating thicknesses 237 µm, 460 µm and 673 µm, which corresponded to relative thicknesses (the ratio of coating thickness to the sintered particle diameter of 120 µm) of 2, 4 and 6 respectively. On the other hand, the authors recommended an optimum relative thickness of 2 in their study. This was because a small deterioration in heat transfer performance was observed in the 460 µm and 673 µm coated surfaces at high heat fluxes. The authors reasoned that a thicker microporous layer increases the hydraulic resistance and impedes liquid-vapour exchange in the channel, leading to heat transfer deterioration at high heat fluxes where intense evaporation takes place. In a related study by Sun et al. [252], the authors also observed adverse effects on heat transfer enhancement at high heat fluxes and recommended the optimum relative thickness of 4 for the flow boiling of FC-72 in a 0.9 mm diameter channel.

A similar effect of coating thickness has also been observed in pool boiling. Chang and You [261] reported that for the pool boiling of FC-72, porous coating thicknesses larger than the thickness of the superheated liquid layer (~100 µm for FC-72 based on Hsu's model for thermal boundary layer thickness during bubble nucleation [109]) was detrimental to heat transfer at high heat fluxes due to the hinderance of liquid-vapour exchange on the boiling surface.

2.9.2.6 Effect of Particle Diameter

Studies in [228], [230], [235], [252] have also addressed the effect of coating particle diameter on the flow boiling heat transfer enhancement. Sintered coatings with mean particle diameters of 35 µm, 120 µm and 240 µm were applied on the bottom surface of a 2.3 mm hydraulic diameter channel in Sun et al. [228]. The porosity of the coatings were between 50% to 59 %. The authors found an optimum particle diameter (i.e. 120 µm) for maximum heat transfer enhancement in the subcooled boiling region for water, but observed only a small influence of particle diameter in the saturated boiling region. In a related study using FC-72, Sun et al. [252] varied the particle diameter from 20 µm, 50 µm and 120 µm in a 0.9 mm hydraulic diameter minichannel. The porosity of the coatings were measured to be around 40 %. However, for FC-72, the highest enhancement ratio was obtained instead using the 50 µm diameter coating, namely at 692 %, at low vapour qualities.

Copper dendrites of nominal diameters 30 µm, 55 µm and 90 µm were sintered on the bottom surface of copper microchannels with a hydraulic diameter of 0.54 mm in Bai et al. [230]. Ethanol was used as the working fluid. The three coated surfaces resulted in relatively similar enhancement effects at low vapour qualities, i.e. $x \sim 0.05$. At $x \sim 0.1$, the 55 µm particle coating begins to exhibit slightly higher heat transfer enhancement compared to the other coated test sections, although experiments were only limited to vapour qualities below $x < 0.3$. Based on their experimental results, the authors stated that the 55 µm produced the optimum pore sizes for bubble nucleation. The authors further reasoned that the majority of the large pores in the 90 µm coating could have been flooded by the fluid, while it is difficult for the fluid to penetrate the small pores on the 30 µm coating. The wettability of the surfaces were not accessed in the study. However, as summarised above, hydrophobic surfaces have been concluded to be more favourable for vapour entrapment [235], [251], [255].

The review above indicate that the particle size of coatings and pore sizes should be optimised carefully in order to induce maximum heat transfer enhancement in microchannels, importantly also based on the working fluid employed. For instance, Sujith-Kumar et al. [235] achieved little to no heat transfer enhancement using a diamond-coated surface over a sand-blasted copper surface. The study also included a carbon-nanotube coated surface which resulted in considerable heat transfer enhancement, as covered in Section 2.9.2.3. The porosity of the

coatings were not analysed. However, from SEM images, the feature size of the diamond coating were around an order of magnitude larger compared to the carbon-nanotubes.

2.9.3 Effect on Critical Heat Flux

The critical heat flux condition tends to occur following wall dryout in two-phase systems, typically in the annular flow regime. Accordingly, surface structures that promote liquid rewetting and highly wetting fluid-surface combinations may help delay the occurrence of critical heat flux during flow boiling. However, as is the case with heat transfer coefficients, the enhancement of, or lack thereof, the critical heat flux limit also appears to be dependent on channel diameter, mass flux and working fluid.

Researchers in [236], [256], [257] have reported an increase in critical heat flux by increasing the hydrophilicity of their channel surfaces. As mentioned above, Kaya et al. [256] obtained a significantly larger flow boiling heat transfer enhancement effect (up to 109 %) in their smaller diameter tube (i.e. 0.25 mm) using water at a given operating condition. Similarly, the pHEMA coated tubes also exhibited higher critical heat fluxes between 8 % to 24 % higher in comparison to the uncoated tube. However, the highest enhancement was observed in the 0.51 mm tube instead for critical heat flux.

In a later study by Cikim et al. [257], the CHF condition of water was delayed by 20.4 % to just over 17000 kW/m^2 at a mass flux of 5000 kg/m^2 s with a 150 nm thick pHEMA coating in a 0.25 mm microtube. As covered above, the study also investigated that effect of coating thickness (from 50 nm to 150 nm) and reported that surface wettability increased with increasing coating thickness. The enhancements obtained in the 50 nm and 100 nm coated tubes were slightly smaller at 17.3 % and 13.2 % respectively.

Morshed et al. [236] enhanced the wettability of water using a Al_2O_3 coating and improved critical heat flux limit in their microchannel. Experiments were conducted at mass fluxes between 23 kg/m^2 s to 92 kg/m^2 s and water inlet temperatures of 21 °C and 37 °C. Critical heat flux increased with increasing mass flux but decreased with lower water inlet temperatures. The critical heat flux was enhanced by between 17 % to 39 %, but also appeared to decreased with increasing mass flux, which has also been observed in [234], [235].

Khanikar et al. [234] investigated the subcooled flow boiling of water in a bare copper channel and a carbon nanotube coated channel of similar dimensions (10 mm wide and 0.37 mm high) at mass fluxes 86, 228 and 368 kg/m^2 s. Bubbly, slug and annular flow were observed in the

bare channel while annular flow prevailed in the coated channel due to high bubble generation rates. At the lowest mass flux condition, the carbon nanotube coated channel exhibited a slightly higher critical heat flux limit of 270 kW/m^2 compared to the plain surface, which was 219 kW/m^2. The critical heat flux limit increased with increasing mass flux in both channels. However, the enhancement obtained using the coating decreased with increasing mass flux and at 368 kg/m^2 s, the critical heat flux obtained in the coated channels (i.e. 435 kW/m^2) was actually lower compared to the plain channels (i.e. 560 kW/m^2). The lower critical heat flux limit at higher mass flux conditions were attributed to the bending of the carbon nanotubes at high mass velocities.

Changes in the morphology of carbon nanotubes at high mass fluxes were also observed in Sujith-Kumar et al. [235] and affected heat transfer enhancement ratios of water (see Section 2.9.2.3). Incidentally, the enhancement in critical heat flux limit were also affected at high mass fluxes, although the authors suggested that this could also be due to nucleate boiling suppression at high mass fluxes. At the highest mass flux condition tested in the study (i.e. 427 kg/m^2 s), the critical heat flux of the carbon nanotube coated channel (i.e. 577 kW/m^2) was only marginally higher compared to the sand-blasted copper channel (i.e. 541 kW/m^2). This brings into question the durability of carbon nanotubes as heat transfer coatings for flow boiling systems where the operational mass flux is moderately high.

From the summary above, it is clear that the critical heat flux limit is typically enhanced by improving surface wettability using coatings. However, coatings may not be effective at high mass fluxes where shear stress dominates over surface tension forces in the system and may pose additional thermal resistance in the channels during dryout conditions. Yang et al. [250] enhanced the critical heat flux of HFE-7000 moderately in a silicon parallel microchannel array with a silicon nanowire coating. Percentage enhancements of between 2 % to 16 % was obtained for mass fluxes between 1108 kg/m^2 s to 1873 kg/m^2 s with a nanowire coating, with the highest enhancement obtained at the lowest mass flux condition. Improvements in the critical heat flux limit was attributed to capillary-induced annular flow in the coated channels, which maintained a thin-liquid film on the channel walls and reduced the liquid entrainment fraction to the vapour core. However, at the highest mass flux investigated, i.e. 2200 kg/m^2 s, the critical heat flux limit was instead reduced by almost 25 % in the coated channels, i.e. dropped from 1578 kW/m^2 to 1186 kW/m^2. The authors stated that at high mass fluxes, the difference in velocity between the liquid and vapour phase is much higher, leading to increased

shear stress at the liquid-vapour interface. Additionally, strong evaporation at high heat fluxes reduce the capillary pressure in the channels, causing shear stress to dominate over the low capillary pressure at high mass flux and heat flux conditions. Consequently, annular flow cannot be sustained in the channels and dryout occurs, inducing critical heat flux condition. Furthermore, during dryout, the layer of coating has high surface roughness (peak-to-peak, 5 μm) and has a higher thermal resistance on compared to the plain channels. Hence at high heat fluxes and high mass flux conditions where dryout occurs in the channel, a lower critical heat flux limit is resulted due to the additional thermal resistance of the coating in the channels.

Importantly, the authors highlighted that HFE-7000 is naturally a highly wetting fluid and incorporating the silicon nanowire coating only enhanced the surface wettability by a small margin. The enhancement percentages in the critical heat flux of water [229], which typically has low wettability on silicon, were notably higher compared to the highly wetting HFE-7000. The critical heat flux limit was successfully extended using a similar nanowire coating by between 165 % to over 300 % compared to a plain silicon parallel channel array. As the wettability of HFE-7000 is not altered significantly with the coating on the plain silicon channels, it is thus clear why only a small enhancement in critical heat flux was observed with the coating in their study using HFE-7000.

As observed in most studies covering surface coatings, the enhancements in critical heat flux depended on mass flux (experimental range between 113 kg/m^2 s to 389 kg/m^2 s). The highest enhancement was obtained at the lowest mass flux condition, i.e. approximately 580 kW/m^2 to 2384 kW/m^2. This was directly attributed to the higher wettability of water on the nanowire-coated surfaces. Additionally, the authors stated that smaller bubble departure size (of less than 5 μm in diameter) were induced in the nucleate boiling region of the coated channels due to the smaller cavity size and lower surface tension forces. A stable annular flow regime with low pressure and temperature fluctuations was observed in the silicon nanowire channels, which led to critical heat flux enhancement.

2.10 Summary

In this chapter, a detailed review of parametric effects, including the influence of heat flux, saturation pressure, mass flux and inlet subcooling on microchannel flow boiling characteristics was presented. It can be concluded that conflicting trends were reported in literature for the effect of operating conditions on flow boiling behaviour in microchannels.

2.10.1 Flow Boiling Heat Transfer

Increasing heat flux generally increased two-phase heat transfer coefficients, unless where affected by flow instabilities and dryout phenomenon in microchannels. It is well established that changes in fluid properties corresponding to saturation pressure have a significant influence on nucleation criteria, bubble growth and departure behaviour, as well as flow oscillations in microscale two-phase flows. While most studies found that increasing system pressure enhanced flow boiling heat transfer, mainly in nucleate boiling dominant regimes, a small number of studies have found that increasing pressure adversely affected heat transfer rates in microchannels. Heat transfer coefficients and two-phase flow pattern development are intrinsically linked to system mass flux.

Most studies agreed that increasing mass velocity extended the critical heat flux limit in microchannels. Flow boiling results reported in literature generally agreed with the conventional theory, i.e. flow boiling heat transfer rates were independent of mass velocity where the nucleate boiling mechanism was dominant, typically at lower heat fluxes, and a notable mass flux effect at flow regimes and heat fluxes where convective boiling prevailed. However, it was also reported that increasing mass flux increased bubble coalescence in the channels, which may trigger intermittent dryout and depreciate two-phase heat transfer coefficients.

The effect of inlet subcooling on flow boiling heat transfer rates were also unclear. A group of researchers found that increasing the degree of subcooling mitigated flow instabilities while another group of researchers reported intensified flow oscillations with higher subcooling degree. Similarly, some studies concluded that inlet subcooling had a negligible effect on flow boiling heat transfer coefficients, while others obtained improved heat transfer rates due to the suppression of flow instabilities. Increasing the degree of inlet subcooling typically delayed the occurrence of critical heat flux. Nonetheless, large degrees of inlet subcooling was

employed in some of these studies, which is not realistically attainable in thermal systems for small-scale applications.

2.10.2 Flow Boiling Pressure Drop

Two-phase pressure drop was mostly reported to increase with increasing heat flux due to higher void fraction in the channels at higher heat flux levels. On the contrary, a small number of studies have found lower magnitudes of pressure drop at higher heat fluxes where flow stratification was observed. Increasing system pressure and the resulting changes in fluid properties typically lowered microchannel two-phase pressure drop. The majority of studies concluded higher pressure drop with increase in mass flux due to higher frictional and acceleration losses. Nonetheless, some studies have found a negligible mass flux effect and even lower pressure drop at higher mass fluxes, the latter attributed to the suppression of flow instabilities. Increasing the degree of subcooling generally reduced two-phase pressure drop owing to lower channel void fraction at a given heat flux condition. Additionally, as mentioned above, increasing inlet subcooling degree may mitigate two-phase flow oscillations and thus also lower flow boiling pressure drop in microchannels.

2.10.3 Flow Pattern Maps

There is no general agreement in flow pattern maps for two-phase flows. The reasons for this may be due to subjectivity during flow pattern identification and different threshold criterion in macro-micro scale channel classification. Furthermore, flow pattern classification based on four primary flow patterns, i.e. bubbly, slug, annular and mist flow, with the use of sub-regimes, for e.g. churn flow for transitional regimes between slug and annular flow, may improve comparison of flow pattern data between independent studies. The use of adiabatic flow maps for diabatic flows as well as singular-channel two-phase flow pattern maps for parallel channel configurations may not be suitable due to differences in flow pattern development and the influence of flow interaction between neighbouring channels.

2.10.4 Flow Boiling Heat Transfer Correlations

To support the implementation of two-phase cooling in industrial applications, accurate prediction tools must be developed to enable optimisation of such systems. Types of heat transfer correlations available in literature, including the (i) enhancement-factor, (ii) nucleate

boiling, (iii) superposition, (iv) asymptotic, (v) predominant mechanism and (vi) criterion-based models were reviewed. For microscale flows, many correlations apply a suppression factor to the nucleate boiling mechanism and an enhancement factor to the convective boiling component in order to predict overall two-phase heat transfer. Accordingly, fluid properties and dimensionless parameters considered for the calculation of the suppression factor and enhancement factors were discussed. There was a large spread in dimensionless parameters considered by two-phase heat transfer correlations, as well as different assumptions and models adopted to calculate the nucleate boiling and convective boiling component.

Overall, the Boiling number, liquid Reynolds number, Martinelli parameter, liquid-only Weber number and the liquid Prandtl number are popular parameters considered in two-phase heat transfer correlations. Additionally, the liquid-vapour density ratio and the reduced pressure ratio are also typically correlated. Nucleate boiling models generally incorporate the Boiling number, liquid-only Reynolds number, liquid-only Weber number and liquid-vapour density ratio. Cooper's nucleate boiling model further considers the surface characteristics of the boiling substrate through the roughness parameter and the molecular weight of the fluid. The molecular weight of the working fluid and fluid dependent parameters may also be used to correlate heat transfer trends in flow boiling.

2.10.5 Flow Boiling Pressure Drop Correlations

Accurate prediction of two-phase pressure drop is also required in application for appropriate pump sizing calculations. The main approaches to the prediction of flow boiling pressure drop are the homogeneous model and the separated flow model, where the main differences are in the friction factor and void fraction definitions. For the separated flow model, correlations are divided into Lockhart-Martinelli based correlations and correlations adopting Chisholm's B-coefficient method. Many of the existing microscale pressure drop correlations are based on the Lockhart-Martinelli model for macroscale flow with a modified expression for Chisholm's parameter. The parameter is correlated to different parameters including hydraulic diameter and mass flux, as well as dimensionless numbers such as Reynolds number, Boiling number and Weber number by different studies. Although there are several methods to predict channel void fraction, the overall significance of the choice of void fraction model may be small. The macroscale correlation of Lockhart-Martinelli has been reported to generally overpredict

microscale two-phase pressure drop, while the Mishima and Hibiki correlation has been found to have good prediction accuracy in several studies.

2.10.6 Flow Boiling Heat Transfer Enhancement

Surface modification by means of a porous coating was established as a cost effective and simple method to enhance bubble nucleation characteristics in flow boiling. Optimised cavities on surface were found to lower boiling incipience wall superheat, thereby mitigating explosive bubble growth instabilities in microchannels. As highlighted in the summary above, suppression of flow instabilities may also improve heat transfer and critical heat flux behaviour in microchannel flow boiling.

Furthermore, several researchers have altered surface wettability using coatings in microchannels. Hydrophobic surfaces were generally found to induce the onset of boiling at lower degrees of wall superheat due to favourable vapour trapping, while hydrophilic surfaces enhanced rewetting behaviour and delayed critical heat flux. However, several studies have also reported that intense bubble nucleation activity following boiling incipience may trigger premature critical heat flux in microchannels. On top of that, a number of studies concluded that critical heat flux enhancement obtained using surface coatings were highly dependent on channel diameter and mass flux, and actually deteriorated critical heat flux limits in certain cases.

Flow boiling heat transfer enhancement of nearly 350 % were reported using porous coatings in microchannels. Similarly, enhancement ratios in two-phase heat transfer rates were also found to be highly influenced by channel diameter, vapour quality, heat flux and mass flux. Evidence suggested that this may have been due to flow patterns and dominant heat transfer mechanism at different operating ranges, however, further work is required to clarify these effects. Several studies concluded that the pore size and thickness of coatings employed in microchannel flow boiling should be optimised to maximise heat transfer enhancement. Additionally, a small number of studies have also observed degradation of surface coatings after experiments. This should be investigated to ensure consistent heat transfer performance in enhanced microchannel heat sinks.

3 Experimental Methodology

3.1 Introduction

In this chapter, the experimental facility is described and details of the experimental methodology is presented. Details of the experimental set-up and equipment, including the test section, are given in Section 3.2. The experimental procedures are listed in Section 3.3 while the data reduction method is presented in Section 3.4. Summaries of the experimental range and uncertainties are given at the end of Section 3.4 and a more detailed propagated error analysis method is presented in Appendix A. In Section 3.5 and 3.6, single-phase validation of the experimental loop and the repeatability of flow boiling experiments in the microchannel test section are discussed respectively.

3.2 Experimental Facility

An experimental facility at Brunel University London, Tower B113, was used for the present study. The experimental loop consists of two flow loops, namely a main flow loop through the test section and an auxiliary loop through a heat exchanger and chiller unit. A schematic diagram of the experimental facility is shown in Figure 3.1.

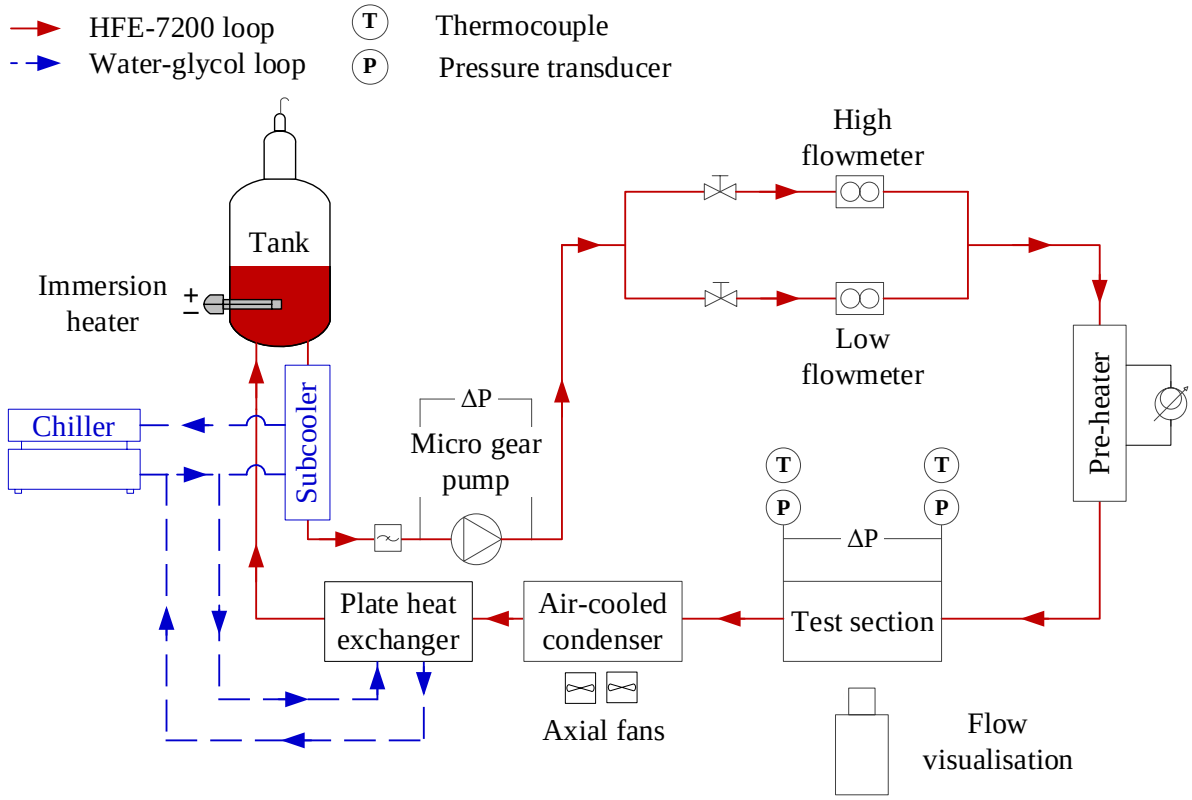

Figure 3.1: Schematic of experimental facility.

The main flow loop uses working fluid HFE-7200. The auxiliary chiller loop, using a water-glycol mixture, is also included. The main loop consists of a reservoir, a subcooler, a gear pump (GJ-N23FF2S from Micropump®), two Coriolis mass flowmeters (OPTIMASS 3000 S01 for mass fluxes up to 300 kg/m^2 s and OPTIMASS 3000 S03 for mass fluxes more than 300 kg/m^2 s from Krohne), a pre-heater, the microchannel evaporator test section, an air-cooled condenser and a heat exchanger. System pressure is regulated using an immersion heater in the reservoir connected to a PID controller. The mass flow rate through the test section is controlled by means of a digital pump drive (ISMATEC Reglo ZS©) connected to the gear pump. Power input to the pre-heater (maximum power input 1500 W) and test section (maximum power input 800 W) are varied using two separate variacs to control fluid inlet temperature and test section heat flux. Two axial fans (ARX FD2412-A3251G) are mounted on the condenser to provide ambient air cooling. The secondary side (cold side) of the plate heat exchanger is connected to the water-glycol loop to provide additional cooling to the working fluid (hot side) prior to return to the reservoir. The water-glycol chiller is also used to control fluid temperature upstream of the pump using the subcooler. The pressure drop across the pump is measured using an Omega™ PX309-030GI differential pressure transducer. A high-speed camera

(Phantom Miro Lab110) was coupled with a Huvitz HSZ-645TR microscope and LED lighting system for flow visualisation, operating at 5000 frames/s and at a resolution of 512 x 512 pixels. All measuring instruments (i.e. thermocouples, pressure transducers and flow meters) were connected to a National Instruments Data Acquisition System (DAQ) and monitored using an in-house LabVIEW program on the computer. Data was acquired for a period of 90 s at a frequency of 1 kHz after steady-state conditions were achieved and the values were averaged for data reduction. Steady-state condition was defined when the readings vary within a range of ±0.2 g/s for mass flow rate, ±0.5 K for inlet/outlet temperature and ±0.05 bar for the inlet/outlet pressure over a period of at least 180 s.

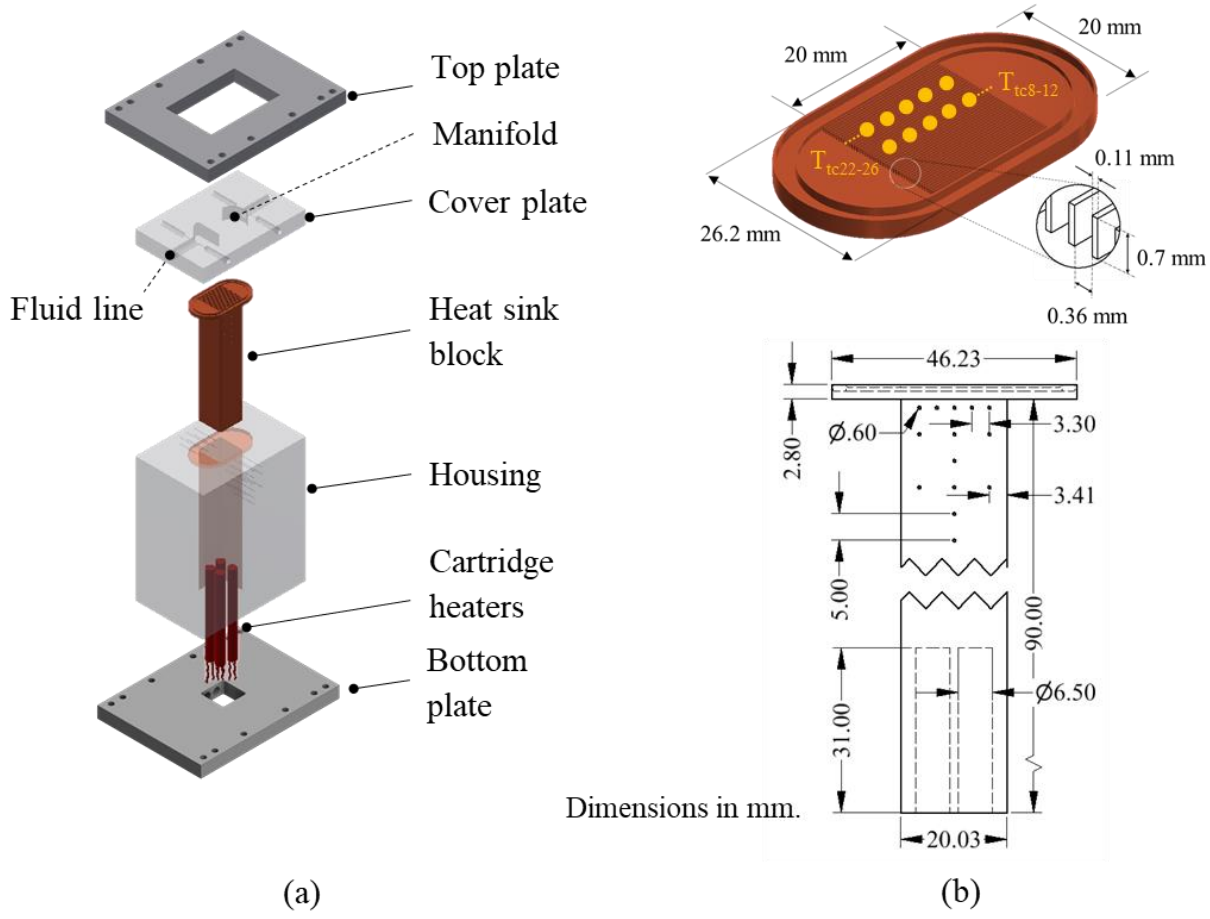

Figure 3.2: Test section (a) Exploded view (b) Details of microchannel heat sink. The locations of wall temperature measurement are annotated.

The test section is shown in Figure 3.2. It consists of an aluminium top plate, polycarbonate cover plate and housing, copper heat sink block, cartridge heaters and an aluminium bottom plate. The heat sink is made up of oxygen-free copper and has dimensions 90.0 mm (H) x 26.2 mm (W) x 46.2 mm (L), including the inlet and outlet plenum at the top of the block. Four cartridge heaters of a maximum heating power of 200 W each were inserted into vertical holes

from the bottom of the block. Forty-four parallel microchannels were machined to a square base area of 20 mm x 20 mm using a high-precision milling machine (Kern HSPC-2216) with a carbide end-mill of 0.35 mm diameter at a speed of 18,000 rpm and a feed rate of 300 mm/min. The channel dimensions were 0.36 mm wide, 0.7 mm deep and 20 mm in length. Table 3.1 summarises the characteristics of the microchannel array. The average surface roughness, Ra, was sampled at five different locations on the channel bottom wall using the Zygo NewView 500 surface profiler and was measured to be around 0.23 μm.

Table 3.1: Dimensions of the microchannel heat sink.

W_{ch} [mm]	H_{ch} [mm]	L_{ch} [mm]	W_f [mm]	N [-]	AR [-]	D_h [mm]	Base area [mm]
0.36	0.7	20	0.1	44	0.51	0.48	20 x 20

Twenty-two K-type thermocouples (accuracy ±0.2 K) were used to measure the temperature distribution in the heat sink block. Five thermocouples, each 3.3 mm apart, were positioned along the channel and inserted into the heat sink to a depth of 10 mm, i.e. to the centre of the block, and 1.6 mm from the channel bottom wall to measure axial temperature. The most upstream and downstream thermocouples are 3.4 mm from the channel inlet and outlet respectively. On another side of the heat sink, five thermocouples were inserted at the same coordinates but only to a depth of 5 mm, i.e. to the quarter plane of the block, to measure traverse temperature distribution. Six thermocouples in the vertical direction, each 5 mm apart and 1.6 mm from the bottom of the channel wall, were used to measure the temperature gradient along the height of the block. The inlet/outlet manifolds are machined in the polycarbonate top plate. The inlet and outlet pressure were measured at the inlet and outlet manifold respectively using two Omega™ PXM409-007BAI pressure transducers. The inlet and outlet fluid temperature were also measured at these points. Lastly, the differential pressure is measured across the manifolds using an Omega™ PX409-015DWUI.

3.3 Experimental Procedure

In this section, the experimental procedure during single-phase and flow boiling experiments are presented. To ensure reproducibility in the experimental results, degassing procedures were conducted prior to experiments in this study. The working fluid was boiled vigorously for at least an hour and degassed air was released through a degassing tap at the top of the reservoir. This process is repeated until the measured temperature and pressure in the tank corresponds to the saturation conditions of pure HFE-7200. These procedures are also detailed in this section.

3.3.1 Degassing Procedures

1. Turn on all power supplies and start LabVIEW program.
2. Open all valves in the experimental loop.
3. Switch on gear pump to 500 rpm and circulate working fluid until no gas bubbles are observed in the test section.
4. Turn off the gear pump and close all valves in the system.
5. Set temperature controller to 120 °C and boil the working fluid in the reservoir for at least an hour.
6. Open degassing valve on reservoir to vent trapped gas to the ambient. Close degassing valve.
7. Compare temperature and pressure readings on LabVIEW with EES. If these do not match, repeat steps 5 and 6.
8. Turn on the chiller and open all valves. Ensure that temperature before pump does not exceed 77 °C before circulating fluid to avoid damage to pump gaskets.

3.3.2 Single-Phase Experiments

For adiabatic experiments where the single-phase pressure drop across the test section is concerned:

1. Ensure degassing procedures are conducted before experiments.
2. Turn on gear pump and set to desired mass flux.
3. Control inlet pressure to desired value using PID controller in the reservoir.
4. Switch on the pre-heater and set heating power using a variac.

5. Log data for at least 90 s when all temperature and pressure readings are stable, as viewed from the plots on the LabVIEW programme.
6. Rename file name on LabVIEW programme with details of test conditions.
7. Repeating steps 2 to 6, record data for different mass fluxes.
8. Gradually reduce gear pump speed and turn off all experimental equipment.

For diabatic single-phase experiments where the single-phase heat transfer coefficient is to be measured:

1. Ensure degassing procedures are conducted before experiments.
2. Turn on gear pump and set to desired mass flux.
3. Control inlet pressure to desired value using PID controller in the reservoir.
4. Switch on the pre-heater and set heating power using a variac.
5. Set heating power on cartridge using a variac and adjust power to set desired base heat flux value calculated on LabVIEW programme.
6. Log data for at least 90 s when all temperature and pressure readings are stable, as viewed from the plots on the LabVIEW programme.
7. Rename file name on LabVIEW programme with details of test conditions.
8. Repeating steps 2 to 7, record data for different mass fluxes.
9. Gradually reduce heating power and gear pump speed. Turn off all experimental equipment when temperatures on test section decrease back to ambient conditions.

3.3.3 Flow Boiling Experiments

1. Ensure degassing procedures are conducted before experiments.
2. Activate flow visualisation software. Align high-speed camera and microscope for flow observation.
3. Turn on gear pump and set to desired mass flux.
4. Control inlet pressure to desired value using PID controller in the reservoir.
5. Switch on the pre-heater and set heating power using a variac. Control inlet temperature to desired inlet subcooling degree.
6. Set heating power on cartridge using a variac and adjust power to set desired base heat flux value calculated on LabVIEW programme.
7. Log data for at least 90 s when all temperature and pressure readings are stable, as viewed from the plots on the LabVIEW programme. Also observe flow patterns on

flow visualisation software and ensure that there are no changes in flow regime in each camera location.

8. Rename file name on LabVIEW programme with details of test conditions.
9. Record high-speed video at first location along the channel and save with details of location and test conditions as the file name.
10. Repeat step 7 for all four locations along the channels.
11. Repeating steps 2 to 10, record data for different heat fluxes.
12. Gradually reduce heating power on the test section and pre-heater. Lower the gear pump speed. Turn off all experimental equipment when temperatures on test section decrease back to ambient conditions.

3.4 Data Reduction

The pressure drop across the microchannel array, ΔP_{ch}, is given by:

$$\Delta P_{ch} = \Delta P_{total} - \Delta P_{loss} \tag{3.1}$$

where ΔP_{total} is the total measured pressure drop, ΔP_{loss} is the total pressure loss, taking into account the losses in the inlet and outlet manifold of the heat sink. Pressure drop in the manifold may account for up to 32 % of the total pressure drop measured across the heat sink. As a result, methods and correlations were selected carefully to best represent the flow and geometrical conditions in the microchannel heat sink to estimate pressure losses in the inlet and outlet manifold.

$$\Delta P_{loss} = \Delta P_{ip} + \Delta P_{sc} + \Delta P_{se} + \Delta P_{op} \tag{3.2}$$

The pressure drop components in the inlet and outlet plenum are ΔP_{ip} and ΔP_{op} respectively, given in Eq. (3.3) and (3.4). These include the pressure losses due to sudden expansion from the fluid line (fluid line radius, R_{fl} = 3 mm) at the inlet manifold, sudden contraction into the fluid line at the outlet manifold and 90° bend in both manifolds (plenum radius, R_p = 9.7 mm), calculated based on the method detailed in Remsburg [262], which was derived for contraction and expansion from multichannel arrays.

$$\Delta P_{ip} = \frac{1}{2}\rho_f \left\{ V_p^2 K_{90} + V_{fl}^2 \left[\alpha_p^2 - 1 + \left(1 - \frac{1}{\alpha_p} \right)^2 \right] \right\} \tag{3.3}$$

$$\Delta P_{op} = \frac{1}{2}\rho_f \left\{ V_p^2 K_{90} + V_{fl}^2 \left[1 - \frac{1}{\alpha_p^2} + \frac{1}{2}\left(1 - \frac{1}{\alpha_p} \right) \right] \right\} \tag{3.4}$$

A coefficient of pressure loss through a 90° bend, K_{90}, of 1.2 was used in Phillips [263] to estimate pressure drop at the plena of microchannel heat sinks. The plenum area ratio, α_p, is defined as the area of the plenum over the cross-sectional area of the fluid line.

The pressure drop components due to sudden contraction into the microchannels and sudden expansion from the microchannels are ΔP_{sc} and ΔP_{se} respectively, where V_{ch} and β are the fluid velocity in the microchannel array and the microchannel area ratio respectively.

$$\Delta P_{sc} = \frac{1}{2}\rho_f V_{ch}^2 \left[1 - \beta^2 + \frac{1}{2}\left(1 - \beta^2 \right) \right] \tag{3.5}$$

$$\Delta P_{se} = \frac{1}{2} \rho_f V_{ch}^2 \left[\frac{1}{\beta^2} - 1 + (1 - \beta)^2 \right] \tag{3.6}$$

The area ratio β is the area flow area of the microchannels over the frontal area of the channel array, i.e. $\beta = (N W_{ch} H_{ch}) / (H_{ch} W)$. The experimental Fanning friction factor in single-phase flow experiments is subsequently found by the relation below:

$$f = \frac{\Delta P_{ch} D_h \rho_f}{2 L_{ch} G^2} \tag{3.7}$$

In two-phase flow experiments, the procedure to calculate pressure drop is as described above, with the exception of the pressure losses in the outlet plenum, $\Delta P_{op,tp}$ and $\Delta P_{se,tp}$, which are estimated based on the two-phase pressure drop equations given in Collier and Thome [100]. This approach was selected as it represented the two-phase nature of the flow at the outlet of the plenum when vapour quality exceeded zero in the channels. $\Delta P_{op,tp}$ consists of two components, namely the two-phase pressure drop through a bend, $\Delta P_{bd,tp}$, and the two-phase pressure loss due to sudden contraction into the fluid line, $\Delta P_{sc,fl,tp}$.

$$\Delta P_{op,tp} = \Delta P_{bd,tp} + \Delta P_{sc,fl,tp} \tag{3.8}$$

The method proposed by Chisholm [264] for two-phase flow in bends was used to calculate $\Delta P_{bd,tp}$, where B is a constant given in Eq. (3.10), R_{bd} is the bend radius of the plenum and D_p is the diameter of the plenum.

$$\Delta P_{bd,tp} = \left\{ \frac{G^2 v_f K_{90}}{2} \right\} * \left\{ 1 + \left[\left(\frac{\rho_f}{\rho_g} - 1 \right) * (B x_e (1 - x_e) + x_e^2) \right] \right\} \tag{3.9}$$

$$B = 1 + \frac{2.2}{K_{90} \left(2 + \frac{R_{bd}}{D_p} \right)} \tag{3.10}$$

Based on the equation derived in Collier and Thome [100], $\Delta P_{sc,fl,tp}$ is calculated as follows:

$$\Delta P_{sc,fl,tp} = \frac{G^2 v_f}{2} \left[\left(\frac{1}{C_c} - 1 \right)^2 + \left(1 - \frac{1}{\alpha_p^2} \right) \right] * \left(1 + \frac{\rho_f}{\rho_g} \right) x_e \tag{3.11}$$

The constant C_c is 0.635 for the current plenum area ratio, based on the relation proposed by Chisholm [265] as cited in Collier and Thome [100]. On the other hand, the two-phase pressure drop due to sudden expansion from the microchannel array may be calculated as follows [100]:

$$\Delta P_{se,tp} = G^2 \, v_f \left[\frac{1}{\beta} \left(1 - \frac{1}{\beta} \right) \right] * \left[\frac{(1 - x_e)^2}{(1 - \alpha_v)} + \left(\frac{v_g}{v_f} \frac{x_e^2}{\alpha_v} \right) \right] \tag{3.12}$$

where the void fraction, α_v, is calculated using the correlation developed by Kawahara et al. [214] for circular microchannels. The correlation for circular channels was adopted due to lack of available correlations for rectangular microchannels in literature.

$$\alpha_v = \frac{0.03 \left(\frac{J_g}{J_g + J_l} \right)^{0.5}}{1 - 0.97 \left(\frac{J_g}{J_g + J_l} \right)^{0.5}} \tag{3.13}$$

The liquid and vapour superficial velocities are J_l and J_g, as given in Eq. (3.14) and (3.15) respectively.

$$J_l = \frac{G (1 - x)}{\rho_f} \tag{3.14}$$

$$J_g = \frac{G x}{\rho_g} \tag{3.15}$$

The exit vapour quality, x_e, and local vapour quality, $x_{(z)}$, are determined using the saturated liquid enthalpy, $i_{f(z)}$, and enthalpy of vapourisation, $i_{fg(z)}$, of the fluid, which are evaluated at the local bulk fluid temperature, $T_{f(z)}$, at the corresponding z location (Eq. (3.17)). The local specific enthalpy, $i_{(z)}$, is evaluated from the energy balance in Eq. (3.18).

$$x_{(z)} = \frac{i_{(z)} - i_{f(z)}}{i_{fg(z)}} \tag{3.16}$$

$$T_{f(z)} = T_i + \frac{q_b'' \, W \, z}{\dot{m} \, c_p} \tag{3.17}$$

$$i_{(z)} = i_i + \frac{q_b'' \, W \, z}{\dot{m}} \tag{3.18}$$

The two-phase pressure drop in the channels, ΔP_{tp}, is thus obtained by the following relation:

$$\Delta P_{tp} = \Delta P_{ch} - \Delta P_{sp} \tag{3.19}$$

Single-phase pressure drop, ΔP_{sp} is the pressure drop in the subcooled region and is calculated based on the single-phase friction factor evaluated using the relation proposed by Shah and London [266] for developing flows, which takes into account the aspect ratio of rectangular channels.

$$\Delta P_{sp} = \frac{G^2 f_{sp} L_{sub} \rho_f}{2 D_h} \tag{3.20}$$

$$f_{sp} = \frac{1}{Re}\left[\frac{3.44}{\sqrt{L_{sub}^{+}}} + \frac{(fRe)_{fd} + \frac{K(\infty)}{4 L_{sub}^{+}} - \frac{3.44}{\sqrt{L_{sub}^{+}}}}{1 + \frac{C^{+}}{\left(L_{sub}^{+}\right)^2}}\right] \tag{3.21}$$

The fully-developed Poiseuille number, $(fRe)_{fd}$, and constants $K(\infty)$ and C^{+} are given as 15.46, 0.97 and 0.00029 respectively for the nominal channel dimensions in this study. The dimensionless subcooled length, L_{sub}^{+}, is determined by $L_{sub}/(Re\, D_h)$. The subcooled length, L_{sub}, is derived iteratively based on Eq. (3.22) – (3.24). An initial value for $T_{sat(z,sub)}$ is assumed and L_{sub} is calculated and substituted into Eq. (3.24) to calculate $P_{sat(z,sub)}$. The saturation temperature at $P_{sat(z,sub)}$ is estimated and compared against the initial value assumed for $T_{sat(z,sub)}$. The iteration is continued until the assumed temperature matches the estimated temperature within an error margin of ± 0.001 K.

$$L_{sub} = \frac{\dot{m}\, c_{p,l}\left(T_{sat(z,sub)} - T_i\right)}{q_b^{"} W} \tag{3.22}$$

where $q_b^{"}$ and T_i are the base heat flux and measured inlet temperature accordingly. The base heat flux is calculated from:

$$q_b^{"} = k_{cu} \left.\frac{dT}{dy}\right|_{y=0} \tag{3.23}$$

The thermal conductivity of copper is represented by k_{cu} while $\frac{dT}{dy}$ is the vertical temperature gradient of the heat sink block. The saturation temperature at the location of zero quality, $T_{sat(z,sub)}$, is evaluated at the local pressure condition, $P_{sat(z,sub)}$, which is found using the formula:

$$P_{sat(z,sub)} = P_{in,ch} - \frac{2 f_{sp} G^2 L_{sub}}{D_h \rho_f} \tag{3.24}$$

The pressure at the inlet of the channel array, $P_{in,ch}$, is corrected for inlet pressure losses, $P_{in,ch} = P_{in} - P_{ip} - P_{sc}$.

The local heat transfer coefficients, h(z), are obtained from thermocouple measurements along the channel bottom wall, at dimensionless locations z/L = 0.17, 0.34, 0.5, 0.67 and 0.83.

$$h_{(z)} = \frac{q_b^{"}\left(W_{ch} + W_{fin}\right)}{\left(T_{w(z)} - T_{f(z)}\right)\left(W_{ch} + 2\,\eta\, H_{ch}\right)} \tag{3.25}$$

In Eq. (3.25), W_{ch}, W_{fin} and H_{ch} are the channel width, fin thickness and channel height respectively. The fin efficiency, η and fin parameter, m, are found iteratively using the formula given in Incropera et al. [267] in Eq. (3.26) and (3.27). W_f is the thickness of the channel fin.

$$\eta = \frac{\tanh (m H_{ch})}{m H_{ch}} \tag{3.26}$$

$$m = \sqrt{\frac{2 h_{(z)}}{k_{cu} W_{fin}}} \tag{3.27}$$

The local wall temperature, $T_{w(z)}$, is extrapolated from the axial thermocouple measurements along the channel, $T_{tc(z)}$, based on energy balance. Y is the distance between the bottom wall of the channel and the topmost thermocouples, i.e. 1.6 mm.

$$T_{w(z)} = T_{tc(z)} - \frac{q_b'' Y}{k_{cu}} \tag{3.28}$$

Note that $T_{f(z)}$ is calculated based on Eq. (3.17) if in the single-phase region or evaluated at the local saturation pressure, $P_{sat(z)}$, if the corresponding z location is in the flow boiling region. $P_{sat(z)}$ is calculated with the assumption of a linear pressure drop in the channels. The assumption of a linear pressure trend along the flow length in the two-phase region is discussed further in Section 4.2.2.

$$P_{sat(z)} = P_{sat(z,sub)} - \left(\frac{z - L_{sub}}{L_{ch} - L_{sub}} \right) \Delta P_{tp} \tag{3.29}$$

The average heat transfer coefficient, $\bar{h}_{(z)}$, is calculated based on all five axial heat transfer measurements with respect to the *total channel length*, see Eq. (3.30), while the average *two-phase* heat transfer coefficient, $\bar{h}_{tp(z)}$, is evaluated using only the heat transfer measurements in the two-phase region based on Eq. (3.31) with respect to the *saturated boiling length*.

$$\bar{h}_{(z)} = \frac{1}{L_{ch}} \int_{L=0}^{L_{ch}} h_{(z)} \, dz \tag{3.30}$$

$$\bar{h}_{tp(z)} = \frac{1}{L_{ch} - L_{sub}} \int_{L_{sub}}^{L_{ch}} h_{(z)} \, dz \tag{3.31}$$

Heat transfer coefficients are presented as a function of wall heat flux, q_w'', in this study.

$$q_w'' = \frac{q_b'' A_b}{A_{ht}} \tag{3.32}$$

where A_b and A_{ht} are the base area and heat transfer area respectively. The former is calculated as $A_b = W_b L_{ch}$ while the latter is expressed as $A_{ht} = N L_{ch} (2H_{ch} + W_{ch})$.

The Nusselt number is defined in Eq. (3.33), where k_f is the liquid thermal conductivity and the average Nusselt number in the microchannels is given by Eq. (3.34).

$$Nu = \frac{h_{(z)} D_h}{k_f} \tag{3.33}$$

$$\overline{Nu} = \frac{1}{L_{ch}} \int_{L=0}^{L_{ch}} \frac{h_{(z)} D_h}{k_f} \, dz \tag{3.34}$$

The thermophysical properties of HFE-7200 were obtained from Engineering Equation Solver (EES). The thermophysical properties of HFE-7200 at a range of pressures are summarized in Table 3.2.

The experimental range investigated in the current study is summarised in Table 3.3. The effect of mass flux was investigated at P = 1 bar and ΔT_{sub} = 10 K, while the effect of subcooling was assessed at P = 1 bar and G = 200 kg/m^2 s. On the other hand, the effect of inlet pressure was assessed at G = 200 kg/m^2 s and ΔT_{sub} = 10 K. For each set of experiment, wall heat flux was increased gradually until exit vapour quality approached 1.

The measurement and propagated experimental uncertainties, the latter evaluated using the method described in Coleman and Steele [268], are listed in Table 3.4 and further detailed in Appendix A. Flow boiling experiments were conducted at mass flux conditions G = 200, 300 and 400 kg/m^2 s, inlet pressures of P = 1 bar, inlet subcooling degree of ΔT_{sub} = 10 K and wall heat fluxes ranging from q_w'' = 24.8 – 234.3 kW/m^2 (corresponding to base heat fluxes q_b'' = 95 – 896 kW/m^2)..

Table 3.2: Thermophysical and environmental properties of HFE-7200 at 1 atm [60].

Boiling point [°C]	Freezing point [°C]	Heat of vapourisation [kJ/kg]	Thermal conductivity [W/m K]	Dielectric constant @ 1 kHz [-]	GWP	ODP	Flash point
76	-138	119	0.068	7.3	55	0	None

Table 3.3: Experimental range.

Fluid	G [kg/m^2 s]	q_w'' [kW/m^2]	q_b'' [kW/m^2]	P [bar]	ΔT_{sub} [K]
HFE-7200	200, 300, 400	24.8 – 234.3	94.9 – 896.5	1.0, 1.5, 2.0	5, 10, 20

Table 3.4: Experimental uncertainties.

Equipment/Parameter	Uncertainty
K-type thermocouple	± 0.2 K
Inlet/outlet pressure transducer	± 0.08 % (full-scale)
Differential pressure transducer	± 0.25 % (full-scale)
Hydraulic diameter	± 0.38 – 0.42 %
Mass flow rate	± 0.035 %
Channel mass flux	± 0.63 %
Fanning friction factor	± 2.39 – 2.46 %
Average Nusselt number	± 5.57 – 11.71%
Channel pressure drop	± 0.1 – 0.57 %
Local heat transfer coefficient	± 3.87 – 9.67%
Local vapour quality	± 2.13 – 9.23 %
Heat flux	± 1.96 – 4.35 %

3.5 Single-Phase Validation

Single-phase experiments were conducted to validate the measurement instruments and the experimental setup. Figure 3.3 and Figure 3.4 show the single-phase experimental friction factor (see Eq. (3.7)) and average single-phase Nusselt number (see Eq. (3.34)) with respect to Reynolds number, Re. The adiabatic experiments were conducted at an inlet pressure of 1 bar, inlet temperature of 40 °C and mass fluxes ranging from G = 251 – 2252 kg/m^2 s, covering a Reynolds number range of 226 – 2038. The diabatic heat transfer experiments were conducted at the same conditions stated above, at a wall heat flux of $q_w^{"}$ ~12 kW/m^2 (i.e. $q_b^{"}$ ~ 5 kW/m^2). The experimental single-phase friction factor appear to be in good agreement with the correlations given in Shah and London [266], proposed for developing and fully developed laminar flows in non-circular horizontal ducts. The average Nusselt number obtained in single-phase heat transfer experiments were well predicted by established correlations for laminar flows in microchannels, namely the Shah and London [266], Peng and Peterson [269] and Stephan and Preusser [270].

The Shah and London [266] and Stephan and Preusser [270] correlations were proposed for thermally developing laminar flow and simultaneously developing flow with a constant wall heat flux. Although these correlations have been developed in circular channel geometries, they are typically employed for non-circular channels with the hydraulic diameter [271]. This could be the reason why the experimental data points at low Reynolds numbers of around ~ 200 to 600 are relatively close to the two correlations. The Peng and Peterson [269] correlation was developed for rectangular channels of hydraulic diameters between D_h = 0.133 mm to 0.367 mm covering a wide Reynolds number range of 50 to 4000. The authors approximated that the transitional Reynolds numbers in microchannels were between 400 < Re < 1000 and fully turbulent flow at Re > 1000. As the turbulent equation developed by Peng and Peterson [269] was employed, it is thus understandable that the experimental data points at Re > 1000 begins to tend towards the Peng and Peterson [269] turbulent correlation. In Figure 3.3, the experimental trend is also better approximated by the developing flow correlation of Shah and London [266]. The single-phase validation results for the coated test section is presented in Section 8.3.

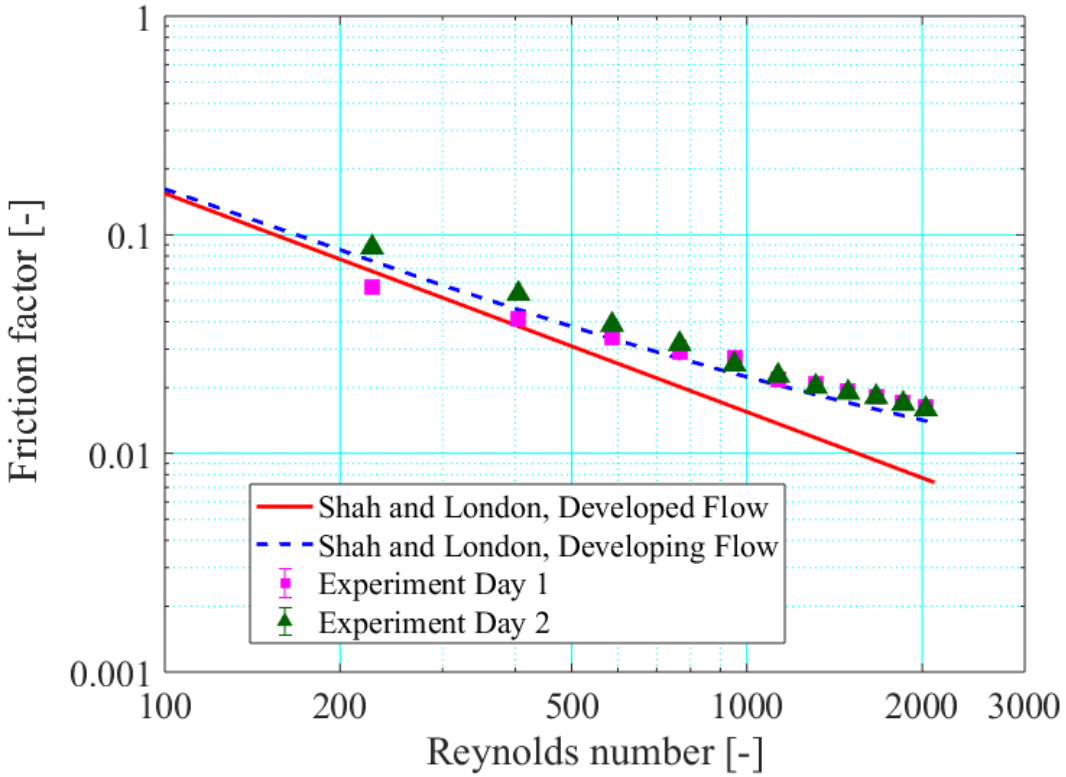

Figure 3.3: Experimental single-phase friction factor vs. Reynolds number. Error bars are between 2.39 – 2.46 % but are too small to be visible in the figure.

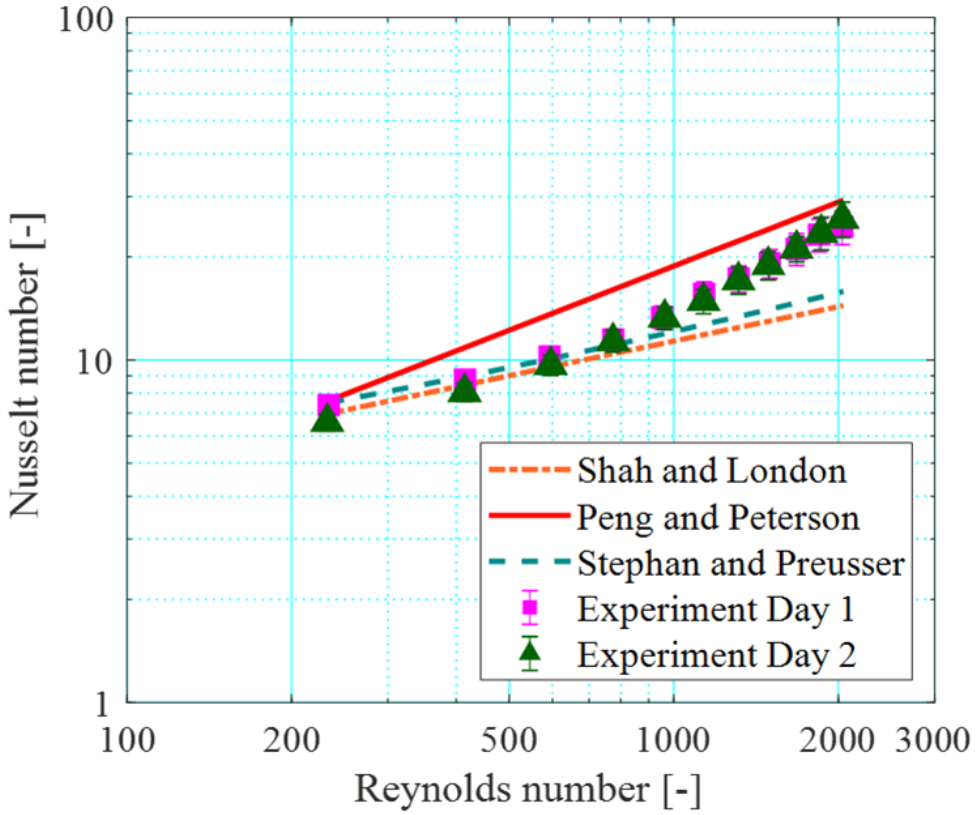

Figure 3.4: Experimental single-phase Nusselt number vs. Reynolds number.

3.6 Repeatability

The repeatability of the experiments, conducted on different days, are shown in Figure 3.5. The mean absolute deviation, MAE, may be used to further assess the repeatability of experiments:

$$\mathrm{MAE} = \frac{1}{n} \sum \left| \frac{j_{day1} - j_{day2}}{j_{day1}} \right| \times 100\ \% \tag{3.35}$$

where j is the experimental parameter and n is the number of data points collected, can be used here to compare the two data sets.

The experimental results of the plain channels on two different days at a set operating condition differ by a MAE of between ± 0.2 % to ± 3.3 % across the heat flux range investigated. Additionally, boiling hysteresis did not occur in the current study, as illustrated in the boiling curves for increasing and decreasing heat fluxes in Figure 3.6.

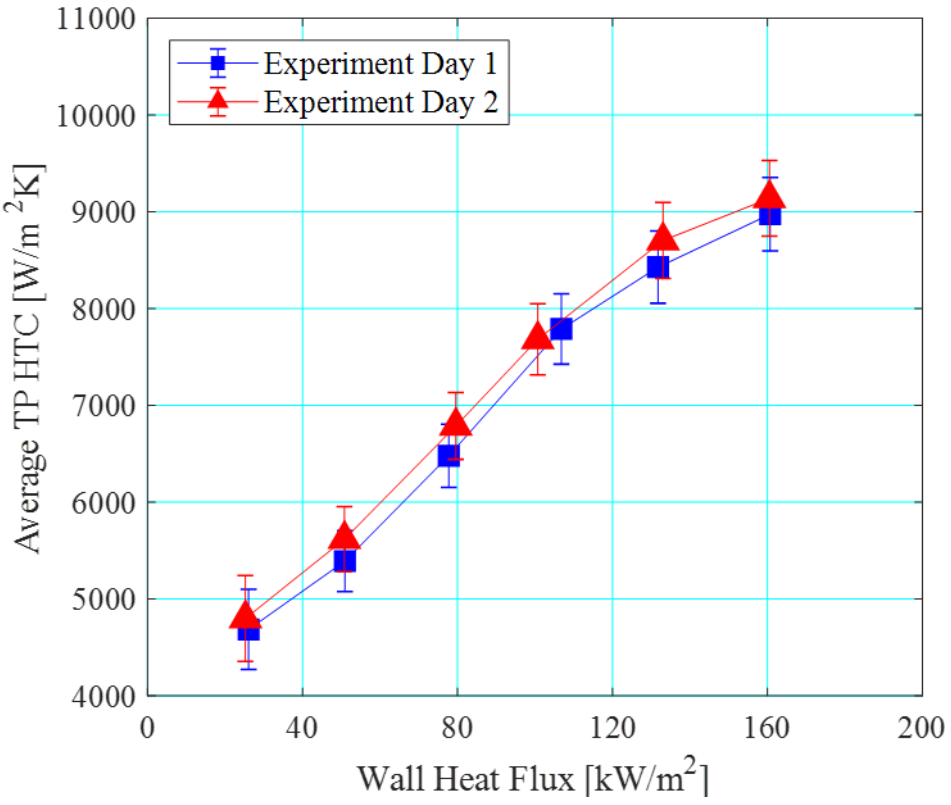

Figure 3.5: Repeatability of two-phase heat transfer coefficients (increasing heat flux) on different days at P = 1 bar, G = 200 kg/m^2 s and ΔT_{sub} = 10 K.

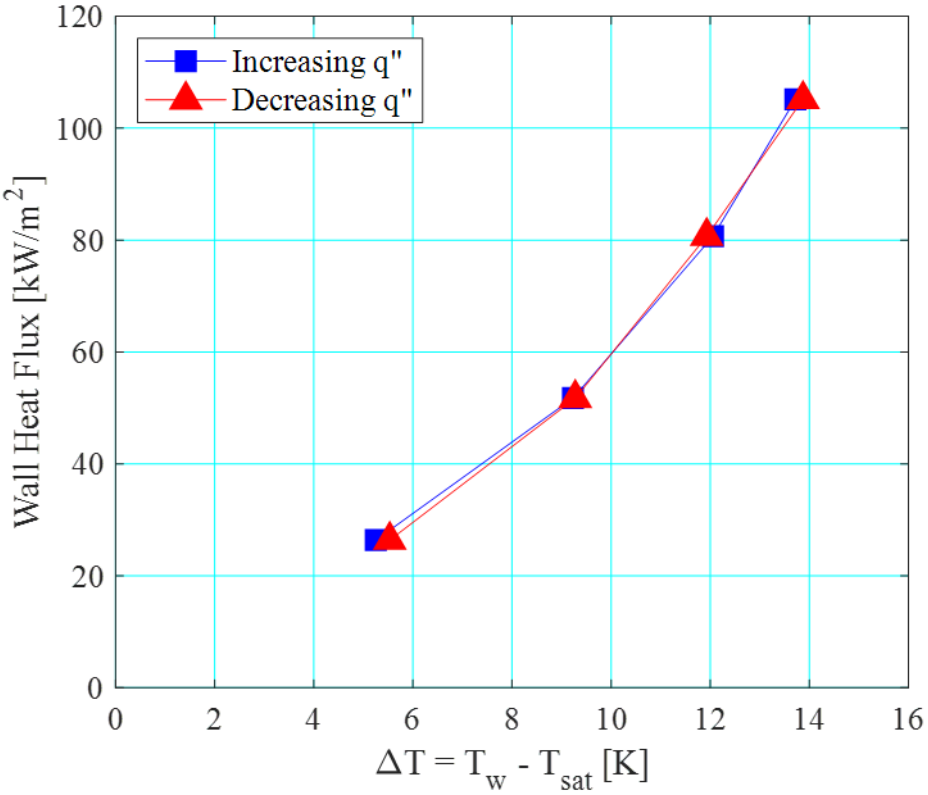

Figure 3.6: Boiling curves obtained with increasing and decreasing heat flux based on the wall temperature at the middle of the plain microchannel heat sink, i.e. z/L = 0.5, at P = 1 bar, G = 200 kg/m^2 s and ΔT_{sub} = 10 K.

3.7 Summary

Flow boiling experiments in a plain and coated copper microchannel heat sink were conducted for a range of experimental conditions for fluid HFE-7200, the properties of which are summarised in Table 3.2. Adiabatic and diabatic single-phase experiments were conducted to validate the experimental set-up. Flow visualisation was carried out during flow boiling experiments to capture flow pattern development using a high-speed camera at the middle of the heat sink along the streamwise direction. High-speed flow visualisation was also performed at certain test conditions at the inlet and outlet plenum to monitor flow instabilities in the heat sink. The measurement uncertainties were analysed and summarised in Table 3.4, as detailed in Appendix A. The repeatability of both single-phase and two-phase experiments in the plain and coated microchannel heat sinks were also validated. These results are presented for the plain channels in Section 3.5. For the coated channels, the single-phase results are discussed in Section 8.3 for ease of comparison of the experimental data.

4 Flow Boiling in Plain Microchannels

4.1 Introduction

Flow boiling experiments were conducted to investigate the effect of heat flux, saturation pressure, mass flux and inlet subcooling degree on microchannel flow boiling characteristics of HFE-7200, including high-speed flow visualisation. The experimental range of the current study is summarised in Table 3.3. In this chapter, flow boiling results obtained from the plain microchannel heat sink are presented. The experimental flow patterns, heat transfer and pressure drop behaviour as a function of heat flux is extensively discussed in Section 4.2. In Sections 4.2 to 4.5, flow boiling trends in relation to varying system pressure, mass flux and inlet subcooling conditions are presented accordingly. Finally, a summary of the experimental findings is given in Section 4.6.

4.2 Effect of Heat Flux

4.2.1 Flow Patterns

Flow visualisation was conducted at four locations along the channel array to capture flow pattern evolution corresponding to each experimental condition. High-speed recordings were conducted at 5000 fps at a magnification of 4.5x and a resolution of 512 x 512 pixels for a duration of 1.3 s at each location. The camera locations are illustrated in Figure 4.1(a). Additionally, high-speed recordings were also conducted at selected operating conditions, under a lower magnification of 2x for an extended duration of 6.5 s at the channel inlet and outlet in order to visualise flow distribution at the manifolds, see Figure 4.1(b).

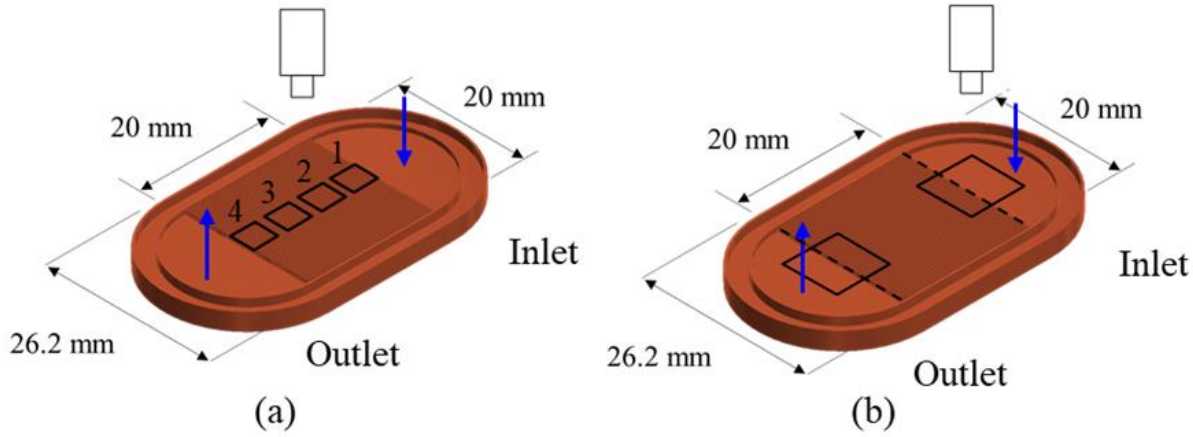

Figure 4.1: Camera locations for flow visualisation. (a) Flow patterns along channel. (b) Flow interaction at the channel inlet and outlet. Length of each frame is 4.4 mm.

It is important to note that the high-speed recordings are not simultaneous. Flow visualisation was conducted when all readings on LabVIEW appear to be at steady-state condition. Steady-state is defined when the fluctuations are within ±0.2 g/s for mass flow rate, ±0.5 K for inlet/outlet temperature and ±0.05 bar for the inlet/outlet pressure over a window of at least 180 s. Therefore, the flow patterns captured remain a good representation of the flow pattern development along the channels, although not simultaneously at each location. This was also verified by repeating the observations on at least two different occasions.

Where more than one flow regime is observed in a recording, especially in the intermittent churn flow regime, the dominant number of frames in the video, sampled at 100 frame intervals of the full-length of the recording, was used to determine the flow regime at a location. It is worth mentioning that more than one flow regime may be observed in two consecutive camera locations on the heat sink. This is because the local vapour quality has yet to exceed the critical transition vapour quality boundary at which flow pattern transition occurs in the channels. Local vapour quality increases according to energy balance along the streamwise length. Actual photographs of the flow regimes captured along the channel at the centre of the heat sink are shown in Figure 4.2 and Figure 4.3 for heat fluxes $q_w^{"}$ = 50.9 kW/m^2 and $q_w^{"}$ = 131.8 kW/m^2 respectively. It is clear that with increasing heat flux and consequently exit vapour quality in the channels, two-phase flow pattern evolved from bubbly to slug, churn and annular flow in the streamwise direction.

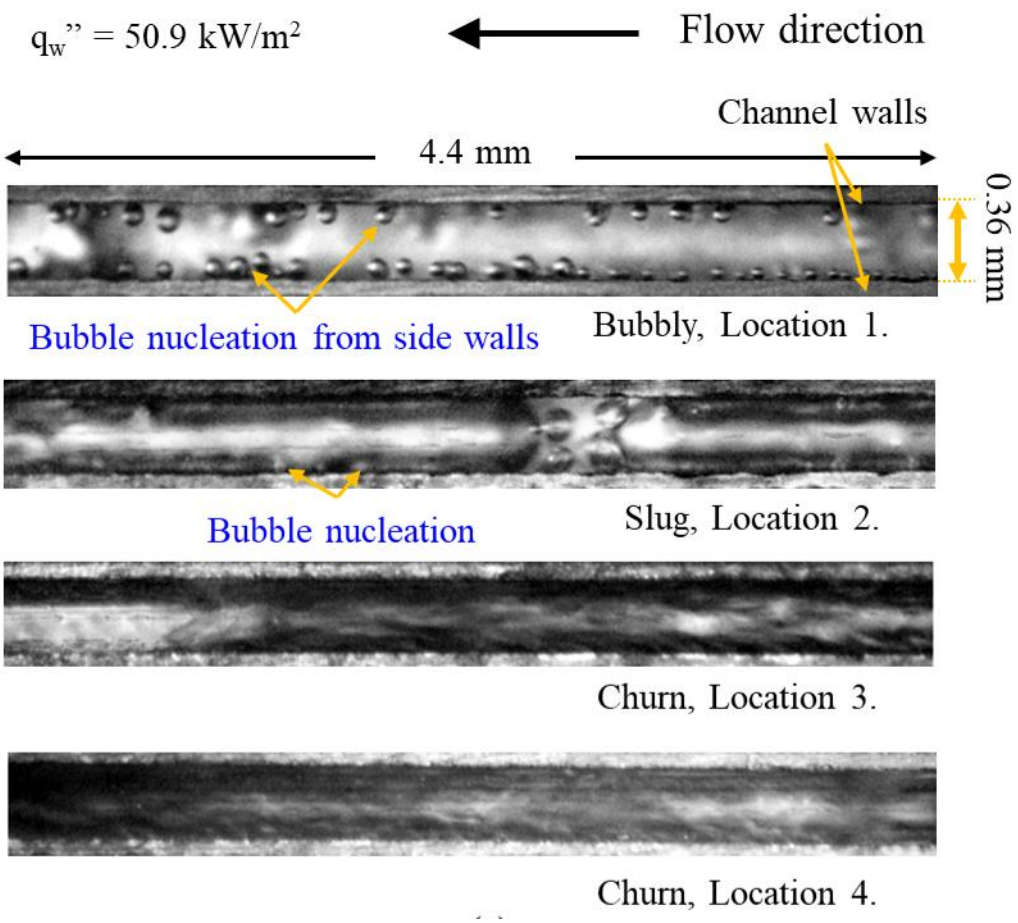

Figure 4.2: Flow patterns observed along the middle of the channel array at P = 1 bar, G = 200 kg/m^2 s, q_w" = 50.9 kW/m^2 and ΔT_{sub} = 10 K.

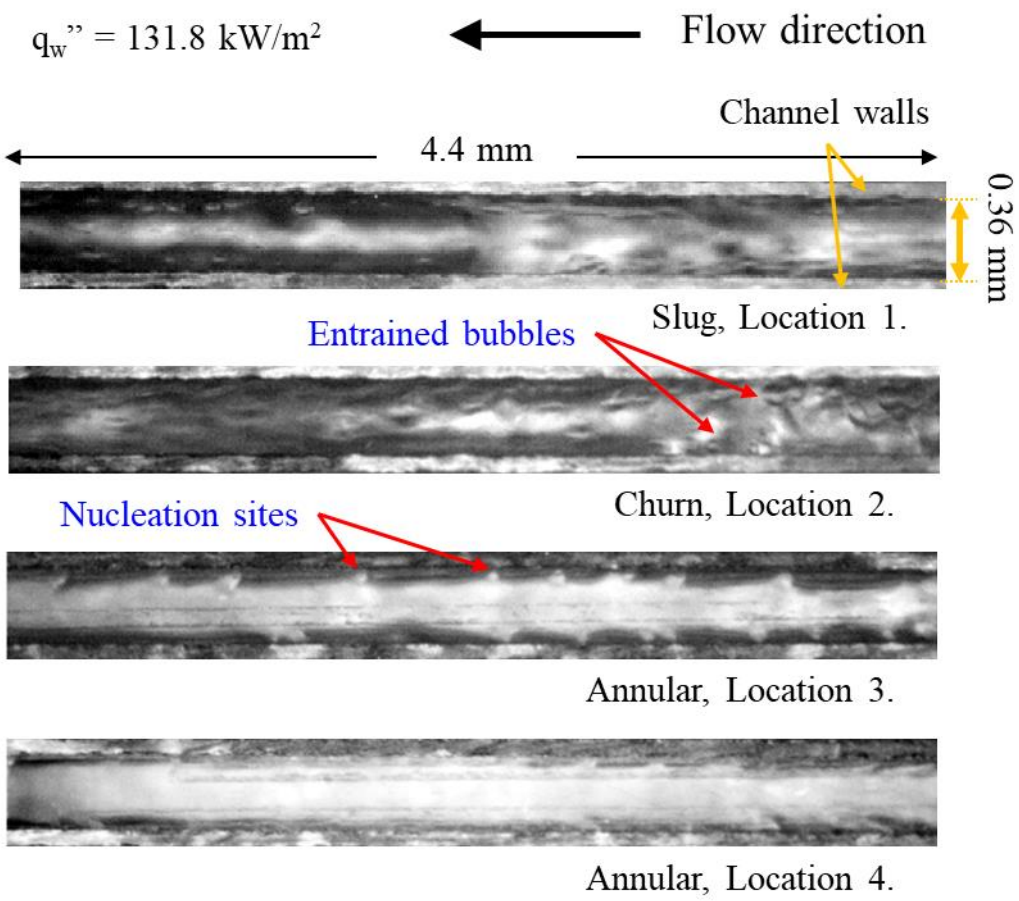

Figure 4.3: Flow patterns observed along the middle of the channel array at P = 1 bar, G = 200 kg/m^2 s, q_w" = 131.8 kW/m^2 and ΔT_{sub} = 10 K.

Bubbly flow was observed at very low heat fluxes, typically just after the onset of boiling in the channels. It is characterised by small bubbles nucleating from the side walls with isolated bubbles flowing within the bulk flow, as shown in Figure 4.2, Bubbly, Location 1. When the bubble reaches a defined bubble departure diameter, drag and surface tension forces are overcome and the bubble departs from the nucleation site. As the bubble departs, a small vapour embryo may be left behind at the nucleation site and the nucleation site remains active in the channel and a new vapour bubble grows from the cavity. This is supported by our flow visualisation results shown in Figure 4.4, where a nucleation site is observed to reactivate shortly following the departure of the previous bubble from the same site.

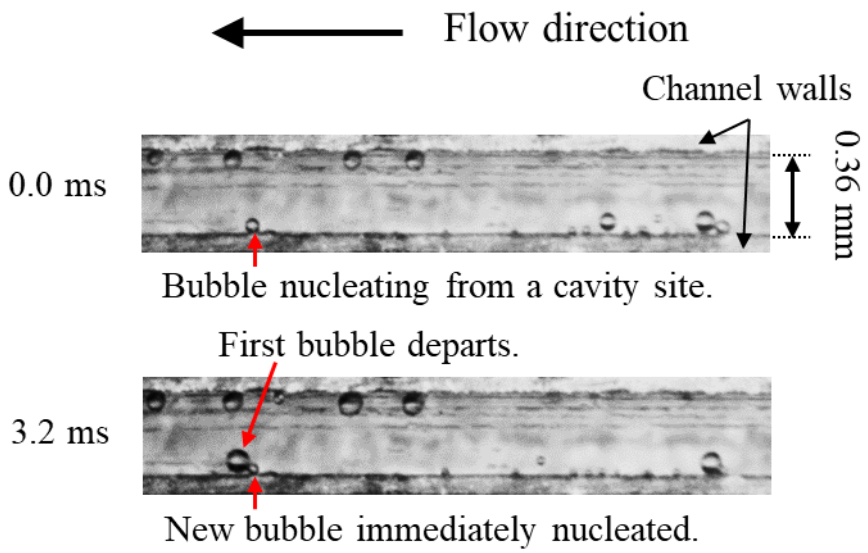

Figure 4.4: Bubble nucleation from the channel side wall at P = 1 bar, G = 200 kg/m^{2}s, $q_w^{"}$ = 26.4 kW/m^2 and ΔT_{sub} = 10 K.

In some cases, particularly in the subcooled region of the heat sink, the liquid layer directly adjacent to the heated channel walls may still become superheated, even if the bulk liquid flow is under subcooled conditions. As a result, nucleation activity from the channel side walls remain active, but departing bubbles shrink or re-condenses back into the flow as it encounters the subcooled bulk fluid, as illustrated in Figure 4.5. The channel is entirely subcooled at this experimental condition and the bubble almost re-condenses into the bulk fluid 1.6 ms after departure.

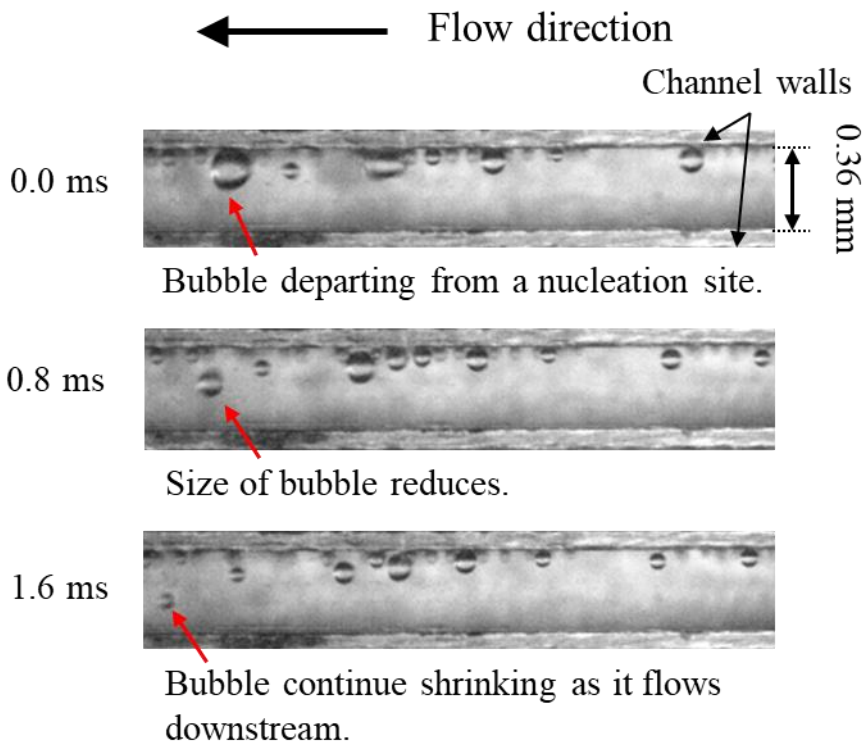

Figure 4.5: Bubble shrinkage in subcooled liquid. Images shown were captured at location 1, under conditions P = 1 bar, G = 200 kg/m^2 s, $q_w^{"}$ = 25.9 kW/m^2 and ΔT_{sub} = 20 K.

After departure, the bubble may slide along the channel wall or directly coagulate with neighbouring bubbles in the bulk flow. Intense bubble nucleation activity also promotes the establishment of slug flow due to increased bubble coalescence in the channels. Bubble coalescence increases the size of the bubbles considerably and eventually become confined by the channel walls. The confined bubbles elongate with further growth and slug flow is established in the channels. Figure 4.6(a) – (g) illustrate the transition from bubbly to slug flow, including the sequence of bubble growth, confinement and elongation in the microchannel. The nucleation and growth dynamics a nucleating bubble is tracked in the series of photographs. Note that the time interval between the frames are not regular. At an arbitrary time of 0 ms, a nucleation site a nucleation site marked in Figure 4.6(a) is activated and a small nucleating bubble is observed. The bubble continues to growth whilst the attached to the cavity for approximately another 3.4 ms (Figure 4.6(b)). It comes into close contact with a bubble in the vicinity and coagulates with the neighbouring bubble at 6.4 ms (Figure 4.6(c)). The newly-merged bubble continues to grow in size approaching the width of the channel and eventually become confined at 11.2 ms (Figure 4.6(d)). As the bubble grows under confinement, it elongates in both the upstream and downstream direction and comes into contact with a bubble

downstream (Figure 4.6(e)). The slug is shown to be merging with the neighbouring bubble in Figure 4.6(f) at 16.6 ms. The slug elongates and moves downstream along the channel in Figure 4.6(g). The slug flow regime is also illustrated in Figure 4.2 (Slug, Location 2) and Figure 4.3 (Slug, Location 1). Isolated bubbles may flow in between successive vapour slugs. Furthermore, slug growth against that of the flow pushes bubbles upstream of the tracked slug toward the inlet manifold, effectively inducing backflow in the channel, as indicated in Figure 4.6(e) – (g). This was similarly reported in Al-Zaidi et al. [57].

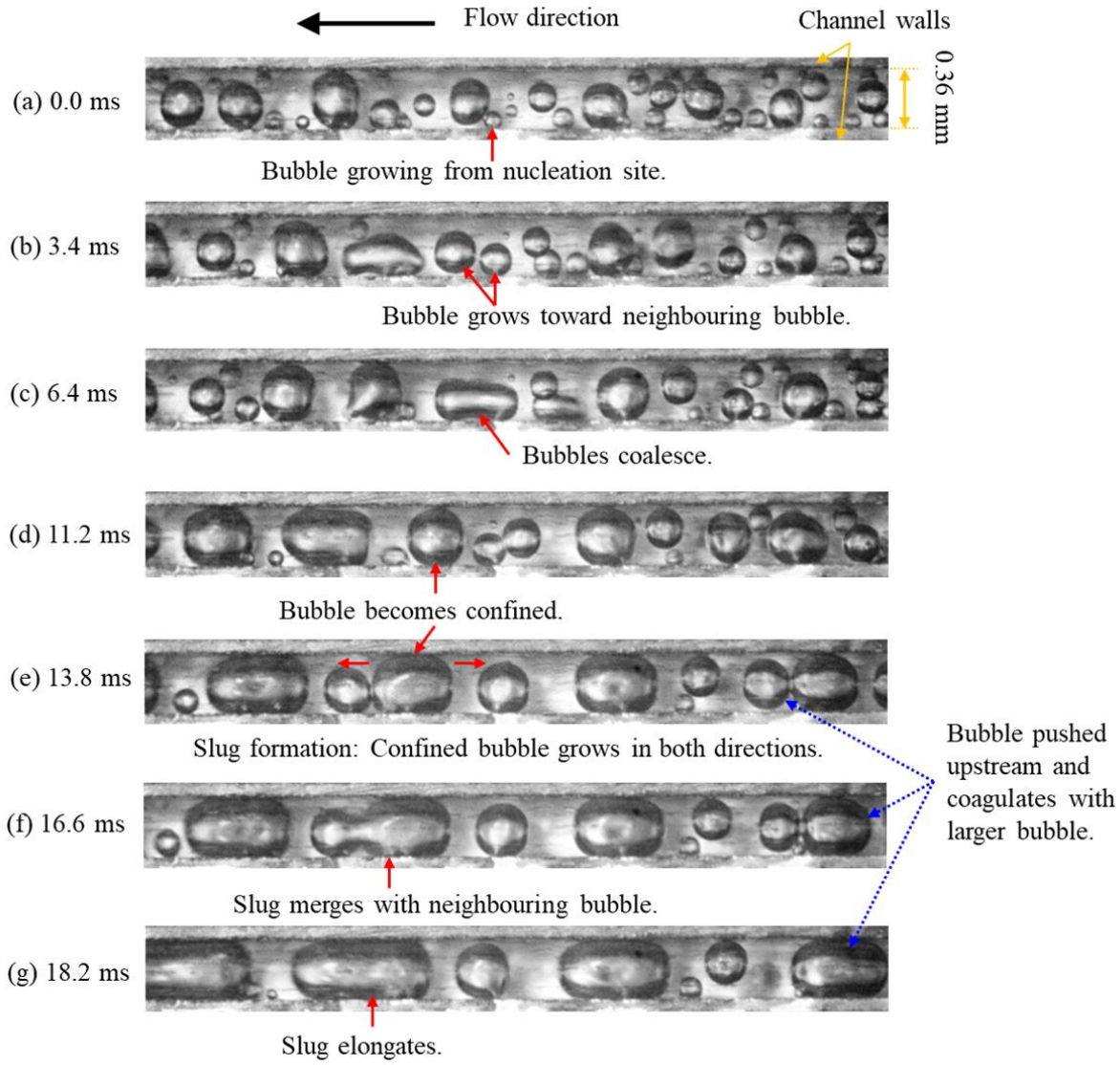

Figure 4.6: Slug formation from bubble confinement captured at camera location 3 and conditions P = 1 bar, G = 200 kg/m^2 s, $q_w^{"}$ = 25.2 kW/m^2 and ΔT_{sub} = 10 K.

With increasing heat flux, more slugs develop along the channel, which may coagulate to form long slugs spanning the full length of the frame (circa 4.4 mm) in the slug flow regime. Liquid

film dryout were occasionally observed in slug flows, typically where long slugs are observed along the channel. While slugs do not immediately suppress nucleation sites in the channel, active nucleation sites were temporarily deactivated on occasions when the liquid film surrounding the slug becomes very thin and in certain cases dries out completely. Figure 4.7(a) shows an active nucleation site on channel side wall, as indicated on the photograph at 0 ms. Note that the time intervals between the frames are irregular. An advancing long slug floods the cavity and nucleation activity is momentarily suspended at 10 ms. Nonetheless, the cavity reactivates soon after and nucleating bubbles are continually observed to rupture from the slug liquid film up until 102 ms. The thickness of the liquid film gradually reduces due to evaporation and completely dries out at 102 ms, as shown in Figure 4.7(e). The nucleation site is suppressed following liquid film dryout. Dryout in the channels persisted for another 110 ms and incoming liquid flow enters the channels at 212 ms (Figure 4.7(f)). The nucleation site appears to be reactivated at 272 ms (Figure 4.7(g)).

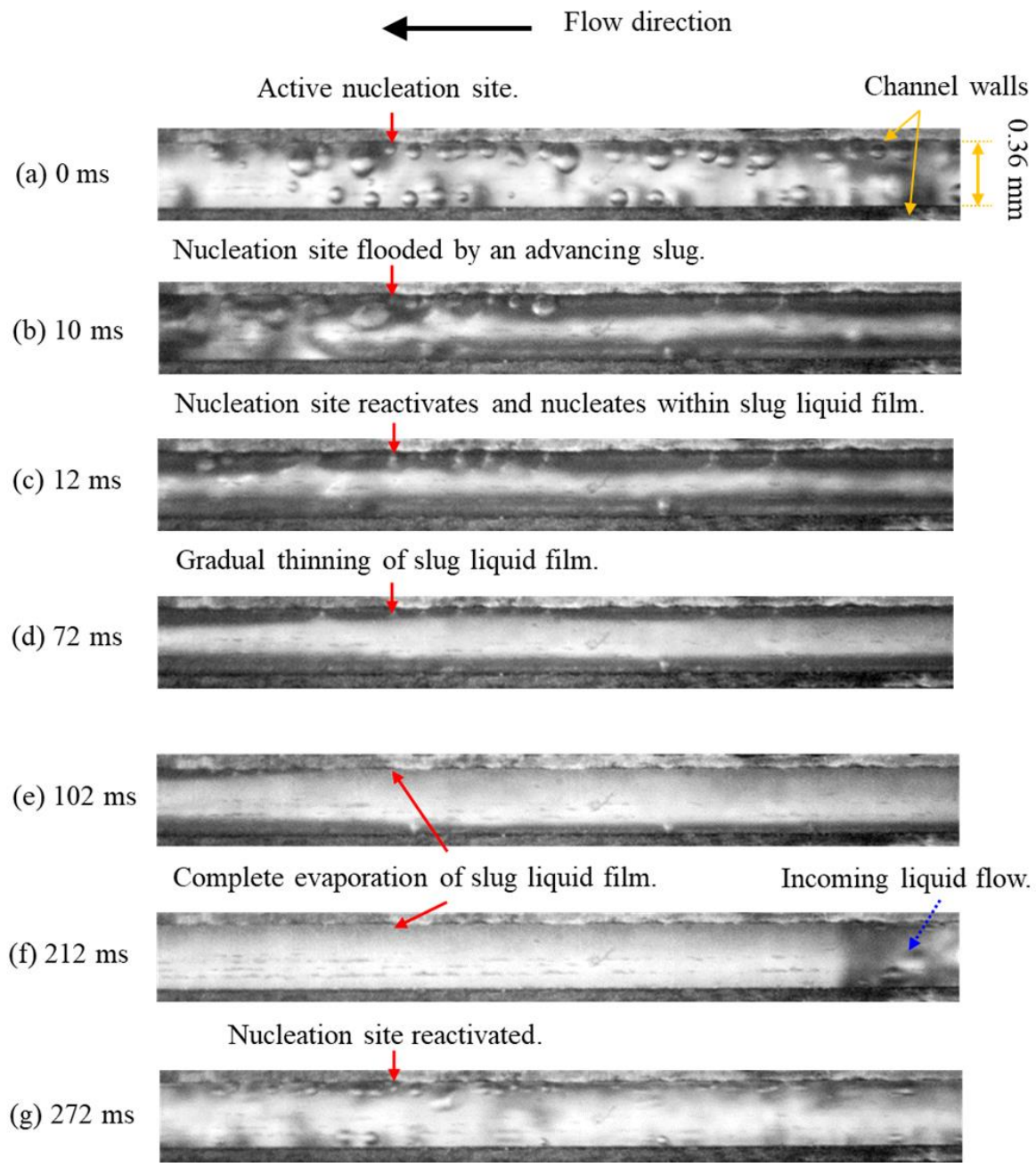

Figure 4.7: Nucleation site suppression by slug liquid film dryout, captured at camera location 2 and conditions P = 1 bar, G = 200 kg/m^{2}s, $q_w^{"}$ = 50.9 kW/m^2 and ΔT_{sub} = 10 K.

Furthermore, the rapid expansion of slugs in the confined channels induce flow reversal in the channels, as the elongation against the flow direction pushes the upstream bubbles in the flow back towards the inlet plena. Flow reversal is captured in a sequence of photographs shown in 200 ms intervals in Figure 4.8(a) – (d). Initially, the flow direction is from the channel inlet towards the channel outlet. Slugs develop along the channel and elongate laterally, see Figure 4.8(b). This causes vapour backflow into the inlet manifold. The incoming subcooled liquid at

the inlet plena pushes the slugs and the vapour in the manifold back along the channel and overcomes backflow in Figure 4.8(d). During flow reversal, slugs also appear to migrate from neighbouring channels through the inlet manifold, as illustrated in Figure 4.9.

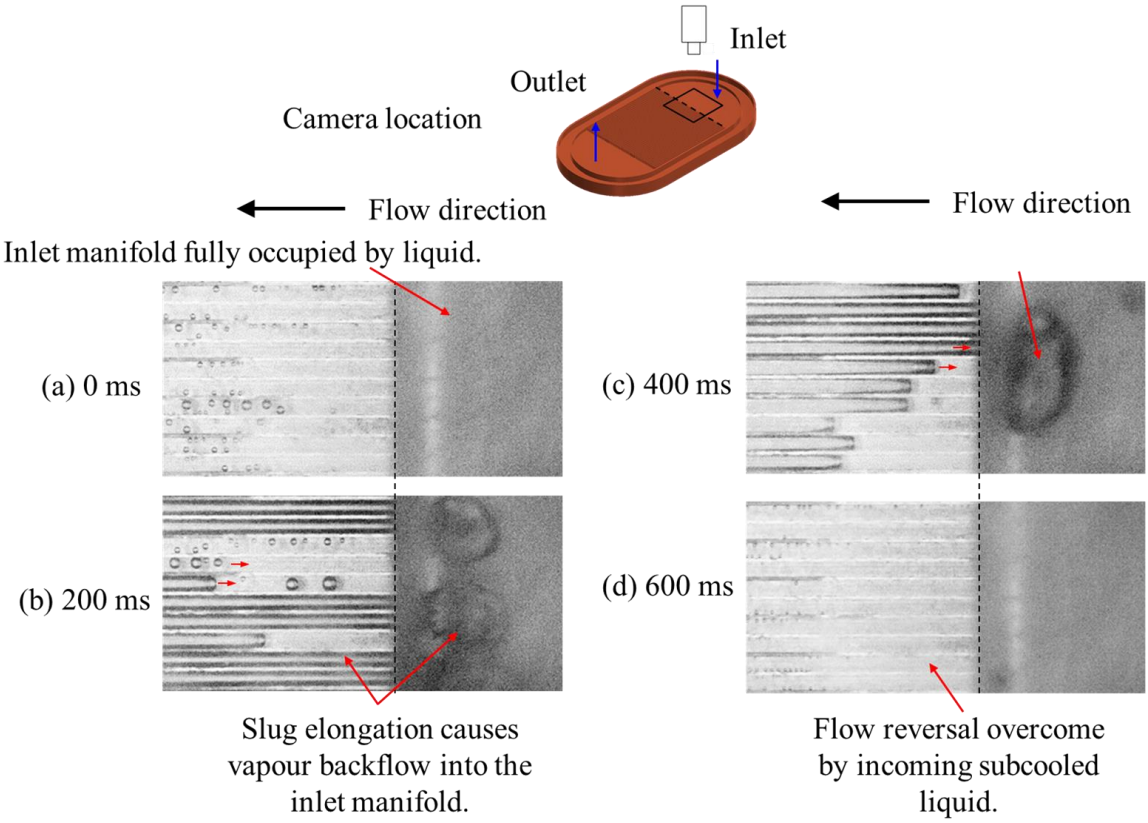

Figure 4.8: Flow reversal captured at the channel inlet and conditions P = 1 bar, G = 300 kg/m^2 s, $q_w^{"}$ = 24.8 kW/m^2 and ΔT_{sub} = 10 K.

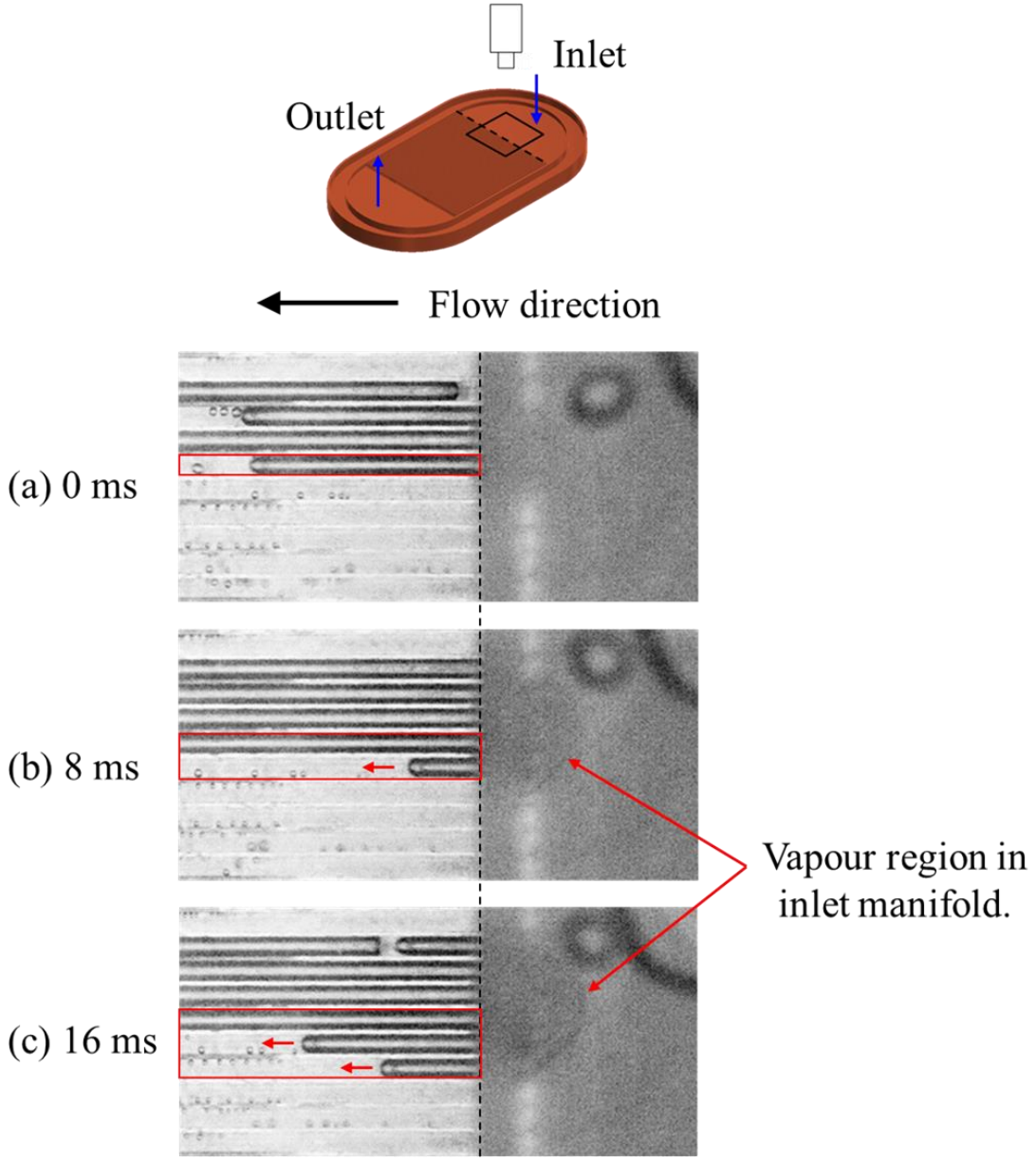

Figure 4.9: Slugs migrating from neighbouring channel through inlet plenum, captured at P = 1 bar, G = 300 kg/m^2 s, q_w" = 24.8 kW/m^2 and ΔT_{sub} = 10 K.

The liquid film surrounding the vapour slug evaporates as it travels along the channel. In Figure 4.10, transition from slug to churn flow occur when the high velocity vapour phase in the slug distorts the shape of the slug and forces the tip to collapse, creating a chaotic mixture of liquid and vapour which flows downstream of the slug. This is captured in the image sequence shown at 1 ms intervals under the condition of P = 1 bar, q_w" = 79.5 kW/m^2, G = 200 kg/m^2 s and ΔT_{sub} = 20 K, captured at camera location 2. At 0 ms to 1 ms, a slug advances in the channel. At 2 ms, the tip of the slug starts to collapse and churn flow develops upstream of the slug tip. The mixture accelerates toward the exit and breaks up individual slugs further downstream.

Entrained bubbles sometimes visible in the dispersed churn wave, as illustrated in Figure 4.3, Churn, Location 2, may have originated from nucleating bubbles stripped from their respective sites as the churn wave advanced past the cavity. As the intermittent churn wave propagates along the channel, a thin liquid layer is left on the channel walls.

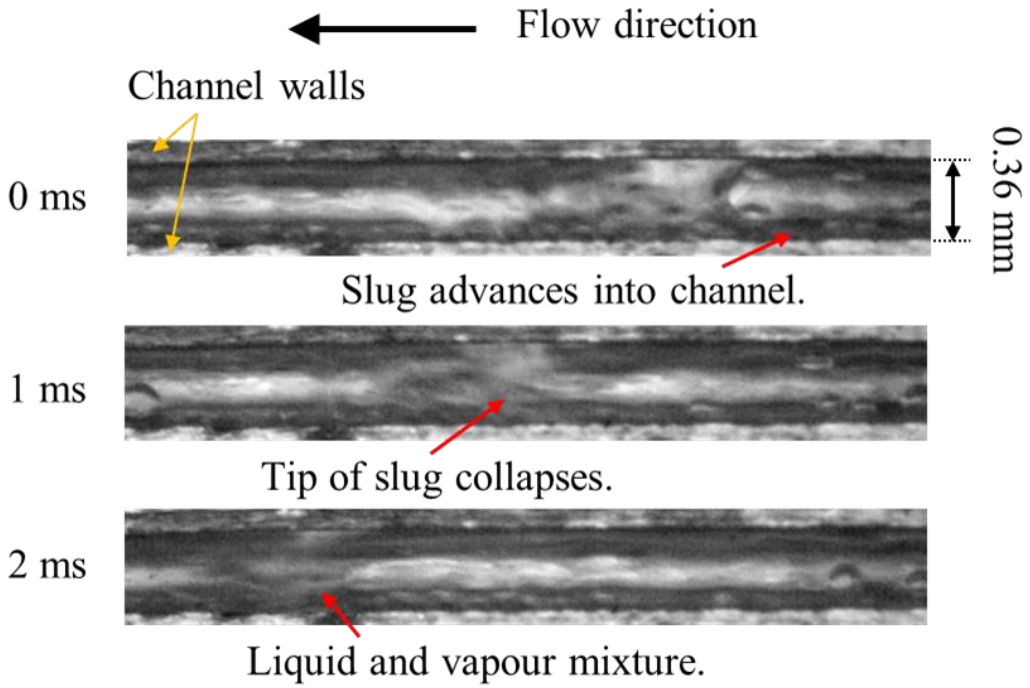

Figure 4.10: Formation of churn flow, captured at P = 1 bar, G = 200 kg/m^2 s, $q_w^{"}$ = 79.5 kW/m^2 and ΔT_{sub} = 20 K.

With increased heat flux, the rate of evaporation is sufficiently high that a continuous vapour phase is established in the middle of the microchannels. Annular flow develops, characterised by a thin liquid film attached to the channel side walls with a clear vapour core along the channels (Figure 4.3, Annular, Location 3 and 4). As mentioned above, long slugs have also been observed in the slug flow regime. The distinction between slug and annular flow, respectively, is the observation of isolated slugs in the interim between subsequent long slugs in slug flow and an uninterrupted vapour core in annular flow. Flow visualisation revealed that nucleation sites remained active within the liquid film in annular flow, see Figure 4.11. As was observed in the slug flow regime, nucleating bubbles were also observed to rupture from the thin liquid film during annular flow in the channels.

Nucleation in the liquid film during annular flow were also reported in Balasubramanian and Kandlikar [272], Harirchian and Garimella [84], Borhani and Thome [273] and Al-Zaidi et al. [57]. The nucleation sites may become suppressed with gradual thinning and dryout of the annular liquid film. Nonetheless, as the liquid layer is nearing depletion or completely evaporated, the dispersed phase (i.e. liquid and vapour mixture) brought about by the intermittent churn flow rewets the channels and a liquid film is re-established on the channel side walls, see Figure 4.12. Due to the rewetting mechanism of the intermittent churn wave, the period of the dryout phenomenon occurring in annular flow were typically much shorter (less than 10 ms, if dryout occurs) compared to the dryout cycle recorded in the slug flow regime (~ 100 ms).

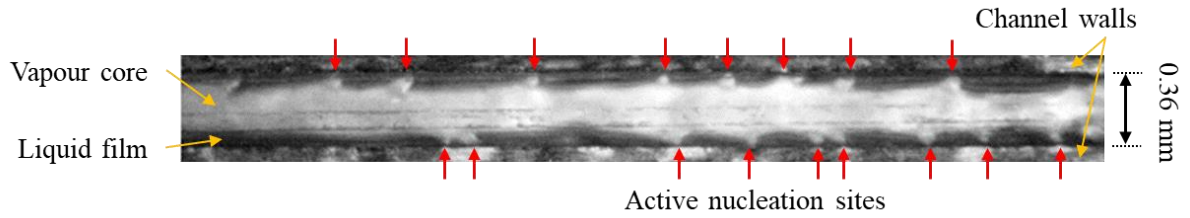

Figure 4.11: Bubbles rupturing from nucleation sites within annular liquid film, captured at camera location 3, under conditions P = 1 bar, G = 200 kg/m^2 s, $q_w^{"}$ = 131.8 kW/m^2 and ΔT_{sub} = 10 K.

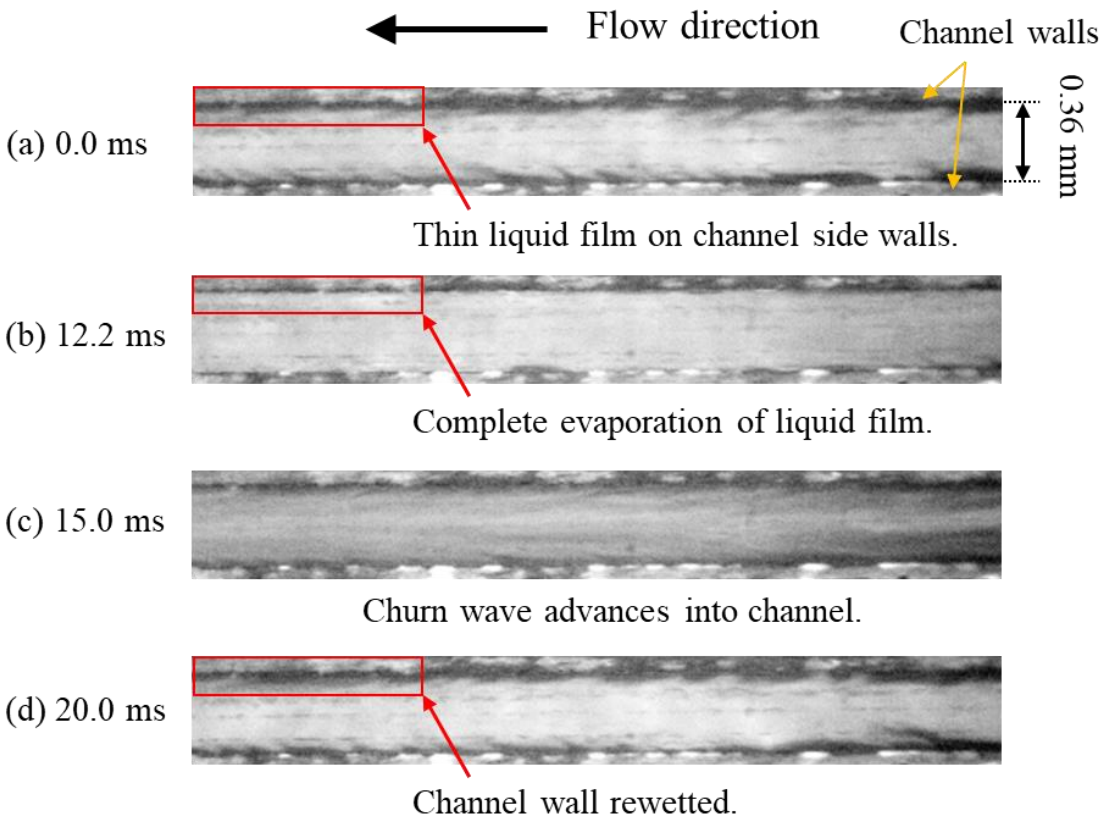

Figure 4.12: Rewetting mechanism by intermittent churn wave, captured at camera location 3, under conditions P = 1 bar, G = 300 kg/m^2 s, q_w'' = 230.8 kW/m^2 and ΔT_{sub} = 10 K.

4.2.2 Heat Transfer

Local heat transfer coefficients were calculated from the temperature measurements at various locations on the heat sink, as detailed in Section 3.2 and illustrated in Figure 3.2. The local heat transfer trend along the channel, at the centre of the heat sink is plotted as a function of vapour quality and dimensionless axial location in Figure 4.13 and Figure 4.14. The respective vapour qualities at which flow pattern transition from bubbly to slug, churn and annular flow, as described in Section 4.2.1 are annotated on Figure 4.13.

Local heat transfer coefficients increase along the channel in the subcooled region. Generally, a peak in local heat transfer coefficients is observed at axial locations near boiling incipience, at low vapour qualities in the channel. After the initial peak at the onset of boiling, the local heat transfer trend decreases moderately along the channel with increasing local vapour quality, also observed in Al-Zaidi et al. [274] using a similar fluid, HFE-7100, and Choi et al. [86], but recovers slightly near the channel exit. Bubbly flow is observed only at very low vapour qualities, i.e. $x < 0.04$. With increase in bubble coalescence in the channels, slug flow is established in the channels, albeit only in a narrow range of vapour qualities up to $x = 0.07$, where transition to churn flow occurred in the channels. The churn flow regime was observed in a large majority of the data points in the channel array. At high heat fluxes and vapour qualities beyond $x = 0.3$, annular flow developed in the channels.

The sharp rise in heat transfer coefficients at low heat fluxes ($q_w^{"}$ = 26.1 and 77.7 kW/m^2) in the subcooled and bubbly flow region is due to the change in heat transfer mode from single-phase liquid convection to nucleate boiling in the channels. As illustrated in Figure 4.2, Bubbly, Location 1, intensive bubble nucleation activity from the channel side walls is observed in the bubbly flow regime. As a result, the nucleate boiling mechanism may be reasonably assumed to dominate in this region. The high heat transfer coefficients could thus be due to the high heat transfer rates arising from micro-layer evaporation underneath nucleating bubbles, as mentioned in Mahmoud and Karayiannis [56], combined with the micro-convection currents induced in the bulk fluid surrounding a nucleating bubble as it departs its nucleation site.

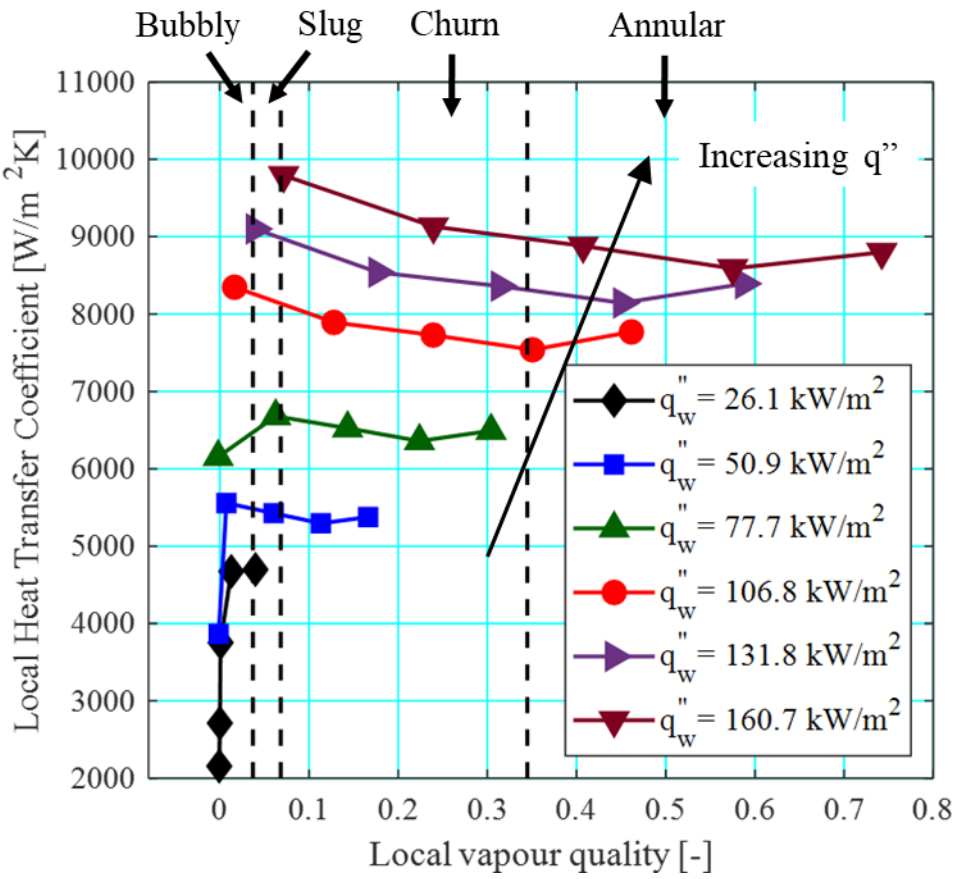

Figure 4.13: Local heat transfer coefficients as a function of vapour quality along the centre of the heat sink at P = 1 bar, G = 200 kg/m^2 s and ΔT_{sub} = 10 K.

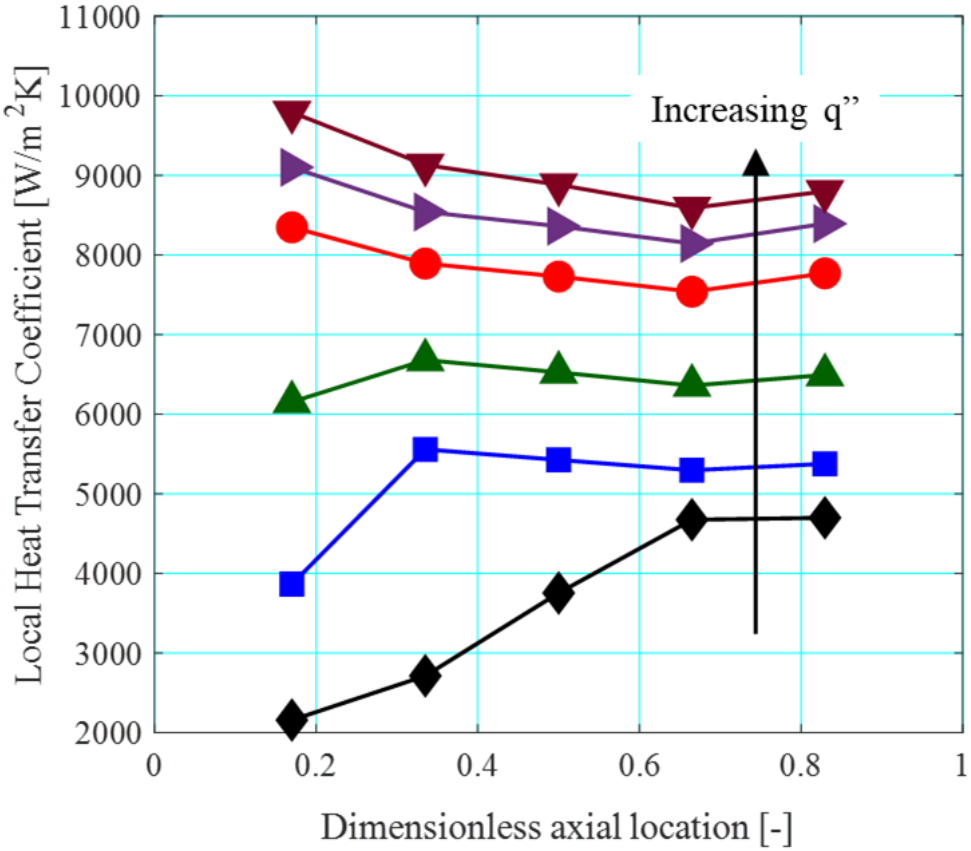

Figure 4.14: Local heat transfer coefficients with respect to axial location for wall heat fluxes q_w" = 26.1 kW/m^2 to 160.7 kW/m^2, refer to Figure 4.13 for symbols, along the centre of the heat sink ($T_{tc8} - T_{tc12}$, see Figure 3.2) at P = 1 bar, G = 200 kg/m^2 s and ΔT_{sub} = 10 K. Empty markers represent heat transfer coefficients in the subcooled region.

Some authors have argued that heat transfer coefficients may be over-predicted, especially near the channel inlet, with the assumption of a linear two-phase pressure drop profile along the channel [208], [275]. The wall temperature profile at five locations along the centre of the heat sink, as well as the corresponding saturation temperature, estimated based on the assumption of linear pressure variation is shown in Figure 4.15. Huang and Thome [208] showed that the local temperature profile decreased in a parabolic trend along their multi-microchannel array, quite different from the linear pressure drop assumption in the two-phase region. They reported that the discrepancy in local saturation temperature (estimated based on the pressure profile) may be as high as 1.5 K, which had a pronounced effect on the resulting local heat transfer prediction, especially near the onset of boiling. Nonetheless, maximum two-phase pressure drop was nearly 70 kPa in [208], which is much larger than the channel pressure drop in this

study (< 12 kPa). The high pressure drops encountered in the abovementioned studies could be due to the smaller hydraulic diameter and high mass fluxes investigated.

The Mishima and Hibiki [205] pressure drop correlation, which has been found to best predict two-phase pressure drop in the current study, see Section 7.2.2, was used to evaluate the effect of the assumption of a linear and parabolic pressure variation on the estimation of local heat transfer coefficients in the channel. This is depicted in Figure 4.16 for an experimental condition of P = 1 bar, G = 200 kg/m^2 s, ΔT_{sub} = 10 K and $q_w^{"}$ = 106.8 kW/m^2. Note that the experimental two-phase pressure drop at this condition is only 2.45 kPa, while the correlation slightly overpredicts the pressure drop to be 3.02 kPa. As a result, the pressure at the outlet of the channels of the parabolic curve is lower than in the linear case. After the onset of boiling, it is clear that the pressure profile with the linear assumption is slightly lower than the parabolic profile. Thereafter, partly due to the overprediction of two-phase pressure drop by the correlation, the parabolic pressure curve is lower than the linear pressure trend. Nevertheless, the local saturation temperature estimated based on the parabolic pressure variation only showed a maximum discrepancy of ± 0.06 K along the channel, in comparison to the linear assumption. The resulting effect of local heat transfer coefficients was less than ±0.4 %, see Figure 4.17, well within the error bar of the experiment (±4.4 % at this condition). This demonstrates that the peak in local heat transfer coefficient near the location of boiling incipience is not significantly inflated due to the assumption of a linear pressure drop profile in the two-phase region.

The subsequent reduction in local heat transfer coefficients with respect to vapour quality could be attributed to the suppression of bubble nucleation sites, as shown in the sequence of images in Figure 4.7 during slug flow as well as during the gradual thinning liquid film in annular flow. Cavity flooding and liquid film dryout partially suppress nucleate boiling due to the impedance of bubble nucleation. At the same time, liquid film evaporation in the slug, churn and annular flow regimes promote convective boiling in the heat sink. Nucleate boiling is a more efficient heat transfer mode compared to convective boiling – the magnitude of nucleate boiling heat transfer coefficients may be several times larger than heat transfer rates associated with the convective boiling mechanism. For instance, the heat transfer correlation proposed by Kim and Mudawar [184], who also noted nucleate boiling suppression in their experimental results, predicts heat transfer coefficients of the nucleate boiling component to be 2 – 3 times larger than that of the convective boiling mechanism. Naturally, the periodic suppression of

nucleation cavities reduces the time-averaged heat transfer coefficient at a given location on the channels. This could explain why local heat transfer coefficients decrease with increasing vapour quality along the channel, corresponding to flow pattern transition to the slug, churn and annular flow regime.

As emphasised in Costa-Patry et al. [83] and Huang et al. [92] , heat transfer coefficients rose with vapour quality when thin-film evaporation occurred near the exit of the channels. The increase in heat transfer coefficient near the channel exit could be due to conjugate effects in the heat sink occurring at the boundaries between the microchannel array and the inlet/outlet plena. As detailed in Figure 3.2 above, heat input is concentrated underneath the square base area where the high surface area microchannel array is situated. Nonetheless, a small percentage of the heat input could have been lost to the plena through conjugate heat effects, in particular the outlet plenum. The heat loss to the outlet plenum is more notable due to the outlet flow quality, whereas subcooled liquid is continuously conveyed into the inlet plenum throughout experiments. Due to the heat loss, temperature measured near the channel exit (at $z/L = 0.83$) could have been artificially lowered, and thus a pseudo higher heat transfer coefficient is estimated near the channel exit based on Eq. (3.25).

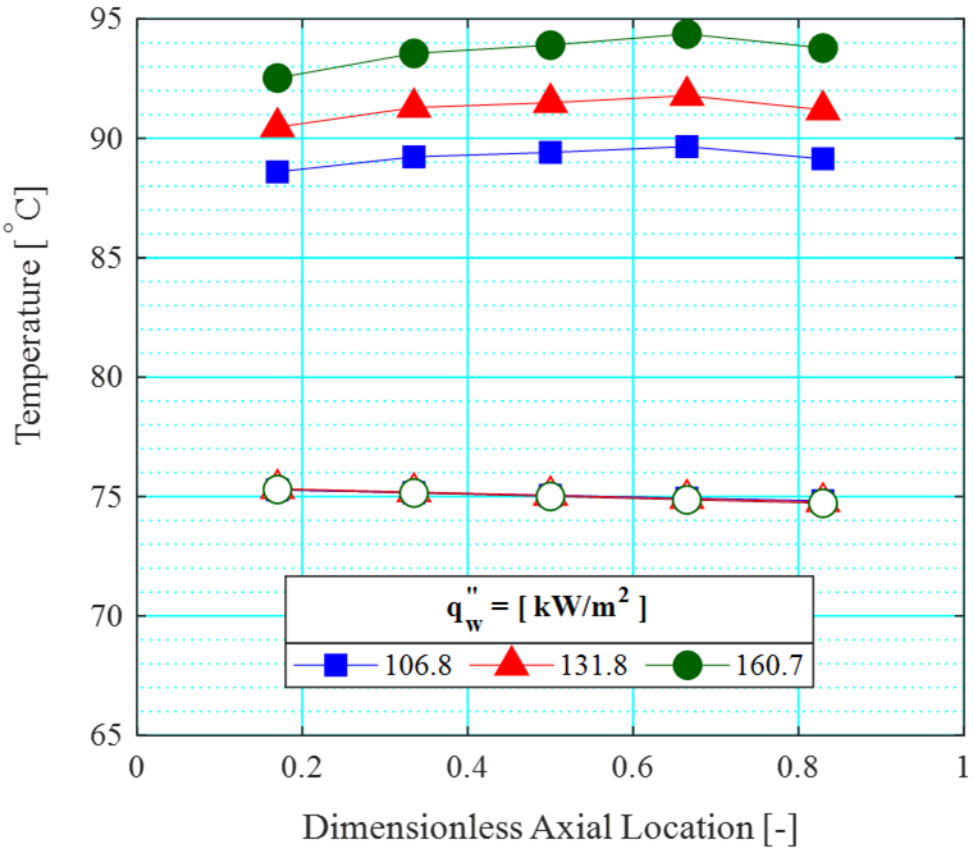

Figure 4.15: Local wall temperatures and the corresponding saturation temperature estimated using the linear pressure drop assumption at P = 1 bar, G = 200 kg/m^2 s and ΔT_{sub} = 10 K.

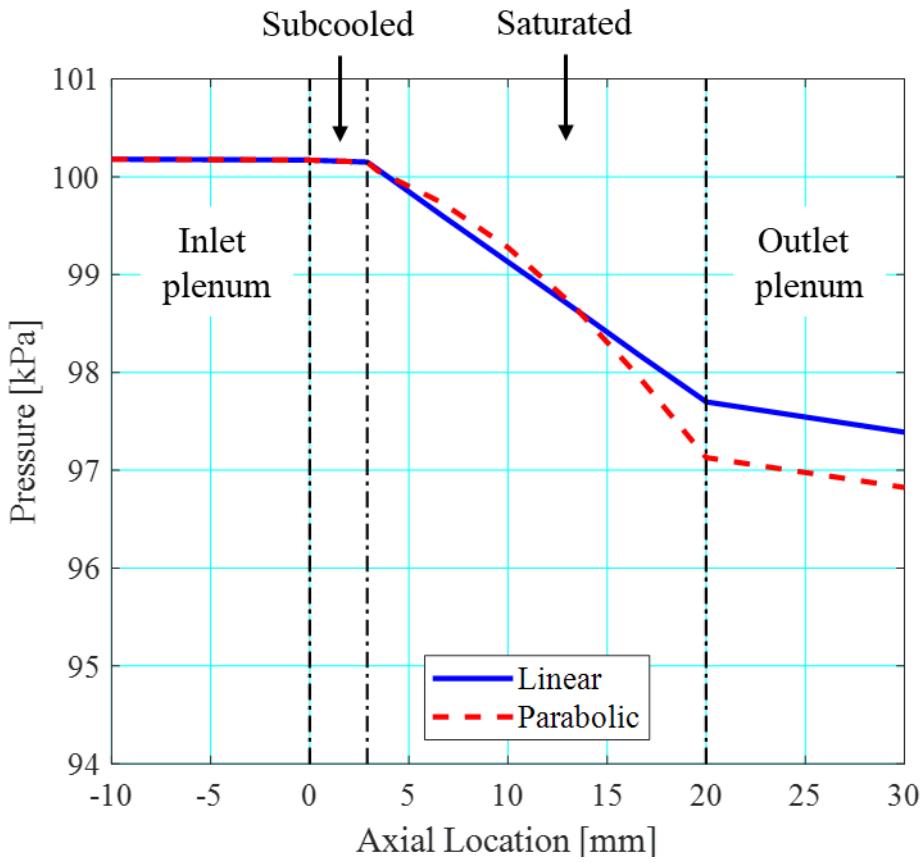

Figure 4.16: Pressure profile in the heat sink with (i) the assumption of a linear pressure drop profile and (ii) parabolic variation estimated using the Mishima and Hibiki [205] correlation.

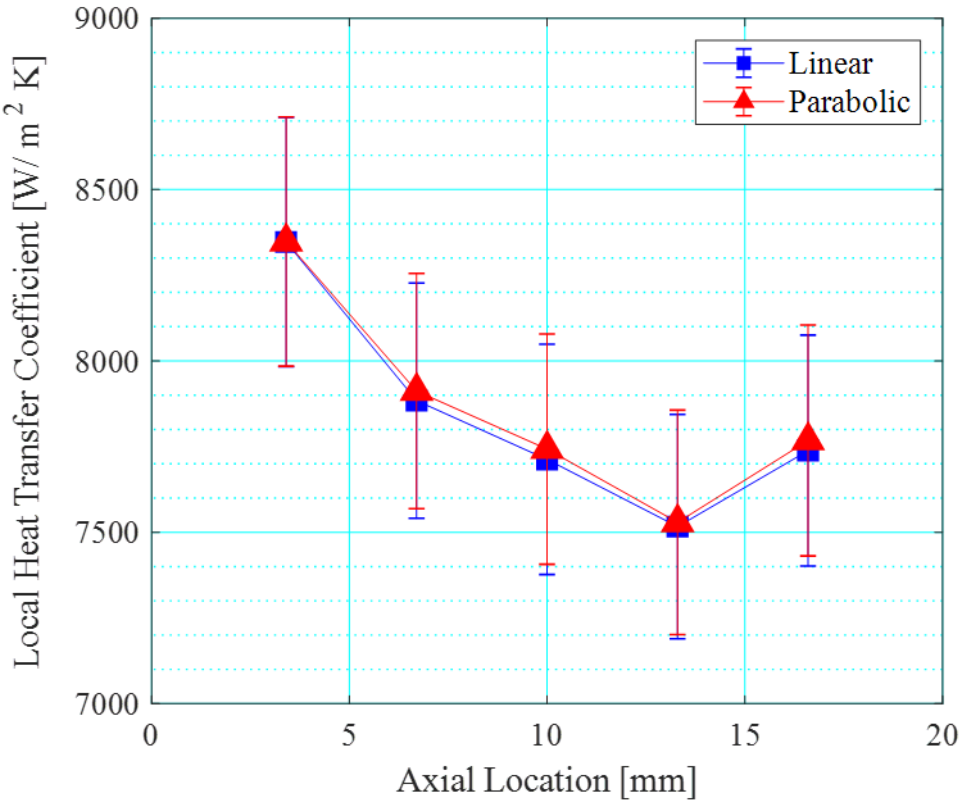

Figure 4.17: Difference in local heat transfer coefficients with the assumption of a (i) linear and (ii) parabolic pressure drop profile in the two-phase region.

A clear heat flux effect may also be inferred from Figure 4.13. All heat transfer coefficients along the channel are seen to increase steadily with increasing heat flux level in the heat sink. The average two-phase heat transfer coefficient, that is, the heat transfer coefficient averaged from only the local heat transfer coefficients in the two-phase region, according to Eq. (3.31), is depicted as a function of wall heat flux in Figure 4.18. Average two-phase heat transfer coefficients increased steadily with increasing wall heat flux (and exit vapour quality), as was also reported by Bertsch et al. [68], [69], Fayyadh et al. [70] and Al-Zaidi et al. [57] for microchannel heat sinks.

The increase in heat transfer coefficients corresponding to increase in heat flux is partly due to the increase in bubble generation frequency with increase in wall heat flux. With increase in bubble nucleation activity in the channels, nucleate boiling heat transfer coefficients increase accordingly. As mentioned above, following flow pattern transition to slug, churn and annular flow, the periodic suppression of some previously active nucleation sites is observed. Nonetheless, the convective boiling mechanism, namely through thin-film evaporation, counteracts against the reduction in nucleate boiling heat transfer coefficients and begins to contribute more to overall heat transfer in the channels. The shared contribution of both the nucleate and convective boiling components are also evident in Figure 4.11, where a considerable number of nucleation sites remain active within the annular liquid film in annular flow. Nucleating bubbles in liquid films have also been reported in Balasubramanian and Kandlikar [272], Harirchian and Garimella [84], Borhani and Thome [273], and Al-Zaidi et al. [57]. As a consequence, average heat transfer coefficients continue to increase with increase in heat flux.

A sudden drop in heat transfer coefficients at high heat fluxes, observed in several studies including the one by Harirchian and Garimella [84], [85], did not occur in the current experimental range. Flow boiling instabilities, which Kim and Mudawar [276] stressed could trigger premature dryout (i.e. dryout at $x < 1$), did not appear to induce premature critical heat flux and ultimately did not adversely affect heat transfer performance in the current range of experiments. This could be because prolonged periods of dryout were not observed in the flow visualisation and all experiments were confined to vapour qualities $x < 1$. The high wettability of the working fluid, HFE-7200, on the copper heat sink substrate might also have encouraged the adherence of the liquid film to the channel walls during annular flow, even at high heat fluxes. Furthermore, the rewetting mechanism of the intermittent churn wave might have

helped mitigated wall dryout in the channels, as depicted in Figure 4.12. The effect of saturation pressure is discussed in detail in Section 4.3.3.

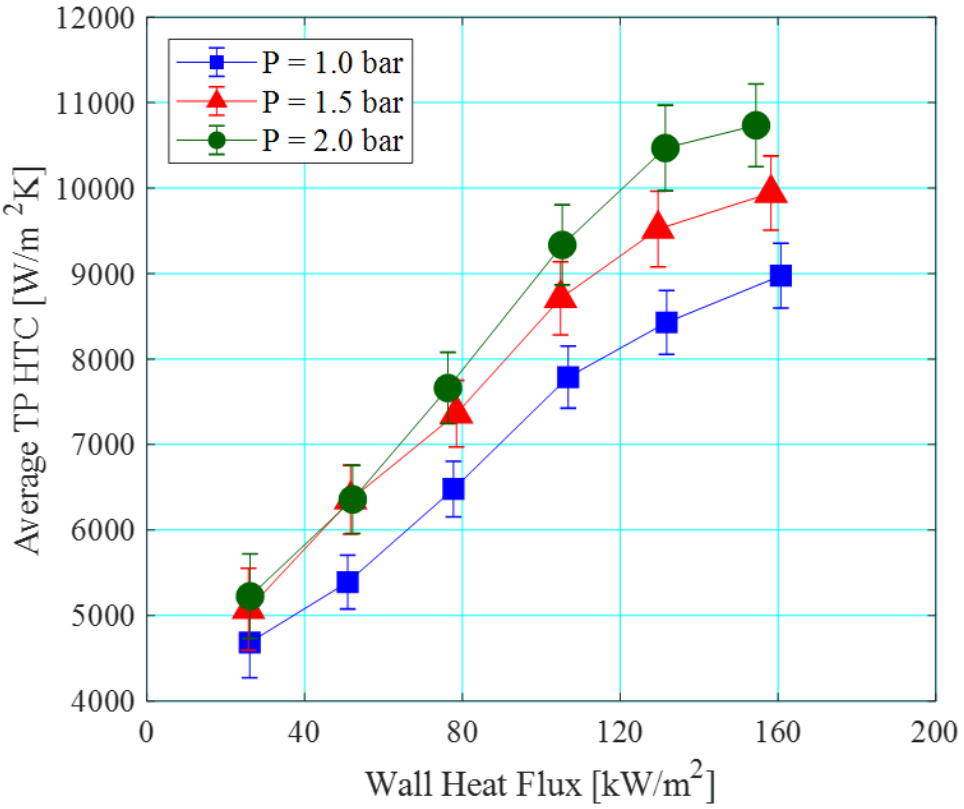

Figure 4.18: Average two-phase heat transfer coefficients with respect to wall heat flux (q_w" = 26.1 – 160.7 kW/m^2), at G = 200 kg/m^2 s and ΔT_{sub} = 10 K for three inlet pressure conditions.

4.2.3 Pressure Drop

Two-phase pressure drop in the channels, calculated based on Eq. (3.19), is shown in Figure 4.19 as a function of wall heat flux. Two-phase pressure drop exhibits a clear increasing trend with increase in wall heat flux, which agrees with the general trend of pressure drop with respect to heat flux in straight microchannel heat sinks [57], [74], [90], [92], [98].

Employing pressure drop prediction models for two-phase system may reveal select physical properties of the fluid that dictate pressure losses in the channels. The total channel pressure drop in the flow boiling region is made up of the frictional pressure drop and gravitational pressure drop components [100]:

$$\Delta P_{total} = \Delta P_{fric} + \Delta P_{acc} \tag{4.1}$$

Applying the principles of the separated flow model, which assumes that the liquid and vapour phase in the channels flow as two segregated streams, the frictional and acceleration pressure gradient are given as:

$$\Delta P_{fric} = \frac{2\, f_{fo}\, G^2\, \nu_f\, L_{tp}}{D_h} \left[\frac{1}{x} \int_0^x \phi_{fo}{}^2 \, dx \right] \tag{4.2}$$

$$\Delta P_{acc} = G^2\, \nu_f \left[\frac{x^2}{\alpha_v} \frac{\rho_f}{\rho_g} + \frac{(1 - x)^2}{(1 - \alpha_v)} - 1 \right] \tag{4.3}$$

In Eq. (4.2), f_{fo} is the liquid-only friction factor, calculated based on the liquid-only Reynolds number, Re_{fo}. The two-phase multiplier, $\phi_{fo}{}^2$, may be estimated using the pioneering model proposed by Lockhart-Martinelli [203]:

$$\phi_{fo}{}^2 = 1 + \frac{C}{X} + \frac{1}{X^2} \tag{4.4}$$

C is the Chisholm constant, which ranges between 5 – 20 depending on the laminar and turbulent conditions of the liquid and vapour regime (Table 4.1). Flow is considered to be turbulent when $Re_k > 2000$, where k refers to either liquid or vapour. The Martinelli parameter, X, is defined as:

$$X = \left(\frac{f_f}{f_g} \right)^{0.5} \left(\frac{\rho_g}{\rho_f} \right)^{0.5} \left(\frac{1 - x}{x} \right) \tag{4.5}$$

Table 4.1: Chisholm constant in Eq. (4.4) [100].

Liquid	Gas	C [-]
Laminar	Laminar	5
Turbulent	Laminar	10
Laminar	Turbulent	12
Turbulent	Turbulent	20

The liquid and gas phase friction factor, f_k, is found from the following:

$$f_k = \frac{16}{Re_k} \quad \text{if} \quad Re_k < 2000 \tag{4.6}$$

$$f_k = \frac{0.079}{Re_k^{0.25}} \quad \text{if} \quad Re_k \geq 2000$$

Lockhart and Martinelli [203] also proposed a correlation to estimate α_v, the void fraction term in Eq. (4.7) as follows:

$$\alpha_v = \frac{1}{1 + 0.28\, X_M} \tag{4.7}$$

$$X_M = \left(\frac{\mu_f}{\mu_g} \right)^{0.07} \left(\frac{\rho_g}{\rho_f} \right)^{0.36} \left(\frac{1 - x}{x} \right)^{0.64} \tag{4.8}$$

The pressure drop components and total two-phase pressure drop predicted using the method detailed in Eq. (4.1) – (4.8) is presented in Figure 4.20 for a system pressure of 1 bar. The model predicted the same increasing trend with respect to heat flux as observed experimentally, but slightly overpredicts two-phase pressure drop at higher heat fluxes. Frictional pressure loss increased with increasing vapour quality, but begins to plateau around x = 0.6 and dropped as the flow approached single-phase gas flow, i.e. x = 1. Acceleration pressure drop varied with vapour quality to the power of 2 and increased exponentially with increase in heat flux and vapour quality. The contribution of the two pressure drop components to the total pressure drop appeared to be relatively equal when x < 0.4, after which the acceleration pressure loss dominated two-phase pressure drop in the system.

As heat flux increases, the vapour quality as well as the overall vapour content in the channels increase accordingly. Slip ratio, S, which defines the velocity of the gaseous phase to the liquid

phase velocity, increased exponentially with increasing vapour quality and void fraction in the system [277], as depicted in Figure 4.21.

$$S = \frac{\rho_f \, x \, (1 - \alpha_v)}{\rho_g \, (1 - x) \, \alpha_v} \tag{4.9}$$

The higher slip ratio, induced by the increase in vapour quality and void fraction with heat flux, result in higher interfacial shear stress between the liquid and gas phase, which increase both the frictional and acceleration pressure drop in the channels. The effect of slip ratio is physically reflected in the two-phase multiplier, ϕ_{fo}^2, which increased exponentially with increasing vapour quality for the frictional pressure loss component in the channels. This is clearly illustrated in Figure 4.22. For acceleration pressure drop, the effect of slip ratio is manifested in the void fraction, which also increased with increasing vapour quality in the channels (Eq. (4.9)), see Figure 4.23.

The rise in ϕ_{fo}^2 is due to significant increase in the gas-phase Reynolds number, Re_g, brought about by the vapour quality increase in the channels, which increases the Chisholm constant, C, the values of which are provided in Table 4.1.

Furthermore, ϕ_{fo}^2 is inversely proportional to the Martinelli parameter, X, given in Eq. (4.10). X is a strongly dependent on vapour quality and decreases exponentially corresponding to an increase in heat flux and thus vapour quality (Figure 4.24). Whilst the liquid-vapour friction factor and the vapour-liquid density ratios both increase with increasing vapour quality, they are weaker controlling terms in X due to the lower exponents associated with the ratios, as can be seen in Eq. (4.8). Thus, an overall decrease in X also resulted in the significant rise in ϕ_{fo}^2 in response to heat flux increase due to the inverse proportionality of the two parameters.

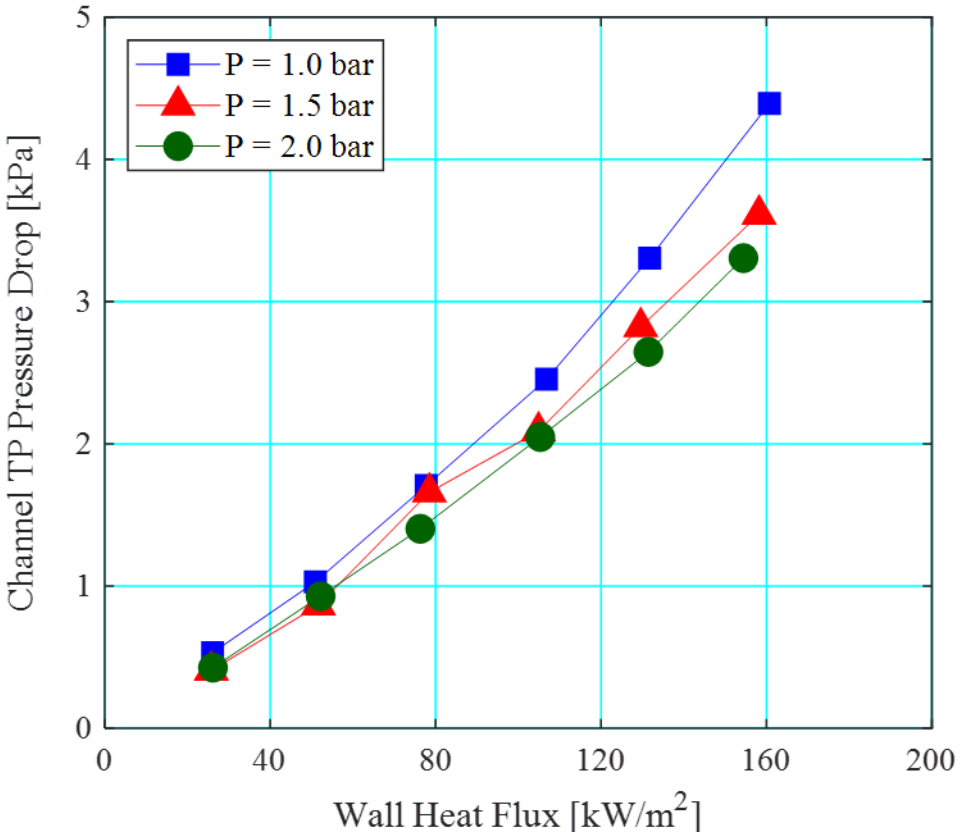

Figure 4.19: Two-phase channel pressure drop with respect to exit quality, at G = 200 kg/m^2 s and ΔT_{sub} = 10 K for three saturation pressures. Error bars are between ± 0.1 – ± 0.4 % but are not visible on the graph.

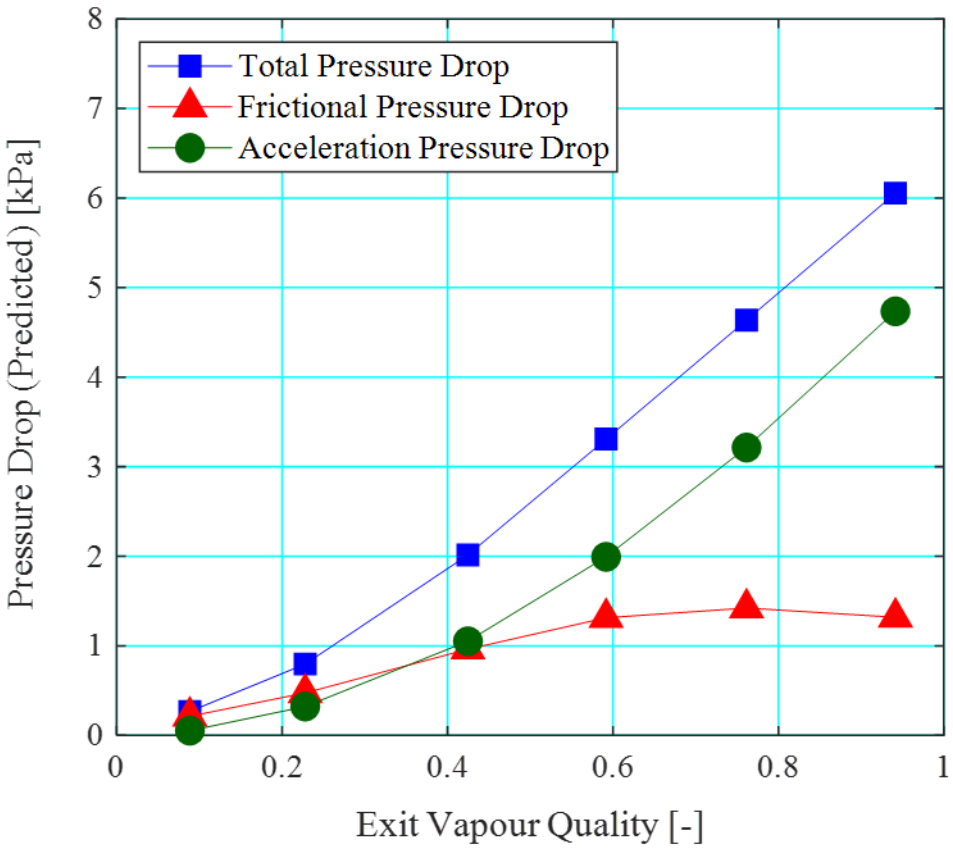

Figure 4.20: Individual pressure drop components predicted using the Lockhart-Martinelli correlation [203] for P = 1 bar, G = 200 kg/m^2 s and ΔT_{sub} = 10 K.

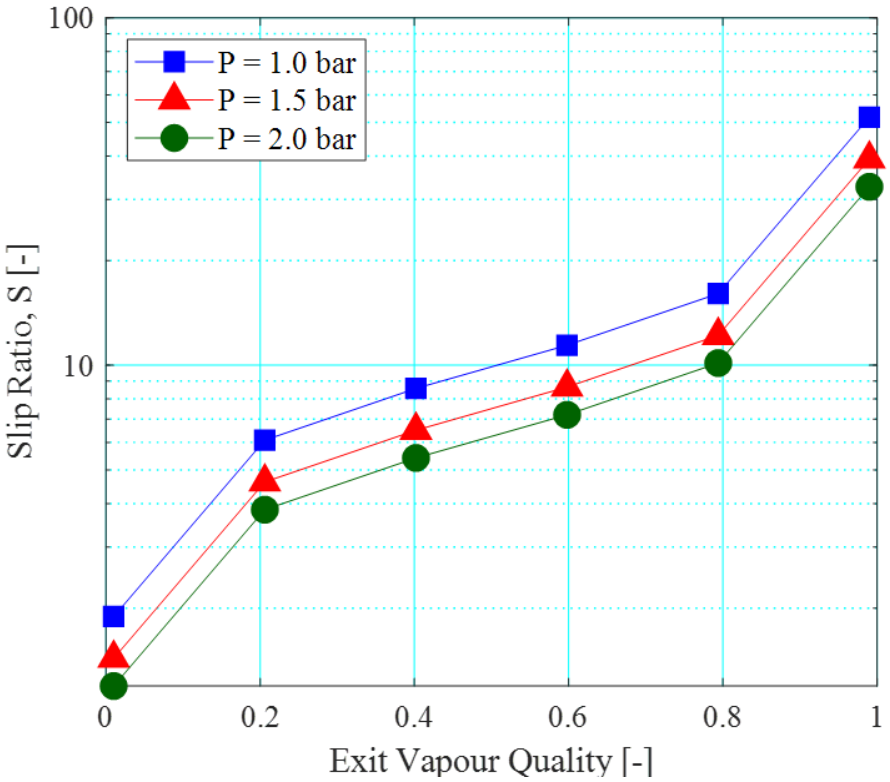

Figure 4.21: Variation of the slip ratio, defined in Eq. (4.9), as a function of exit quality for G = 200 kg/m^2 s and ΔT_{sub} = 10 K.

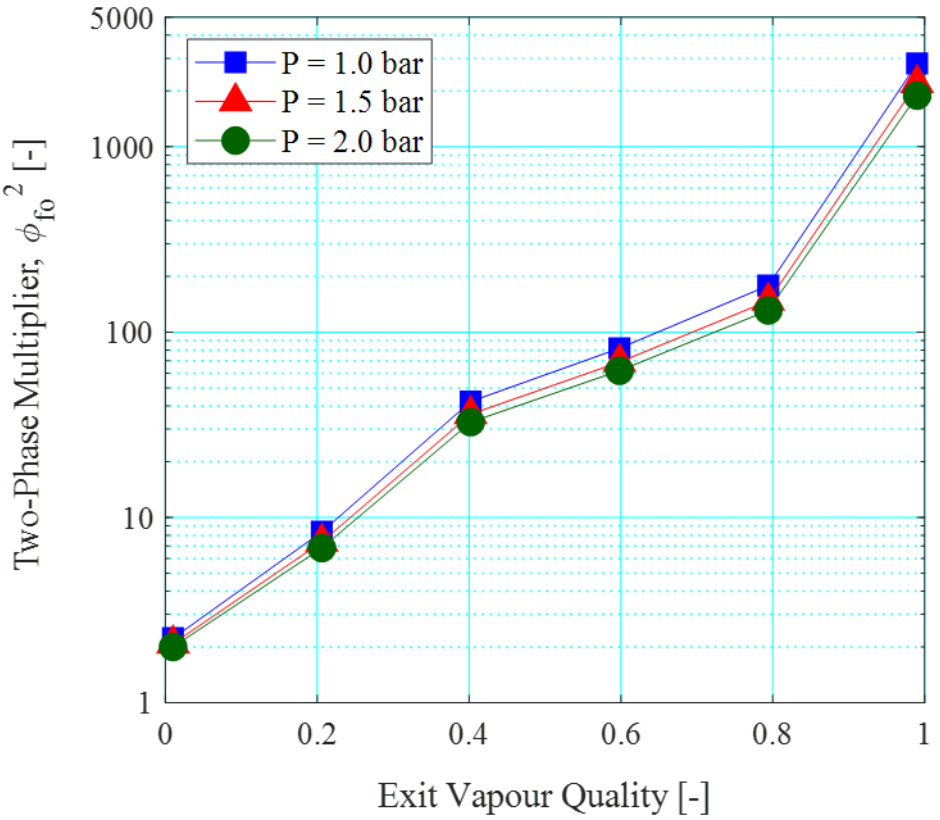

Figure 4.22: Variation of the two-phase multiplier (Eq. (4.4)) with respect to exit quality, calculated using the Lockhart-Martinelli correlation [203] for G = 200 kg/m^2 s and ΔT_{sub} = 10 K.

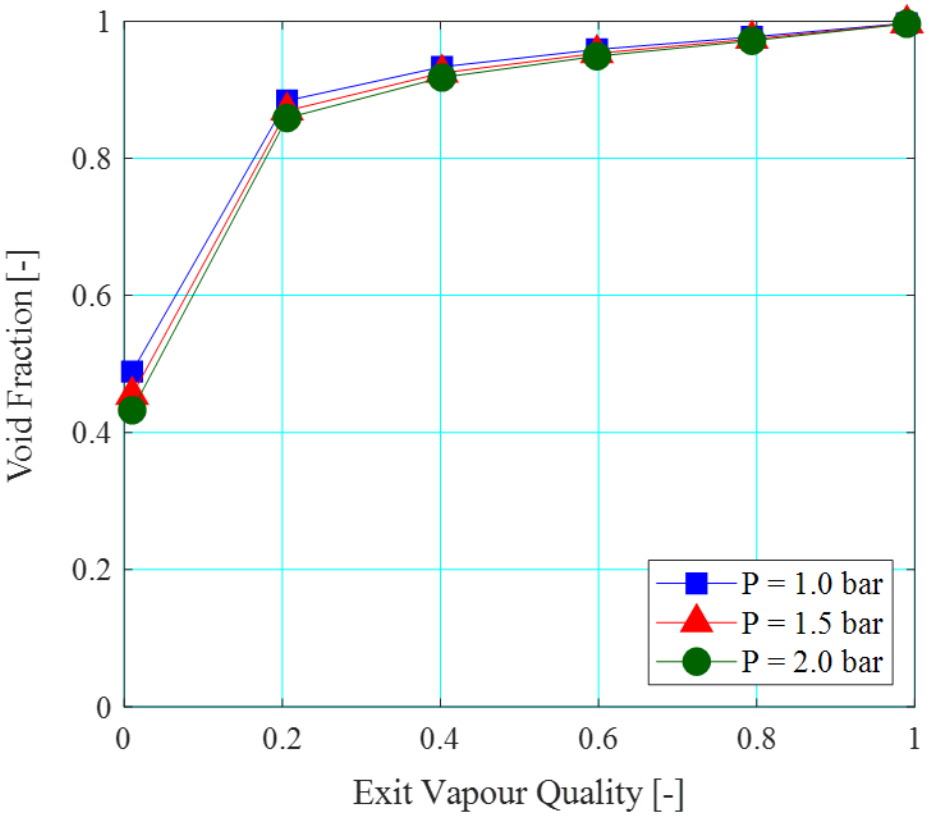

Figure 4.23: Void fraction (Eq. (4.7)) with respect to exit quality, calculated using the Lockhart-Martinelli correlation [203] for G = 200 kg/m^2 s and ΔT_{sub} = 10 K.

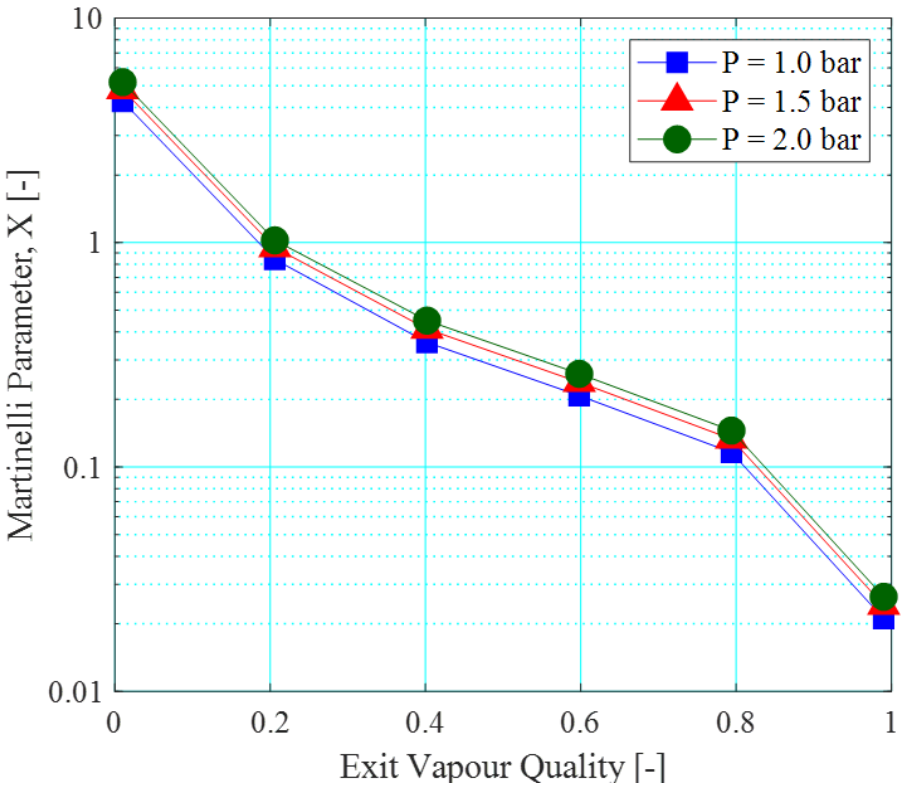

Figure 4.24: Variation of the Martinelli parameter, defined in Eq. (4.8), with respect to exit quality for G = 200 kg/m^2 s and ΔT_{sub} = 10 K.

4.3 Effect of Saturation Pressure

As highlighted above, fluid property change with system pressure could have a significant effect on flow boiling characteristics in microchannels. Relevant fluid properties of the working fluid, HFE-7200, at system pressures from P = 1 bar to P = 2 bar are summarised in Table 4.2 and Table 4.3.

Table 4.2: Properties of fluid HFE-7200 at different saturation pressures.

P_{sat} [bar]	T_{sat} [°C]	c_p [J/kg K]	i_{fg} [kJ/kg]	ρ_f [kg/m^3]	ρ_g [kg/m^3]	μ_f [kPa s]	μ_g [kPa s]	σ [mN/m]
1.0	75.1	1086	110	1303	9.7	0.36	0.012	9.6
1.5	88.7	1135	107	1267	14.3	0.31	0.013	8.4
2.0	99.0	1175	105	1239	19.0	0.27	0.013	7.5

Table 4.3: Property ratios and dimensionless numbers of fluid HFE-7200 at different saturation pressures.

P_{sat} [bar]	$\left(\frac{\rho_f}{\rho_g}\right)$ [-]	$\left(\frac{\mu_f}{\mu_g}\right)$ [-]	P_r [-]	Ja [-]
1.0	134	29.2	0.05	17.8
1.5	88.4	24.3	0.07	9.1
2.0	65.3	20.7	0.10	5.5

Corresponding to a pressure increase from 1 bar to 1.5 bar, liquid viscosity and surface tension dropped by -13 % and -12.4 % while the vapour density of the fluid rose by +47.5 %. Liquid density only dropped by a maximum of -2.8 % over the pressure range of this study. The large rise in vapour density resulted in a -34.1 % fall in liquid to vapour density ratio while the reduction in liquid viscosity decreased liquid to vapour viscosity ratio by -16.7 %. Additionally, the reduced pressure ratio (P_{sat}/P_{crit}) increased significantly by +50 % with as inlet pressure was increased to 1.5 bar. On the other hand, liquid density, gas viscosity, specific heat and latent heat of evaporation of HFE-7200 did not vary significantly in the range of this study (varied by less than 5 % between 1 bar and 1.5 bar). Between P = 1.5 bar and P = 2 bar, a proportional fall in liquid viscosity (-12 %) and surface tension (-10.5 %) was recorded. Vapour density varied less between operating pressures of 1.5 bar and 2 bar, and rose by only +32.2 % compared to the +47.5 % in the previous pressure increment. This contributed to a -26.1 % drop in liquid to vapour density ratio and a -14.8 % reduction in liquid to vapour viscosity ratio. The reduced pressure ratio rose moderately by +33.3 % when pressure was increased from 1.5

bar to 2 bar. Similarly, the variation in liquid density, gas viscosity, specific heat and latent heat of evaporation were negligible with pressure increment to 2 bar.

Additionally, in the Hsu model previously presented in Eq. (2.15), the size of active nucleation cavities was associated with the physical properties of the working fluid, saturation temperature and subcooling, as well as the thickness of the thermal boundary layer surrounding a nucleating bubble. The saturation temperature of the fluid is in turn influenced by the system pressure. Therefore, the relation is used to predict the active cavity size radii, r_c, for operating pressures in the range of P = 1 – 2 bar, with the assumption of zero subcooling in the system and D_h = 475 µm (Figure 4.25).

The range of active nucleation sites increased rapidly with superheat, especially in the low wall superheat region, namely where 0 K < ΔT_{sup} < 5 K. The largest cavity radius in the active nucleation range is around 55 µm and appeared to be insensitive to pressure change, at least within the pressure range of this study (P = 1 – 2 bar). The minimum cavity size, in contrast, varied distinctly with change in saturation pressure. This is mainly due to the notable increase in vapour density with pressure increase (Table 4.2). For a nominal ΔT_{sup} of 10 K, minimum r_c extended from 0.11 µm to 0.08 µm with pressure increase from P = 1 bar to P = 1.5 bar, and further to 0.06 µm with respect to subsequent pressure increase to P = 2 bar.

In conclusion, increasing system pressure had a remarkable effect on vapour density and the reduced pressure of fluid HFE-7200. Surface tension and liquid viscosity also fell moderately with pressure increase. Nonetheless, a smaller variation in fluid properties were observed between pressures P = 1.5 bar and P = 2 bar. The range of active nucleation sites, as predicted using Hsu's model [109] increased with increasing wall superheat and extended slightly with increase in saturation pressure.

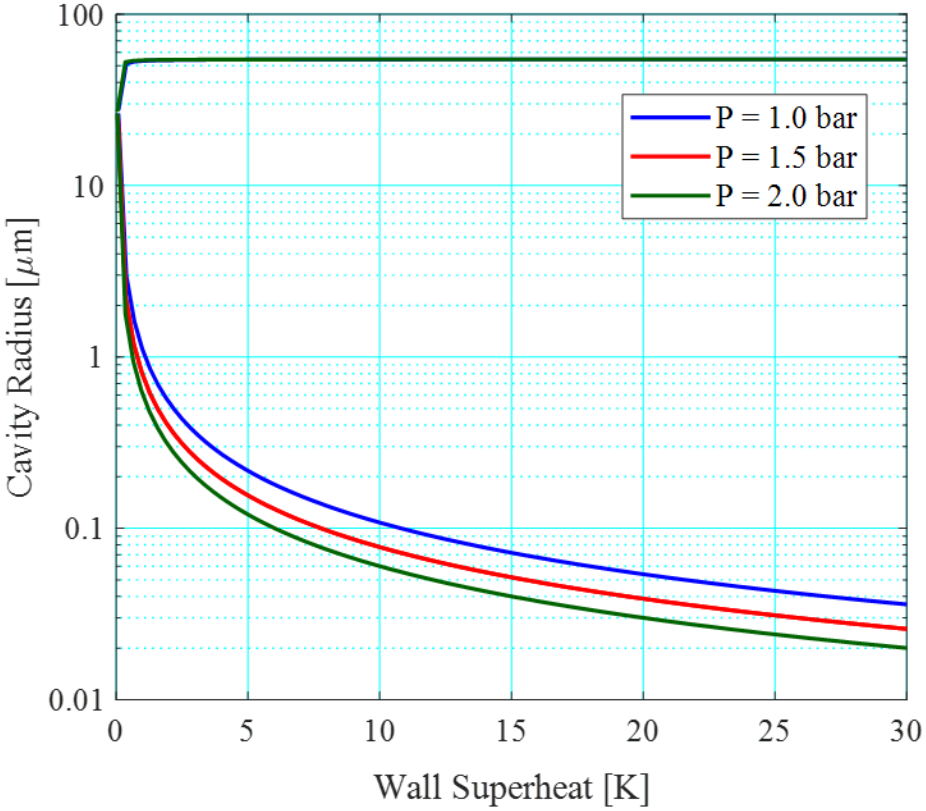

Figure 4.25: Effect of system pressure on the size range of active nucleation sites using HFE-7200, based on the nucleation model by Hsu [109].

4.3.1 Flow Patterns

Flow patterns developed in a similar manner at all three investigated pressure conditions, i.e. from bubbly, slug, churn to annular flow (see flow patterns depicted in Figure 4.2 and Figure 4.3). Generally, there was an increase in flow pattern transition vapour quality with increase in saturation pressure, as summarised in Table 4.4. The was a notable delay in transitional boundaries between pressures P = 1.0 bar and P = 1.5 bar. For instance, transition from bubbly to slug flow occurred accordingly at x = 0.04 at P = 1 bar, x = 0.06 at P = 1.5 bar and x = 0.07 at P = 2 bar. With pressure increase from P = 1.5 bar and P = 2 bar, there was a smaller difference in flow pattern transition vapour qualities.

Table 4.4: Flow pattern transition vapour qualities at G = 200 kg/m^2 s and ΔT_{sub} = 10 K for wall heat fluxes ranging from $q_w^{"}$ = 26.1 – 161.6 kW/m^2.

P [bar]	x_{B-S} [-]	x_{S-C} [-]	x_{C-A} [-]
1.0	0.037	0.068	0.304
1.5	0.064	0.119	0.314
2.0	0.066	0.122	0.353

Delayed transition from bubbly to slug flow could be due to smaller bubble departure diameters at higher saturation pressures, as illustrated in Figure 4.26. The bubble diameters were measured using ImageJ in one random channel, at five separate frames sampled from the corresponding high-speed video. Figure 4.27, Figure 4.28 and Figure 4.29 show the distribution of bubble diameters observed in the bubbly flow regime at $q_w^{"}$ ~ 50 kW/m^2 for inlet pressure conditions of 1 bar, 1.5 bar and 2 bar respectively. Bubble size was observed to decrease with increasing system pressure, as evidenced by the shift in distribution peak to lower bubble diameters at higher operating pressures. The median bubble diameter calculated from each distribution decreased from 98.5 µm to 82 µm between P = 1 bar and P = 1.5 bar, i.e. a percentage difference of -16.8 %, and at P = 2 bar decreased further to 67 µm (by -18.3 %). Smaller bubbles have a smaller tendency to coalesce in the channels, thus explaining the delay in transition from bubbly to slug flow at higher system pressures. Smaller bubble sizes at higher operating pressure conditions were also observed by Euh et al. [103], Prodanovic et al. [106] and Yuan et al. [104] in macrotubes, as well as Kuo and Peles [101] for parallel microchannels.

Amongst these studies, Euh et al. [103] cited the change in vapour density with system pressure increase as the main reason for the reduction in bubble departure diameter. the reduction in liquid-vapour density ratio, $\left(\frac{\rho_f}{\rho_g}\right)$, with pressure increase was also cited as a physical property that controlled bubble departure diameters in flow boiling by Prodanovic [106]. Accordingly, $\left(\frac{\rho_f}{\rho_g}\right)$ decreased by -34.1 % and -26.1 % with pressure increase to P = 1.5 bar and P = 2 bar respectively. Vapour density has also been cited as an important parameter in bubble nucleation dynamics [56], [101], [103], especially in the force balance models developed by Situ et al. [107] and Klausner et al. [108] to estimate flow boiling bubble departure diameter. The drag force acting on a nucleating bubble, both in the streamwise direction as well as the direction normal to the flow, is a function of bubble growth rate [56], which is estimated based on the correlation by Zuber [278] in the model of Situ et al. , and using the model developed by Mikic et al. [279] in Klausner's drag equation. Zuber's correlation is given as follows [278]:

$$\dot{r}_b = \frac{1}{2\sqrt{t}} \frac{2\, b\, Ja \sqrt{\alpha_f}}{\sqrt{\pi}} \tag{4.11}$$

where b is a constant between 1 and $\sqrt{3}$ and α_f is the liquid thermal diffusivity. Jakob number, Ja, is defined as follows:

$$Ja = \frac{\rho_f\, c_{p,f}\, (T_w - T_{sat})}{\rho_g\, i_{fg}} \tag{4.12}$$

On the other hand, the model developed by Mikic et al. [279] is given below:

$$\dot{r}_b = \frac{1}{2\sqrt{t}} \sqrt{\frac{12\, \alpha_f}{\pi}}\, Ja \left(1 - \frac{T_v - T_{sat}}{T_w - T_{sat}} \right) \tag{4.13}$$

Evidently, bubble growth rate is a function of Ja, which represents the ratio of sensible heat to latent heat absorbed during phase change. As mentioned above, liquid density, specific heat and latent heat of vapourisation did not vary significantly with pressure, at least in the range of this study. The notable increase in vapour density, namely by +47.5 % at P = 1.5 bar and +32.2 % at P = 2 bar, result in reductions in Ja by -49.1 % and -39.3 % respectively. The smaller Jakob number drastically reduces the drag force acting on a bubble growing from a nucleation site. Since less drag force is imposed on the bubble, the force balance equations are violated more easily, thus resulting in smaller bubble departure diameters and bubble sizes in the channels at higher saturation pressures.

Other than drag force on a bubble, Lee [280] concluded surface tension forces are also dominant forces controlling bubble departure diameter. Surface tension dropped by –12.4 % between P = 1 bar and P = 1.5 bar, and by a further –10.5 % with pressure increase to P = 2 bar. The resultant lower surface tension forces on bubbles at higher system pressures could also have contributed to smaller bubble departure diameters. Additionally, bubble departure diameter is intrinsically linked to bubble generation frequency, as reviewed in Situ et al. [107]. Although bubble generation frequency could not be independently verified in this study for a nominal cavity, the higher number of bubbles identified in the channels (Figure 4.27, Figure 4.28 and Figure 4.29) could be an indication of higher bubble generation frequencies at larger operating pressures. The wider range of nucleation cavity sizes predicted using Hsu's model, as illustrated in Figure 4.25, also supports this observation. With increase in system pressure, smaller nucleation sites, that is, if available on the surface of the boiling substrate, could have been activated, increasing the overall bubble generation rate in the channels.

Furthermore, average liquid film thickness reduced with increase in saturation pressure. The initial liquid film thickness, that is, the thickness of the replenished liquid film on the channel walls immediately after a dryout (complete and incomplete) cycle in annular flow was found to decrease with increasing system pressure. The mean liquid film thickness is averaged from measurements in 5 frames of the high-speed video recording at $q_w^{"} \sim 131$ kW/m^2, in one random channel at location 3 where annular flow has established in the channel array at all three pressures. An example of the measurement is shown in Figure 4.30. Mean liquid film thickness decreased from $\delta_{film} = 0.11$ mm at P = 1 bar, to $\delta_{film} = 0.075$ mm at P = 1.5 bar to $\delta_{film} = 0.066$ mm at P = 2 bar. On the contrary, In and Jeong [120] suggested that with increase in gas density along with saturation pressure, bubble passing time increased and the liquid film thickness around elongated bubbles decreased instead with a reduction in system pressure. Nonetheless, the study employed R134a as a working fluid and only assumed that the elongated bubble regime dominated in their microchannel, as flow visualisation was not included in the setup.

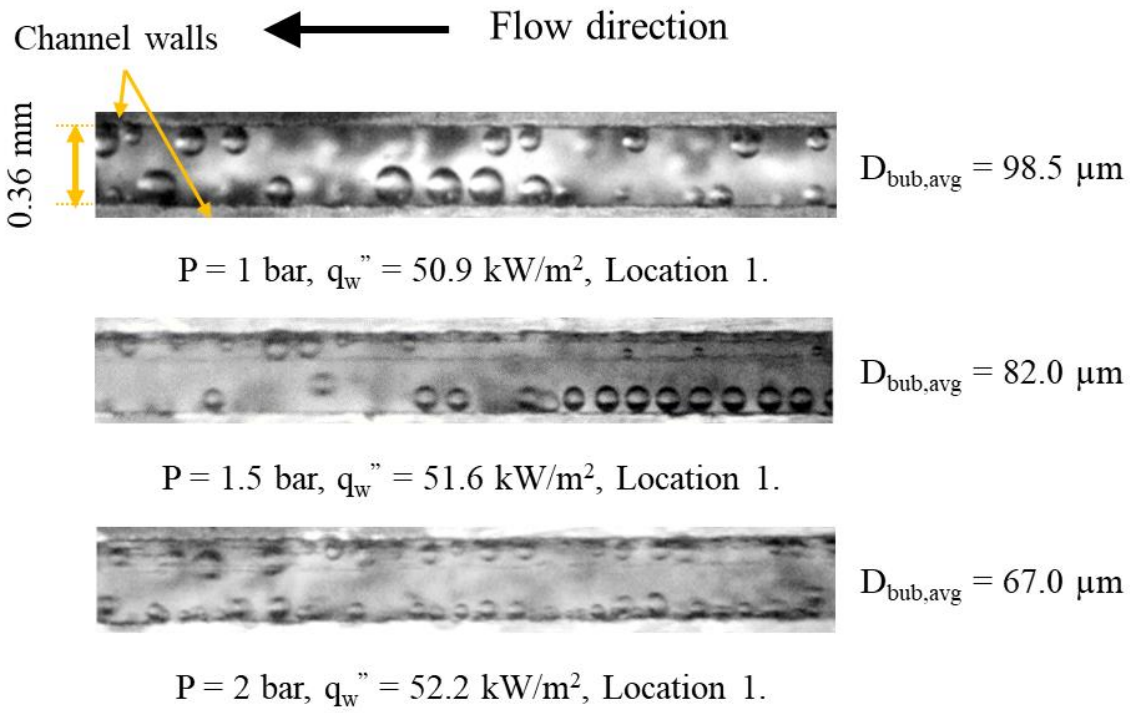

Figure 4.26: Average bubble diameters in bubbly flow at different system pressures, captured at camera location 1 (Figure 4.1) at q_w" ~ 50 kW/m^2.

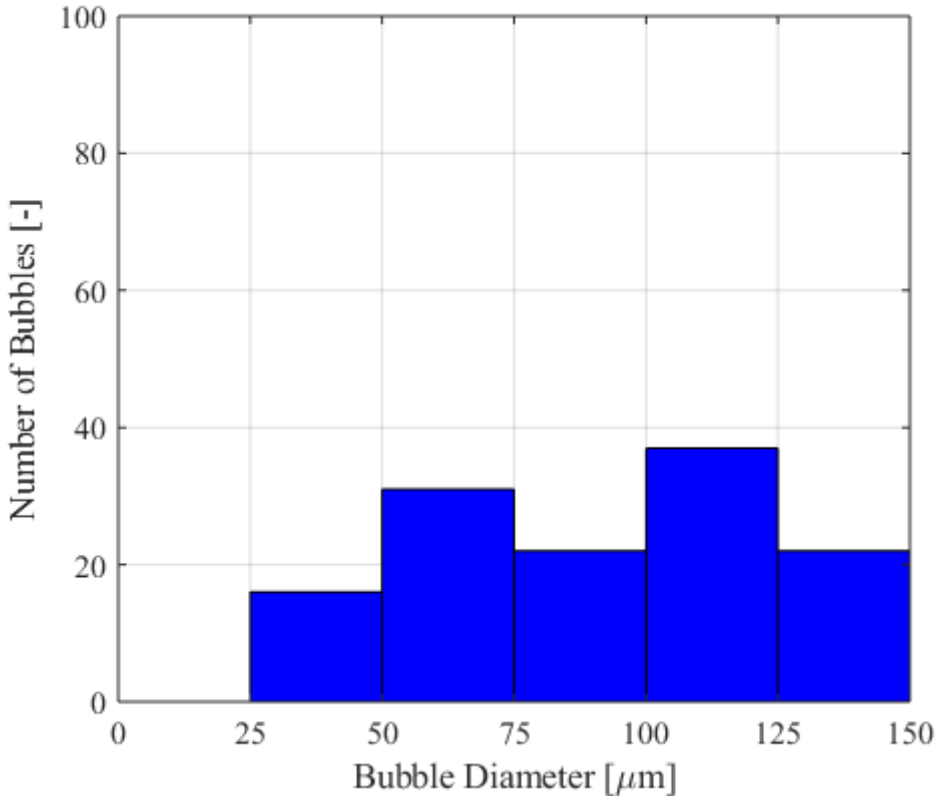

Figure 4.27: Distribution of bubble diameters measured on five still frames of the high speed recording at P = 1 bar, G = 200 kg/m^2 s, ΔT_{sub} = 10 K and q_w" = 50.9 kW/m^2.

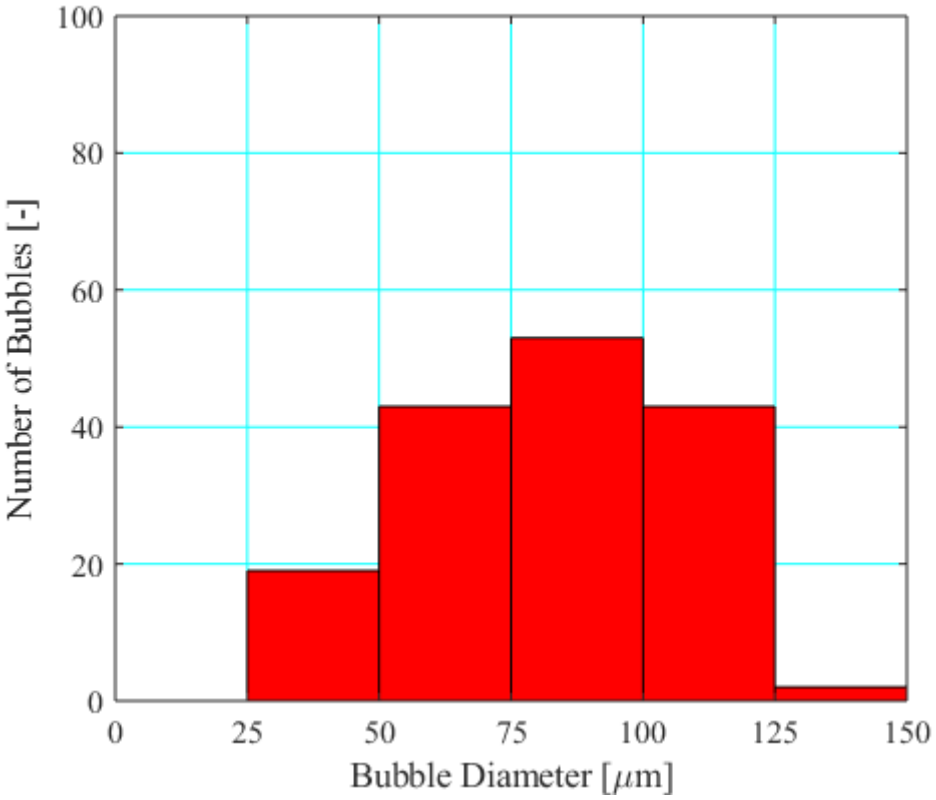

Figure 4.28: Distribution of bubble diameters measured on five still frames of the high speed recording at P = 1.5 bar, G = 200 kg/m^2 s, ΔT_{sub} = 10 K and $q_w^{"}$ = 51.6 kW/m^2.

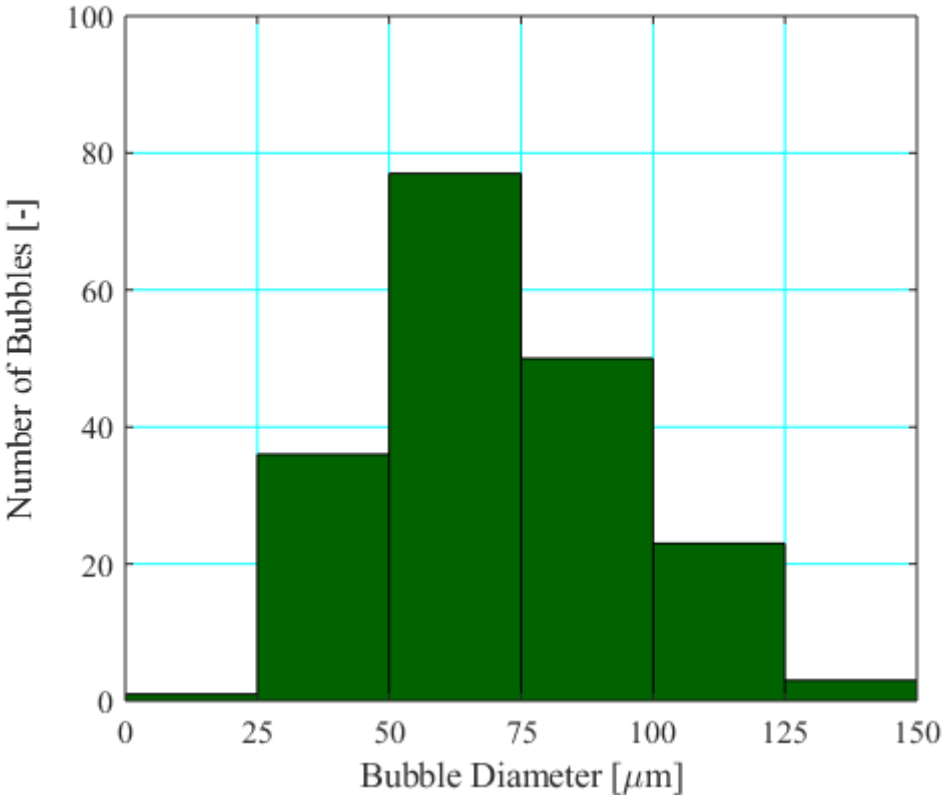

Figure 4.29: Distribution of bubble diameters measured on five still frames of the high speed recording at P = 2 bar, G = 200 kg/m^2 s, ΔT_{sub} = 10 K and $q_w^{"}$ = 52.2 kW/m^2.

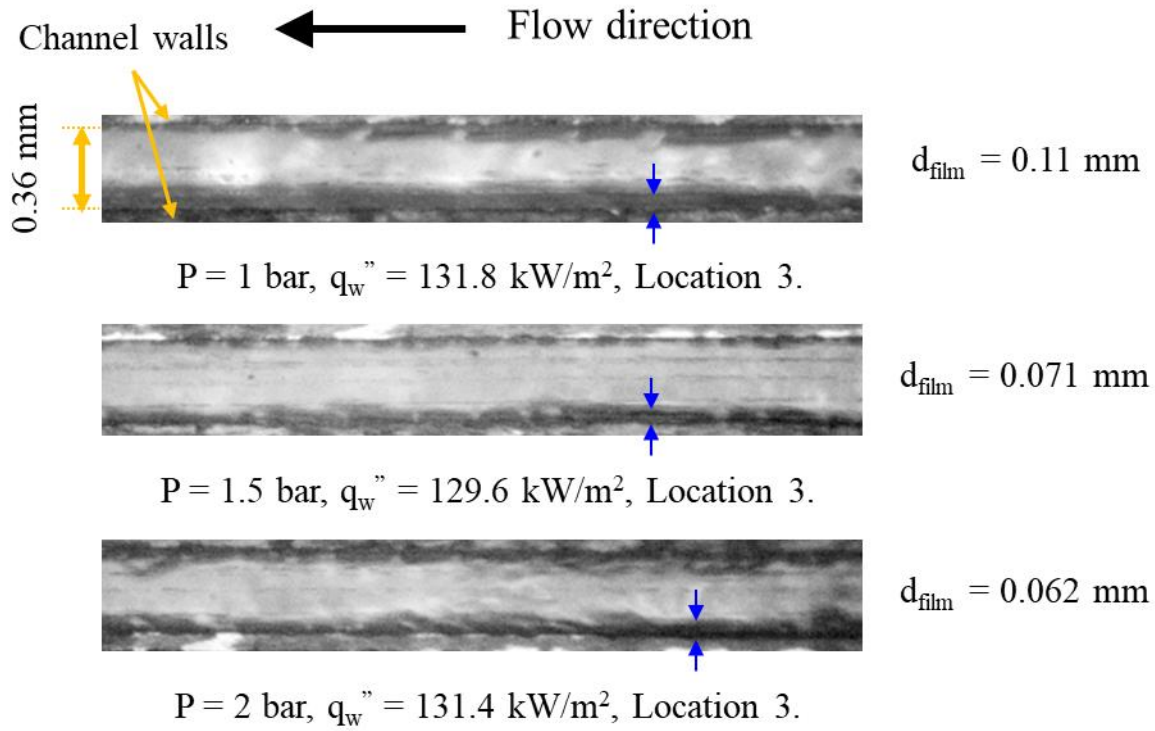

Figure 4.30: Liquid film thickness in annular flow at different system pressures, captured at camera location 3 (Figure 4.1) at q_w" ~ 131 kW/m^2.

4.3.2 Flow Instability

As covered in Section 2.3.1, Kuo and Peles [101], [110] found that increasing the exit pressure from 50 kPa to 205 kPa mitigated flow oscillations due to rapid bubble growth of water microchannel flow boiling due to a reduction in boiling incipience wall superheat. Notably, there was a considerably larger influence of saturation pressure on the active nucleation range of water, as compared to the current range of pressures investigated for HFE-7200, see Figure 4.25. It was unclear whether the degree of liquid inlet subcooling was kept constant in the study. In the current study, the effect of saturation pressure is isolated from the effect of inlet subcooling as the degree of subcooling was maintained at ΔT_{sub} = 10 K.

From Section 4.2.1, see Figure 4.8 and Figure 4.9, flow instabilities are typically observed in the slug flow regime at low wall heat fluxes near the onset of boiling in the heat sink. The measured pressure drop signal across the heat sink may be used to assess the extent of flow oscillations in the microchannels at different saturation pressures. The standard deviation of an experimental parameter, $\sigma(\Delta j)$, may be calculated as follows:

$$\sigma(\Delta j) = \sqrt{\frac{\sum_{n=1}^{n} \left(j_n - \bar{j_n} \right)^2}{n}} \tag{4.14}$$

where j represents the experimental parameter and n is the number of data points.

Kuo and Peles [101] used local transient temperature signals to study stages of unstable boiling in their silicon microchannel heat sink while researchers in [141], [142], [281] have also demonstrated the use of pressure and temperature signals to characterise flow boiling instability phenomenon in microchannel heat sinks. In the present measurement setup, the response time of the 0.5 mm diameter K-type thermocouple used to measure fluid inlet temperature was specified by the manufacturer to be around 0.03 s [282]. As events such as bubble in flow reversal occurs over a considerably shorter time period, as short as 16 ms as seen from Figure 4.9, temperature measurement techniques with higher response rates should be employed. As the response time of the differential pressure transducer is less than 1 ms [283], based on manufacturer's specifications, the instrumentation to measure heat sink pressure drop is sufficient to capture flow oscillations due to vapour backflow in the current study.

Accordingly, the standard deviation of the measured pressure drop signal across the heat sink is presented in Figure 4.31 for $q_w" \sim 26$ kW/m^2 in order to assess the effect of inlet pressure on flow boiling instabilities in the microchannel heat sink near the onset of boiling. The peaks and dips in the pressure drop signal may correspond to the occurrence of vapour backflow and recovery from flow reversal in the inlet plenum respectively, see Figure 4.8(b) – (d). As mentioned in Section 4.2.1, flow visualisation was not conducted simultaneously with data recording in the current study. However, high speed recordings were only conducted when all readings on LabVIEW appear to be at steady-state condition for at least a window of 90 s and the flow phenomenon is observed to be quasi-steady. Hence while flow reversal phenomenon captured may not be directly linked to the pressure drop signals depicted in Figure 4.31, it remains a good indication of the different stages of flow instability in the microchannel heat sink.

Increasing the operating pressure from P = 1 bar to P = 2 bar at the lowest wall heat flux condition (corresponding to an exit vapour quality of x = 0.1) reduced pressure drop oscillations in the heat sink. The standard deviation in total pressure drop was 0.42 kPa at P = 1 bar, which reduced to 0.26 kPa and 0.17 kPa with pressure increment to P = 1.5 bar and P = 2 bar respectively. This is mainly because of the delay in flow regime transition to slug flow in the heat sink at higher pressures, as discussed extensively in Section 4.3.1, see Table 4.4. The delay in flow pattern transition was mainly due to smaller bubble diameters at higher pressures, as illustrated in Figure 4.26. Similarly, Kuo and Peles [101] also found that increasing the operating pressure suppressed temperature oscillations at low vapour qualities of up to x = 0.15 due to lower wall superheat and smaller bubble departure diameters. The magnitude of temperature oscillations were almost 40 % lower at 205 kPa compared to at 101 kPa at a given vapour quality condition.

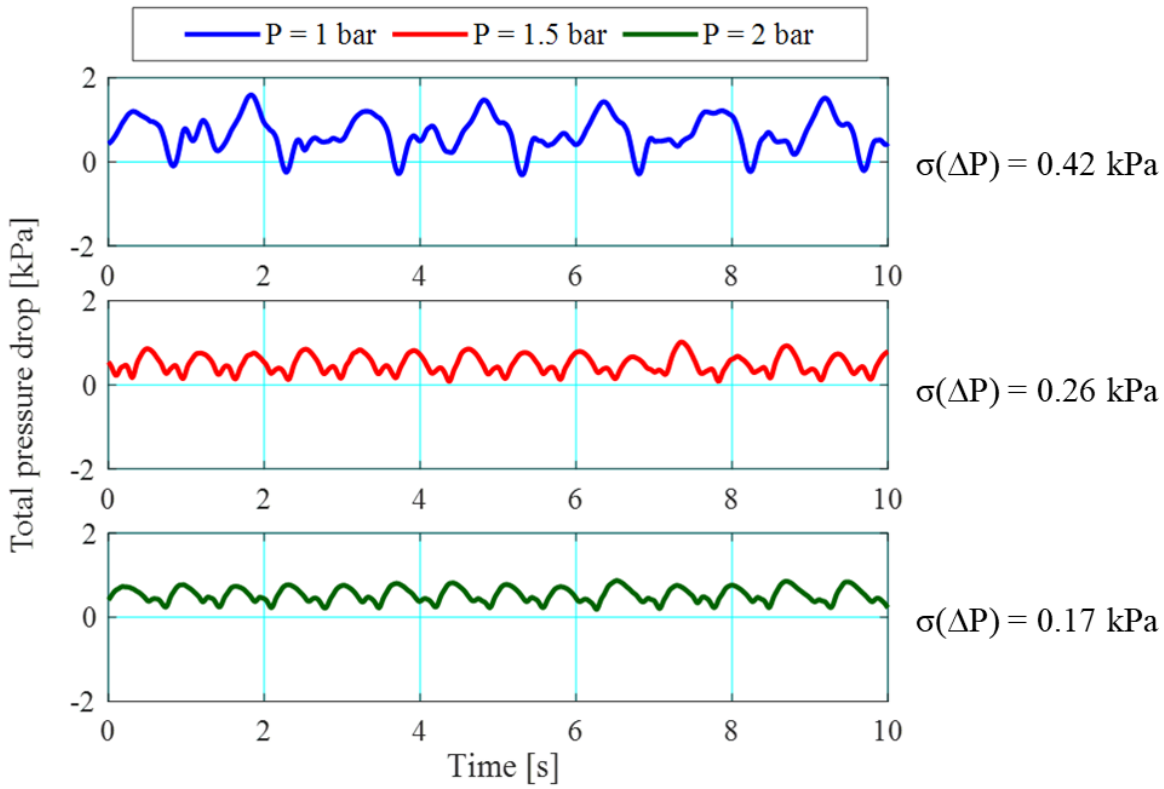

Figure 4.31: Measured pressure drop across the heat sink at $q_w^{"} \sim 26$ kW/m^2 over a window of 20 s for G = 200 kg/m^2 s and ΔT_{sub} = 10 K at system pressures 1 bar to 2 bar.

4.3.3 Heat Transfer

The effect of inlet pressure on average two-phase heat transfer coefficient at a fixed mass flux of G = 200 kg/m^2 s and inlet subcooling of ΔT_{sub} = 10 K for wall heat fluxes in the range of $q_w^{"}$ = 26.3 – 164.2 kW/m^2 may be inferred from Figure 4.18. The inlet temperature was varied at each pressure condition (i.e. 65, 79 and 88 °C) to maintain inlet subcooling at 10 K. Since the mass flux and inlet subcooling were kept constant in the experiments, the effect of pressure is isolated from effects of mass flux and inlet subcooling in this analysis.

With inlet pressure increase from 1 bar to 1.5 bar, there is a slight increase in heat transfer coefficients across the range of heat fluxes investigated, except at the lowest heat flux level ($q_w^{"}$ ~ 26 kW/m^2). The pressure effect is less significant between operating pressures 1.5 bar and 2 bar at low heat fluxes, but begin to diverge slightly toward high heat fluxes ($q_w^{"}$ ~ 134 – 157 kW/m^2). In fact, at low heat fluxes ($q_w^{"}$ ~ 26 kW/m^2 and $q_w^{"}$ ~ 50 kW/m^2), increasing inlet pressure from 1.5 bar to 2 bar did not appear to have an effect on heat transfer coefficient in the channels. Figure 4.32 shows the local heat transfer coefficients with respect to streamwise location at $q_w^{"}$ ~ 51 kW/m^2. The subcooled and saturated region calculated based on energy balance detailed in Eq. (3.22) are annotated on the graph. Heat transfer coefficients in the subcooled region exhibited a similar pressure effect to that found in the flow boiling region. Figure 4.33 and Figure 4.34 clearly depict a more pronounced pressure effect on heat transfer coefficients at moderate and high heat fluxes ($q_w^{"}$ ~ 110 kW/m^2 and $q_w^{"}$ ~ 160 kW/m^2 respectively).

It is clear from Figure 4.18 that there is a slight increase in heat transfer coefficient when inlet pressure increased from P = 1 bar to P = 1.5 bar, and in the moderate and high heat flux regions between P = 1.5 bar and P = 2 bar. In the low heat flux region, $q_w^{"}$ ~ 26 – 50 kW/m^2, bubbly flow dominated over at least half the channel length, implying that nucleate boiling is dominant at these conditions. Hence the heat transfer enhancement at low heat fluxes could be due to an increase in bubble generation frequency with increase in saturation pressure. This is explained above using Hsu's model (Figure 4.25), and is also supported by our flow visualisation results, where a larger number of bubbles were identified at higher operating pressures as illustrated in Figure 4.27, Figure 4.28 and Figure 4.29.

Incidentally, the reduced pressure, P_r, is an important parameter in the estimation of nucleate boiling heat transfer coefficient, for instance in Cooper's correlation [159], where boiling heat

transfer coefficient in the nucleate regime, h_{nb}, is directly correlated to reduced pressure, surface roughness and molecular weight (see Eq. (4.15)).

$$h_{nb} = 55\, P_r^{0.12 - 0.434 \ln Rp} (-\log P_r)^{-0.55}\, M^{-0.5}\, q^{0.67} \tag{4.15}$$

Note that the roughness parameter in the correlation, Rp, is in units of µm.

The reduced pressure ratio doubled between P = 1 bar and P = 1.5 bar. At a wall heat flux of $q_w^{"} = 50$ kW/m^2, Cooper's correlation predicts an increase in h_{nb} from 1399 W/m^2 K to 1753 W/m^2 K i.e. by +25.3 % between these conditions.

Other than that, the change in fluid properties, namely vapour density and surface tension could also have played a role in the enhancing two-phase heat transfer at higher system pressures. Vapour density increased by almost +50 % while surface tension fell by -12 % corresponding to pressure increase from P = 1 bar to P = 1.5 bar. Karayiannis et al. [55] and Xu et al. [115] suggested that a reduction in surface tension is beneficial to flow boiling heat transfer.

Interestingly, at heat flux levels $q_w^{"} \sim 26$ kW/m^2 and $q_w^{"} \sim 50$ kW/m^2, no significant enhancement in heat transfer between P = 1.5 bar and P = 2 bar was recorded. Incidentally, flow pattern transition boundaries differed less between these pressures (see Table 4.4). This could be related to the slightly smaller rise in P_r by only +33.3 % between the aforementioned pressures. A lower percentage change in vapour density and surface tension at the higher pressures, compared to P = 1 bar to P = 1.5 bar, could also have led to a slightly smaller change in drag and surface tension forces, which resulted in the pressure effect observed between these pressures compared to the lowest pressure condition.

At moderate and high heat fluxes, churn and annular flow tended to dominate the flow pattern in the channels. Alongside nucleate boiling, the convective boiling mechanism also begin to dominate in these flow regimes due to liquid film evaporation from the heated channel walls. The pressure effect between P = 1 bar and P = 1.5 bar remained constant, whilst a stronger pressure effect manifests between P = 1.5 bar and P = 2 bar.

This observation is in contradiction with the conclusion reported by Wen et al. [119], Karayiannis et al. [55] and In and Jeong [120], where insignificant saturation pressure effects

on heat transfer coefficient were found at high vapour qualities where convective boiling were assumed to dominate. Nonetheless, these studies were for minichannels and microtubes. Additionally, Wen et al. [119] reported that heat transfer coefficients depreciated sharply in the convective boiling region with respect to vapour quality, as well as dryout in the annular flow regime. However, in the current study, a drop in average heat transfer coefficient was not recorded in the channels, even at high vapour qualities. Furthermore, wall dryout in the annular flow regime was in fact, less severe than in the slug flow regime, as discussed in Section 4.2.1.

The effect of pressure in the heat flux region where thin-film evaporation dominates could be understood by applying the three-zone model proposed by Thome et al. [151]. The model estimates convective boiling heat transfer coefficients in the elongated bubble regime under constant heat flux condition. Local heat transfer coefficient is evaluated at a fixed location, z, in a heated microchannel and assumes the passage of: (i) a saturated liquid slug, (ii) an elongated bubble and (iii) a dry vapour zone (if present), as shown in Eq. (4.16). The time-averaged heat transfer coefficient at the specific location, h(z), is averaged over period τ, the time period between successive cycles, with thin-film evaporation of the elongated bubble being the main heat transfer mechanism in the channel. Full equations and the model assumptions may be found in the original paper by Thome et al. [151].

$$h(z) = \frac{1}{\tau} \left(t_l h_l + t_{film} h_{film} + t_{dry} h_{dry} \right) \tag{4.16}$$

In the above equation, h_{film} is the heat transfer coefficients through the evaporating thin-liquid film and t_{film} is time period over which thin-film evaporation occurs. h_l and h_{dry} are the heat transfer coefficients in the liquid and vapour slug region and the corresponding time periods are t_l and t_{dry}, the latter if dryout is predicted to occur in the channel.

τ is inversely proportional to the bubble generation frequency, f:

$$\tau = \frac{1}{f} = \left(\frac{q_w''}{q_{ref}''} \right)^{1.74} \tag{4.17}$$

The reference heat flux, q_{ref}'' is related to P_r by $q_{ref}'' = 3328\ P_r^{-0.5}$. Since P_r increases with increasing system pressure, the bubble generation frequency increases for a given wall heat flux condition. Consequently, the residence time of the elongated bubble regime decreases, and thus the duration between successive cycles of slug passage, τ, reduces according to Eq. (4.17).

For instance, at a wall heat flux of $q_w^{"}$ = 160 kW/m^2, with system pressure increase to P = 1.5 bar and later to P = 2 bar, *f* increased from 62.2 Hz to 88.5 Hz and further to 113.6 Hz. This caused τ to drop from 0.016 s to 0.011 s and 0.009 s (i.e. by -29.7 % and -22.2 %), which produced a considerable rise in the time-averaged heat transfer coefficient, h(z). At a fixed location in the channels where local vapour quality is x = 0.8, the respective reduction in τ resulted in an increase of h(z) from 21623 W/m^2 K at P = 1 bar to 26033 W/m^2 K at P = 1.5 bar, and further to 29193 W/m^2 K at P = 2 bar.

The main factor affecting the increase in average heat transfer coefficient is the increase of the thin-film evaporation region, h_{film}. h_{film} increased from 21623 W/m^2 K to 29193 W/m^2 K corresponding to pressure increase from P = 1 bar to 2 bar at x = 0.8. This may be attributed to the dryout time period, t_{film}. The shorter t_{film} at higher system pressures is a direct consequence of the reduction in τ with increase in saturation pressure and bubble generation frequency, as explained above.

Although the three-zone model correctly predicts the trend with respect to system pressure, the average heat transfer coefficients predicted are much higher than the experimental results. This is because the liquid film thickness predicted using based on the method of [151] is several orders thinner than the liquid film thickness in the annular flow regime in this study (see Table 4.5). Additionally, liquid film thickness increased with increasing pressure, contrary to the observation in the current study. The thinner liquid film thickness predicted overall resulted in inflated heat transfer coefficients in the thin-film evaporation regime.

Table 4.5: Average liquid film thickness in the annular flow regime, measured at location 4 at $q_w^{"}$ ~ 160 kW/m^2 compared to the predicted film thickness [151], [153].

P [bar]	$\delta_{film,exp}$ [µm]	$\delta_{film,Thome\ et\ al.}$ [µm]	$\delta_{film,Magnini\ and\ Thome}$ [µm]
1.0	82.0	0.47	2.9
1.5	54.0	0.55	2.8
2.0	44.8	0.62	2.7

Notice also that there is a smaller difference in the liquid film thickness between P = 1.5 bar and P = 2 bar, which could be related to the weaker pressure effect observed between these pressures.

More recently, Magnini and Thome [153] proposed an updated method on the original three-zone model by Thome et al. [151]. Amongst the modifications, the authors highlighted the much smaller liquid film thickness predicted when applying the Moriyama and Inoue [284] correlation. The authors argued that an increase in *f* resulted in a decrease in liquid slug length, i.e. short liquid slugs, such that the thickness of the liquid film is reduced due to the development of a thinner viscous boundary layer. The model showed that the film thickness reduced with increasing bubble generation frequency, which in turn increased with saturation pressure [153]. From Table 4.5, the new model shows a slight improvement in the prediction of the liquid film, but importantly predicts the trend in liquid film thickness with respect to saturation pressure.

Heat transfer prediction results obtained by applying the updated three-zone model to estimate the initial liquid film thickness, as summarised above, at the exit of the channels where exit vapour qualities ranged from x_e = 0.04 – 0.7 for wall heat fluxes between 26 kW/m^2 – 154 kW/m^2 at G = 200 kg/m^2 s are shown in Figure 4.35 for the three investigated saturation pressures. Experimental data obtained at P = 1 bar and z/L = 0.83 (nearest to channel exit), at the abovementioned wall heat fluxes are also presented.

The model predicts that heat transfer coefficients increased with increasing heat flux and vapour quality in the channels. Time-averaged heat transfer coefficient plateaus approaching high heat fluxes and eventually a slight drop is observed at x ~ 0.6. Compared to the experimental data, an under-prediction of heat transfer coefficient at the lowest heat flux and vapour quality condition, where bubbly flow and thus nucleate boiling, rather than thin-film evaporation, is dominant, is observed. The over-prediction in heat transfer coefficients may be attributed to the still slightly thinner liquid film thickness estimated using the revised model. As expected, the liquid film thickness predicted using the model decreased with increasing pressure. Although the model typically predicted liquid film thickness to be an order of magnitude smaller than the average liquid film thickness measured from flow visualisation, it is nonetheless an improvement from the original model. The much more realistic magnitudes of heat transfer coefficients predicted using the updated model is a direct result of the improved prediction of liquid film thickness.

Contrary to the experimental data, which show a steady increasing trend with regard to heat flux and vapour quality, the model predicts that the time-averaged heat transfer coefficient drops slightly toward high heat fluxes and vapour qualities. This is mainly because the dryout period estimated in the model increase with increasing heat flux and vapour quality, which eventually result in the drop in time-averaged heat transfer coefficient in the channel (Figure 4.35). Nonetheless, as illustrated above, the rewetting churn wave mechanism observed in this study appear to prevent prolonged periods of dryout in the channel walls. This could explain why the experimental trend increases steadily without a fall in heat transfer coefficient, even at high heat fluxes and vapour quality conditions.

Interestingly, in accordance with the experimental observations, where a weak pressure effect between P = 1.5 bar and P = 2 bar was observed at low heat fluxes, the model also predicted a similar phenomenon. Again, this could be due to the smaller increase in bubble generation frequency as the increase in P_r is less between these pressures and its subsequent effect on the residence time period, τ in Eq. (4.17). On the other hand, at moderate to high heat fluxes and vapour qualities, an enhancement in time-averaged heat transfer coefficient is predicted with increasing saturation pressure, mainly due to the reduction in residence time and partly caused by the reduction in the estimated liquid film thickness in the channel. This was also concluded in Magnini and Thome [153] and could be the reason for the pressure effect at moderate and high heat fluxes as observed in Figure 4.18. The reinstated pressure effect between P = 1.5 bar and P = 2 bar toward high heat fluxes where churn and annular flow dominates, could also be explained through the reduction in liquid film thickness with increasing operating pressure in the channels.

In general, enhanced heat transfer coefficients at low heat fluxes, where nucleate boiling is believed to dominate in the channels, could be attributed to an increase in P_r with increase in saturation pressure. The variation in vapour density and surface tension could also have contributed to heat transfer enhancement at higher pressures.

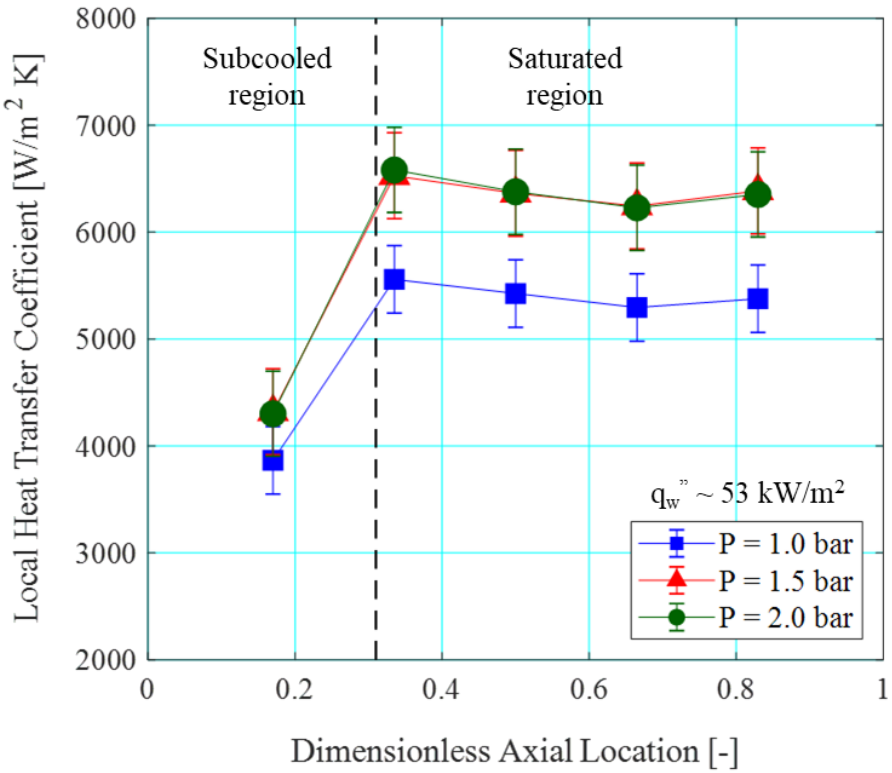

Figure 4.32: Local heat transfer coefficients as a function of streamwise location on the channels, at G = 200 kg/m^2 s, ΔT_{sub} = 10 K and $q_w^{"}$ ~ 50 kW/m^2 .

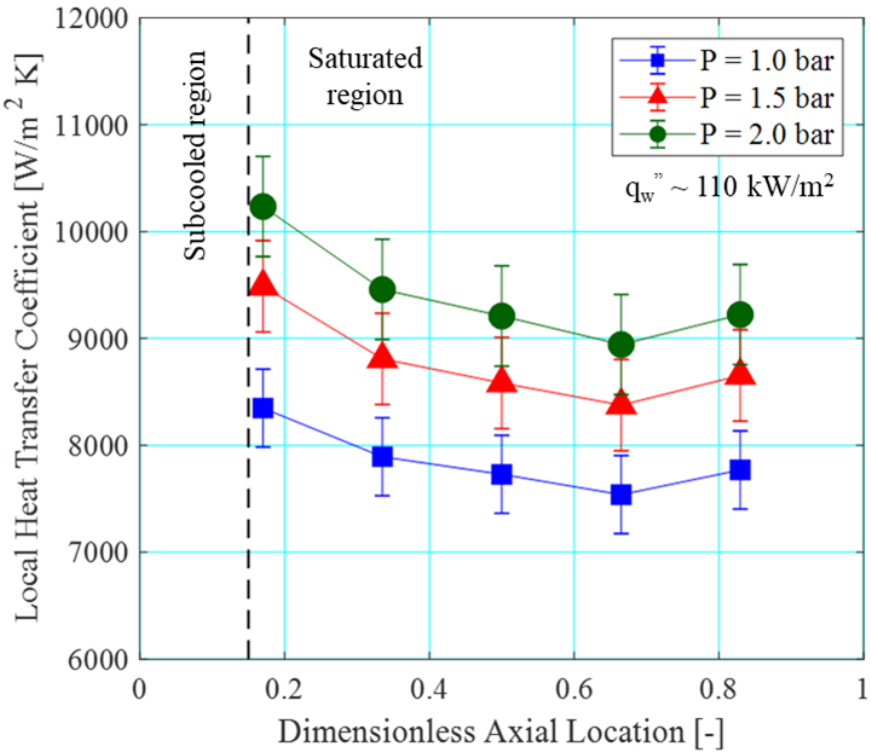

Figure 4.33: Local heat transfer coefficients as a function of streamwise location on the channels, at G = 200 kg/m^2 s, ΔT_{sub} = 10 K and $q_w^{"}$ ~ 110 kW/m^2 .

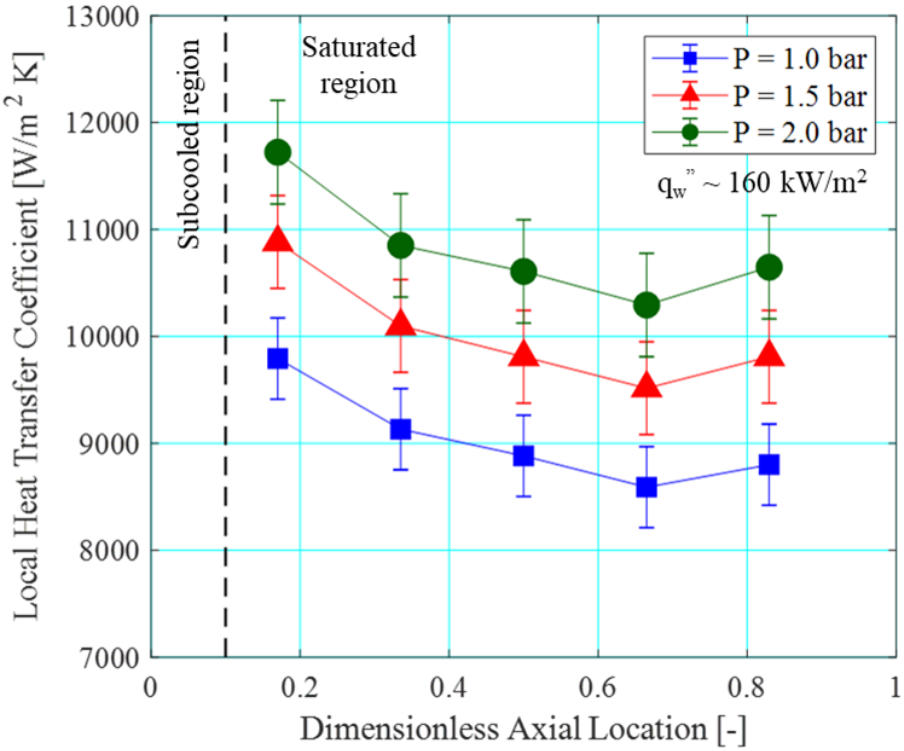

Figure 4.34: Local heat transfer coefficients as a function of streamwise location on the channels, at G = 200 kg/m^2 s, ΔT_{sub} = 10 K and $q_w^{"}$ ~ 160 kW/m^2.

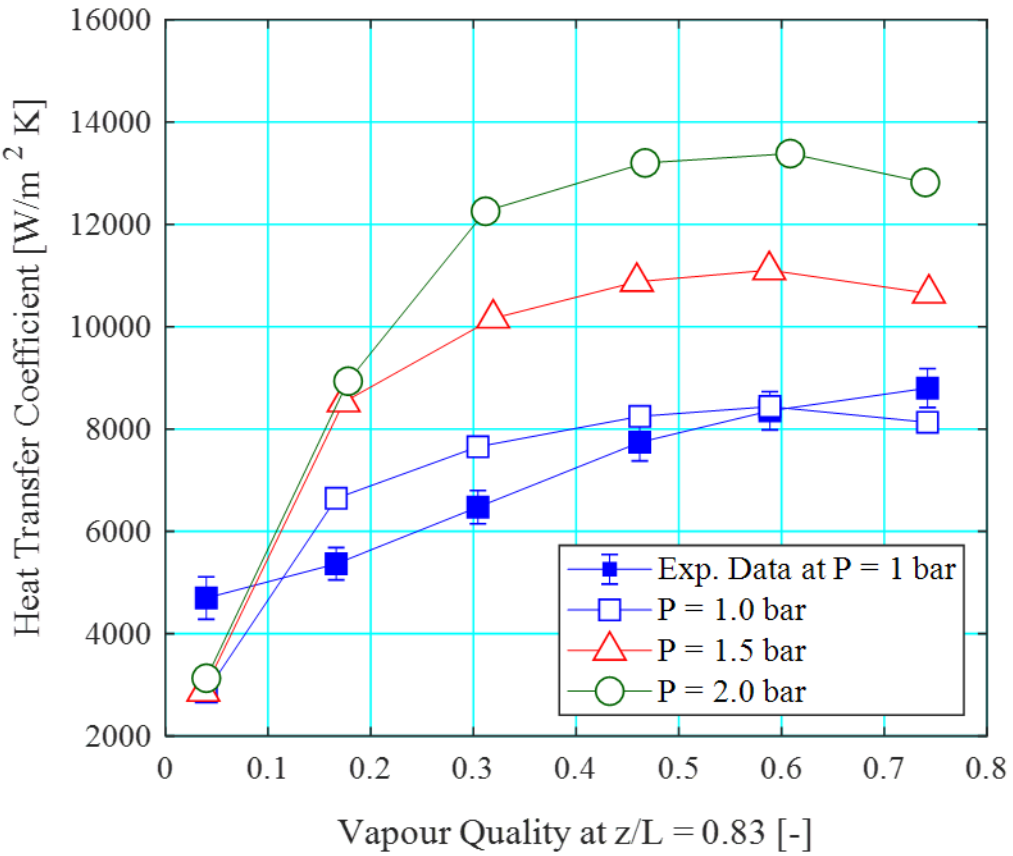

Figure 4.35: Time-averaged heat transfer coefficient predicted using the updated three-zone model by Magnini and Thome [153] at conditions corresponding to location z/L = 0.83, G = 200 kg/m^2 s and ΔT_{sub} = 10 K.

4.3.4 Pressure Drop

The effect of system pressure on two-phase pressure drop in the channels are shown in Figure 4.36 as a function of wall heat flux. Increasing the inlet saturation pressure reduced the two-phase pressure drop across the microchannel heat sink, although a weaker pressure effect is observed between saturation pressures P = 1.5 bar and P = 2 bar. The deviation in pressure drop with system pressure is likely unrelated to flow pattern development in the channels. As reported above, flow patterns developed accordingly across all inlet pressures, with a small delay in flow pattern transition vapour qualities at higher pressures. A reduction in two-phase pressure drop in response to system pressure increase was also reported by Kuo and Peles [101], Saisorn et al. [102] and Dário et al. [97].

As highlighted above, frictional pressure loss and acceleration pressure loss are dependent on fluid properties, such as density and viscosity (see Eq. (4.2) and (4.3)), which have been shown to vary significantly with pressure changes in Table 4.2. In fact, the effect of pressure can be observed in the slip ratio in Figure 4.21, two-phase multiplier in Figure 4.22 as well as the Martinelli parameter in Figure 4.24. With increase in saturation pressure, all the above-mentioned parameters decreased considerably due to changes in the physical properties of the fluid. The resultant frictional pressure drop and gravitational pressure drop components, as predicted based on the Lockhart-Martinelli correlation [203] (see Eq. (4.1) – (4.8)) for the operating pressures investigated are shown in Figure 4.37 and Figure 4.38 respectively. Frictional pressure drop decreased with increase in pressure, especially between P = 1 bar and P = 1.5 bar, while a weaker pressure effect was observed between P = 1.5 bar and P = 2 bar. A similar trend was found for the acceleration pressure drop component.

As established above, frictional pressure loss is largely influenced by the magnitude of the two-phase multiplier. It was mentioned earlier that a large rise in vapour density of up to +47.5 % was registered with system pressure increase from P = 1 bar to P = 1.5 bar. This resulted in a notable rise in the vapour to liquid density ratio, $\left(\frac{\rho_g}{\rho_f}\right)$, namely by +51.7 %. For a given vapour quality condition, X mainly increased with an increase in the density ratio at higher operating pressures (Eq. (4.5)). The increase in X resulted in a decrease in $\phi_{fo}^{\ 2}$ (depicted in Figure 4.22 and Figure 4.24) which ultimately lowered frictional pressure loss with increase in saturation pressure in the system, as shown in Figure 4.37. Other than that, liquid viscosity, μ_f, decreased

by -13 % while gas viscosity, μ_g, rose by a mere +4.5 % corresponding to inlet pressure increase from P = 1 bar to P = 1.5 bar. The respective changes in viscosity affect the Reynolds number of the liquid as well as gas flow, and by extension the friction factor of the liquid and gas phase in accordance with Eq. (4.6). Nonetheless, only a moderate drop in liquid-vapour friction factor ratio of -15.8 % occurred between P = 1 bar and P = 1.5 bar. The small change in friction factor ratio with pressure increase had a negligible effect on X. Instead, the increase in parameter X in response to pressure increase, which produced a reduction in $\phi_{fo}^{\ 2}$ and thus frictional pressure drop, was mainly governed by the change in vapour-liquid density ratio, in direct relation to the increase in system pressure for a given heat flux and vapour quality condition in the heat sink.

The weaker pressure effect between P = 1.5 bar and P = 2 bar could be due to the comparatively smaller increase in vapour density between pressures of 1.5 bar and 2 bar. (+32.2 % compared to +47.5 % at the lower pressure) This brought about a milder increase in density ratio in the fluid (+35.2 % compared to +51.7 % at the lower pressure), which slightly narrowed the disparity in parameter X as well as $\phi_{fo}^{\ 2}$ for a given vapour quality between P = 1.5 bar and P = 2 bar (Figure 4.24). Consequently, a smaller deviation in frictional pressure drop trend is observed between these pressures in Figure 4.37.

The model also predicted a drop in two-phase acceleration pressure drop with increase in system pressure in the system (Figure 4.38). Evident from Eq. (4.3), acceleration pressure drop is directly related to the liquid-to-vapour density ratio, $\left(\frac{\rho_f}{\rho_g}\right)$, of the fluid. As noted above, liquid density remain largely unaltered across the pressure range studied while the vapour density increased by up to +50 % at the lower pressure increase and by just over +30 % with further increase in operating pressure to 2 bar. $\left(\frac{\rho_f}{\rho_g}\right)$ decreased by -34.1 % and -26.1 % accordingly. As a direct consequence, acceleration pressure drop decreased with increasing saturation pressure for a given heat flux and vapour quality condition. The softer pressure effect observed between P = 1.5 bar and P = 2 bar, as concluded above, could be due to the smaller corresponding increase in vapour density, which produced a smaller decrease in $\left(\frac{\rho_f}{\rho_g}\right)$ of only -26.1 % between these pressures. Whilst the notable change in vapour density also affects the void fraction

through X_M (see Eq. (4.7) and (4.8)), the ultimate decrease in α_v was insignificant, owing to the small range as well as magnitude of α_v, as illustrated in Figure 4.23.

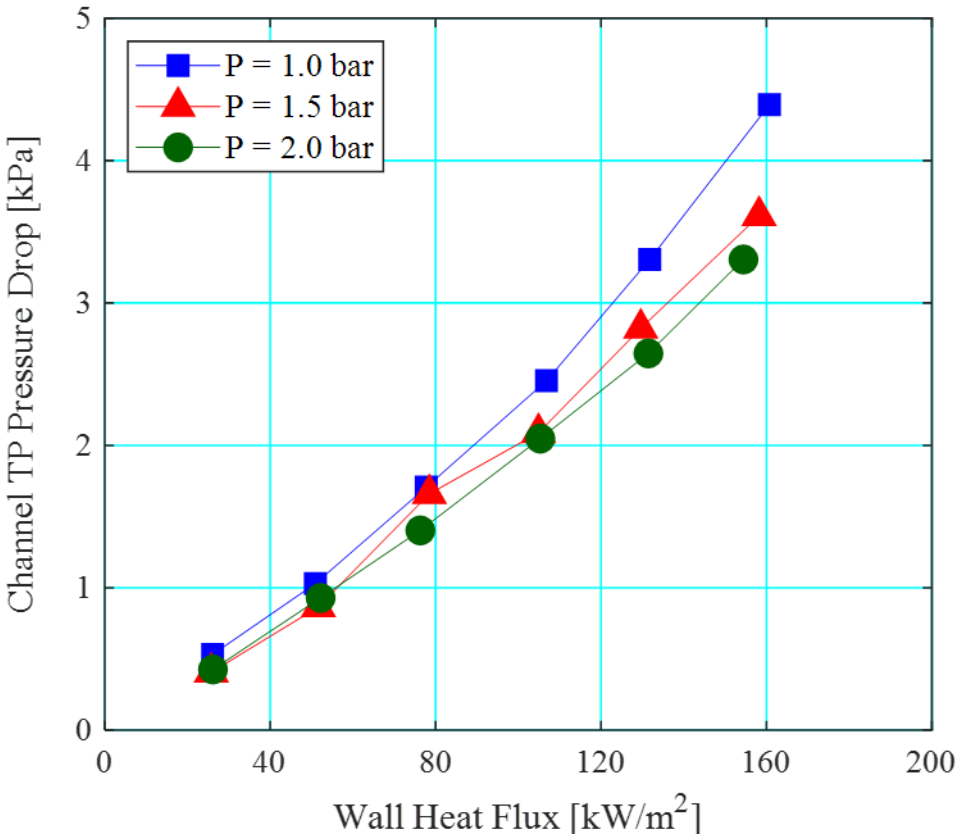

Figure 4.36: Two-phase pressure drop in the channels with respect to wall heat flux at G = 200 kg/m^2 s and ΔT_{sub} = 10 K for three inlet pressure conditions.

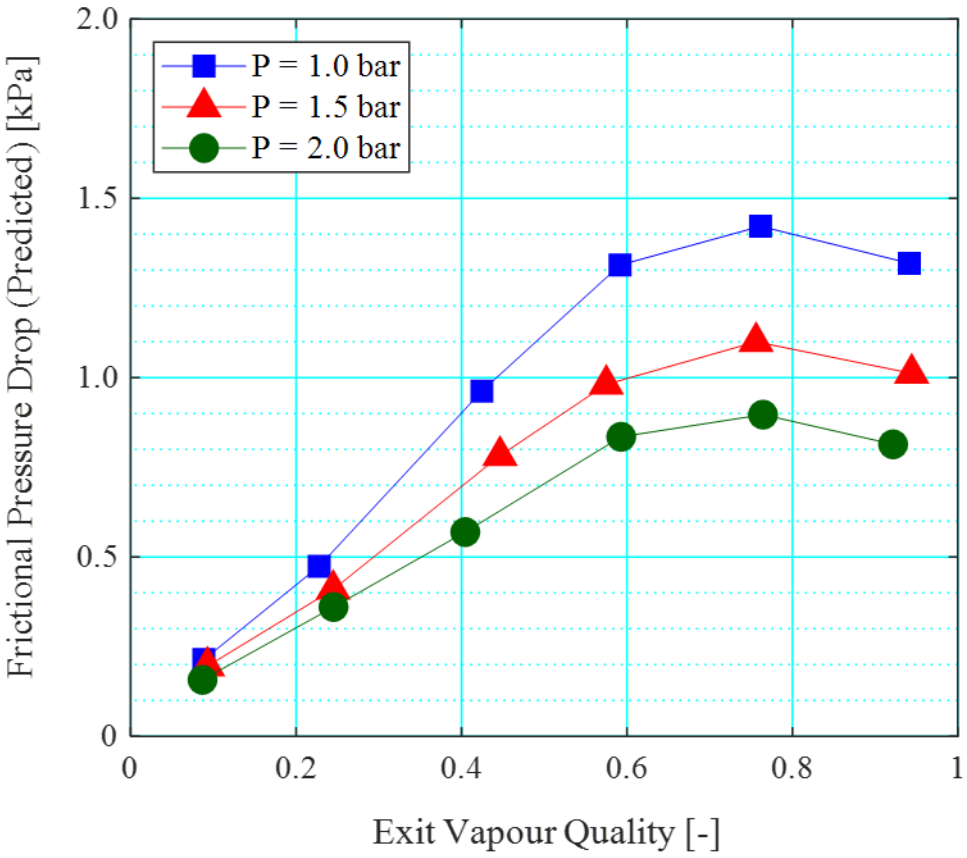

Figure 4.37: The two-phase frictional pressure drop component with respect to exit quality, calculated using the Lockhart-Martinelli correlation [203] for G = 200 kg/m^2 s and ΔT_{sub} = 10 K.

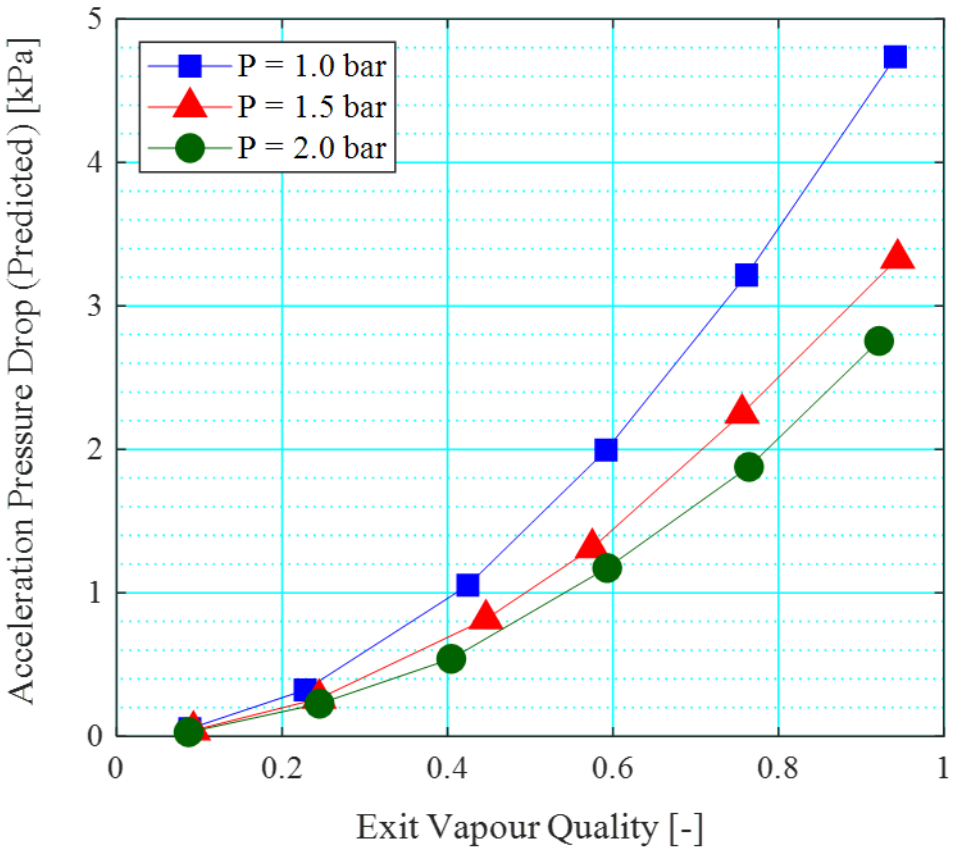

Figure 4.38: The two-phase acceleration pressure drop component with respect to exit quality, calculated using the Lockhart-Martinelli correlation [203] for G = 200 kg/m^2 s and ΔT_{sub} = 10 K.

4.4 Effect of Mass Flux

4.4.1 Flow Patterns

In order to investigate the effect of mass flux on flow boiling heat transfer, pressure drop as well as flow pattern evolution in the channels, experiments were conducted at channel mass velocities of G = 200 kg/m^2 s, 300 kg/m^2 s and 400 kg/m^2 s for wall heat fluxes ranging from $q_w^{"}$ = 24.8 – 234.3 kW/m^2. The inlet pressure and inlet subcooling degree was remained at P = 1 bar and ΔT_{sub} = 10 K respectively.

As discussed above, the main flow regimes observed in this study are bubbly, slug, churn and annular flow. Flow patterns developed accordingly with increase in heat flux across all mass fluxes investigated. In particular, flow pattern transition boundaries shifted to lower vapour qualities with increasing mass velocity. Table 4.6 summarises the vapour qualities at which flow pattern transition from bubbly to slug (x_{B-S}), slug to churn (x_{S-C}) and churn to annular flow (x_{C-A}) occurs at nominal mass flux conditions of G = 200 kg/m^2 s, 300 kg/m^2 s and 400 kg/m^2 s respectively. Accelerated flow pattern transitions at higher mass fluxes were also reported by Harirchian and Garimella [84], Huang et al. [92], Costa-Patry et al. [83] and Yin et al. [285].

It has already been highlighted earlier that bubbly flow only occurred over a narrow range of vapour qualities in the microchannels, even at the lowest mass flux condition of G = 200 kg/m^2 s. Nonetheless, the range of vapour qualities at which bubbly flow is observed narrowed further with increase in mass flow rate. This could be due to a higher rate of bubble coalescence in the channels due to higher flow inertia, which accelerated the transition from bubbly to slug flow, subsequently to churn flow and finally to annular flow in the heat sink. Annular flow occurred at x = 0.3 at G = 200 kg/m^2 s, but shifted towards lower vapour qualities to x = 0.195 and x = 0.169 at G = 300 kg/m^2 s and G = 400 kg/m^2 s respectively. The average liquid film thickness in the annular flow regime was also characteristically thinner at a given heat flux, as illustrated in Figure 4.43. This phenomenon was also observed by Harirchian and Garimella [84], who attributed it to an increase in vapour velocity at higher mass velocities. Flow reversal was observed at all mass fluxes, especially at low heat fluxes where the bubbly and slug flow regime developed in the channels.

Although it could be argued that smaller bubble departure diameters (Figure 4.39) at higher mass fluxes could lead to less bubble coalescence in the channels and delay the development

of slug flow, the stronger flow inertia at higher mass fluxes could have prevailed over the effect of reduced bubble diameters in the channel, increasing the velocity of the bubbles in the flow and resulting in an overall increase in the rate of bubble coagulation in the channels. Increasing rates of bubble coalescence with mass flux was also demonstrated in Revellin and Thome [160] for refrigerant flows in microtubes.

From Figure 4.39, it is shown that average bubble diameters at a given wall heat flux condition decreased with increasing mass velocity in the channels, especially when mass flux increased to G = 400 kg/m^2 s. Furthermore, the number of bubbles at G = 300 kg/m^2 s and G = 400 kg/m^2 s were about twice the number of bubbles identified in the selected frame at the lowest mass flux condition. Smaller bubble diameters at larger mass velocities were also observed in Harirchian and Garimella [84], Yin et al. [285] and Al-Zaidi [286]. The average bubble diameters were calculated from the median of the histogram shown in Figure 4.40, Figure 4.41 and Figure 4.42. Notably, bubble diameters measured at the lowest mass flux were as large as 300 µm. On the other hand, there was a clear peak in the distribution of bubble diameters between 75 µm – 100 µm and 50 µm – 75 µm at G = 300 kg/m^2 s and G = 400 kg/m^2 s respectively. At G = 200 kg/m^2 s, the distribution was more scattered and bubble diameters as large as 300 µm may be identified on the channels.

An understanding of relative forces acting on the liquid-vapour interface of a growing bubble in the channel could reveal controlling parameters in the development of flow patterns, heat transfer and flow instability in the microchannel heat sink. Kandlikar [287] considered a growing, confined bubble in a microchannel, surrounding by a body of fluid, as shown in Figure 4.44. F_σ, F_I, F_τ, F_B and F_M and are the surface tension force, inertia force, shear force, buoyancy force and evaporative momentum force respectively. These expressions are summarised in Eq. (4.18) – (4.22), based on the analysis by Kandlikar [287]. Alam et al. [121] extended this work by incorporating the effect of contact angle and heating surface orientation in the analysis.

$$F_\sigma \sim \frac{\sigma}{D_h} \tag{4.18}$$

$$F_I = \frac{G^2}{\rho} \tag{4.19}$$

$$F_\tau = \frac{\mu G}{\rho D_h} \tag{4.20}$$

$$F_B = \left(\rho_f - \rho_g\right) g\, D_h \tag{4.21}$$

$$F_M \sim \left(\frac{q_w''}{i_{fg}}\right)^2 \frac{1}{\rho_g} \tag{4.22}$$

F_I and F_τ are calculated assuming liquid flow and all fluid properties are evaluated based on at the saturation temperature condition at P = 1 bar while G is the channel mass flux, and g is the acceleration due to gravity. The magnitude of forces estimated at a fixed mass flux of G = 200 kg/m^2 s for wall heat fluxes ranging from q_w'' ~ 26 – 160 kW/m^2 are shown in Figure 4.45.

Earlier flow pattern transitions in the channel array at higher mass fluxes, postulated to be due to higher flow inertia at higher mass velocities, could be better understood through the analysis of forces at different mass flow rate conditions. Figure 4.46 present the relative forces with increasing mass flux at (a) a low wall heat flux condition of q_w'' ~ 26 kW/m^2 and (b) a high heat flux condition of q_w'' ~ 161 kW/m^2. Evident from Eq. (4.18) – (4.22), the surface tension, buoyancy and evaporation momentum force are insensitive to changes in mass flux at a given applied wall heat flux condition. On the other hand, at a fixed heat flux condition, increasing mass flux produces a considerable rise in inertia force and a moderate increase in shear force acting on the liquid-vapour interface. Again, the dominant forces in the channel appear to be the inertia force, surface tension force and buoyancy force, in increasing order. Notably, the evaporation momentum force was over an order of magnitude higher at q_w'' ~ 161 kW/m^2 compared to at q_w'' ~ 26 kW/m^2.

The significant increase in inertia force with increase in channel mass flux from G = 200 kg/m^2 s to G = 400 kg/m^2 s support the theory that an increase in the probability of bubble coagulation in the channels increase with increasing mass flux at a given wall heat flux, which would then shift flow pattern transition boundaries forward. This agrees with the inferences made from our flow visualisation, where earlier flow pattern transitions were recorded at increased mass fluxes (summarised in Table 4.6). The significant increase in flow inertia also indicate that the strong inertia force at higher mass flow rates dominated the effect of mass flux on bubble coagulation rate, rather than reduced bubble departure diameters in the channel observed during bubbly flow (Figure 4.39).

The thinner liquid film measured from flow visualisation with increasing mass flux, see Figure 4.43, could be due to the higher interfacial shear stress between the vapour and liquid phase,

indicated by the dependence of the frictional and acceleration pressure drop in the channels on G^2 (see Eq. (4.2) and (4.3)), as well as the increasing shear force in the channels from Figure 4.46, could have contributed to the thinner liquid film in the annular flow regime at higher mass fluxes.

Table 4.6: Flow pattern transition vapour qualities at P = 1 bar and ΔT_{sub} = 10 K for wall heat fluxes ranging from $q_w^{"}$ = 24.8 – 234.3 kW/m^2.

G [kg/m^2 s]	x_{B-S} [-]	x_{S-C} [-]	x_{C-A} [-]
200	0.037	0.068	0.304
300	0.008	0.041	0.195
400	0.001	0.037	0.169

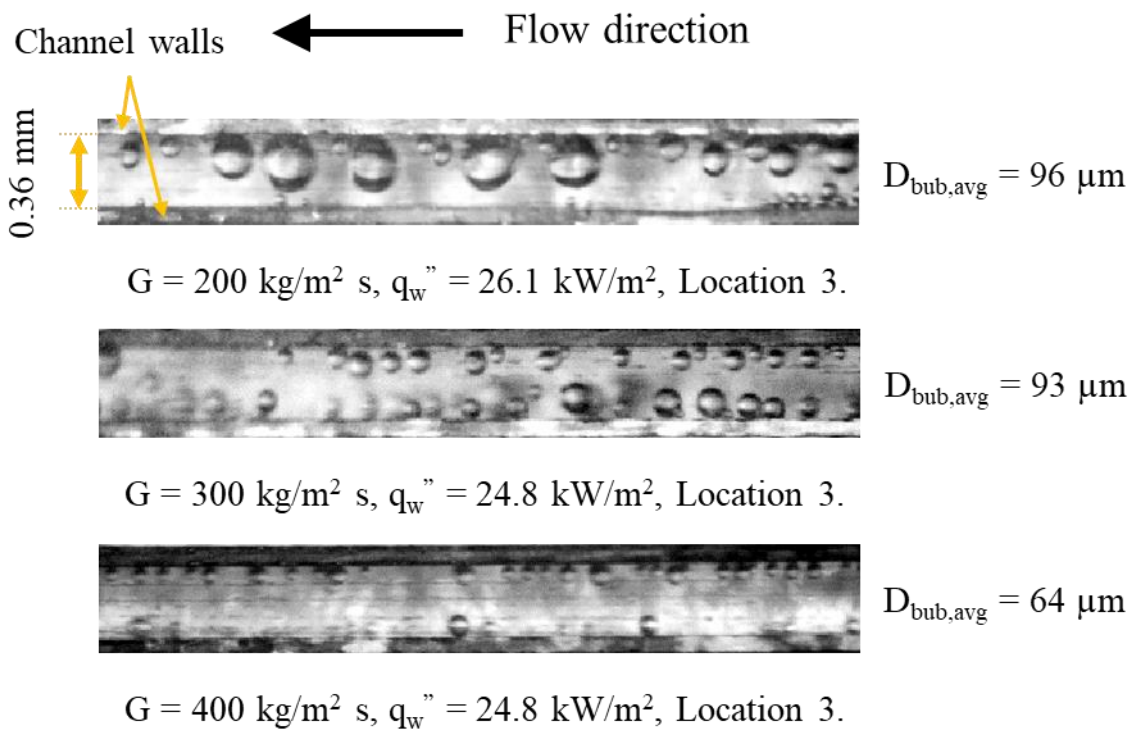

Figure 4.39: Average bubble diameters in bubbly flow at different mass fluxes, captured at camera location 3 (see Figure 4.1 for locations) at q_w" ~ 26 kW/m^2.

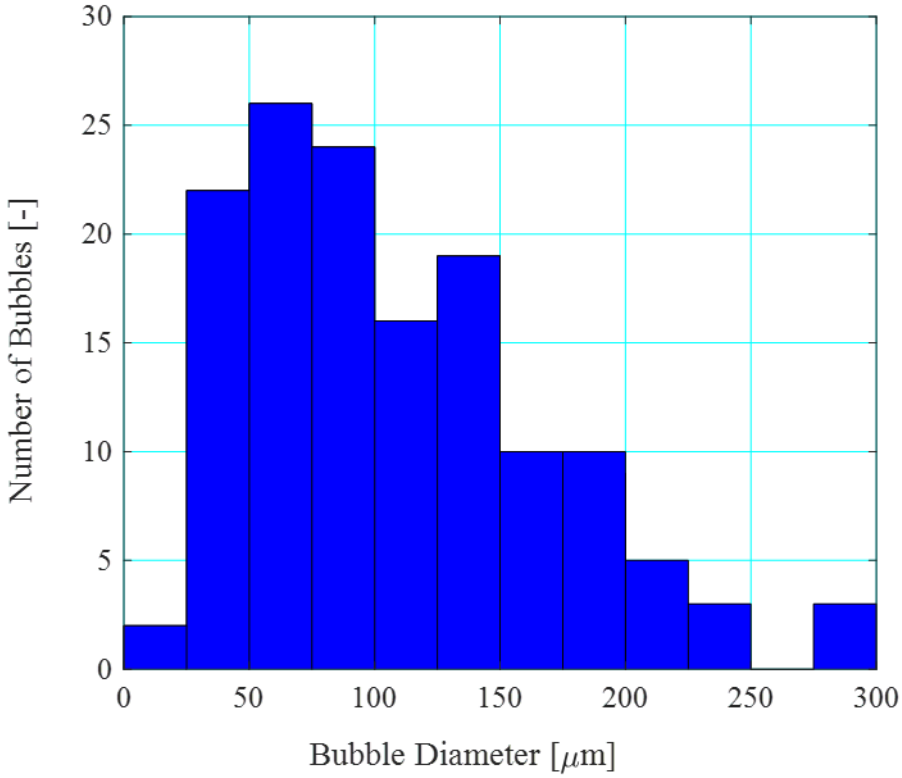

Figure 4.40: Distribution of bubble diameters measured on five still frames of the high speed recording at P = 1 bar, G = 200 kg/m^2 s, ΔT_{sub} = 10 K and q_w" = 26.1 kW/m^2.

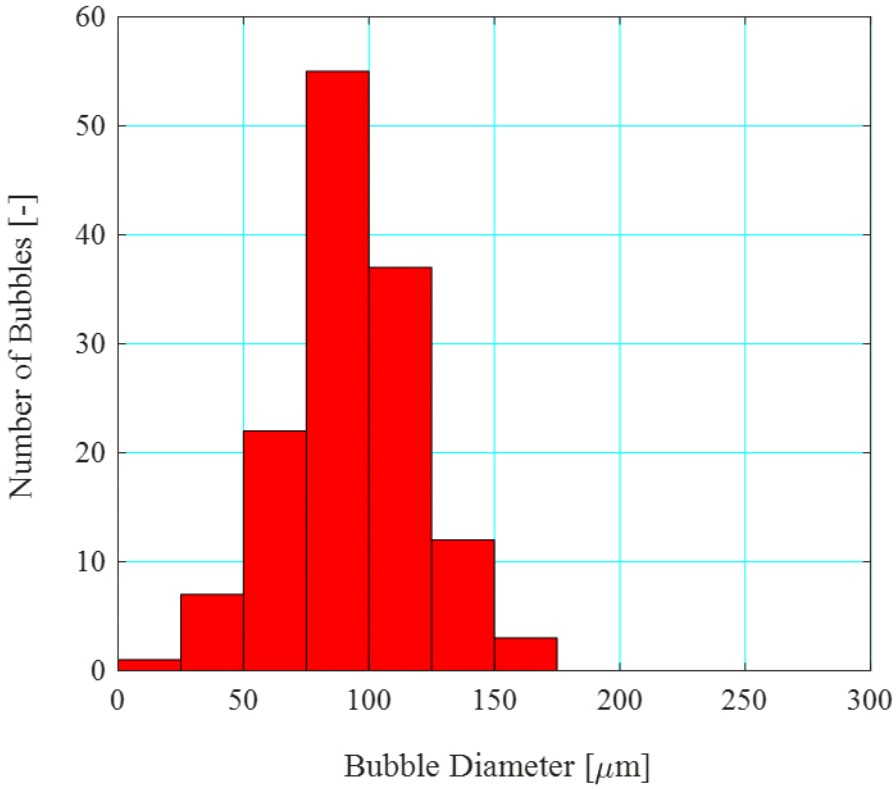

Figure 4.41: Distribution of bubble diameters measured on five still frames of the high speed recording at P = 1 bar, G = 300 kg/m^2 s, ΔT_{sub} = 10 K and q_w" = 24.8 kW/m^2.

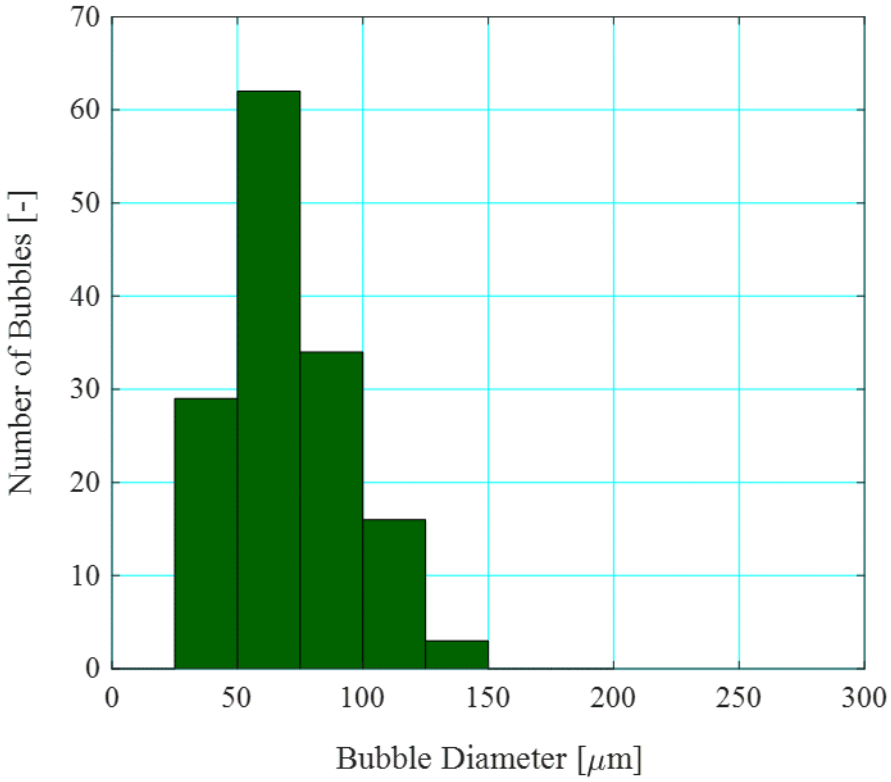

Figure 4.42: Distribution of bubble diameters measured on five still frames of the high speed recording at P = 1 bar, G = 400 kg/m^2 s, ΔT_{sub} = 10 K and $q_w^{"}$ = 24.8 kW/m^2.

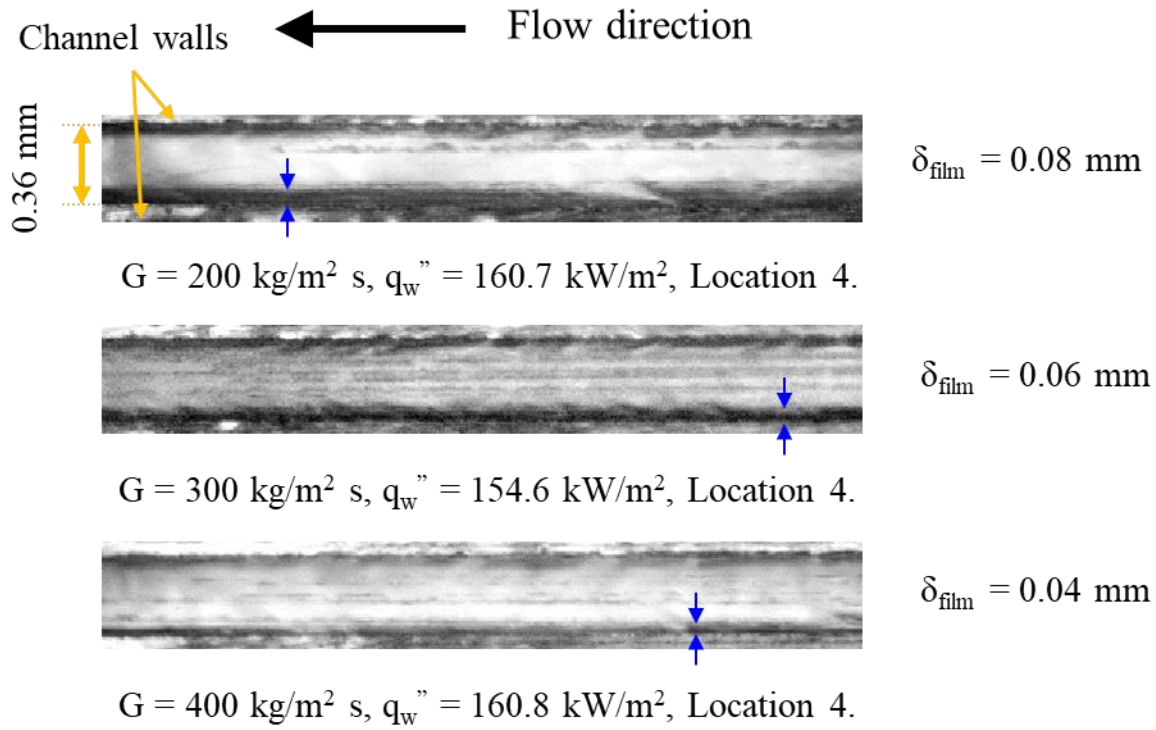

Figure 4.43: Liquid film thickness in annular flow at different mass fluxes, captured at camera location 4 (see Figure 4.1 for locations) at $q_w^{"}$ ~ 160 kW/m^2.

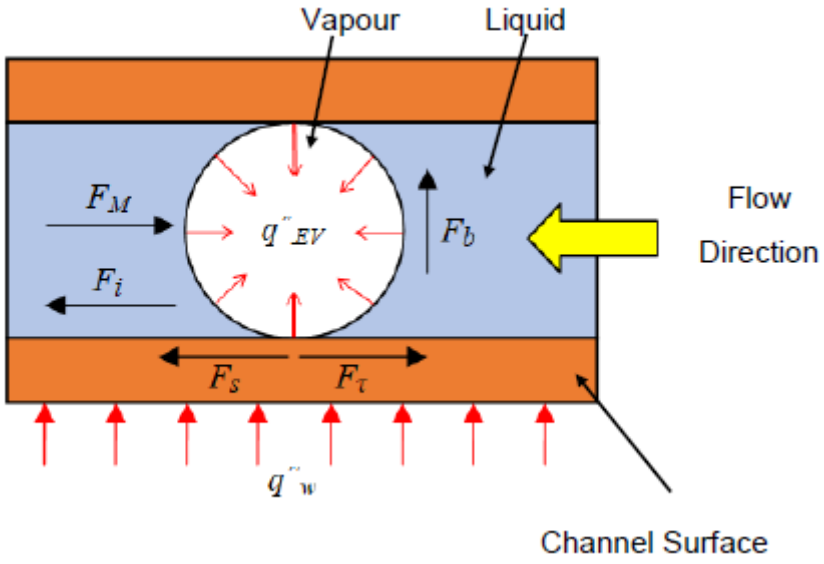

Figure 4.44: Forces acting on the liquid-vapour interface of a confined bubble growing in a microchannel. Illustration from Al-Zaidi [286].

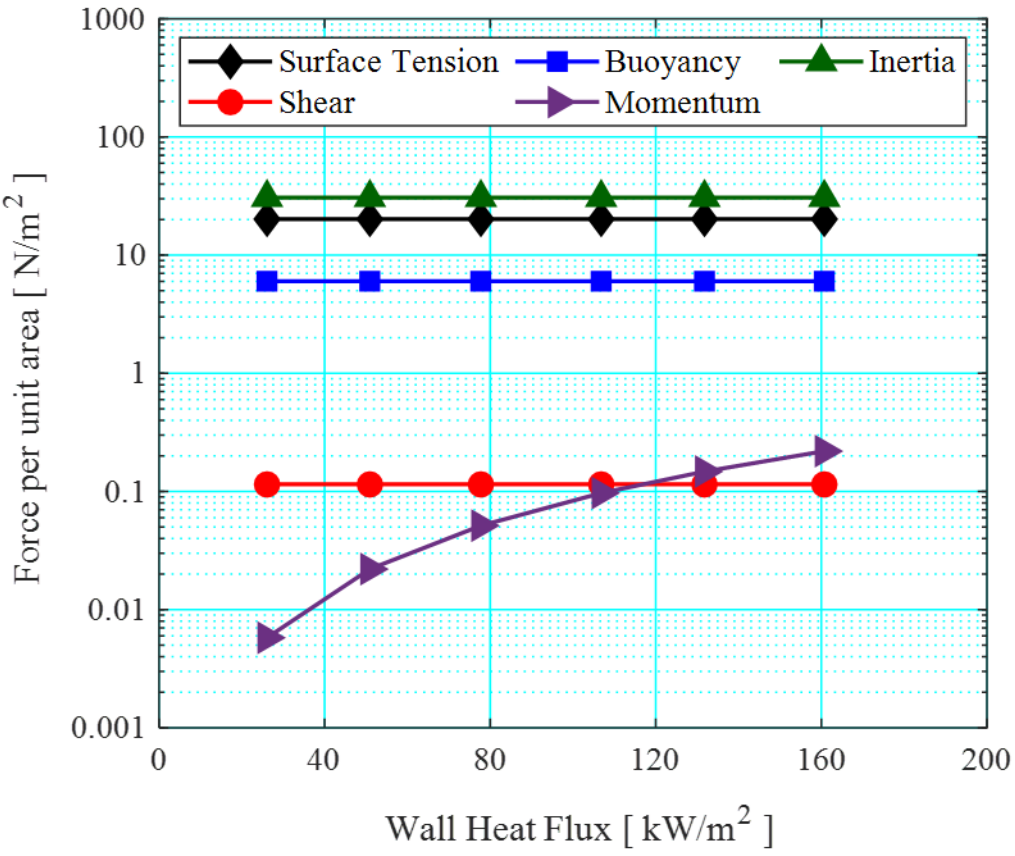

Figure 4.45: Magnitudes of relative forces acting on a growing bubble at P = 1 bar, G = 200 kg/m^2 s for q_w'' ~ 26 – 160 kW/m^2.

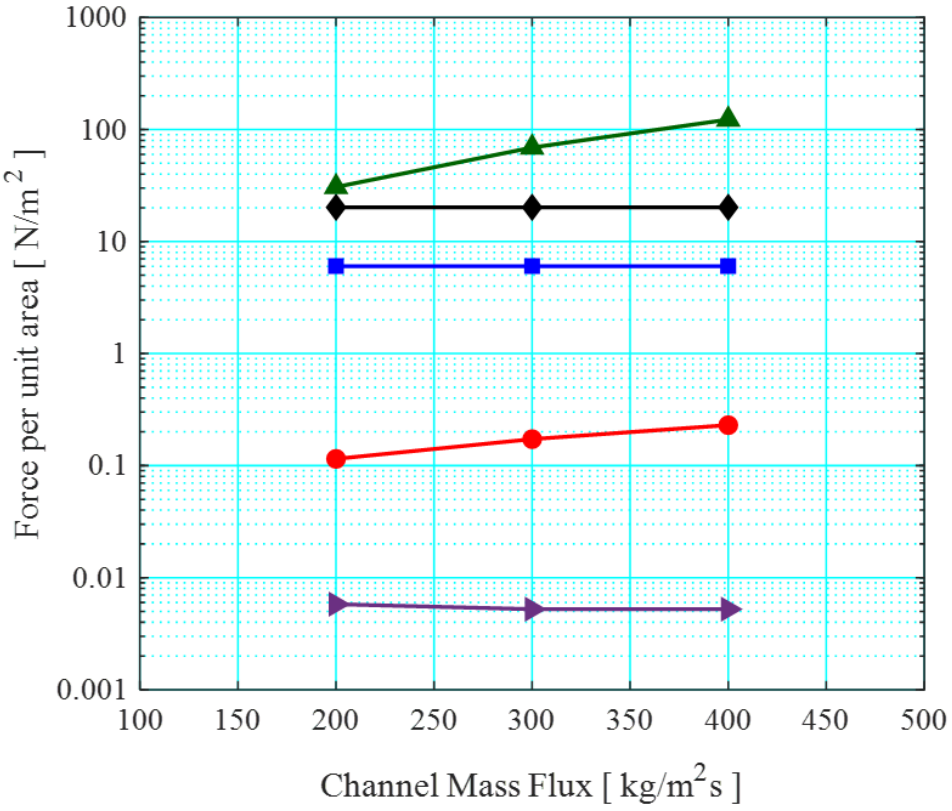

(a)

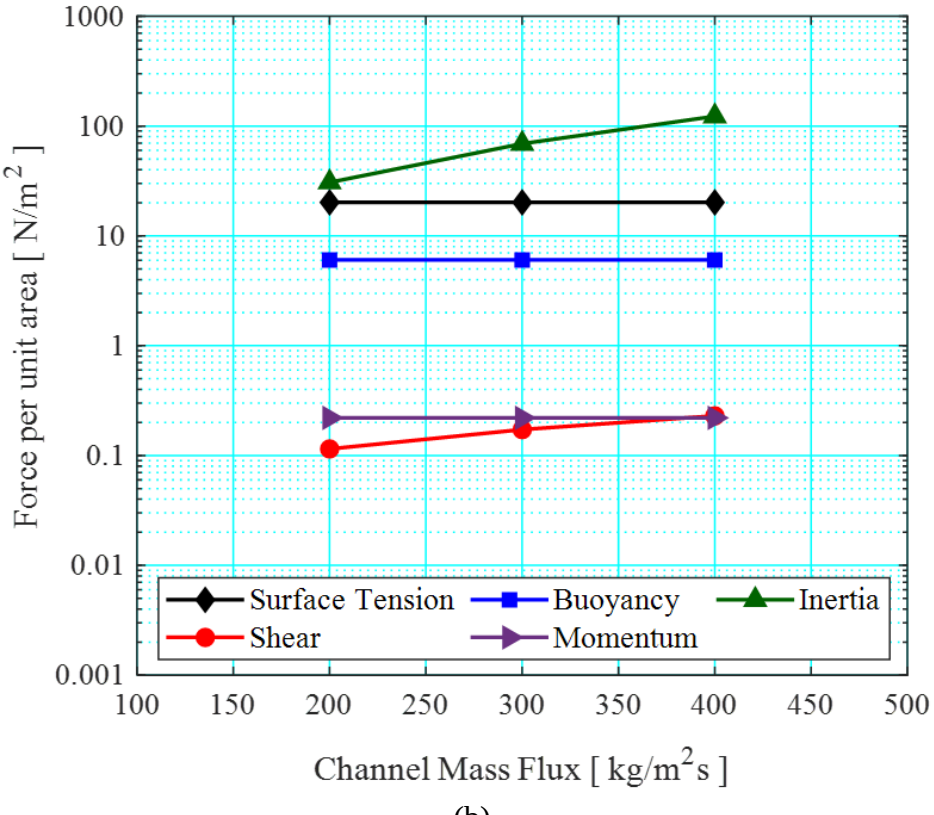

(b)

Figure 4.46: Magnitudes of relative forces acting on a growing bubble at P = 1 bar and G = 200, 300 and 400 kg/m^2 s for (a) q_w'' ~ 26 kW/m^2 and (b) q_w'' ~ 161 kW/m^2.

4.4.2 Heat Transfer

The boiling curves at the dimensionless location of z/L = 0.5 are plotted in terms of wall heat flux for the investigated mass flux conditions in Figure 4.47. As there is no data available for the region where wall superheat is between 0 K – 5 K, temperature overshoot prior to the commencement of boiling cannot be independently verified in this study. Nonetheless, in a similar heat sink configuration employing HFE-7100, a working fluid in the same series as the HFE-7200 used in the current study, Al-Zaidi et al. [57] stated that boiling incipience occurred without temperature overshoot at slightly smaller wall superheat (i.e. 2 K to 3.7 K).

From Figure 4.47, at the lowest heat flux condition, a slightly higher wall superheat accompanied higher channel mass flux. The boiling incipience superheat was between 6 to 11 K, with slightly higher wall superheat at higher mass fluxes. Boiling incipience occurred immediately at $q_w^{"}$ = 26.1 kW/m^2 at G = 200 kg/m^2 s while boiling was only triggered at $q_w^{"}$ = 50.6 kW/m^2 at G = 400 kg/m^2 s. Delayed boiling incipience heat flux and larger wall superheat at higher mass flow rates have also been reported in Harirchian and Garimella [85] and Drummond et al. [39]. At moderate heat fluxes between $q_w^{"}$ ~ 78 to 132 kW/m^2, the boiling curves appear to be independent of mass flux. A small effect of mass flux is recorded in the high heat flux region, as seen in Figure 4.47. In the high heat flux region where $q_w^{"}$ > 132 kW/m^2, the boiling curves begin to diverge from each other with increasing heat flux. The effect of mass flux in the high heat flux region could be due to the increasing contribution of the convective boiling mechanism following flow pattern transition to churn and annular flow.

At higher mass fluxes, the subcooled length in the channel increases accordingly due to the larger applied heat flux required to achieve saturation temperature conditions in the flow. In other words, for a given wall heat flux, increasing mass flow rate extended the subcooled region in the channels, as illustrated in Figure 4.48, which delayed boiling incipience heat flux as well as boiling incipience wall superheat in the channels. Subcooled length decreases exponentially with increase in wall heat flux. At $q_w^{"}$ ~ 26.1 kW/m^2, there is a notable difference in subcooled length with increase in mass velocity. In fact, at G = 400 kg/m^2 s, the entire channel is in subcooled boiling mode (i.e. $L_{sub} = L_{ch}$ = 20 mm). At G = 300 kg/m^2 s, the saturated boiling region only occurred toward the exit of the channels, while flow boiling was activated over almost half the length of the heat sink at G = 200 kg/m^2 s.

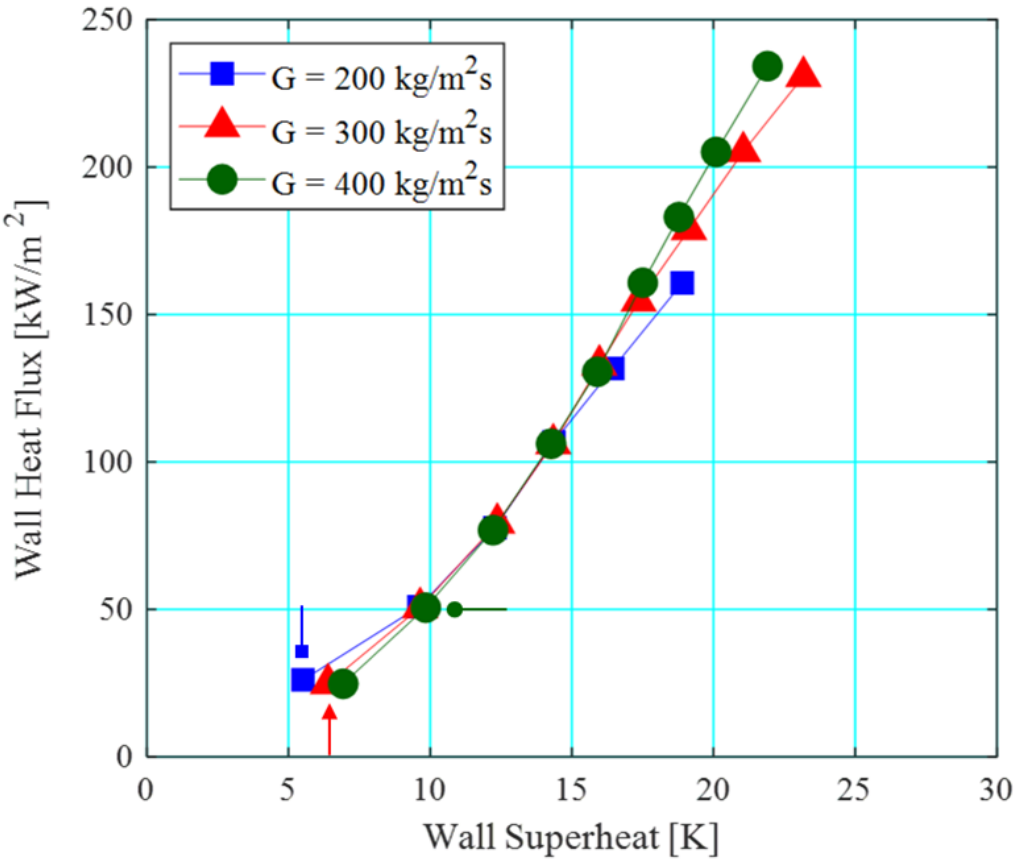

Figure 4.47: Boiling curves for mass fluxes G = 200, 300 and 400 kg/m^2 s as a function of wall heat flux at P = 1 bar and ΔT_{sub} = 10 K. Arrows with the corresponding markers indicate boiling incipience wall heat flux on the figure. The error bars in wall heat flux and wall superheat range between 2 % – 4.3 % and 0.2 K – 0.6 K respectively but are not visible in the figure.

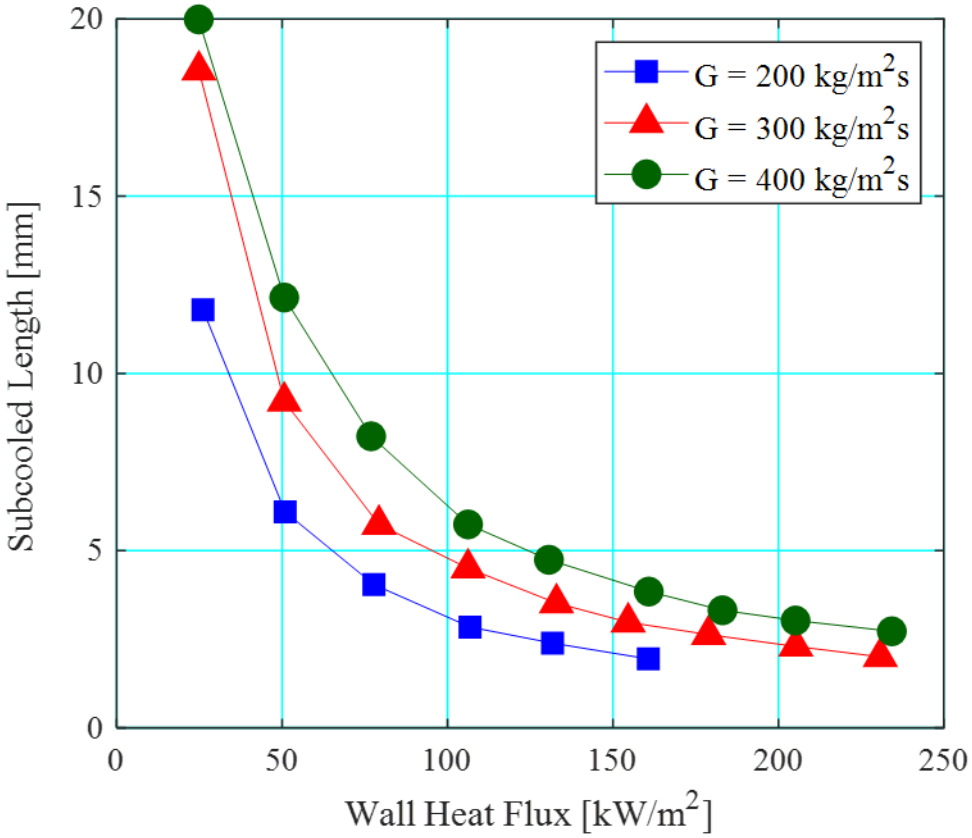

Figure 4.48: Subcooled length with respect to wall heat flux for G = 200, 300 and 400 kg/m^2 s at P =1 bar and ΔT_{sub} = 10 K.

The effect of mass flux on flow boiling heat transfer coefficients is depicted in Figure 4.49 as a function of wall heat flux. Average two-phase heat transfer coefficients increase with increasing heat flux. Similar to the trend exhibited by the boiling curves in Figure 4.47, some dependency of heat transfer coefficients on mass flux is detected at high heat fluxes but is negligible at low and moderate heat flux levels. Notice that the data point at the lowest wall heat flux (q_w" ~ 26 kW/m^2) is removed from the plot of G = 300 kg/m^2 s and G = 400 kg/m^2 s respectively. This is because all local heat transfer coefficients measured at this heat flux level fall within the subcooled region of the channels.

A similar mass flux trend is observed when assessing the overall heat transfer coefficients in the channel (see Figure 4.50), that is, taking into consideration also heat transfer coefficients in the subcooled region and averaging local heat transfer coefficients over the entire channel length based on Eq. (3.30). At low heat fluxes (q_w" ~ 26 to 51 kW/m^2), the lower overall heat transfer coefficients in the channel at higher mass fluxes is due to the considerable extension of the subcooled region in the channel array with increasing mass flux, as seen from Figure 4.48. As the magnitude of heat transfer coefficients in the subcooled region is naturally lower than heat transfer coefficients typically measured under saturated conditions, a lower overall heat transfer coefficient is observed at low heat fluxes. At moderate and high heat fluxes (q_w" ~ 161 to 234 kW/m^2), the subcooled length shrinks considerably and the effect of mass flux on subcooled length become insignificant, as the subcooled length of the channels is negligible compared to the saturated boiling length, which is established over a large portion of the channels.

Nonetheless, a mass flux effect is still prevalent in the high heat flux region. In the initial stages of boiling in microchannels, the nucleate boiling mechanism is likely the primary contributor to total heat transfer coefficients in the channel. This is supported by our flow visualisation results, where intensive nucleation activity is observed on the channel walls. Following flow pattern transition to slug, churn and annular flow, as noted in Section 4.2.1, nucleation sites are periodically suppressed (owing to liquid film thinning) and the contribution of the convective boiling mechanism, namely thin-film evaporation, increases in these regimes. The effect of mass flux observed between q_w" ~ 161 to 234 kW/m^2 could have captured the early stages where the contribution of the convective boiling mechanism to total heat transfer begins to overtake the nucleate boiling mechanism in the channels. This is evident from Figure 4.49, where an increase in channel mass flux produced a mild rise in average flow boiling heat

transfer coefficients, only apparent in the high heat flux region (i.e. q_w" ~ 161 to 234 kW/m^2). Enhanced heat transfer coefficients with increasing mass velocities at heat fluxes where convective boiling dominates was also reported by Harirchian and Garimella [85], Huang et al. [92], Thiangtham et al. [117] and Agostini et al. [87]. From flow visualisation, it is clear that annular flow prevails over at least half the length of the channels in the heat sink in this heat flux range.

Furthermore, average liquid film thickness in the annular flow regime decreased with increase in mass flux, see Figure 4.43. Higher thin-film evaporation rates could be associated with the thinner liquid film in the annular flow regime in the channels at higher mass flux conditions. Despite the fact that thinner liquid films could also more prone to dryout, the rewetting mechanism brought about by the intermittent churn wave appeared to have prevented prolonged dryout in the channels, and was consistently observed through flow visualisation at all mass flux conditions investigated in this study.

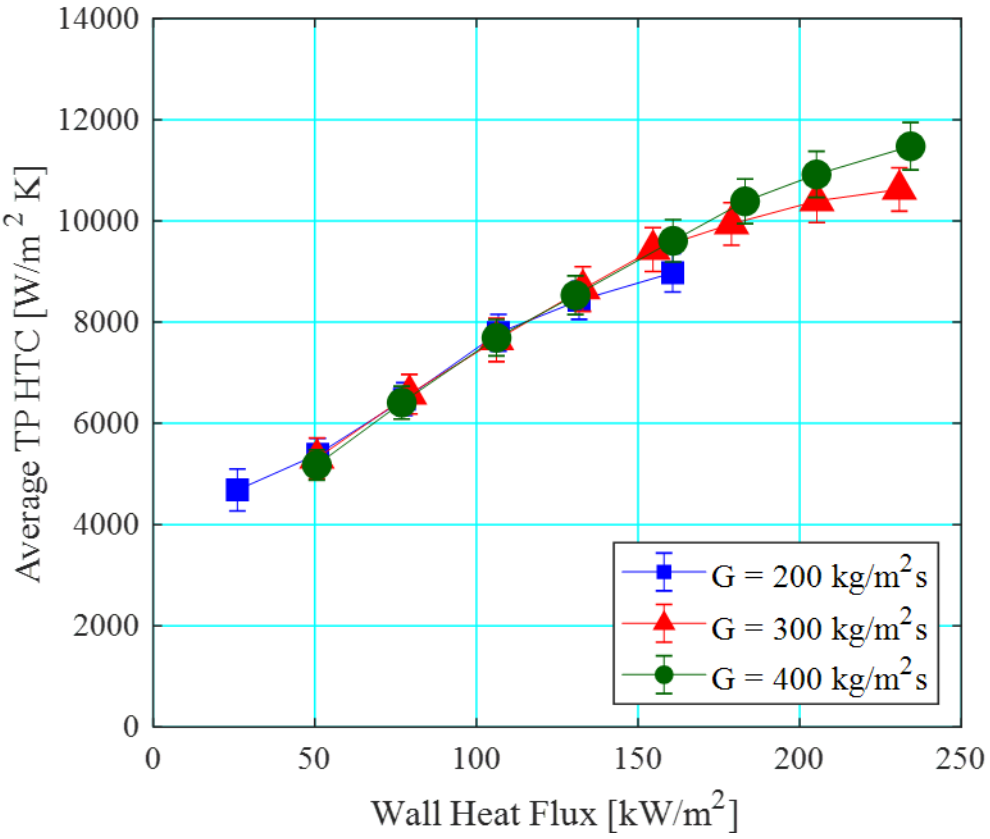

Figure 4.49: Average flow boiling heat transfer coefficients with respect to wall heat flux for G = 200, 300 and 400 kg/m^2 s at P = 1 bar and ΔT_{sub} = 10 K.

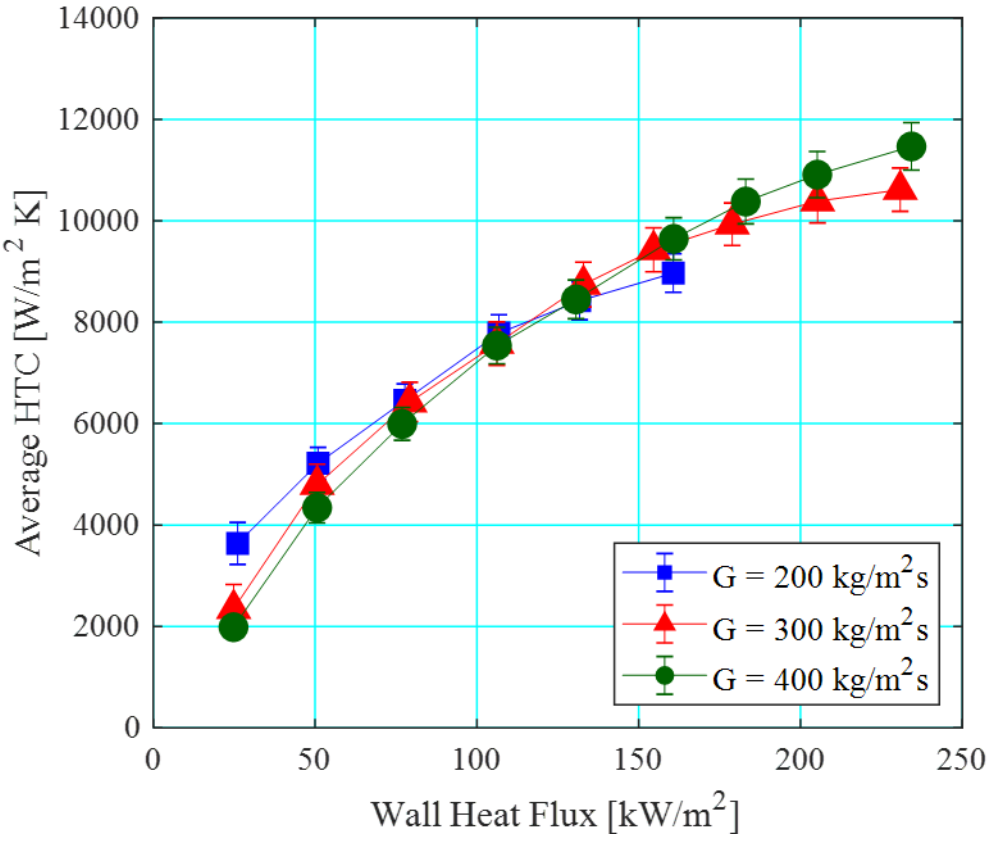

Figure 4.50: Overall heat transfer coefficients with respect to wall heat flux for G = 200, 300 and 400 kg/m^2 s at P = 1 bar and ΔT_{sub} = 10 K.

4.4.3 Pressure Drop

Figure 4.51 and Figure 4.52 show the effect of mass flux on two-phase pressure drop in the microchannel heat sink. The magnitude of two-phase pressure drop was relatively small (less than 12 kPa) in the microchannel heat sink, owing to the short channel length and relatively low vapour volume of the working fluid. As expected, two-phase pressure drop increases with increasing wall heat flux, as well as increasing mass flux in the channels. The pressure drop profile is steeper at higher mass velocities in the channel. The observations for the effect of mass flux conform to the general agreement in literature (see Section 2.4). Accordingly, at higher flow rates, interfacial shear as well as energy loss due to fluid acceleration increase, thereby increasing the frictional pressure drop and acceleration pressure loss components of the system.

As explained above, two-phase pressure drop in the channels is made up of the frictional and acceleration pressure drop component as shown in Eq. (4.2) and (4.3). Both components are strongly related to mass flux and vapour quality. At a given heat flux condition, increasing channel mass velocity decreases lowers the vapour quality in the channels, according to Eq. (3.16) to (3.18). Hence the effect of mass flux on vapour quality must be considered when assessing the individual pressure loss contributions in the channel.

The respective rise in the frictional and acceleration pressure drop components, predicted using the Lockhart-Martinelli [203] correlation based on the experimental data are presented in Figure 4.53 and Figure 4.54 accordingly for all mass fluxes investigated in this study. Frictional pressure drop increases steeply with increasing vapour quality, but plateaus as the flow approaches single-phase gas flow. The pressure drop gradient, with respect to vapour quality, increases with increasing mass flux, since $\Delta P_{fric} \propto G^2$. Additionally, at a given exit vapour quality the two-phase frictional multiplier generally increases with increasing mass flux, as shown in Figure 4.55. This is mainly due to an increase in the liquid and gas Reynolds number, which resulted in a reduction in the liquid-gas friction factor ratio in Eq. (4.5). Subsequently, the smaller Martinelli parameter, inversely proportional to the two-phase multiplier, results in a higher frictional multiplier in Eq. (4.4). On the other hand, at a fixed exit vapour quality condition, acceleration pressure drop increases with increasing mass flux, as given by Eq. (4.3).

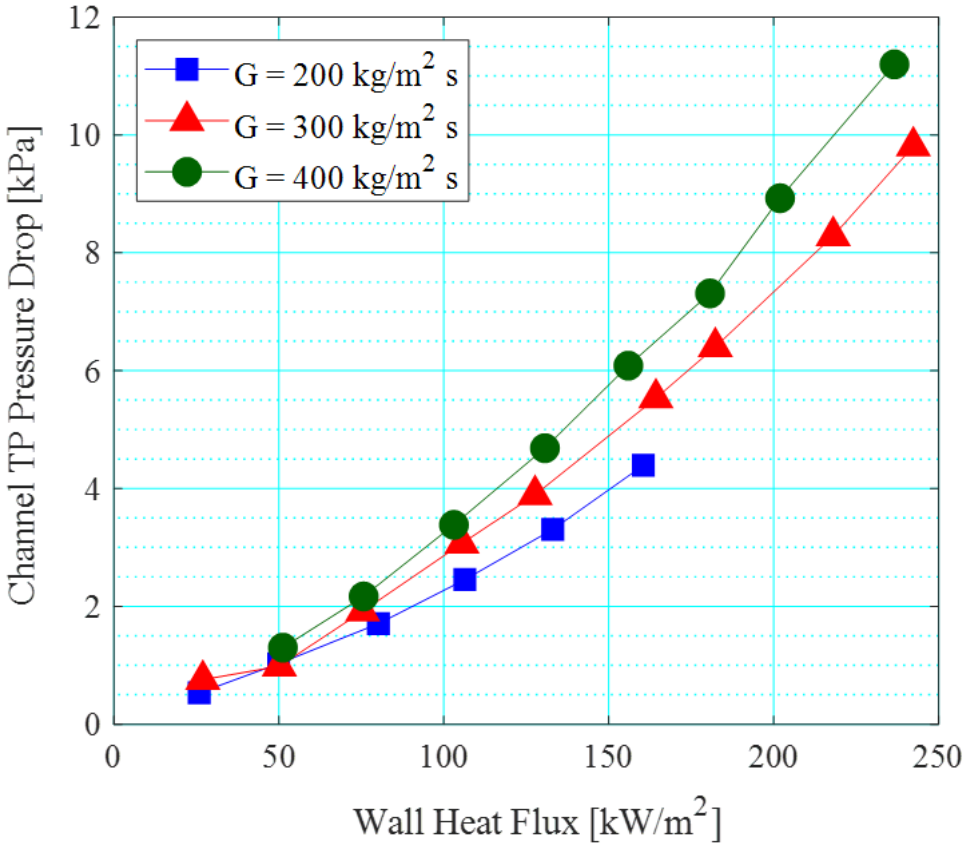

Figure 4.51: Two-phase pressure drop with respect to wall heat flux for G = 200, 300 and 400 kg/m^2 s at P = 1 bar and ΔT_{sub} = 10 K.

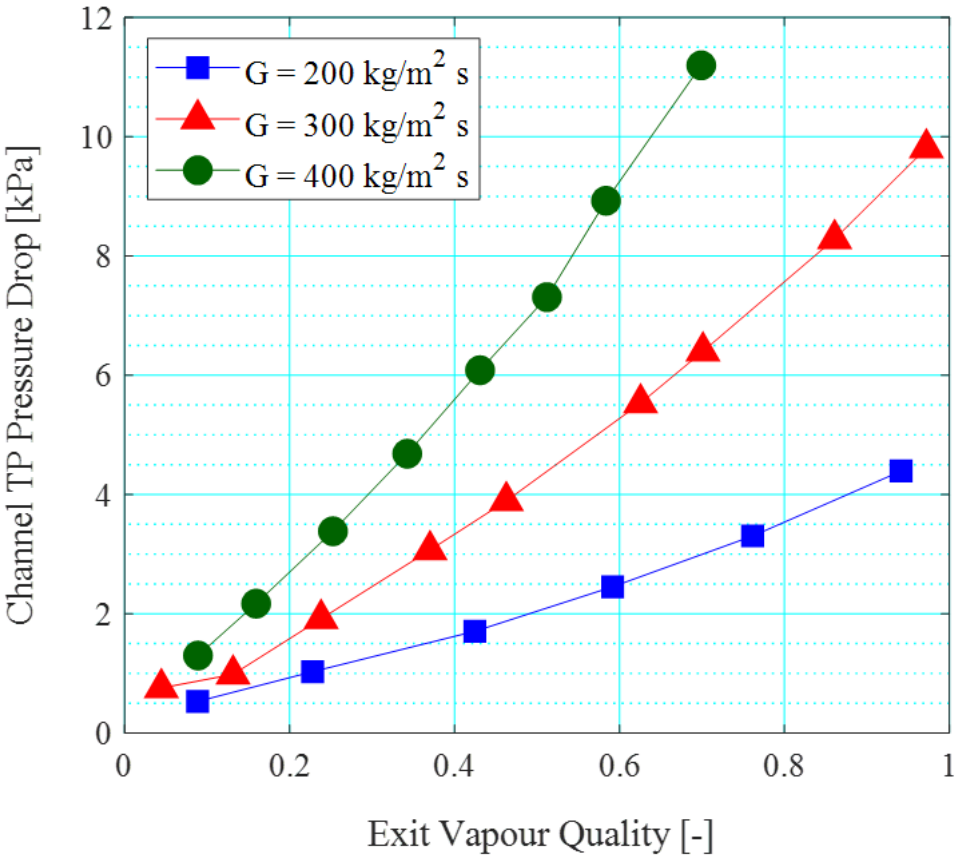

Figure 4.52: Two-phase pressure drop as a function of exit vapour quality for G = 200, 300 and 400 kg/m^2 s at P = 1 bar and ΔT_{sub} = 10 K.

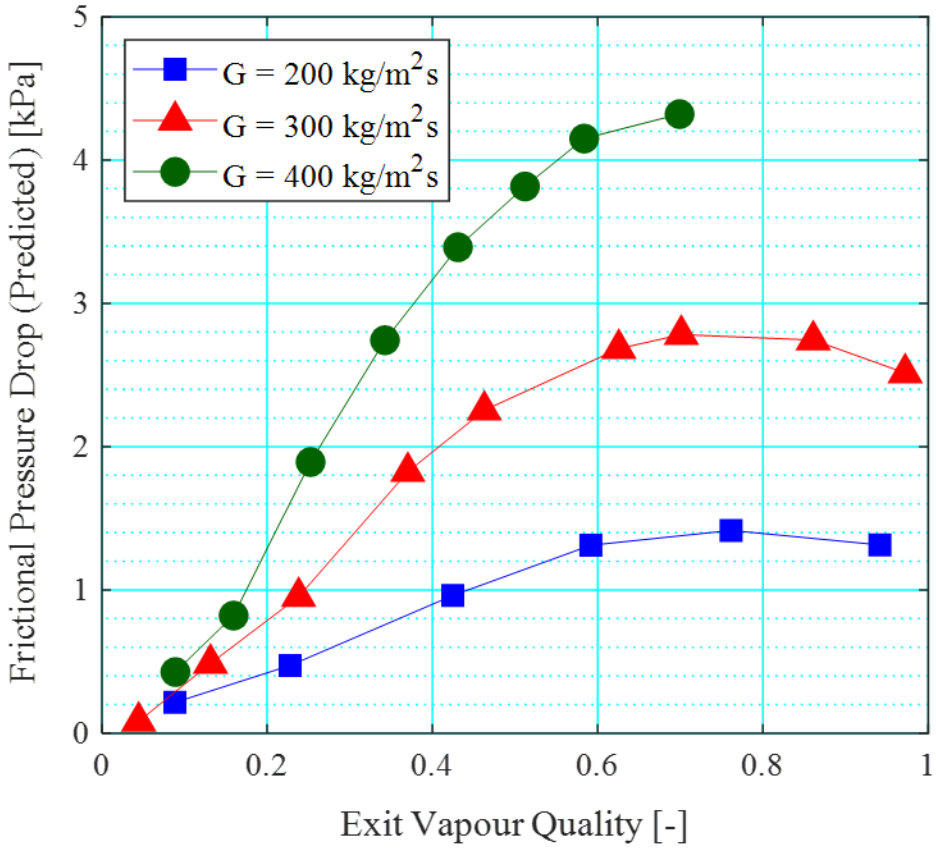

Figure 4.53: Two-phase frictional pressure drop with respect to exit vapour quality, predicted using the Lockhart-Martinelli correlation [203] for G = 200, 300 and 400 kg/m^2 s at P = 1 bar and ΔT_{sub} = 10 K.

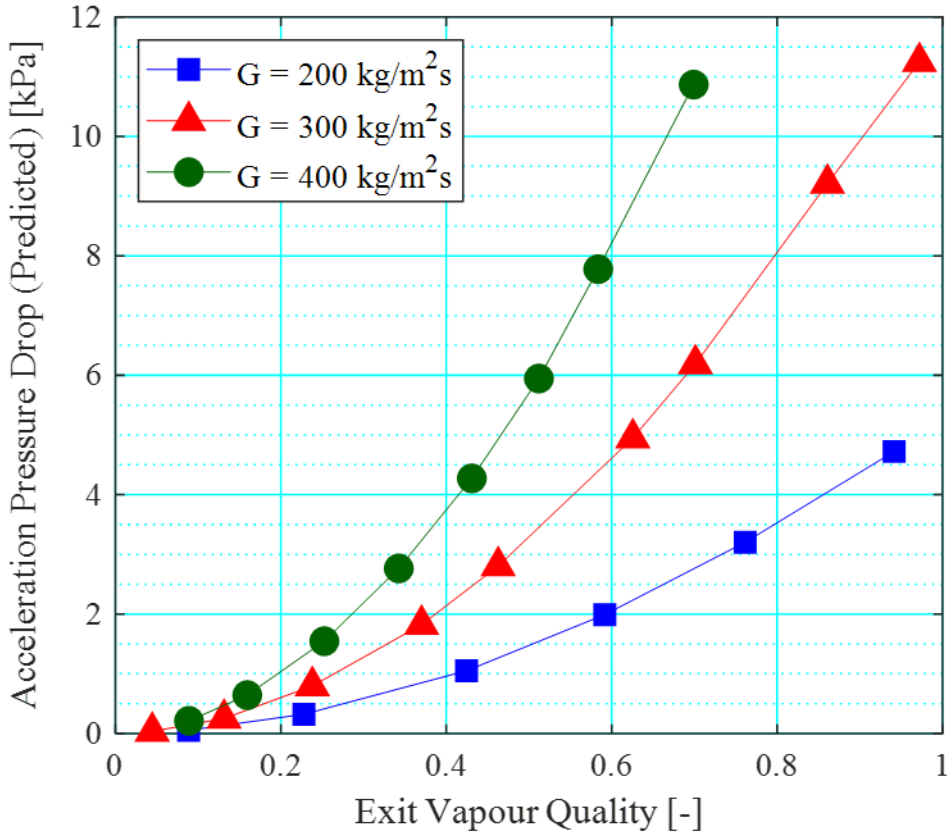

Figure 4.54: Two-phase acceleration pressure drop with respect to exit vapour, predicted using the Lockhart-Martinelli correlation [203] for G = 200, 300 and 400 kg/m^2 s at P = 1 bar and ΔT_{sub} = 10 K.

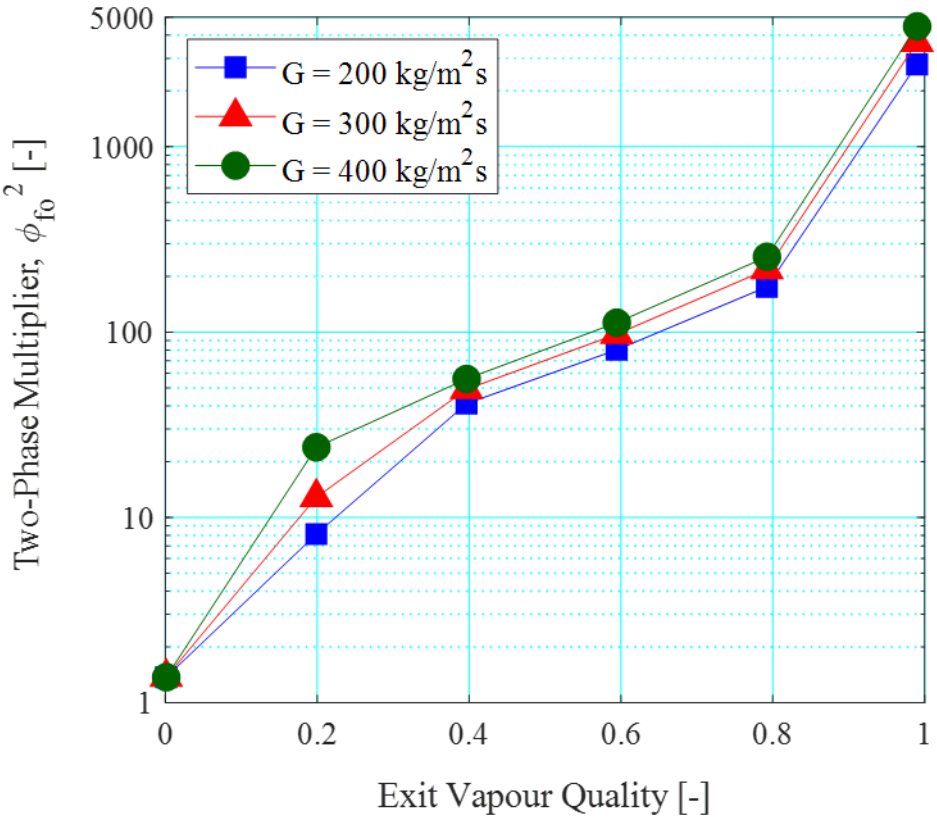

Figure 4.55: Two-phase frictional multiplier with respect to exit vapour, calculated using the Lockhart-Martinelli correlation [203] for G = 200, 300 and 400 kg/m^2 s at P = 1 bar and ΔT_{sub} = 10 K.

4.5 Effect of Inlet Subcooling

Flow boiling experiments were conducted to investigate the effect of inlet subcooling, namely at ΔT_{sub} = 5 K, 10 K and 20 K for wall heat fluxes ranging from $q_w^{"}$ = 25.9 kW/m^2 to 180.7 kW/m^2. This corresponds to vapour qualities from 0 to 1 at the exit of the microchannel heat sink. The channel mass flux and inlet pressure were kept constant at P = 1 bar, while the saturation temperature of HFE-7200 at 1 bar is 75.05 °C.

Notably, the repeatability of experiments at ΔT_{sub} = 5 K was less repeatable in comparison with the experiments conducted at inlet subcooling conditions of ΔT_{sub} = 10 K and 20 K. The mean absolute deviation of experiments at the higher subcooling conditions were around ± 3 – ± 4 %, while the mean absolute deviation was up to ±12.3 % at ΔT_{sub} = 5 K, as shown in Figure 4.56. The deviation in the data was slightly higher at lower heat fluxes in the channel at this subcooling condition. This could be related to flow reversal in the channel due to slug growth following the onset of boiling and potential upstream compressibility effects in the channel, which could affect heat transfer characteristics in microchannels [288], [289]. Flow reversal and hence possible effects on reproducibility is expected to be weaker at higher mass fluxes. This was the case when mass flux was increased to G = 300 and 400 kg/m^2 s, where the mean absolute deviation of experiments ranged between ± 0.1 to ± 4.5 %. Similar results were observed in Al-Zaidi [286] for reproducibility comparisons at higher mass fluxes.

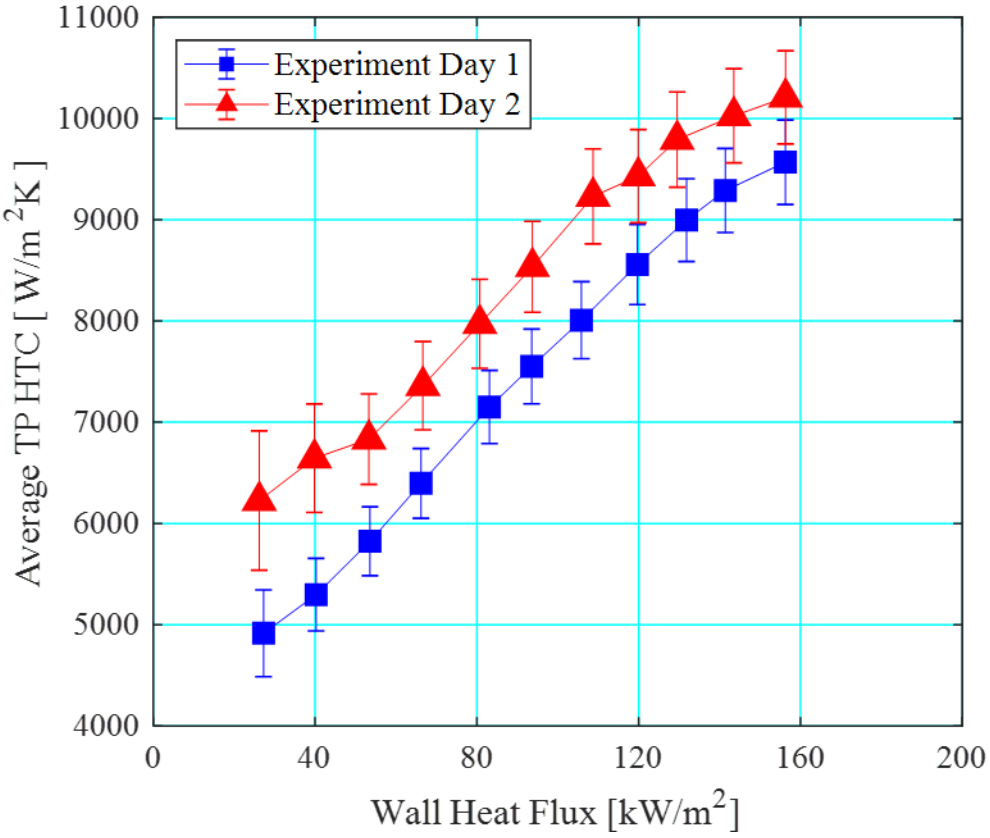

Figure 4.56: Repeatability of experiments at P = 1 bar, G = 200 kg/m^2 s and ΔT_{sub} = 5 K. The mean average deviation of the experimental data is ±12.3 %.

4.5.1 Flow Patterns

Flow patterns developed accordingly from bubbly to slug, churn and annular flow in the channels at all subcooling conditions. Flow regime transition boundaries were delayed to larger vapour qualities at higher inlet subcooling conditions (i.e. lower inlet temperatures). This agrees with the observations of Chen et al. [89] and Zeng et al. [77]. At a given wall heat flux condition of $q_w^{"} \sim 107$ kW/m^2, flow patterns monitored at the channel inlet (camera location 1, see Figure 4.1) evolved from churn to slug and bubbly flow with increasing subcooling, as shown in Figure 4.57. Accordingly, the vapour quality at which transition from bubbly to slug flow occurred in the channels increased with increase in inlet subcooling, as summarised in Table 4.6. From Table 4.7, it is clear that the quality for transition from bubbly to slug flow, as well as from churn to annular flow, increased gradually with subcooling. At higher degrees of subcooling, the development of annular flow was also delayed. Nonetheless between ΔT_{sub} = 5 K and ΔT_{sub} = 10 K, only a small shift in the slug-churn transition boundary was observed in the heat sink. However, this change was more evident as ΔT_{sub} increased to 20 K.

In the subcooled region of the channels, the liquid layer directly adjacent to the heated channel walls may still become superheated, even when the bulk liquid temperature is below saturation. Bubbles were captured to nucleate from the channel side walls, but shrink and eventually re-condense into the bulk flow soon after departure, as illustrated previously in Section 4.2.1, Figure 4.5. Due to bubble shrinkage in the subcooled region at higher subcooling, it follows that the potential for bubble coalescence in the channels is lower at higher inlet subcooling conditions. Additionally, increasing the inlet subcooling degree effectively extends the subcooled region in the channels. From Figure 4.58, it is clear that subcooled length decreases with heat flux but increases with inlet subcooling. As a result, transition from bubbly to slug flow occurs at higher vapour qualities in the heat sink at higher inlet subcooling conditions. Similarly, the subsequent flow regime transition boundaries were residually affected, i.e. slug-churn and churn-annular transition were also delayed to higher vapour qualities at higher inlet subcooling conditions.

The model proposed by Hsu [109], given previously in Eq. (2.15), was applied to predict the range of nucleation sites at inlet subcooling conditions of ΔT_{sub} = 5 K, 10 K and 20 K. This is shown in Figure 4.59. It is clear that the range of active nucleation sites become smaller with increasing degree of subcooling. Cavities with radii larger than 10 μm are significantly affected

by the subcooling degree, while the nucleation activity from small cavities are less sensitive to changes in system subcooling, for the range of subcooling investigated in the current study. The less vigorous bubble nucleation activity (lower bubble generation frequency) at higher subcooling conditions could also have contributed to the delay in flow pattern transition, owing to less bubble coagulation in the channels. Lower bubble generation frequencies at higher subcooling conditions were also suggested by Euh et al. [103] and Goel et al. [135] for macroscale boiling.

From Figure 2.1, it is clear from the comparison in active nucleation range between water and HFE-7200 that the model is highly dependent on working fluid due to differences in fluid properties applied in Eq. (2.15). Similarly, the range of active nucleation sites may also exhibit different sensitivities to degree of inlet subcooling. Furthermore, for fluids where annular flow develops very quickly in microchannels due to very high bubble generation frequencies, for e.g. water, the extent of the influence of subcooling may be lower as bubbly flow only occurs for a very narrow range of vapour qualities. This topic is worth investigating further for a conclusion.

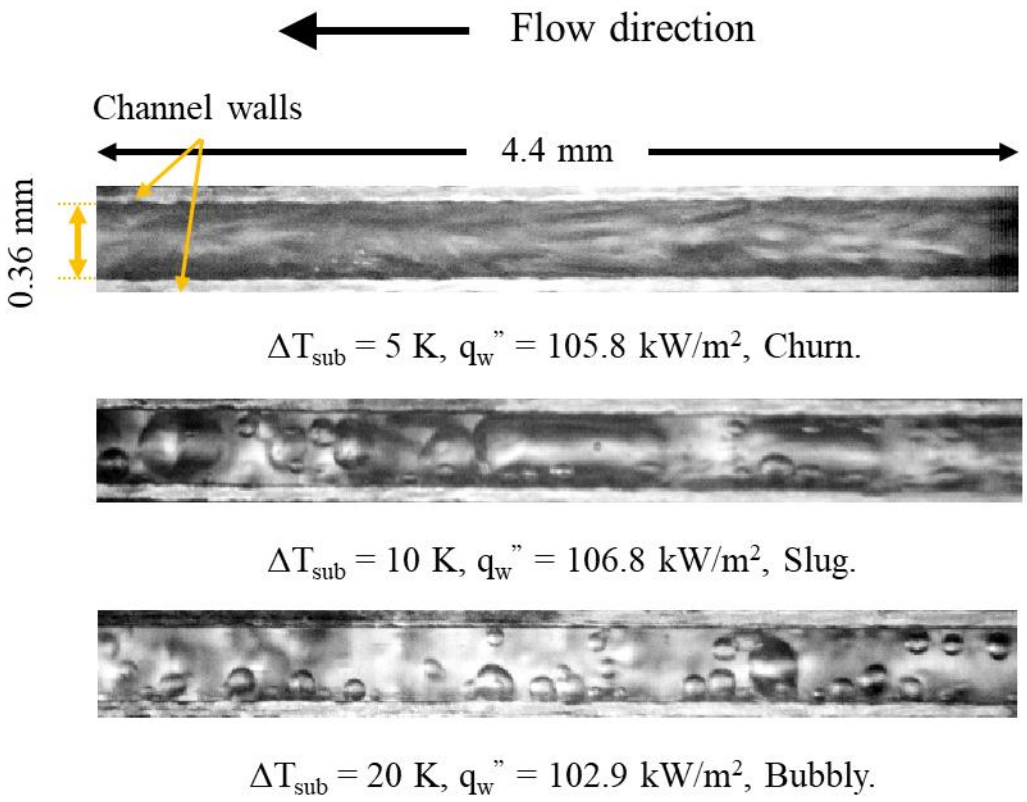

Figure 4.57: Flow patterns observed at camera location 1 (near channel inlet, see Figure 6), at three inlet subcooling conditions for an approximate wall heat flux of $q_w" \sim 107$ kW/m^2.

Table 4.7 : Flow pattern transition vapour qualities at P = 1 bar and G = 200 kg/m^2 s for wall heat fluxes ranging from $q_w^{"}$ = 25.9 – 180.7 kW/m^2.

ΔT_{sub} [K]	x_{B-S} [-]	x_{S-C} [-]	x_{C-A} [-]
5	0.012	0.064	0.23
10	0.037	0.068	0.30
20	0.049	0.125	0.34

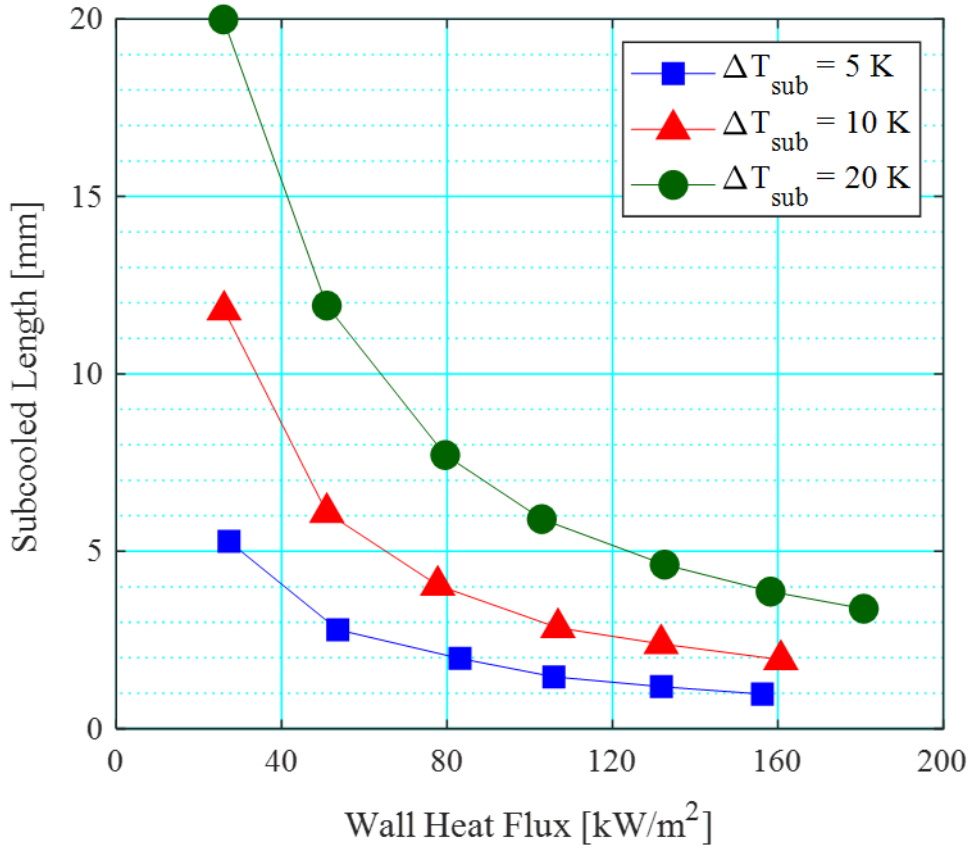

Figure 4.58: Subcooled length as a function of wall heat flux for inlet subcooling ΔT_{sub} = 5 K, 10 K and 20 K.

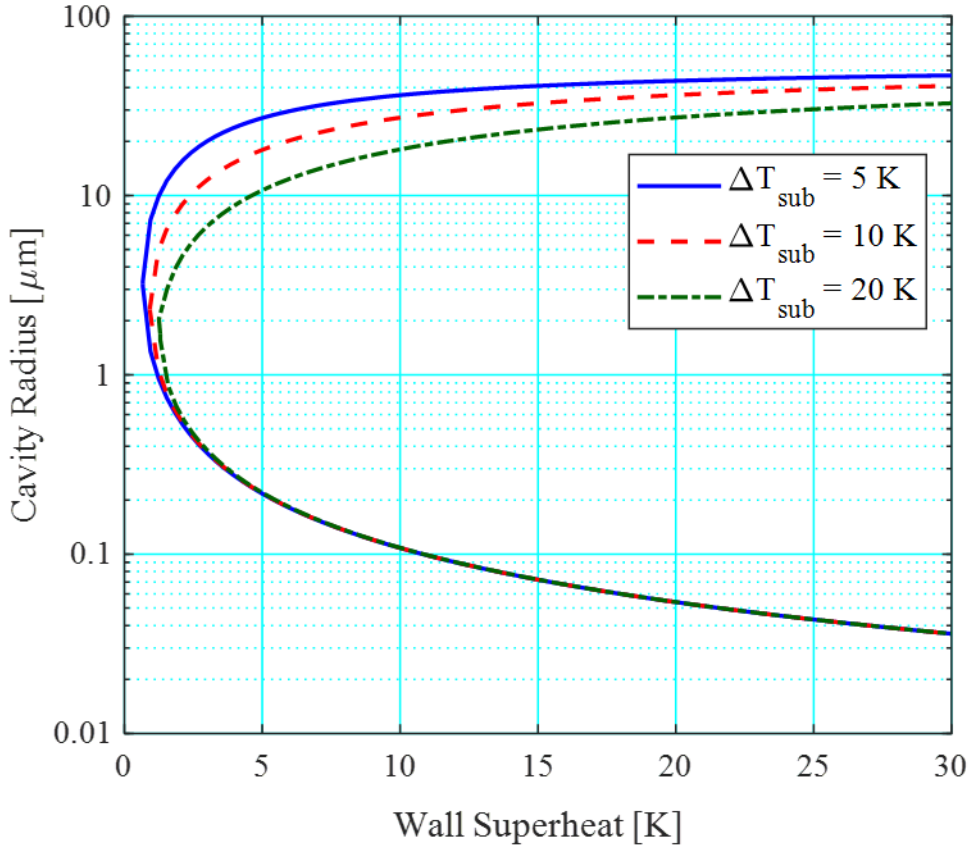

Figure 4.59: Range of active nucleation cavity radii as a function of wall superheat at subcooling conditions of ΔT_{sub} = 5, 10 and 20 K, as predicted using Hsu's model [109].

4.5.2 Flow Instability

It has previously been highlighted in Section 2.5 that there is an unclear dependence of subcooling on flow instabilities in microchannels. Authors in [89], [139], [140] found that increasing the degree of inlet subcooling suppressed two-phase oscillations in microchannels while authors in [80], [141], [142] reported significantly higher flow instabilities at higher degrees of inlet subcooling for microchannel flow boiling.

As discussed in Section 4.3.2, the standard deviation of the measured pressure drop signal may be used as an indication of the magnitude of flow oscillations in the heat sink at a particular operating condition. The standard deviation of the measured pressure drop signal across the heat sink is presented in Figure 4.60(a) and (b) for $q_w^{"} \sim 51$ kW/m^2 and $q_w^{"} \sim 132$ kW/m^2 respectively in order to assess the effect of inlet subcooling on flow boiling instabilities in the microchannel heat sink. The standard deviation is calculated based on Eq. (4.14). As mentioned in Section 4.3.2, pressure and temperature measurement signals are commonly used to characterise flow instability in [101], [141], [142], [281]. Kuo and Peles [101] used local temperature measurements to identify bubble nucleation, dryout and upstream flooding stages in microchannel flow while pressure drop oscillations were attributed to alternating vapour flow into the inlet plenum and the incoming subcooled liquid in Bogojevic et al. [141]. In Kingston et al. [142], [281], fluctuations in the pressure drop, temperature and mass flux signals were correlated to periodic occurrences of rapid bubble growth and confined bubble expansion in the channel array.

Pressure drop oscillations observed in the current study may be associated with flow reversal triggered by the expansion of vapour slugs in the channels, which is frequently observed in the presence of confined slugs. Flow reversal captured at the inlet of the heat sink showed a typical cycle of flow reversal to be between 350 – 600 ms long, with slug expansion causing vapour backflow to be as short as 16 ms. Flow reversal captured in the current study has previously been illustrated in Figure 4.8 and Figure 4.9. Due to limitations in camera memory, flow visualisation at extended time periods of 6.5 s at the inlet plenum (normal flow pattern visualisation along the channel are only for a duration of 1.3 s) were only conducted at select operating conditions to monitor the full occurrence of flow reversal phenomenon in this study. While the flow conditions illustrated in Figure 4.8 and Figure 4.9 do not directly correspond to the range of operating conditions presented in the current section, they are a good

representation of the type of flow reversal observed in the heat sink at low heat fluxes. This is confirmed through the observation of flow patterns captured along the channels at different mass fluxes, including G = 200 kg/m^2 s of the present range, for various heat flux conditions. Additionally, as covered in Section 4.2.1, high speed flow visualisation was conducted at quasi-steady state but not simultaneous to data recording.

The peak in pressure drop readings may be associated with upstream pressurisation due to vapour expansion in the upstream direction (see Figure 4.8(b) – (c)). As the slugs grow to the full length of the channels, the flow resistance is reduced and results in a drop in measured pressure drop across the heat sink. This corresponds to the pressure drop instability phenomenon observed in Kingston et al. [142] during confined bubble expansion. In order to capture these occurrences, the response time of the measuring instrument must be shorter than the time period of the flow phenomenon. As mentioned in Section 4.3.2, based on the manufacturer's specification, the response time of the differential pressure transducer is less than 1 ms [283], hence the instrumentation was suitable for capturing the pressure oscillations. The response time of the 0.5 mm diameter K-type thermocouple used to measure fluid inlet temperature is given as 0.03 s [282]. In order to obtain a meaningful measurement of the dynamic temperature behaviour corresponding to flow reversal in the microchannels, temperature measurement techniques such as temperature sensors [141] that allows for higher response rates should be employed. Hence only the signal obtained from the differential pressure transducer will be used in the discussions on flow boiling instabilities in the current study.

At low heat flux, increasing inlet subcooling, particularly to 20 K, reduced pressure oscillations in the heat sink. The standard deviation of the measured pressure drop signal at 5 K was 0.58 kPa. Increasing inlet subcooling mitigated pressure drop oscillations to 0.1 kPa at 20 K, see Figure 4.60(a). This could be due to the delayed development of slug flow due to less intensive bubble coalescence phenomenon in the channels at higher subcooling for a given wall heat flux condition. At $q_w^{"} \sim 51$ kW/m^2, the slug flow regime was observed near the inlet of the heat sink at 5 K and 10 K, while bubbly flow was largely observed in the heat sink at 20 K. As mentioned above, the expansion of vapour slugs in the channels trigger vapour backflow into the inlet plenum, and is believed to contribute to the larger pressure drop oscillations observed at lower inlet subcooling. Kingston et al. [142] also found that increasing inlet subcooling at a given

wall heat flux condition delayed the onset of pressure drop instabilities in their parallel microchannel heat sink using fluid HFE-7100.

The magnitude of two-phase oscillations stabilised in the churn and annular flow regime are evident by comparing the signals illustrated in Figure 4.60(a) and (b). This could be due to the presence of a stable vapour core in the annular flow regime, which could have resulted in lower flow resistance in the channels, lower upstream compressibility and thus less severe vapour backflow to the inlet plenum of the heat sink. However, increasing inlet subcooling at wall heat fluxes where the annular flow regime is dominant increased the pressure fluctuations slightly. The standard deviation of the measured heat sink pressure drop increased from 0.05 kPa at 5 K to 0.1 kPa at 20 K. This agrees with the observation of Bogojevic et al. [141] and Deng et al. [80] who found higher flow oscillations at higher degrees of subcooling in their parallel channel heat sinks. This could be because both studies used water as the working fluid and annular flow was the predominant flow pattern in the heat sink. Bogojevic et al. [141] attributed the lower flow oscillations to improved flow distribution at higher inlet water temperatures in the heat sink.

In summary, a complex dependency of two-phase flow instability on the degree of subcooling was observed. Increasing the degree of subcooling resulted in a reduction in pressure drop fluctuations when the flow was dominated by slug flow. On the other hand, when heat flux was increased and annular flow dominated in the channels, increasing inlet subcooling increased the pressure fluctuations, although only slightly.

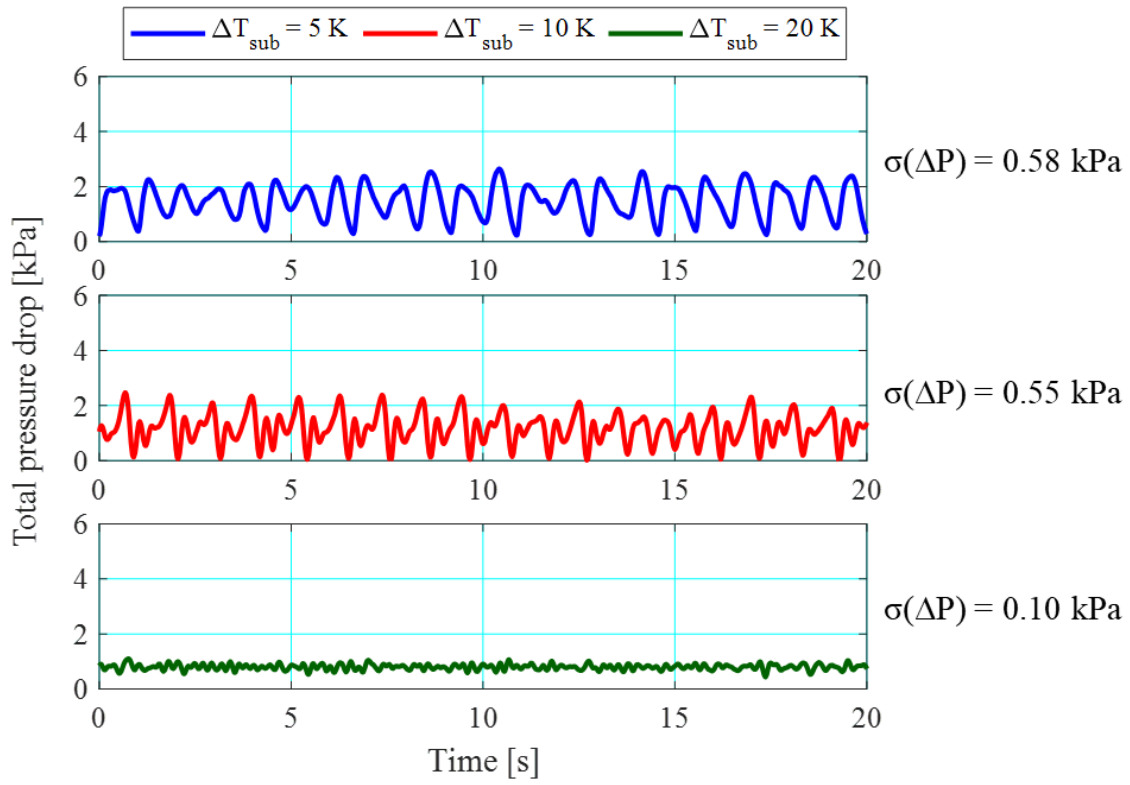

(a)

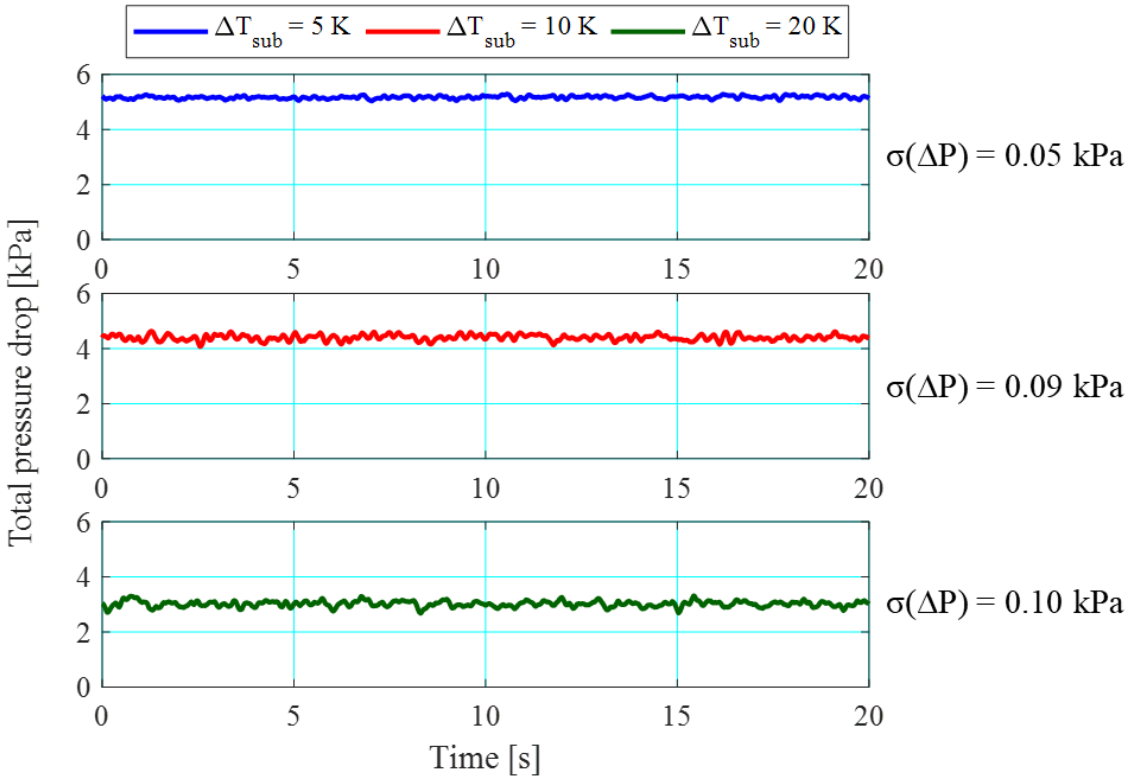

(b)

Figure 4.60: Measured pressure drop across the heat sink at (a) $q_w^{"} \sim 51$ kW/m^2 and (b) $q_w^{"} \sim 132$ kW/m^2 over a window of 20 s for G = 200 kg/m^2 s and inlet subcooling conditions 5, 10 and 20 K.

4.5.3 Heat Transfer

In order to assess the effect of subcooling on heat transfer coefficient separately in the subcooled and saturated boiling region of the channels, the local heat transfer trends at the three subcooling conditions are plotted in Figure 4.61, Figure 4.62 and Figure 4.63 for wall heat fluxes $q_w^{"} \sim 52$ kW/m^2, $q_w^{"} \sim 107$ kW/m^2 and $q_w^{"} \sim 161$ kW/m^2 respectively. The wall heat fluxes selected represent the low, medium and high heat flux condition. The empty markers represent subcooled flow boiling heat transfer coefficients while the filled markers denote flow boiling heat transfer coefficients in the saturated region. As per energy balance, at a given wall heat flux condition, increasing inlet subcooling decreases the local vapour quality along the channels due to the extension of the subcooled region at higher inlet subcooling.

As discussed in Section 4.2.2, local heat transfer coefficients rose sharply in the subcooled region and generally peaked at the location of boiling incipience. The sharp rising trend of heat transfer coefficients in the subcooled region is also an indication of subcooled boiling, which was also confirmed by flow visualisation. After the initial peak at the onset of boiling, the local heat transfer trend decreases moderately along the channel with increasing local vapour quality, also observed in Al-Zaidi et al. [57] using a similar fluid, HFE-7100, and Choi et al. [163], but recovers slightly near the channel exit.

Bubbly flow is typically prevalent in the subcooled region as well as near the location of boiling incipience. Hence the nucleate boiling mechanism may be reasonably assumed to dominate in this region. The high heat transfer coefficients, as explained in Section 4.2.2, may be attributed to high heat transfer rates arising from micro-layer evaporation underneath nucleating bubbles, combined with micro-convection currents induced in the bulk fluid surrounding a nucleating bubble as it departs its nucleation site. Heat transfer coefficients drop gradually along the channel after the initial peak due to nucleate boiling suppression corresponding to slug formation in the channels, as presented in Section 4.2.2. Heat transfer coefficients increase again near the exit of the channels, which could be due to liquid film thinning during thin-film evaporation or small heat losses to the outlet plenum.

In the subcooled region, increasing inlet subcooling generally resulted in a reduction in heat transfer coefficients, evident from Figure 4.61 and Figure 4.62 at $\Delta T_{sub} = 10$ K and 20 K. This is in agreement with the trends reported by Agostini et al. [87]. It could be attributed to higher

bubble departure frequencies and shorter waiting times between successive bubble ebullition cycles at lower subcooling, as the higher bulk liquid temperatures will inevitably require a shorter time period to reach the sufficient wall superheat degree for bubble nucleation.

At the low heat flux condition, flow boiling heat transfer coefficients in the saturated boiling region at ΔT_{sub} = 20 K were marginally higher than that at ΔT_{sub} = 5 K and 10 K, Figure 4.61. At this heat flux, bubbly flow was observed in the channels at ΔT_{sub} = 20 K while slug as well as churn flow have already developed in the channels at ΔT_{sub} = 5 K and 10 K. The high saturated flow boiling heat transfer coefficients observed at the highest inlet subcooling condition could be due to the presence and dominance of nucleate boiling near the location of boiling incipience. The predominance of bubbly flow in the channels at this condition also supports this observation. As slug and churn flow tend to suppress some nucleation activity on the channel walls, the contribution of the nucleate boiling mechanism is reduced, and thus slightly lower heat transfer coefficients are observed at ΔT_{sub} = 10 K at this heat flux level.

Increasing inlet subcooling resulted in a small reduction in heat transfer coefficients in the saturated boiling region. This is more apparent in Figure 4.62(b) and Figure 4.63(b), i.e. medium and high heat fluxes, where the local heat transfer trend is plotted with respect to vapour quality. As shown in Figure 4.59, the range of active nucleation sites become smaller with increasing subcooling. This indicates lower bubble generation frequency in the channels at higher subcooling, i.e. lower nucleate boiling heat transfer coefficients at higher subcooling. Accordingly, delayed flow pattern transitions were also observed at higher inlet subcooling conditions, see Table 4.7, although at medium to high heat fluxes, annular flow was predominantly observed in the channels at all subcooling degrees.

Slightly lower heat transfer coefficients in the saturated region where annular flow is observed could also be due to the effect of subcooling on local vapour quality. At a given heat flux, increasing subcooling decreases the vapour quality at a specific location along the channels. Heat transfer coefficients have been demonstrated to increase with vapour quality in the annular flow regime in Costa-Patry et al. [83], Huang and Thome [93] and Falsetti et al. [71]. A combination of lower nucleate boiling heat transfer coefficients (due to reduced bubble generation activity) and lower contribution of thin-film evaporation (due to delayed flow regime transition to annular flow) to total heat transfer could explain the lower heat transfer coefficients observed in the saturated region at higher degrees of inlet subcooling. Evidently,

varying the degree of inlet subcooling by 5 – 20 K has some effect on flow boiling heat transfer coefficients, although small (i.e. about ±10%) in the saturated boiling region, as also concluded by studies in [87], [137], [143].

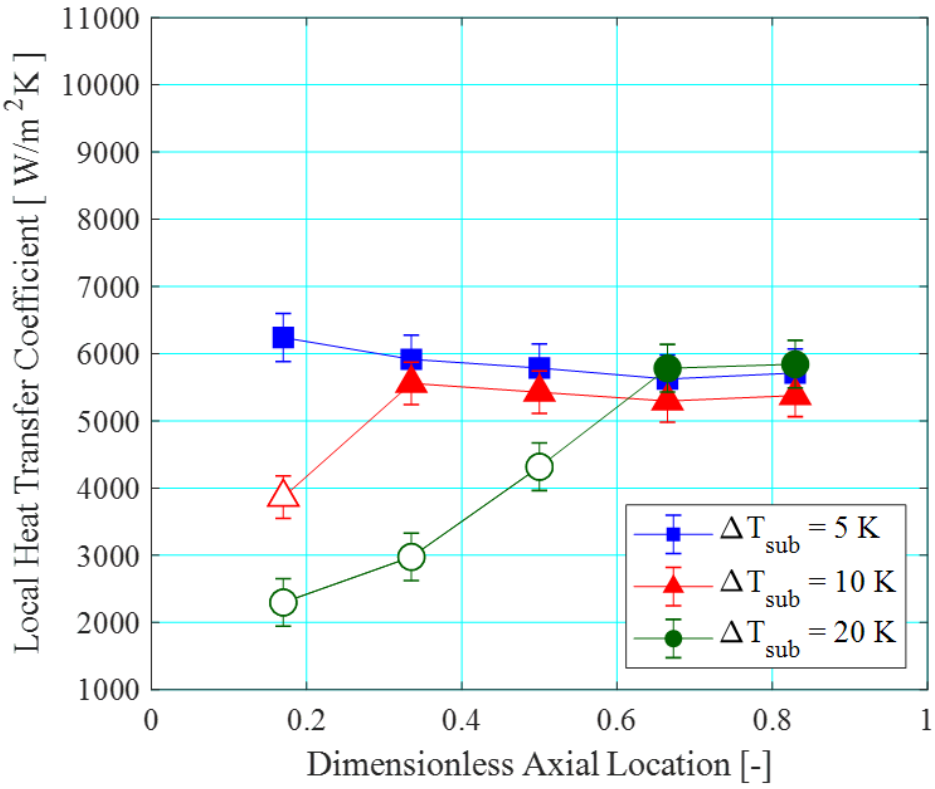

(a)

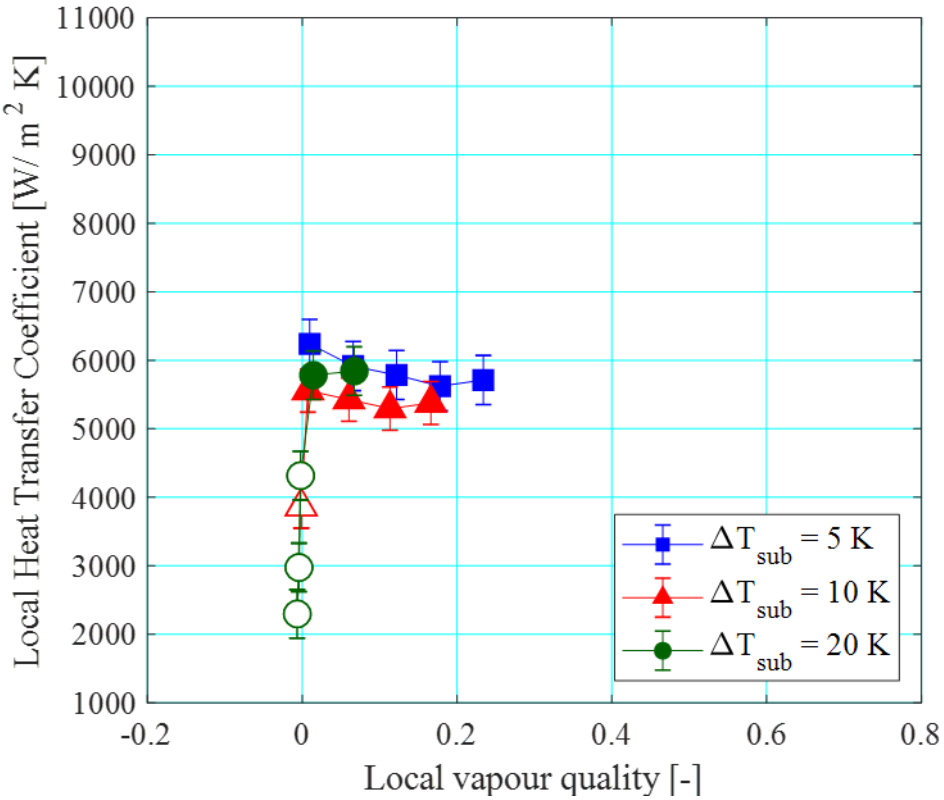

(b)

Figure 4.61: Local heat transfer coefficients along the heat sink at P = 1 bar, G = 200 kg/m^2 s and q_w" ~ 52 kW/m^2. Empty and filled markers denote heat transfer coefficients measured in the subcooled and saturated boiling region respectively.

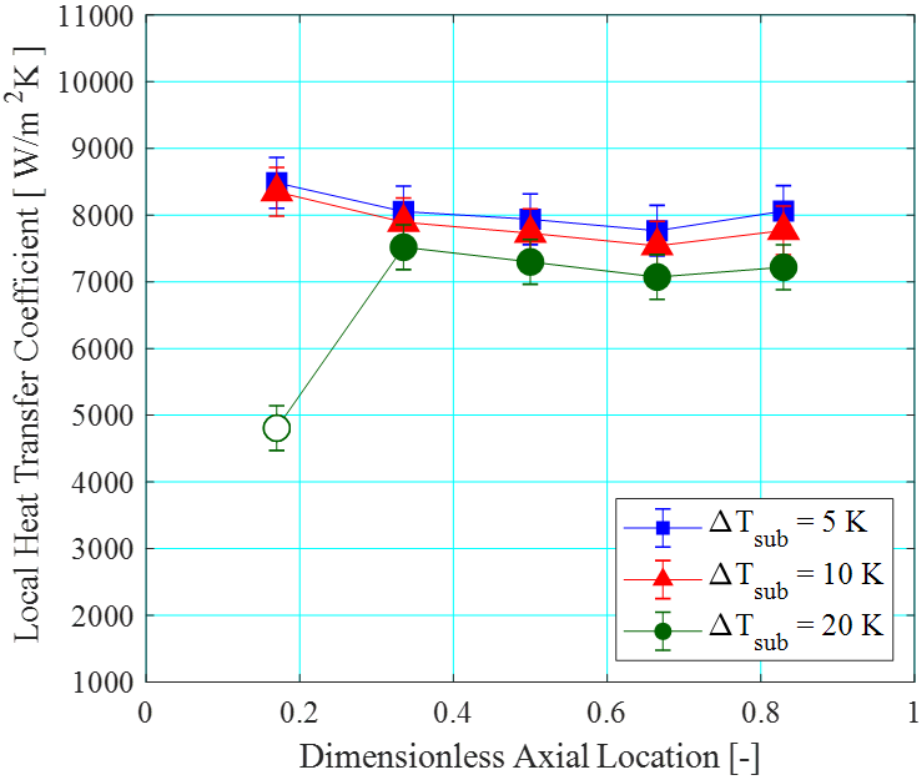

(a)

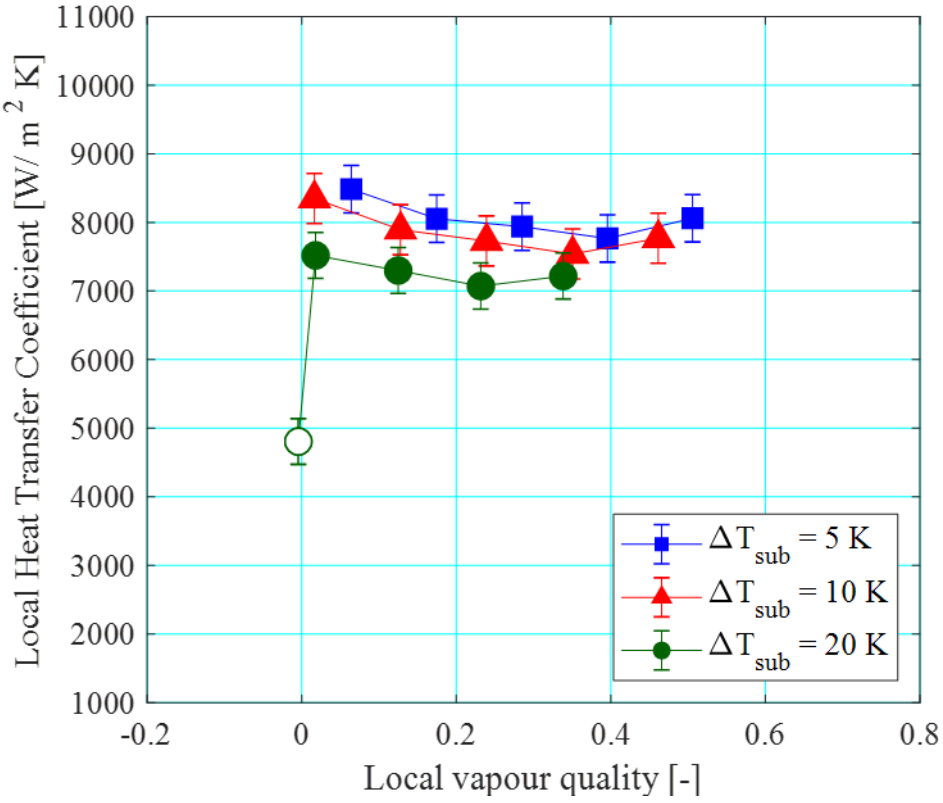

(b)

Figure 4.62: Local heat transfer coefficients along the heat sink at P = 1 bar, G = 200 kg/m^2 s and q_w" ~ 107 kW/m^2. Empty and filled markers denote heat transfer coefficients measured in the subcooled and saturated boiling region respectively.

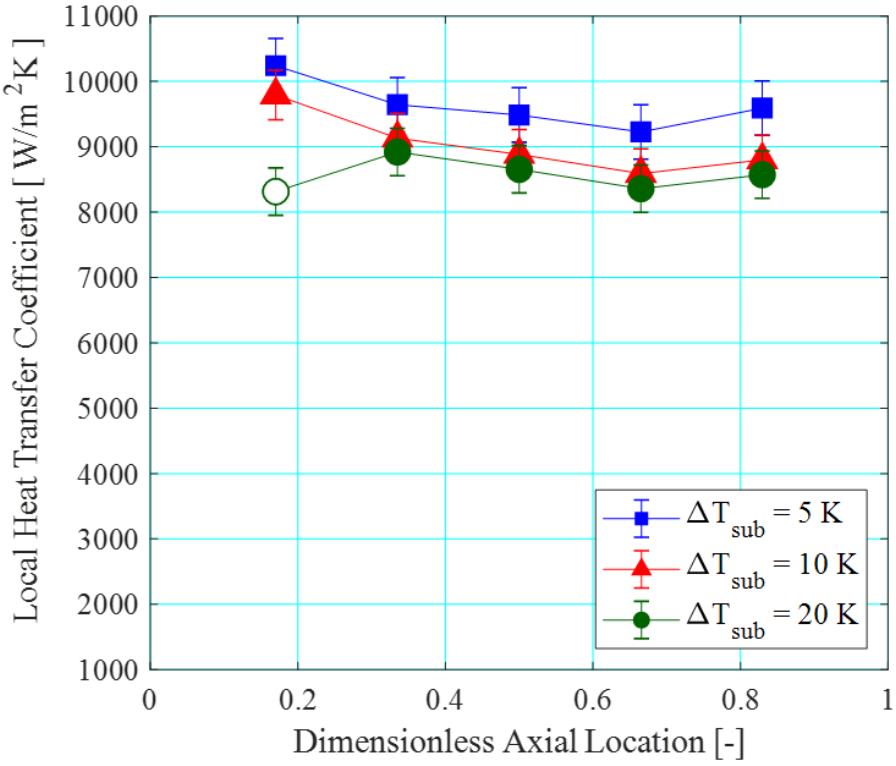

(a)

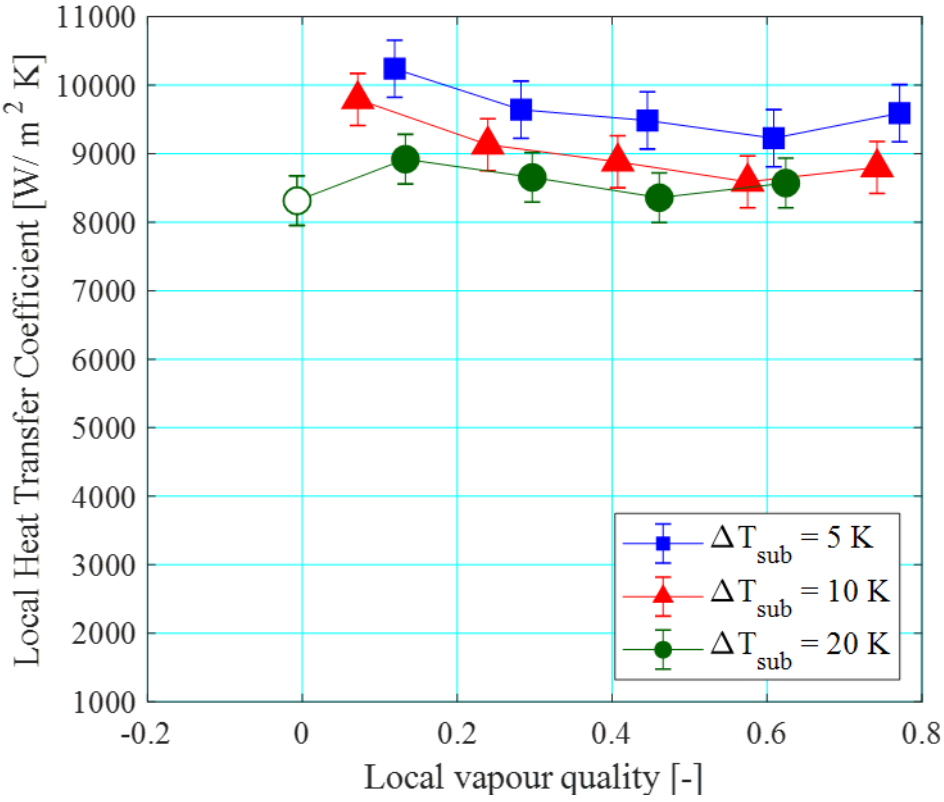

(b)

Figure 4.63: Local heat transfer coefficients along the heat sink at P = 1 bar, G = 200 kg/m^2 s and $q_w^{"}$ ~ 161 kW/m^2. Empty and filled markers denote heat transfer coefficients measured in the subcooled and saturated boiling region respectively.

The effect of inlet subcooling on average heat transfer coefficients in the heat sink is depicted in Figure 4.64. Note that the average heat transfer coefficients referred to here are averaged from heat transfer coefficients along the channel and includes local heat transfer coefficients in the subcooled region, i.e. based on Eq. (3.30). Average heat transfer coefficients increase slightly with decreasing inlet subcooling. At the lowest heat flux condition, there is a marked rise in average heat transfer coefficients in the channel at lower inlet subcooling conditions.

As mentioned earlier, see Figure 4.58, increasing the degree of inlet subcooling at a given wall heat flux increases the length of the subcooled region in the channels. Although local heat transfer coefficients in the subcooled region rises steeply along the channel, the magnitude of subcooled heat transfer coefficients are nonetheless lower than heat transfer coefficients typically observed in the saturated boiling region. Consequently, average heat transfer coefficients are lower at high subcooling for a given wall heat flux condition in the heat sink. From Figure 4.58, it is clear that the subcooled region constitutes a substantial fraction of the total channel length at wall heat fluxes $q_w^{"} \sim 26$ to 52 kW/m^2. As a result, the subcooled heat transfer coefficients have a larger effect on overall heat transfer coefficients in the channel. Hence a stronger effect of subcooling is observed in the low heat flux region.

Overall, the effect of subcooling on local heat transfer coefficients was found to be more pronounced in the subcooled region where subcooled boiling was observed. This was attributed to higher bubble departure frequencies and shorter waiting times between successive bubble ebullition cycles at lower subcooling. The effect of subcooling was generally smaller in the saturated boiling region. Similarly, average heat transfer coefficients exhibited a strong dependency on the degree of inlet subcooling, particularly at low wall heat fluxes, due to the substantial length of the subcooled region. The subcooled length decreases with heat flux, and as a result the effect of inlet subcooling is smaller with increasing wall heat flux.

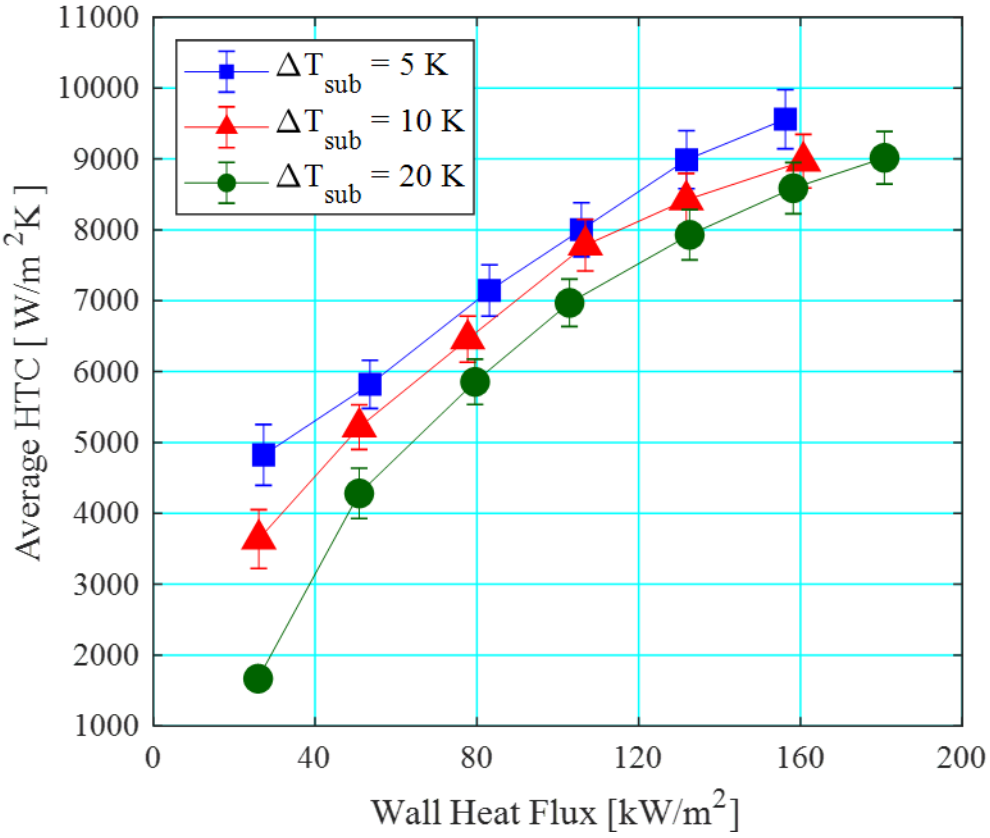

Figure 4.64: Effect of inlet subcooling on average heat transfer coefficients along the channel for wall heat fluxes between $q_w^{"}$ = 25.9 – 180.7 kW/m^2 at P = 1 bar and G = 200 kg/m^2 s.

4.5.4 Pressure Drop

Figure 4.65 shows the total pressure drop in the microchannels, i.e. ΔP_{ch}, see Eq. (3.1), as a function of wall heat flux. On the other hand, the pressure drop in the two-phase region (i.e. ΔP_{tp}, see Eq. (3.19) at the same conditions are shown in Figure 4.66(b). Note that the two-phase pressure drop at the lowest wall heat flux condition, i.e. $q_w^{"} = 26$ kW/m^2, is zero as the channels were entirely subcooled at $\Delta T_{sub} = 20$ K.

As expected, total pressure drop increases with wall heat flux due to an increase in overall void fraction in the channels, which is associated with higher flow resistance at higher heat fluxes [100]. Additionally, pressure drop in the microchannel heat sink decreases with increasing inlet subcooling at a given wall heat flux condition. This is mainly because single-phase liquid pressure drop, which is much smaller compared to two-phase pressure drop, has a larger contribution to total pressure drop in the heat sink at higher subcooling, due to the longer subcooled length in the channels, see Figure 4.58. Similar observations were also reported in Deng et al. [124], Chen et al. [89] and Huang and Thome [208].

Similarly, the effect of inlet subcooling on two-phase pressure drop was negligible between $\Delta T_{sub} = 5$ K and $\Delta T_{sub} = 10$ K, especially at wall heat fluxes below $q_w^{"} = 83$ kW/m^2. On the other hand, at a given wall heat flux condition, the magnitude of the two-phase pressure drop at $\Delta T_{sub} = 20$ K is notably smaller compared to lower degrees of inlet subcooling.

As mentioned above, flow pattern transitions occurred at higher vapour qualities (summarised in Table 4.7) with increasing degrees of inlet subcooling, particularly at $\Delta T_{sub} = 20$ K. This was attributed to less vigorous bubble coagulation in the channels due to the condensation of bubbles in the subcooled region, which was extended with higher inlet subcooling at a given wall heat flux condition. This could also have contributed to a smaller void fraction in the channels at higher degrees of subcooling for a nominal wall heat flux level. Furthermore, Figure 4.59 predicts a smaller range of active nucleation sites at higher degrees of inlet subcooling, which may also indicate a smaller channel void fraction as a direct result of lower bubble nucleation activity in the channels at higher degrees of subcooling. As both the acceleration component in two-phase pressure drop is strongly dependent on the void fraction [100], the smaller void fraction at larger inlet subcooling could have resulted in the lower two-phase pressure drop in the heat sink.

In summary, pressure drop characteristics were found to be affected by changes in the degree of subcooling. Increasing the inlet subcooling decreased both the total pressure drop and two-phase pressure drop in the channels (i.e. ΔP_{ch} and ΔP_{tp} respectively), particularly when the subcooling was increased to ΔT_{sub} = 20 K. The reduction in pressure drop values was attributed to the delay in flow pattern development and smaller channel void fraction with increase the degree of subcooling.

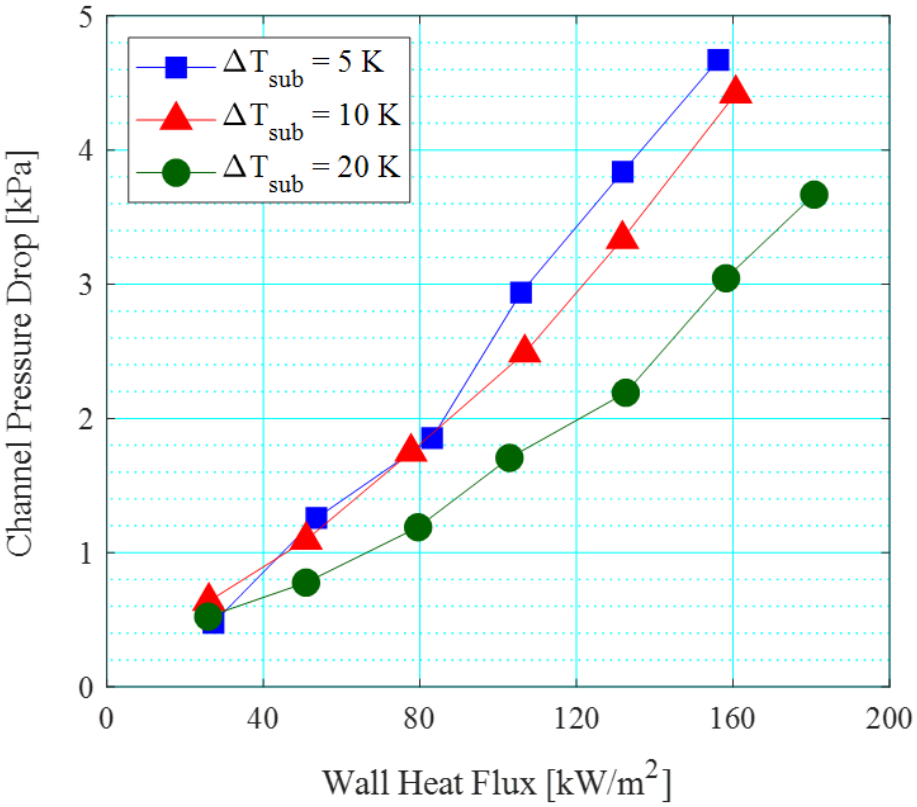

Figure 4.65: Effect of subcooling on total pressure drop (single and two-phase) for wall heat fluxes q_w'' = 25.9 – 180.7 kW/m^2 at P = 1 bar and G = 200 kg/m^2 s.

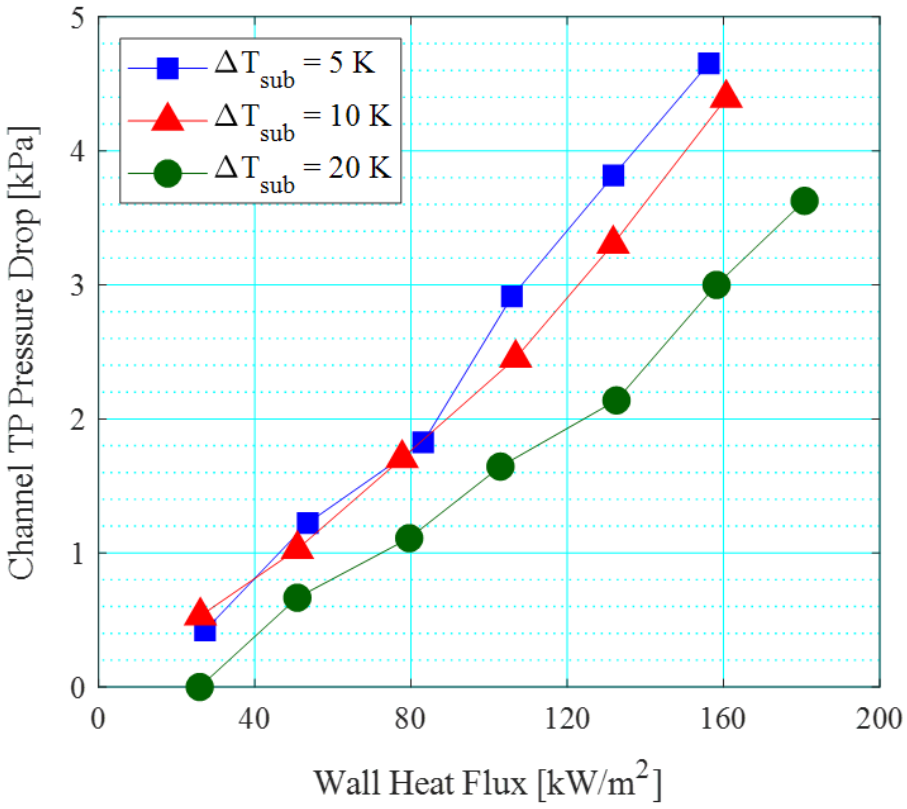

Figure 4.66: Effect of subcooling on two-phase pressure drop in the channel for wall heat fluxes $q_w^{"}$ = 25.9 – 180.7 kW/m^2 at P = 1 bar and G = 200 kg/m^2 s.

4.6 Summary

Flow pattern development, flow instability along with heat transfer and pressure drop characteristics in a plain microchannel heat sink was presented in this section. The effects of operating parameters, namely heat flux, system pressure, mass velocity and degree of inlet subcooling on microchannel flow boiling behaviour were assessed independently.

High-speed flow visualisation along the channel showed that with increasing heat flux and exit vapour quality, flow patterns evolved from bubbly to slug, churn and annular flow in the heat sink. Flow regime transitions were mainly governed by increase in bubble nucleation activity, bubble coalescence and superficial vapour velocity in the channels. Increasing saturation pressure and inlet subcooling degree delayed flow pattern transitions in the plain microchannel heat sink. On the other hand, increasing mass flux accelerated flow regime transitions in the plain channels. The active cavity range for HFE-7200 was shown to be significantly influenced by degree of inlet subcooling as well as system pressure. Bubble nucleation was observed from the channel side walls during bubbly flow. Flow visualisation revealed that nucleation sites on the side walls remained active in the slug and annular flow regime. However, nucleation sites were observed to be periodically suppressed with liquid film thinning in slug and annular flow. Wall dryout in slug flow may persist for over 100 ms. In annular flow, the rewetting mechanism brought about by the churn flow regime mitigated prolonged periods of wall dryout in the channels.

Flow reversal was typically triggered in slug flow due to slug expansion in the upstream direction towards the inlet plenum. Vapour backflow were also observed to result in cyclic wall dryout on the channels, which as mentioned above, periodically suppressed nucleation sites on the side walls. There was evidence to suggest that increasing system pressure and subcooling degree may mitigate pressure drop oscillations resulting from bubble growth instabilities, which was found to be particularly prominent at low heat fluxes where slug flow was dominant in the heat sink.

Local and average heat transfer trends were reported in the current study. Local heat transfer coefficients generally reached a maximum near the location of boiling incipience and decreased

along the channel with local vapour quality. The peak in heat transfer coefficient near onset of boiling was attributed to the high heat transfer rates in the nucleate boiling regime. Following that, the decrease in heat transfer coefficients along the channel was attributed to nucleate boiling suppression corresponding to flow pattern development towards annular flow in the channel. Average two-phase heat transfer coefficients generally increased with increasing heat flux. This was attributed to the increase in bubble generation activity from the channel walls with increasing degree of wall superheat at higher heat fluxes. Increasing system pressure enhanced flow boiling heat transfer in the channels. This may be because of the increase in vapour density with pressure increment, which reduced waiting times between successive bubble ebullition cycles from cavities in the channels at higher pressures. Varying the degree of inlet subcooling had a notable effect on heat transfer coefficients in the subcooled region, but only a minimal effect in the saturated boiling region. Experiments at the lowest subcooling condition of 5 K had a lower repeatability, which could be due to upstream compressibility effects during flow reversal. The effect of mass flux on two-phase heat transfer was insignificant at low to moderate heat fluxes, where the nucleate boiling mechanism is dominant. At higher heat fluxes where annular flow dominates in the heat sink, the contribution of the convective boiling mechanism increases and the effect of mass flux begins to manifest.

Two-phase pressure drop increased with heat flux and mass flux in the present study. The frictional and acceleration pressure drop components increase with heat flux due to higher void fraction in the channels. Increasing mass velocity increase pressure losses due to flow acceleration and higher interfacial shear in the microchannels. Increasing saturation pressure resulted in a notable reduction in vapour density, which reduced two-phase pressure drop in the microchannels. As mentioned above, increasing the degree of inlet subcooling delayed flow pattern development in the channels and also lowered flow boiling pressure drop in the heat sink.

5 Comparison with Flow Pattern Maps

5.1 Introduction

Flow patterns in the heat sink were captured using high-speed imaging along the length of the microchannel at each experimental condition. The range of relevant dimensionless numbers in the current experimental range, see Table 3.3, is summarised in Table 5.1.

Table 5.1: Range of dimensionless parameters.

Dimensionless number	Experimental range
Bo [-]	$0.56 \times 10^{-3} – 8.2 \times 10^{-3}$
Bd [-]	0.25 – 0.32
Co [-]	1.76 – 2
Re_{fo} [-]	265.9 – 540.6
Re_{go} [-]	7261 – 15679
We_{fo} [-]	1.3 – 5.7
We_{go} [-]	121.6 – 754.6

Flow patterns observed in this study were categorised into four main flow regimes, namely bubbly, slug, churn and annular flow. As covered in Section 4.2.1, where more than one flow regime is observed in a recording, especially in the intermittent churn flow regime, the dominant number of frames in the video, sampled at 100 frame intervals of the full-length of the recording, was used to determine the flow regime at a location. More than one flow regime may be observed in two consecutive camera locations on the heat sink. This is because the local vapour quality has yet to exceed the critical transition vapour quality boundary at which flow pattern transition occurs in the channels. Local vapour quality increases according to energy balance along the streamwise length.

With increasing heat flux, flow patterns developed from bubbly towards slug, churn and annular flow. Increasing mass flux accelerated flow transition boundaries while increasing system pressure and degree of inlet subcooling delayed flow regime transitions in the plain heat sink.

The experimental flow pattern data obtained at P = 1 bar and ΔT_{sub} = 10 K for a range of wall heat flux and mass fluxes are presented in Figure 5.1 as a function of the local liquid and vapour superficial velocity, calculated based on the local vapour qualities corresponding to each axial location along the channel. The vapour superficial velocity increases with vapour quality along the channel and heat flux, while the liquid superficial velocity decreases. The trends shift upwards with increasing mass flux.

Whilst bubbly flow appears to only be observed at the lowest mass flux condition on the flow map, at higher mass velocities, bubbly flow was only observed in the subcooled region (i.e. J_g < 0 m/s) and hence are not visible on the figure. At the lowest mass flux condition, bubbly flow was observed up to J_g ~ 0.3. However, at higher mass fluxes, slug flow has already developed in the channels for the same vapour superficial velocity. As explained above, this could be due to an increase in the rate of bubble coalescence in the channels at higher mass velocities, also observed by Revellin and Thome [160]. Generally, at vapour superficial velocities higher than J_g > 1.5 m/s, churn and annular flow dominate in the channels. In this chapter, flow pattern results obtained using HFE-7200 in the current parallel microchannel configuration are assessed against flow pattern maps in literature.

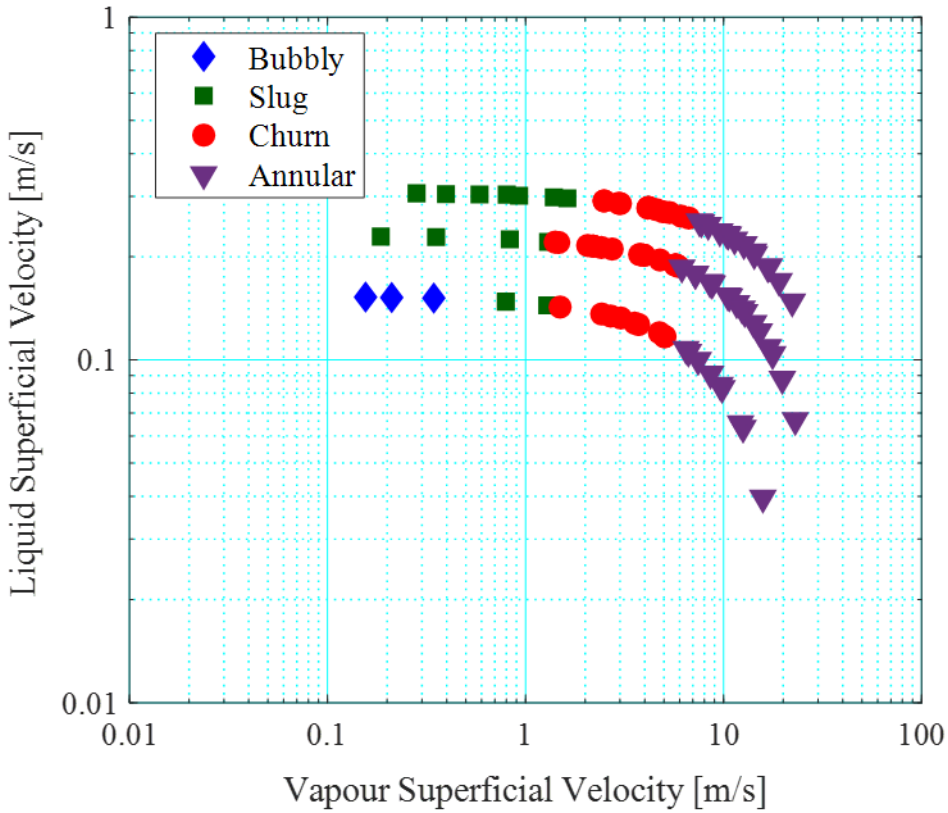

Figure 5.1: Flow patterns observed at P = 1 bar and ΔT_{sub} = 10 K for wall heat fluxes and mass fluxes ranging from $q_w^{"}$ = 24.8 – 234.3 kW/m^2 and G = 200 – 400 kg/m^2 s respectively.

5.2 Comparison with Mahmoud and Karayiannis [162]

The model developed by Mahmoud and Karayiannis [162] has previously been presented in Section 2.6, see Eq. (2.9) – (2.14). At the lowest mass flux condition, bubbly and slug flow are well predicted by the map. Nonetheless, early transition from bubbly to slug flow at higher mass fluxes was not captured by the flow map and over half of the slug data points are incorrectly predicted to be in the bubbly flow regime. This could be because the flow regime map was proposed based on experiments in single tubes and relatively larger diameter channels (1.1 mm – 4.26 mm). In parallel microchannel configurations, flow instabilities and vapour backflow into the inlet plenum may also trigger transition from bubbly to slug flow, as demonstrated in Figure 4.8. The applicability of single channel studies have also been questioned by Ribatski [167] on similar grounds. Although the model takes into consideration several possible mechanisms that could trigger transition from slug to churn flow, the flow map overpredicted this boundary and also underpredicted churn-annular transition. The flow map predicted a relatively narrow range for churn flow.

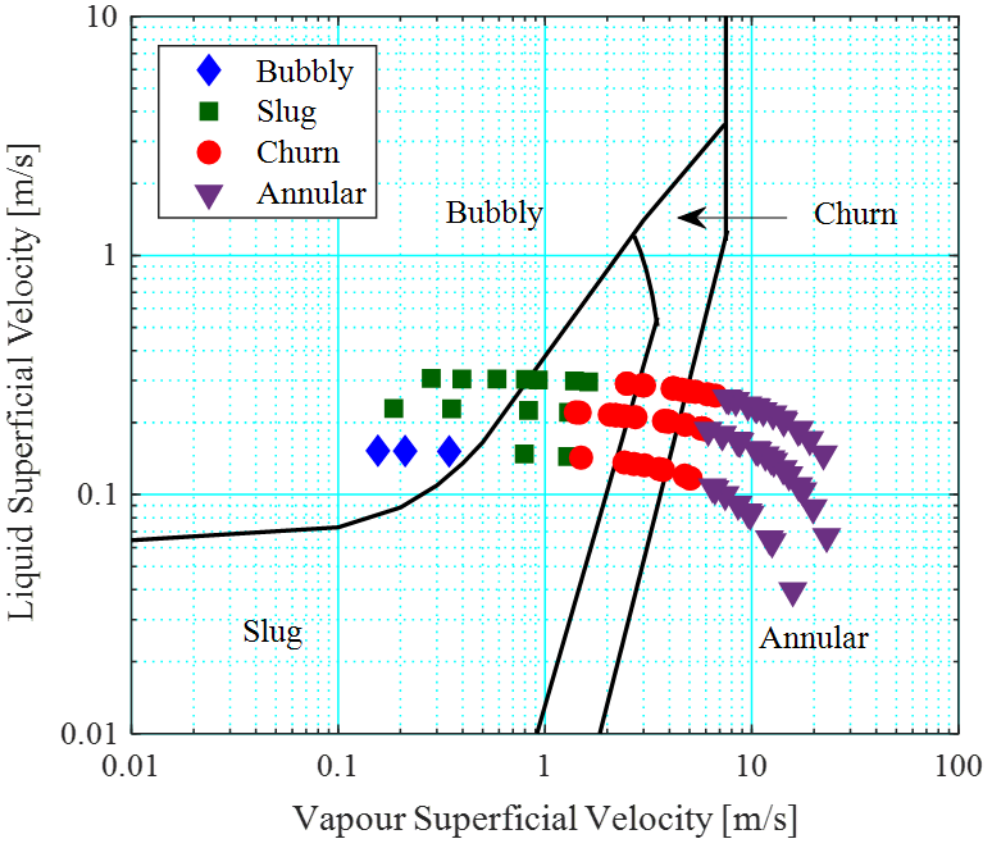

Figure 5.2: Comparison of HFE-7200 flow pattern data (G = 200 to 400 kg/m^2 s) with the Mahmoud and Karayiannis [162] flow map.

5.3 Comparison with Harirchian and Garimella [157]

The Harirchian and Garimella [157] flow map, see Section 2.6, Eq. (2.6) – (2.7), classified data points obtained at the two higher mass fluxes (i.e. G = 300 and 400 kg/m^2 s) to be unconfined flow. This appears to capture the phenomenon of smaller bubble diameters at higher mass fluxes, as shown in Figure 4.39. Bubbly flow was well predicted by the map. However, slug flow data were scattered in both the confined slug and bubbly flow regions. The boundary between slug and churn/annular flow was relatively accurate. In the current study, a thin-liquid film attached to the walls, separated by a vapour core through the centre of the channels was always observed in annular flow. This was classified as confined annular flow in the original paper, i.e. no vapour confinement observed in unconfined churn and annular flow. From Figure 5.3, it is clear that the map incorrectly placed the majority of the confined annular flow points in the unconfined flow region. Notably, the mass fluxes in the current experimental range was in the lower range of the experimental database used to develop the flow map (G = 224 – 1461 kg/m^2 s).

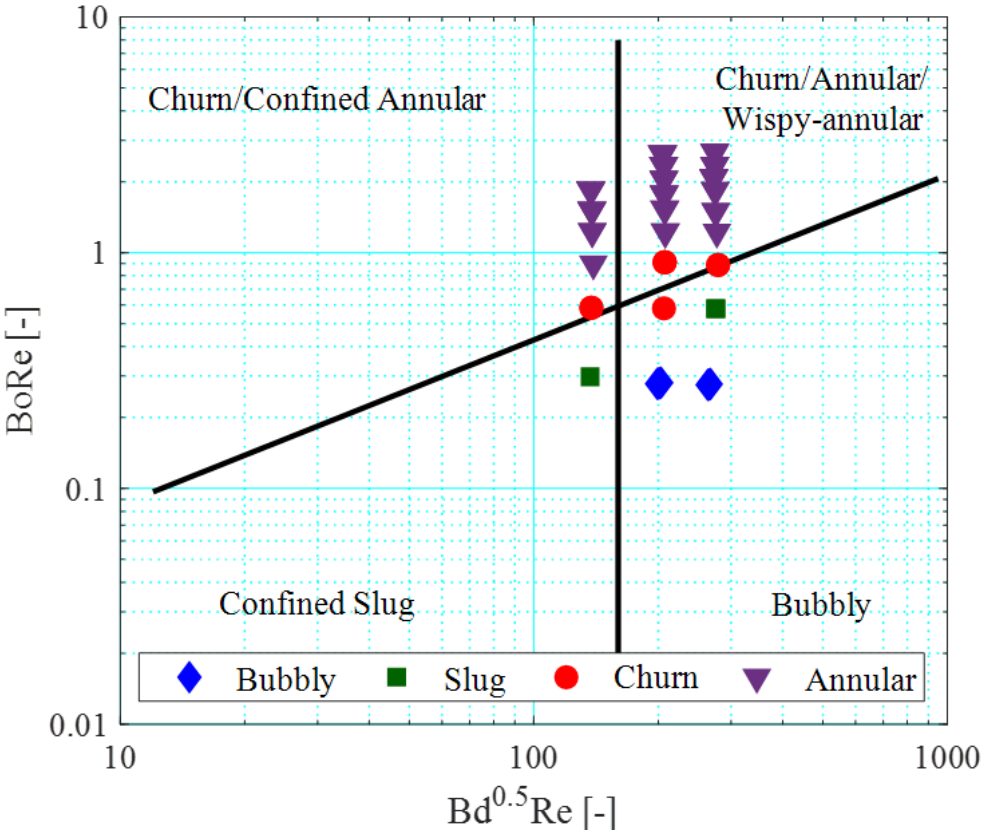

Figure 5.3: Comparison of HFE-7200 flow pattern data (G = 200 to 400 kg/m^2 s) with the Harirchian and Garimella [157] flow map.

5.4 Comparison with Revellin and Thome [160], Ong and Thome [161] and Costa-Patry et al. [168]

The comparison with the flow regime maps produced by the group of Thome are shown collectively in Figure 5.4, see Section 2.6, Eq. (2.1) – (2.5), Note that the Revellin and Thome [160] and Ong and Thome [161] correlation predicting the transition vapour quality from the IB to SB regime is sensitive to wall heat flux, evident from Eq. (2.1) and Eq. (2.3). Similarly, Costa-Patry et al. [168] also found that the transition from the CB to A regime varied with heat flux, see Eq. (2.5). It is worth mentioning that in the current study, flow regime transitions did not appear to be a function of wall heat flux. This agrees with the work of Al-Zaidi et al. [57] for parallel microchannel heat sinks. For the purposes of the comparison, the criterion to select wall heat flux applied in Eq. (2.1) and Eq. (2.3) is based on the local vapour quality, which is measured at five axial locations along the channel (see Figure 3.2). The wall heat flux considered is set to the minimum wall heat flux level where saturated conditions are achieved in the channels (i.e. any of the five axial vapour qualities exceed zero). For Eq. (2.5), the wall heat flux level at which annular flow was first observed in the channels at the lowest mass flux condition, i.e. $q_w^{"} \sim 80$ kW/m^2, was selected for the comparison in Figure 5.4. Based on the classification given in Ong and Thome [161], the IB regime includes both bubbly and slug flow, while the coalescing bubble regime could include slug, churn and slug-annular flow. Annular flow is considered for wavy-annular and smooth-annular flow.

5.4.1 Revellin and Thome [160]

The IB/CB transition vapour quality decreased with increasing mass flux. This agrees with the experimental observation of earlier flow regime transitions at higher mass velocities. Additionally, the IB/CB transition boundary predicted the transition from slug to churn flow moderately well in the channels. The CB/A transition boundary was overpredicted for the lower mass fluxes, but was relatively accurate at G = 400 kg/m^2 s. This could be related to the comparatively lower range of mass fluxes investigated in this work.

5.4.2 Ong and Thome [161]

Only a small difference resulted from implementing the method of Revellin and Thome [160] and the proposed method for the IB/CB transition in the current experimental range. Nonetheless, the flow map captured the transition from slug to churn flow more accurately, see

Figure 5.4. The model also exhibited good dependency on mass flux and is in line with the experimental observation (i.e. transition boundaries shift to lower vapour qualities with mass flux). Although the flow map was developed based on flow boiling in singular and circular horizontal tubes, the validity of the correlation proposed for the IB/CB transition boundary was also verified in Costa-Patry et al. [168] for parallel rectangular microchannel arrays. Since slug-annular flow was not observed in this study, the CB/A transition is considered to be the churn-annular boundary. The vapour quality at which transition from churn to annular flow occurs is underpredicted.

5.4.3 Costa-Patry et al. [168]

The Ong and Thome [161] model for IB/CB transition was recommended for this flow map and predicts the slug-churn transition boundary relatively well, as discussed earlier. At a wall heat flux level of $q_w^{"} \sim 80$ kW/m^2, the CB/A transition was overpredicted for lower mass fluxes, but performed well at the highest mass flux, even though the range of mass fluxes investigated in the study was relatively close to the current experimental range (G = 205 – 569 kg/m^2 s).

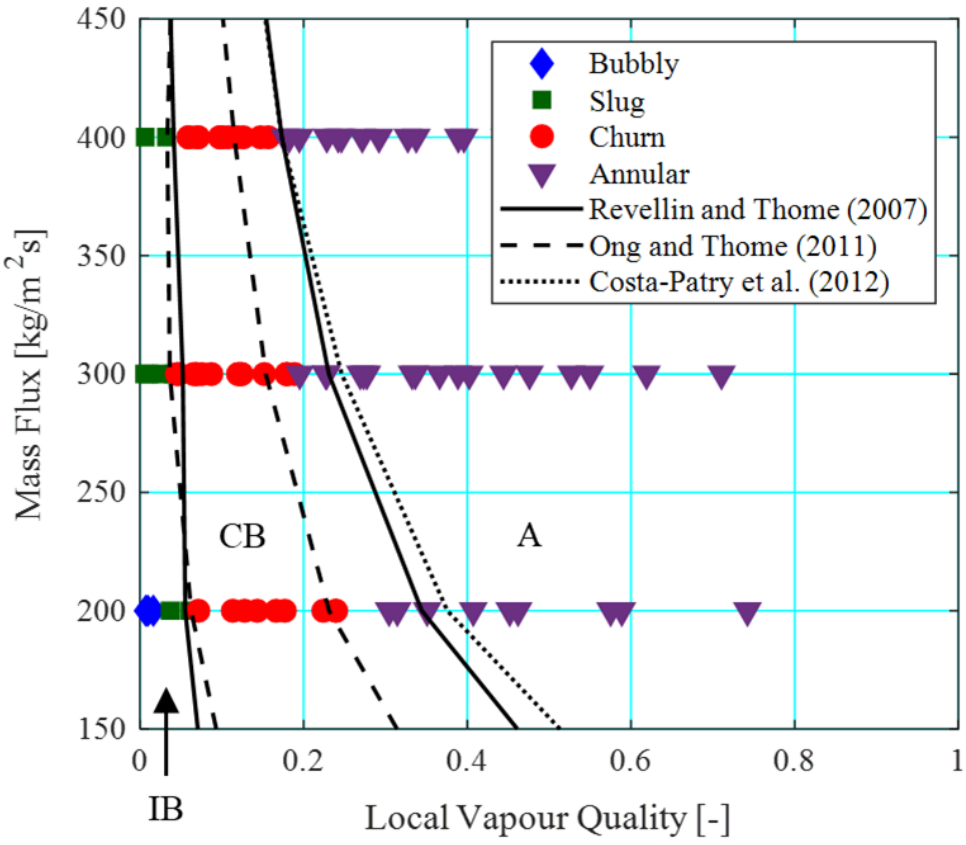

Figure 5.4: Comparison of HFE-7200 flow pattern data (G = 200 to 400 kg/m^2 s) with the flow maps developed from the group of Thome [160], [161], [168].

5.5 Comparison with Choi et al. [163]

Based on the convention of this flow pattern map, churn and annular flow may be considered singularly as annular flow, see Section 2.6, Eq. (2.8). As the flow map only attempts to dissociate the nucleate boiling (bubbly/slug) and convective boiling (annular) dominant regimes, only two regions are present on the map. Generally, the transition from bubbly/slug flow to annular (churn and annular) flow was overpredicted. This could be related to the low heat flux range investigated in the original study, namely 3.2 – 49 kW/m^2. The heat fluxes investigated in the current experimental range was much larger, at 24.8 – 234.3 kW/m^2. Additionally, the length of the channels of the copper heat sink investigated in Choi et al. [163] was 40 mm, which is three times the length of the channels in the present study (L_{ch} = 20 mm).

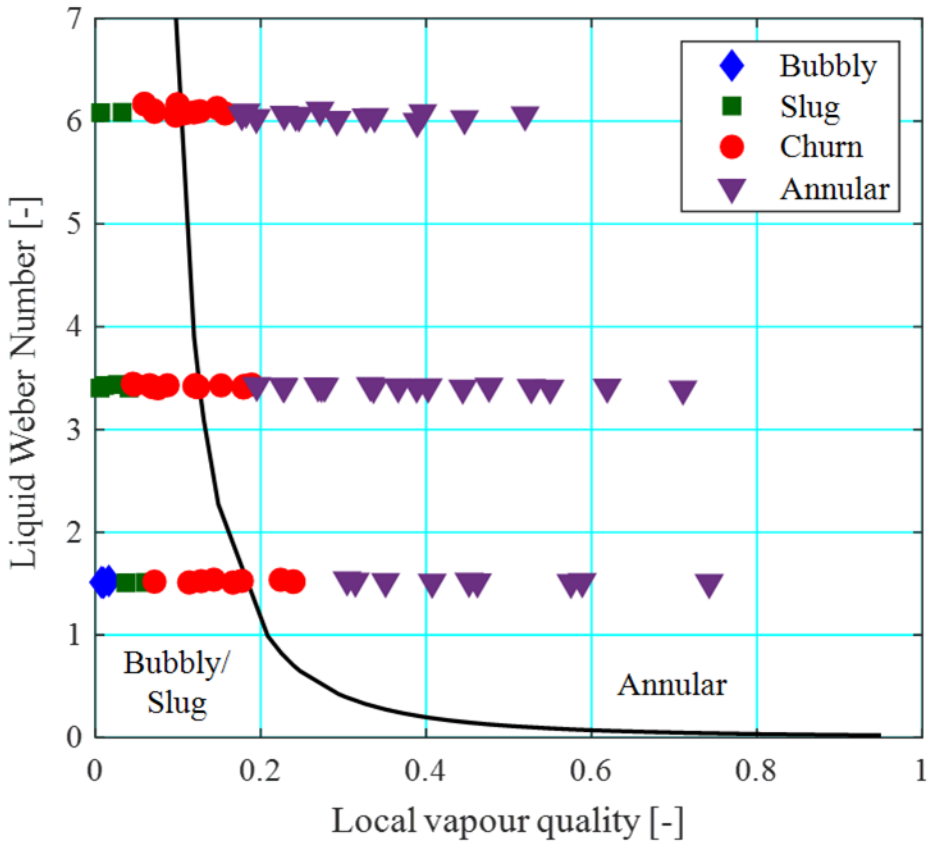

Figure 5.5: Comparison of HFE-7200 flow pattern data (G = 200 to 400 kg/m^2 s) with the Choi et al. [163] flow map.

5.6 Effect of Operating Parameters

Assessing all flow maps for its sensitivity to mass flux, system pressure and degree of subcooling, the Revellin and Thome [160] and Ong and Thome [161] correlation predicted the delay in flow pattern transition with increase in saturation pressure and inlet subcooling as well as the effect of mass flux for HFE-7200 under the current experimental conditions. This is despite the original study of Revellin and Thome [160] finding no effect of inlet subcooling (subcooling varied from 2 to 15 K) on the transitional boundaries of fluid R134a and R245fa. The effect of pressure and inlet temperature on vapour density and surface tension is accounted for in the Weber number and Reynolds number in Eq. (2.1) and (2.2). The model of Ong and Thome [161] also takes into account the effect of saturation pressure and inlet temperature in the confinement number and liquid-to-vapour density ratio in Eq. (2.3) – (2.4). The Costa-Patry et al. [168] flow map correctly predicted the trend of saturation pressure for CB/A transition, but the opposite trend with regards to the effect of inlet subcooling on flow pattern behaviour. Nonetheless, the groupings of the abovementioned methods into the IB and CB regimes do not dissociate clearly between bubbly, slug and churn flow, although the IB/CB transition corresponds to slug-churn transition relatively well.

A shift in flow pattern boundaries to lower superficial gas velocity with increase in system pressure, predominately in the slug-churn and churn-annular boundaries, was reported in Chen [165], who proposed the original flow map which was later modified by Mahmoud and Karayiannis [162]. Chen [165] attributed this to an increase in vapour density and reduction in surface tension with increasing pressure. Accordingly, the slug-churn and churn-annular transition lines shift to the left (i.e. lower vapour superficial velocities) with increasing pressure. In the current study, at a given mass flux condition of G = 200 kg/m^2 s and a fixed subcooling of ΔT_{sub} = 10 K, transition from churn to annular flow was also observed to have occurred at lower vapour superficial velocities with increasing saturation pressure. Although the flow map predicts a similar trend, i.e. delayed flow regime transitions at higher pressures, in line with the present experimental observation for the effect of pressure at a given mass flux, flow regime boundaries were generally not well predicted by this flow map.

The convective-confinement number, $Bd^{0.5}Re$, proposed by Harirchian and Garimella [157] captured the effect of saturation pressure, but not the effect of inlet subcooling, on flow pattern

development. The flow map predicted that there is a smaller confinement effect at higher operating pressures, and that transition from bubbly to slug, as well as that the churn/annular flow regimes are delayed with increasing pressure. This agrees with the experimental observation, where smaller average bubble sizes were captured at higher pressures, leading to a slower transition to slug flow and the subsequent flow regimes at higher saturation pressures.

5.7 Summary

The effect of heat flux, mass flux, inlet pressure and degree of inlet subcooling on flow pattern development of HFE-7200 during flow boiling in a parallel copper microchannel heat sink was investigated. Flow patterns were captured at four locations at the centre of the heat sink along the flow direction. Flow patterns were classified into bubbly, slug, churn and annular flow. Flow patterns monitored near the centre of the heat sink developed accordingly with increasing heat flux due to the increase in local vapour quality. Flow pattern transition boundaries were shifted to higher vapour qualities with increasing pressure and inlet subcooling degree. This could be attributed to changes in fluid properties, such as vapour density and surface tension, on bubble nucleation behaviour in the channels. On the other hand, increasing channel mass velocity accelerated flow regime transition in the channels, which was linked to an increase in the rate of bubble coalescence in the channels with higher flow inertia.

Several flow pattern maps were accessed for the experimental flow pattern data. The transition model proposed by Ong and Thome [161] for the boundary between the isolated bubbly regime and the coalescing bubbly flow regime predicted transition from slug to churn flow well. The coalescing bubbly-annular flow regime was underpredicted. The Revellin and Thome [160] map also predicted slug-churn transition relatively well in the flow map, but overpredicted the transition boundary of churn and annular flow at lower mass fluxes. Both maps also captured the effect of saturation pressure and inlet subcooling on flow pattern development in the channels. The Costa-Patry et al. [168] flow map displayed the correct sensitivity to operating pressure but the opposite trend with regards to the effect inlet subcooling on flow pattern behaviour.

The convective-confinement number proposed by Harirchian and Garimella [157] correctly represented the effect of saturation pressure on flow confinement in the channels and agreed with the experimentally observed trends. The Mahmoud and Karayiannis [162] flow map predicted churn-annular transition at lower vapour qualities but do not generally predict the flow transition boundaries well in the channel. The flow map of Choi et al. [163] did not predict the experimental data well, possibly due to the low heat fluxes and long channel length investigated in the original study.

The applicability of the Ong and Thome [161] flow map, originally developed for flow boiling in singular tubes, to multichannel configurations was verified. This was also reported by Costa-Patry et al. [168]. The Ong and Thome map correctly predicted the trends of mass flux, saturation pressure and inlet subcooling on two-phase flow pattern development. However, the flow pattern classifications do not clearly dissociate between the four main flow patterns, although the isolated bubbly-coalescing bubbly boundary corresponded well with the slug-churn transition boundary. The transition from churn to annular flow was underpredicted. A comprehensive flow regime map adhering to the four main flow pattern classifications for multichannel flow boiling configurations is still required in the community.

6 Comparison with Heat Transfer Correlations

6.1 Introduction

In this chapter, flow boiling heat transfer data of HFE-7200 in a multi-microchannel heat sink is evaluated against existing heat transfer correlations, which are selected based on a sensitivity matrix specific to the operational parameters of the current experimental study. At least three correlations from the (i) enhancement-factor, (ii) nucleate boiling, (iii) superposition, (iv) asymptotic, (v) predominant mechanism and (vi) criterion-based models are assessed in order to evaluate the effectiveness of the heat transfer models adopted in each category in predicting the current experimental trends.

As mentioned above, several approaches may be adopted to develop predictive models for two-phase heat transfer at the macroscale and microscale level. The heat transfer correlations analysed in this study are presented in Table 6.7 and include three prediction methods from (i) enhancement-factor, (ii) nucleate boiling, (iii) superposition, (iv) asymptotic, (v) predominant mechanism and (vi) hybrid models. All correlations studied in this section have been proposed for the prediction of saturated flow boiling in single tubes or multichannel configurations as well as for vertical and horizontal diabatic two-phase flows using various working fluids. While most are specific to microscale heat transfer applications, some are also recommended for the macroscale range. Individual parameters included in each correlation is carefully marked against the parameters found to vary significantly across the operating range of the current study, i.e. based on the findings from Section 6.2. These results are summarised in Table 6.1 and Table 6.2. Correlations incorporating a fluid-dependent parameter and developed based on a databank of multiple fluids are also identified. Additional considerations of scaling parameters such as the liquid Prandtl number, confinement number, which is typically used as a criterion to classify macro/microscale applicability [290], molecular mass of the working fluid and surface roughness of the channel are also highlighted.

6.2 Sensitivity Study

A sensitivity study was conducted in order to identify relevant dimensionless parameters as well as fluid properties typically considered in heat transfer correlations that vary significantly under different operating conditions, i.e. at different wall heat flux, mass flux, system pressure and degree of subcooling. The dimensionless parameters are grouped into three categories, namely (i) general dimensionless parameters, (ii) liquid-phase dimensionless parameters and (iii) vapour-phase dimensionless parameters. The thermophysical properties evaluated were: (i) liquid-vapour density ratio, (ii) liquid-vapour viscosity ratio and (iii) reduced pressure.

The effect of wall heat flux, corresponding to exit vapour qualities of $x_e = 0 – 1$ on the relevant dimensionless parameters are presented in Figure 6.1(a) – (c). The analysis was conducted based on the actual experimental data for conditions of P = 1 bar, G = 200 kg/m^2 s and ΔT_{sub} = 10 K. All thermophysical properties are evaluated at the measured temperature and pressure at the inlet of the heat sink. Since the inlet temperature and pressure have been kept constant, the main fluid properties remained relatively unchanged across the heat flux range.

Parameters Bo, Cv and X_{tt} varied by more than ±30 % as the wall heat flux increased from 26.1 kW/m^2 to 160.7 kW/m^2. Bo is a direct function of $q_w^{"}$ and i_{fg}, while Cv and X_{tt} are partly dependent on x_e. Similarly, due to their dependency on the exit vapour quality, Fr_f, Re_f and Re_g both vary notably with increasing heat flux, as shown in Figure 6.1(b) and (c).

On the other hand, increasing the system mass flux from G = 200 to 300 and 400 kg/m^2 s at a nominal wall heat flux condition of $q_w^{"} \sim 80$ kW/m^2 result in notable variations in Bo, Cv and X_{tt} as well as the Fang number, Fa, owing to their proportionality to mass flux (see Figure 6.2). From Figure 6.2(b) and (c), most of the liquid and vapour-phase specific dimensionless parameters also change significantly at different mass flux conditions, with the exception of Prandtl number alongside the gas-phase Reynolds number. The liquid and gas-phase Prandtl number remained constant across the mass flux range since the inlet temperature and pressure at which the fluid properties are evaluated on have been kept constant at different mass flux levels. Re_g decreased only moderately with increasing mass flux at the nominal wall heat flux condition due to the effect of mass flux on exit vapour quality.

In the current study, the boiling number varied significantly with increase in heat flux as well as mass flux (as depicted in Figure 6.1(a) and Figure 6.2(b) respectively). For a nominal wall heat flux condition, the liquid Reynolds number and liquid-only Weber number increase notably with increase in system mass flux. This is mainly due to their dependency on wall heat flux, mass flux and vapour quality. The Martinelli parameter captures the effect of heat flux, mass flux and inlet subcooling.

The reduced pressure ratio increases while the liquid-to-vapour density ratio decreases with increasing saturation pressure. The former is directly proportional to the system pressure while the latter decreases due to a notable increment in vapour density with saturation pressure. Several other parameters that are functions of vapour density such as Cv and We_{go} also vary moderately with system pressure, although these variations are less than the benchmark ± 30 %.

The fluid inlet temperature is lower at higher system subcooling. This effectively extends the subcooled length of the channels and hence the exit vapour quality decreases with increasing subcooling at a given wall heat flux condition. Accordingly, parameters Cv, Fr_f and X_{tt} which are inversely proportional to the exit vapour quality, increase notably with increasing system subcooling.

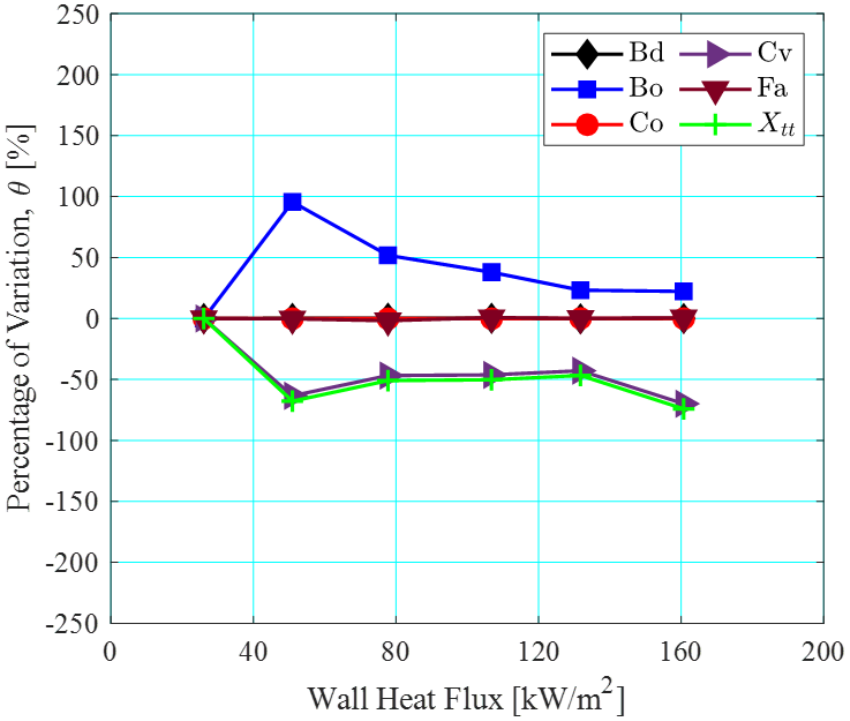
Bd
Cv
Bo
Fa
Co
X_{tt}
Percentage of Variation, θ [%]
Wall Heat Flux [kW/m^2]
250
200
150
100
50
0
-50
-100
-150
-200
-250
0
40
80
120
160
200

(a)

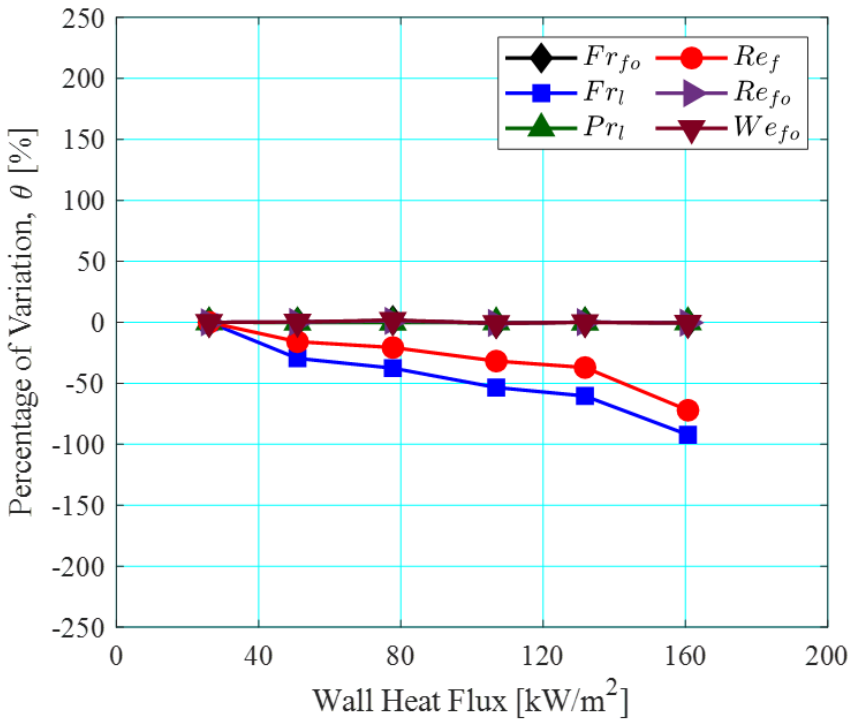
Fr_{fo}
Re_f
Fr_l
Re_{fo}
Pr_l
We_{fo}
Percentage of Variation, θ [%]
Wall Heat Flux [kW/m^2]
250
200
150
100
50
0
-50
-100
-150
-200
-250
0
40
80
120
160
200

(b)

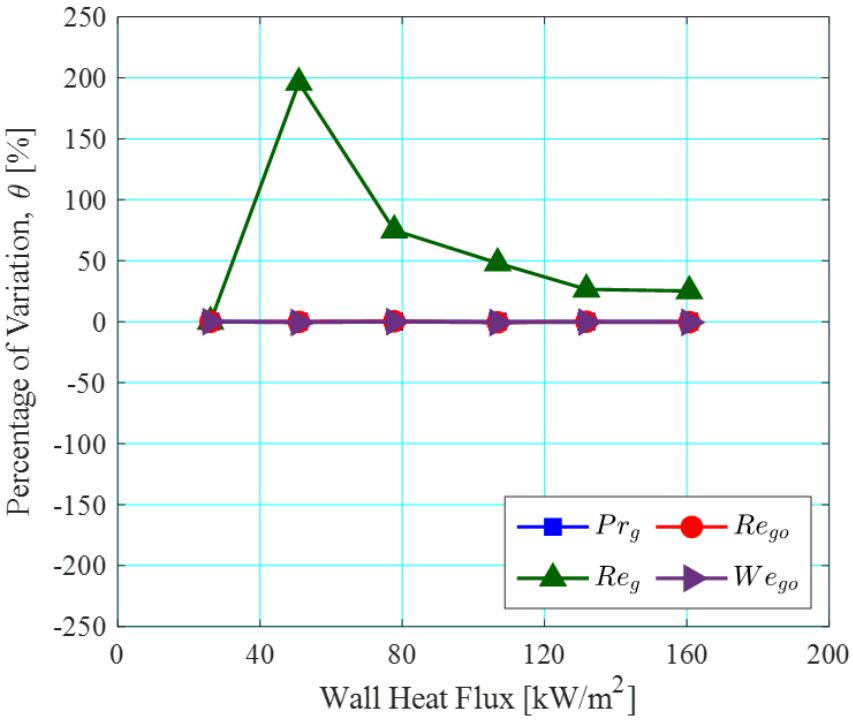

(c)

Figure 6.1: Effect of heat flux on (a) general dimensionless numbers, (b) liquid-specific dimensionless numbers and (c) gas-specific dimensionless numbers commonly considered in heat transfer correlations.

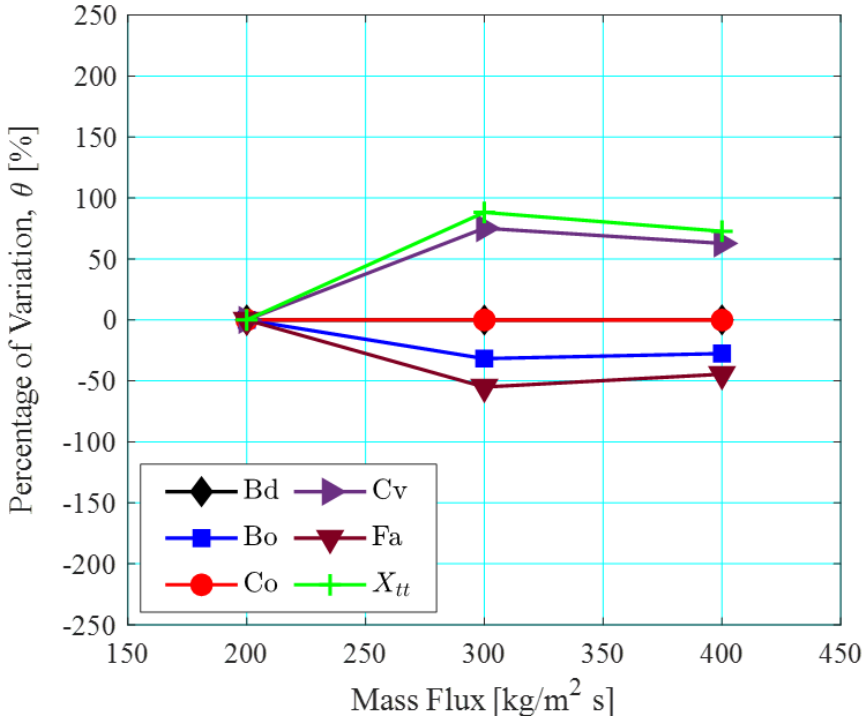
Percentage of Variation, θ [%]
Mass Flux [kg/m^2 s]
Bd
Cv
Bo
Fa
Co
X_{tt}

(a)

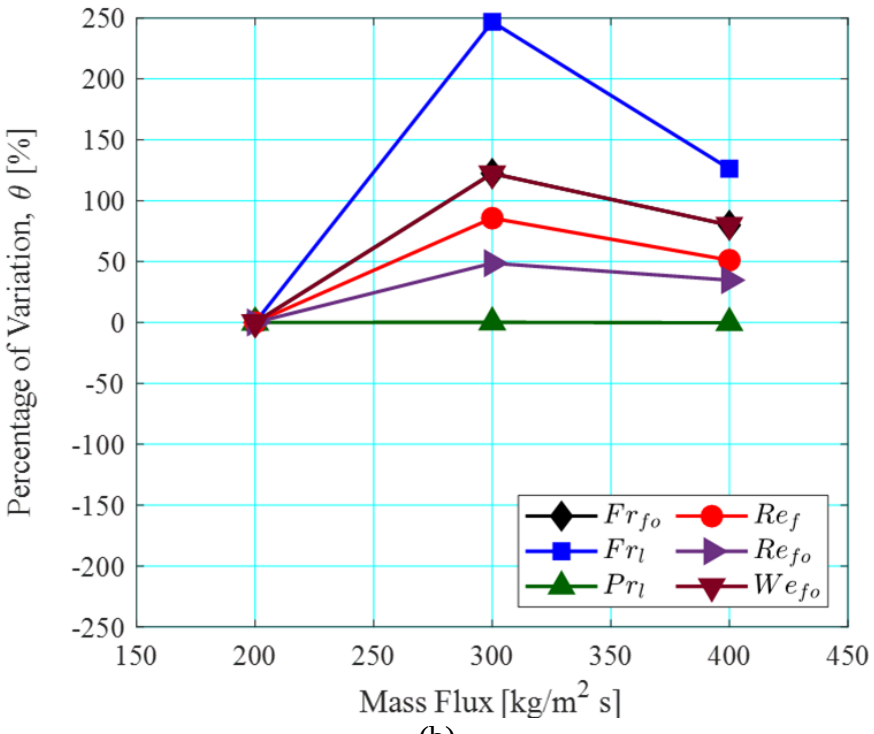
Percentage of Variation, θ [%]
Mass Flux [kg/m^2 s]
Fr_{fo}
Re_f
Fr_l
Re_{fo}
Pr_l
We_{fo}

(b)

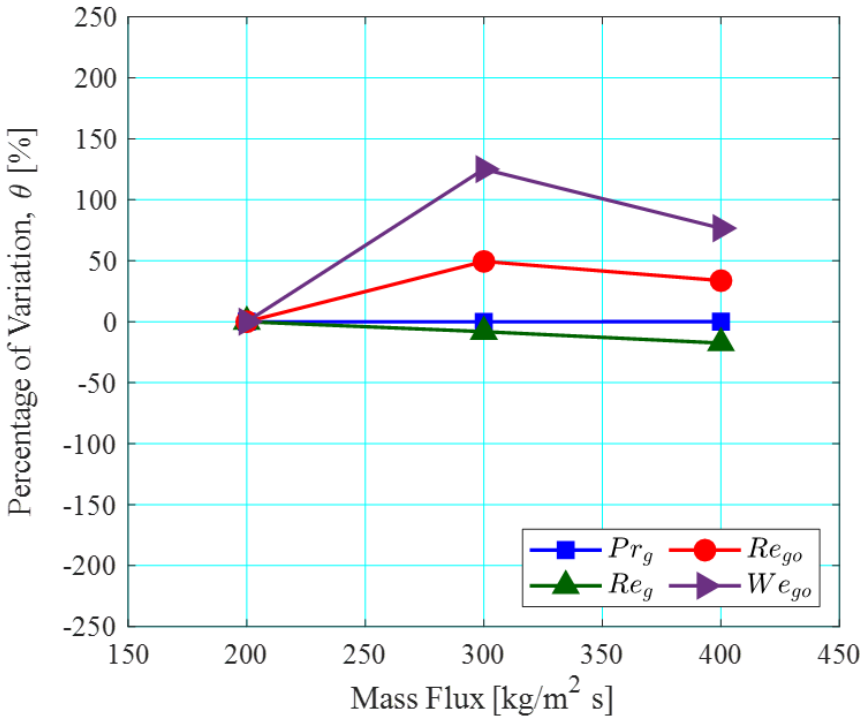

(c)

Figure 6.2: Effect of mass flux on (a) general dimensionless numbers, (b) liquid-specific dimensionless numbers and (c) gas-specific dimensionless numbers commonly considered in heat transfer correlations.

6.3 Evaluation of Heat Transfer Correlations

The correlations presented previously in Section 2.7 and listed in Table 6.7 were compared with the flow boiling results of HFE-7200 in a multi-microchannel heat sink at $q_w^{"}$ = 24.8 – 234.3 kW/m^2, P = 1 – 2 bar, G = 200 – 400 kg/m^2 s and ΔT_{sub} = 5 – 20 K. The mean absolute error (MAE) and the percentage of data points predicted within ±30% error band, θ_{30}, were used to evaluate the accuracy of each correlation, where n is the number of data points.

$$MAE = \frac{1}{n}\left| \frac{\bar{h}_{tp,exp} - \bar{h}_{tp,pred}}{\bar{h}_{tp,exp}} \right| \times 100\ \% \tag{6.10}$$

$$\theta_{30} = \frac{n_{pred}}{n_{exp}} \times 100\ \% \tag{6.11}$$

Based on the analysis in Section 6.2, the correlations are separated into four groups as follows: (i) correlations considering less than four parameters (as listed in Table 6.1 and Table 6.2) and developed based on a specific working fluid, (ii) correlations considering less than four parameters and developed for multiple working fluids. These are summarised in Table 6.3 and Table 6.4. Heat transfer correlations in group (iii) considers at least four parameters and have been developed based on data on a specific fluid, while correlations in group (iv) are developed for multiple working fluids. Correlations in group (ii) and (iv), i.e. developed based on multiple working fluids generally involve a large databank of flow boiling data from various sources. These are presented in Table 6.5 and Table 6.6.

As some of the existing correlations were proposed based on experimental studies with fully-heated channels, a correction factor was used to account for the heat transfer results obtained with three-sided heating condition in the current study using the Nusselt number relations proposed by Shah and London [266]. This approach was also adopted by Al-Zaidi et al. [57], Qu and Mudawar [221] and Kim and Mudawar [291]. The predicted heat transfer coefficient, HTC_{pred}, is thus expressed as follows:

$$HTC_{pred} = \frac{Nu_3}{Nu_4} \times HTC_{cor} \tag{6.12}$$

where Nu_3 and Nu_4 are the Nusselt number expressions for three-sided heating and four-sided heating configurations. The original predicted heat transfer coefficient by each correlation is represented by HTC_{cor}.

The top three performing correlations were the Sun and Mishima [176], Kim and Mudawar [184] and Kandlikar and Balasubramaniam [187], as depicted in Figure 6.3 to Figure 6.5. The

top correlations concluded in this study appear to have some agreement with the evaluation of Fang et al. [171] for a large database of almost 11,000 data points for up to 19 different working fluids. Aside from their own correlation (i.e. Fang et al. [171]), the authors cited the Kim and Mudawar [184] model to be one of the top performing heat transfer correlations, especially for vertical flows. The comparison also found that the Sun and Mishima [176] correlation predicted the experimental data for working fluids such as water, R134a and R245fa to relatively high accuracies. The Kandlikar and Balasubramaniam [187] correlation was also found to predict the database of ammonia well.

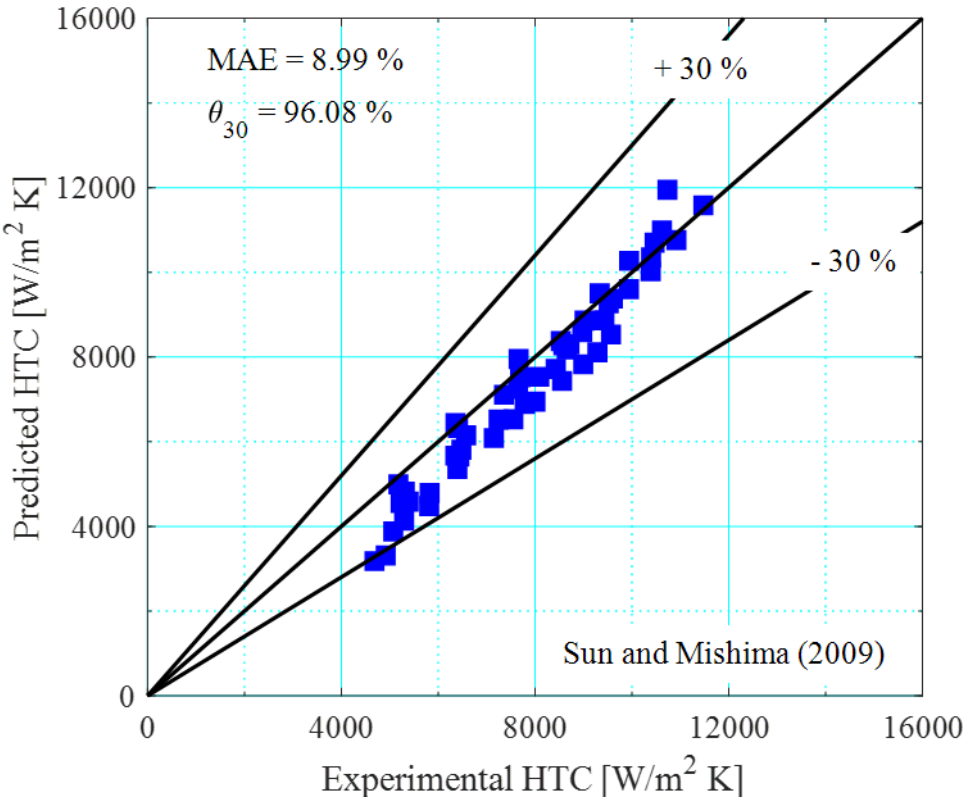

Figure 6.3: Comparison of flow boiling data with the Sun and Mishima correlation [176].

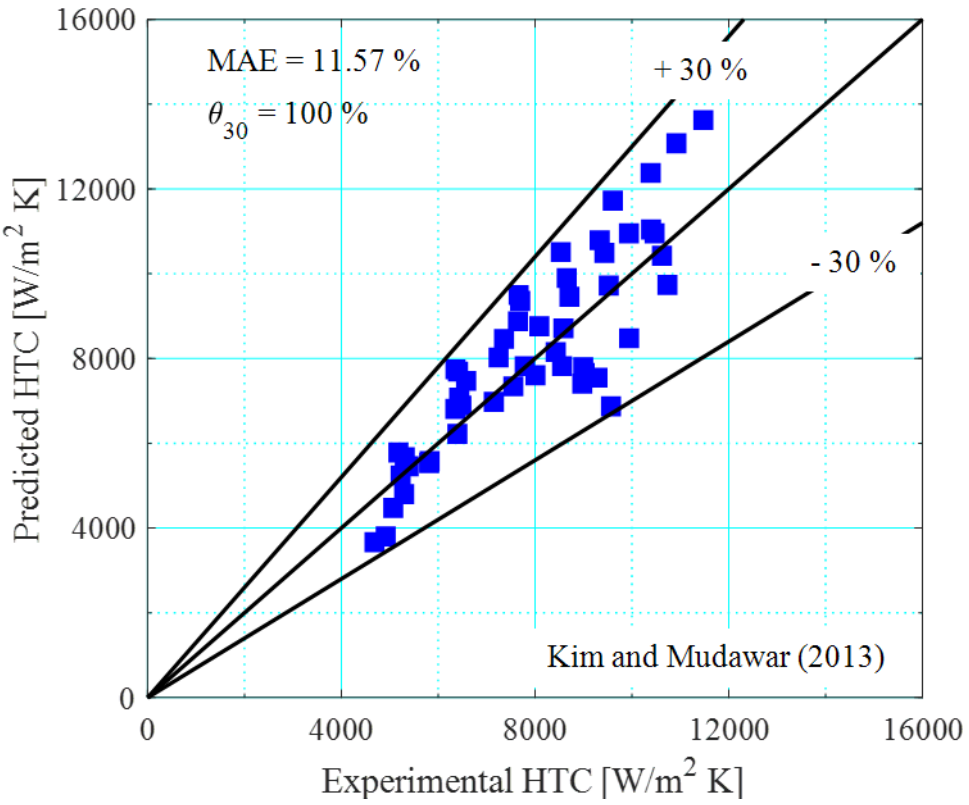

Figure 6.4: Comparison of flow boiling data with the Kim and Mudawar correlation [184].

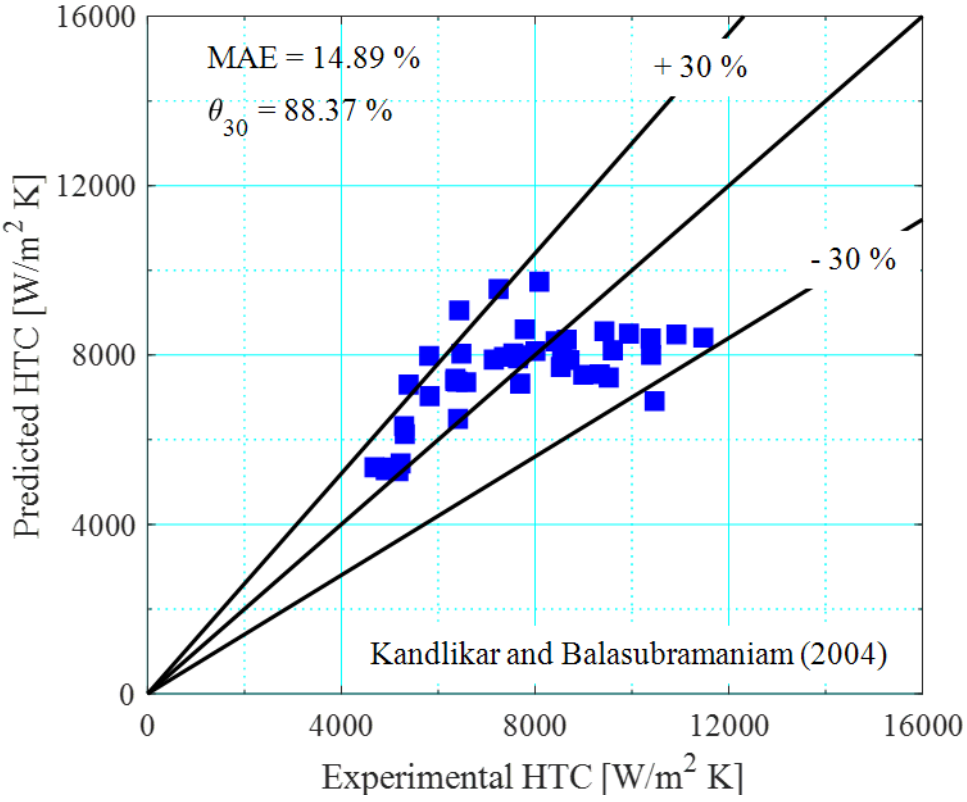

Figure 6.5: Comparison of flow boiling data with the Kandlikar and Balasubramaniam correlation [187].

Additionally, the top performing correlations mentioned above were in group (iv) – all microscale correlations developed based on relatively large databases involving multiple working fluids, as well as considering more than four of the dimensionless parameters evaluated in Table 6.1 and Table 6.2. The MAE was lower than ±20 % and at least 85 % of the experimental data was captured within the ±30 % error band. Overall, the correlations in group (iv) resulted in the lowest MAE of ±30.7 % and the highest θ_{30} of 63.6 % of the four groups.

Correlations in group (i) considering less than four parameters generally performed poorly in the prediction of heat transfer coefficient, with a mean MAE of ±62.4 % and θ_{30} of 11.8 %. Correlations in group (ii) developed for multiple working fluids, performed slightly better at a MAE of ±42.4 % and θ_{30} of 17.8 %. This could be because heat transfer correlations developed for multiple working fluids typically also involved a larger experimental database. Correlations in group (iii), which considered at least four parameters but only one fluid, resulted in a mean MAE of ±136.5 % and θ_{30} of 9.3 %. This excludes the correlation of Eraghubi et al [194], which could skew the comparison as it has been developed for a similar class of fluid, i.e. the

HFE-7000. The correlation predicted 70.6 % of the data within the ±30 % band, with a MAE of ±22.7 %.

A direct correlation between the number of dimensionless parameters included was not observed in the current assessment. Nevertheless, flow boiling heat transfer correlations proposed based on a database of multiple working fluids and considered more than four relevant parameters (i.e. group (iv), see Table 6.6) appear to have a wider range of fluid applicability and generally predicted the experimental heat transfer results to a higher degree of accuracy compared to the other groups in this study.

The Boiling number was considered in many correlations assessed in this study, including the top three correlations. The nucleate boiling model of Sun and Mishima [176], developed for 2505 flow boiling data points of 11 working fluids including R134a and water correlated two-phase heat transfer to $Bo^{0.54}$. The asymptotic-based correlation of Kim and Mudawar [184] contained a large databank of nearly 11,000 data points for multiple working fluids used the boiling number to calculate both the nucleate and convective boiling heat transfer coefficients. The predominant-mechanism model of Kandlikar and Balasubramaniam [187], developed for over 10,000 data points for 14 working fluids, also considered the boiling number in both flow boiling components. The boiling number is a dimensionless form of heat flux, which increases with heat flux and decreases with mass flux, as depicted in Figure 6.1(a) and Figure 6.2(b) respectively. Correlations employing Cooper-type nucleate boiling formulations directly include wall heat flux as a parameter.

The liquid Weber number appear to be effective in capturing the effects of surface tension in microscale heat transfer. The liquid Weber number increased significantly with mass flux for a nominal wall heat flux condition in the current study. The liquid Weber number is included in the Sun and Mishima [176] and Kim and Mudawar [184] correlation. The liquid-only Reynolds number and liquid Reynolds number was also considered in the top three correlations. Sun and Mishima [176] directly correlated their two-phase heat transfer coefficient to the liquid-only Reynolds number while Kim and Mudawar [184] correlation used the Dittus-Boelter turbulent flow equation to calculate single-phase liquid heat transfer. Kandlikar and Balasubramaniam [187] recommended the laminar flow condition to be at $Re_{fo} < 1600$ and identified a transition region between $1600 \leq Re_{fo} < 3000$.

The liquid-to-vapour density ratio and reduced pressure ratio also varied notably with changes in operating pressure, due to the increase in the vapour density of fluid HFE-7200 with increase in pressure. As mentioned above, bubble nucleation and growth rate have been shown to be related to the liquid-vapour density of the working fluid [56], [108]. Sun and Mishima [176] directly correlated the liquid-to-vapour density ratio in their prediction model. Kim and Mudawar [184] included the reduced pressure ratio for the nucleate boiling component and the density ratio for the convective boiling component. The Kandlikar and Balasubramaniam [187] considered the convection number in their heat transfer correlation. The convection number varies significantly with heat flux and mass flux (see Figure 6.1(a) and Figure 6.2(a)) but only by up to +20 % with pressure in the present study. This is because the density ratio is correlated to the power of 0.5 in the convection number.

Furthermore, the Martinelli parameter is relatively sensitive to changes in heat flux, mass flux and inlet subcooling (see Figure 6.1(a) and Figure 6.2(a))). This is mainly due to the dependence of the Martinelli parameter on exit vapour quality. The parameter is also employed in many Chen-type correlations [182], [194], as well as the Kim and Mudawar [184] correlation to calculate convective boiling enhancement.

The Shah [150] correlation considered several parameters mentioned above, including the boiling number, liquid Reynolds number and convection number. Additionally, the gas-only Weber number and liquid-only Froude number, which increased significantly with mass flux, was also included. Nevertheless, the correlation performed only moderately in the prediction HFE-7200 flow boiling heat transfer, as depicted in Figure 6.6. This could be because the nucleate boiling correlation was only weakly related to the boiling number, namely by $Bo^{0.5}$ and if parameter J is between $0.1 < J \leq 1$, to $Cv^{-0.1}$. The liquid-only Froude number was only given as a condition to calculate parameter J in the model, which was set to $J = Cv$ if $Fr_{fo} \geq 0.04$. Parameter F in the correlation, which includes the gas-only Weber number, was set to $F = 1$, as recommended by the model if the actual calculated F is less than 1. On the other hand, the convective boiling heat transfer coefficient was estimated based on the convection number, which varied with heat flux, mass flux and inlet subcooling. The predominant-mechanism model was consistently selected the nucleate boiling mechanism as the dominant heat transfer mode across the operating range investigated in the present study, which could have

contributed to the overprediction of heat transfer coefficients (see Figure 6.6). The Kandlikar and Balasubramaniam [187], which typically selected the convective boiling mechanism as the dominant heat transfer mode when $x_e > 0.4$ performed much better in the prediction of HFE-7200 heat transfer.

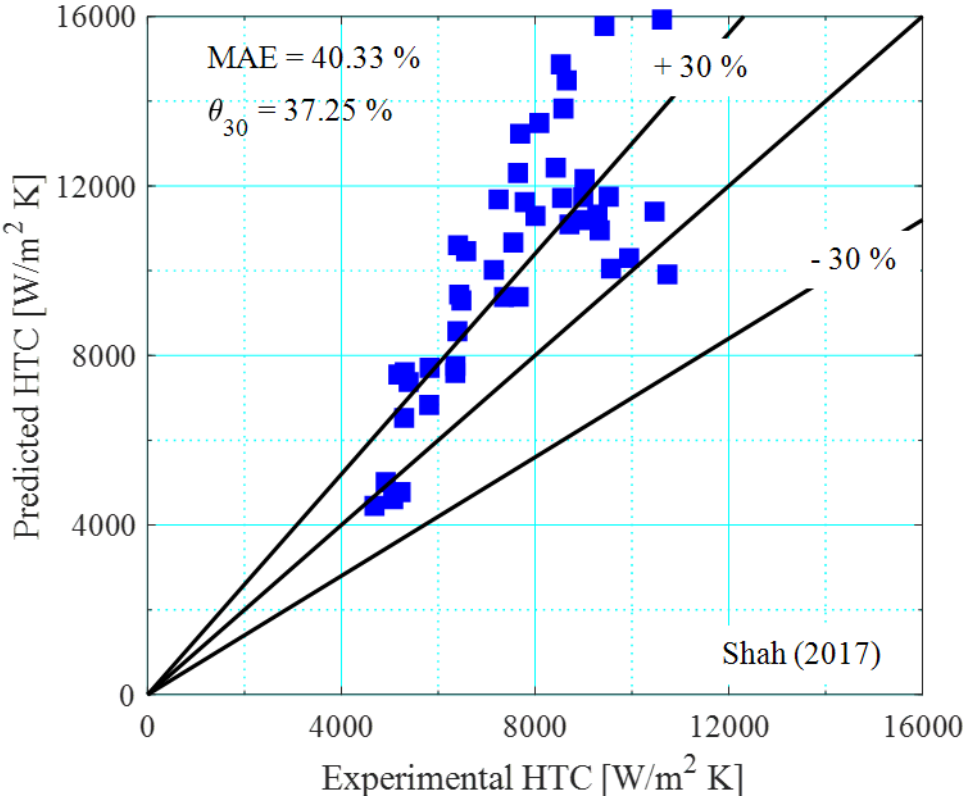

Figure 6.6: Comparison of flow boiling data with the Shah correlation [150].

The Fang et al. [171] and Lee and Mudawar [190] correlation in group (iv) also did not perform satisfactorily in the prediction of HFE-7200 flow boiling heat transfer. The Fang et al. [171] resulted in a MAE of ±45.2 while the Lee and Mudawar [190] produced an even higher MAE of ±76.7 %. This could be because the latter was developed for only water and R134a data. The Fang et al. [171] correlation was found to consistently outperform all correlations in the prediction of heat transfer data in the assessment conducted by Fang et al. [171]. This disparity could be due to the fluid dependent parameter in the model, which is not available for HFE-7200.

Some approach and assumptions of these correlations, believed to affect the prediction accuracy, are discussed below.

6.3.1 On the Fluid Dependent Parameter

The Fang et al. [171] and Kandlikar and Balasubramaniam [187] models both recommended a fluid dependent parameter in their correlations. Although a fluid parameter was not available for HFE-7200, the latter predicted heat transfer results well in this study (see Figure 6.5). On the contrary, the Fang et al. [171] generally overpredicted the flow boiling heat transfer coefficient of HFE-7200 (see Figure 6.7). The correlation was developed based on a large database of 13 fluids and incorporates a fluid-dependent parameter, which is not currently available for HFE-7200. The authors recommended a standard value of $F_f = 1850$ where is this the case but encouraged the determination of a suitable constant based on vigorous experimental data fitting. Since the magnitude of the fluid parameter is relatively large in the Fang et al. [171] correlation, compared to the Kandlikar and Balasubramaniam [187] correlation, the predicted heat transfer coefficient is relatively sensitive to the constant assigned for each fluid. A fluid constant for HFE-7200 could be proposed if a more comprehensive flow boiling database becomes available.

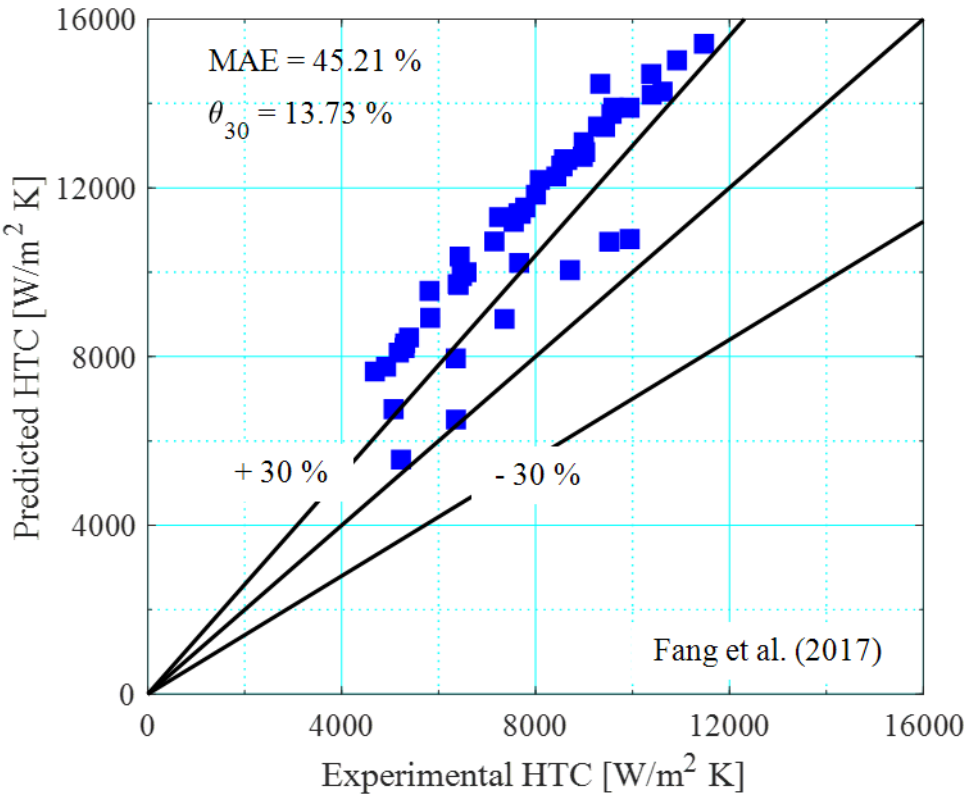

Figure 6.7: Comparison of flow boiling data with the Fang et al. correlation [174].

6.3.2 On Cooper's Nucleate Boiling Model

Correlations adopting the nucleate pool boiling equation of Cooper [159], such as the Liu and Winterton [183], Mahmoud and Karayiannis [182] and Bertsch et al. [181] typically underpredicted the experimental heat transfer results of HFE-7200 (see Figure 6.8, Figure 6.9(a) and Figure 6.10(a)). This was due to the small magnitude of the nucleate boiling component in the respective correlations. This could be because of the enhanced bubble nucleation activity in flow boiling (thus higher nucleate boiling heat transfer coefficients) compared to the pool boiling mode due to additional inertia forces that affect bubble departure behaviour in microchannels.

Replacing Cooper's correlation with the Sun and Mishima [176] model (see Figure 6.3) or the Tran et al. [177] model (see Figure 6.11) developed for flow boiling data to estimate the nucleate boiling mechanism generally improved the accuracy of all the above-mentioned models. For instance, using the Sun and Mishima [176] model in the nucleate boiling component of the Mahmoud and Karayiannis [182] model reduced the MAE from ±35 % to ±26 % and significantly improved θ_{30} from 29 % to 73 % (see Figure 6.9(b)). Bertsch et al. [181] obtained a MAE of ±23 % and much higher θ_{30} of 75 % using the correlation Sun and Mishima [176] correlation as the nucleate boiling relation improved from ±41 % and 26 % respectively using the original correlation using Cooper's pool boiling relation (see Figure 6.10(b)).

On exception to this is the Eraghubi et al. [194] heat transfer correlation (see Figure 6.12). The correlation merely replaced the original nucleate boiling model of Chen [180] with the pool boiling equation of Cooper [159]. However, the study did not measure the average surface roughness of their 8 mm tube and recommended applying a default roughness parameter of 1 μm. This augmented the nucleate boiling heat transfer coefficient, which would otherwise be several times lower with the actual roughness parameter (i.e. R_p = 0.23 μm) in the current study.

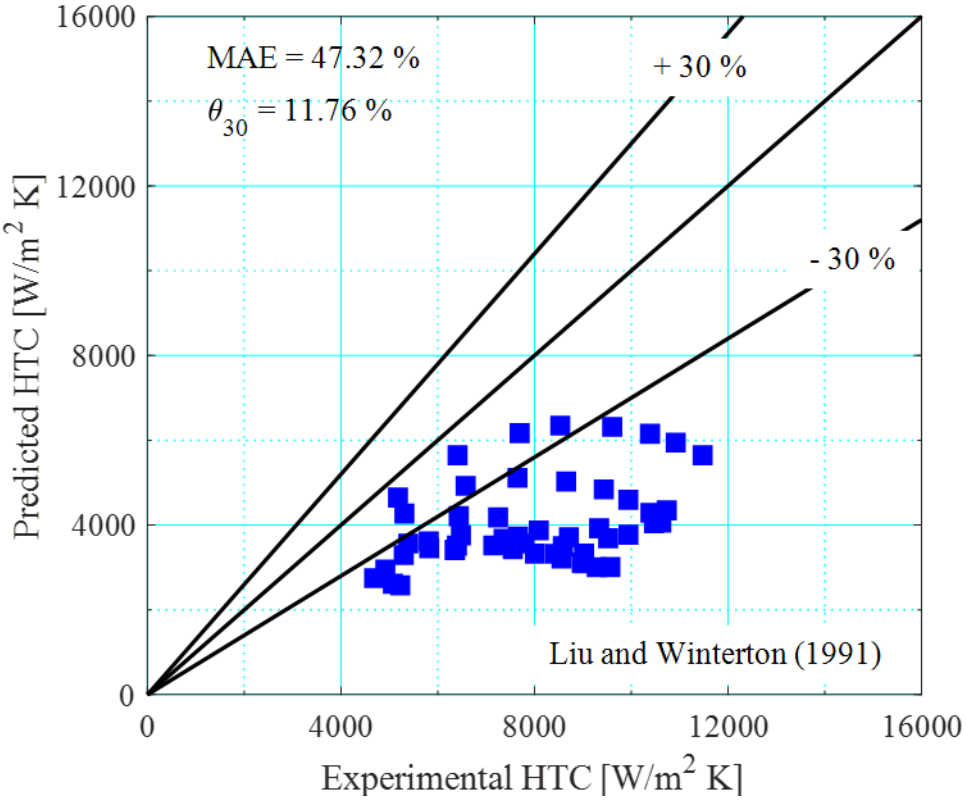

Figure 6.8: Comparison of flow boiling data with the Liu and Winterton correlation [183].

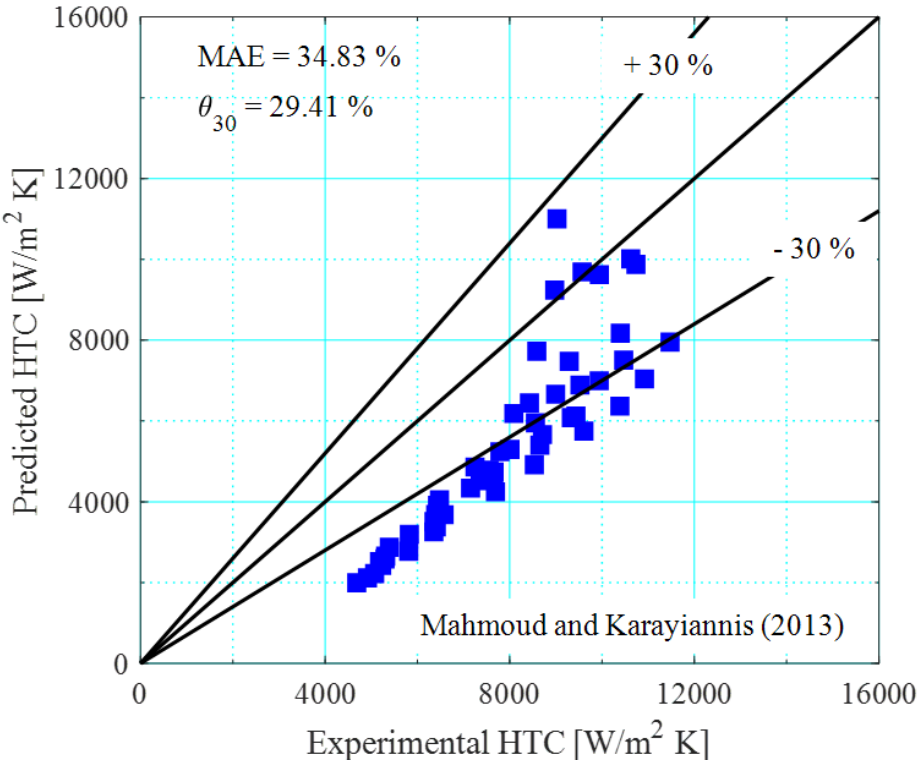

(a)

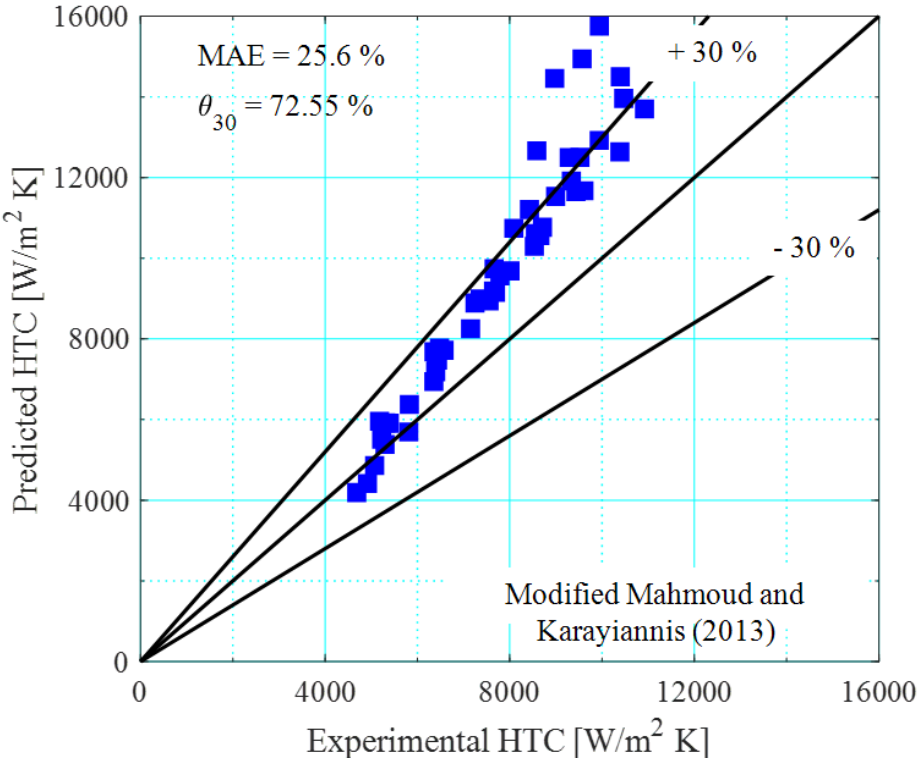

(b)

Figure 6.9: (a) comparison of flow boiling data with the Mahmoud and Karayiannis correlation [182] and (b) with a modified nucleate boiling model.

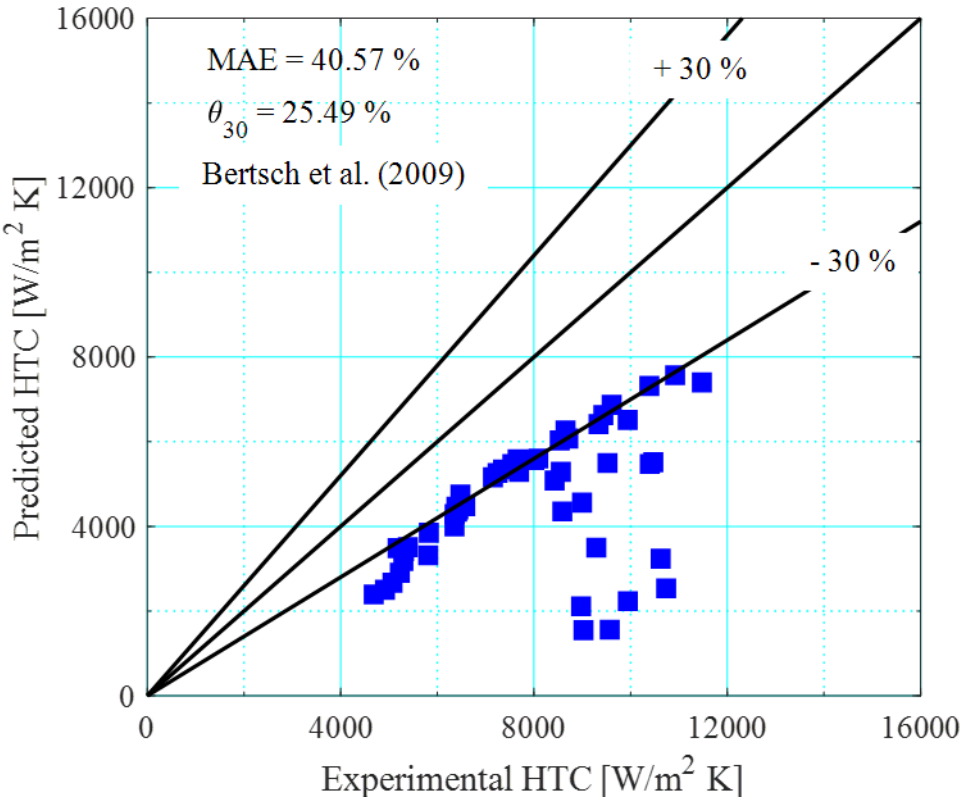

(a)

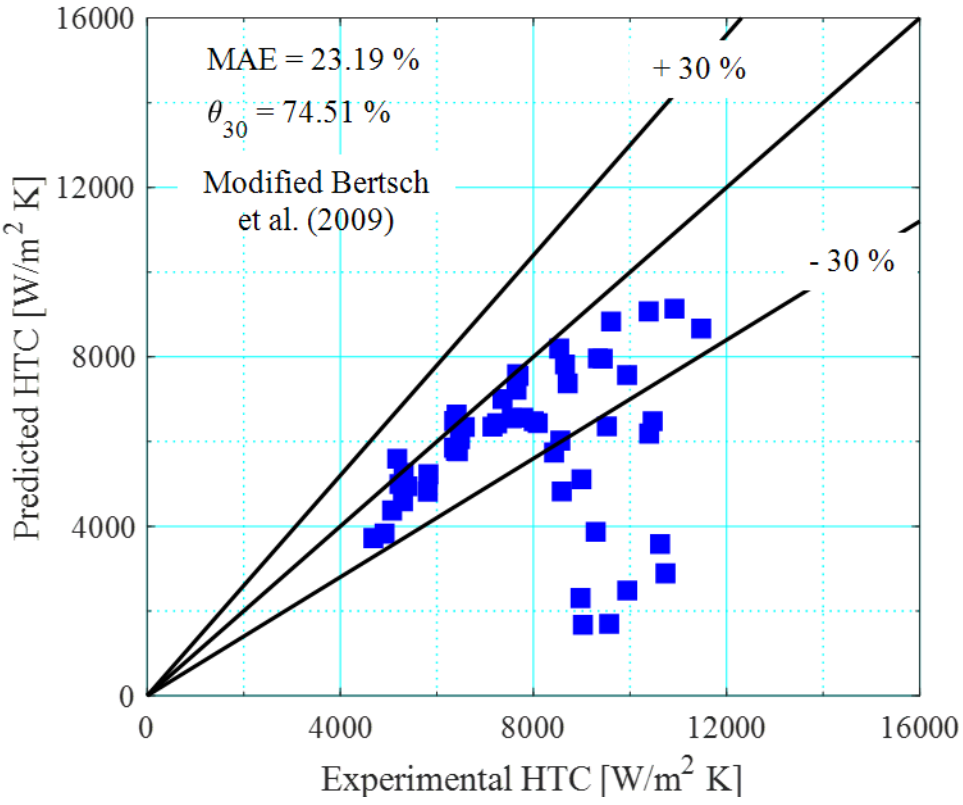

(b)

Figure 6.10: (a) comparison of flow boiling data with the Bertsch et al. correlation [181] and (b) with a modified nucleate boiling component.

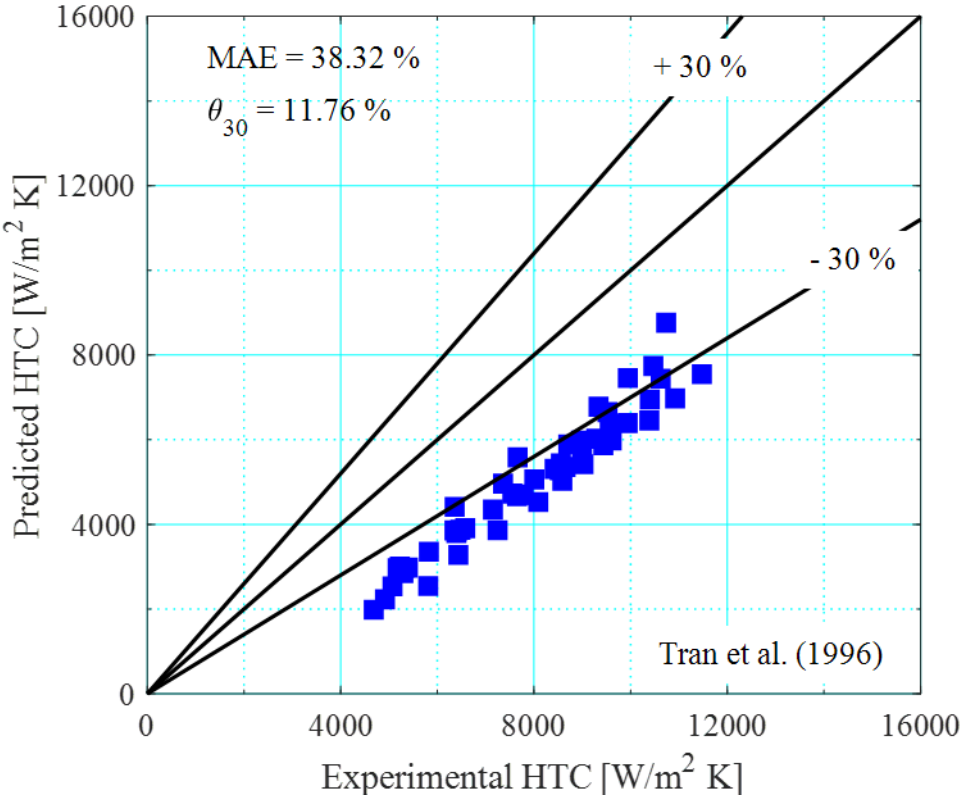

Figure 6.11: Comparison of flow boiling data with the Tran et al. correlation [177].

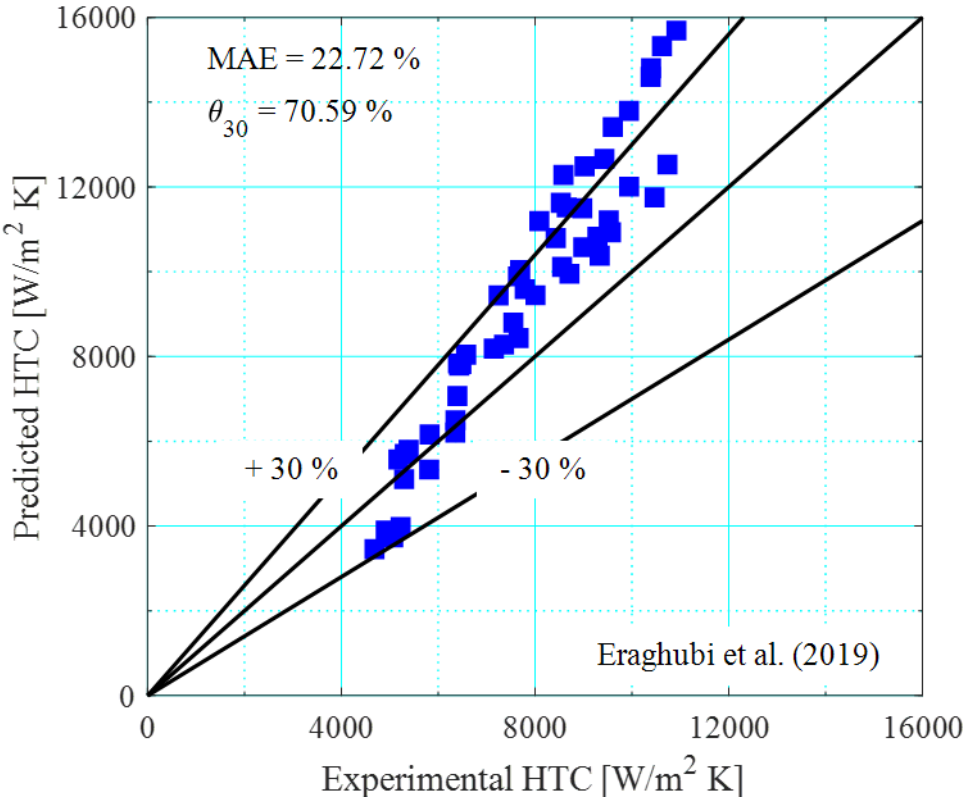

Figure 6.12: Comparison of flow boiling data with the Eraghubi et al. correlation [194].

6.3.3 On the Assumption of Laminar Single-Phase Gas Flow

The Bertsch et al. [181] and Lee and Mudawar [190] correlation included the single-phase gas heat transfer coefficient. Lee and Mudawar [190] recommended the Dittus-Boelter turbulent flow equation to calculate the single-phase gas heat transfer coefficient for vapour Reynolds numbers above $Re_g > 2000$. The single-phase all-gas heat transfer coefficient is estimated based on three-sided heating Nusselt number (refer to Eq. (2.5)).

On the contrary, Bertsch et al. [181] employed the Hausen correlation (see Eq. (2.6)) to estimate both the liquid and gas-phase single-phase heat transfer component. While the liquid-phase in microchannels in the current mass flux range is indeed in the laminar range, the vapour-phase is relatively turbulent. Re_g ranges from 594 up to 10523 in the current study. Accordingly, adopting the Dittus-Boelter correlation for the vapour-only single-phase heat transfer further improves the accuracy of the model. In Section 6.3.2, using the Sun and Mishima [176] correlation instead of Cooper's nucleate boiling correlation resulted in large improvements in the accuracy of the prediction model (i.e. MAE = ±23 % and θ_{30} = 75 %). Adopting the Dittus-Boelter correlation further improves the model, bringing the MAE down to ±15 % and θ_{30} to 88 %, as depicted in Figure 6.13.

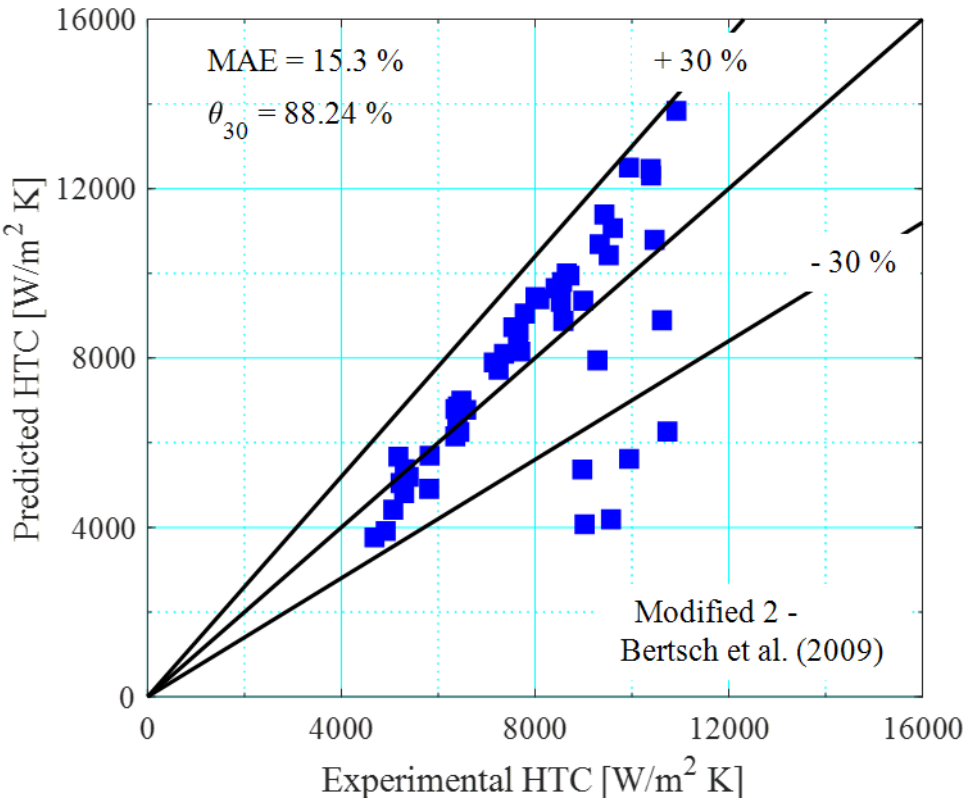

Figure 6.13: The Bertsch et al. correlation [181] with a modified nucleate boiling model and the Dittus-Boelter correlation for single-phase gas heat transfer.

6.3.4 On the Local Heat Transfer Trend and Type of Model Adopted

The local heat transfer trend at P = 1 bar, G = 200 kg/m^2 s and ΔT_{sub} = 10 K at $q_w^{"}$ = 106.8 kW/m^2 was used to evaluate the performance of the abovementioned prediction models in predicting the experimental heat transfer trend with respect to local vapour quality. Local heat transfer coefficients along the channel generally decreased from a peak near the onset of boiling toward the channel exit. A slight increase at the downstream location nearest to the channel exit is potentially related to heat losses to the exit plenum. Furthermore, the contribution of both nucleate boiling and convective boiling mechanisms has been verified from flow visualisation in the current study. Bubble nucleation in the liquid film in the annular flow regime was observed in our flow visualisation, indicating the contribution of both the nucleate boiling and convective mechanisms even in the high vapour quality region. The prediction results are presented in Figure 6.14(a) and (b).

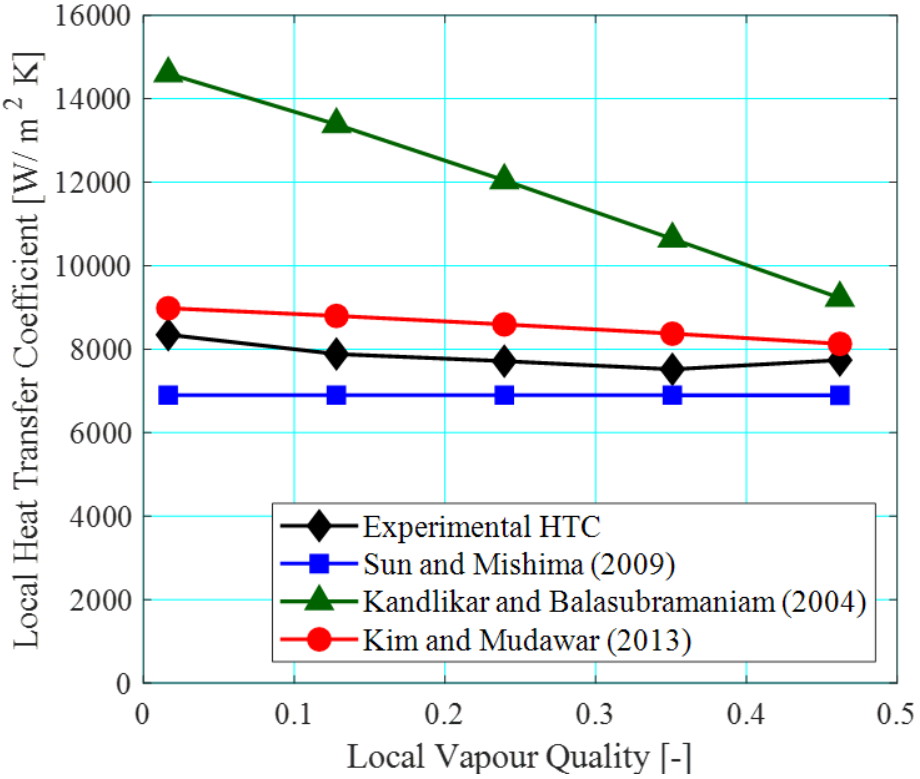

(a)

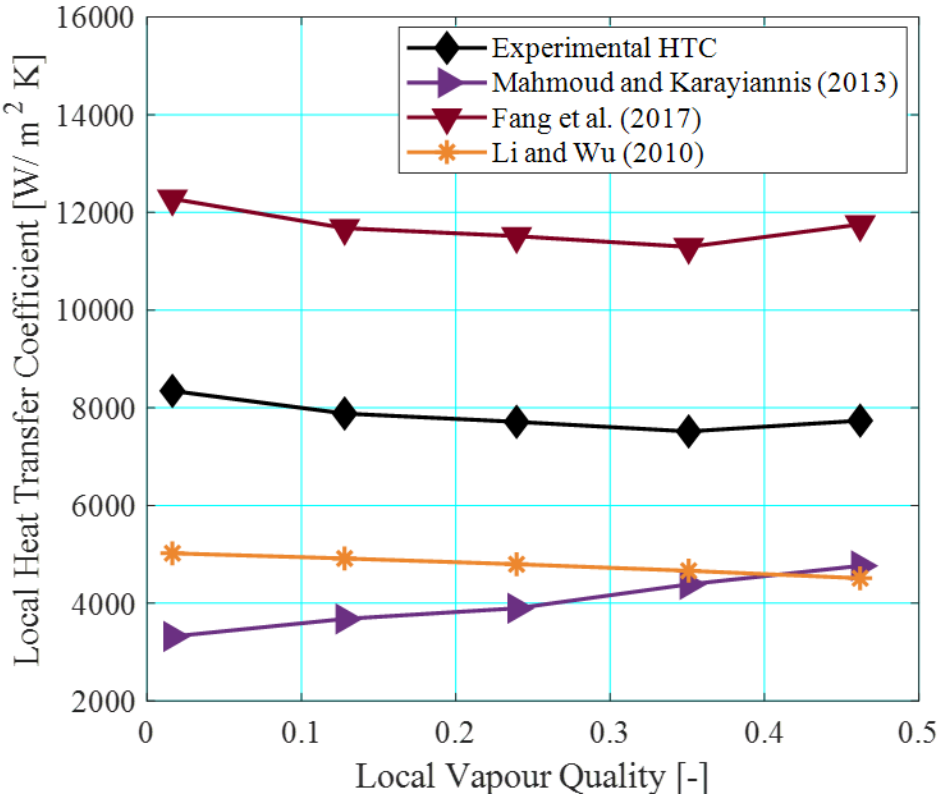

(b)

Figure 6.14: Prediction of the local heat transfer trends at P = 1 bar, G = 200 kg/m^{2}s and ΔT_{sub} = 10 K at $q_w^{"}$ = 106.8 kW/m^2. (a) top three heat transfer correlations, (b) selected correlations from the superposition, enhancement-factor and hybrid models.

The nucleate boiling model of Sun and Mishima [176] did not predict the peak in local heat transfer coefficients near the onset of boiling. Local heat transfer coefficients predicted by the model remained largely constant with local vapour quality. The main reason for this is the rather weak dependency of the dimensionless parameters considered in the model, namely Bo, We_{fo} and Re_{fo}, with vapour quality. These parameters varied more significantly with wall heat flux. The magnitude of heat transfer coefficients predicted by the model, however, is relatively close to the experimental heat transfer coefficient.

The predominant-mechanism model of Kandlikar and Balasubramaniam [187] assumed dryout incipience at vapour qualities larger than 0.7 and limited the application of their correlation to flow boiling data below the dryout quality. The model generally determined a nucleate boiling dominant trend up to vapour qualities around $x_e = 0.4$. Nucleate boiling heat transfer coefficients at low vapour qualities (i.e. $x_e < 0.4$) were several times the experimental heat transfer coefficient, even though trend of nucleate boiling suppression with increasing vapour quality was captured. Similarly, heat transfer coefficients in the convective boiling dominant region, as determined by the model, was also overpredicted. The predominant-mechanism correlation of Shah [150] on the other hand, selected the nucleate boiling heat transfer component to be the dominant heat transfer mechanism consistently for all vapour qualities, which could have contributed to the general overprediction of the experimental heat transfer data (see Figure 6.6). The model also predicted local heat transfer coefficients to increase with vapour quality along the channel, which is opposite to the experimental trend.

The Kim and Mudawar [184] correlation, based on the asymptotic model considered both the contribution of the nucleate boiling and convective boiling regimes. Accordingly, the correlation captured the peak in local heat transfer coefficient near boiling incipience as well as the decreasing heat transfer trend with respect to vapour quality along the channel. The magnitude of the heat transfer coefficients is very close to the experimentally obtained heat transfer coefficients. The $(1 - x_e)^{-0.51}$ term in the model appears to capture nucleate boiling suppression relatively well. The Martinelli parameter and the density ratio, used in several other models [180], [183] to correlate convective boiling enhancement, also appeared to be effective.

The superposition model also takes into account both the nucleate boiling and convective boiling contributions to estimate two-phase heat transfer. Nonetheless, the local heat transfer trend predicted by the Mahmoud and Karayiannis [182] correlation increases with vapour quality, which is opposite to the experimental trends observed This is because the nucleate boiling suppression factor decreases slightly with increasing vapour quality at a given wall heat flux. In fact, most superposition models evaluated in this study appear to predict smaller suppression factors with increasing vapour quality at a given wall heat flux condition. The magnitude of heat transfer coefficients is much lower than the experimental value, due to the adoption of Copper's pool boiling correlation, as discussed in Section 4.3.3.

Enhancement-type factor models generally predicted heat transfer data poorly, especially if the correlation has been proposed for specific fluids, for example the Thiangtham et al. [117] and Fang [173] correlation, both for fluid R134a. As discussed in Section 6.3.1, the strong dependency of the Fang et al. [174] correlation on the fluid parameter led to an overprediction of the magnitude of heat transfer coefficient for fluid HFE-7200. However, the correlation managed to capture the local heat transfer trend almost perfectly along the channel. This is due to the inclusion of the (μ_{lf}/μ_{lw}) viscosity ratio in the model. Nonetheless, the wall temperature measurement may not be readily available to evaluate μ_{lw} in commercial applications.

Hybrid models generally did not predict the experimental data well. For instance, the model of Qi et al. [192] assumed dryout incipience at $x > 0.3$ and heat transfer coefficients dropped to almost zero in this region. On the other hand, the peak in local heat transfer coefficients in the low vapour quality region ($x < 0.05$) where bubble nucleation was dominant was vastly under-predicted by the Lee and Mudawar [190] model. The criterion $BdRe_f^{0.5}$ predicted the peak in heat transfer coefficients near the onset of boiling as well as the subsequent decrease in local heat transfer coefficients along the channel. This is mainly due to the variation of liquid Reynolds number with vapour quality along the channel. Nevertheless, the magnitude of heat transfer coefficients predicted was much lower than the experimental value.

Table 6.1: Analysis of selected correlations adopting the enhancement factor, nucleate boiling and superposition models.

	Applicability	ρ_f/ρ_g [-]	P_r [-]	Bo [-]	Cv [-]	Fa [-]	Fr_{fo} [-]	Re_f [-]	Re_g [-]	Re_{fo} [-]	We_{fo} [-]	We_{go} [-]	X parameter [-]	Fluid constant [-]	No. of parameters considered [-]	Additional considerations
Enhancement-factor models																
Fang et al. [174]	Macro/ microscale	✓	✓	✓			✓							✓	5	• (μ_{lf}/μ_{lw}), Bd, MW. • For multiple fluids.
Fang [173]	Macro/ microscale	✓		✓		✓		✓							3	• (μ_{lf}/μ_{lw}), Pr_f.
Thiangtham et al. [117]	Microscale	✓		✓						✓	✓				4	•
Nucleate boiling models																
Yu et al.	Nucleate pool boiling	✓		✓							✓				3	•
Tran et al. [177]	Microscale	✓		✓							✓				3	• For R12 and R113.
Sun and Mishima [176]	Microscale	✓		✓						✓	✓				4	• For multiple fluids.
Superposition models																
Bertsch et al. [181]	Microscale		✓							✓					2	• $h_{sp,g}$, Pr_f, Co, MW, R_p, L_{ch}. • For multiple fluids.
Mahmoud and Karayiannis [182]	Microscale	✓	✓					✓					✓		4	• Pr_f, Co, MW, R_p.
Eraghubi et al. [194]	Macroscale	✓	✓					✓					✓		4	• Pr_f, MW, R_p.

Table 6.2: Analysis of selected correlations adopting the asymptotic, predominant-mechanism and hybrid models.

	Applicability	ρ_f/ρ_g [-]	P_r [-]	Bo [-]	Cv [-]	Fa [-]	Fr_{fo} [-]	Re_f [-]	Re_g [-]	Re_{fo} [-]	We_{fo} [-]	We_{go} [-]	X parameter [-]	Fluid constant [-]	No. of parameters considered [-]	Additional considerations
Asymptotic models																
Liu and Winterton [183]	Macroscale	✓	✓					✓							3	• Pr_f, MW,R_p. • For multiple fluids.
Kim and Mudawar [184]	Microscale	✓	✓	✓							✓		✓		5	• Pr_f, P_H, P_w. • For multiple fluids.
Choi et al. [163]	Microscale			✓				✓			✓				3	• Pr_f, Co, $We_{f,m}$.
Predominant-mechanism models																
Kandlikar and Balasubramanian [187]	Microscale			✓	✓			✓						✓	4	• Nu_3. • For multiple fluids.
Docoulombier et al. [188]	Microscale	✓	✓	✓				✓					✓		5	• Pr_f, MW, R_p.
Shah [150]	Macro/ microscale			✓	✓		✓	✓				✓			5	• D_{hp}. • For multiple fluids.
Hybrid models																
Qi et al. [192]	Microscale			✓			✓				✓		✓		5	• K_p.
Li and Wu [191]	Microscale			✓											2	• Bd, $BdRe_f^{0.5}$. • For multiple fluids.

Lee and Mudawar [190]	Microscale	✓		✓					✓		✓		✓		5	• $h_{sp,g}$, Nu_3. • For R134a and water.

Table 6.3: Correlations for only 1 fluid and considering less than 4 parameters.

Author(s)	Applicability	Type of model	No. of parameters [-]	MAE [%]	Θ_{30} [%]	Remarks
Yu et al.	Microscale	Nucleate boiling	3	77.13	0	• For water. • Heat transfer coefficients generally overpredicted.
Bertsch et al. [213]	Microscale	Superposition	2	40.57	25.49	• Nucleate boiling heat transfer coefficients relatively small using Cooper's correlation. • Laminar gas phase assumed by model. • Suppression factor decreases with vapour quality for a given wall heat flux.
Fang [205]	Macro/ microscale	Enhancement-factor	3	50.88	21.57	• For R134a. • Wall temperature required to evaluate viscosity ratio. • Lower accuracy at low and high vapour quality.
Choi et al. [160]	Microscale	Asymptotic	3	80.95	0	• For FC-72. • Proposed nucleate and convective boiling relation using a modified Weber number. • Heat transfer coefficients significantly underpredicted.

Table 6.4: Correlations for more than 1 fluid and considering less than 4 parameters.

Author(s)	Applicability	Type of model	No. of parameters [-]	MAE [%]	Θ_{30} [%]	Remarks
Liu and Winterton [215]	Macroscale	Asymptotic	3	47.32	11.76	• Nucleate boiling heat transfer coefficients relatively small using Cooper's correlation. • Nucleate boiling suppression factor decreases with vapour quality for a given wall heat flux.
Tran et al. [209]	Microscale	Nucleate boiling	3	38.32	11.76	• For R12 and R113. • Heat transfer coefficients generally underpredicted.
Li and Wu [222]	Macro/ microscale	Hybrid	2	41.58	29.79	• Valid for $x > 0.1$. • Current experimental range deemed to be in microscale. • Bd used to account for surface tension effect in microchannel correlation. • Heat transfer coefficient generally underpredicted.

Table 6.5: Correlations for only 1 fluid and considered at least 4 parameters.

Author(s)	Applicability	Type of model	No. of parameters [-]	MAE [%]	Θ_{30} [%]	Remarks
Qi et al. [223]	Microscale	Hybrid	5	90.24	0	• For N_2. Nucleate boiling assumed to dominate at x < 0.3 and convective boiling dominates at x > 0.3. • Heat transfer coefficients are significantly underpredicted.
Mahmoud and Karayiannis [214]	Microscale	Superposition	4	34.83	29.41	• For R134a. Nucleate boiling heat transfer coefficients relatively small using Cooper's pool boiling correlation • Suppression factor decreases with vapour quality for a given wall heat flux.
Docoulombier et al. [219]	Microscale	Predominant-mechanism	5	160.6	7.84	• For CO_2. Adopts modified Cooper's correlation by Cheng et al. [196] to calculate nucleate boiling component. • Heat transfer coefficients significantly overpredicted.
Thiangtham et al. [114]	Microscale	Enhancement-factor	4	260.36	0	• For R134a. • Heat transfer coefficients significantly overpredicted.
Eraghubi et al. [227]	Macroscale	Superposition	4	22.72	70.59	• For HFE-7000. Cooper's correlation for nucleate boiling component with default R_p = 1 μm. • Nucleate boiling heat transfer coefficients several times lower if the measured R_p is used. • Heat transfer coefficients slightly overpredicted.

Table 6.6: Correlations for more than 1 fluid and considered at least 4 parameters.

Author(s)	Applicability	Type of model	No. of parameters [-]	MAE [%]	Θ_{30} [%]	Remarks
Kandlikar and Balasubramanian	Microscale	Predominant-mechanism	4	15.63	89.19	• Only valid for $x_e < 0.7$ (dryout assumed). • Nucleate boiling and convective boiling component correlated to Cv, Bo and fluid parameter. • Nucleate boiling component dominant up to $x_e \sim 0.4$. Relatively large nucleation heat transfer coefficients. • Reduction in heat transfer coefficient with vapour quality captured by $(1-x_e)$ term.
Lee and Mudawar [221]	Microscale	Hybrid	5	76.67	25.49	• For R134a and water. • Regions segregated by vapour quality do not agree with experimental observation. • Heat transfer coefficients at $x > 0.55$ significantly underpredicted.
Sun and Mishima [208]	Microscale	Nucleate boiling	4	8.99	96.08	• Changes in fluid properties and operating conditions well captured by density ratio, Re_{fo} and We_{fo}. • Bo captures effect of wall heat flux. • Predicted local heat transfer trend does not vary significantly with vapour quality.
Kim and Mudawar [184]	Microscale	Asymptotic	5	11.57	100	• Changes in fluid properties and operating conditions well captured by density ratio, P_r and We_{fo}. • Perimeter ratio used to relate 3 and 4 -sided heating configurations. • Bo captures effect of wall heat flux. • Nucleate boiling suppression correlated to $(1 - x_e)$. • Trend of decreasing heat transfer with vapour quality captured.

Shah [147]	Macro/ microscale	Predominant-mechanism	5	40.33	37.25	• Convective boiling correlated to Cv. • Nucleate boiling correlated to Bo and Cv. • Nucleate boiling component consistently selected as dominant heat transfer mechanism. • Local heat transfer trend increases with vapour quality at nominal wall heat flux.
Fang et al. [206]	Macro/ microscale	Enhancement-factor	5	45.21	13.73	• Author recommends fluid parameter (F_f = 1850) if unavailable. Unavailable for HFE-7200. • Wall temperature required to evaluate viscosity. • Heat transfer coefficients generally overpredicted. • Local heat transfer trend well captured by wall temperature dependent viscosity term.

6.4 Summary

In this section, a sensitivity study on common fluid parameters considered in heat transfer correlations was conducted. Dimensionless parameters that vary significantly within the range of operating conditions include the Boiling number, liquid Reynolds number, liquid-only Weber number and Martinelli parameter. The liquid-vapour density ratio and reduced pressure ratio, in particular, varied notably with operating pressure.

The density ratio was relatively sensitive to changes in system pressure, due to the increase in the vapour density of fluid HFE-7200 with increase in pressure. As expected, the reduced pressure ratio also increased with increasing system pressure. These parameters could be useful in capturing the effect of saturation pressure on bubble nucleation behaviour. Using the force balance model of Klausner et al. [108], Mahmoud and Karayiannis [56] also showed that bubble nucleation and growth rate were strongly related to the liquid-vapour density of the working fluid, see Section 4.3.3. On the other hand, the liquid Prandtl number remained relatively constant due to small variations in the liquid specific heat, liquid viscosity and thermal conductivity of the liquid phase in the current range of operation.

The convection number, considered in Shah [150] and Kandlikar and Balasubramaniam [187] exhibited a significant dependency on heat flux and mass flux, due to their influence on vapour quality. Increasing system subcooling at a given wall heat flux condition also have a significant effect on the convection number owing to its proportionality with exit vapour quality. The confinement number, which appears in Choi et al. [163], Qi et al. [192], Mahmoud and Karayiannis [182] and Bertsch et al. [181] remained relatively unchanged throughout the range of operating conditions in this study, with a marginal decrease of Co = 1.9 to 1.8 with pressure increase from P = 1 bar to 2 bar owing to the increase in vapour density with system pressure.

The Fang number considered in Fang [173] decreased with mass flux. On the other hand, the liquid-only Froude number considered in Fang et al. [174] and Shah [150] increased with mass flux. The Bond number in Li and Wu [191] varied with the square of the hydraulic diameter, which was kept constant in the current study.

Eighteen flow boiling heat transfer correlations recommended for various flow directions (i.e. horizontal and vertical) and channel configurations (i.e. single or multichannels) were evaluated. At least three correlations from the (i) enhancement-factor, (ii) nucleate boiling, (iii) superposition, (iv) asymptotic, (v) predominant mechanism and (vi) criterion-based models were assessed in order to evaluate the effectiveness of the heat transfer models adopted in each category in predicting the current experimental trends. In addition to that, the parameters in each correlation were analysed against the relevant fluid parameters identified from the sensitivity study. The heat transfer correlations were catagorised into four groups, namely (i) correlations considering less than four parameters and developed based on a specific working fluid, (ii) correlations considering less than four parameters and developed for multiple working fluids, (iii) correlations considering at least four parameters and have been developed based on data on a specific fluid and (iv) correlations developed for multiple working fluids. Correlations in group (ii) and (iv), i.e. developed based on multiple working fluids generally involve a large databank of flow boiling data from various sources.

The top three performing correlations in the prediction of the flow boiling results of fluid HFE-7200 in a parallel microchannel heat sink were the Sun and Mishima [176], Kim and Mudawar [184] and Kandlikar and Balasubramaniam [187], which belonged to group (iv). This could be partly because correlations in group (iv) typically involve a large databank of flow boiling data from various sources and working fluids.

Common parameters in the above-mentioned correlations were the density ratio, boiling number and liquid-only Weber number. Boiling number is a non-dimensional form of heat flux. It captured the effect of heat flux and mass flux on flow boiling heat transfer. The density ratio as well as the reduced pressure ratio represented the effect of pressure on flow boiling behaviour well. The liquid-only Weber number along with the Reynolds numbers reflected changes in system mass flux. The former correlated the effect of surface tension in microscale heat transfer while the latter was sensitive to vapour quality. On top of that, the Martinelli parameter, employed in many Chen-type correlations [182], [194] as well as the Kim and Mudawar model [184] to calculate the enhancement factor of the convective boiling mechanism, captured the effect of heat flux, mass flux and degree of subcooling.

Nevertheless, a direct correlation between the number of dimensionless parameters included in the heat transfer prediction method was not observed in the current assessment. Furthermore, heat transfer correlations employing Cooper's nucleate pool boiling correlation, such as the Mahmoud and Karayiannis [182] and Bertsch et al. [181], were found to under-predict the experimental heat transfer coefficient. Replacing the nucleate boiling correlation with the Sun and Mishima [176] nucleate boiling model, developed specifically for flow boiling, showed vast improvements in their prediction accuracy. This could be because of the enhanced bubble nucleation activity in flow boiling (thus higher nucleate boiling heat transfer coefficients) compared to the pool boiling mode due to additional inertia forces that affect bubble departure behaviour in microchannels. The assessment also found that the prediction results of the Bertsch et al. [181] correlation, which assumes a developing laminar single-phase gaseous flow can be improved with the adoption of the turbulent Dittus-Boelter relation.

The prediction capability of the heat transfer correlations was also assessed for the local heat transfer trend obtained at P = 1 bar, G = 200 kg/m^{2}s and ΔT_{sub} = 10 K at $q_w^{"}$ = 106.8 kW/m^2. Local heat transfer coefficients peaked near the onset of boiling and generally decreased along the channel with vapour quality. Bubble nucleation in the liquid film in the annular flow regime was observed in our flow visualisation, indicating the contribution of both the nucleate boiling and convective mechanisms even in the high vapour quality region.

The evaluation showed that the asymptotic model of Kim and Mudawar [184], which considered both the nucleate boiling and convective boiling mechanism performed very well in both the prediction of the average two-phase heat transfer coefficient as well as the local heat transfer trend with respect to local vapour quality. In contrast, the nucleate boiling model of Sun and Mishima [176] predicted no change in local heat transfer coefficients with vapour quality. The superposition model, which also takes into account both heat transfer mechanisms in flow boiling, predicted an increasing heat transfer trend with respect to vapour quality. This was because the nucleate boiling suppression factor decreased with vapour quality at a nominal wall heat flux and mass flux condition. The trend of the suppression factor in superposition models should be investigated further, but appeared to be well correlated with the exit vapour quality or the liquid Reynolds number, the latter which decreases with increasing vapour quality.

Other than that, the correlation of Fang et al. [174] managed to capture the variation in local heat transfer coefficients with vapour quality along the channel, although the magnitude of heat transfer coefficients were several times larger the experimental heat transfer value, due to the fluid-dependent parameter. This is attributed to the liquid viscosity ratio, which is evaluated at the wall temperature of the channel. However, this correlation may not be suitable in applications where intricate surface temperature measurements are not readily obtainable. This is also the case for flow-pattern based heat transfer models, such as the three-zone model of Thome et al. [151], which have to be used in conjunction with flow pattern maps that currently do not show agreement in the community.

Table 6.7: Flow boiling heat transfer correlations.

Author(s)	Correlation	Remarks
Enhancement-factor models		
Fang [173]	$h_{tp} = \left(\frac{k_f}{D_h}\right)\left[\frac{0.0061\,(S+F)\,Re_f\,Pr_f^{0.4}Fa^{0.11}}{\ln\left(\frac{1.023\,\mu_{lf}}{\mu_{lw}}\right)}\right]$ If $Bo < 0.0026$, $S = 30000\,Bo^{1.13}$ If $Bo \geq 0.0026$, $S = 36$ $F = \left(\frac{1 - x_e}{x_e}\right)^{0.95}\left(\frac{\rho_f}{\rho_g}\right)^{0.4}$	Fluid: R134a Single/multichannels $D_h = 0.19 – 8$ mm $G = 42 – 1500$ kg/m^2 s $q_w^{"} = 1 – 165$ kW/m^2 $x = 0 – 1$ $P_{sat} = 3 – 13$ bar
Thiangtham et al. [117]	$h_{tp} = \left(\frac{k_f}{D_h}\right)\left[\frac{10^{16.7}\,We_{fo}^{2.7}\,Bo^{0.3}}{Re_{fo}^{2.7}\left(\frac{\rho_f}{\rho_g}\right)^{0.9}}\right]$	Fluid: R134a Multichannels $D_h = 0.42$ mm $G = 150 – 600$ kg/m^2 s $q_w^{"} = 3 – 127$ kW/m^2 $x = 0.05 – 0.92$ $T_{sat} = 13 – 23$ °C
Fang et al. [174]	$h_{tp} = \left(\frac{k_f}{D_h}\right)\left[\frac{F_f\,M^{-0.18}\,Bo^{0.98}\,Fr_{fo}^{0.48}Bd^{0.72}\left(\frac{\rho_f}{\rho_g}\right)^{0.29}Y}{\ln\left(\frac{\mu_{lf}}{\mu_{lw}}\right)}\right]$ If $P_r \leq 0.43$, $Y = 1$ If $P_r > 0.43$, $Y = 1.28 - P_r^{1.15}$ $F_f = 1850$ (for fluids not defined)	Fluids: 13 fluids Single/multichannels $D_h = 0.21 – 32$ mm $G = 10 – 1782$ kg/m^2 s $q_w^{"} = 0.2 – 4788$ kW/m^2 $x = 0 – 1$ $P_r = 0.0045 – 0.93$
Nucleate boiling models		
Tran et al. [177]	$h_{tp} = 84000\left(Bo^2\,We_{fo}\right)^{0.3}\left(\frac{\rho_f}{\rho_g}\right)^{-0.4}$	Fluids: R12, R113 Single $D_h = 2.4 – 2.92$ mm $G = 50 – 832$ kg/m^2 s $q_w^{"} = 7.5 – 129$ kW/m^2 $P_r = 0.045 – 0.2$
Yu et al. [178]	$h_{tp} = 6400{,}000\left(Bo^2\,We_{fo}\right)^{0.27}\left(\frac{\rho_f}{\rho_g}\right)^{-0.2}$	Fluid: Water Single $D_h = 2.98$ mm $G = 50 – 200$ kg/m^2 s $q_w^{"} = 50 – 200$ kW/m^2 $P_{sat} = 2$ bar

Sun and Mishima [176]	$h_{tp} = \frac{6\ Re_{fo}^{1.05}\ Bo^{0.54}}{We_{fo}^{0.191}\left(\frac{\rho_f}{\rho_g}\right)^{0.142}}$	Fluids: 11 fluids Single D_h = 0.21 – 6.5 mm G = 44 – 1500 kg/m^2 s $q_w^{"}$ = 5 – 109 kW/m^2
Superposition models		
Bertsch et al. [181]	$h_{tp} = h_{nb}S + h_{cv}F$ $h_{nb} = 55\ P_r^{0.12 - 0.434 \ln Rp}(-\log P_r)^{-0.55}\ M^{-0.5}\ q_w^{" 0.67}$ $h_{cv} = h_{cv,f}\ (1 - x_e) + h_{cv,g}\ x_e$ $h_{cv,i} = \left(\frac{k_f}{D_h}\right)\left[3.66 + \frac{0.0668\left(\frac{D_h}{L_{ch}}\right)Re_{fo}Pr_f}{1+ 0.04\left[\left(\frac{D_h}{L_{ch}}\right)Re_{fo}Pr_f\right]^{2/3}}\right]$ $S = (1 - x_e)$ $F = 1 + 80(x_e^2 - x_e^6)\ EXP\ (-0.6\ Co)$	Fluids: 12 Single/multichannel D_h = 0.16 – 2.92 mm G = 20 – 3000 kg/m^2 s $q_w^{"}$ = 4 – 1150 kW/m^2 x = 0 – 1 Co = 0.3 – 0.4
Mahmoud and Karayiannis [182]	$h_{tp} = h_{nb}S + h_{cv}F$ $h_{nb} = 55\ P_r^{0.12 - 0.434 \ln Rp}(-\log P_r)^{-0.55}\ M^{-0.5}\ q_w^{" 0.67}$ If $Re_f \le 2000$, $h_{cv} = 4.36\left(\frac{k_f}{D_h}\right)$ If $Re_f > 2000$, $h_{cv} = 0.023\ Re_f^{0.8}\ Pr_f^{0.4}\left(\frac{k_f}{D_h}\right)$ $F = \left(1+\frac{2.812\ Co^{-0.408}}{X_M}\right)^{0.64}$ $X_M = \left(\frac{f_f}{f_g}\right)^{0.5}\left(\frac{\rho_g}{\rho_f}\right)^{0.5}\left(\frac{1 - x_e}{x_e}\right)$ $S = \frac{1}{1 + 2.56 \times 10^{-6}\left(Re_f\ F^{1.25}\right)^{1.17}}$	Fluid: R134a Single D_h = 0.52 – 4.26 mm G = 100 – 700 kg/m^2 s $q_w^{"}$ = 1.7 – 158 kW/m^2 $x < x_{dryout}$ P_{sat} = 6 – 14 bar
Eraghubi et al. [194]	$h_{tp} = h_{nb}S + h_{cv}F$ $h_{nb} = 55\ P_r^{0.12 - 0.434 \ln Rp}(-\log P_r)^{-0.55}\ M^{-0.5}\ q_w^{" 0.67}$ $h_{cv} = 0.023\ Re_f^{0.8}\ Pr_f^{0.4}\left(\frac{k_f}{D_h}\right)$ $S = \frac{1}{1 + 2.56 \times 10^{-6}\left(Re_f\ F^{1.25}\right)^{1.17}}$ If $\frac{1}{X_{tt}} > 0.1$, $F = 2.35\left(\frac{1}{X_{tt}} + 0.213\right)^{0.736}$ If $\frac{1}{X_{tt}} \le 0.1$, $F = 1$ $X_{tt} = \left(\frac{\mu_f}{\mu_g}\right)^{0.1}\left(\frac{\rho_g}{\rho_f}\right)^{0.5}\left(\frac{1 - x_e}{x_e}\right)^{0.9}$	Fluid: HFE-7000 Single D_h = 8 mm G = 50 – 150 kg/m^2 s $q_w^{"}$ = 2.5 – 60 kW/m^2 P_{sat} = 1.2 bar
Asymptotic models		

Liu and Winterton [183]	$h_{tp} = [(h_{nb}S)^2 + (h_{cv}F)^2]^{0.5}$ $h_{nb} = 55\ P_r^{0.12 - 0.434 \ln Rp}(-\log P_r)^{-0.55}\ M^{-0.5}\ q_w{}^{" 0.67}$ $h_{cv} = 0.023\ Re_f^{0.8}\ Pr_f^{0.4}\left(\frac{k_f}{D_h}\right)$ $S = \frac{1}{1 + 0.055\ F^{0.1} Re_f^{0.16}}$ $F = \left[1 + x_e\ Pr_f\left(\frac{\rho_f}{\rho_g} - 1\right)\right]^{0.35}$	Fluids: 9 fluids Single D_h = 2.95 – 32 mm G = 12.4 – 8179.3 kg/m^2 s $q_w{}^{"}$ = 0.3 – 262 kW/m^2 P_r = 0.0023 – 0.895
Kim and Mudawar [184]	$h_{tp} = [(h_{nb})^2 + (h_{cv})^2]^{0.5}$ $h_{nb} = h_{sp,f}\left[2345\left(Bo\ \frac{P_H}{P_w}\right)^{0.7} P_r^{0.38}\ (1 - x_e)^{-0.51}\right]$ $h_{cv} = h_{sp,f}\left[5.2\left(Bo\ \frac{P_H}{P_w}\right)^{0.08} We_{fo}^{-0.54} + 3.5\left(\frac{1}{X_{tt}}\right)^{0.94}\left(\frac{\rho_g}{\rho_f}\right)^{0.25}\right]$ $h_{sp,f} = 0.023\ Re_f^{0.8}\ Pr_f^{0.4}\left(\frac{k_f}{D_h}\right)$	Fluids: 18 fluids Single/multichannel D_h = 0.19 – 6.5 mm G = 19 – 1608 kg/m^2 s x = 0 – 1 P_r = 0.005 – 0.69
Choi et al. [163]	$h_{tp} = [(h_{nb})^2 + (h_{cv})^2]^{0.5}$ $h_{nb} = 0.17\ Re_f^{0.17}\ We_{f,m}^{-0.23}\ Bo^{-0.44}\left(\frac{k_f}{D_h}\right)$ $h_{cv} = 0.27\ Re_f^{0.51}\ We_{f,m}^{-0.23}\ Co^{-0.46}\left(\frac{k_f}{D_h}\right)$ $We_{f,m} = 0.021 + We_{fo}\ (1 - x_e^{2.458})$	Fluids: FC-72 Multichannel D_h = 0.28 mm G = 100 – 458 kg/m^2 s $q_w{}^{"}$ = 5.6 – 49 kW/m^2 x = 0 – 0.96
Predominant mechanism models		
Kandlikar and Balasubramaniam [187]	$h_{tp} = MAX\{h_{nb}, h_{cv}\}$ $h_{nb} = h_{sp,f}\ (1 - x_e)^{0.8}\left[0.6683\ Cv^{-0.2} + 1058 Bo^{0.7} F_f\right]$ $h_{cv} = h_{sp,f}\ (1 - x_e)^{0.8}\left[1.136\ Cv^{-0.9} + 667.2 Bo^{0.7} F_f\right]$ $F_f = 1$ $h_{sp,f} = Nu_3\left(\frac{k_f}{D_h}\right)$	Fluids: 14 fluids Single/Multichannels D_h = 0.19 – 32 mm G = 13 – 8179 kg/m^2 s $q_w{}^{"}$ = 5.5 – 90.8 kW/m^2 x < 0.8 (dryout)
Docoulombier et al. [188]	$h_{tp} = MAX\{h_{nb}, h_{cv}\}$ $h_{nb} = 131\ P_r^{-0.0063}(-\log P_r)^{-0.55}\ M^{-0.5}\ q_w{}^{" 0.58}$ If Bo ≥ 1.1 x 10^{-4} $h_{cv} = h_{sp,f}\left[1.47 \times 10^4\ Bo + 0.93\left(\frac{1}{X_{tt}}\right)^{2/3}\right]$ If Bo < 1.1 x 10^{-4} $h_{cv} = h_{sp,f}\left[1 + 1.8\left(\frac{1}{X_{tt}}\right)^{0.986}\right]$ $X_{tt} = \left(\frac{\mu_f}{\mu_g}\right)^{0.1}\left(\frac{\rho_g}{\rho_f}\right)^{0.5}\left(\frac{1 - x_e}{x_e}\right)^{0.9}$	Fluid: CO_2 Single D_h = 0.529 mm G = 200 – 1200 kg/m^2 s $q_w{}^{"}$ = 10 – 30 kW/m^2

	$h_{sp,f} = 0.023\ Re_f^{0.8}\ Pr_f^{0.4} \left(\frac{k_f}{D_h}\right)$	
Shah [150]	$h_{tp} = F\ h_{sp,f}\ MAX\{E, S\}$ $h_{sp,f} = 0.023\ Re_f^{0.8}\ Pr_f^{0.4} \left(\frac{k_f}{D_h}\right)$ $F = 2.1 - 0.008\ We_{go} - 110Bo$ We_{go} and Fr_{fo} based on D_{hp}, all others based on D_h. $D_{hp} = \frac{4\ (W_{ch}H_{ch})}{W_{ch} + 2H_{ch}}$ If $Fr_{fo} \geq 0.04$, $J = Cv$ If $Fr_{fo} < 0.04$, $J = 0.38\ Fr_{fo}^{-0.3}\ Cv$ $S = 1.8\ J^{-0.8}$ If $J > 1$ and $Bo \geq 3 \times 10^{-5}$ $E = 230\ Bo^{0.5}$ If $J > 1$ and $Bo < 3 \times 10^{-5}$ $E = 1 + 46\ Bo^{0.5}$ If $0.1 < J \leq 1$ $E = F_{nb}\ Bo^{0.5}\ EXP(2.47\ J^{-0.1})$ If $Bo \geq 11 \times 10^{-4}$, $F_{nb} = 14.7$ If $Bo < 11 \times 10^{-4}$, $F_{nb} = 15.3$	Fluids: 30 fluids Single/multichannel $D_h = 0.38 – 27.1$ mm $G = 15 – 2437$ kg/m^2 s $P_r = 0.0046 – 0.787$
Hybrid models		
Lee and Mudawar [190]	If $0 < x_e \leq 0.05$ $h_{tp} = 3.856\ X_{M,i}^{0.267}\ h_{sp,f}$ If $0.05 < x_e \leq 0.55$ $h_{tp} = 436.48\ Bo^{0.522}\ We_{fo}^{0.351}\ X_{M,i}^{0.665}\ h_{sp,f}$ If $0.55 < x_e \leq 1$ $h_{tp} = MAX\{108.6\ X_{M,i}^{1.665} h_{sp,f}, h_{sp,g}\}$ $h_{sp,f} = Nu_3 \left(\frac{k_f}{D_h}\right)$ If $Re_g \leq 2000$, $h_{sp,g} = Nu_3 \left(\frac{k_g}{D_h}\right)$ If $Re_g > 2000$, $h_{sp,g} = 0.023\ Re_g^{0.8}\ Pr_g^{0.4} \left(\frac{k_g}{D_h}\right)$ If $Re_f \leq 2000$ and $Re_g \leq 2000$, $X_{M,i} = X_{tt}$ If $Re_f \leq 2000$ and $Re_g > 2000$, $X_{M,i} = \left(\frac{f_f\ Re_g^{0.25}}{0.079}\right)^{0.5} \left(\frac{\rho_g}{\rho_f}\right)^{0.5} \left(\frac{1 - x_e}{x_e}\right)^{0.5}$	Fluids: For $x < 0.05$, water. For $0.05 < x < 0.55$, water and R134a. For $x > 0.55$, R134a. Multichannel $G = 127 – 654$ kg/m^2 s $P_{sat} = 1.44 – 6.6$ bar

	f_f based on Shah and London [266]	
Qi et al. [192]	If $x_e < 0.3$ $h_{tp} = 1059.83\ Bo^{0.454}\ We_{fo}^{0.045}\ K_p^{0.106}\ X_{tt}^{0.107}\ Co^{-1.825}\ \left(\frac{k_f}{D_h}\right)$ If $x_e \geq 0.3$ $h_{tp} = 0.0042\ Bo^{-0.872}\ We_{fo}^{-0.059}\ K_p^{0.293}\ X_{tt}^{0.065}\ Co^{-1.704}\ \left(\frac{k_f}{D_h}\right)$ $K_p = \frac{P_i}{\left[\sigma\ g\ \left(\rho_f - \rho_g\right)\right]^{0.5}}$	Fluids: N_2 Single $D_h = 0.531 – 1.931$ mm
Li and Wu [191]	If $BdRe_f^{0.5} \leq 200$ (Microscale) $h_{tp} = 22.9\ \left(BdRe_f^{0.5}\right)^{0.355}\ \left(\frac{k_f}{D_h}\right)$ If $BdRe_f^{0.5} > 200$ (Macroscale) $h_{tp} = 30\ \ Re_{fo}^{0.857}\ Bo^{0.714}\ \left(\frac{k_f}{D_h}\right)$	Fluids: 12 fluids Single/multichannels $D_h = 0.19 – 3.1$ mm $G = 20.3 – 1500$ kg/m^2 s $q_w^{"} = 0 – 715$ kW/m^2

7 Comparison with Pressure Drop Correlations

7.1 Introduction

In the current study, the flow boiling pressure drop of HFE-7200 was measured in a multi-microchannel array using a differential pressure transducer across the heat sink. The data reduction procedure applied to isolate the two-phase pressure drop data from the total measured pressure drop data are presented in Section 3.3. In summary, two-phase pressure drop in the channels increased with heat flux and exit vapour quality. Increasing the channel mass flux increased two-phase pressure drop while increasing the system pressure decreased flow boiling pressure drop at a nominal wall heat flux condition. The effect of inlet subcooling on two-phase pressure loss was less significant between ΔT_{sub} = 5 K and 10 K. Increasing the degree of subcooling to ΔT_{sub} = 20 K resulted in a notable reduction in flow boiling pressure drop.

The observed trends of pressure drop may be explained as follows. An increase in wall heat flux increases bubble nucleation activity and consequently the channel void fraction. The increased void fraction accelerates the flow, increasing the momentum pressure loss in the channels. The acceleration of the flow result in a steeper velocity gradient at the channel wall, also resulting in an increase in the frictional pressure drop. Increasing mass flux also result in an acceleration of the flow. Additionally, the effect of mass flux on two-phase pressure losses are depicted in Eq. (2.2) and (2.5), where both the frictional and acceleration pressure drop components are related to the term G^2. Increasing the operating pressure typically increases the vapour density and hence a notable reduction in the liquid-to-vapour density ratio present in the acceleration pressure drop component (see Eq. (2.5)). The larger vapour density induces a deceleration in the flow, yielding a smaller velocity gradient at the channel wall as well as lower frictional losses in the flow. On the other hand, the reduction of two-phase pressure drop with increasing degree of subcooling, particularly at ΔT_{sub} = 20 K, was attributed to delayed flow regime transitions from bubbly to slug, churn and annular flow in the heat sink.

7.2 Evaluation of Pressure Drop Correlations

The homogeneous flow model and existing macroscale and microscale two-phase pressure drop correlations based on the separated flow model were evaluated. These have been

discussed previously in Section 2.8 and summarised in Table 7.1. The prediction results are compared against the experimental data of HFE-7200 and assessed using the mean average deviation of the models, MAE, and percentage of data points captured within a ±30 % error band, θ_{30}. The void fraction model in the acceleration pressure drop component specified by each correlation is employed in the current evaluation. Where the void fraction correlation is not specified by the model [199], [205], the void fraction was calculated based on Lockhart-Martinelli's void fraction model (see Eq. (2.15)).

7.2.1 Macroscale Correlations

The prediction results of the macroscale correlations evaluated in this study are presented in Figure 7.1 and Figure 7.2. The homogeneous flow model [100] and the separated flow model of Lockhart-Martinelli [203] both tended to overpredict the pressure drop of HFE-7200 in the current study. Interestingly, the homogeneous model, which is generally believed to be appropriate for dispersed flows, performed better compared to the model proposed by Lockhart-Martinelli. The homogeneous model predicted the 42.3 % of the experimental data within the ±30 % error band, with a MAE of ±43.2 %, while the Lockhart-Martinelli predicted merely 17.3 % of the data with a much higher MAE of ±113.4 %. Microscale studies in [57], [81], [202], [209] also found that the Lockhart-Martinelli [203] correlation overpredicted their pressure drop data.

The two-phase friction factor employed in the homogeneous model is $f_{tp} = 0.003$, based on the recommendation of Qu and Mudawar [206]. The homogeneous model was found to be highly dependent on f_{tp}. Evaluating f_{tp} based on the mixture viscosity model of Cicchitti et al. [201] and McAdams et al. [200] result in a much higher MAE of ±127.1 % and ±66.6 % respectively compared to $f_{tp} = 0.003$ was employed. The sensitivity of the prediction accuracy of the homogeneous model on the two-phase viscosity model was also concluded by Kim and Mudawar [202].

The B-coefficient method of Chisholm [211] performed the best amongst the macroscale correlations assessed in this study, predicting over 70 % of the pressure drop data with a MAE of only ±28.4 %. Notably, two-phase pressure drop at the inlet subcooling degree of 20 K was significantly overpredicted by all macroscale models, including the Chisholm B-coefficient

method. Pressure drop in the two-phase region ranged from 0.67 kPa to 3.63 kPa at this subcooling condition.

7.2.2 Microscale Correlations

The correlation of Mishima and Hibiki [205] and Qu and Mudawar [206] were the top two predictions overall, capturing almost 80 % of the data within a ±30 % error band with a MAE of only ±22.7 % and ±25.2 % respectively. Authors in [57], [81], [206], [213] have also obtained relatively high prediction accuracies of pressure drop data using the Mishima and Hibiki [205] correlation.

The frictional multiplier in both correlations are calculated based on the laminar-liquid and laminar-vapour Martinelli parameter. The Mishima and Hibiki [205] model gives Chisholm's C parameter as a function of the hydraulic diameter, which in this case is C = 3. Qu and Mudawar [206] considered the additional effect of mass velocity in the channels in the C parameter. C ranged from C = 2.64 – 5.15 at the highest mass flux condition. The void fraction model of Lockhart-Martinelli is applied for the Mishima and Hibiki [205] correlation while Zivi's void fraction model was used to estimate acceleration pressure loss in Qu and Mudawar [206]. Nonetheless, the choice of void fraction correlations did not appear to significantly affect (less than ±2 % for the MAE and θ_{30} in the case of the above-mentioned correlations) the prediction results of microscale pressure drop methods with the assumption of the separated flow model. As mentioned above, this was similarly concluded in Kim and Mudawar [202].

Similar to the Qu and Mudawar [206] correlation, the Lee and Garimella [81] model, also expresses Chisholm's parameter as a function of mass flux and hydraulic diameter. Nonetheless, the latter generally overestimated two-phase pressure drop, only capturing 30.8 % of the data within the error band. Both correlations were in fact developed for the flow boiling of water in parallel microchannel heat sinks. The latter was proposed based on an investigation of several heat sinks with hydraulic diameters ranging from D_h = 0.16 to 0.57 mm while the former only investigated one hydraulic diameter (i.e. D_h = 0.35 mm).

Overall, the top three performing pressure drop prediction methods were the Mishima and Hibiki [205], Qu and Mudawar [206] and Chisholm's B-coefficient [211] model.

Although the Kim and Mudawar [202] correlation was developed based on a large database of pressure drop data involving several working fluids and configurations, the present evaluation found that the model tended to underpredict pressure drop results at low vapour quality and overpredict two-phase pressure drop at moderate to high vapour qualities. The pressure drop correlation given by Keepaiboon et al. [207] also resulted in underpredictions at low exit vapour qualities and overpredictions at moderate to high exit vapour qualities. The correlation predicted only 34.6 % of datapoints with a MAE of ±48.1 %. This could be because only 288 datapoints from the consolidated database (with a total of 2378 points) were related to rectangular multichannel configurations. Nevertheless, the Chisholm parameter in Li and Hibiki [199], proposed specifically for multichannel heat sink configurations overpredicted most of the pressure drop data. The correlation only predicted 32.7 % of the multi-microchannel pressure drop data of HFE-7200 with a relatively large MAE of ±54 %. The databank considered by Li and Hibiki [199] also included experimental work on micro-pin fins [292] and trapezoidal channels [293].

Tran et al. [212], Huang and Thome [208] and Markal et al. [209] predicted less than 30 % of the experimental pressure drop results in the current study. Interestingly, Chisholm's parameter in Markal et al. [209] resulted in a negative value. This resulted in mostly a negative two-phase multiplier and hence negative frictional pressure drop values. Incidentally, two-phase pressure drop was generally underpredicted by this model.

Notably, all correlations overpredicted most of the two-phase pressure drop data obtained at ΔT_{sub} = 20 K. These points are indicated by red outlines in Figure 7.1 to Figure 7.5. The pressure drop at the highest subcooling condition was lower at a given mass flux and wall heat flux condition due to a delay in flow regime transition. As mentioned above, the delayed flow pattern transitions could be due to lower bubble nucleation activity and lower channel void fraction at higher degrees of inlet subcooling, thus decreasing two-phase pressure drop in the channels.

The general overprediction of two-phase pressure drop at the highest degree of subcooling could be related to delayed flow pattern transitions in the channel. Quibén and Thome [294] found that flow pattern effects, which are particularly important at low mass fluxes and in the high vapour quality region, were not accounted for in most two-phase pressure drop models. The authors segregated their experimental pressure drop data of R134a, R22 and R410A in

horizontal tubes according to the Wojtan et al. [295] flow pattern map. Friction factor correlations were proposed for each flow regime based on simplified interfacial flow structures including of the bubbly, slug, annular and mist flow regimes. Quibén et al. [296] extended the previous work and modified the annular friction factor relation for flattened copper tubes with equivalent diameters of 5.3 mm – 8.6 mm. Similarly, Choi and Kim [297] also noted a strong dependency of microchannel two-phase frictional pressure losses on flow patterns. In order to improve the pressure drop prediction of adiabatic two-phase flows in singular rectangular microchannels (D_h = 0.14 – 0.49 mm), the authors proposed individual Chisholm's constants for the bubbly, transition and liquid ring flow regime. The above studies show that two-phase pressure drop is intrinsically related to flow regimes and have a significant effect on the prediction accuracy of two-phase pressure drop.

Increasing the degree of inlet subcooling decreases the exit vapour quality and saturated length in the channels at a nominal wall heat flux condition. Additionally, the gas viscosity, evaluated at the inlet temperature of the heat sink, decreases with increasing inlet subcooling. This indirectly affected the calculation of the two-phase frictional multiplier through the Martinelli parameter, Chisholm's constant as well as Γ in Chisholm [211] and Tran et al. [212]. The estimated void fraction using the three void fraction models also did not exhibit a significant dependency on inlet subcooling. However, lower bubble nucleation activity at higher subcooling could affect channel void fraction at higher subcooling.

Furthermore, in Eq. (2.2) and (2.5), the exit vapour quality, the term G^2 and density ratio were relatively effective in capturing the effects of wall heat flux, mass flux and system pressure on two-phase pressure drop. On the other hand, changes in fluid properties and dimensionless parameters with increasing subcooling at a given mass flux condition were subtler compared to property variations corresponding to changes in the other operating parameters.

Further investigations should be conducted in order to clarify the effect of inlet subcooling on flow patterns, as well as the inter-dependence of flow patterns and flow boiling pressure drop in microchannels.

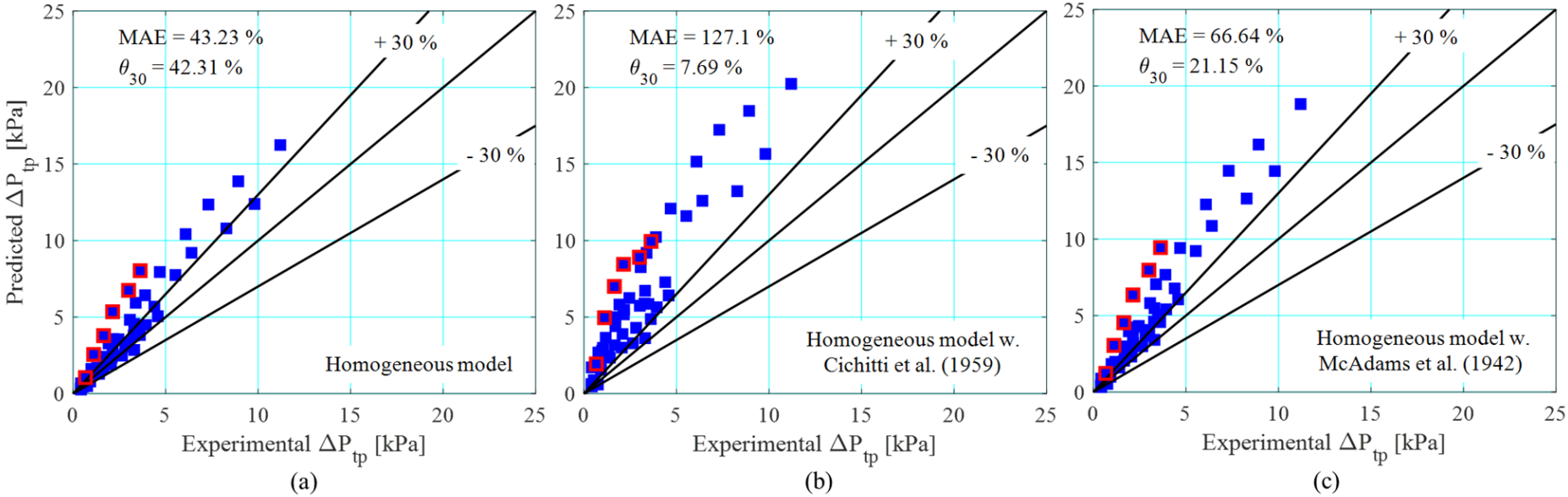

Figure 7.1: Comparison of HFE-7200 flow boiling pressure drop data with the homogeneous model based on (a) f_{tp} = 0.003 [206], (b) the mixture viscosity model of Cichitti et al. [201] and (c) the mixture viscosity model of McAdams et al. [200].

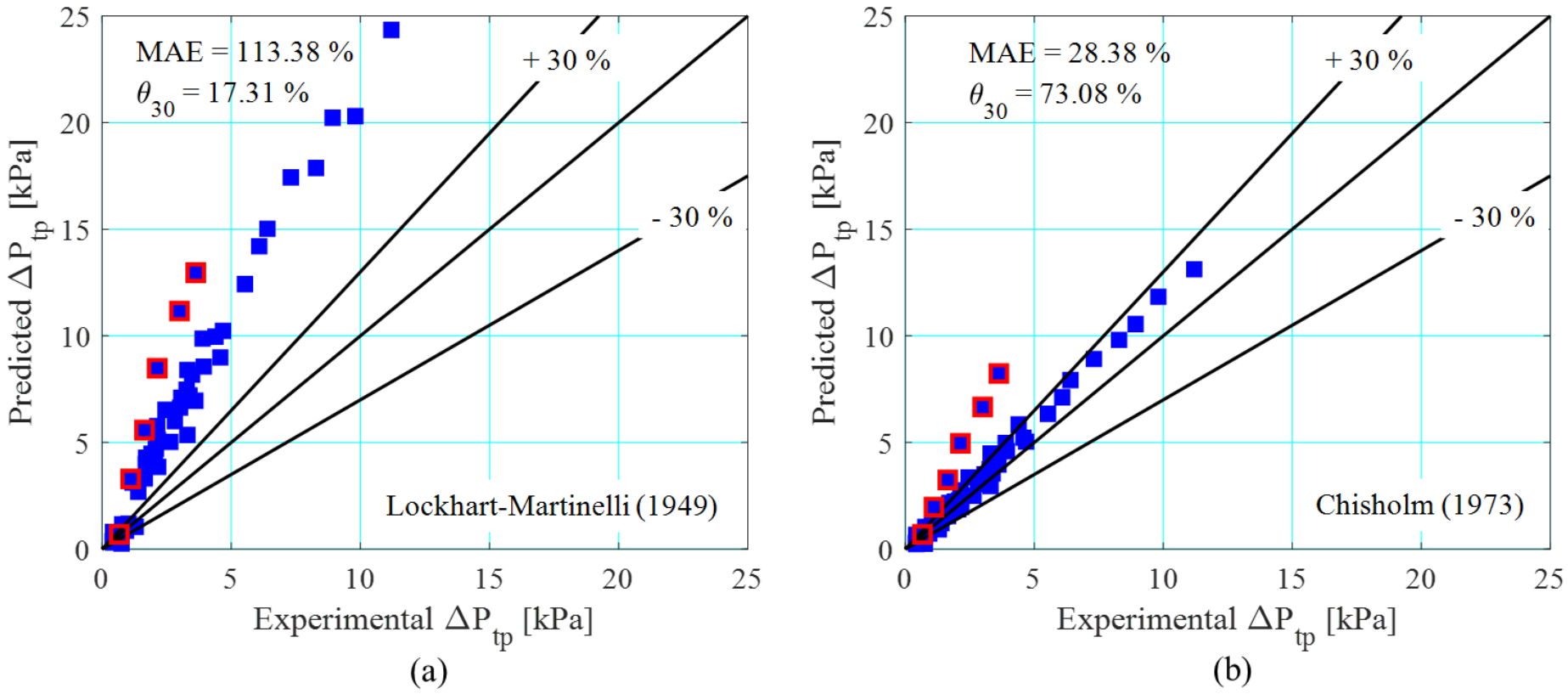

Figure 7.2:Comparison of HFE-7200 flow boiling pressure drop data with (a) the Lockhart-Martinelli [203] correlation and (b) Chisholm's B-coefficient method [211].

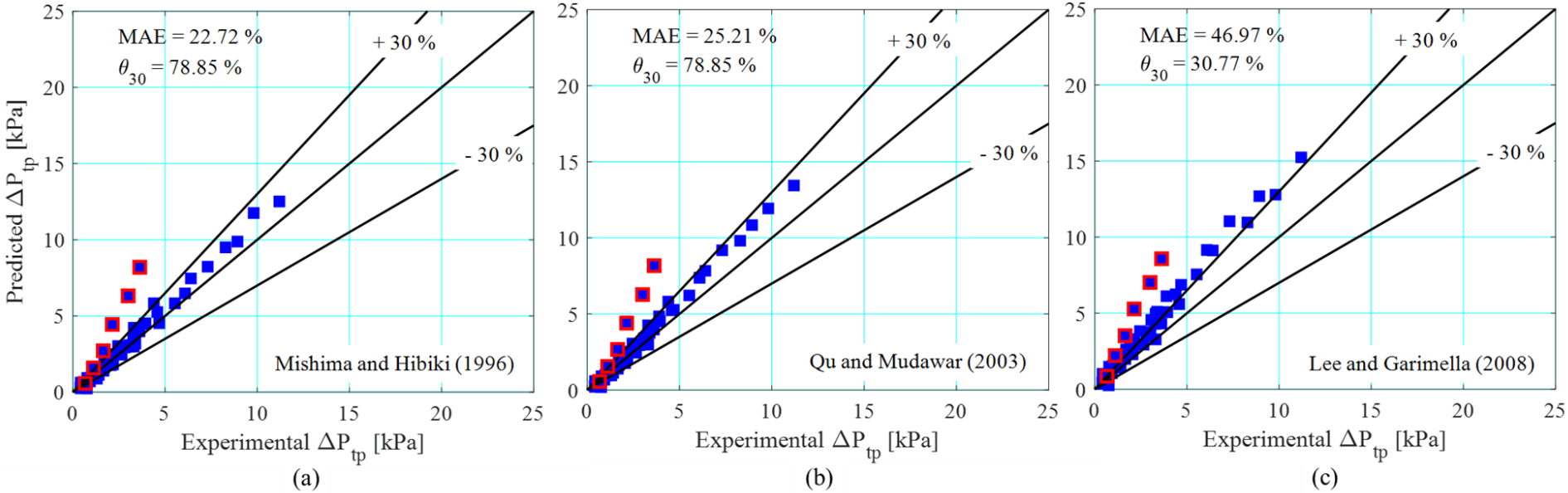

Figure 7.3: Comparison of HFE-7200 flow boiling pressure drop data with the correlations of (a) Mishima and Hibiki [205], (b) Qu and Mudawar [206] and (c) Lee and Garimella [81].

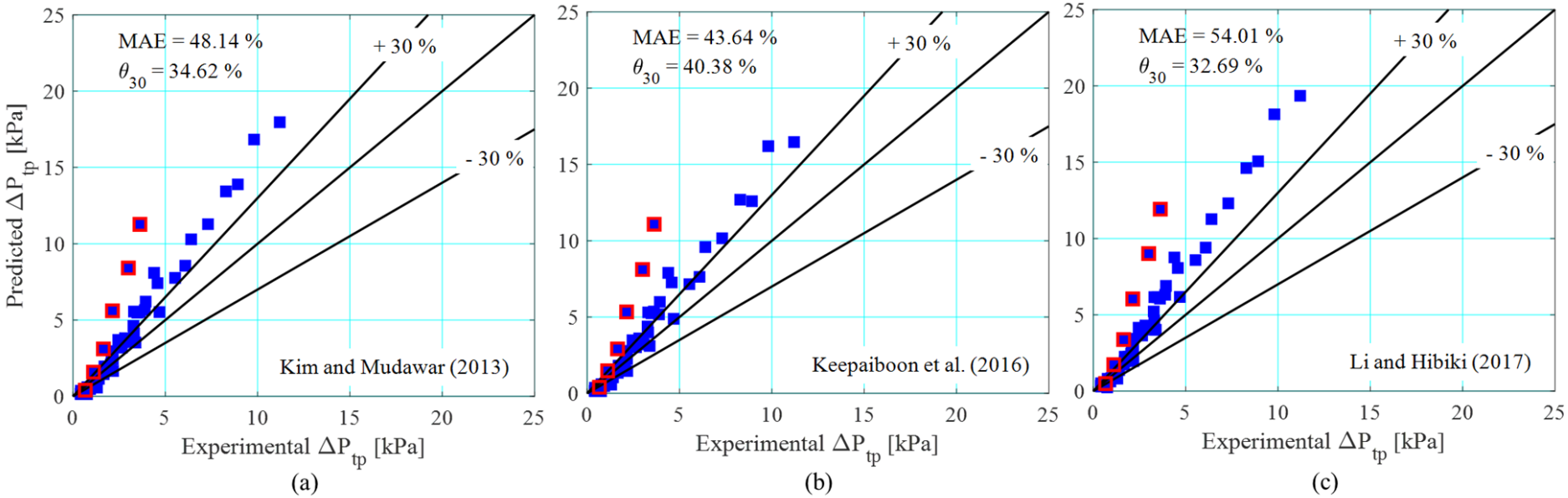

Figure 7.4: Comparison of HFE-7200 flow boiling pressure drop data with the correlations of (a) Kim and Mudawar [202], (b) Keepaiboon et al. [207] and (c) Li and Hibiki [199].

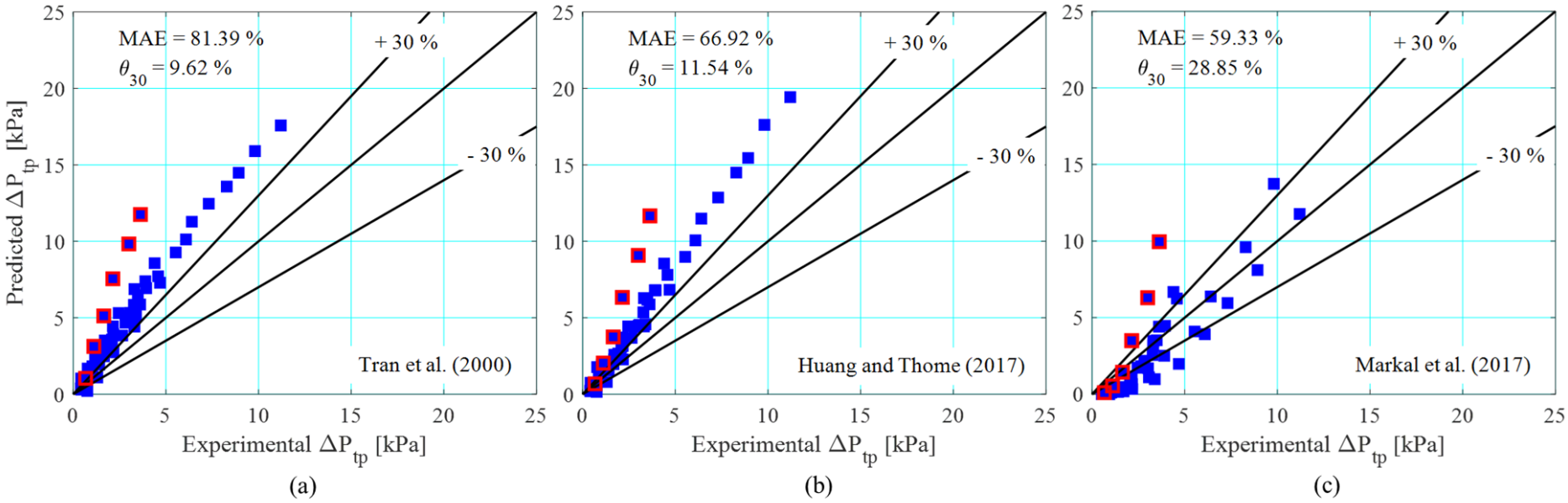

Figure 7.5: Comparison of HFE-7200 flow boiling pressure drop data with the correlations of (a) Tran et al. [212], (b) Huang and Thome [208] and (c) Markal et al. [209].

7.3 Summary

Macroscale and microscale two-phase pressure drop correlations were evaluated against the flow boiling pressure drop results of HFE-7200 in the plain microchannels. The accuracy of the homogeneous model was highly dependent on the two-phase viscosity model employed for the calculation of the two-phase friction factor. The top performing correlations were the Mishima and Hibiki [205] and Qu and Mudawar [206] correlations developed for microscale flow based on Chisholm's coefficient, and the B-coefficient method of Chisholm [211] proposed for macroscale flows. The Mishima and Hibiki [205] correlation has predicted two-phase pressure drop data well in several other studies. Employment of either the Lockhart-Martinelli or Zivi void fraction model was found to only have a small effect on prediction accuracy. There was a general overprediction of flow boiling pressure drop at the subcooling condition of 20 K by the correlations assessed in the current study. This could be because of delayed flow regime development in the channels, as flow pattern effects were typically not accounted for in the pressure drop prediction methods. A number of other studies have also noted the dependency of flow boiling pressure drop on dominant flow regimes and should be investigated further in order to improve the prediction of two-phase pressure drop in microchannels.

Table 7.1: Two-phase pressure drop correlations.

Model/Author(s)	Correlation	Remarks
Homogeneous flow model [100]	$\Delta P_f = \frac{2 f_{tp} L_{sat} G^2 v_f}{D_h} \left[1 + \left(\frac{x_e}{2} \right) \left(\frac{v_{fg}}{v_f} \right) \right]$ $\Delta P_{acc} = G^2 v_{fg} x_e$ $f_{tp} = 0.003$ as recommended by Qu and Mudawar [206]	The liquid and vapour phase are assumed to flow in the channel at the same velocity.
Lockhart-Martinelli [203]	$\Delta P_f = \frac{L_{sat}}{x_e} \left[\int_{x=0}^{x=x_e} \frac{2 f_f G^2 (1 - x_e)^2 v_f}{D_h} \phi_f^2 \, dx \right]$ The two-phase frictional multiplier is calculated based on the method proposed by Chisholm [204]: $\varphi_f^2 = 1 + \frac{C}{X} + \frac{1}{X^2}$ where For laminar liquid-laminar vapour (vv), i.e. $Re_f < 2000$ and $Re_g < 2000$: $C = 5$ $X_{vv} = \left(\frac{\mu_f}{\mu_g} \right)^{0.5} \left(\frac{\rho_g}{\rho_f} \right)^{0.5} \left(\frac{1 - x_e}{x_e} \right)^{0.5}$ For turbulent liquid-laminar vapour (tv), i.e. $Re_f < 2000$ and $Re_g < 2000$: $C = 10$ $X_{tv} = \left(\frac{f_f}{f_g} \right)^{0.5} \left(\frac{\rho_g}{\rho_f} \right)^{0.5} \left(\frac{1 - x_e}{x_e} \right)$ For laminar liquid-turbulent vapour (vt), i.e. $Re_f < 2000$ and $Re_g < 2000$: $C = 12$ $X_{vt} = \left(\frac{f_f}{f_g} \right)^{0.5} \left(\frac{\rho_g}{\rho_f} \right)^{0.5} \left(\frac{1 - x_e}{x_e} \right)$ For turbulent liquid-turbulent vapour (tt), i.e. $Re_f > 2000$ and $Re_g > 2000$: $C = 20$ $X_{tt} = \left(\frac{\mu_f}{\mu_g} \right)^{0.1} \left(\frac{\rho_g}{\rho_f} \right)^{0.5} \left(\frac{1 - x_e}{x_e} \right)^{0.9}$ If $Re_k < 2000$, based on Shah and London [266] for rectangular channels: $f_k Re_k = 24 \left(1 - 1.355AR + 1.946AR^2 - 1.7012AR^3 + 0.9564AR^4 - 0.2537AR^5 \right)$	Separated flow model. $D_h = 1.49 – 25.83$ mm. Developed for water, benzene and oil.

	If $2000 \leq Re_k < 20{,}000$ $f_k = \frac{0.079}{Re_k^{0.25}}$ If $Re_k \geq 20{,}000$ $f_k = \frac{0.046}{Re_k^{0.2}}$ where k is represents f or g $\Delta P_{acc} = G^2 \nu_f \left[\frac{x_e^2}{\alpha_v} \frac{\rho_f}{\rho_g} + \frac{(1 - x_e)^2}{(1 - \alpha_v)} - 1 \right]$ $\alpha_v = \frac{1}{1 + 0.28 X_M}$ $X_M = \left(\frac{\mu_f}{\mu_g} \right)^{0.07} \left(\frac{\rho_g}{\rho_f} \right)^{0.36} \left(\frac{1 - x_e}{x_e} \right)^{0.64}$	
Chisholm B-coefficient method [211]	$\Delta P_f = \frac{L_{sat}}{x_e} \left[\int_{x=0}^{x=x_e} \frac{2 f_{fo} G^2 v_f}{D_h} \varphi_{fo}^2 \, dx \right]$ $\varphi_{fo}^2 = 1 + (\Gamma^2 - 1) [B x_e^{0.875} (1 - x_e)^{0.875} + x_e^{1.75}]$ $\Gamma = \left(\frac{\mu_g}{\mu_f} \right)^{0.5} \left(\frac{v_g}{v_f} \right)^{0.5}$ where If $G \leq 500$ and $\Gamma \leq 9.5$ $B = 4.8$ If $G \leq 500$ and $\Gamma \geq 9.5$ $B = \frac{15000}{\Gamma^2 G^{0.5}}$ If $G > 600$ and $9.5 \leq \Gamma \leq 28$ $B = \frac{21}{\Gamma}$ If $G \leq 600$ and $9.5 \leq \Gamma \leq 28$ $B = \frac{520}{\Gamma^2 G^{0.5}}$ If $500 \leq G \leq 1900$ and $\Gamma \leq 9.5$ $B = \frac{2400}{G}$ If $G > 1900$ and $\Gamma \leq 9.5$ $B = \frac{55}{G^{0.5}}$ If $Re_{ko} < 2000$, f_{ko} is based on Shah and London [266] for rectangular channels:	Developed for evaporating two-phase mixtures.

	$f_k\ Re_{ko} = 24\ 24\ \left(\begin{array}{c} 1 - 1.355AR + 1.946AR^2 - 1.7012AR^3 \\ + 0.9564AR^4 - 0.2537AR^5 \end{array} \right)$ If $2000 \le Re_{ko} < 20000$, $f_{ko} = \frac{0.079}{Re_{ko}^{0.25}}$ If $Re_{ko} \ge 20000$, $f_{ko} = \frac{0.046}{Re_{ko}^{0.2}}$ where k represents f or g $\Delta P_{acc} = G^2\ \nu_f \left[\frac{x_e^2}{\alpha_v} \frac{\rho_f}{\rho_g} + \frac{(1 - x_e)^2}{(1 - \alpha_v)} - 1 \right]$ $\alpha_v = 1 + \left(\frac{1 - x_e}{x_e} \right) \left(\frac{\rho_g}{\rho_f} \right) \sqrt{(1 - x_e) \left(1 - \frac{\rho_f}{\rho_g} \right)}$	
Mishima and Hibiki [205]	$\Delta P_f = \frac{L_{sat}}{x_e} \left[\int_{x=0}^{x=x_e} \frac{2\ f_f\ G^2\ (1 - x_e)^2\ v_f}{D_h} \phi_f^2\ dx \right]$ $\varphi_f^2 = 1 + \frac{C}{X_{vv}} + \frac{1}{X_{vv}^2}$ where $C = 21\ [\ 1 - e^{(-319\ D_h)}\ ]$ $\Delta P_{acc} = G^2\ \nu_f \left[\frac{x_e^2}{\alpha_v} \frac{\rho_f}{\rho_g} + \frac{(1 - x_e)^2}{(1 - \alpha_v)} - 1 \right]$ $\alpha_v = \frac{1}{1 + 0.28\ X_M}$ $X_M = \left(\frac{\mu_f}{\mu_g} \right)^{0.07} \left(\frac{\rho_g}{\rho_f} \right)^{0.36} \left(\frac{1 - x_e}{x_e} \right)^{0.64}$	$D_h = 1.05 – 4$ mm. Developed for various adiabatic flows including air–water in circular and rectangular ducts.
Tran et al. [212]	$\Delta P_f = \frac{L_{sat}}{x_e} \left[\int_{x=0}^{x=x_e} \frac{2\ f_{fo}\ G^2\ v_f}{D_h} \varphi_{fo}^2\ dx \right]$ $\varphi_{fo}^2 = 1 + (4.3\Gamma^2 - 1)\ [\ Co\ x_e^{0.875}\ (1 - x_e)^{0.875} + x_e^{1.75}\ ]$ $\Delta P_{acc} = G^2\ \nu_f \left[\frac{x_e^2}{\alpha_v} \frac{\rho_f}{\rho_g} + \frac{(1 - x_e)^2}{(1 - \alpha_v)} - 1 \right]$ $\alpha_v = \frac{1}{1 + \left(\frac{1 - x_e}{x_e} \right) \left(\frac{v_f}{v_g} \right)^{2/3}}$	$D_h = 2.46 – 2.92$ mm. $q_w'' = 2.2 – 129$ kW/m^2 $G = 44 – 832$ kg/m^2 s $P_{sat} = 1.38 – 8.35$ bar Developed for flow boiling pressure drop of R134a, R12 and R113 in circular and rectangular ducts.

Qu and Mudawar [206]	$\Delta P_f = \frac{L_{sat}}{x_e}\left[\int_{x=0}^{x=x_e} \frac{2 f_f G^2 (1-x_e)^2 v_f}{D_h} \phi_f^2 \, dx\right]$ $\varphi_f^2 = 1 + \frac{C}{X_{vv}} + \frac{1}{X_{vv}^2}$ where $C = 21\,[\,1 - e^{(-319 D_h)}\,](0.00418G + 0.0613)$ $\Delta P_{acc} = G^2 v_f \left[\frac{x_e^2}{\alpha_v}\frac{\rho_f}{\rho_g} + \frac{(1-x_e)^2}{(1-\alpha_v)} - 1\right]$ $\alpha_v = \frac{1}{1 + \left(\frac{1-x_e}{x_e}\right)\left(\frac{v_f}{v_g}\right)^{2/3}}$	D_h = 0.35 mm. G = 135 – 402 kg/m^2 s Developed for flow boiling of water in a parallel microchannel heat sink.
Lee and Garimella [81]	$\Delta P_f = \frac{L_{sat}}{x_e}\left[\int_{x=0}^{x=x_e} \frac{2 f_f G^2 (1-x_e)^2 v_f}{D_h} \phi_f^2 \, dx\right]$ $\varphi_f^2 = 1 + \frac{C}{X_{vv}} + \frac{1}{X_{vv}^2}$ where $C = 2566\, G^{0.5466} D_h^{0.8819}\,[\,1 - e^{(-319 D_h)}\,]$ $\Delta P_{acc} = G^2 v_f \left[\frac{x_e^2}{\alpha_v}\frac{\rho_f}{\rho_g} + \frac{(1-x_e)^2}{(1-\alpha_v)} - 1\right]$ $\alpha_v = \frac{1}{1 + \left(\frac{1-x_e}{x_e}\right)\left(\frac{v_f}{v_g}\right)^{2/3}}$	D_h = 0.162 – 0.571 mm. Developed for the flow boiling of water in silicon parallel microchannel heat sinks.
Kim and Mudawar [202]	$\Delta P_f = \frac{L_{sat}}{x_e}\left[\int_{x=0}^{x=x_e} \frac{2 f_f G^2 (1-x_e)^2 v_f}{D_h} \phi_f^2 \, dx\right]$ $\varphi_f^2 = 1 + \frac{C}{X} + \frac{1}{X^2}$ where If $Re_f < 2000$ $C = C_{non\text{-}boiling}\left[1 + 530 We_{fo}^{0.52}\left(Bo\frac{P_H}{P_W}\right)^{1.09}\right]$ If $Re_f \geq 2000$ $C = C_{non\text{-}boiling}\left[1 + 60 We_{fo}^{0.32}\left(Bo\frac{P_H}{P_W}\right)^{0.78}\right]$ For laminar liquid-laminar vapour (vv), i.e. $Re_f < 2000$ and $Re_g < 2000$: $C_{non\text{-}boiling} = 3.5 \times 10^{-5} Re_{fo}^{0.44} Su_{go}^{0.5}\left(\frac{\rho_f}{\rho_g}\right)^{0.48}$	D_h = 0.35 – 5.35 mm. G = 33 – 2738 kg/m^2 s Developed for the flow boiling of 9 working fluids including water, R134a, R245fa and FC-72 For single and multichannel configurations.

	For turbulent liquid-laminar vapour (tv), i.e. $Re_f \geq 2000$ and $Re_g < 2000$: $C_{non\text{-}boiling} = 8.7 \times 10^{-4}\ Re_{fo}^{0.17} Su_{go}^{0.5} \left(\frac{\rho_f}{\rho_g} \right)^{0.14}$ For laminar liquid-turbulent vapour (vt), i.e. $Re_f < 2000$ and $Re_g \geq 2000$: $C_{non\text{-}boiling} = 0.0015\ Re_{fo}^{0.59} Su_{go}^{0.19} \left(\frac{\rho_f}{\rho_g} \right)^{0.36}$ For turbulent liquid-turbulent vapour (tt), i.e. $Re_f \geq 2000$ and $Re_g \geq 2000$: $C_{non\text{-}boiling} = 0.39\ Re_{fo}^{0.03} Su_{go}^{0.1} \left(\frac{\rho_f}{\rho_g} \right)^{0.35}$ $\Delta P_{acc} = G^2 \nu_f \left[\frac{x_e^2}{\alpha_v} \frac{\rho_f}{\rho_g} + \frac{(1 - x_e)^2}{(1 - \alpha_v)} - 1 \right]$ $\alpha_v = \frac{1}{1 + \left(\frac{1 - x_e}{x_e} \right) \left(\frac{v_f}{v_g} \right)^{2/3}}$	
Keepaiboon et al. [207]	$\Delta P_f = \frac{L_{sat}}{x_e} \left[\int_{x=0}^{x=x_e} \frac{2 f_f G^2 (1 - x_e)^2 \nu_f}{D_h} \phi_f^2 \, dx \right]$ $\varphi_f^2 = 1 + \frac{C}{X} + \frac{1}{X^2}$ where $C = 1.93 \times 10^5\ Re_{fo}^{-1.18} Co^{-27.99} X^{0.93}$ $\Delta P_{acc} = G^2 \nu_f \left[\frac{x_e^2}{\alpha_v} \frac{\rho_f}{\rho_g} + \frac{(1 - x_e)^2}{(1 - \alpha_v)} - 1 \right]$ $\alpha_v = \frac{1}{1 + \left(\frac{1 - x_e}{x_e} \right) \left(\frac{v_f}{v_g} \right)^{2/3}}$	$D_h = 0.68$ mm $q_w'' = 7.63 – 49.46$ kW/m^2 $G = 600 – 1400$ kg/m^2 s $T_{sat} = 23$, 27 and 31 °C Developed for R134a in a single microchannel.
Li and Hibiki [199]	$\Delta P_f = \frac{L_{sat}}{x_e} \left[\int_{x=0}^{x=x_e} \frac{2 f_f G^2 (1 - x_e)^2 \nu_f}{D_h} \phi_f^2 \, dx \right]$ $\varphi_f^2 = 1 + \frac{C}{X} + \frac{1}{X^2}$ where For laminar liquid-laminar vapour (vv), i.e. $Re_f < 1000$ and $Re_g < 1000$: $C = 1.87\ Re_{tp}^{0.38} x_e^{0.35} N_{\mu tp}^{0.12}$	$D_h = 0.109$ to 4 mm $q_w'' = 6 – 6140$ kW/m^2 $G = 44 – 1114$ kg/m^2 s Developed for 8 working fluids including water, R134a, R245fa and CO_2.

	For turbulent liquid-laminar vapour (tv), i.e. $Re_f > 2000$ and $Re_g < 1000$: $C = 2.23\ Re_{tp}^{0.54}\ x_e^{0.25}\ N_{\mu tp}^{0.51}$ For laminar liquid-turbulent vapour (vt), i.e. $Re_f < 1000$ and $Re_g > 2000$: $C = 7.63\ Re_{tp}^{0.66}\ x_e^{0.43}\ N_{\mu tp}^{1.2}$ $\Delta P_{acc} = G^2\ v_f \left[\frac{x_e^2}{\alpha_v} \frac{\rho_f}{\rho_g} + \frac{(1 - x_e)^2}{(1 - \alpha_v)} - 1 \right]$ $\alpha_v = \frac{1}{1 + 0.28\ X_M}$ $X_M = \left(\frac{\mu_f}{\mu_g} \right)^{0.07} \left(\frac{\rho_g}{\rho_f} \right)^{0.36} \left(\frac{1 - x_e}{x_e} \right)^{0.64}$	For multichannel configurations.
Huang and Thome [208]	$\Delta P_f = \frac{L_{sat}}{x_e} \left[\int_{x=0}^{x=x_e} \frac{2\ f_f\ G^2\ (1 - x_e)^2\ v_f}{D_h}\ \phi_f^2\ dx \right]$ $\varphi_f^2 = 1 + \frac{C}{X} + \frac{1}{X^2}$ where For laminar liquid-laminar vapour (vv), i.e. $Re_f \leq 2000$ and $Re_g \leq 2000$: $C = 0.037\ Re_g^{1.7}\ Re_{fo}^{-0.83}$ For laminar liquid-turbulent vapour (vt), i.e. $Re_f \leq 2000$ and $Re_g > 2000$: $C = 0.9\ Re_g^{0.034}\ Re_{fo}^{0.2}$ For R1233zd(E) and if $Re_f < 2000$, $f_f = \frac{8.058}{Re_f}$ For all other fluids and $Re_f < 2000$, f_f is based on Shah and London [266] for rectangular channels: $f_f\ Re_f = 24 \left(1 - 1.355AR + 1.946AR^2 - 1.7012AR^3 + 0.9564AR^4 - 0.2537AR^5 \right)$ For all fluids and if $Re_f > 2000$, $f_f = \frac{0.079}{Re_f^{-0.25}}$ $\Delta P_{acc} = G^2\ v_f \left[\frac{x_e^2}{\alpha_v} \frac{\rho_f}{\rho_g} + \frac{(1 - x_e)^2}{(1 - \alpha_v)} - 1 \right]$	$q_w" = 200 – 640\ kW/m^2$ $G = 1250 – 2750\ kg/m^2 s$ Developed for flow boiling pressure drop in silicon microchannels. Working fluids: R1233zd(E), R245fa and R236fa.

	$\alpha_v = \dfrac{1}{1 + \left(\dfrac{1 - x_e}{x_e}\right)\left(\dfrac{v_f}{v_g}\right)^{2/3}}$	
Markal et al. [209]	$\Delta P_f = \dfrac{L_{sat}}{x_e}\left[\int_{x=0}^{x=x_e} \dfrac{2 f_f G^2 (1 - x_e)^2 v_f}{D_h} \phi_f^2 \, dx\right]$ $\varphi_f^2 = 1 + \dfrac{C}{X} + \dfrac{1}{X^2}$ where $C = -7.1 + \left[\dfrac{(1 - x_e)^{1.766}}{Re_{fo}^{0.12} AR^{0.031} Bo^{0.165} We_{fo}^{0.074} \left(\dfrac{v_f}{v_g}\right)^{0.233} \left(\dfrac{L_{sat}}{D_h}\right)^{0.247}}\right]$ $\Delta P_{acc} = G^2 v_f \left[\dfrac{x_e^2}{\alpha_v}\dfrac{\rho_f}{\rho_g} + \dfrac{(1 - x_e)^2}{(1 - \alpha_v)} - 1\right]$ $\alpha_v = \dfrac{1}{1 + \left(\dfrac{1 - x_e}{x_e}\right)\left(\dfrac{v_f}{v_g}\right)^{2/3}}$	$D_h = 0.1 – 0.25$ mm $q_w'' = 36 – 121.8$ kW/m^2 $G = 51 – 324$ kg/m^2 s Developed for water in multichannel heat sinks.

8 Flow Boiling in Coated Microchannels

8.1 Introduction

In this chapter, flow boiling results obtained in the coated microchannel heat sink are presented and evaluated against the baseline results obtained in the plain microchannel test section (discussed in Chapter 4). Flow visualisation was also conducted in the coated channels and the range of experimental conditions were similar to the plain heat sink, as summarised in Table 3.3. Section 8.2 compares the surface topology of the plain and coated channel walls. Single-phase validation results using the coated test section is detailed in Section 8.3. An assessment of the single-phase results against the results obtained in the plain microchannel heat sink is also included. The repeatability of two-phase experiments in the coated channels is evaluated in Section 8.4. Flow boiling results obtained in the coated microchannel heat sink at varying heat flux, system pressure, mass flux and inlet subcooling conditions with respect to the baseline results are discussed thoroughly in Section 8.5. The effect of the surface coating on the suppression of flow instabilities, heat transfer enhancement and pressure drop penalty were also analysed. A summary of the coating effect is given in Section 8.6.

8.2 Surface Characterisation

As reviewed extensively in Section 2.7, surface characteristics and operating parameters, which affect fluid properties, significantly influence bubble nucleation behaviour on boiling surfaces. Microchannel two-phase flow pattern development, heat transfer and pressure drop behaviour are accordingly influenced by bubble nucleation and growth. Since the working fluid and range of operating conditions investigated in this study were kept constant in the plain and coated microchannel heat sinks, the primary difference in bubble generation behaviour is likely caused by differences in the surface structure of the plain and coated channel walls. In order to achieve a better understanding of the physics behind the effects of the coating on flow boiling behaviour, in relation to the baseline tests conducted in the plain heat sink, the surface topography of the bottom wall of the CNC micro-milled plain copper microchannels and coated microchannels were analysed using scanning electron microscopy (SEM). SEM analysis was conducted using the LEO 1455VP at the Experimental Techniques Centre in Brunel University London.

8.2.1 Plain Surface

Figure 8.1 depict the surface characteristics analysed at the bottom wall of a random channel in the plain microchannel heat sink. The magnification was set to 5000x on the electron microscope. Defects on the copper surface, produced by feed marks, smeared material and material debris during the micro-milling process result in cavities which, with sufficient wall superheat, may support bubble nucleation in flow boiling. Examples of potential nucleation cavities are marked accordingly on the figure. Shallow cavities are typically observed on the milled copper surface.

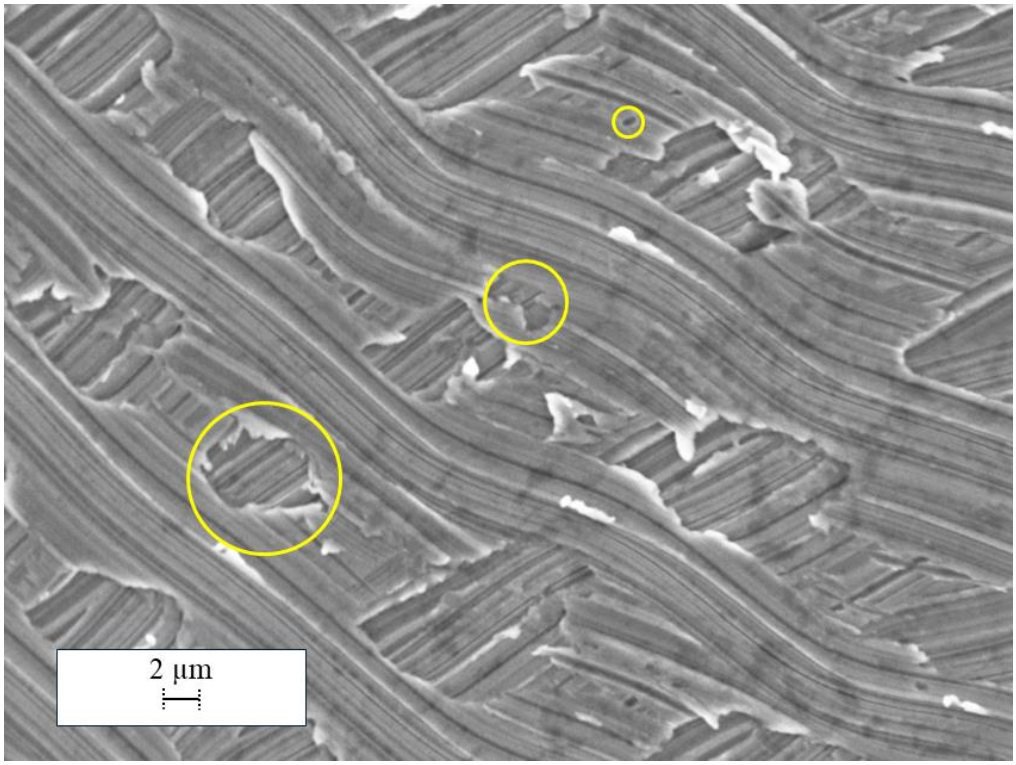

Figure 8.1: SEM image of the bottom channel wall on the end-milled plain microchannel heat sink at a magnification of 5000x.

A nominal square area of 35 µm x 35 µm was selected from Figure 8.1 to conduct an analysis, using ImageJ, of the cavity radius sizes found on the plain copper surface. This is shown in Figure 8.2. The radius of the cavities was approximated by assuming a circular area, using the area of the cavities identified by the software. A total of 15 cavities were identified on the surface, with pore area ranging from 0.2 μm^2 to 64.8 μm^2 and cavity radius ranging from 0.25 µm to 4.5 µm. The outlines of the cavities identified and distribution of the cavities are

illustrated in Figure 8.1(a) and Figure 8.1(b) accordingly. Importantly, the range of cavity sizes lie within the range of active nucleation sites as predicted using Hsu's model for HFE-7200 and operating conditions of P = 1 bar and ΔT_{sub} = 10 K for a hydraulic diameter of 475 µm, as shown in Figure 8.3.

The distribution and number of cavities identified on the plain channel are also superimposed on the plot. Note that the curve correspond to the bottom axes (i.e. Wall Superheat [K]) while the bars correspond to the top axes (i.e. Number of cavities [-]). The figure shows that nucleation may be triggered from wall superheat degree of 1 K onwards, with a minimum cavity radius of around 2 µm. Based on the distribution, no cavities between the size range of 2 µm to 2.5 µm are available on the surface for nucleation. Hence onset of nucleation is delayed to higher degrees of wall superheat. For a nominal wall superheat of 5 K, cavities within the range of 0.2 µm to 10.8 µm may be activated. From the plain channels, cavities between the range 0.25 µm to 4.5 µm were identified. This means that all 15 cavities on the area examined will be activated at a wall superheat degree of 5 K.

The working fluid, HFE-7200, is highly wettable on copper and has a contact angle of around 12°. The contact angle of HFE-7200 on a copper surface was measured using the static sessile droplet method at atmospheric conditions using an in-house contact angle goniometer setup, which includes high speed video imaging. The images were processed using FTA32 software, see Figure 8.4. As the test section was too large to fit into the measurement chamber, a flat copper surface was used for the contact angle measurements. The flat copper sample had an average surface roughness 0.073 µm, which is much smaller than the average surface roughness of the bottom wall of the actual plain copper channels, i.e. 0.23 µm (see Section 3.2). Nevertheless, the contact angle is not used in any calculations and only serves as a reference for the wettability of the working fluid on copper.

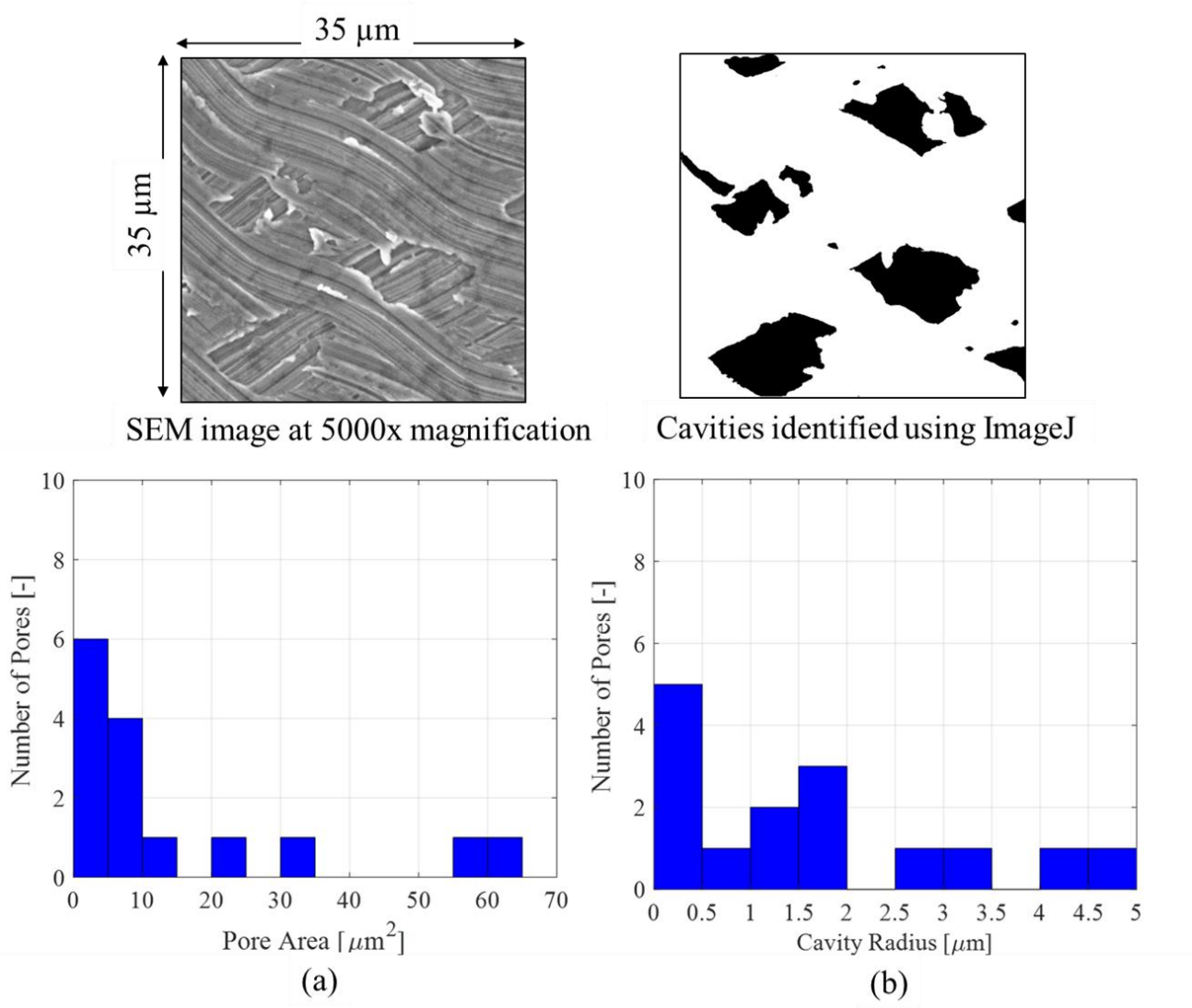

Figure 8.2: Results from image analysis on the plain channel, showing (a) the distribution of pore area and (b) the distribution of cavity radius on the surface.

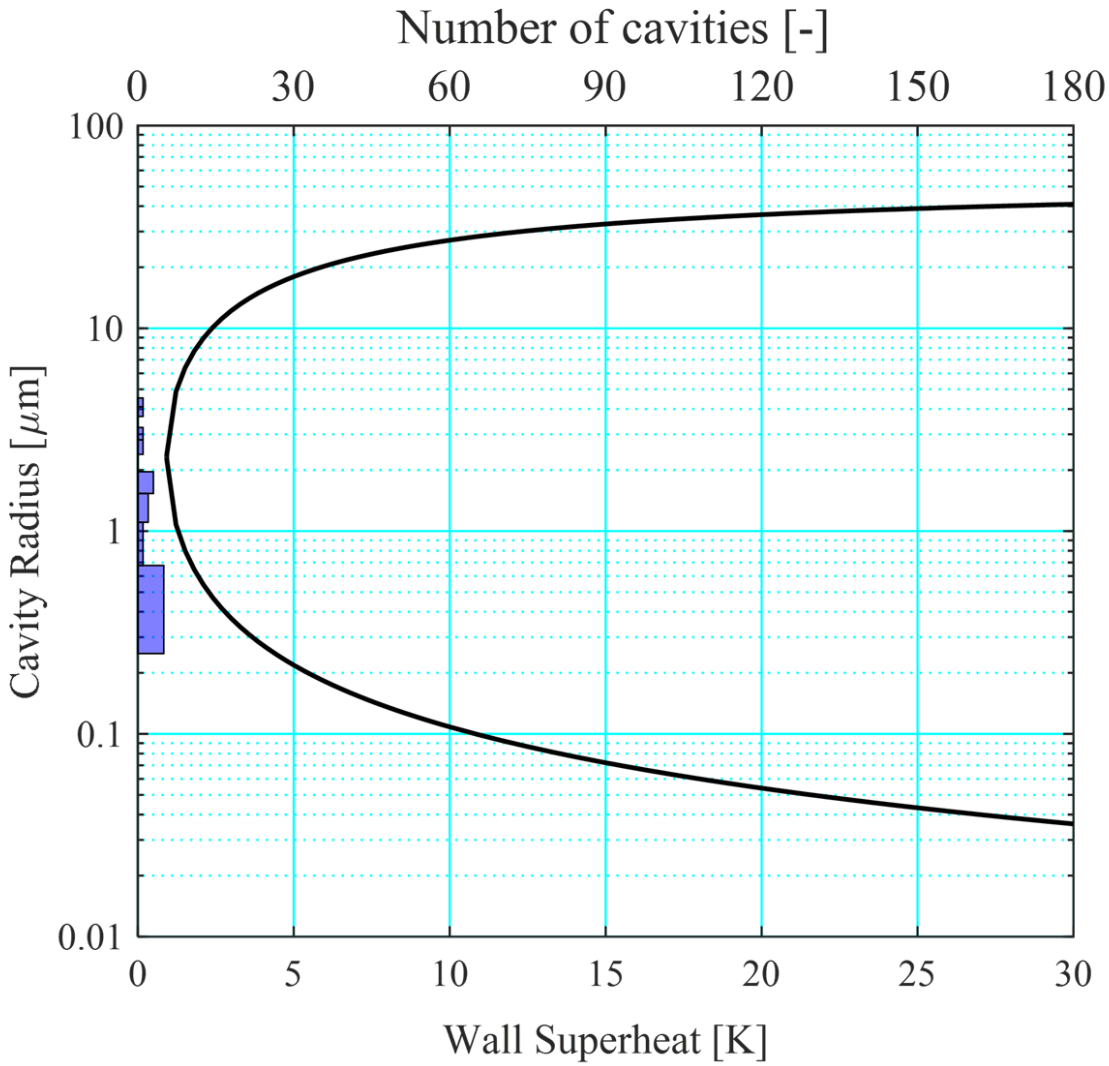

Figure 8.3: Comparison of surface cavities on the plain channel with the active cavity range predicted using Hsu's model at P = 1 bar and ΔT_{sub} = 10 K. The curves correspond to the bottom axes (i.e. Wall Superheat [K]) while the bars correspond to the top axes (i.e. Number of cavities [-]).

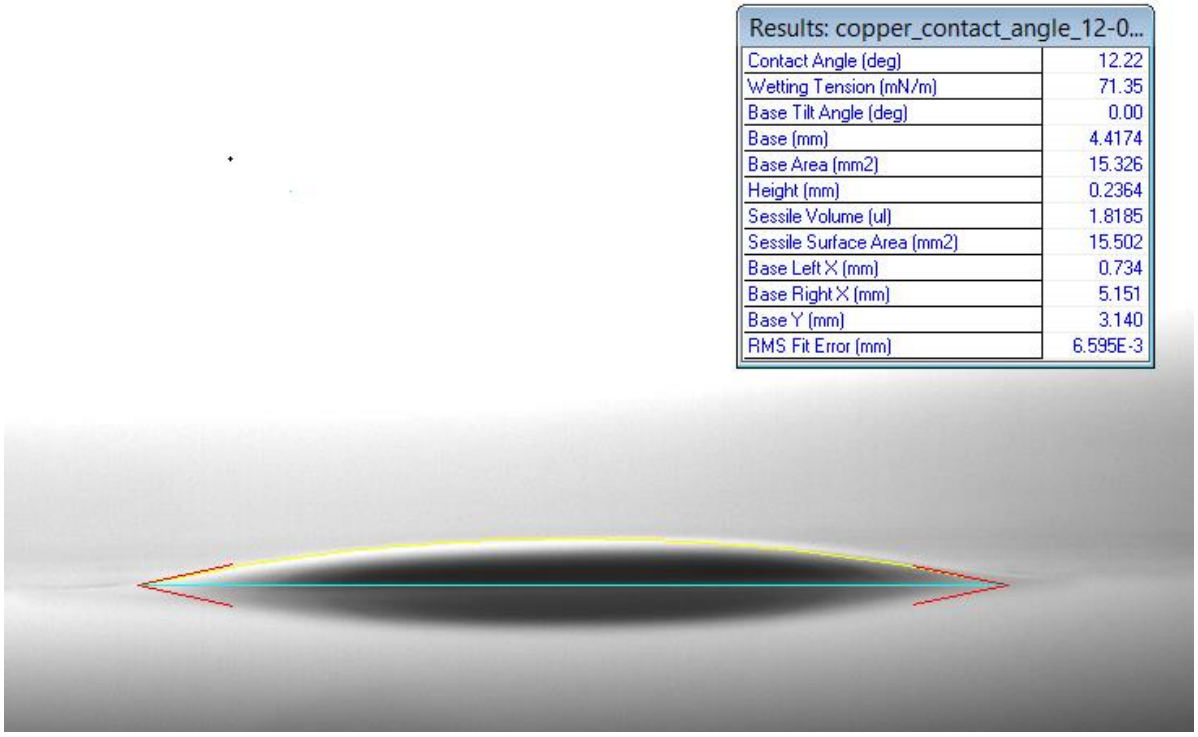

Figure 8.4: Contact angle of HFE-7200 measured on a flat copper sample at atmospheric conditions using the static sessile drop method. The contact angle is estimated to be 12.2 °.

8.2.2 Coated Surface

An SEM image of the coated channel surface, taken at the bottom wall of a random channel is shown in Figure 8.5. The image shown was taken at the same magnification, i.e. 5000x, as for the plain channels in Figure 8.1. A uniform layer of dendrite structures was deposited in random orientations on the channel. These could produce irregular pores that may potentially serve as nucleation sites on the coated surface. Examples of such cavities are marked on the figure. The thickness of the coating was measured to be around 5 µm to 10 µm, based on the width of the channel. This resulted in a maximum reduction in hydraulic diameter by ±4.2 % (the nominal hydraulic diameter of the plain channels is 475 µm), and the hydraulic diameter considered for the coated channels is 456 µm.

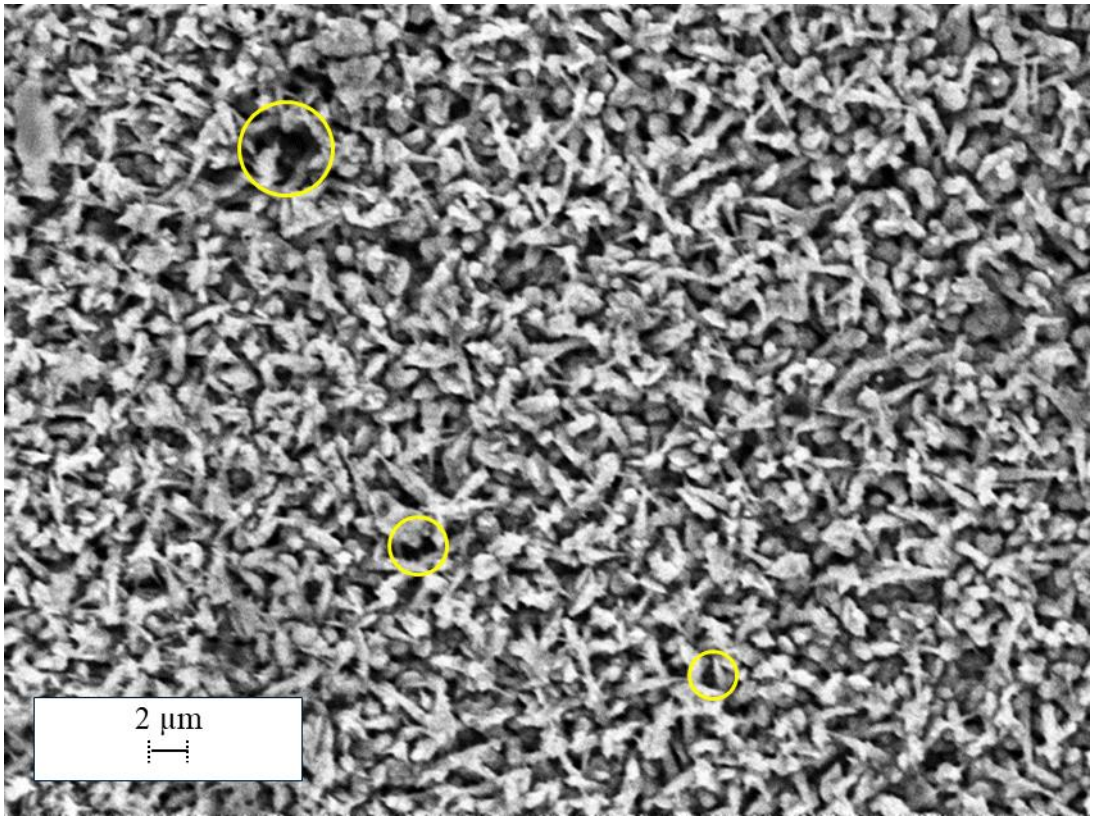

Figure 8.5: SEM image of the bottom channel wall on the coated microchannel heat sink at a magnification of 5000x.

Whilst Figure 8.5 is representative of the coating structure observed at the bottom wall of most channels, there were some variation in the coating structure, typically near the corners of the walls. This is shown in Figure 8.6. Nonetheless, this variation in coating structure was only observed in select channels under the SEM. Additionally, the size range of cavities resulting

from the different structure from these selected areas remained similar to those observed in Figure 8.5. Hence Figure 8.5 may be reasonably taken as the good representation of the coating structure on the channel bottom wall.

Agglomerates were also found near the top of the fins and the channel side walls. These are visible from Figure 8.7, shown at a smaller SEM magnification of 400x, near the edge of a fin on the coated heat sink. Additionally, Figure 8.8 shows agglomerates collected on the corners of certain channels, which was captured at a magnification of 500x from the top of the microchannels. Figure 8.7 and Figure 8.8 demonstrate the contrast in coating structure on the fins and on the corners of the channels. A relatively uniform layer of coating is observed to be deposited on the bottom wall of the channels. On the other hand, an uneven coating structure with agglomerates is visible on the top of the fins. The variation in coating structure near the channel corners and formation of agglomerates are related to the coating process. The hydraulic diameter assumed for the coated channel, i.e. 456 μm, is based on the maximum coating thickness of 10 μm, which accounts for the variation in coating structure on the channels. Overall, the heat transfer area of the coated channels is possibly also higher than the plain channels, owing to the additional surface area provided by the irregular structures of the coating.

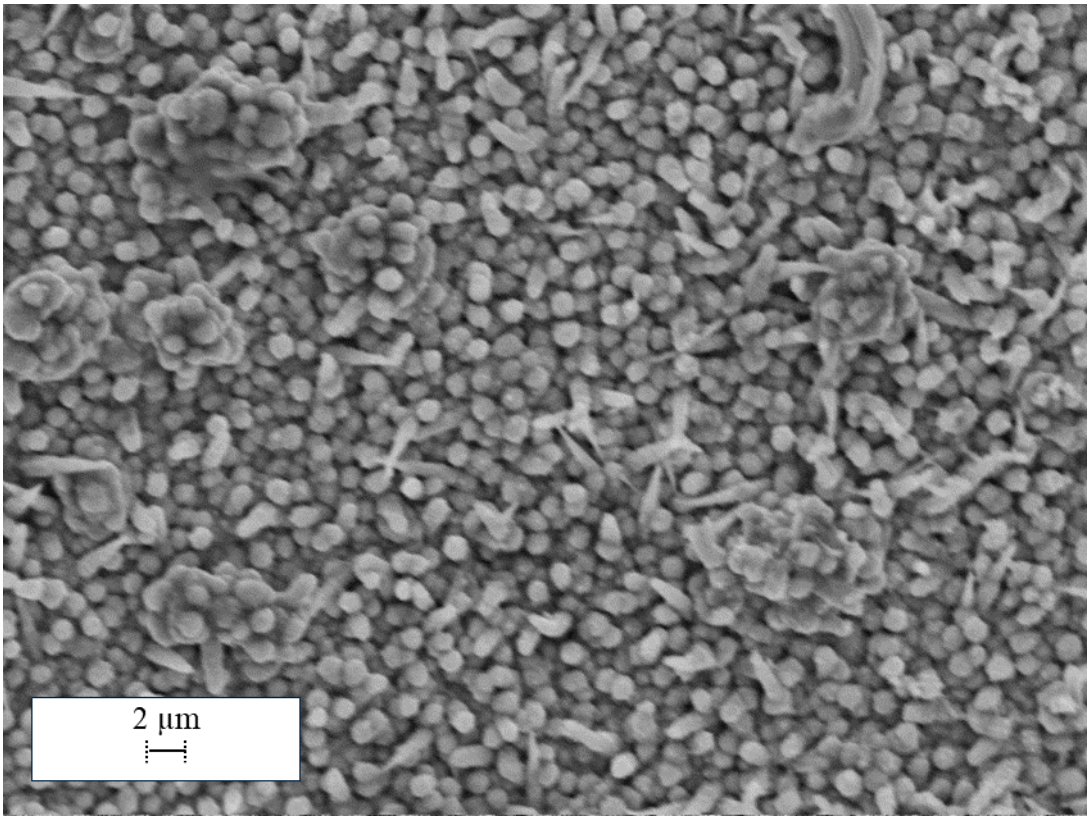

Figure 8.6: SEM of the coating structure near the channel corner on the bottom wall, taken at a magnification of 5000x.

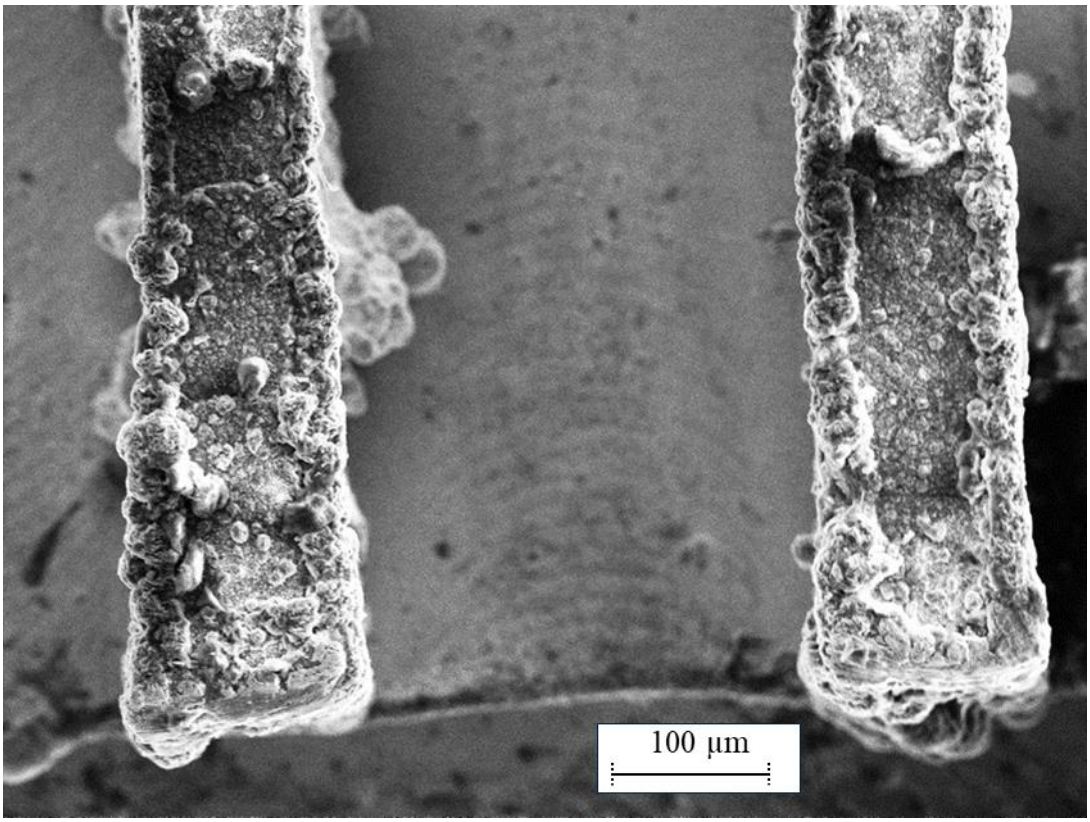

Figure 8.7: SEM image showing agglomerates on the top of the channel fins and down the side wall of the channel, taken at a magnification of 400x.

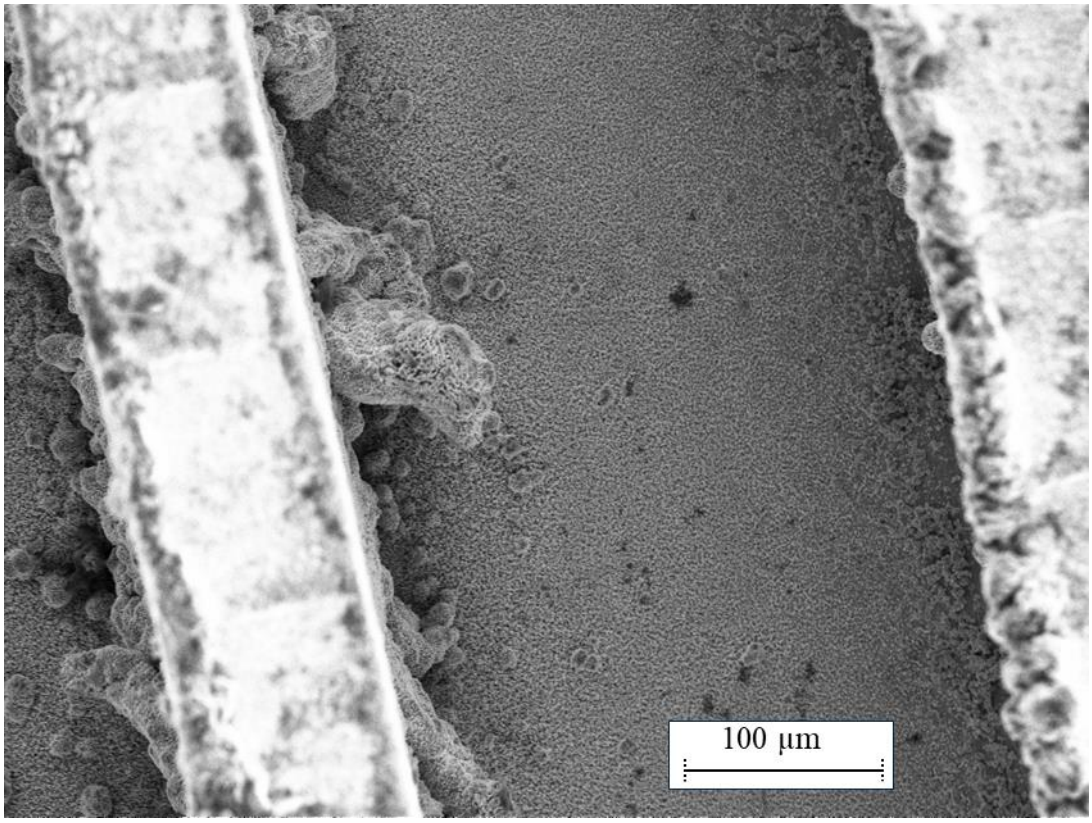

Figure 8.8: SEM image from the top of the channels showing agglomeration deposited in the corners but a relatively uniform coating structure on the channel bottom wall, taken at a magnification of 500x.

Notably, comparing the surface cavities marked in Figure 8.5 with the cavities observed on the plain channels, cavities identified on the coated surface appear to be more defined and deeper, in contrast to the shallow surface cavities observed on the plain, CNC-milled microchannels. This could encourage vapour trapping in the cavities and increase bubble generation frequency in the channels. It is important to note that features of larger sizes suitable as nucleation sites on both the plain and coated microchannels may be found at lower magnifications on the SEM. The images shown in Figure 8.1 and Figure 8.5 are only a comparison between the two surfaces at the equivalent magnification. Furthermore, the treated surface is clearly more densely populated with smaller cavities in comparison to the plain channels.

Image analysis was conducted using the same procedure as the plain channels above, i.e. based on a square area of 35 µm x 35 µm from an SEM image of the coating taken at 5000x magnification. The distribution of cavity size and radius on the coating is presented in Figure 8.9. The size of the cavities provided by the coating was between 0.1 µm to 1.7 µm, with the majority of cavity radii smaller than 1 µm on the image analysed. Typical cavity sizes are smaller in comparison to the plain channels, which exhibited cavities radii of up to 4.5 µm (see Figure 8.2). Nonetheless, the number of cavities are significantly higher on the coated surface in comparison to the plain surface. The total number of cavities identified on the same area on the plain area was 15 while the total number of cavities identified on the coated surface was 479. This means that the number of potential nucleation sites on the coated surface was almost 32 times higher than the CNC-milled plain copper channels.

Importantly, the size of cavities on the coated surface are also within the range of active nucleation sites, as predicted using Hsu's model for HFE-7200, see Figure 8.10. This has previously shown in Figure 8.3 for the plain microchannels. Comparing the two figures, it is clear that the coatings provide cavities in the smaller range for nucleation. It is also clear that the number of cavities available on the coated surface is substantially higher compared to the plain surface, as highlighted in Figure 8.9. For instance, both surfaces are populated with cavities between 0.25 µm and 4.5 µm, which would be activated with wall superheat degrees of 1 K to 4.5 K on the surface. There are 15 and 361 cavities on the plain and coated surface respectively within this range. Furthermore, as mentioned above, the cavities on the plain channels are relatively shallow, which might be difficult for vapour entrapment. Agglomerates found on the channel corners (see Figure 8.7 and Figure 8.8) may also act to trap vapour pockets, which could also potentially support bubble nucleation.

As highlighted in Section 8.2.1, HFE-7200 exhibits high wettability properties on copper. A flat copper sample was coated in a similar procedure as the coated microchannel test section in order to obtain a measure of the effect of the coating on contact angle. The contact angle measured on the coated flat sample was around 12.7 °, see Figure 8.11. This is similar to the value obtained on the flat copper sample, which indicates that the coating had a negligible effect on surface wettability in this study. Surface roughness measurements on the coated sample were also attempted, but was not quantified as the available measurement techniques were not suitable for the average roughness range.

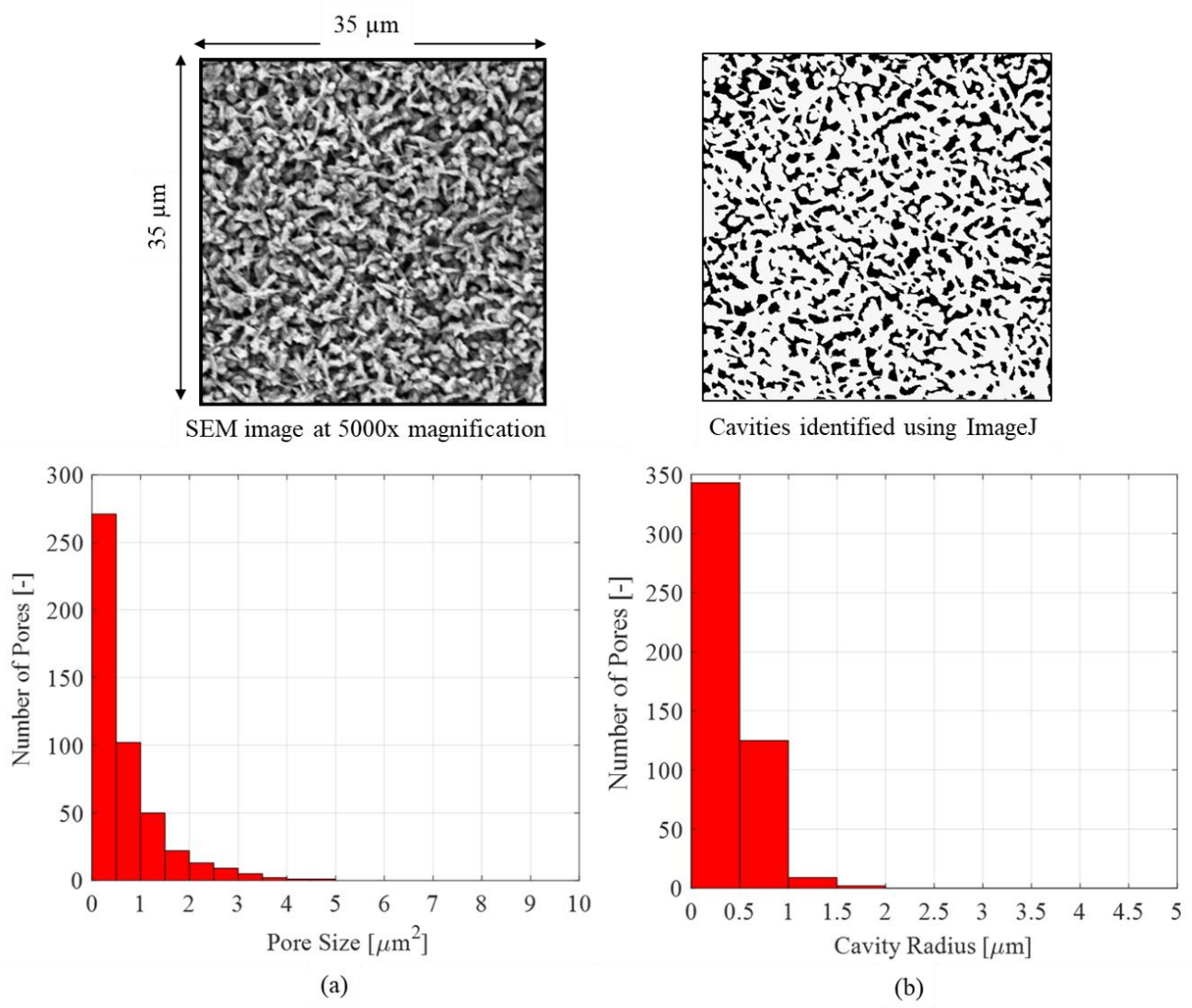

Figure 8.9: Results from image analysis on the coated channel, showing (a) the distribution of pore area and (b) the distribution of cavity radius on the surface.

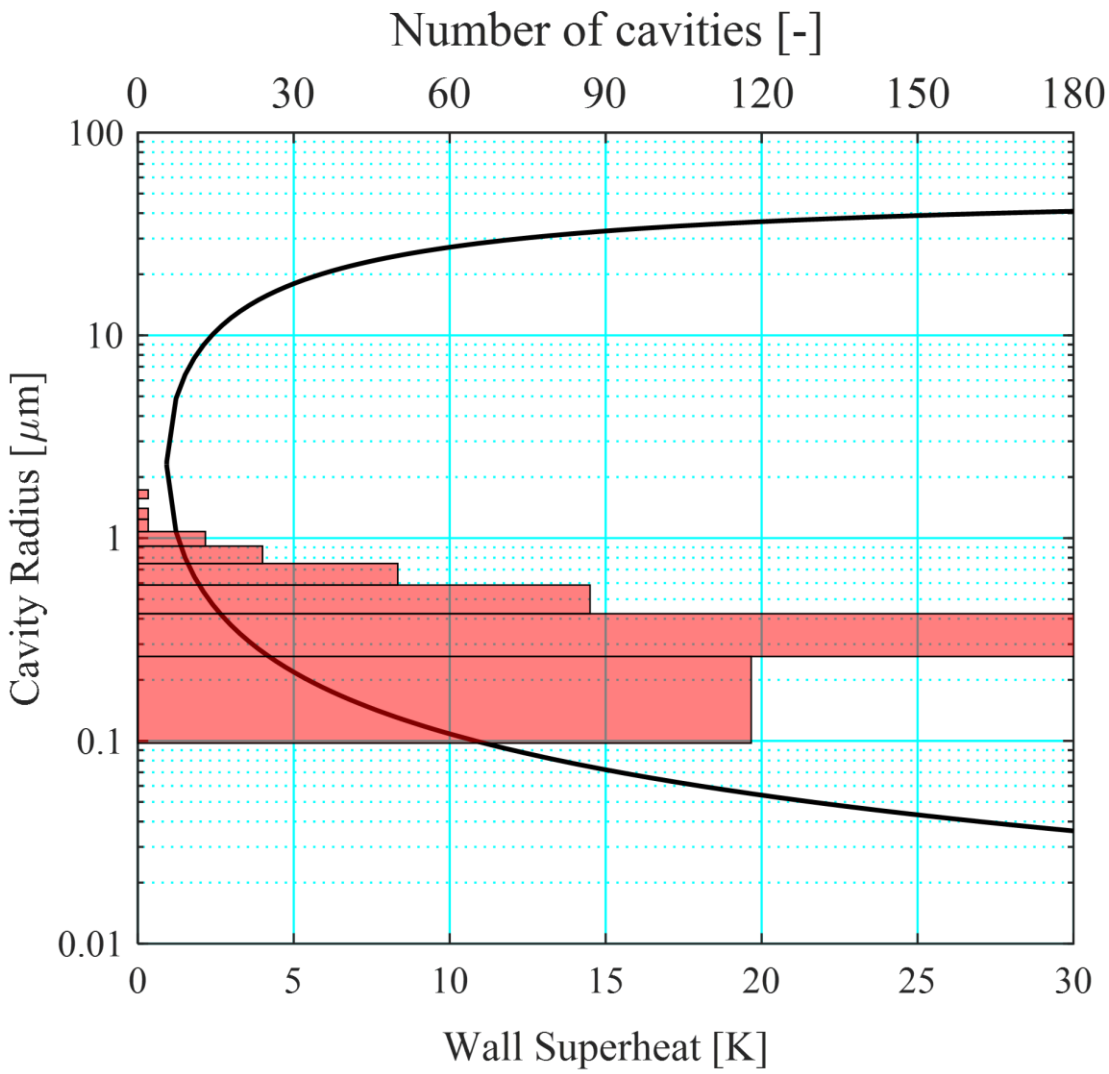

Figure 8.10: Comparison of surface cavities on the coated channel with the active cavity range predicted using Hsu's model at P = 1 bar and ΔT_{sub} = 10 K. The curves correspond to the bottom axes (i.e. Wall Superheat [K]) while the bars correspond to the top axes (i.e. Number of cavities [-]).

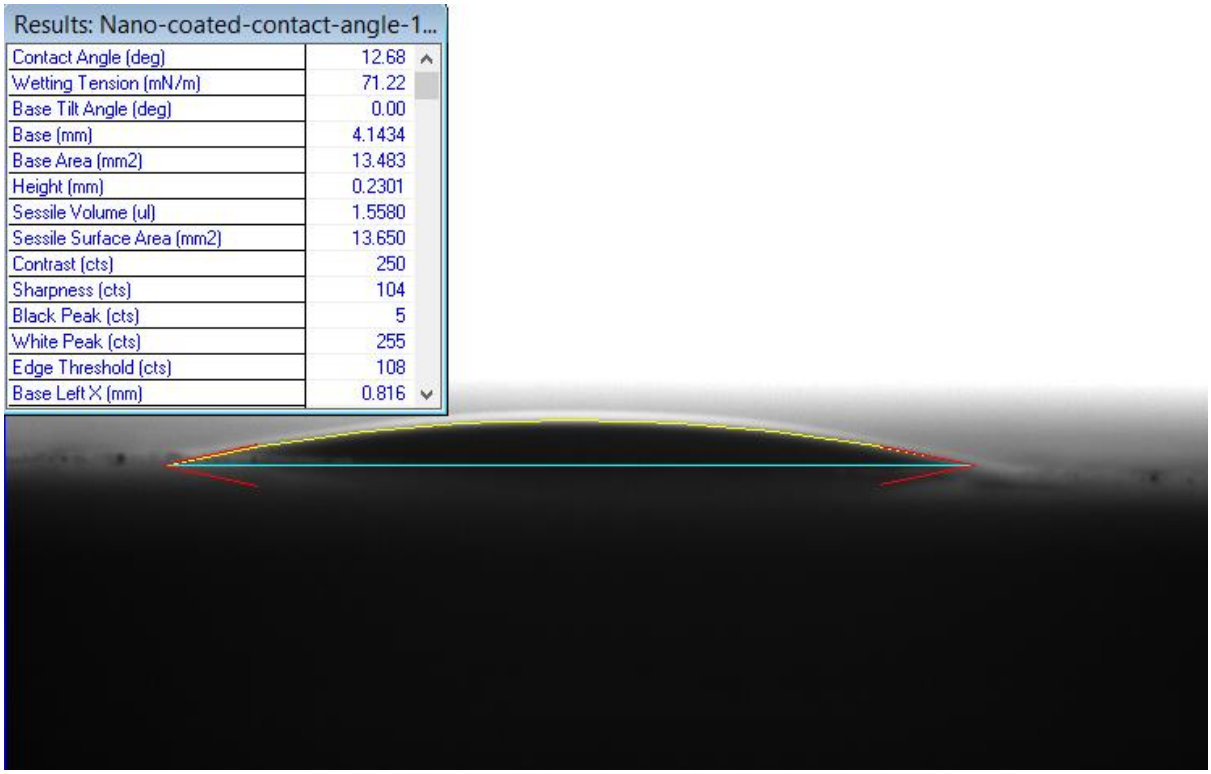

Figure 8.11: Contact angle of HFE-7200 measured on a flat coated sample at atmospheric conditions using the static sessile drop method. The contact angle is estimated to be 12.7 °.

8.3 Single-Phase Validation

As in the plain microchannel test section, single phase experiments were conducted on the coated test section in order ensure consistency and also to validate experimental measurements in the test facility. Single-phase adiabatic experiments were conducted using the working fluid at mass fluxes G = 250 to 2250 kg/m^2 s at an inlet pressure and temperature condition of 1 bar and 40 °C respectively. For diabatic tests, a fixed wall heat flux of $q_w^{"}$ = 1.3 kW/m^2 (corresponding base heat flux, $q_b^{"}$ = 5 kW/m^2) was applied to the test section for the range of mass fluxes quoted above at an inlet pressure of 1 bar and inlet temperature of 40 °C. The Reynolds number range covered is 226 to 2038. Furthermore, the repeatability of both sets of experiments were verified. As mentioned above, the layer of coating is between 5 µm to 10 µm thick on the three heated walls of the channel. The resulting hydraulic diameter considered for the coated microchannels is 456 µm, assuming a maximum coating thickness of 10 µm on the bottom and side walls of the channels. Nonetheless, the results obtained in the coated test section remain comparable to the plain test section, where D_h = 475 µm, since the hydraulic diameters only vary by a maximum of 4 %.

Figure 8.12 and Figure 8.13 show the experimental Fanning friction factor (see Eq. (3.7)) and average Nusselt number (see Eq. (3.34)) as a function of Reynolds number respectively. The uncertainty in friction factor varied between ±2.39 % to ±2.46 % while the experimental uncertainty in Nusselt number ranged from ±7.68 % to ±12.68 % with increasing Reynolds number. These error ranges are similar to those observed in the uncoated test section (see Section 3.5). The single-phase friction factor obtained experimentally was relatively close to the correlation of Shah and London [266] for developing flows in conventional rectangular channels at Re < 500 and begins to diverge from the correlation at Re > 500. This may be attributed to higher frictional losses generated due to local turbulence brought about by the rough structure of the coated channel walls, which is clearly illustrated in Figure 8.5 to Figure 8.8.

From Figure 8.13, the experimental Nusselt number in the coated channels is notably higher than the conventional microchannel predictions given by the Shah and London [266], Peng and Peterson [269] and Stephan and Preusser [270] correlations, which are valid for plain and unmodified rectangular ducts. The higher experimental Nusselt number could be a result of the slightly smaller hydraulic diameter of the coated channels as well as the higher single-phase

heat transfer coefficients (discussed further in Section 8.3.1) in the enhanced test section in comparison to regular and unmodified microchannels. Heat transfer rates may have been promoted due to the increased heat transfer area provided by the structure of the coating as well as induced mixing on the surfaces of the coated channel walls.

Furthermore, single-phase experiments in the coated test section was demonstrated to be highly repeatable. Similar to the observation in the plain microchannel test section, the deviation in single-phase friction factor when Re < 500 was marginally larger compared to friction factors obtained at higher Reynolds numbers due to the relatively small magnitude of single-phase pressure drop and resulting error at low Reynolds number conditions.

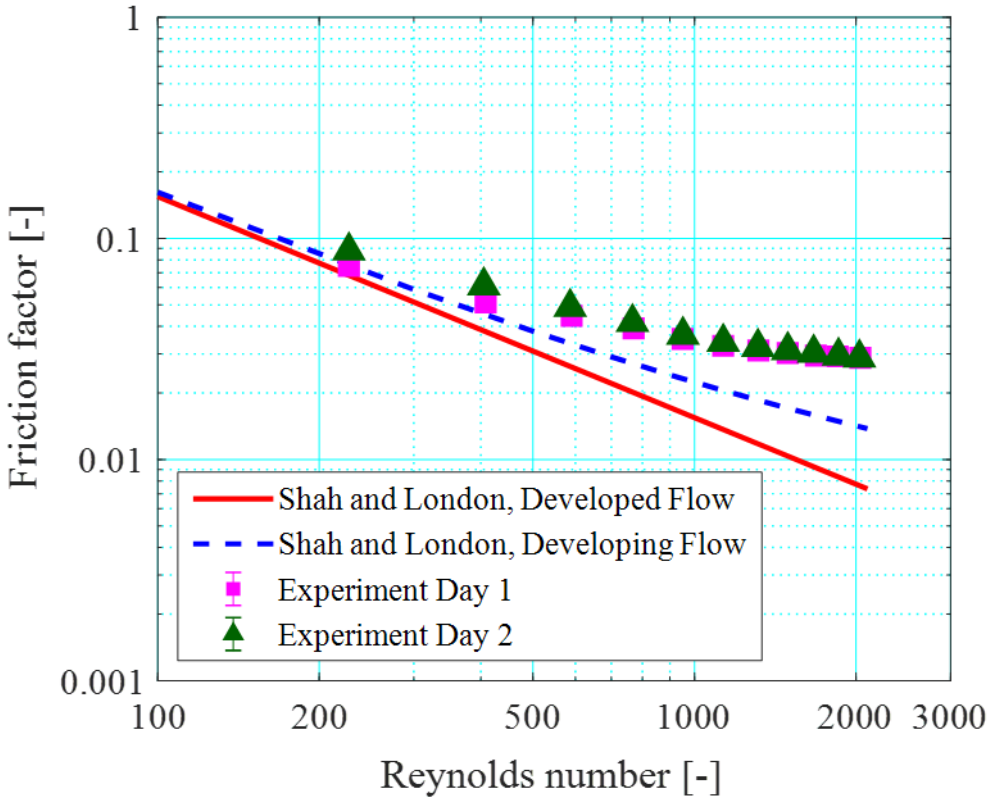

Figure 8.12: Experimental single-phase friction factor vs. Reynolds number obtained in the coated test section. Error bars are between ±2.39 – 2.46 % but are too small to be visible in the figure.

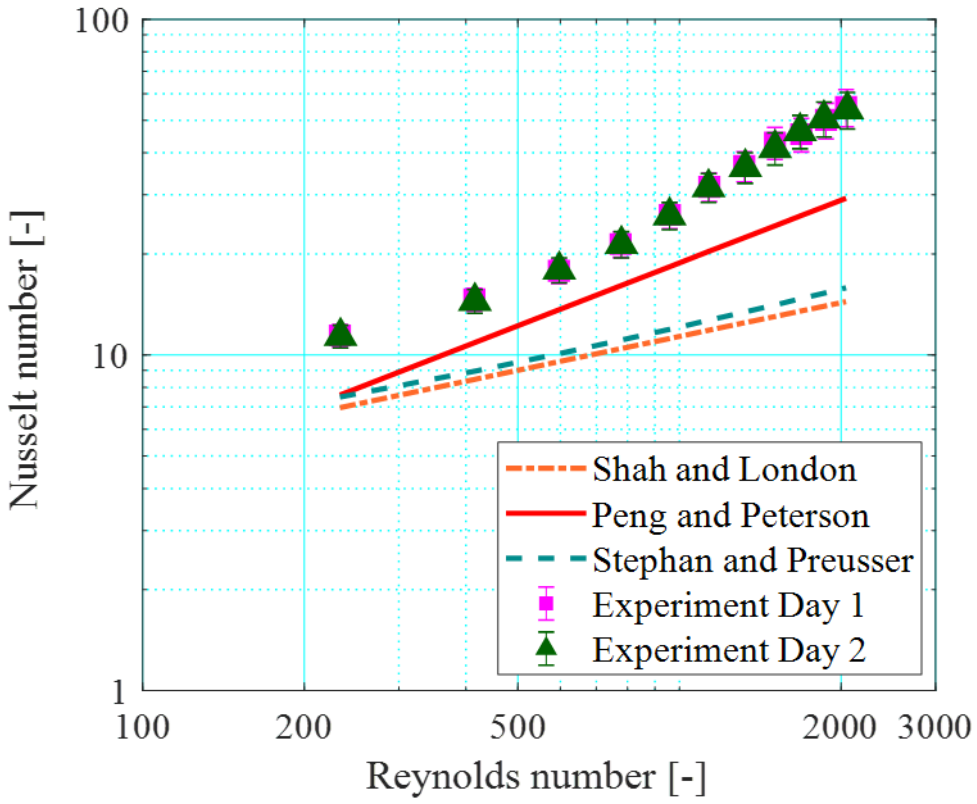

Figure 8.13: Experimental single-phase Nusselt number vs. Reynolds number obtained in the coated test section.

8.3.1 Comparison with Single-Phase Results in the Plain Test Section

Figure 8.14 and Figure 8.15 depict the single-phase friction factor and Nusselt number obtained in the plain and coated microchannel test section respectively. Evidently, both the friction factor and Nusselt number of the coated microchannels are notably larger compared to the single-phase results of the uncoated test section. The friction factor was between 50 % to 81 % higher in the coated test section while the experimental Nusselt number was between 54 % and 120 % higher in the coated test section.

As mentioned above, the higher friction factor in the coated channels could be due to the higher roughness characteristics of the coating compared to the plain channels. The higher experimental Nusselt number observed in the coated test section was a result of higher single-phase heat transfer coefficients in the coated channels as well as the slightly smaller hydraulic diameter considered in the coated channels (i.e. 456 μm). The enhancement in average single-phase heat transfer coefficient in the coated channels were found to be between 40 % to 103 % in relation to the plain test section (see Figure 8.16). The enhancement generally increased with Reynolds number and mass flux in the channels. Improvements in single-phase heat transfer coefficients in the coated test section could have been induced by the structure of the coating, which provided a larger heat transfer area and enhanced fluid mixing on the channel walls. Nevertheless, single-phase results obtained in the coated microchannel test section, albeit offset to higher values, appear to follow the general trend of classical microchannel theory.

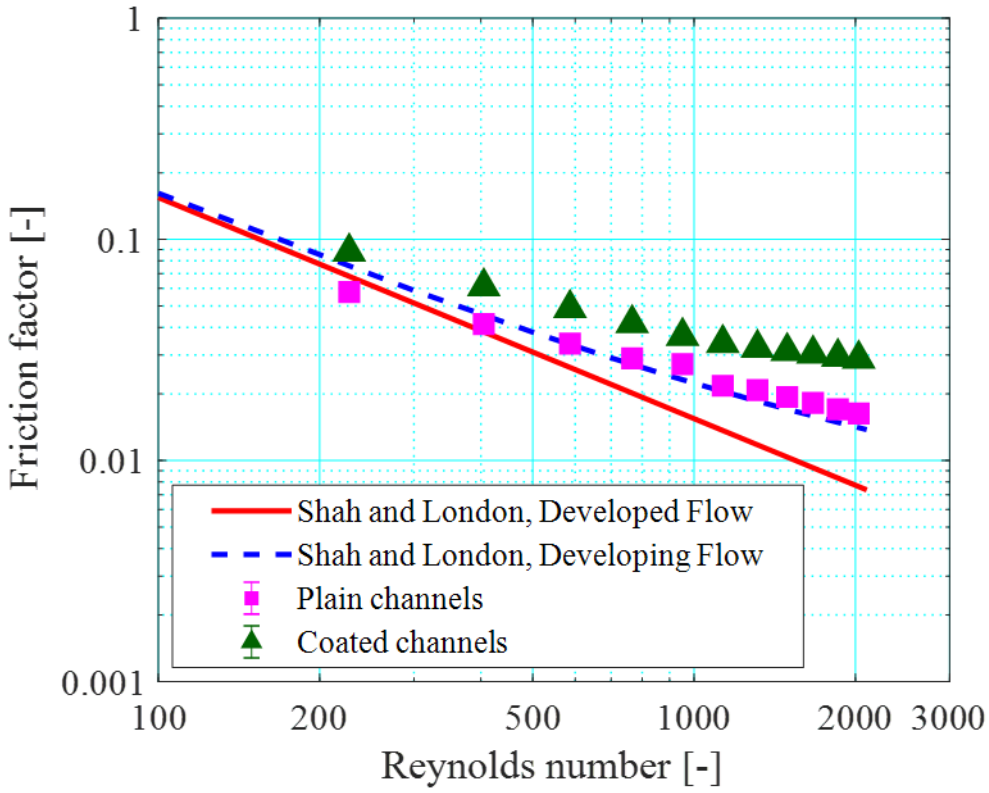

Figure 8.14: Experimental single-phase friction factor as a function of Reynolds number obtained in the plain and coated test sections respectively. Error bars are included but are too small to be visible in the figure.

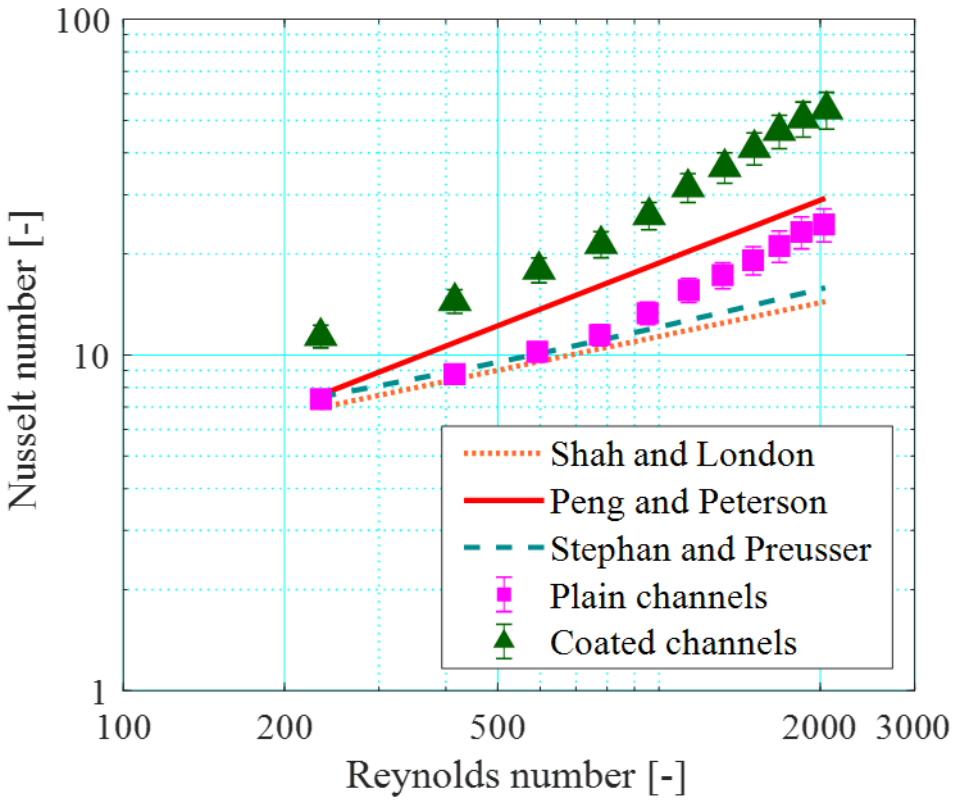

Figure 8.15: Experimental Nusselt number as a function of Reynolds number obtained in the plain and coated test sections respectively.

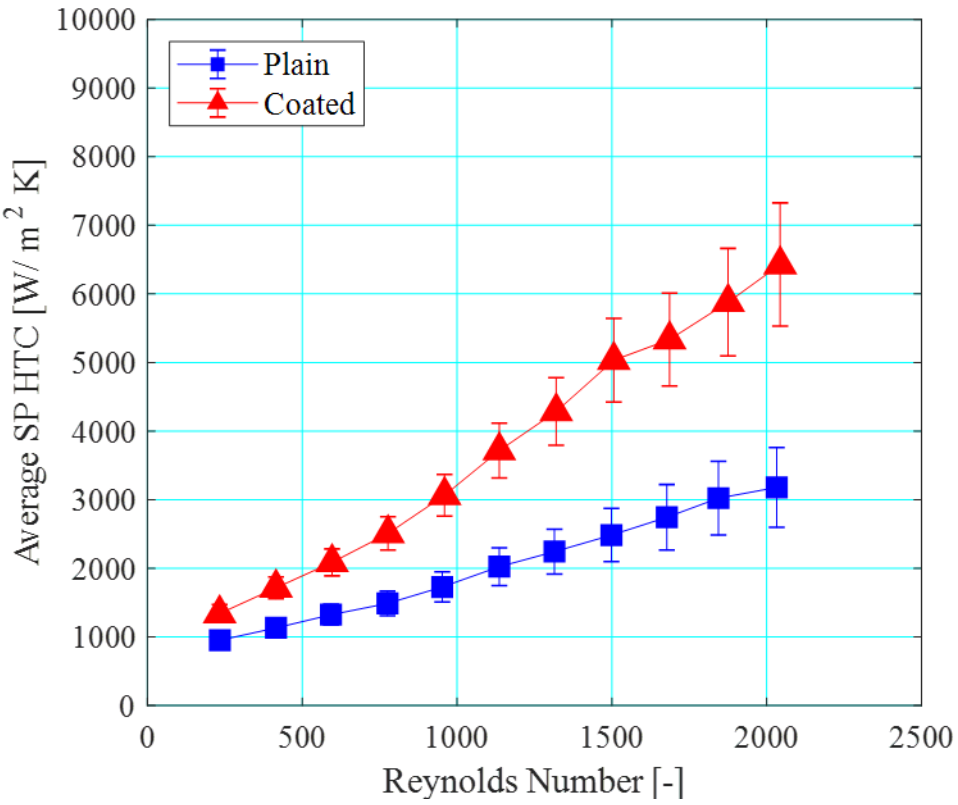

Figure 8.16: Average single-phase heat transfer coefficients with respect to Reynolds number in the plain and coated microchannel test sections.

8.4 Repeatability

The repeatability of flow boiling experiments were verified at P = 1 bar, G = 200 kg/m^2 s and ΔT_{sub} = 10 K for wall heat fluxes $q_w^{"}$ = 24.5 – 153.3 kW/m^2 (see Figure 8.17). The mean deviation of the experimental data was ± 2.6 %, with a slightly higher discrepancy at low heat fluxes. The MAE of two-phase heat transfer coefficients were ± 8.7 % at the lowest heat flux condition (i.e. $q_w^{"}$ = 24.5 kW/m^2) but decreases with increasing heat flux. A slightly higher deviation in experimental data was also observed in the plain microchannel test section at low heat fluxes, as shown previously in Section 4.5. As mentioned before, the slightly larger discrepancy at low heat flux could be related to slug expansion and flow reversal in the channels following boiling incipience, which could have triggered upstream compressibility effects near the inlet of the heat sink [288], [289].

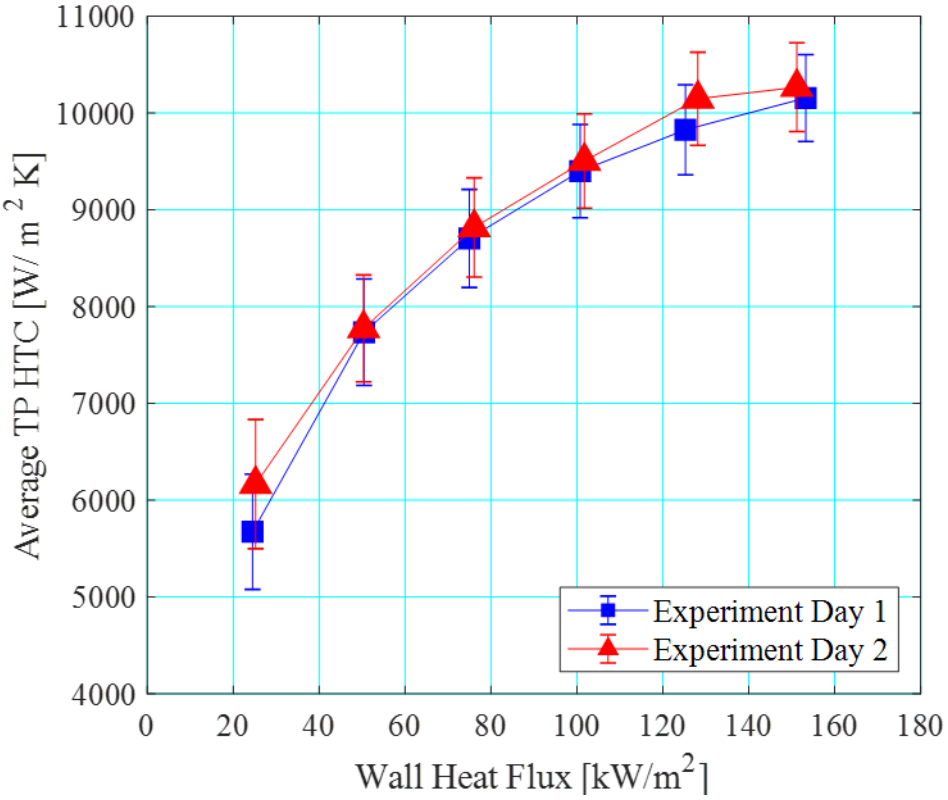

Figure 8.17: Repeatability of flow boiling experiments at P = 1 bar, G = 200 kg/m^2 s and ΔT_{sub} = 10 K in the coated test section. The mean average deviation of the experimental data is ±2.6 %.

8.5 Flow Boiling Results and Comparison with Plain Microchannels

Flow boiling experiments were conducted at channel mass fluxes of G = 200 kg/m^2 s, 300 kg/m^2 s and 400 kg/m^2 s for wall heat fluxes ranging from $q_w^{"}$ = 24.5 – 171.8 kW/m^2. The corresponding base heat fluxes were between $q_b^{"}$ = 93.7 – 656.4 kW/m^2. The inlet pressure and inlet subcooling degree was kept constant at P = 1 bar and ΔT_{sub} = 10 K respectively. Additionally, the effect of pressure as well as the effect of inlet subcooling degree were assessed in this study. For the former, channel mass flux and inlet subcooling degree were fixed at G = 200 kg/m^2 s and ΔT_{sub} = 10 K respectively for inlet pressures of P = 1, 1.5 and 2 bar. For the latter, mass flux and inlet pressure were fixed at P = 1 bar and G = 200 kg/m^2 s respectively. Finally, two-phase heat transfer and pressure drop results in the coated microchannel test section were compared against the results obtained in the plain microchannel test section under similar operating conditions. In particular, the effect of the nanocoating on wall superheat at a given wall heat flux condition, flow boiling heat transfer coefficient and two-phase pressure drop in the heat sink was assessed. As per the plain microchannel test section, flow visualisation were conducted along the microchannel evaporator in order to capture the flow pattern evolution corresponding to each operating condition. The recordings were carried out at 5000 fps at a magnification of 4.5x and resolution of 512 x 512 pixels for a duration of 1.3 s at each location (see Figure 4.1 for the locations).

8.5.1 Boiling Curve

The boiling curves, with increasing and decreasing heat flux, based on the dimensionless location of z/L = 0.5 (i.e. middle of the heat sink) in the coated channels at P = 1 bar, G = 200 kg/m^2 s and ΔT_{sub} = 10 K are depicted in Figure 8.18. As in the plain microchannel test section, boiling hysteresis was not observed in the coated microchannel heat sink. The lack of hysteresis phenomena could indicate that a similar size range of nucleation cavities were activated in the channels with both increasing and decreasing heat flux [298].

A comparison of the boiling curves of the plain and coated heat sink is plotted in Figure 8.19 for increasing wall heat flux at the operating conditions listed above. At a given wall heat flux condition, the wall superheat on the coated channels was on average 2.8 K smaller compared to the plain channels. For instance, at a wall heat flux of q_w" ~ 50 kW/m^2, wall superheat on the surface of the coated channels was 6.7 K, while on the plain channels the wall superheat measured was nearly 10 K. The lower degree of wall superheat on the enhanced microchannels could be due to the availability and activation of more nucleation sites within the activation range, see Section 8.2.2, provided by the coating. In practical terms, this means that for a given level of wall heat flux, the surface temperature of the heat sink, with the coating applied, will be around 3 K lower compared to the plain copper channels. Hence for a given junction temperature rating, the design heat flux may be higher using the coated heat sink. Since flow boiling experiments did not extend to wall superheats lower than 4 K, the effect of the porous coating on boiling incipience wall superheat is not apparent in the current study.

From Figure 8.1 and Figure 8.5, as presented in Section 8.2, it is evident that the surface of the plain copper microchannels was characterised by relatively larger and shallower cavities in comparison to the topography of the coated microchannels. The characteristically deeper cavities of the coating may also encourage vapour trapping and increase bubble nucleation frequency. Furthermore, the coated surface has a substantially higher number of cavities available as nucleation sites, as depicted in Figure 8.9, in contrast to the plain channel in Figure 8.3. The higher nucleation activity (contributes to higher nucleate boiling heat transfer coefficients) explains the lower degree of wall superheat on the coated channel for a given wall heat flux.

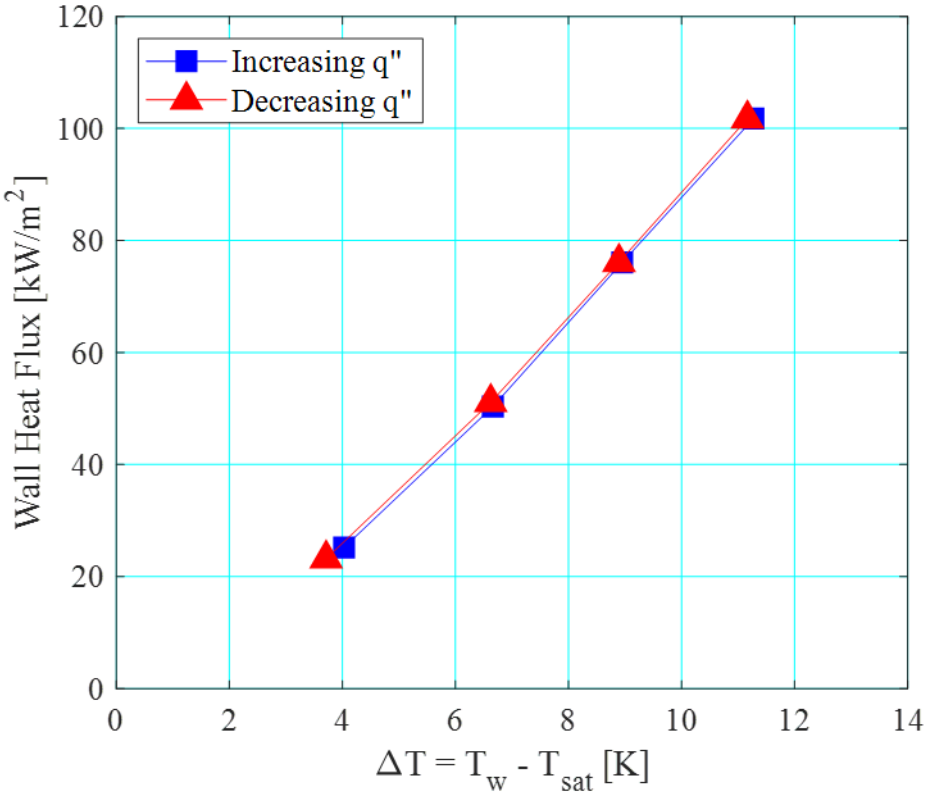

Figure 8.18: Boiling curves obtained with increasing and decreasing heat flux based on the wall temperature at the middle of the coated heat sink (i.e. z/L = 0.5) at P = 1 bar, G = 200 kg/m^2 s and ΔT_{sub} = 10 K.

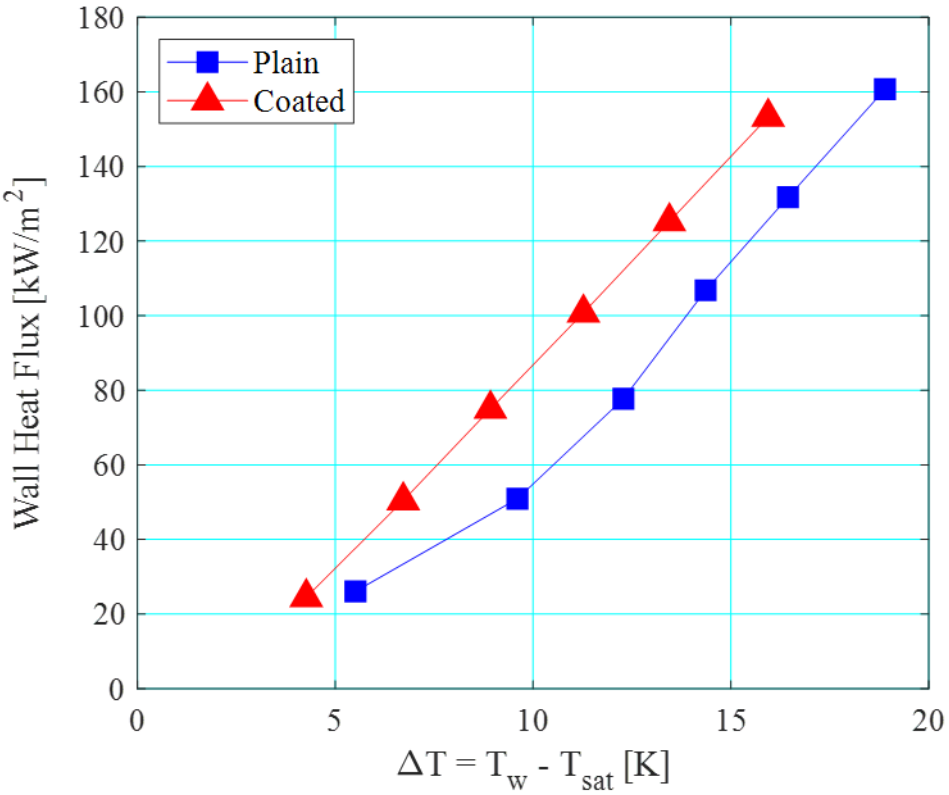

Figure 8.19: Boiling curves of the plain and coated microchannel heat sink at the middle of the heat sink (i.e. z/L = 0.5) at P = 1 bar, G = 200 kg/m^2 s and ΔT_{sub} = 10 K.

8.5.2 Effect of Heat Flux

8.5.2.1 Flow Patterns

As mentioned above, flow pattern evolution in both the plain and coated channels were monitored using high speed recording. During the coating process, in addition to the layers of coating deposited on the bottom and side walls of the channels, a layer of coating is also resulted on the top of the fins. As a result, fluid flow in the channels were not completely isolated as the top plate was not able to seal sufficiently given the irregular surface at the top of the fins. Consequently, some fluid transfer over the tops of the fins were observed in flow visualisation, predominantly during churn and annular flow. Nevertheless, flow interactions between the channels were fairly minor and flow pattern development were mainly controlled by bubble generation and flow dynamics in two-phase flow.

Images of the flow regimes in the coated microchannel heat sink, captured along the channel length, at the centre of the heat sink (see Figure 4.1, Locations 1 to 4) are shown in Figure 8.20 and Figure 8.21 for wall heat fluxes $q_w^{"}$ = 50.4 kW/m^2 and $q_w^{"}$ = 125.2 kW/m^2 respectively. Note that the fins of the coated channels appear thicker in comparison to the plain microchannels due to the additional layer of coating. As mentioned above, even with the layer of coating, the difference in hydraulic diameter between the two test sections is less than ±4 % and thus remain fairly comparable within the scope of this study.

Similar to the observations in the plain microchannel heat sink, two-phase flow pattern developed from bubbly to slug, churn and annular flow at a given location with increasing heat flux or vapour quality. During bubbly flow in the coated test section, bubble nucleation is observed on the side walls and also appear to nucleate from the bottom wall of the channel (see Figure 8.20, Bubbly, Location 1). Slug flow develops following bubble coalescence in the channels (see Figure 8.20, Slug, Location 2). As was observed in the plain channel test section, active nucleation sites may be suppressed with the gradual thinning of the slug liquid film. This was previously illustrated in Figure 4.7. With further increase in vapour quality, the tips of the slug collapse due to the high velocity of the vapour phase and breaks up individual slugs downstream of the channel (see Figure 8.20, Churn, Location 3 and 4).

In churn flow, intermittent waves of a liquid and vapour mixture accelerates toward the channel exit. Growing bubbles may be stripped from their respective nucleation sites during the surge

and are entrained into the wave. Figure 8.20, Churn, Location 3 shows small entrained vapour bubbles within a chaotic mixture of liquid and vapour in the churn flow regime. Furthermore, active nucleation sites were observed to be periodically suppressed, in-phase with the dispersed churn wave. As noted above, some fluid transfer from the tops of the fins may occur in churn flow. Annular flow, which develops after churn flow, is characterised by a clear vapour core and thin liquid film visibly attached to the channel side walls. Distinct from long slugs observed in slug flow, no bubbles or slugs pass intermittently in annular flow and the vapour core is largely uninterrupted. Additionally, from Figure 8.21, Location 3 and 4, it is clear that there is a substantial number of active nucleation sites within the annular liquid film. Similar to the suppression mechanism observed in the slug flow regime, these sites are periodically deactivated with liquid film dryout. As illustrated in Figure 4.12, intermittent churn waves rewet the channel walls to re-establish a liquid film on the walls and nucleation sites are reactivated accordingly.

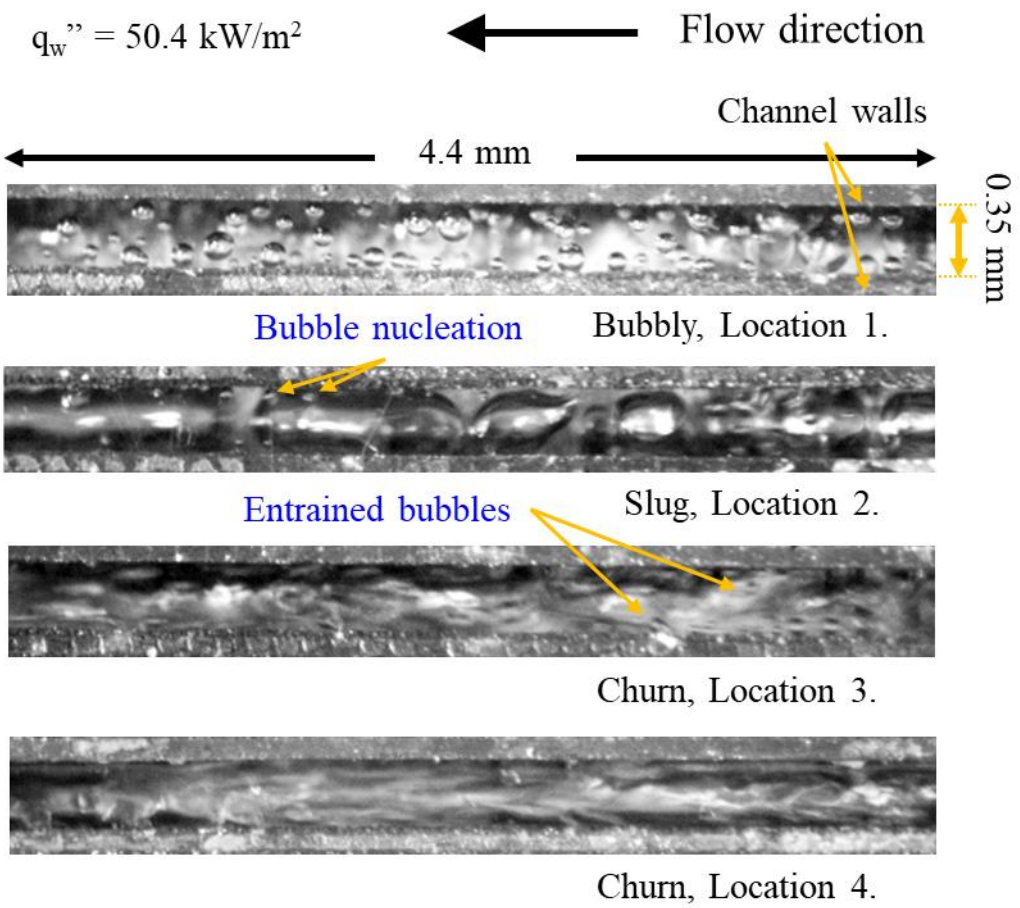

Figure 8.20: Flow patterns along the coated microchannel heat sink at q_w" = 50.4 kW/m^2, see Figure 4.1 for locations. Slugs and the churn wave pass intermittently in the frame shown.

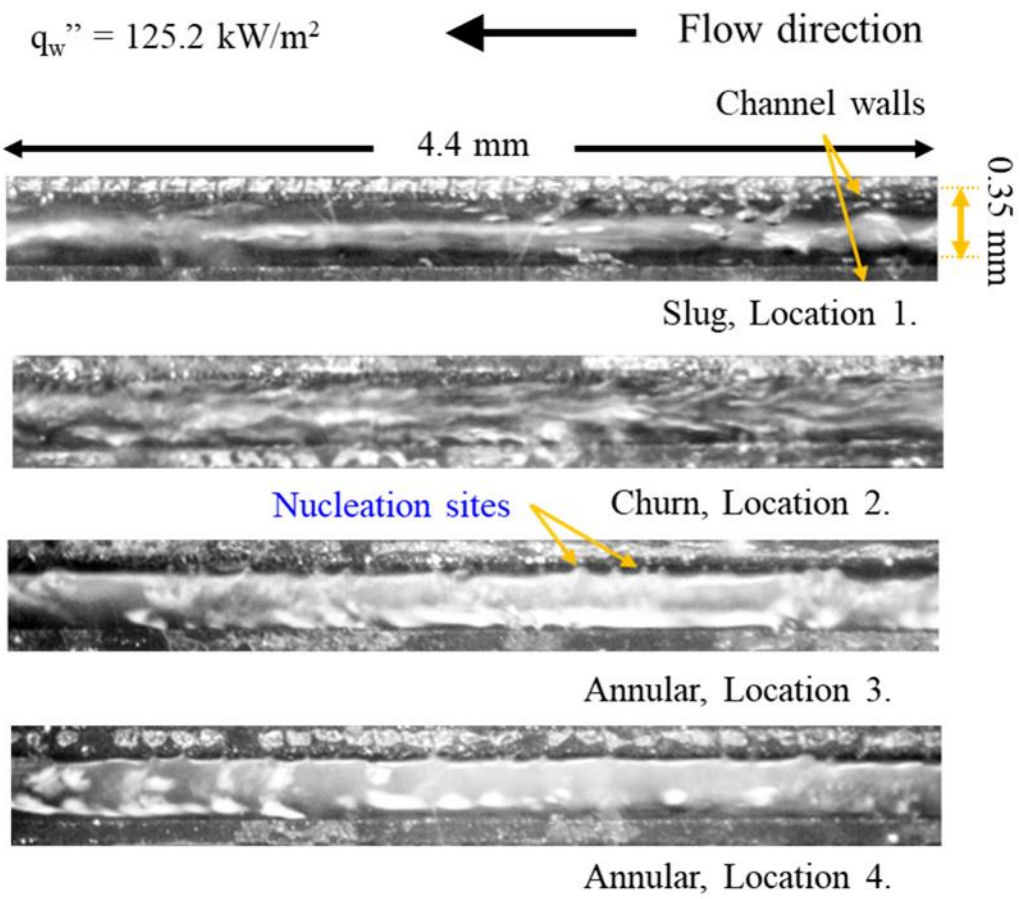

Figure 8.21: Flow patterns along the coated microchannel heat sink at q_w" = 125.2 kW/m^2, see Figure 4.1 for locations. Slugs and the churn wave pass intermittently in the frame shown.

Previously in Figure 4.2 and Figure 4.3, flow regimes captured in the plain microchannels are depicted for q_w" = 50.9 kW/m^2 and q_w" = 131.8 kW/m^2 respectively under similar pressure, mass flux and subcooling conditions in the test section. A comparison of flow morphologies in the coated and uncoated microchannels would greatly benefit the understanding of differences in flow boiling behaviour between the two samples. Flow patterns in the plain microchannel test section has previously been presented in much detail in Section 4.2.1.

At q_w" ~ 50 kW/m^2, bubbly flow occurs in both microchannels at Location 1, near to the inlet of the channels. On the plain microchannels, bubbles several times smaller than the width of the channel are observed to nucleate from the channel side walls (see Figure 4.2, Bubbly, Location 1). On the coated channels, there is a notably higher density of bubbles nucleation from the walls (see Figure 8.20, Bubbly, Location 1). This indicates a comparatively higher bubble generation frequency in the coated channels in relation to the plain channels. As explained in Section 8.2, the higher bubble generation frequency is likely a direct result of the

abundance of nucleation sites as well as more defined cavities provided by the porous coating. With increasing vapour quality along the channel, slug and churn flow develops in Location 2 to 4 toward the exit of the channels in both heat sinks.

In the plain microchannel heat sink, wall dryout due to vapour slug expansion in the slug flow regime was observed at G = 200 kg/m^2 s and $q_w^{"}$ = 50.9 kW/m^2, see Figure 4.7. At a similar wall heat flux condition, dryout was not observed in the coated heat sink. This could indicate flow instability suppression using the coating at a similar operating condition, which may be caused by lower wall superheat at boiling incipience in the coated channels, as indicated in Figure 8.19. Flow morphologies of the slug and churn flow regimes appear similar in both test sections. Bubble nucleation is active in slug flow, as shown by the arrows in Location 2 of Figure 4.2 and Figure 8.20 while in churn flow, entrained bubbles are sometimes observed in the wake of the churn wave. The latter is shown in Figure 8.20, Location 3 for the coated test section and captured at $q_w^{"}$ ~ 132 kW/m^2, Figure 4.3, Location 2 for the plain microchannel test section.

At the higher heat flux condition of $q_w^{"}$ ~ 130 kW/m^2, slug flow develops immediately near the inlet of the channels, followed by churn and annular flow in both heat sinks (see Figure 4.3 and Figure 8.21, Location 1 to 4). At $q_w^{"}$ ~ 130 kW/m^2, annular flow is captured at Location 3 and 4 in both test sections (see Figure 4.3 and Figure 8.21 for the coated and plain microchannels respectively). As in slug flow, nucleation sites on the side walls, as indicated by the arrows in Location 3 in the abovementioned figures, remain active as long as the wall is sufficiently wetted, i.e. thin liquid film has not evaporated completely.

Although the classified two-phase flow patterns between the plain and coated test section do not vary significantly when assessed at fixed locations along the channel, the bubbly and annular flow regime, in particular, manifests differently in the coated channels. Firstly, a higher density of bubbles are observed in bubbly flow for a nominal wall heat flux condition while the liquid-vapour interface in annular flow appear to be wavier in the coated channels. The latter may be due to some irregularities in the coating structure. As presented in Section 8.2.2, agglomerates were observed on the bottom walls in some sections of the channel and also in the corners of some of the sampled channels (see Figure 8.7 and Figure 8.8).

The higher number of bubbles observed in bubbly flow is indicative of higher bubble generation frequency in the enhanced channels, which appear to confirm higher bubble nucleation activity and the activation of a larger number of nucleation sites on the coated surface, as hypothesised in Section 8.2. Higher bubble nucleation activity in the channels could also be indicative of a more efficient nucleate boiling mechanism (i.e. higher nucleate boiling heat transfer coefficients and lower wall temperatures on the heat sink). This is in-line with our observations in Figure 8.19, which show a lower wall superheat for a given wall heat flux level in the coated test section.

Dryout and rewetting cycles around 30 ms, with around 3 ms of continuous wall dryout, at G = 200 kg/m^2 s in the coated channels were periodically observed during annular flow at q_w" = 153.3 kW/m^2. This is presented in Figure 8.22 at camera location 4 at 10 ms intervals. In the plain heat sink, shorter dryout cycles of around 23 ms, with wall dryout of 2 ms, were observed in the annular flow regime at q_w" = 160.7 kW/m^2. The slightly longer dryout period could be due to higher bubble nucleation and liquid film evaporation in the coated channels. As covered in Section 4.2.1, dryout cycles in the annular flow regime were typically much shorter compared to dryout cycles observed in the slug flow regime, which could last up to 100 ms.

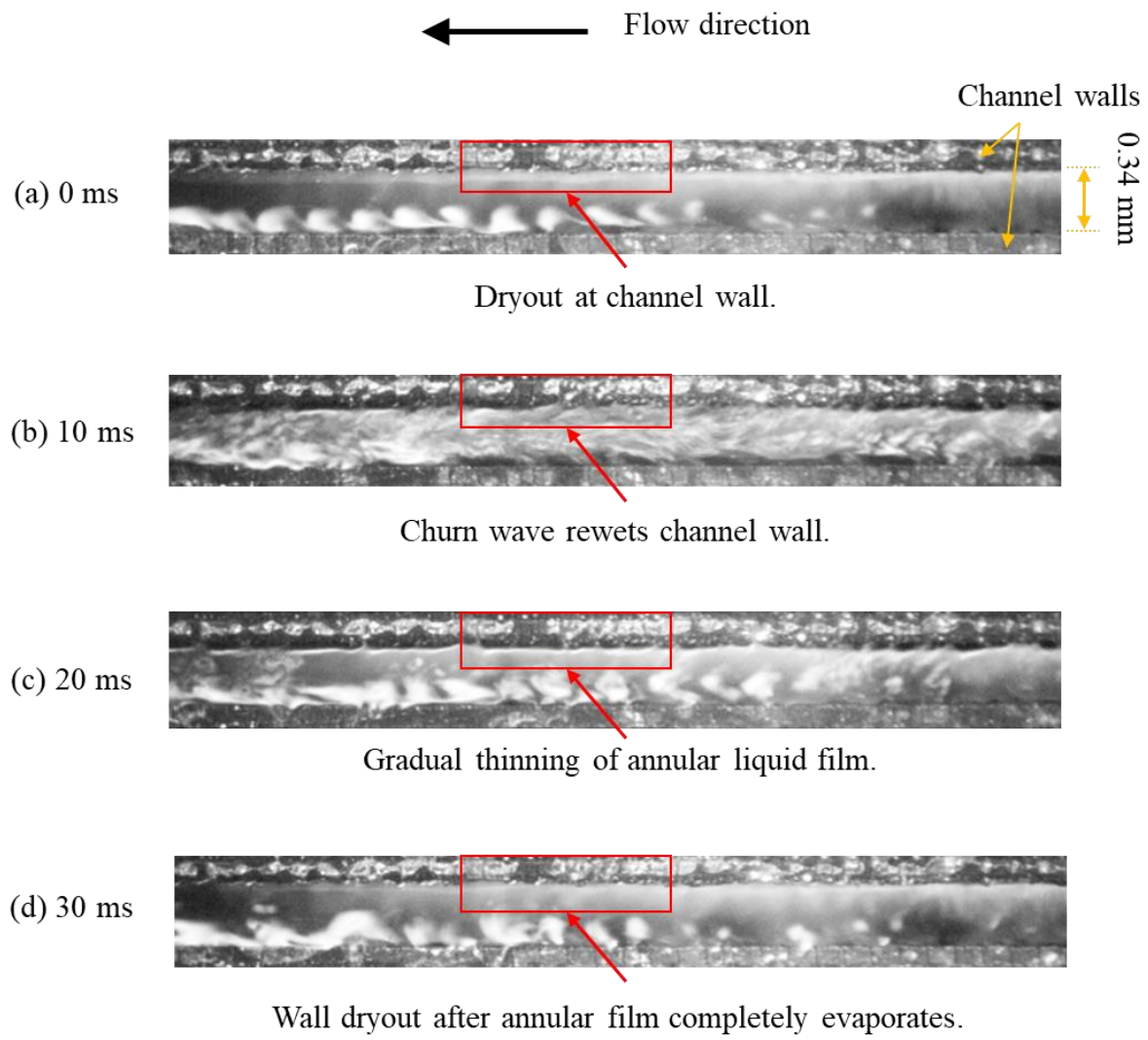

Figure 8.22: Dryout and rewetting cycle captured during annular flow in the coated channels at camera location 4, for operating conditions $q_w^{"}$ ~ 130 kW/m^2, P = 1 bar, G = 200 kg/m^2 s and ΔT_{sub} = 10 K.

Overall, flow pattern transition boundaries shifted to lower vapour qualities in the coated test section for a similar wall heat flux range compared to the plain channels, see Table 8.1. Bubbly-slug flow transition occurred at x = 0.04 and x = 0.01 in the plain and coated test section respectively. There was only a small disparity between the flow transition boundaries of slug-churn and churn-annular flow, as it may be controlled by flow properties such as mass flux and fluid properties such as vapour density.

The tips of individual slugs collapse when the superficial velocity of the vapour phase increases sufficiently and consequently induces transition to churn flow. Higher vapour phase flow velocity also promotes the development of a clear vapour core characteristic of annular flow in

the channel. Vapour superficial velocity is governed by Eq. (3.15) and is dependent on heat flux and vapour quality for a nominal mass flux condition. While high bubble generation activity induces earlier transition from bubbly to slug flow, subsequent transitions from slug to churn and annular flow is predominantly controlled by the superficial vapour velocity. Since the flow pattern visualisation were obtained at similar mass flux, inlet pressure and subcooling conditions for both the plain and coated test section at comparable ranges of wall heat fluxes, the superficial gas velocities do not differ significantly at a nominal wall heat flux level. This could explain similar vapour qualities at slug-churn and churn-annular transition in both test sections.

Table 8.1: Flow pattern transition vapour qualities in the plain and coated heat sink at P = 1 bar and ΔT_{sub} = 10 K for wall heat fluxes ranging from $q_w^{"}$ = 24.5 – 160.7 kW/m^2.

Test section	x_{B-S} [-]	x_{S-C} [-]	x_{C-A} [-]
Plain	0.037	0.068	0.30
Coated	0.008	0.067	0.30

8.5.2.2 Heat Transfer

The local heat transfer coefficients, measured at the middle of the heat sink along the channels (namely at z/L = 0.17, 0.34, 0.5, 0.67 and 0.83) are shown for wall heat fluxes ranging from $q_w^{"}$ = 24.5 to 153.3 kW/m^2 in Figure 8.23. Vapour qualities at which flow pattern transition occurs are also annotated on the figure.

Similar to the observations in the plain microchannel test section, local heat transfer coefficients rise sharply with increasing vapour quality in the subcooled region while a peak in heat transfer coefficient is typically observed at vapour qualities near x = 0. As discussed in Section 4.2.2, the high heat transfer coefficients at low vapour qualities may be associated with high heat transfer rates in nucleate boiling. This is further supported by the observation of bubbly and slug flow corresponding to the peak in local heat transfer coefficients in the low vapour quality region.

The decrease in local heat transfer coefficients following the initial peak is caused by the periodic suppression of nucleation sites (thus the nucleate boiling mechanism) with liquid film thinning in slug flow and similarly in annular flow. Furthermore, transient variations in local heat transfer coefficients at a fluxed location along the channels, owing to periodic dryout and rewetting cycles, could also have contributed to a drop in the measured time-averaged heat transfer coefficients based on the three-zone model of Thome et al. [151]. For example, wall dryout in slug flow could last up to 100 ms based on flow visualisation (see Figure 4.7). Although film evaporations increase along with liquid film thinning, heat transfer coefficients are relatively low in the dryout phase of the cycle. The time averaged heat transfer coefficients may therefore be adversely affected in flow regimes prone to cyclic wall dryout.

Notably, there is a less pronounced increase in local heat transfer coefficients near to the channel exit in the coated test section (see Figure 8.23) in comparison to the plain microchannel test section (see Figure 4.13). As explained in Section 4.2.2, the increase in heat transfer coefficient could be related to heat loss at the outlet plenum of the heat sink. The smaller heat loss effect manifested in the coated channels could be due to the relatively larger magnitude of heat transfer coefficients obtained in the enhanced test section as compared to the plain test section.

Furthermore, comparing the flow pattern transition boundaries in Table 8.1, it is clear that bubbly-slug flow transition occurred earlier, namely at x = 0.01, in the coated test section than in the plain microchannel test section, where bubbly-slug transition was observed at x = 0.04. This could be due to heightened bubble coalescence phenomenon as a result of higher bubble nucleation activity as well as bubble generation frequency in the coated channels.

As depicted in Figure 8.5, cavities on the coated surface appear deeper and more defined compared to the shallow surface defects observed on the bottom wall of the plain end-milled microchannels. Such deeper cavities could induce a stronger pinning effect on departing bubbles, producing residual vapour pockets in the cavities from the preceding departing bubble. A new bubble may grow immediately from the remaining vapour embryo, thus reducing the waiting time between subsequent ebullition cycles on the coated channels. This could also contribute to the higher density of bubbles observed in the coated channels (see Figure 8.20, Bubbly, Location 1). As a consequence of increased nucleation sites as well as higher bubble generation frequency from the coated surface, transition from bubbly to slug flow occurs at a lower vapour quality in the enhanced test section due to higher coalescence rate in the channels compared to the plain channels.

On the other hand, the slug-churn (where x = 0.068 in plain channel and x = 0.067 in coated channel) boundary were relatively comparable in the plain and coated test sections. The similar transitional boundaries in slug-churn and churn-annular flow observed in the plain and coated channels is due to different flow mechanisms, other than bubble generation, inducing flow regime transition in from slug to churn and annular flow. As discussed earlier, higher bubble generation frequency could have accelerated the transition from bubbly to slug flow, as well as induced slightly longer dryout periods in the coated channels.

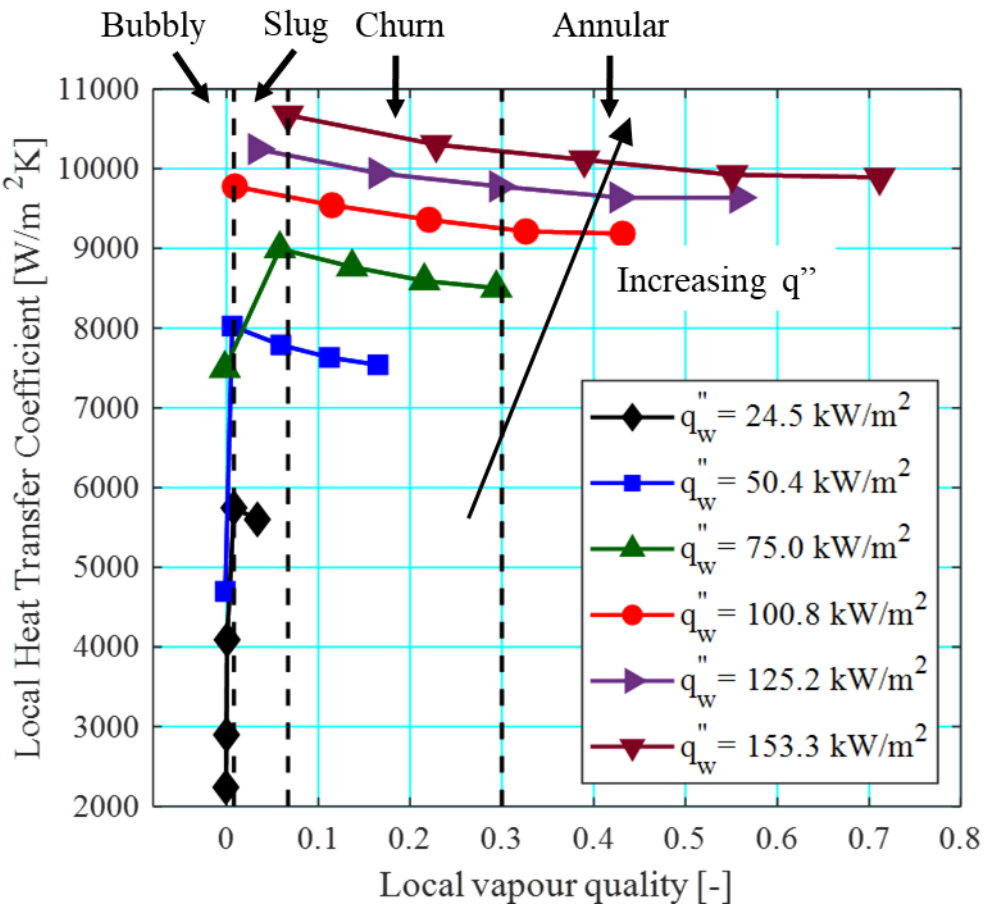

Figure 8.23: Local heat transfer coefficients as a function of vapour quality in the coated channels at P = 1 bar, G = 200 kg/m^2 s and ΔT_{sub} = 10 K.

As can be inferred from Figure 4.13 and Figure 8.23, heat transfer coefficients increase with increasing wall heat flux in both microchannel heat sinks. Figure 8.24 plots the average heat transfer coefficients in the two-phase region (based on Eq. (3.31)) with respect to wall heat flux in the plain and coated channels. Both trends indicate that average flow boiling heat transfer coefficient increase with increasing wall heat flux. Additionally, average two-phase heat transfer coefficients obtained in the coated test section is significantly higher compared to the plain microchannel test section.

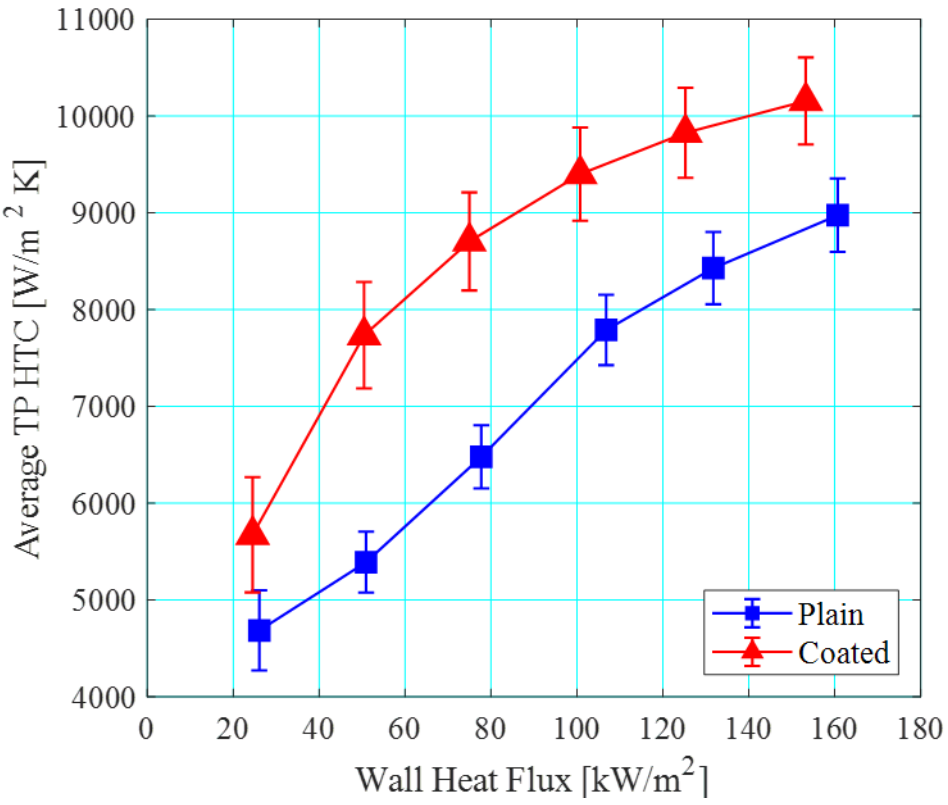

Figure 8.24: Average two-phase heat transfer coefficients in the plain and coated heat sink at P = 1 bar, G = 200 kg/m^2 s and ΔT_{sub} = 10 K.

To further quantify the enhancement effect of the coating on flow boiling heat transfer coefficients, an enhancement percentage, E_{HTC}, is defined as follows:

$$E_{HTC} = \frac{\bar{h}_{tp,coated} - \bar{h}_{tp,plain}}{\bar{h}_{tp,plain}} \times 100\ \% \qquad (8.16)$$

where E_{HTC} is calculated as a function of the average two-phase heat transfer coefficient in the plain (i.e. $\bar{h}_{tp,plain}$) and coated (i.e. $\bar{h}_{tp,coated}$) channels respectively. The percentage enhancement of average two-phase heat transfer coefficients by means of a porous coating in a microchannel heat sink is depicted in Figure 8.25.

Importantly, Figure 8.25 shows that two-phase heat transfer enhancement is highly dependent on wall heat flux. Heat transfer enhancement obtained using the coating increases steeply at low wall heat fluxes but depreciates at medium to high heat flux levels. An appreciable enhancement of 21.1 % in average two-phase heat transfer coefficient is recorded at the lowest heat flux level of q_w" ~ 25 kW/m^2. With further increase to q_w" ~ 51 kW/m^2, the percentage enhancement more than doubled and reached a maximum of 43.5 %. This peak corresponds to an exit vapour quality of x = 0.22 in the heat sink. However, subsequent increase in heat flux in the medium and high heat flux region induced a sharp decrease in heat transfer enhancement effect. After the peak at q_w" ~ 51 kW/m^2, percentage enhancement dropped from 34.4 % at q_w" ~ 76 kW/m^2 to 13.2 % at the highest heat flux condition of q_w" ~ 157 kW/m^2. The observation of peak heat transfer enhancement at low vapour qualities (i.e. near the onset of boiling) and depreciating enhancement effect with subsequent increase in exit vapour quality, agree with the results of Bai et al. [230] and Sun et al. [252] using porous coatings, as covered in Section 2.9.2.2.

The dependency of two-phase heat transfer enhancement on wall heat flux is due to the influence of flow patterns in the microchannel heat sink. At low wall heat fluxes and low exit vapour qualities, bubbly and slug flow are the dominant flow patterns (i.e. observed in over half the length of the channel array) in the microchannel heat sink. In the bubbly flow regime, the two-phase heat transfer mechanism is highly controlled by bubble nucleation activity in the channels, i.e. the nucleate boiling component contributes primarily to two-phase heat transfer. In the slug flow regime, bubble nucleation is still highly active, since the high bubble generation activity triggers bubble coagulation and bubble confinement in the channels. Despite the fact that nucleation sites are periodically suppressed with liquid film dryout (see

Figure 4.7), especially with the formation of long slugs, bubble nucleation activity remains very high in the coated channels (see Figure 8.20, Slug, Location 2). Thus, the nucleate boiling mechanism continues to be a major contributor to two-phase heat transfer. Furthermore, thin-film evaporation from the slug also begins to contribute to overall two-phase heat transfer in the channels in the slug flow regime.

The bubble nucleation activity in the coated channels is significantly higher in comparison to the plain channels. In fact, a much earlier transition from bubbly to slug flow was observed in the coated microchannels compared to the plain microchannel heat sink, see Table 8.1. This is attributed to the abundance of potential nucleation sites formed by dendritic structures of the coating on the surface of the channels (see Figure 8.5). As highlighted in Section 8.5.2.1, the deeper cavities are also believed to encourage vapour entrapment and consequently increase bubble generation frequency from cavities. Since higher bubble generation activity is intrinsically linked to higher nucleate boiling heat transfer coefficients, higher average two-phase heat transfer coefficients may be obtained in the coated channels, where bubble nucleation was more active.

A heat transfer enhancement of 21.1 % and a peak enhancement of 43.5 % were obtained at q_w" ~ 25 kW/m^2 and q_w" ~ 51 kW/m^2 respectively. Authors in [230], [252], [260] have also reported peak flow boiling heat transfer enhancement effect at low vapour qualities (between x = 0.03 to x = 0.1) using coatings compared to untreated microchannels. Heat transfer enhancement diminished with increasing vapour qualities in the abovementioned studies. The wall heat flux at which the highest enhancement effect was obtained, i.e. q_w" ~ 51 kW/m^2, corresponds to a vapour quality of x = 0.22 at the exit of the channels.

The moderate heat transfer enhancement obtained at the lowest heat flux condition (i.e. q_w" ~ 25 kW/m^2) could be due to the relatively short saturated flow boiling length, i.e. 8 mm compared to the full channel length of 20 mm. Additionally, the lower wall superheat and consequent activation of fewer nucleation sites on the surface by comparison to q_w" ~ 51 kW/m^2, where the highest enhancement of 43.5 % was recorded, may also have resulted in a lower enhancement effect at this low wall heat flux. The range of active nucleation sites increase with increasing wall superheat, especially at low wall superheat degrees, based on Hsu's nucleation model [109] (see Figure 8.10). The wall superheat was just above 4 K at q_w" ~ 25 kW/m^2 and increased to 7 K at q_w" ~ 51 kW/m^2. Notably, the flow pattern was

predominantly slug flow at q_w" ~ 51 kW/m^2, where the maximum percentage enhancement is recorded. As highlighted above, the earlier transition to the slug flow regime indicates much higher bubble generation in the coated channels. The higher nucleate boiling heat transfer coefficients, combined with the accelerated contribution of the thin-film evaporation mechanism to two-phase heat transfer (owing to earlier transition to slug flow) compared to the plain channels, could have resulted in a peak in enhancement effect at this wall heat flux condition.

Following the peak at q_w" ~ 51 kW/m^2, the enhancement in average two-phase heat transfer coefficient depreciates in the medium to high heat flux region, namely q_w" = 76 kW/m^2 to 157 kW/m^2 (or exit vapour quality x > 0.22). As mentioned above, diminishing heat transfer enhancement effect beyond a certain vapour quality was also observed in [230], [252], [260]. In the current study, decreasing enhancement effect corresponded to more severe nucleate boiling suppression in the channel, as churn and annular flow begins to dominate in the heat sink, compared to at lower wall heat fluxes where slug flow is dominant. As the nucleate boiling mechanism is believed to be the more efficient method in two-phase heat transfer (as discussed in Section 4.2.2), as thin-film evaporation increasingly overtakes nucleate boiling as the main mode of heat transfer in the channels, the overall heat transfer coefficient decreases in the channel. Nonetheless, the decreasing trend appears to slow slightly between namely q_w" ~ 104 kW/m^2 to 157 kW/m^2. Incidentally, this corresponds to the dominance of annular flow in the heat sink (i.e. annular flow observed in at least half of the channel length (in total 20 mm).

At medium to high heat fluxes, churn and annular flow are mainly observed in the heat sink. As discussed in Section 4.2.1, bubble nucleation activity appears to be suppressed intermittently in churn flow while nucleation sites in the liquid film of annular flow are also periodically suppressed with gradual thinning of the film. Accordingly, the contribution of the nucleate boiling mechanism to two-phase heat transfer decreases, while the contribution of the convective boiling mechanism increases through thin-film evaporation in the churn and annular flow regime. Since the heat transfer augmentation provided by the coating is strongly related to bubble nucleation and by extension, the nucleate boiling heat transfer mechanism, the enhancement effect drops, understandably, in the churn and annular flow dominant heat fluxes, where the contribution of the nucleate boiling mechanism diminishes.

It is important to note that the nucleate boiling component does not deplete completely, evident from Figure 4.3, Annular, Location 3 and also Figure 8.21, Annular, Location 3, where a considerable number of nucleation sites on the side walls remain active during annular flow, at least in periods when the wall is wetted by a thin-liquid film. Therefore, some amount of heat transfer enhancement remain observable between $q_w^{"}$ = 76 kW/m^2 and 160 kW/m^2 in the heat sink. Another possible enhancement effect could be due to the irregularity of the coating structure (see Figure 8.7 and Figure 8.8) and the resulting higher surface area provided by the coating, by comparison to the plain microchannels. Liquid film evaporation rates in the coated channels could have been promoted by the increased heat transfer area as well as increased wall turbulence induced by perturbations on the coated walls. Larger surface area and improved fluid mixing were also postulated as reasons for the enhancement effect observed in the coated test section for single-phase flow (see Section 8.3.1).

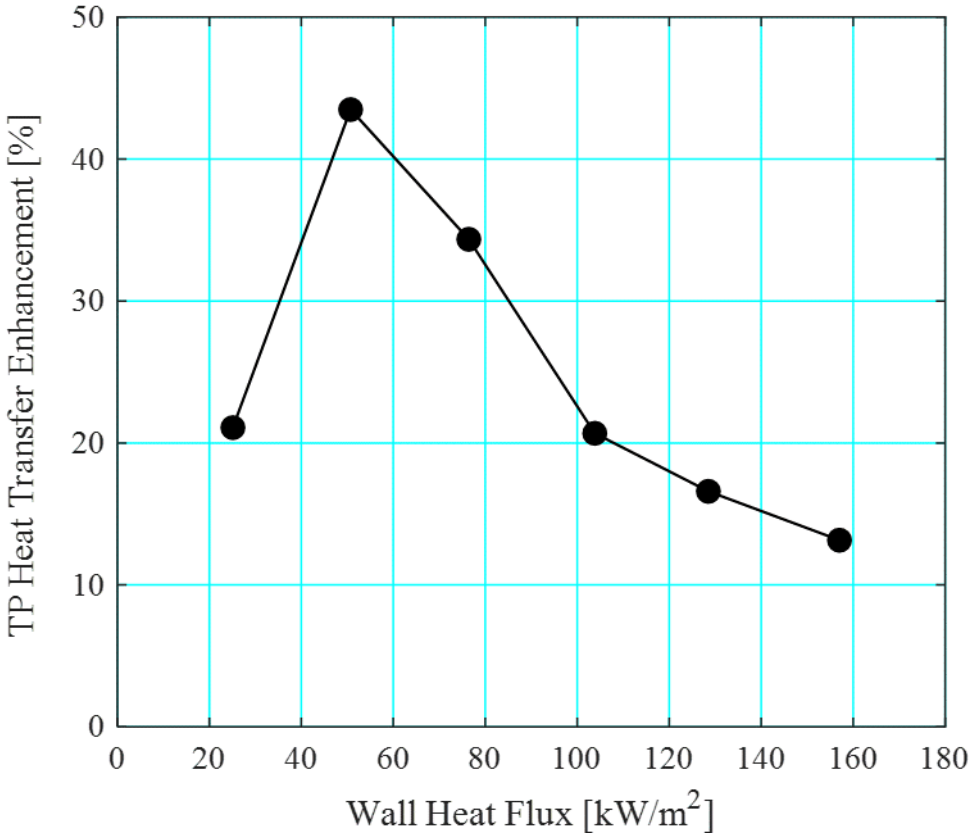

Figure 8.25: Percentage of two-phase heat transfer enhancement (based on Eq. (8.16)) using the coated microchannels at P = 1 bar, G = 200 kg/m^2 s and ΔT_{sub} = 10 K.

8.5.2.3 Pressure Drop

Microchannel pressure drop in the two-phase region is depicted in Figure 8.26 for the plain and coated test section. In both heat sinks, two-phase pressure drop increases with increasing wall heat flux. This is mainly due to the effect of higher void fraction in the channels with increasing heat flux on the frictional and acceleration pressure drop components. The difference in two-phase pressure drop between the plain and coated heat sink appears to increase with increasing wall heat flux. At a given wall heat flux condition, flow boiling pressure drop in the coated channels is higher in comparison to the plain channels. As highlighted in Section 8.5.2.1, higher bubble nucleation activity was observed in coated microchannel heat sink. While the channel void fraction was not directly measured, the higher nucleation activity indicates higher void fraction in the coated channels. Accordingly, flow pattern transitions were also accelerated in the coated test section, especially the bubbly-slug transition boundary (see Table 8.1).

Notably, two-phase pressure drop in the coated heat sink rose significantly from 3.7 kPa to 6.1 kPa between wall heat fluxes $q_w^{"}$ = 125 kW/m^2 and 153 kW/m^2. The region where annular flow is observed in the heat sink extended with the increase in wall heat flux, however, persistent wall dryout was not observed in flow visualisation and the critical heat flux limit was not reached at the highest wall heat flux condition in the coated heat sink. Interestingly, the magnitude of flow oscillations increased with the corresponding increase in wall heat flux. From Figure 8.27, the standard deviation of the total pressure drop across the heat sink doubled from 0.05 kPa to 0.1 kPa between $q_w^{"}$ = 125 kW/m^2 and 153 kW/m^2 in the coated microchannel test section.

To further investigate the increase in flow boiling pressure drop posed by the coating, the percentage difference in two-phase pressure drop between the plain and coated channels are calculated according to Eq. (8.17) and plotted in Figure 8.28. The pressure drop penalty posed by the coating is shown to be highly dependent on wall heat flux.

$$\Delta P_{pen} = \frac{P_{tp,coated} - P_{tp,plain}}{P_{tp,plain}} \times 100\ \% \tag{8.17}$$

At the lowest wall heat flux condition of $q_w^{"}$ = 25 kW/m^2, flow boiling pressure drop in the coated heat sink was 5.5 % higher in the coated heat sink compared to the plain heat sink. This is despite of the fact that slug flow has already developed in the coated microchannels at the lowest wall heat flux, while the two-phase flow pattern remained predominantly in the bubbly

region in the plain heat sink (see Figure 4.13 and Figure 8.23). The relatively low percentage penalty could be due to the short two-phase length in the region (i.e. 8 mm) in the heat sink in relation to the total length of the channels (i.e. 20 mm). The coating had a smaller effect on slug-churn and churn-annular flow pattern transition boundaries in the microchannel heat sink (i.e. similar flow regimes were observed in both heat sinks at a given wall heat flux condition).

Two-phase pressure drop penalty dropped slightly to 3.1 % with increase in wall heat flux to $q_w^{"}$ = 51 kW/m^2. This could be a result of smaller pressure drop oscillations in the coated heat sink, owing to lower wall superheat at the same heat flux condition. Lower degree of superheat have been found to suppress rapid bubble growth instabilities near the onset of boiling. At this wall heat flux condition, bubbly flow is observed near the channel inlet of both heat sinks. The standard deviation in total pressure drop across the plain and coated heat sinks were 0.55 kPa and 0.22 kPa respectively, while the coating lowered wall superheat from 9.6 K to 6.8 K, see Figure 8.29. Incidentally, no dryout was observed in the coated channels while dryout lasting for over 100 ms was observed in the plain heat sink at this heat flux condition (see Figure 4.7).

Following that, flow boiling pressure drop penalty rose from 10.5 % to 13.1 % as churn and annular flow begins to dominate in the heat sink between $q_w^{"}$ = 76 to 104 kW/m^2. Pressure drop penalty dropped slightly again to 10.8 % at $q_w^{"}$ = 128 kW/m^2 when annular flow was the dominant flow regime in both heat sinks. The relatively stable pressure drop penalty in this range of heat fluxes could be because similar flow regimes (mainly churn and annular flow) were observed in both heat sinks at a given wall heat flux condition, with the higher pressure drop being induced by the slightly smaller hydraulic diameter of the coated channels as well as higher channel void fraction due to more active bubble nucleation in the coated heat sink. At the highest wall heat flux condition where annular flow was dominant in the coated microchannels, there was a large jump in two-phase pressure drop penalty of almost 40 %. This may be attributed to the sharp rise in channel two-phase pressure drop in the coated heat sink at $q_w^{"}$ = 153 kW/m^2, as highlighted earlier from Figure 8.26 and may be related to larger pressure drop oscillations in the heat sink. Incidentally, slightly longer dryout and rewetting cycles were observed in the coated heat sink (i.e. 10 ms) compared to the plain heat sink (i.e. 3 ms) at $q_w^{"}$ = 153 kW/m^2 and $q_w^{"}$ = 160.7 kW/m^2 respectively, as presented in Section 8.5.2.1.

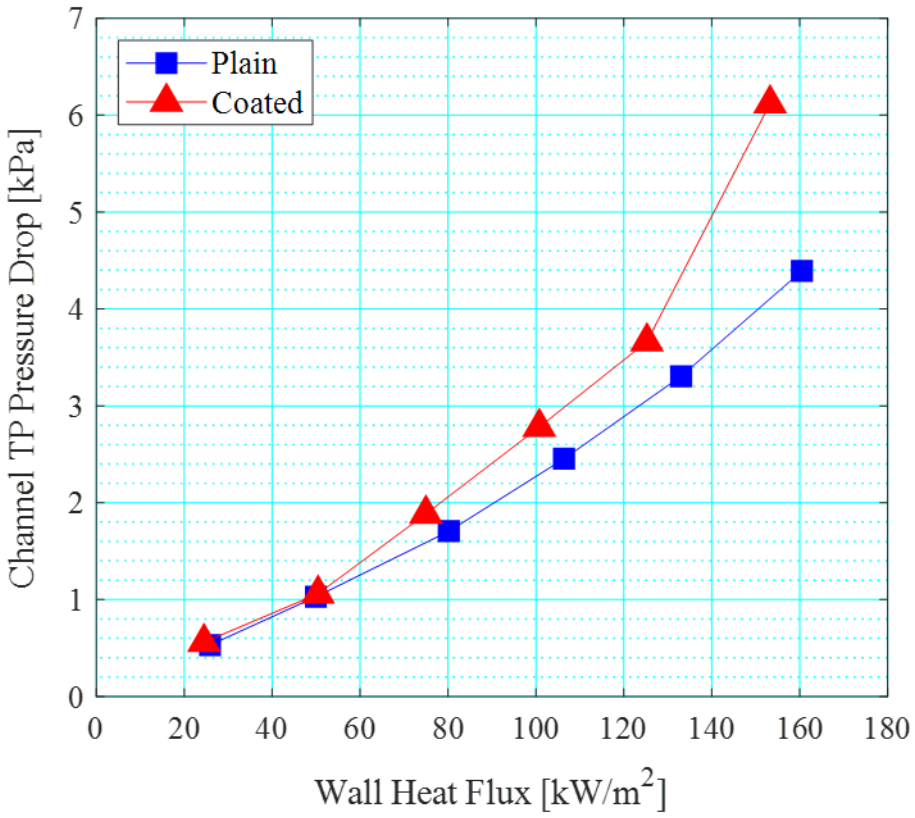

Figure 8.26: Two-phase pressure drop in the plain and coated microchannels P = 1 bar, G = 200 kg/m^2 s and ΔT_{sub} = 10 K.

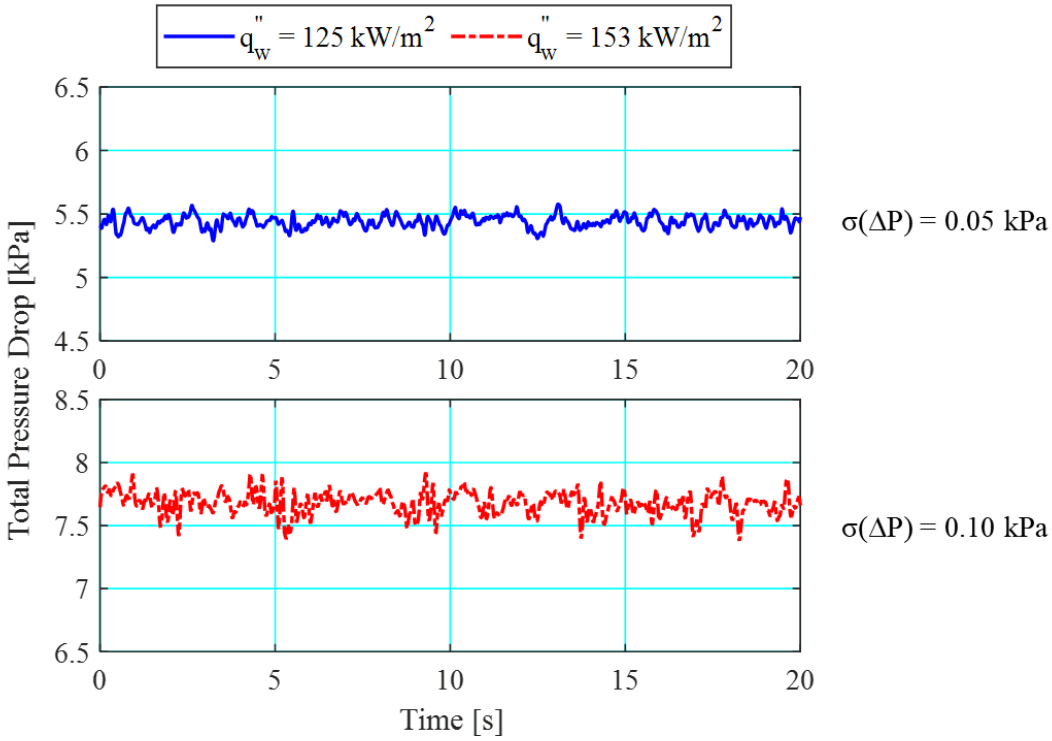

Figure 8.27: Measured pressure drop across the coated heat sink at q_w" ~ 125 kW/m^2 and q_w" ~ 153 kW/m^2 over a window of 20 s for G = 200 kg/m^2 s and ΔT_{sub} = 10 K.

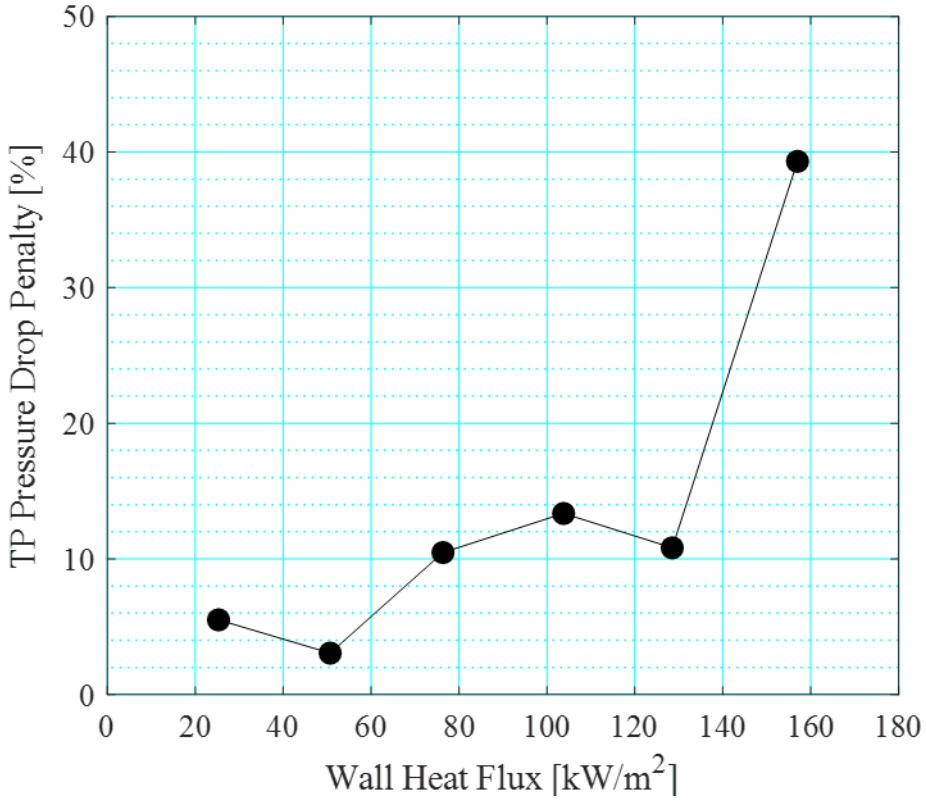

Figure 8.28: Two-phase pressure drop penalty as a result of the coating in the microchannel heat sink at P = 1 bar, G = 200 kg/m^2 s and ΔT_{sub} = 10 K.

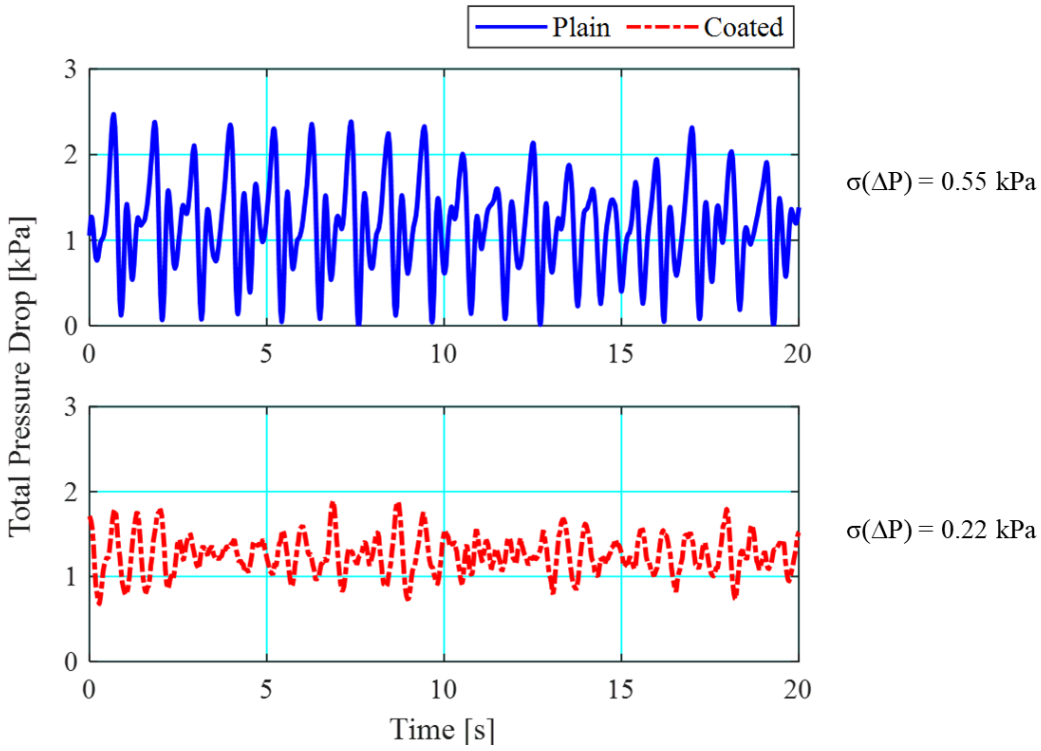

Figure 8.29: Measured pressure drop across the plain and coated heat sink respectively at q_w" ~ 51kW/m^2 over a window of 20 s for G = 200 kg/m^2 s and ΔT_{sub} = 10 K.

8.5.3 Effect of Saturation Pressure

8.5.3.1 Flow Patterns

In order to investigate the effect of inlet pressure on flow boiling characteristics in the coated microchannel heat sink, experiments were conducted at inlet pressures of P = 1, 1,5 and 2 bar for wall heat fluxes between $q_w^{"}$ = 24.5 to 154.3 kW/m^2. The mass flux and inlet subcooling degree were maintained at G = 200 kg/m^2 s and ΔT_{sub} = 10 K respectively. Increasing the inlet pressure in the coated microchannel heat sink accelerated two-phase flow pattern transitions from bubbly to slug, churn and annular flow, as summarised in Table 8.2.

Transition from bubbly to slug flow in the coated microchannels occurred at lower vapour qualities with increasing pressure, particularly between P = 1 bar and P = 1.5 bar. Bubbly-slug transition occurred at x = 0.008 for P = 1 bar and x = 0.005 for P = 1.5 bar and P = 2 bar respectively. Accelerated flow pattern transitions, especially between P = 1 bar and P = 1.5 bar, could be due to higher bubble generation activity and more intense bubble coalescence phenomenon in the channels at higher saturation pressures. As illustrated in Figure 4.25, increasing saturation pressure increases the range of active nucleation cavities, especially for smaller scale cavities with mouth radii less than 1 μm. Furthermore, as discussed in Section 4.3.1, increasing system pressure decreases the vapour density of the working fluid. Based on force balance theory [108], lower vapour densities allow for smaller bubble departure diameters (thus shorter bubble growth time) as a lower drag force is imposed on the bubble growing from a nucleation site. As a consequence, higher bubble generation frequencies at a given site may be observed at higher pressures owing to the shorter waiting time between successive bubble nucleation cycles. This was also reported in the study of Euh et al. [103] concerning macroscale flow boiling, from which bubble departure dynamics in microscale flow boiling may be understood. The above justifies the higher bubble nucleation activity in the coated channels at higher saturation pressures.

In fact, smaller bubble diameters at higher system pressures were captured in flow visualisation for the plain microchannels. These are depicted in Figure 4.27 to Figure 4.29 and thoroughly discussed in Section 4.3.1. Kuo and Peles [101] also observed smaller bubble sizes with increasing system pressure in their parallel microchannel array. On the contrary, increasing system pressure in the plain microchannel heat sink delayed flow pattern transitions in the channel. This was attributed to smaller mean bubble diameters in the channel, which had a

smaller tendency to coalesce even though the overall bubble generation frequency may be higher in the channel at higher saturation pressures. In the case of the coated microchannels, it would appear that the effect of higher bubble generation frequency in the channels preceded over the effect smaller bubble diameters in the channel, thus accelerating flow pattern transitions in the channels between P = 1 bar and P = 1.5 bar. The smaller shift between bubbly-slug transition between P = 1.5 bar and P = 2 bar could be because the effect of smaller diameter overcame the effect of bubble generation frequency in the channels.

The subsequent flow regime transitions were also residually affected. The higher vapour content in the microchannels at higher pressures, owing to higher bubble nucleation activity, could have promoted the establishment of a clear vapour core characteristic of annular flow in the heat sink. The vapour quality at which flow regime transition from churn to annular flow was observed decreased from x = 0.3 to x = 0.23 and subsequently to x = 0.19 corresponding to pressure increase from P = 1 to 2 bar. Higher vapour density at higher saturation pressures may also have influenced earlier transition to annular flow in the microchannels.

Notably, prolonged wall dryout lasting for an average of 27 ms was observed in the coated heat sink at P = 1.5 bar and $q_w^{"}$ = 154.3 kW/m^2 in the annular flow regime. The sequence of complete wall dryout and rewetting by the churn wave mechanism has previously been depicted in Figure 4.7. At a similar wall heat flux at P = 2 bar, where annular flow was also dominant in the coated heat sink, dryout lasted for approximately 30 ms. In the plain heat sink at a similar wall heat flux condition (i.e. $q_w^{"}$ ~ 160 kW/m^2), dryout cycles observed were much shorter, namely between 7 ms to 8 ms for both P = 1.5 bar and P = 2 bar. Longer wall dryout periods in the coated heat sink at a given operating condition may be attributed to higher bubble generation frequency and higher film evaporation rates (due to larger heat transfer area) in the coated channels.

Table 8.2: Flow pattern transition vapour qualities in the coated heat sink at different system pressures for G = 200 kg/m^2 s and ΔT_{sub} = 10 K.

P [bar]	x_{B-S} [-]	x_{S-C} [-]	x_{C-A} [-]
1.0	0.008	0.067	0.30
1.5	0.005	0.064	0.23
2.0	0.005	0.057	0.19

8.5.3.2 Heat Transfer

Flow boiling heat transfer coefficients generally increased with increasing heat flux at all system pressures investigated in the coated microchannel heat sink, as shown in Figure 8.30. Nonetheless, critical heat flux phenomenon was observed when heat flux was increased to q_w" ~ 129 kW/m^2 at P = 1.5 bar and similarly at P = 2 bar. Experiments at P = 1 bar did not exceed the critical heat flux limit. Notably, increasing saturation pressure increased average two-phase heat transfer coefficients in the coated microchannel heat sink. This was similarly observed in the plain microchannel heat sink, although a smaller pressure effect on average two-phase heat transfer coefficients was recorded between P = 1.5 bar and P = 2 bar (see Figure 4.18).

Higher average two-phase heat transfer coefficients at higher system pressures could be due to larger nucleate boiling heat transfer coefficients and its resultant effect on the magnitude of two-phase heat transfer in the channels. This is further supported by flow pattern observations, where accelerated flow regime transitions, particularly from bubbly to slug flow, with increasing saturation pressures were recorded in the coated microchannel heat sink (see Table 8.2).

The critical heat flux limits exhibited at P = 1.5 bar and P = 2 bar may be due to excessive bubble generation activity in the annular liquid film, which exacerbated persistent wall dryout in the coated channels. Wall dryout persisted for nearly 30 ms at P =1.5 bar and P = 2 bar, as highlighted in Section 8.5.3.1. In contrast, in the plain channels where wall dryout only lasted for around 7 ms to 8 ms, critical heat flux phenomenon was not observed at a similar wall heat flux condition. More frequent intermittent wall dryout could have reduced the time-averaged heat transfer coefficient measured. As a result, a sudden drop in average two-phase heat transfer coefficient, signifying critical heat flux phenomenon, were observed at q_w" ~ 129 kW/m^2 at the higher saturation pressures.

The enhancement in two-phase heat transfer in the coated microchannel heat sink as compared to the plain microchannel heat sink is depicted in Figure 8.31 for the three inlet pressures investigated at a nominal mass flux of G = 200 kg/m^2 s and inlet subcooling degree of ΔT_{sub} = 10 K.

As presented above, at P = 1 bar, the percentage of flow boiling heat transfer enhancement increases in the low heat flux region, peaking at $q_w^{"} \sim 51$ kW/m^2 where the nucleate boiling mechanism is most dominant in the microchannels. Nucleate boiling suppression increases with increasing heat flux and the convective boiling mechanism gradually takes precedence over nucleate boiling in two-phase heat transfer. Therefore, the enhancement effect of the coating drops sharply following the peak with increasing wall heat flux. The depreciation in two-phase heat transfer enhancement in the coated channels appear to tend towards a plateau between $q_w^{"} \sim 104$ kW/m^2 and 157 kW/m^2.

On the contrary, at P = 1.5 bar and P = 2 bar, relatively high heat transfer enhancement factors are readily observed from low wall heat fluxes. At $q_w^{"} \sim 25$ kW/m^2, the two-phase heat transfer enhancement recorded is 37.5 % and 45.5 % for P = 1.5 bar and P = 2 bar respectively, whereas it is just over 20 % at P = 1 bar at a similar wall heat flux level.

As discussed in Section 8.5.2.2, improvements in two-phase heat transfer by means of porous coatings are highly flow regime dependent. From Section 8.5.3.1, increasing system pressure in the coated channels brought about earlier flow pattern transitions in the coated channels (see Table 8.2). This was attributed to higher bubble generation activity in the coated heat sink at higher pressures, thus increasing the rate of bubble coalescence in the channels, consequently inducing earlier flow regime transition from bubbly to slug flow. At the lowest wall heat flux condition of $q_w^{"} \sim 25$ kW/m^2, slug flow is already observed in over half the length of the coated channels (namely the downstream half) at P = 1.5 bar and P = 2 bar. On the other hand, for a similar wall heat flux, slug flow is only observed towards the exit of the channel array at P = 1 bar. Slug flow becomes dominant at a wall heat flux of $q_w^{"} \sim 25$ kW/m^2, where the enhancement in two-phase heat transfer peaks at P = 1 bar.

Interestingly, in the plain channels, the opposite was the case, i.e. increasing saturation pressure delayed flow regime transitions instead, see Table 4.4. This was because the effect of smaller bubble diameters overcame the effect of higher bubble nucleation activity at higher pressures in the plain heat sink. In the plain microchannel heat sink, the flow pattern observed was largely bubbly flow and slug flow did not develop, even near the channel exit, at $q_w^{"} \sim 25$ kW/m^2. Since larger improvements in average two-phase heat transfer coefficient is observed where the nucleate boiling mechanism has a large contribution to two-phase heat transfer and thin-film evaporation just begins to contribute to flow boiling heat transfer (i.e. the slug flow

regime), relatively high percentage enhancements are immediately observed from low wall heat fluxes at P = 1.5 bar and P = 2 bar.

Following that, there is a slight drop in enhancement effect with increasing wall heat flux to q_w" ~ 78 kW/m^2 at P = 1.5 bar. Further increase in heat flux beyond q_w" ~ 78 kW/m^2 towards q_w" ~ 157 kW/m^2 resulted in a sharp depreciation in flow boiling heat transfer improvement. At P = 2 bar, two-phase heat transfer augmentation increased slightly from 45.5 % to 49 % between q_w" ~ 25 kW/m^2 and 51 kW/m^2 but fell slightly to 46.6 % with further heat flux increase to q_w" ~ 78 kW/m^2. The decrease in heat transfer augmentation is related to nucleation suppression in the channels with flow pattern development.

Beyond q_w" ~ 78 kW/m^2, the improvement in two-phase heat transfer in the coated channels in relation to the plain channels decreased steeply with increasing heat flux, as observed for P = 1.5 bar. As a matter of fact, two-phase heat transfer augmentation is only around 8 % at P = 1.5 bar and P = 2 bar at the highest heat flux condition, i.e. q_w" ~ 157 kW/m^2, and is lower than that of P = 1 bar, i.e. 13.1 % at a similar wall heat flux level. This is due to the critical heat flux phenomenon, induced by wall dryout (of nearly 30 ms) in the annular flow regime, observed at the two higher pressures, as highlighted in Section 8.5.3.1.

Notably, there is a relatively consistent difference in flow boiling heat transfer enhancement between P = 1.5 bar and P = 2 bar when wall heat flux ranged from q_w" ~ 26 to 78 kW/m^2. This gradually narrows with further increase in heat flux and diminishes as the critical heat flux limit is exceeded at q_w" ~ 157 kW/m^2. The diminishing difference between the trends of P = 1.5 bar and P = 2 bar could indicate more intense nucleate boiling suppression at P = 2 bar at a given wall heat flux condition. This may be caused by much higher bubble nucleation activity at lower wall heat fluxes (evidenced by accelerated flow pattern transition between bubbly and slug flow at P = 2 bar as well as almost 50 % in two-phase heat transfer enhancement) which may have exacerbated channel wall dryout and nucleate boiling suppression at P = 2 bar, leading to a reduction in the enhancement effect at higher system pressures toward high heat fluxes.

Overall, the higher enhancement effect exhibited by the coating for a given wall heat flux at higher pressures may be twofold. Firstly, higher nucleation site density and higher bubble generation activity (owing to the deeper cavities) induce larger two-phase heat transfer

coefficients in the coated channels as compared to the plain channels. Secondly, as discussed extensively in Section 4.3.1, shorter bubble growth times at higher system pressures could also act to further increase the bubble generation frequency on the coated surface, which is substantially more populated with cavities, hence increasing the flow boiling heat transfer coefficients in the coated channels.

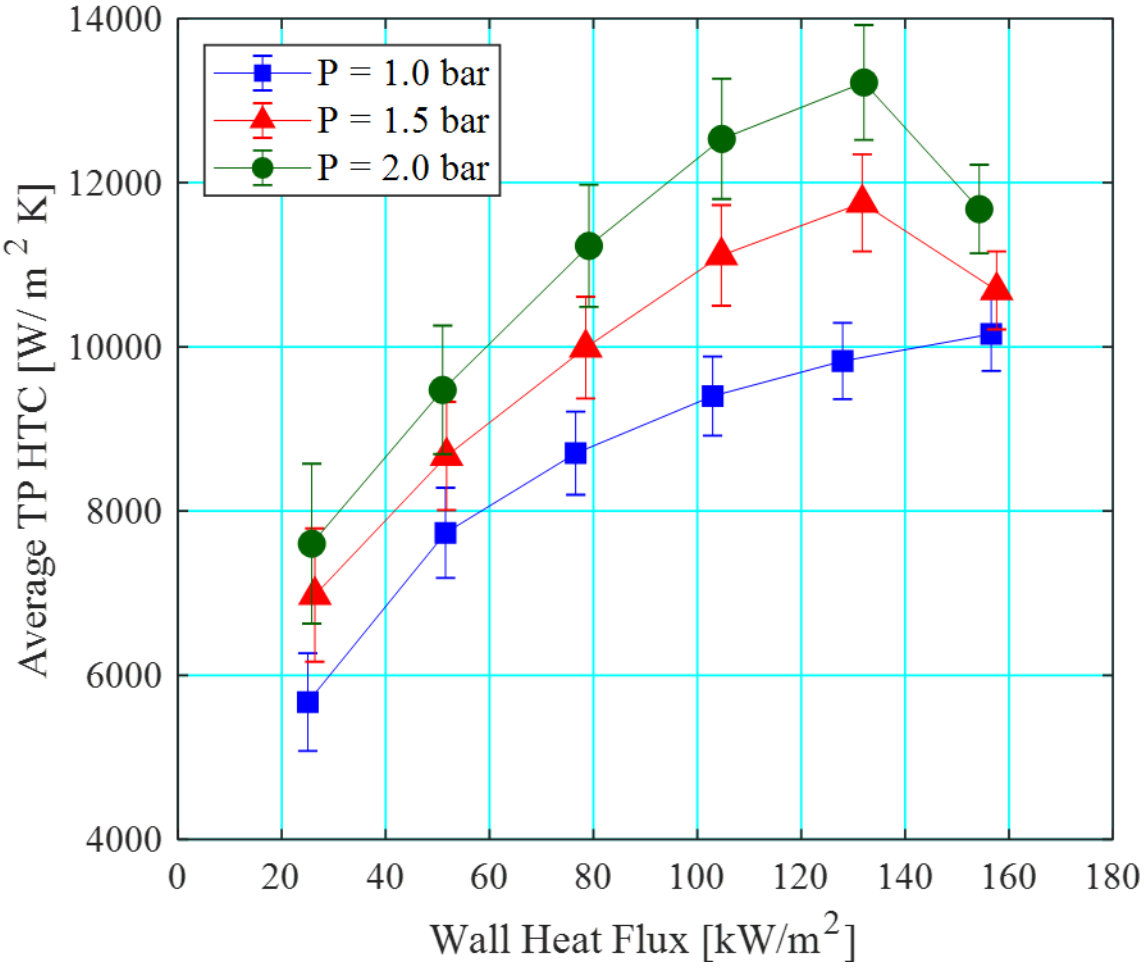

Figure 8.30: Effect of system pressure on average two-phase heat transfer coefficients as a function of wall heat flux in the coated heat sink for G = 200 kg/m^2 s and ΔT_{sub} = 10 K

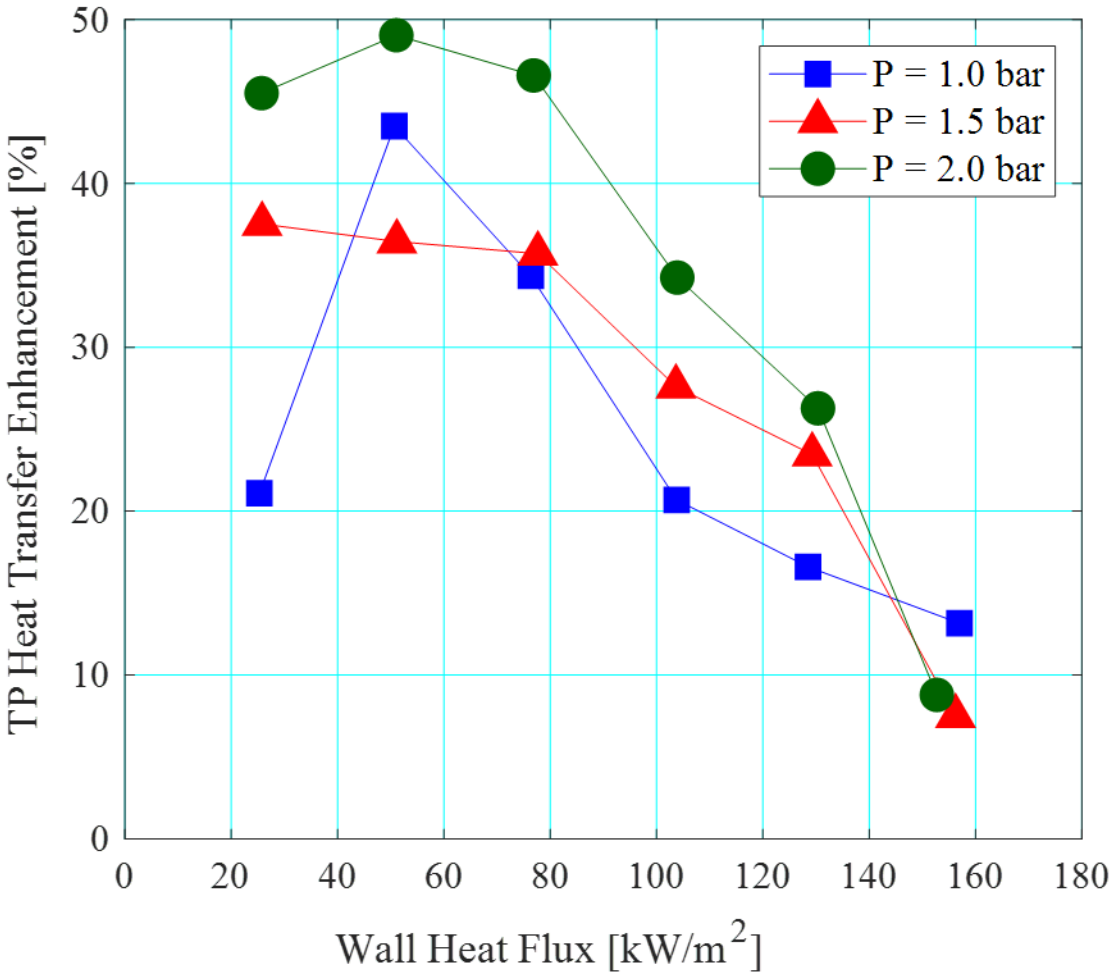

Figure 8.31: Percentage enhancement in heat transfer at different system pressures with respect to wall heat flux, for operating conditions of G = 200 kg/m^2 s and ΔT_{sub} = 10 K.

8.5.3.3 Pressure Drop

Two-phase pressure drop in the coated microchannels are depicted in Figure 8.32 for three saturation pressures investigated. Across all pressures, flow boiling pressure drop increased gradually with increasing wall heat flux. This may be attributed to the increase in channel void fraction due to increase in bubble nucleation activity at higher wall heat fluxes, leading to an increase in the frictional and acceleration pressure drop component in the channels. As covered in Section 8.5.2.3, the sharp rise in channel pressure drop at the highest wall heat flux condition when P = 1 bar may be related to two-phase flow oscillations in the heat sink, see Figure 8.27.

Two-phase pressure drop is generally lower at a given wall heat flux condition with increment in system pressure. This was similarly observed in the plain test section and has been reported in [97], [101], [102]. Additionally, at moderate wall heat fluxes (with the exception of $q_w^{"} \sim 153$ kW/m^2), the effect of system pressure on flow boiling pressure drop is weaker between P = 1 bar and P = 1.5 bar in the coated microchannel heat sink. The change in fluid properties with increasing pressure could have been overcome by the increase in bubble nucleation activity at P = 1.5 bar. The noticeably lower magnitudes of two-phase pressure drop may also be related to the suppression of flow boiling oscillations, as presented in Section 4.3.2. A potential relationship between the magnitude of two-phase pressure loss and flow instabilities, as well as dryout are discussed in Section 8.5.5.3. On the contrary, in the plain channels, a weaker pressure effect is observed between saturation pressures P =1.5 and P = 2 bar. This was attributed to correspondingly smaller changes in fluid properties as well as a smaller difference between flow pattern transition boundaries (bubbly slug and slug-churn transition) between the higher pressures.

The two-phase pressure drop penalty at different saturation pressures in comparison to the plain microchannels is shown in Figure 8.33. Pressure drop penalty generally increased with increasing heat flux at low wall heat fluxes. This is clear from the trends of P = 1.5 bar and P = 2 bar, and may be attributed to accelerated flow regime transition from bubbly to slug flow in the coated heat sink in comparison to the plain microchannel heat sink (see Table 4.4 and Table 8.2). For instance, at P = 1.5 bar, bubbly-slug transition occurred at x = 0.005 in the coated heat sink, significantly earlier than in the plain heat sink, i.e. x = 0.064.

As covered in Section 8.5.2.3, a drop in flow boiling pressure drop penalty, observed at $q_w"$ = 51, 78 and 104 kW/m^2 respectively for increment in system pressure from P = 1 bar to 2 bar, may be a result of the suppression of flow boiling instabilities in the coated microchannel heat sink in comparison to the plain heat sink (see Figure 8.29 for P = 1 bar). This is typically the case where bubbly flow is observed near the inlet of the channels, as rapid bubble growth instabilities tend to occur in this flow regime. Flow boiling pressure drop penalty rise again after the dip as churn and annular flow begins to dominate in the heat sink. As observed in Section 8.5.2.3, two-phase pressure drop penalty tend to fluctuate where churn and annular flow is commonly observed as the dominant flow regime in both heat sinks. Notably, the critical heat flux limit is exceeded at P = 1.5 bar and P = 2 bar in the coated heat sink. As presented in Section 8.5.3.1, persistent channel wall dryout of nearly 30 ms was periodically observed at these conditions. Nevertheless, critical heat flux phenomenon do not have a clear effect on two-phase pressure drop penalty, as it drops sharply at P = 1.5 bar and appear to reach a plateau at P = 2 bar.

At the lowest wall heat flux condition, the negligible effect of pressure could be due to the short length of the boiling region (i.e. ~ 8 mm compared to the total channel length of 20 mm) in both heat sinks. However, the pressure effect becomes more significant with increasing wall heat flux. Two-phase pressure drop penalty was the highest at P = 1.5 bar, except at $q_w"$ = 153 kW/m^2 where a sharp rise in flow boiling pressure drop was recorded in the coated microchannel heat sink. As covered above, this is potentially related to two-phase oscillations in the heat sink.

The larger pressure drop penalty measured at the system pressure of P = 1.5 bar in comparison to P = 1 bar could be due to the larger difference in flow pattern transition boundaries between the plain and coated heat sink at P = 1.5 bar (see Table Table 4.4 and Table 8.2). At P = 1 bar, slug-churn transition occurred at x = 0.068 and x = 0.067 in the plain and coated channels respectively, while transition to annular flow was observed at x = 0.3 in both heat sinks. At P = 1.5 bar, bubbly-slug and churn flow transition occurred much earlier in the coated heat sink, at x = 0.005 and x= 0.064 respectively, compared to at x = 0.064 and x = 0.119 respectively in the plain microchannel heat sink. Furthermore, increasing system pressure increased bubble nucleation activity in the channels. This is supported by the generally improved two-phase heat transfer enhancement percentages shown in Figure 8.31. Higher bubble nucleation activity could indicate higher channel void fraction at higher saturation pressures, thereby increasing

two-phase pressure drop in the channels and resulting in higher pressure drop penalty at higher pressures at a given wall heat flux condition at P = 1.5 bar compared to P = 1 bar.

Nonetheless, the two-phase pressure drop penalty at P = 2 bar is significantly lower in comparison to P = 1.5 bar across most wall heat fluxes, even with higher bubble nucleation activity (thus higher channel void fraction) at P = 2 bar. This could be due to the effects of flow instability on the magnitude of two-phase pressure drop, as presented in Section 8.5.2.3 and 8.5.5.3. Increasing system pressure decreased flow boiling instabilities in the channels, see Section 4.3.2, which may also reduce pressure loss in the microchannels. Whilst accelerated flow regimes due to increased bubble nucleation activity may increase two-phase pressure drop, at P = 2 bar, the flow instabilities in the channel may be sufficienly negated such that the two-phase pressure loss is lowered.

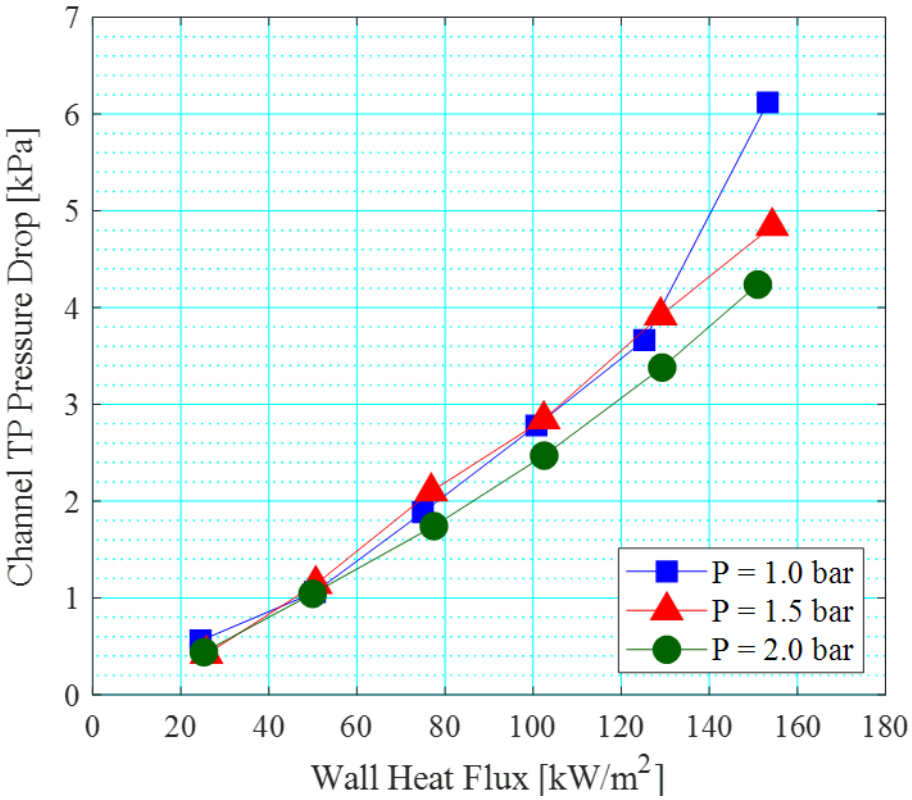

Figure 8.32: Two-phase pressure drop in the coated microchannels at different system pressures with respect to wall heat flux, for operating conditions of G = 200 kg/m^2 s and ΔT_{sub} = 10 K.

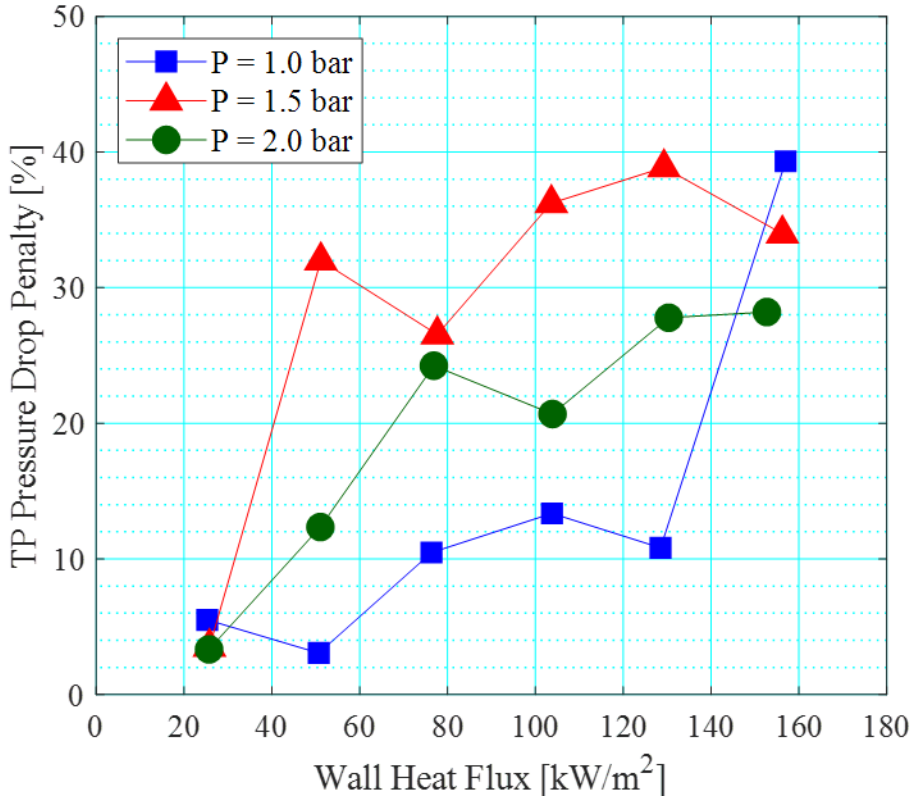

Figure 8.33: Microchannel two-phase pressure drop penalty as a result of the coating at different system pressures with respect to wall heat flux for G = 200 kg/m^2 s and ΔT_{sub} = 10 K.

8.5.4 Effect of Mass Flux

8.5.4.1 Flow Patterns

In order to investigate the effect of mass flux on flow boiling heat transfer, pressure drop as well as flow pattern evolution in the channels, experiments were conducted at channel mass velocities of G = 200 kg/m^2 s, 300 kg/m^2 s and 400 kg/m^2 s for wall heat fluxes ranging from $q_w^{"}$ = 24.8 – 234.3 kW/m^2 in the coated microchannel heat sink. The inlet pressure and inlet subcooling degree was remained at P = 1 bar and ΔT_{sub} = 10 K respectively.

Increasing mass flux from G = 200 kg/m^2 s to 400 kg/m^2 s accelerated flow regime transition from bubbly to slug, churn and annular flow in the coated heat sink. Earlier flow pattern transitions were also observed with increasing mass flux in the plain microchannel heat sink, see Table 4.6. This may be attributed to increased rate of bubble coalescence with higher flow inertia at higher channel mass fluxes, triggering earlier transition from bubbly to slug flow in the channels. The difference in transition vapour qualities were generally smaller between G = 300 kg/m^2 s and G = 400 kg/m^2 s in both heat sinks. The higher flow inertia may also have encouraged the establishment of a clear vapour core characteristic of annular flow in the channels, thus inducing earlier annular flow development in the channels at higher mass fluxes. Churn-annular transition occurred at x = 0.3, x = 0.19 and x = 0.15 with for mass fluxes G = 200, 300 and 400 kg/m^2 s respectively.

For a given mass flux condition, flow pattern transition occurred at lower vapour qualities in the coated heat sink in comparison to the plain heat sink. This was observed for G = 200 kg/m^2 s, as summarised in Table 8.1. This was also the case at the higher mass flux conditions of G = 300 kg/m^2 s and G = 400 kg/m^2 s, see Table 4.6 and Table 8.3. The difference between the slug-churn and churn-annular flow transition boundaries in the plain and coated heat sinks were larger at G = 300 kg/m^2 s and 400 kg/m^2 s, see Table 4.6 and Table 8.3. At G = 200 kg/m^2 s, there was a large shift in the bubbly-slug transition boundary between the plain and coated heat sink, however, vapour qualities at which the subsequent flow regime transitions occurred varied only slightly (less than 1.5 % smaller) between the two microchannel heat sinks.

As highlighted in Section 8.5.2.1, cyclic dryout lasting around 100 ms was observed in the plain microchannel heat sink (see Figure 4.7), but was not observed in the coated heat sink at G = 200 kg/m^2 s and a similar heat flux of $q_w^{"}$ ~ 51 kW/m^2. On the other hand, dryout and

rewetting cycles averaging around 30 ms at G = 200 kg/m^2 s in the coated channels were periodically observed during annular flow at $q_w^{"}$ = 153.3 kW/m^2.

Increasing system mass flux appeared to mitigate cyclic dryout in the coated microchannel heat sink in the annular flow regime. Persistent wall dryout was not observed at G = 300 kg/m^2 s and 400 kg/m^2 s in the coated heat sink. That is to say that wall dryout during annular flow was rewetted periodically by the churn wave mechanism (see Figure 4.12). Although transition to annular flow occurred earlier at higher mass fluxes, the higher flow inertia could have enhanced the liquid film rewetting capability and prevented dryout in the annular flow regime.

Table 8.3: Flow pattern transition vapour qualities in the coated heat sink at P = 1 bar and ΔT_{sub} = 10 K for wall heat fluxes ranging from $q_w^{"}$ = 24.8 – 234.3 kW/m^2.

G [kg/m^2 s]	x_{B-S} [-]	x_{S-C} [-]	x_{C-A} [-]
200	0.008	0.067	0.30
300	0.007	0.047	0.19
400	0.001	0.036	0.15

8.5.4.2 Heat Transfer

The effect of mass flux on average two-phase heat transfer coefficients in the coated microchannel heat sink is presented in Figure 8.34. Note that the data points at $q_w^{"} \sim 25$ kW/m^2 for G = 300 kg/m^2 s and 400 kg/m^2 s are omitted as all local heat transfer measurements are in the subcooled region. The influence of mass flux on average two-phase heat transfer coefficient is negligible between wall heat fluxes $q_w^{"} \sim 51$ to 130 kW/m^2, but grows with further increase in wall heat flux beyond $q_w^{"} \sim 130$ kW/m^2. A similar mass flux effect, i.e. insignificant mass flux effect at wall heat fluxes below $q_w^{"} \sim 161$ kW/m^2 but a prevalent mass flux effect in the high heat flux region, was also observed in the plain microchannel test section, see Figure 4.49.

The weak effect of channel mass flux at lower wall heat fluxes is attributed to the dominance of the nucleate boiling mechanism in the microchannels. With increasing wall heat flux, churn and annular flow begin to dominate in the heat sink and the contribution of the convective boiling mechanism to total heat transfer increases. Convective boiling increases with increasing mass velocity, as reported by Harirchian and Garimella [85], Huang et al. [92], Thiangtham et al. [117] and Agostini et al. [87] for microchannels. As flow pattern transition to the annular flow regime occurs earlier in the coated heat sink compared to the plain heat sink (see Table 8.1), it follows that the wall heat flux at which the mass flux effect begins to manifest is lower, i.e. $q_w^{"} \sim 130$ kW/m^2 in the coated test section and $q_w^{"} \sim 161$ kW/m^2 in the plain test section.

Figure 8.35 depicts the percentage enhancements in average two-phase heat transfer coefficients using the porous coating at an inlet pressure and subcooling of P = 1 bar and ΔT_{sub} = 10 K for the three mass fluxes investigated. Wall heat flux ranged between $q_w^{"}$ = 25.8 and 206.6 kW/m^2. Note that at $q_w^{"} \sim 26$ kW/m^2, flow boiling conditions are not yet established in the channels at G = 300 and 400 kg/m^2 s. Since the enhancement is specific to flow boiling heat transfer coefficients, the larger two mass fluxes have been omitted from the figure.

Generally, the enhancement effect of the coating reached a maximum at low wall heat fluxes and decreased with increasing wall heat flux. At the lowest mass flux condition, i.e. at G = 200 kg/m^2 s, the enhancement percentage decreased steeply between $q_w^{"} \sim 51$ to 104 kW/m^2 but begin to recover slightly beyond $q_w^{"} \sim 104$ kW/m^2. On the contrary, at the two higher mass fluxes of G = 300 and 400 kg/m^2 s, two-phase heat transfer augmentation depreciated sharply between $q_w^{"} \sim 51$ to 130 kW/m^2 but stabilised at around 25 % with increasing heat flux beyond

q_w" ~ 130 kW/m^2. Furthermore, the coating generally induced higher enhancement percentages at G = 300 kg/m^2 s compared to at G = 200 and 400 kg/m^2 s.

As highlighted previously, two-phase heat transfer enhancement by means of the porous coating peaked at a wall heat flux where the slug flow regime was dominant in the coated channels. At G = 200 kg/m^2 s, two-phase heat transfer enhancement jumped from 21.1 % to a maximum of 43.5 % between q_w" ~ 25 and 51 kW/m^2. The steep rise in percentage enhancement could be due to a larger number of nucleation sites being activated at higher wall superheats, i.e. higher nucleate boiling heat transfer coefficients in the channel. Notably, the transition boundary between bubbly and slug flow shifted to much lower vapour qualities in the coated heat sink compared to the plain heat sink (see Table 8.1). As discussed above, high bubble nucleation activity in the slug flow regime indicate that the nucleate boiling mechanism dominates flow boiling heat transfer, as is also the case in the bubbly flow regime. At the same time, thin-film evaporation occurring from the slug liquid film and also begins to contribute to two-phase heat transfer, much earlier than in the plain channels due to accelerated flow pattern transitions in the coated heat sink. The combined effects of the above could have resulted in a peak in coating enhancement effect at wall heat flux levels where slug flow is dominant.

Similarly, at G = 300 and 400 kg/m^2 s, the percentage enhancement peaked at q_w" ~ 51 kW/m^2, where slug flow was established in at least half of the full length of the microchannel array (i.e. 20 mm). The peak enhancement of 43.6 % at G = 300 kg/m^2 s, was close to the value observed at G = 200 kg/m^2 s (i.e. 43.5 %). As mentioned above, at G = 200 kg/m^2 s, bubbly flow transitioned into slug flow much earlier in the coated channels compared to the plain channels (see Table 8.1). Flow visualisation also show a higher density of bubbles in the coated heat sink in the bubbly flow regime (see Figure 8.20, Bubbly, Location 1). The higher probability of bubble coalescence in the channels induced earlier transition to slug flow. Although higher bubble densities were also observed in the coated channels at the higher mass flux of G = 300 kg/m^2 s, bubbly to slug flow transition occurred only at a slightly lower vapour quality of x = 0.007 in the coated heat sink as compared to x = 0.008 in the plain heat sink (i.e. coating has a smaller effect on flow pattern transition boundaries at higher mass fluxes). As bubbly flow is only observed up to very low vapour qualities, both in the plain and coated microchannel heat sinks at the higher mass flux conditions due to the influence of flow inertia on the rate of bubble coalescence in the microchannels, the enhancement effect of the coating may have been suppressed due to accelerated flow pattern development in the microchannel heat sink. This

could be the reason why a similar percentage enhancement is observed at G = 200 and 300 kg/m^2 s at q_w" ~ 51 kW/m^2.

Similarly, the maximum enhancement recorded for G = 400 kg/m^2 s was lower, i.e. 36.8 % at q_w" ~ 51 kW/m^2. Furthermore, increasing mass velocity tends to decrease bubble generation frequency from an active nucleation site, as found by Euh et al. [103]. Incidentally, flow pattern transition vapour qualities were also only mildly lower in the coated heat sink as compared to the plain heat sink at G = 400 kg/m^2 s. Longer waiting times are required to re-establish the wall superheat required to sustain bubble growth from a cavity as steeper temperature gradients are found on thinner thermal boundary layers. Whilst higher bubble generation frequencies may have resulted from the deeper cavities found on the coated surface (see Figure 8.5), thus improving heat transfer coefficients in the coated channels, the high mass flux could have acted to partly subdue the high bubble generation frequencies from cavities of the coating. From Table 8.3, there is also a much earlier transition to the annular flow regime at G = 400 kg/m^2 s, i.e. x = 0.15, which could have brought about earlier nucleate boiling suppression in the channels, decreasing the effect of the coating on heat transfer enhancement. Transition to annular flow only occurred at x = 0.3 and x = 0.19 at G = 200 kg/m^2 s and 300 kg/m^2 s respectively. Even at the lowest subcooling condition of ΔT_{sub} = 5 K, flow regime transition to annular flow was only observed at x = 0.22 (see Table 8.4 in Section 8.5.5.1).

The smaller percentage enhancement observed could also be because of the narrower range of active nucleation sites in the channel with increasing mass flux. As discussed in Section 2.9.1, increasing mass flux decreases the thickness of the thermal boundary layer on the microchannel walls, thus resulting in a steeper temperature gradient within the layer. This delays the onset of nucleate boiling, subsequently decreasing the range of active nucleation sites on a surface. At G = 400 kg/m^2 s, the active cavity range may have shrunk sufficiently to leave a portion of the small cavities provided by the coating outside of the finite range of active nucleation sites. This means that these cavities will not be able to sustain nucleation even with substantial degrees of wall superheat on the surface. As a result, the nucleate boiling heat transfer coefficients and by extension, average two-phase heat transfer coefficients, are enhanced to a lower degree at the highest mass flux condition.

At wall heat fluxes beyond q_w" = 51 kW/m^2, nucleate boiling is increasingly suppressed in the channels as churn flow dominates in the heat sink. As highlighted above, growing bubbles may

be prematurely stripped from nucleation sites by dispersed waves in the churn flow regime. Hence the enhancement the porous coating, which increases the density of nucleation sites on the channel walls, is less effective in this region and drops sharply with increasing heat flux. This is generally observed for all mass fluxes investigated between q_w" ~ 51 to 104 kW/m^2.

However, for G = 200 kg/m^2 s, the depreciation in two-phase heat transfer enhancement slows slightly from q_w" = 101 kW/m^2, just as annular flow begins to take precedence in the heat sink. Annular flow is established in at least half of the channel length at q_w" = 125 and 153 kW/m^2. Firstly, convective boiling contributes significantly to two-phase heat transfer in the annular flow regime and bubble nucleation on the channel walls is periodically suppressed with liquid-film thinning. Hence the enhancement observed at heat fluxes where annular flow is mainly observed in the heat sink is considerably lower than at heat fluxes where the slug flow regime is dominant.

Secondly, owing to the coating structure, the heat transfer area of the coated channels is, on the whole, larger compared to the plain microchannels. The larger heat transfer area could have promoted thin-film evaporation heat transfer rates in the coated channels, thus slowing the decrease in two-phase heat transfer enhancement at high heat fluxes where annular flow is mainly observed in the microchannel array. Nonetheless, heat transfer improvement in the coated heat sink continue on a decreasing trend with increasing heat flux in the high heat flux region, potentially due to more severe liquid film dryout in the annular flow regime as a result of larger heat transfer rates in the coated channels.

At the higher mass fluxes of G = 300 and 400 kg/m^2 s, the improvement in average two-phase heat transfer coefficient appears to stabilise between heat fluxes q_w" ~ 130 and 207 kW/m^2. This corresponds to the annular flow regime being observed in at least half the total length of the channels (i.e. 20 mm). Additionally, the percentage augmentation at G = 300 and 400 kg/m^2 s are higher than the lowest mass flux condition of G = 200 kg/m^2 s, which was not the case for G = 400 kg/m^2 s at lower wall heat fluxes. As highlighted above, bubble nucleation is periodically suppressed in the annular flow regime and thin-film evaporation contributes highly to two-phase heat transfer. The enhancement mechanism of the coating in thin-film evaporation may be partly attributed to the higher heat transfer area of the coated channels. However, higher evaporation rates also exacerbate wall dryout in the channels, especially during annular flow.

Hence the depreciating trend in heat transfer improvement continues between $q_w^{"}$ = 125 and 153 kW/m^2 at G = 200 kg/m^2 s where annular flow is dominant.

On the contrary, at higher mass fluxes, the higher flow inertia is able to replenish the annular liquid at a higher rate than at lower mass fluxes, where channel wall dryout could have inhibited heat transfer improvement, as presented in Section 8.5.4.1 where dryout periods were reduced or eliminated at higher mass fluxes. Therefore, the enhancement percentage stabilises at around 25 % and 23 % at G = 300 and 400 kg/m^2 s respectively, while the percentage enhancement drops at high wall heat fluxes at G = 200 kg/m^2 s. A similar mass flux effect was also observed in Li et al. [233] with a silicon nanowire coating, where water was used as a working fluid and two-phase heat transfer enhancement was only observed at higher mass fluxes (namely G > 238 kg/m^2 s). Annular flow was prevalent in the channels and flow boiling heat transfer coefficients were found to be lower than in the plain channels at low mass fluxes due to wall dryout. The slightly lower enhancement effect in the annular flow regime at the highest mass flux condition may still be attributed to the narrower range of active nucleation sites on the surface, since nucleate boiling continues to contribute partly to two-phase heat transfer in the channels. This is evident from the active bubble nucleation sites observed in annular flow as shown in Figure 4.3, Annular, Location 3 and Figure 8.21, Annular, Location 3.

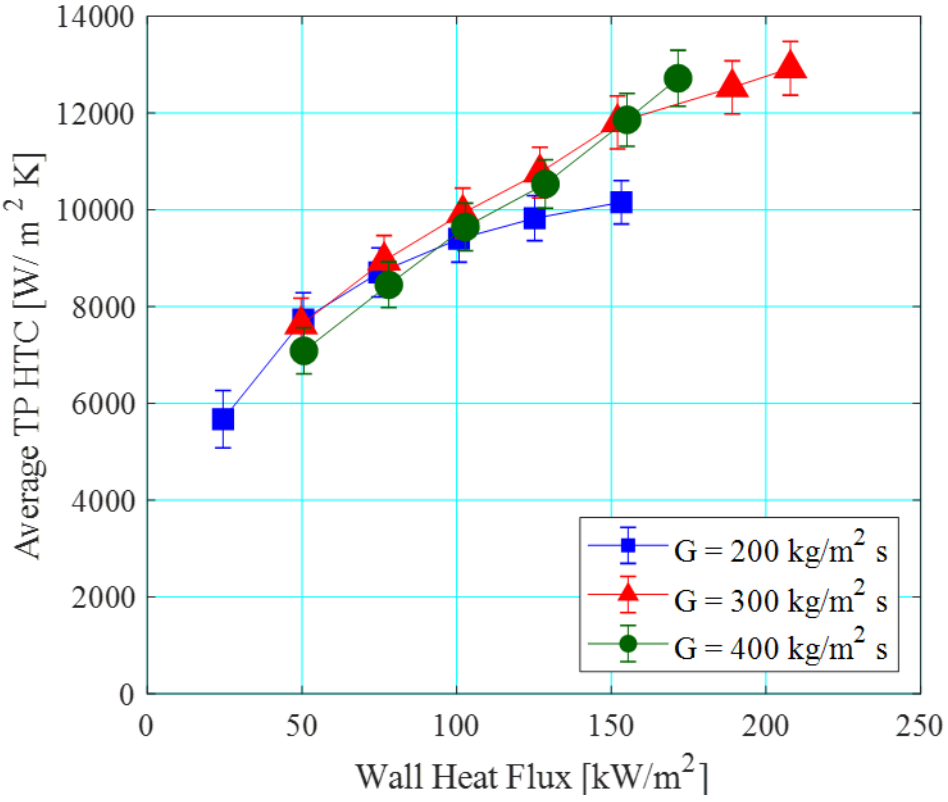

Figure 8.34: Average two-phase heat transfer coefficients in the coated heat sink at P = 1 bar and ΔT_{sub} = 10 K for mass fluxes G = 200, 300 and 400 kg/m^2 s.

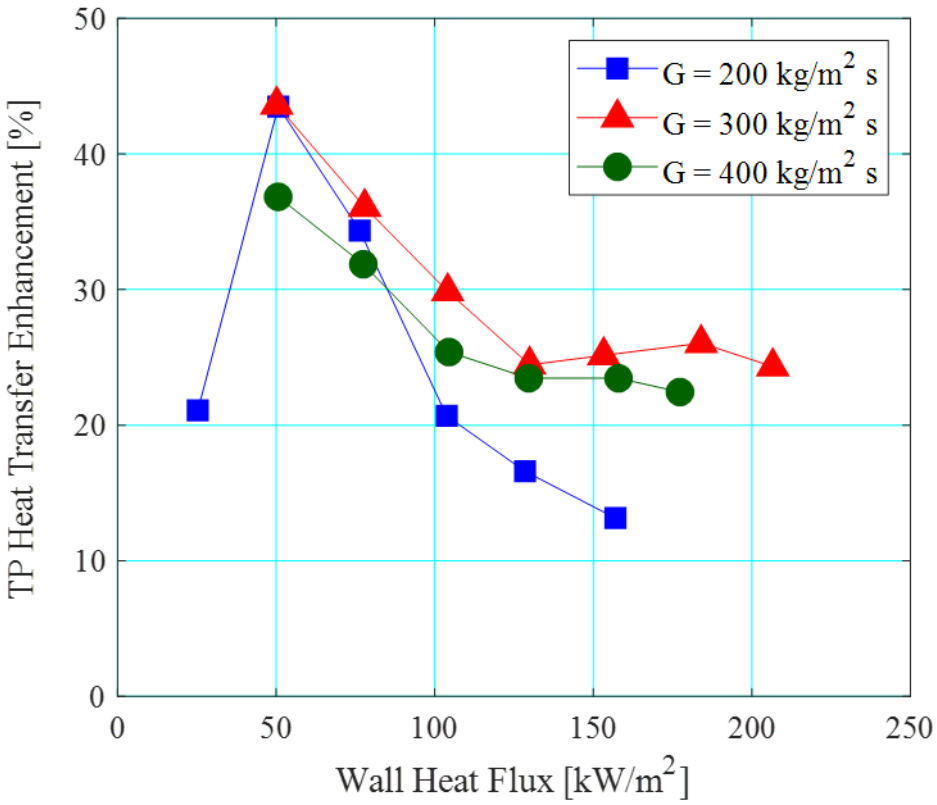

Figure 8.35: Percentage enhancement in heat transfer at different mass fluxes with respect to wall heat flux, for operating conditions of P = 1 bar and ΔT_{sub} = 10 K.

8.5.4.3 Pressure Drop

As expected, flow boiling pressure drop in the coated channels increase with increasing mass flux for a given wall heat flux condition, as depicted in Figure 8.36. This is a result of higher frictional and acceleration pressure drop in the microchannels at higher mass fluxes, and was similarly observed for the plain microchannels in Figure 4.51. Note that the point at G = 400 kg/m^2 s and $q_w^{"}$ = 26.3 kW/m^2, the channel is entirely subcooled and thus is omitted from the graph. The mass flux effect is slightly weaker between G = 300 kg/m^2 s and 400 kg/m^2 s. This could be due to the smaller difference in flow pattern transition vapour qualities, especially between the higher mass fluxes, in comparison to between G = 200 kg/m^2 s and 300 kg/m^2 s (see Table 8.3).

Two-phase pressure drop penalty is depicted in Figure 8.37 for three different mass flux condition. The pressure drop penalty at the lowest mass flux condition of G = 200 kg/m^2 s was typically the lowest at a given wall heat flux condition. This could be because there is a much smaller difference between the slug-churn and churn-annular flow transition boundaries in the plain and coated heat sink at G = 200 kg/m^2 s (see Table 8.1) by comparison to the larger mass fluxes. Whilst there was a notable shift in bubbly-slug flow transition between the plain and coated heat sink, the suppression of flow instabilities at low wall heat fluxes near boiling incipience could have reduced pressure drop penalty in this region, see Section 8.5.2.3.

At the lowest wall heat flux condition of $q_w^{"}$ ~ 26 kW/m^2, the relatively small flow boiling pressure drop penalties at G = 200 kg/m^2 s and 300 kg/m^2 s may be caused by the short saturated boiling lengths in the channel (i.e. 8 mm and 2.5 mm at G = 200 kg/m^2 s and 300 kg/m^2 s respectively). At G = 300 kg/m^2 s and 400 kg/m^2 s, the penalty in two-phase pressure drop rose sharply with increase in heat flux at $q_w^{"}$ = 50 kW/m^2 and $q_w^{"}$ = 77 kW/m^2 respectively, corresponding to slug flow development as well as the extended saturated boiling region in the channels (i.e. increasing two-phase pressure drop contribution compared to single-phase pressure drop). As mentioned above, the slight drop in pressure drop penalty with increase in wall heat flux at G = 200 kg/m^2 s may be attributed to the suppression of flow boiling instabilities due to a lower degree of wall superheat near the onset of boiling in the coated heat sink (see Figure 8.29).

A slight decrease in pressure drop penalty was observed where churn flow became dominant in the heat sink. This was observed for G = 300 kg/m^2 s and 400 kg/m^2 s between q_w" ~ 78 kW/m^2 and 104 kW/m^2. A reduction in pressure drop penalty was also observed at G = 200 kg/m^2 s when q_w" ~ 128 kW/m^2. Following that, flow boiling pressure drop penalty increased slightly from 43.2 % to 49 % at G = 400 kg/m^2 s between heat fluxes q_w" = 104 kW/m^2 to 130 kW/m^2. This could be because of the accelerated transition to annular flow in the coated heat sink at the highest mass flux condition. Churn-annular transition occurred at x = 0.169 and x = 0.152 in the plain and coated heat sink respectively (see Table 4.6 and Table 8.3). Two-phase pressure drop penalty stabilised between 47.3 % and 49.8 % at G = 400 kg/m^2 s in the wall heat flux range of q_w" = 130 kW/m^2 and 177 kW/m^2. This is mainly where annular flow is the dominant flow regime in both the plain and coated heat sink.

On the other hand, at G = 300 kg/m^2 s, pressure drop penalty fluctuated quite significantly between q_w" = 104 kW/m^2 to 207 kW/m^2. Annular flow was predominantly observed in both heat sinks at the abovementioned range of wall heat fluxes. Incidentally, there was also a sharp increase in two-phase pressure drop penalty at G = 200 kg/m^2 s at q_w" = 153 kW/m^2, where the magnitude of pressure drop oscillations across the coated microchannel heat sink increased considerably (see Figure 8.27). Increasing magnitude of pressure drop oscillations in the annular flow dominant region was also observed in the plain microchannel test section at G = 300 kg/m^2 s, increasing from 0.05 kPa to 0.14 kPa between q_w" = 106 kW/m^2 to 205 kW/m^2.

In contrast, at G = 400 kW/m^2 in the coated heat sink, pressure drop oscillations decreased from 0.06 kPa to 0.04 kPa between q_w" = 105 kW/m^2 to 175 kW/m^2, where annular flow was dominant in the coated heat sink. The pressure drop oscillations could be related to the dryout and rewetting cycle in the annular flow regime and should be investigated further in future studies. The higher flow inertia at G = 400 kg/m^2 s could have suppressed an increase in two-phase oscillations in the annular flow regime at a similar range of wall heat flux in the heat sink, which helped stabilise pressure drop penalty. Interestingly, Deng et al. [78] also found increasing standard deviation in pressure drop where the annular flow regime was observed in a pin-fin microchannel evaporator at mass fluxes ranging from 125 kg/m^2 s to 300 kg/m^2 s with water and ethanol as working fluids.

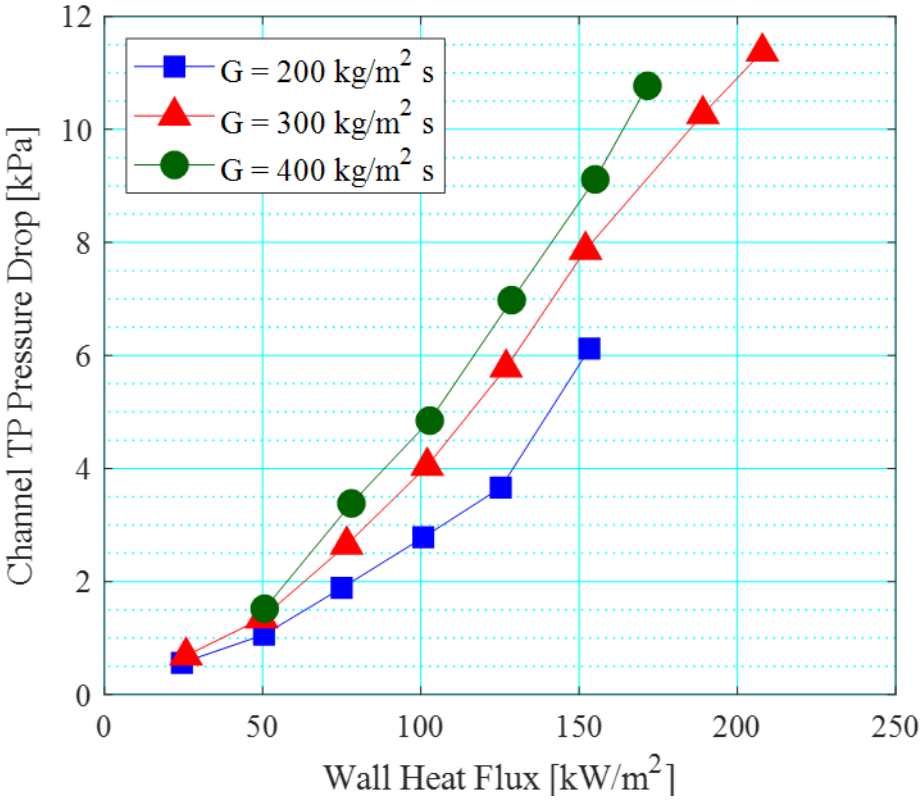

Figure 8.36: Two-phase pressure drop in the coated microchannels at different mass fluxes with respect to wall heat flux, for operating conditions of P = 1 bar and ΔT_{sub} = 10 K.

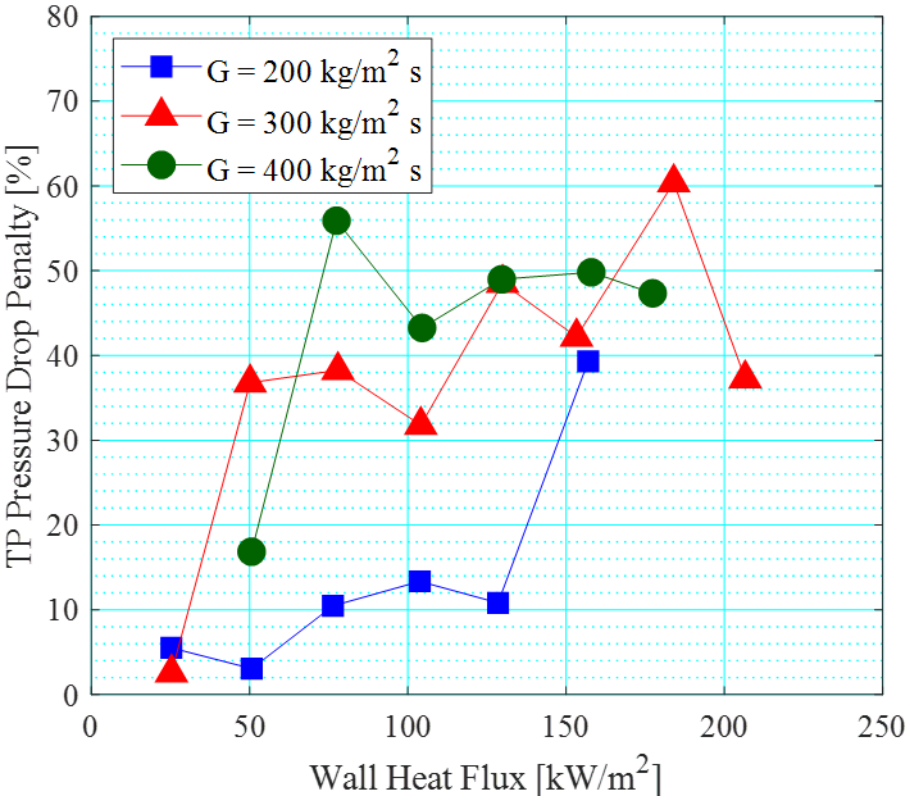

Figure 8.37: Microchannel two-phase pressure drop penalty as a result of the coating at different mass fluxes with respect to wall heat flux for P = 1 bar and ΔT_{sub} = 10 K.

8.5.5 Effect of Inlet Subcooling

8.5.5.1 Flow Patterns

The effect of inlet subcooling on flow pattern development in the coated microchannel heat sink was investigated at ΔT_{sub} = 5, 10 and 20 K. For the range of inlet subcooling investigated, increasing the degree of inlet subcooling delayed flow pattern transition from bubbly to slug, churn and annular flow in the coated microchannel heat sink, as summarised in Table 8.4. Delayed flow pattern transitions with increasing degree of subcooling was similarly observed in the plain microchannel heat sink (see Table 4.7). This is attributed to the extended subcooling region in the channels and lower bubble nucleation activity at higher inlet subcooling conditions, which decrease the rate of bubble coalescence in the microchannels (see Section 4.5.1). This in turn triggered flow pattern development at higher vapour qualities with increasing inlet subcooling at a given wall heat flux condition.

In comparison to the plain microchannel heat sink, flow regime transition occurred at lower vapour qualities in the coated heat sink at all inlet subcooling conditions, particularly for bubbly-slug and slug-churn regime transition. Transition from churn to annular flow occurred at x = 0.23 and x = 0.22 in the plain and coated channels respectively at ΔT_{sub} = 5 K. Similarly, at the higher inlet subcooling conditions, churn-annular transition occurred at similar vapour qualities in both heat sinks, i.e. at x = 0.30 and x = 0.34 for ΔT_{sub} = 10 K and 20 K respectively. This could be because transition to annular flow, which is characterised by a continuous vapour core in the middle of the channels, is not only controlled by bubble generation activity in the channels. Flow properties corresponding to the operating condition may also have a significant influence in regime transition between churn and annular flow. For instance, with increasing pressure (i.e. higher vapour density) and mass flux (i.e. higher flow inertia), there is a large shift in churn-annular transition in both the plain (see Table 4.4 for pressure effect and Table 4.6 for mass flux effect) and coated microchannel heat sink (see Table 8.2 for pressure effect and Table 8.3 for mass flux effect).

Notably, severe wall dryout was observed during the slug flow regime at $q_w^{"}$ = 26 kW/m^2 at ΔT_{sub} = 5 K in the coated channels, as presented in Figure 8.38. Dryout was triggered by the expansion of vapour slugs towards both the upstream and downstream direction of the flow. Dryout lasted for just over 145 ms before subcooled liquid from the inlet of the heat sink overcame vapour backflow and rewetted the channel walls. At a similar operating condition in

the plain channels, persistent wall dryout was not observed. This could be because of comparatively lower bubble nucleation activity in the plain heat sink by comparison to the coated heat sink, which resulted in lower rate of bubble coalescence in the channels. Dryout behaviour improved with increasing subcooling degree.

Furthermore, at $q_w^{"} = 174.2$ kW/m^2 when $\Delta T_{sub} = 20$ K, prolonged wall dryout lasting around 9 ms were observed in the coated heat sink. At a similar operating condition in the plain microchannel heat sink, wall dryout periods were slightly shorter and occurred over an average of 5 ms in the channels.

Table 8.4: Flow pattern transition vapour qualities in the coated heat sink at different inlet subcooling conditions for P = 1 bar and G = 200 kg/m^2 s.

ΔT_{sub} [K]	x_{B-S} [-]	x_{S-C} [-]	x_{C-A} [-]
5	0.005	0.055	0.22
10	0.008	0.067	0.30
20	0.016	0.071	0.34

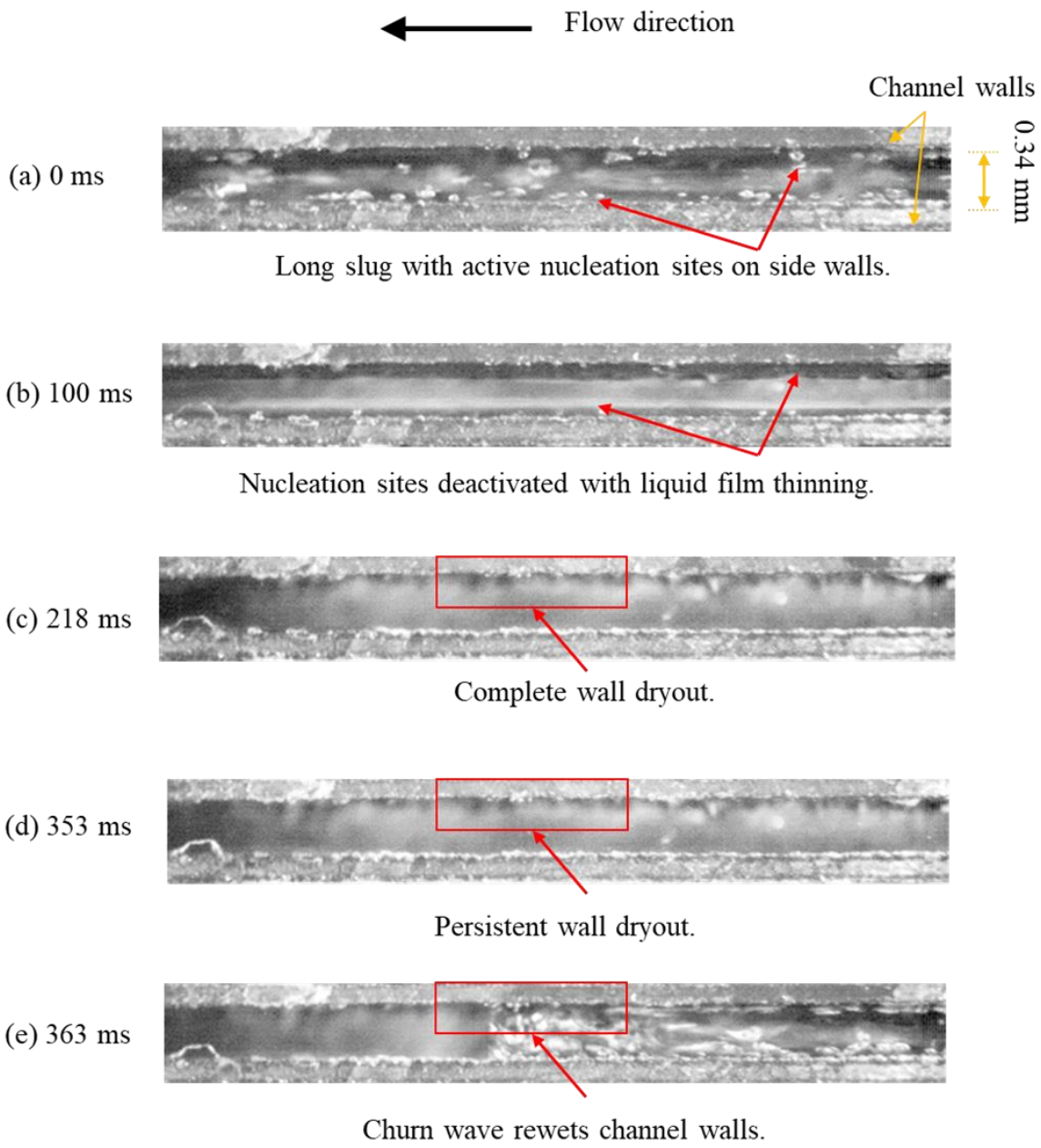

Figure 8.38: Prolonged wall dryout captured in the coated channels, camera location 3, during slug flow at $q_w^{"}$ = 26 kW/m^2 when ΔT_{sub} = 5 K. Wall dryout persisted for around 145 ms.

8.5.5.2 Heat Transfer

Figure 8.39 depicts the effect of subcooling degree on average flow boiling heat transfer coefficients in the coated channels at P = 1 bar and G = 200 kg/m^2 s. Average two-phase heat transfer coefficients increased with increasing wall heat flux in the microchannel heat sink but appeared to be largely unaffected by the degree of inlet subcooling. However, critical heat flux condition was reached at a wall heat flux of $q_w^{"}$ = 174.2 kW/m^2 when ΔT_{sub} = 20 K.

From Section 4.5.2, local heat transfer coefficients in the saturated boiling region was only marginally dependent on the degree of subcooling. Flow boiling heat transfer coefficients decreased only slightly with increasing inlet subcooling and a more pronounced effect of inlet subcooling was found in the subcooled boiling region. Nonetheless, critical heat flux was not observed at the three degrees of inlet subcooling degree investigated in the plain test section.

The enhancement in flow boiling heat transfer coefficients at different degrees of inlet subcooling is depicted in Figure 8.40. The effect of the porous coating on average two-phase heat transfer coefficients is shown to be strongly dependent on flow boiling regimes on top of the range of active nucleation sites in the channel. The enhancement effect increased with increasing heat flux in the region where bubbly and slug flow are dominant in the heat sink. This is mainly attributed to the large contribution of the nucleate boiling regime to overall heat transfer due to the increase in active nucleation sites provided by the coating, as discussed in Section 8.5.2.2. The wall heat flux at which peak enhancement in two-phase heat transfer was observed to shift to higher heat flux levels when inlet subcooling was increased to ΔT_{sub} = 20 K. This is attributed to delayed flow regime transitions at the higher inlet subcooling condition, as discussed in detail in Section 8.5.5.1. At wall heat fluxes where churn and annular flow begins to dominate in the heat sink, nucleate boiling is increasingly suppressed. Hence, the nucleate boiling enhancement effect in the coated channels depreciate with further increase in wall heat flux.

At $q_w^{"}$ ~ 51 kW/m^2, a peak in two-phase heat transfer enhancement of 25.5 % and 43.5 % was observed at ΔT_{sub} = 5 K and 10 K respectively. The subcooled length were negligible (i.e. L_{sub} = 3 mm and 6 mm accordingly) compared to the total channel length (i.e. 20 mm) at both degrees of inlet subcooling. The smaller peak percentage enhancement observed at ΔT_{sub} = 5 K could be because of relatively high nucleation activity in the plain channels at this low

subcooling condition, thus rendering a smaller enhancement effect using the coated channels compared to when ΔT_{sub} = 10 K. On the other hand, the subcooled length at $q_w^{"}$ ~ 51 kW/m^2 when ΔT_{sub} = 20 K was over half the full channel length at L_{sub} = 12 mm and slug flow only developed towards the end of the heat sink. This indicates lower bubble nucleation activity in the coated channels at $q_w^{"}$ ~ 51 kW/m^2 in comparison to at lower subcooling conditions, where slug flow was observed at multiple locations on the heat sink. Consequently, a peak in percentage enhancement was not observed at this wall heat flux condition when ΔT_{sub} = 20 K. Instead, a maximum enhancement of 35.8 % was observed at $q_w^{"}$ ~ 78 kW/m^2, where bubbly and slug flow dominated in the coated heat sink.

Following the peak in flow boiling heat transfer enhancement, a larger enhancement effect is observed with increasing degrees of inlet subcooling for a given wall heat flux condition, particularly when ΔT_{sub} = 20 K. As mentioned above, increasing the degree of subcooling decreases the range of active nucleation sites on a surface, with a stronger effect on larger sized cavities as shown in Figure 4.59 using Hsu's model [109]. Despite nucleation suppression at medium to high wall heat fluxes, the nucleate boiling mechanism continue to contribute substantially to overall two-phase heat transfer in the heat sink. The enhancement effect exhibited by the coating, which provides favourable nucleation cavities typically in the range of 0.1 µm to 1.7 µm (see Figure 8.10), appeared to be stronger at higher inlet subcooling conditions. This is potentially due to the comparatively smaller finite range of nucleation sites at lower subcooling degrees and the size range of coating cavities being within the range of nucleation at ΔT_{sub} = 20 K. This is also supported by the much larger shift in the bubbly-slug flow transition boundaries between the plain and coated heat sink at ΔT_{sub} = 20 K. Bubbly-slug flow transition occurred at x = 0.049 in the plain heat sink and x = 0.016 in the coated heat sink.

Importantly, the critical heat flux limit is reached at $q_w^{"}$ = 174.2 kW/m^2 and x_e = 0.92 when ΔT_{sub} = 20 K. Average two-phase heat transfer coefficient approaches a plateau between $q_w^{"}$ = 155.2 and 174.2 kW/m^2. On the contrary, at slightly higher wall heat flux condition in the plain heat sink (i.e. $q_w^{"}$ = 180.7 kW/m^2), two-phase flow pattern in the heat sink was also predominantly annular flow, however, critical heat flux phenomenon was not observed and average heat transfer coefficients continue to rise with heat flux. At $q_w^{"}$ = 174.2 kW/m^2 in the coated channels, the predominant flow regime was annular flow. Interestingly, persistent wall dryout of around 9 ms was observed at $q_w^{"}$ = 174.2 kW/m^2, where the critical heat flux limit

appears to be reached. However, persistent wall dryout could well occur if wall heat flux was increased further (i.e. exceeding the critical heat flux limit), causing a significant drop in average heat transfer coefficient, as observed in Figure 8.30, where the dryout period was nearly 30 ms. Despite this, the comparatively lower critical heat flux limit in the coated heat sink may still be attributed to higher bubble nucleation activity as well as higher liquid film evaporation rates owing to the higher heat transfer area of the coated channels. The above is supported by the small 10.8 % enhancement in average two-phase heat transfer coefficient at $q_w^{"} \sim 180$ kW/m^2 compared to the plain microchannels, i.e. at the critical heat flux limit of the coated heat sink when $\Delta T_{sub} = 20$ K.

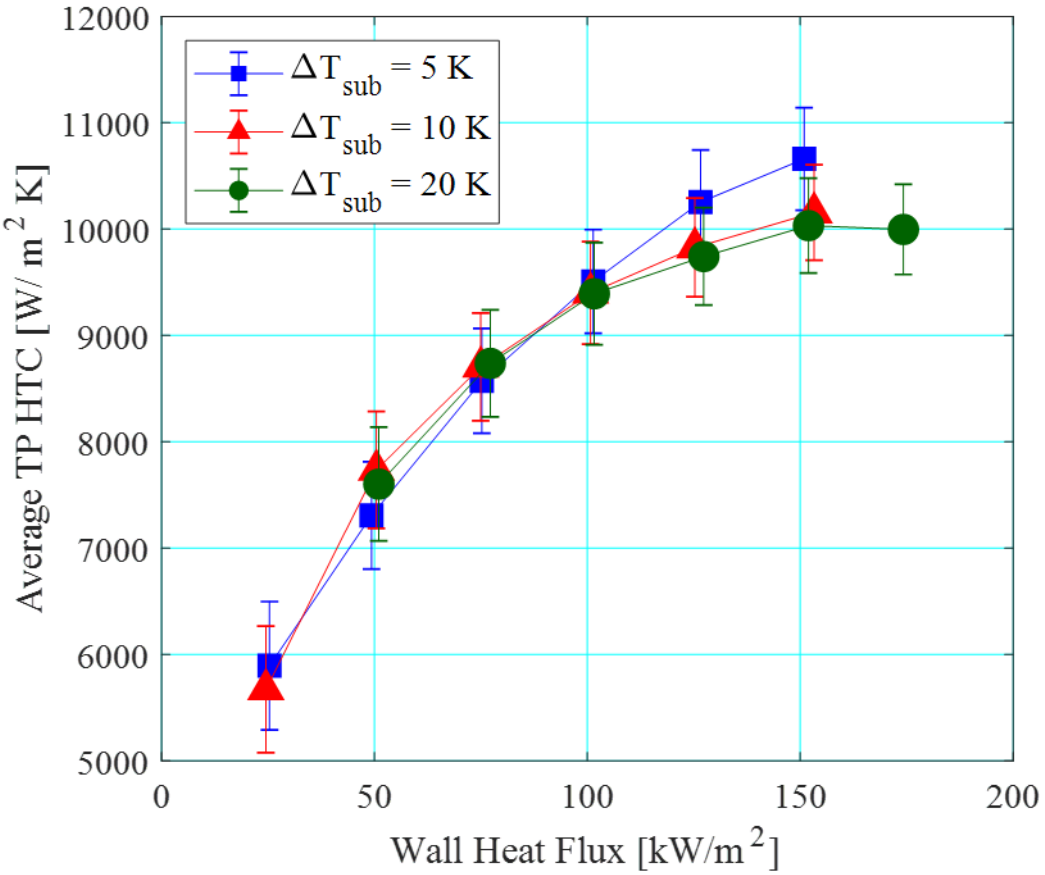

Figure 8.39: Effect of inlet subcooling on average two-phase heat transfer coefficients as a function of wall heat flux in the coated heat sink for P = 1 bar and G = 200 kg/m^2 s.

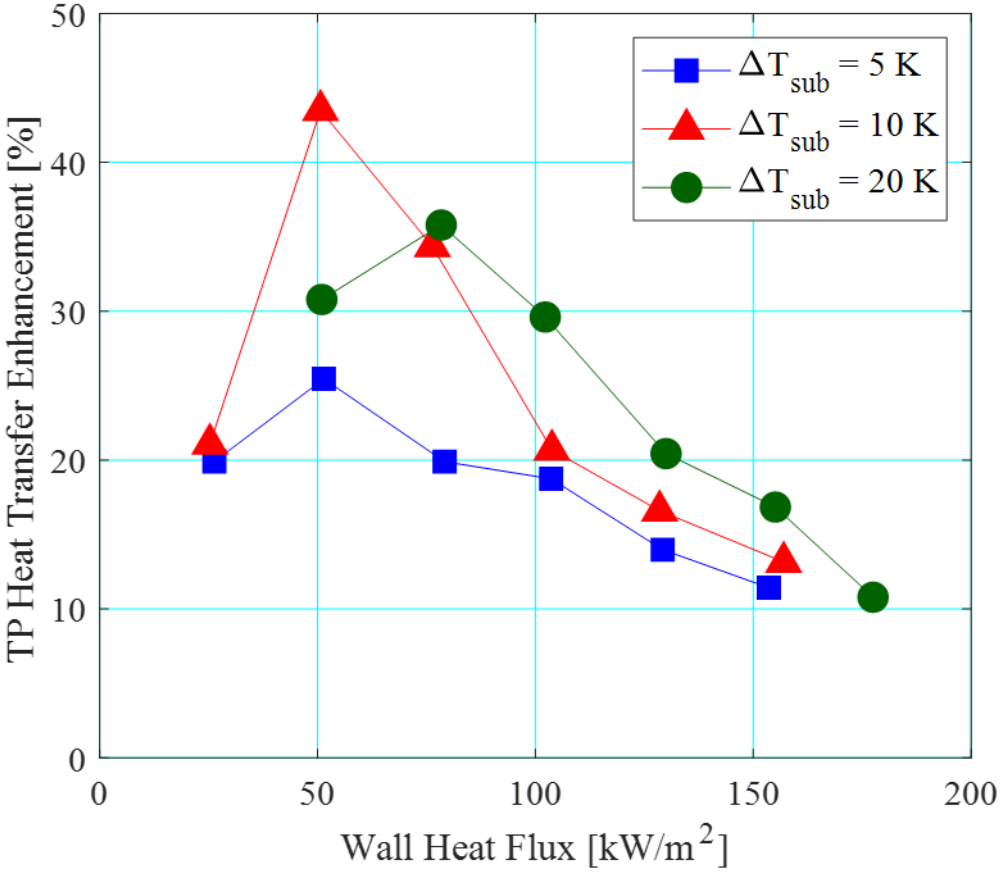

Figure 8.40: Percentage enhancement in heat transfer at different degrees of inlet subcooling with respect to wall heat flux, for operating conditions of P = 1 bar and G = 200 kg/m^2 s.

8.5.5.3 Pressure Drop

Flow boiling pressure drop in the channels increase with increasing wall heat flux across all three degrees of inlet subcooling, as depicted in Figure 8.41. Note that in Figure 8.41, the pressure drop at ΔT_{sub} = 20 K is zero as the subcooled length covers the entire length of the channel array (i.e. 20 mm). As mentioned before, the increasing trend of pressure drop with respect to wall heat flux is due to the increase in the acceleration component of two-phase pressure drop with increasing void fraction in the channels as flow patterns transition from bubbly towards annular flow. At a given wall heat flux condition, increasing the degree of subcooling decreases the magnitude of two-phase pressure drop in the channels. This is due to delayed flow pattern transition boundaries in the microchannel heat sink with increasing inlet subcooling, as discussed in Section 8.5.5.1. Delayed flow pattern transitions and lower two-phase pressure drop were similarly observed in the plain microchannel test section with increasing degree of subcooling. The subcooling effect on flow boiling pressure drop appears to be smaller between ΔT_{sub} = 10 K and 20 K, except at the wall heat flux condition of $q_w^{"}$ ~ 170 kW/m^2. The smaller effect of subcooling could be due to the smaller differences in flow pattern transition boundaries between ΔT_{sub} = 10 K and 20 K compared to between ΔT_{sub} = 5 K and 10 K, particularly for slug-churn and churn-annular transition in the channels. For instance, churn to annular transition occurred at a vapour quality of x = 0.22 at ΔT_{sub} = 5 K while at ΔT_{sub} = 10 K and 20 K, annular flow is only observed from x = 0.3 and x = 0.34 respectively in the coated microchannel heat sink.

On the other hand, the sharp rise in flow boiling pressure drop between $q_w^{"}$ ~ 130 kW/m^2 and 160 kW/m^2 at ΔT_{sub} = 10 K may be a combination of higher channel void fraction at higher wall heat flux and more severe flow oscillations due to vapour backflow into the inlet plenum during the annular flow regime. The standard deviation of the pressure drop signal from 0.05 kPa to 0.1 kPa doubled between $q_w^{"}$ ~ 130 kW/m^2 and 160 kW/m^2, as depicted previously in Figure 8.27. Dryout cycles lasting for around 30 ms, with 3 ms of persistent wall dryout were also observed at the highest wall heat flux condition, as covered in Section 8.5.2.1.

Combining flow boiling results of the plain channel, the pressure drop penalty associated with the coating for the three degrees of inlet subcooling and range of wall heat fluxes investigated are depicted in Figure 8.42. Note that a negative value for the percentage of two-phase pressure drop penalty signifies a lower two-phase pressure drop in the coated channels in comparison

to the plain microchannels. Furthermore, the data point at the lowest wall heat flux condition at ΔT_{sub} = 20 K is omitted as it is entirely in the subcooled region.

At ΔT_{sub} = 5 K, the penalty in two-phase pressure drop peaks at the lowest wall heat flux condition and decreases with increasing wall heat flux, eventually stabilising at just under 50 % between $q_w^{"}$ ~ 100 kW/m^2 to 150 kW/m^2. At ΔT_{sub} = 10 K and 20 K, pressure drop penalty generally increases with increasing heat flux and stabilises for a distinct range of wall heat fluxes, typically where churn or annular flow is dominant in the heat sink. Following that for ΔT_{sub} = 10 K, two-phase pressure drop penalty was relatively constant at 10 % between heat fluxes $q_w^{"}$ ~ 78 kW/m^2 and 130 kW/m^2. For ΔT_{sub} = 20 K, the percentage of pressure drop penalty posed by the coating increases steeply between $q_w^{"}$ ~ 51 kW/m^2 to 130 kW/m^2 and appear to plateau with further increase in heat flux. In fact, the coating lowered flow boiling pressure drop in the microchannel heat sink at a similar operating condition at $q_w^{"}$ ~ 51 kW/m^2 for ΔT_{sub} = 20 K, namely by 9.5 % compared to the plain channels.

The highest penalty in flow boiling pressure drop of over 84 % was observed at $q_w^{"}$ ~ 26 kW/m^2 when ΔT_{sub} = 5 K. As covered above, the coating enhances bubble generation activity in the channels in comparison to the plain microchannels. This resulted in earlier flow pattern transitions in the coated channel, by comparison to the plain channels (see Table 8.4 and Table 4.7 respectively). Accordingly, the higher channel void fraction at a given wall heat flux condition in the coated channels, hence increasing both the frictional and acceleration pressure drop in the channels. Furthermore, flow visualisation revealed severe vapour backflow at $q_w^{"}$ ~ 26 kW/m^2 in the coated channels when ΔT_{sub} = 5 K, as presented in Figure 8.38. Wall dryout lasted for around 145 ms in the coated microchannels, while wall dryout was not observed in the plain heat sink at a similar operating condition, possibly due to lower bubble nucleation activity in the channels. Complete dryout of the channel walls could have increased flow resistance in the channels during the rewetting cycle typically observed in slug flow. A combination of the above may have resulted in the peak in pressure drop penalty at the lowest subcooling condition of ΔT_{sub} = 5 K.

With increasing wall heat flux, churn flow becomes the dominant flow pattern in both test sections and the pressure drop penalty decreases in this flow regime. This could be due to the churn wave rewetting mechanism (shorter period of wall dryout or no wall dryout altogether) as well as the generally smaller magnitude of flow oscillations in churn flow. Between $q_w^{"}$ ~

105 kW/m^2 to 160 kW/m^2 where annular flow was prevalent in both the plain and coated heat sink, pressure drop penalty was fairly stable between 44 % to 50 %. This could be because the annular flow regime was established in both the plain and coated microchannels at these wall heat fluxes. Transition from churn to annular flow were similar in the two heat sinks, at x = 0.23 and x = 0.22 in the plain and coated microchannels respectively (see Table 8.4 and Table 4.7). Fairly stable pressure drop penalties were also observed where similar flow regimes, i.e. annular flow are established in both test sections, as shown at different pressures and mass fluxes in Figure 8.37 and Figure 8.33.

As highlighted above, two-phase pressure drop in the coated channels were lower in comparison to the plain microchannels at $q_w^{"} \sim 51$ kW/m^2 when $\Delta T_{sub} = 20$ K. This is despite of the fact that flow pattern transition was accelerated using the coating and slug flow is observed over a longer length of the coated channels in comparison to the plain channels, where slug flow only developed near the channel outlet at this wall heat flux condition. Interestingly, the magnitude of pressure drop oscillations were much smaller in the coated channels at this operating condition. The standard deviation of the differential pressure drop (measured across the heat sink) was smaller in the coated channels, namely at 0.03 kPa, while the standard deviation of the pressure drop signal in the plain channels at a similar wall heat flux was 0.1 kPa. This is presented in Figure 8.43. Lower wall superheat at a given wall heat flux in the coated channels, evident from Figure 8.19, could have mitigated against instabilities related to rapid bubble growth in the coated channels, thus reducing two-phase pressure drop at low wall heat flux conditions near boiling incipience [299]. The degree of wall superheat in the plain and coated channels were 8.2 K and 6.8 K respectively.

With increasing wall heat flux, the effect of void fraction and flow pattern (typically higher channel void fraction and accelerated flow pattern transitions in coated channels at a given heat flux due to higher bubble nucleation activity) takes over and the pressure drop in the coated channels rise above that of the plain microchannels. The percentage of pressure drop penalty stabilised immediately at $\Delta T_{sub} = 10$ K while an increasing trend is observed at $\Delta T_{sub} = 20$ K for heat fluxes between $q_w^{"} \sim 78$ kW/m^2 and 130 kW/m^2. This could be because very similar flow pattern boundaries, except bubbly flow, were observed in the plain and coated channels at $\Delta T_{sub} = 10$ K. From Table 8.4 and Table 4.7, transition from slug to churn and churn to annular flow occurred at x ~ 0.068 and x = 0.3 respectively in both heat sinks. On the other hand, the difference in flow pattern boundaries were more significant between the two heat

sinks at ΔT_{sub} = 20 K. Slug to churn flow transition occurred at x = 0.125 and x = 0.071 respectively in the plain and coated channels. However, churn to annular flow transition were similar in both heat sinks (i.e. x = 0.34), thus explaining the plateau toward high heat fluxes in Figure 8.42. Two-phase pressure drop penalty fluctuated slightly where annular flow is dominant in both heat sinks (as observed previously in Figure 8.37 and Figure 8.33). However, it does not appear to spike even as the critical heat flux limit appears to be reached at $q_w^{"}$ = 174.2 kW/m^2 (see Figure 8.42).

Notably, there is a sharp jump in pressure drop penalty between $q_w^{"}$ ~ 130 kW/m^2 and 160 kW/m^2 when ΔT_{sub} = 10 K. As discussed in Section 8.5.2.3, the sharp jump in pressure drop penalty between $q_w^{"}$ ~ 130 kW/m^2 and 160 kW/m^2 and could be related to more severe flow instabilities at the highest wall heat flux condition (see Figure 8.27). The results observed in Figure 8.27 and Figure 8.43 indicate a tangible relation between two-phase flow oscillations and flow boiling pressure drop in microchannels.

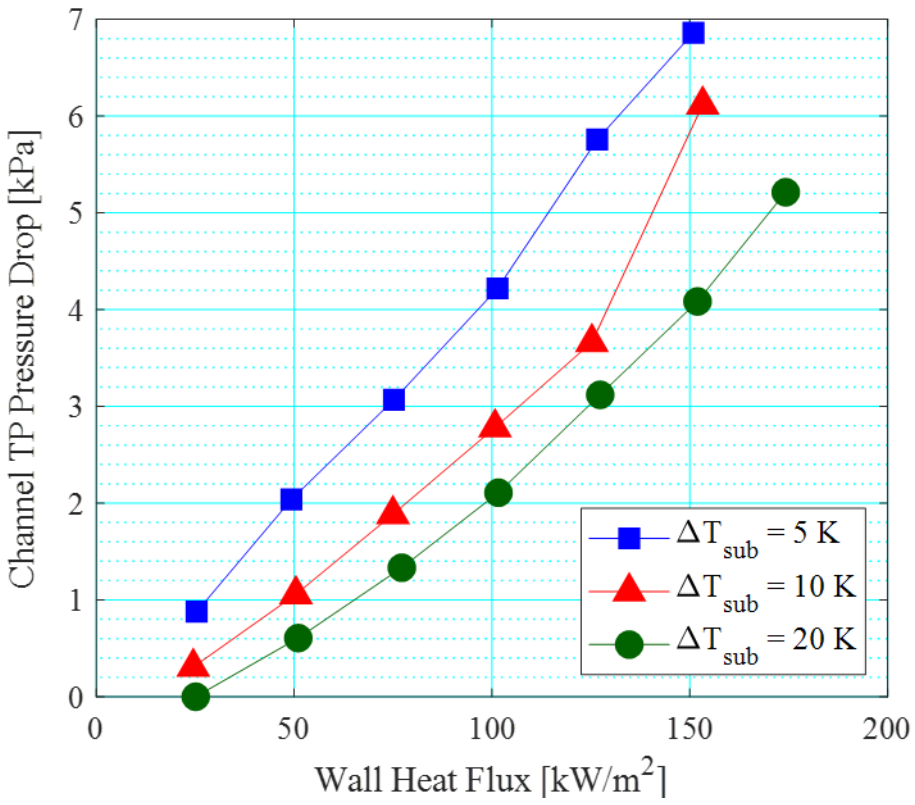

Figure 8.41: Two-phase pressure drop in the coated microchannels at different degrees of inlet subcooling with respect to wall heat flux, for operating conditions of P = 1 bar and G = 200 kg/m^2 s.

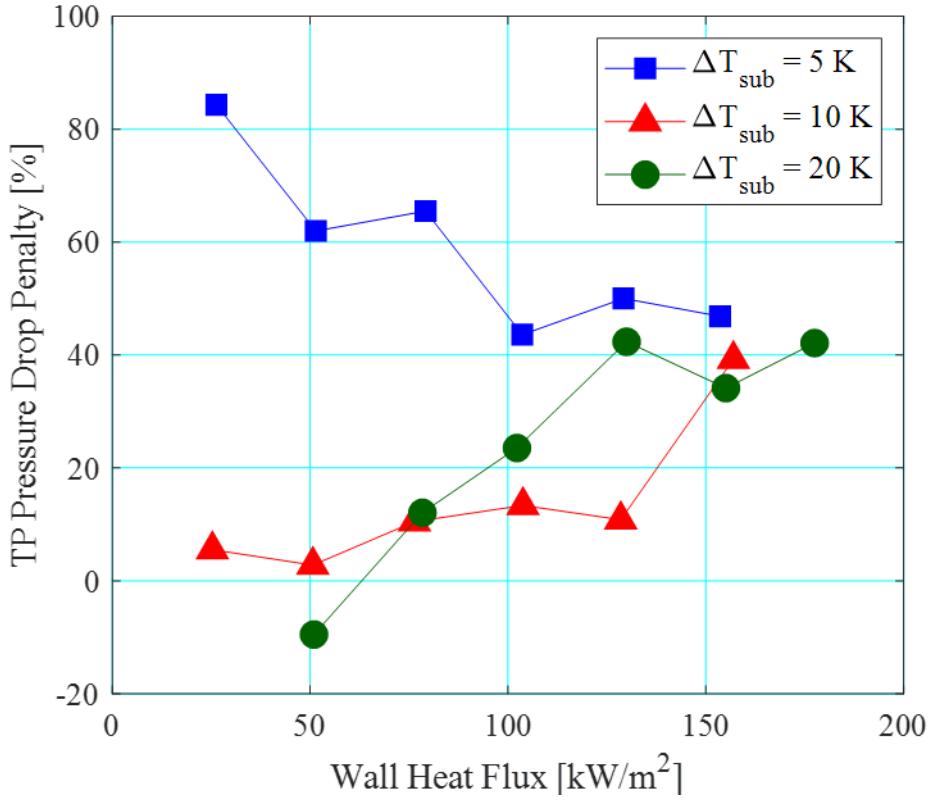

Figure 8.42: Microchannel two-phase pressure drop penalty as a result of the coating at different degrees of inlet subcooling with respect to wall heat flux for P = 1 bar and G = 200 kg/m^2 s.

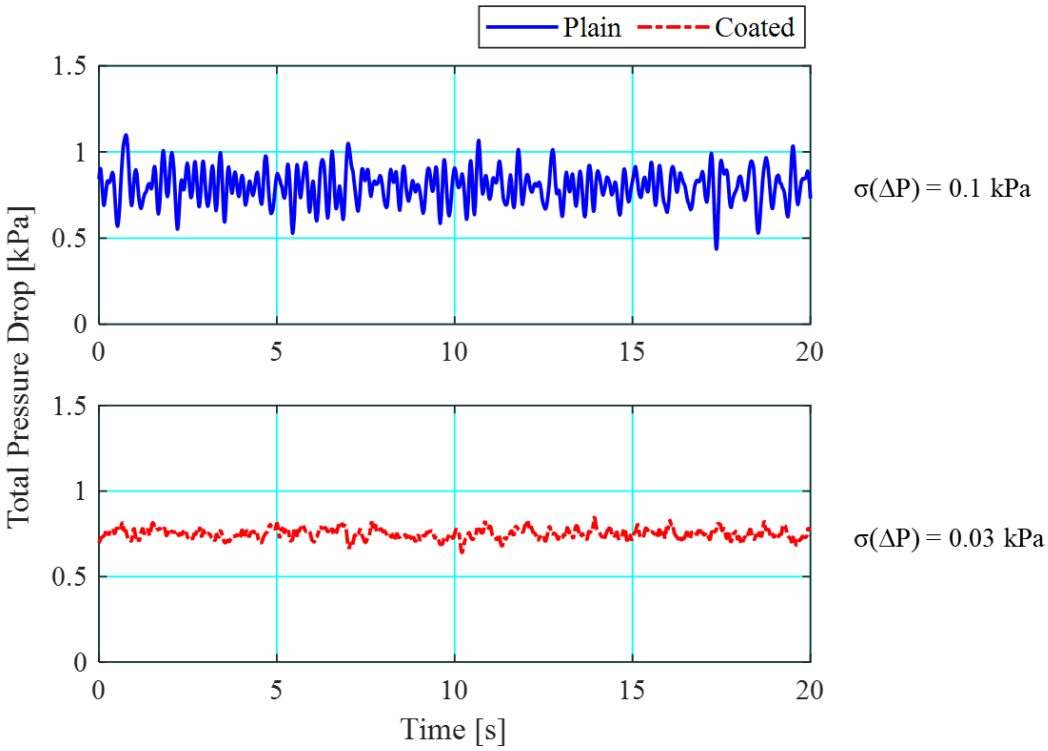

Figure 8.43: Measured pressure drop across the plain and coated heat sink respectively at q_w" ~ 51kW/m^2 over a window of 20 s for G = 200 kg/m^2 s and ΔT_{sub} = 20 K.

8.6 Summary

Flow boiling experiments, including high-speed flow visualisation, were conducted in a coated microchannel heat sink with a similar configuration to the plain copper microchannels discussed in Chapter 4. Comparison of the results obtained at similar working conditions in the plain and coated heat sink were presented in this chapter.

SEM analysis was conducted in order to characterise and compare the surfaces of the milled copper channels and the coated channel walls. Shallow cavities between 0.25 µm and 4 µm were typically found on the plain microchannels, while smaller and more defined cavities between 0.1 µm and 1.7 µm were identified on the coated surface. The cavity ranges present on both samples were within the active nucleation range for HFE-7200. The number of cavities present on the coated surface was 32 times higher compared to the plain surface. As HFE-7200 is a highly wetting fluid, applying the layer of porous coating did not appear to alter the wettability characteristics of the surface significantly.

Single-phase friction factor and Nusselt number in the coated microchannels were higher compared to the plain heat sink. The higher frictional losses was attributed to the rougher walls of the coated channels while the increase in single-phase heat transfer was attributed to the increase in surface area and enhanced mixing near the walls due to the layer of coating.

In flow boiling experiments, wall superheat degree was reduced by an average of 3 K compared to the plain channels at a nominal heat flux condition. This was related to the higher density of nucleation sites present on the coated surface. Furthermore, the deeper cavities identified on the coated surface was also believed to encourage vapour trapping and further enhance bubble generation frequency in flow boiling. Lower degree of wall superheat on the coated channels appeared to suppress rapid bubble growth instabilities in the coated heat sink.

From flow visualisation, at a similar operating condition, bubble nucleation activity in the coated heat sink was higher than the plain microchannels. Consequently, flow pattern transitions were generally accelerated in the coated heat sink compared to the plain microchannels. Similar to the observations for the plain heat sink, increasing mass flux and subcooling degree accelerated and delayed flow regime transitions in the coated heat sink respectively. In contrast, an opposite effect of system pressure was observed in the coated heat

sink, i.e. flow pattern transitions occurred earlier with increasing pressure. This was postulated to be due to high coalescence rates in the coated heat sink with higher bubble generation activity, which overcame the effect of smaller bubble diameter in the channels.

Furthermore, excessive bubble nucleation activity and higher liquid film evaporation rates from the coated surface may induce wall dryout in the coated channels where not observed in the plain heat sink. Prolonged periods of channel wall dryout in the heat sink were also correlated with critical heat flux phenomenon in the coated heat sink. Increasing mass velocity and subcooling degree may have mitigated or shorted the duration of periodic dryout on the coated channels. Additionally, there was tangible evidence to suggest a relationship between flow instability, magnitude of pressure drop and wall dryout.

Local heat transfer trends in the coated microchannel heat sink were similar to the observations in the plain microchannels. Local heat transfer coefficients peaked at low vapour qualities near the onset of boiling and decreased along the streamwise direction corresponding to flow pattern development and nucleation site suppression. Average two-phase heat transfer coefficients typically increased with increasing heat flux and system pressure. The degree of inlet subcooling also only had a marginal effect on average two-phase heat transfer coefficients, but influenced overall heat transfer coefficients at low heat fluxes due to the substantial length of the subcooled region. As was concluded for the plain microchannels, a weak mass flux effect was observed at low to moderate heat fluxes but became more apparent at high heat fluxes where annular flow was dominant. This was due to the suppression of nucleate boiling and the increasing contribution of the convective boiling mechanism to total heat transfer.

Flow boiling heat transfer enhancement of up to 50 % were obtained using the porous coating. The enhancement effect was most prominent at heat fluxes where the bubbly and slug flow regime where observed in the heat sink, when nucleate boiling was very active. This was mainly due to the increase in nucleation site density as well as the deeper cavities which promoted vapour entrapment on the coated channels. This agreed with flow pattern observations, where flow regime development generally occurred earlier in the coated heat sink compared to the plain channels. Additionally, the increase in surface area could also have augmented liquid film evaporation rates in the coated microchannel heat sink. With increasing heat flux, dominant flow patterns in the heat sink transitioned towards annular flow and the enhancement percentage depreciated.

The enhancement effect of the coating were found to be highly dependent on operating conditions. Percentage enhancement typically increased with saturation pressure, particularly at low heat fluxes. This was attributed to higher bubble generation frequency at higher pressures in the more defined cavities on the coated surface. The enhancement effect generally increased with increasing subcooling degree. On the other hand, the enhancement ratio increased between 200 kg/m^2 s and 300 kg/m^2 s, but decreased slightly between 300 kg/m^2 s and 400 kg/m^2 s. These may be because of the size of cavities on the coated surface within the active range of nucleation sites for HFE-7200 in each experimental condition.

As highlighted above, excessive bubble nucleation activity in the coated channels resulted in prolonged periods of wall dryout, in most cases not observed at a similar operating condition in the plain heat sink. Wall dryout phenomenon observed in flow visualisation were linked to critical heat flux in the coated heat sink. Increasing mass velocity appeared to alleviate channel wall dryout in the annular flow regime and stabilised the enhancement ratio in the coated channels.

Two-phase pressure drop in the coated channels increased with heat flux and mass flux, but decreased with increasing saturation pressure and degree of inlet subcooling. This agreed with the experimental observations in the plain microchannel heat sink. The magnitude of flow boiling pressure drop were generally higher in the coated heat sink compared to the plain heat sink for a similar operating condition. This was mainly attributed to accelerated flow pattern development due to higher bubble generation activity in the coated channels. The higher channel void fraction resulted in higher frictional and acceleration pressure losses in the coated heat sink.

Pressure drop penalty typically increased with increasing heat flux and mass flux. A higher pressure drop penalty was observed where there is a larger difference in dominant flow pattern between the plain and coated microchannels. Accordingly, the pressure drop penalty increased between 1 bar and 1.5 bar but decreased between 1.5 bar and 2 bar. This was postulated to be related to the reduction in flow oscillations at higher system pressures.

The pressure drop penalty of 83 % was the highest at the lowest subcooling condition of 5 K. From flow visualisation, flow reversal triggered periodic wall dryout lasting for around 145 ms

in the coated microchannels. Wall dryout was significantly less severe in the plain channels at a similar working condition due to lower bubble nucleation activity. On the other hand, at the highest subcooling condition of 20 K, the coating actually lowered the magnitude of two-phase pressure drop in the channels at low heat fluxes. This was attributed to the suppression of flow boiling instabilities due to lower wall superheat in the coated heat sink at a given heat flux condition. A possible link between pressure drop oscillations, channel wall dryout and pressure drop magnitude were highlighted for further investigation.

9 Small-Scale Integrated Two-Phase Thermal Management System

9.1 Introduction

As highlighted in Section 1.1, implementation of two-phase microchannel cooling in industry has been slow due to poor understanding of fundamental issues in flow boiling. In the current study, many of these aspects were evaluated in order to facilitate the uptake of microchannel flow boiling technology for thermal management in high heat flux applications. In this section, the practical implications of operating conditions and performance of the microchannel heat sinks investigated are discussed. Furthermore, a design for a small-scale, integrated thermal management system adopting two-phase flow in microchannels is proposed and some design considerations are explored.

9.2 Microchannel Heat Sink Performance

Based on the results obtained in the current study, flow boiling (in the present plain and coated microchannel configurations) result in relatively uniform temperatures on the heat sink. The highest temperature difference obtained in the experimental range investigated is less than 2 K and 1 K at base heat fluxes of up to 800 kW/m^2 (i.e. power dissipation of 320 W on a base area of 20 mm x 20 mm) in the plain and coated heat sink respectively. The maximum wall temperature on the heat sink was 96.8 °C and 94.5 °C in the plain and coated microchannels respectively, which is below the typical allowable junction temperature of 125 °C and 150 °C for devices in military platforms and industrial applications.

Lee and Mudawar [38] previously demonstrated maximum cooling performance of 7 MW/m^2 using HFE-7100 as a working fluid, at very high inlet subcooling degrees (i.e. temperature of -30 °C at the inlet of the heat sink). As highlighted in Section 2.5, the cascade refrigeration cycle used to achieve the low coolant temperatures are not practical in the viewpoint of small-scale devices. The authors also did not report on temperature uniformity on their microchannel heat sink.

Whilst flow boiling instabilities, typically at low heat fluxes, was observed in the current study, two-phase oscillations did not deteriorate heat transfer performance in the microchannels,

except near the critical heat flux limit. Critical heat flux phenomenon was only observed at very high heat fluxes and at higher pressures in the coated heat sink, due to excessive bubble nucleation activity on the coated surface (see Section 8.5.3.2 and 8.5.5.2). Provided that the system operates within a safe range of operation below the critical heat flux limit, these results confirm that flow boiling in microchannels are able to deliver efficient cooling to high heat flux devices. Based on their extensive work on two-phase microchannel heat sinks using several working fluids, Kim and Mudawar [59] developed prediction models for important design parameters including premature critical heat flux and dryout incipience to predict the operational limits of a particular working fluid in a specific microchannel configuration. Such design models are paramount for the implementation of two-phase microchannel cooling technology in industry. The proposed models was not able to accurately predict critical heat flux and dryout incipience in the current study. Nevertheless, the heat transfer correlation of Kim and Mudawar [184] performed well in the prediction of HFE-7200 heat transfer coefficients (see Section 6.3).

9.3 Power Consumption

In the present study, the total pressure drop across the experimental loop was measured, see Section 3.2. Based on the current draw of the gear pump employed in the current study (see Section 3.2) for a range of pressure drop values [300], the power consumption curve of the pump is depicted in Figure 9.1.

Accordingly, this allows for the assessment of the power consumption in the microchannel heat sink, as well as the system power consumption of the complete experimental loop. Furthermore, the pressure drop across the heat sink and the pressure loss in the experimental loop is plotted in Figure 9.2 for the plain and coated heat sink for a nominal operating condition of P = 1 bar, G = 200 kg/m^2 s and ΔT_{sub} = 10 K. The filled markers represent the pressure drop in the experimental system while the blank markers represent pressure drop in the microchannel heat sink. The resulting power consumption in the system and the heat sink was calculated based on a curve fit of the power consumption data shown in Figure 9.1. This is depicted in Figure 9.3.

Total pressure drop across the heat sink ranged from 0.3 kPa to 5.9 kPa in the plain heat sink and 0.4 kPa and 7.7 kPa in the coated microchannel heat sink at G = 200 kg/m^2 s. As discussed

above, this is mainly due to the small mass flow rates employed in the current study. Whilst the two-phase pressure drop penalty was as high as 84 % in the coated test section (see Section 8.5.5.3), due to the relatively small pressure drop values observed in this study, the corresponding increase in power consumption across the heat sink is relatively small. The maximum heat sink power consumption in the coated heat sink was 1.7 W, which is only 0.2 W higher than the maximum power consumption of 1.5 W in the plain microchannel heat sink.

Furthermore, the majority of the pressure losses in the system (thus also the power consumption) is in fact in the experimental loop aside of the heat sink assembly, even though high pressure drop in microchannels is frequently cited as a limitation to two-phase cooling performance [301]. The highest pressure loss encountered across the experimental loop, was 36.1 kPa and 45.9 kPa using the plain and coated heat sink respectively at the highest base heat flux level at the nominal operating condition. The corresponding system power consumption was 9.4 W and 10.4 W accordingly. The pressure drop penalty posed by the coating results in only a 1 W increase in system power consumption. This penalty is very small if one considers the power consumption of the total experimental system.

For the range investigated in the current study, the highest pressure loss in the experimental loop obtained using the plain and coated heat sink was 75.2 kPa and 123.3 kPa respectively at an operating condition of G = 300 kg/m^2 s and q_b" ~ 800 kW/m^2. The corresponding pressure drop across the heat sink was 9.3 kPa (i.e. 1.9 W) and 14.1 kPa (i.e. 2.8 W) in the plain and coated test section respectively. The penalty in power consumption increases at the higher mass flux and base heat flux condition from 0.2 W (as discussed above) to 0.9 W. On the other hand, the system power consumption was 15.1 W and 24.4 W in the plain and coated microchannel heat sink respectively at this operating condition. The penalty in system power consumption increased from 1 W to 9.3 W using the coated heat sink at the higher mass flux and base heat flux condition. Note that the pressure loss data at the highest mass flux condition of G = 400 kg/m^2 s is not comparable with the lower mass flux conditions due to a difference in flow path through a different flowmeter (see Section 3.2).

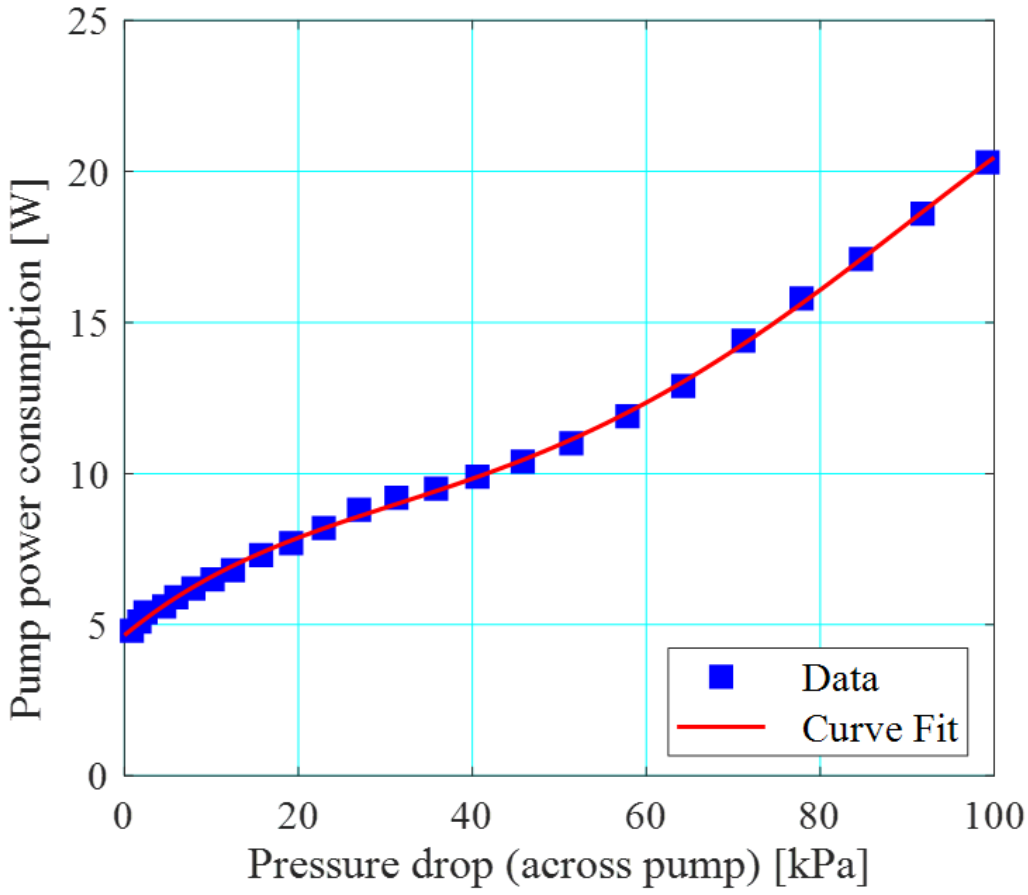

Figure 9.1: Power consumption of the pump for pressure drop values of up to 100 kPa.

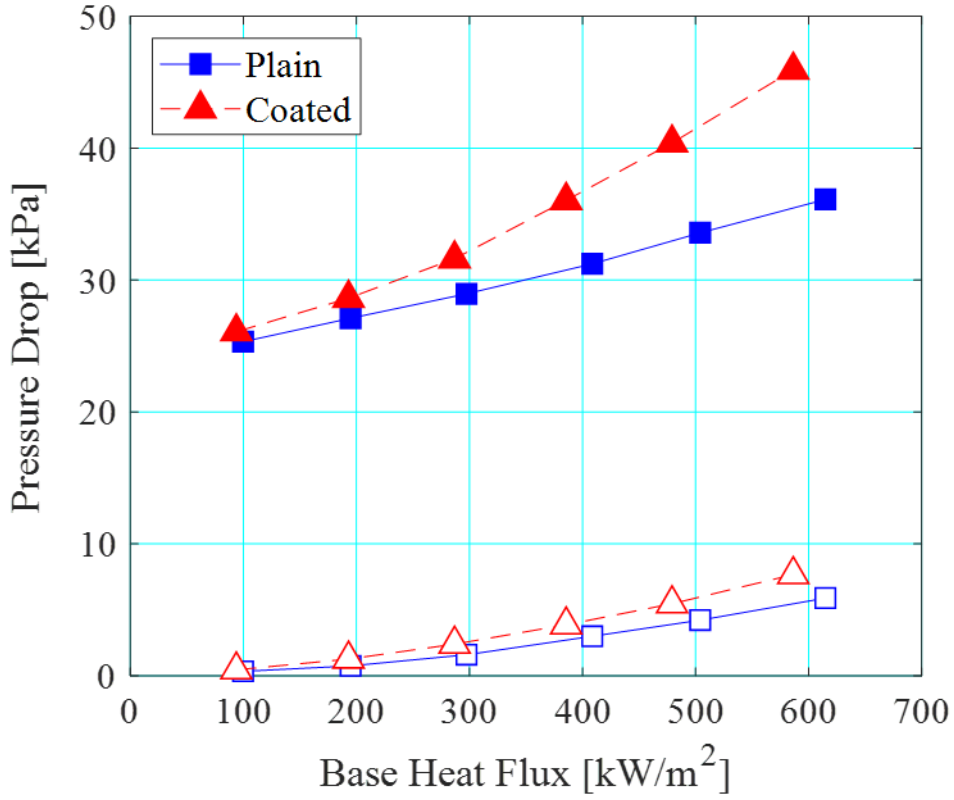

Figure 9.2: Pressure drop as a function of base heat flux in the experimental loop (filled markers) and the heat sink (blank markers) for the plain and coated microchannel configurations.

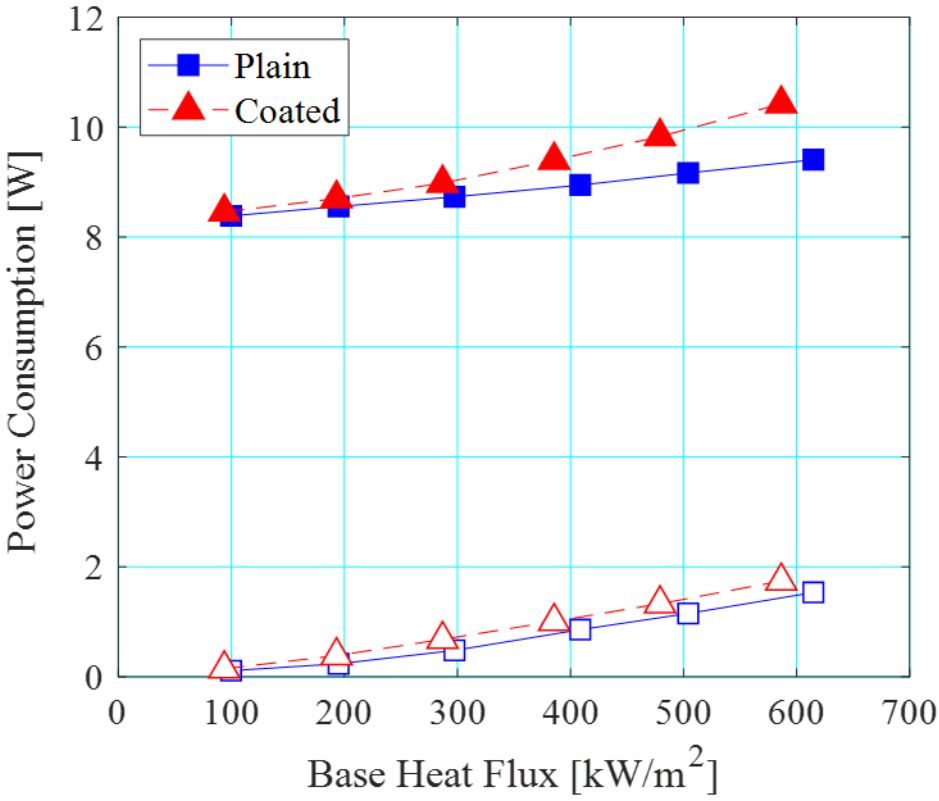

Figure 9.3: Power consumption of the pump as a function of base heat flux in the experimental loop (filled markers) and the heat sink (blank markers) for the plain and coated microchannel configurations.

9.4 Proposed Design of a Small-Scale Two-Phase Pumped Cooling System

In a small-scale thermal management system, measuring equipment present in the experimental loop is not required and the two-phase pumped loop may be simplified to one shown in Figure 9.4. As discussed briefly in Section 1.2, microchannel evaporators may be employed for the cooling of high heat flux devices in a two-phase cooling loop consisting of a receiver, pump, microchannel evaporator plate and a condenser. The condenser should interface with the global cooling strategy of the specific application. For example, avionics packages are typically air-cooled using conditioned engine bleed air in the avionics bay [6]. For this configuration, the condenser on the electronics module should be designed to reject heat to the cooling airflow provided by the environmental control system onboard. Aircraft fuel is sometimes also used as the ultimate heat sink in more demanding aerospace applications. In this case, the condenser should be liquid-cooled and have flow paths which interface with the fuel cooling circuit. Additionally, the design should consider the overall size, weight, power and cost of the system.

Furthermore, microchannel evaporator plates may be designed to manage multiple heat sources within an electronics package, as shown in Figure 9.5. The PTS6900 power electronics module from TMD Technologies Ltd. is shown in Figure 9.5(i) [302], with eight heat sources in the package. Two microchannel evaporator plates, each with four identical microchannel heat sinks similar to the configuration used in the current study, is mounted on top of the heat sources. The proposed design for the complete two-phase cooling loop is depicted in Figure 9.6. The dielectric properties of HFE-7200 and the low operating pressures pose less concerns on the sealing of the system. Due to the small refrigerant charge required by the system, a small pump would suffice for the application, along with a small reservoir contained within the electronics chassis. A manifold is connected prior to the evaporator plates to distribute flow evenly to each microchannel heat sink. The two-phase mixture is condensed in a microchannel condensing unit located outside the electronics chassis, which interfaces with the global cooling strategy, as discussed above. Cooling fins with fans or flow paths for fuel cooling may be integrated on the condenser.

A prototype of a similar two-phase pumped cooling loop for multiple heat sources should be investigated, with particular attention to the overall weight and size, as well as power consumption of the cooling system, including condenser fans (if present) and power draw of

the pump circulating the working fluid. Microchannel-based condensers are an active area of research in the flow boiling community [303], [304]. The promising results obtained at low degree of HFE-7200 subcooling (i.e. between 5 K to 20 K) in the current study poses a lower condenser load in the system and hence suitably sized condenser may be used for a small-scale thermal management solution, without compromising the weight of the overall system.

In applications where the ambient operating temperature is high, care must be taken to select a working fluid and operating pressure with a boiling point above the ambient temperature. Alternatively, a vapour-compression refrigeration cycle may be considered, and would widen the selection of working fluids suitable for such applications. Nevertheless, there are currently still concerns about the reliability of small-scale compressors, as highlighted in Section 1.2. The effect of gravitational orientation must also be clarified for implementation in airbourne or zero gravity environments. Research in this field is on-going for both microscale and macroscale flow boiling and condensation [305], [306].

Based on the system power consumption of the experimental loop, the power consumption of the proposed two-phase pumped cooling loop is estimated to be less than 50 W for mass fluxes in each heat sink of up to 300 kg/m^2 s managing up to 320 W power dissipation from each chip.

This estimation is based on the pressure drop across the microchannel evaporator plates (i.e. total of around 112 kPa and 24 W) and lower pressure losses due to less piping requirement in the real-life system (thus lower pressure loss and power consumption outside of the microchannel assembly). Pressure losses in the microchannel condenser should be relatively low due to the low refrigerant charge in the system and larger flow area in the condenser. Electrical power consumption by the condensing fans on cooling fins attached to the condenser should be additionally considered. The cooling fans employed in the current study had a power consumption of less than 20 W. Thus, the power required to operate the two-phase cooling system is likely to only make up less than 10 % of the power input to the device, which is almost 850 W for the PTS6900 module. The above indicates the viability of employing two-phase cooling in high heat flux electronics packages.

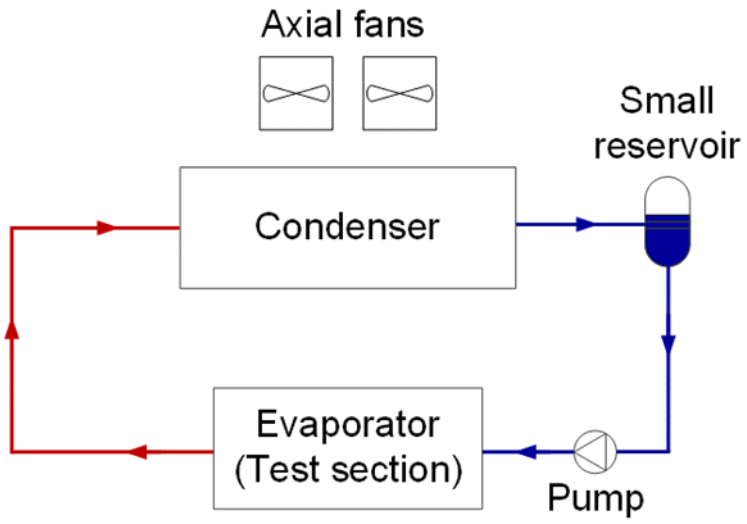

Figure 9.4: Illustration of a two-phase cooling loop.

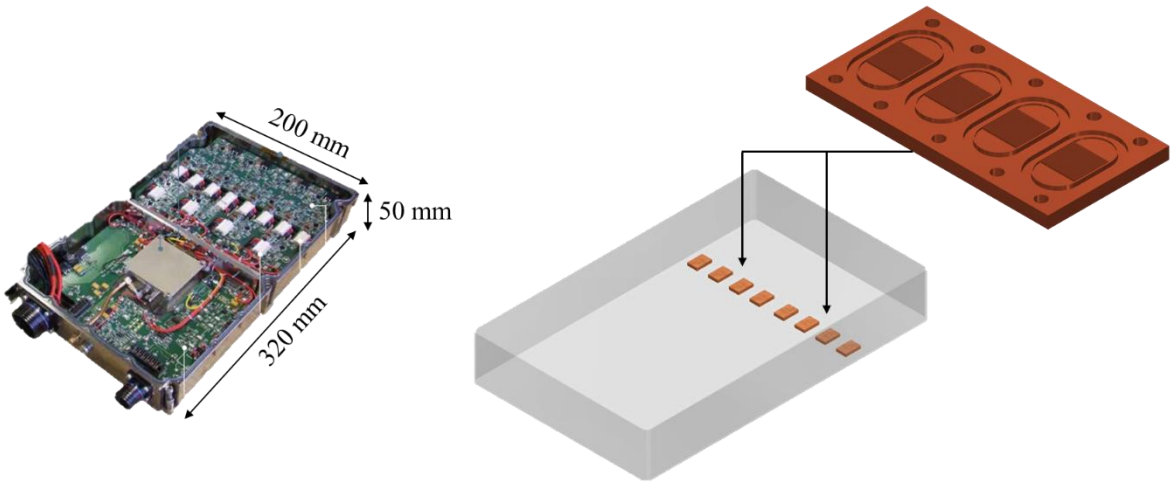

(i) Power electronics module from TMD Technologies (PTS6900) with eight heat sources

(ii) Two microchannel evaporator plates, each managing four heat sources

Figure 9.5: Example of electronics package with multiple heat sources shown in (i) and the conceptual design of microchannel evaporator plates is shown in (ii).

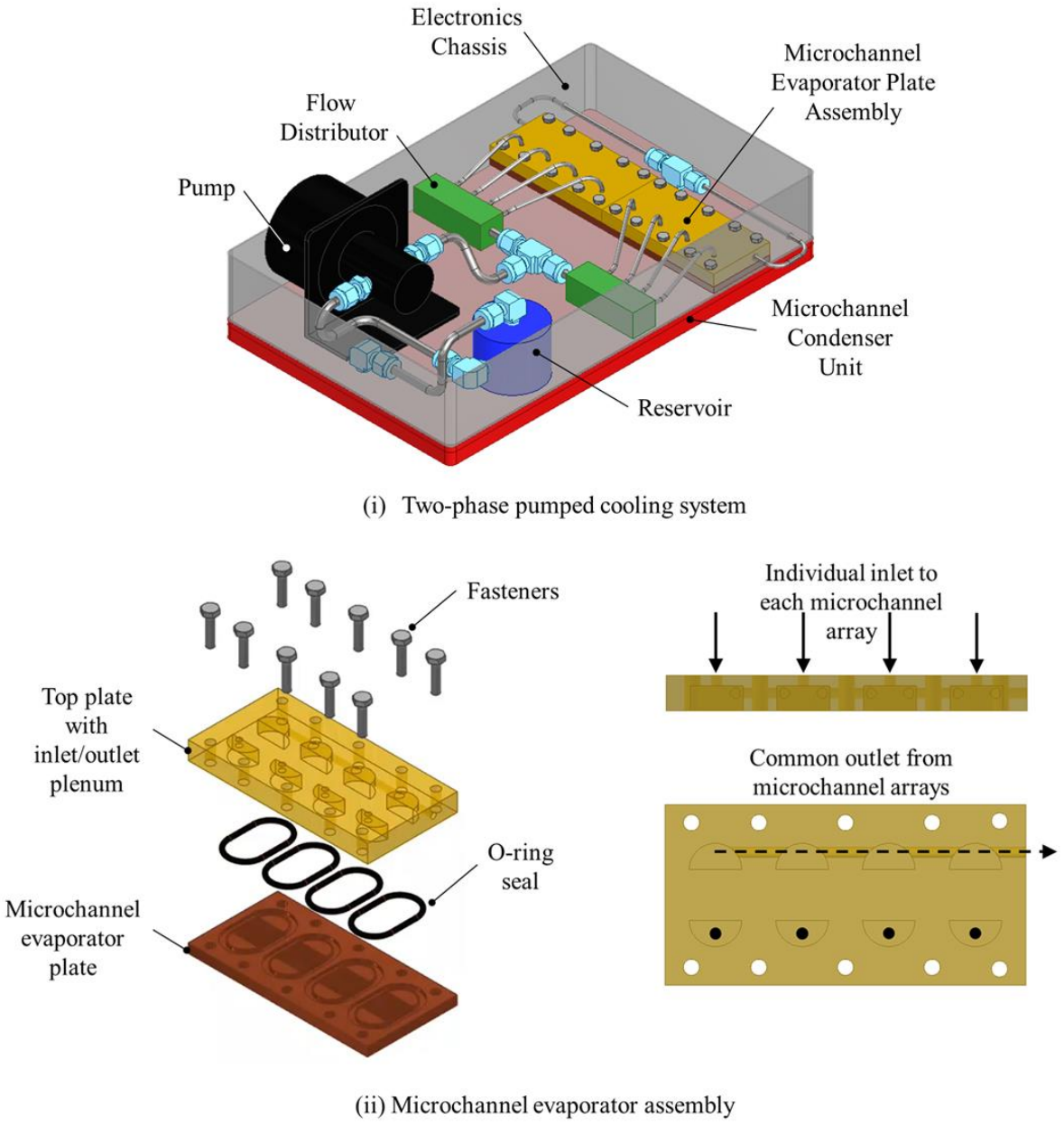

Figure 9.6: Conceptual design of an integrated two-phase pumped cooling loop with microchannel evaporator plates and a microchannel condenser.

9.5 Summary

In summary, the experimental results obtained in the current study were assessed for the practical implementation of a two-phase microchannel cooling system. The present study demonstrated a cooling capacity of 800 kW/m^2 using flow boiling in microchannel heat sinks at a mass flux of 300 kg/m^2 s and low inlet subcooling condition of 10 K. Good temperature uniformity of 2 K was demonstrated on the plain microchannel heat sink. The porous coating on the microchannel heat sink further improved isothermality to 1 K. The maximum heat sink wall temperatures at the highest heat flux condition (i.e. 94.5 °C in the enhanced channels) were below the maximum allowable limits for industrial and military applications.

Two-phase flow oscillations did not adversely affect heat transfer performance in the current study. Provided that the microchannel heat sink is designed to operate within a safe working range below the critical heat flux limit, efficient cooling can be delivered to high heat flux devices at low power consumption. Experimental data showed only a small penalty in power consumption using the coated heat sink and that the majority of pressure losses in the experimental loop was outside of the heat sink assembly. At the highest heat flux capacity, the power consumption was 15 W and 24 W using the plain and coated heat sink respectively.

Lastly, a design of an integrated small-scale thermal management system was proposed for a power electronics device with multiple heat sources. The two-phase pumped loop consisted of a small reservoir, gear pump, microchannel heat sink plates and a microchannel condenser assembly contained within the footprint of the electronics chassis. Based on experimental data, the power consumption of the integrated cooling system was projected to be less than 50 W and less than 10 % of the power input to the device (i.e. 850 W). The study concluded that two-phase pumped cooling loops are a viable thermal management solution for electronic assemblies with multiple high power density heat sources. For avionics cooling, attention should be paid to the overall size, weight, power as well as cost to operate the cooling system. The microchannel condenser acts as the ultimate heat sink to reject heat from the electronics enclosure, and should be appropriately interfaced with the global cooling system.

10 Conclusions and Recommendations

10.1 Conclusions

The present study investigates the flow boiling of HFE-7200, including high-speed flow visualisation, in a multi-microchannel copper heat sink of base area 20 mm x 20 mm with 44 channels of width 350 µm and height 700 µm. The channel-to-channel wall thickness was 100 µm and the channel hydraulic diameter was 475 µm. In particular, the effect of heat flux, mass flux, system pressure and degree of inlet subcooling on two-phase flow patterns, heat transfer, pressure drop and flow instability was examined. The experimental range covered was between inlet pressures of 1 – 2 bar, mass fluxes of 200 – 400 kg/m^2 s, subcooling degree of 5 – 20 K for wall and base heat fluxes 24.8 – 234.3 kW/m^2 and 93.7 – 896.3 kW/m^2 respectively.

The effect of surface coatings on microchannel flow boiling behaviour was also investigated in the current study. The coating, nanoFLUX®, was applied on the bottom and side walls of the conventionally milled copper microchannels and is a proprietary coating provided by Oxford nanoSystems Ltd consisting of a metallic dendritic nano and microstructure allowing for optimisable porosity for bubble nucleation. SEM analysis was conducted on the bottom wall of the channels in order to characterise the surface of the plain and coated heat sink.

Shallow cavities with diameters between 0.25 µm and 4.5 µm were typically observed on the plain surface. On the coated surface, slightly smaller but deeper and more defined cavities of diameters between 0.1 µm to 1.7 µm were identified. On a given size area, there were 24 times more cavities on the coated channels in comparison to the plain channels.

Crucially, the size range of all cavities (identified both on the plain as well as the coated channels) are within the active nucleation range (i.e. 0.04 µm to 40 µm at P = 1 bar and ΔT_{sub} = 10 K) as predicted using Hsu's model for HFE-7200 and wall superheat degrees of up to 30 K. This means that the cavities are able to act as bubble nucleation sites for the flow boiling of HFE-7200 within the operating range investigated in the current study.

Flow boiling experiments in the coated microchannel heat sink was conducted at similar operating conditions as in the plain heat sink, along with the corresponding flow visualisation.

The hydraulic diameter considered for the coated channels was 456 µm (as opposed to 475 µm for the plain channels) due to the thickness of the layer of coating. The effectiveness of the coating was assessed based on two-phase heat transfer enhancement and pressure drop penalty in the heat sink.

Single-phase experiments showed that results from the coated test section followed traditional microchannel theory, albeit with higher channel friction factor (i.e. 54 % to 120 %) and higher Nusselt number (i.e. 50 % to 81 %) compared to the plain microchannels. The higher frictional loss in the coated test section was postulated to be due to the rougher channel walls owing to the layer of coating on the enhanced channels. The higher experimental Nusselt number in the coated heat sink was attributed to higher heat transfer area and improved fluid mixing on the surfaces of the coated walls.

10.1.1 Two-Phase Flow Patterns

Flow visualisation was conducted in the middle of the heat sink at four locations in the streamwise direction along the channels for each experimental condition. High-speed recordings were taken at steady-state conditions at 5000 fps for a duration of 1.3 s. The key findings from the flow visualisation results are summarised below:

i. Four flow regimes, namely bubbly, slug, churn and annular flow were observed in this study. Two-phase flow patterns developed from bubbly to slug, churn and annular flow with increasing heat flux in the microchannel heat sink.

ii. Bubbly flow was observed at low heat fluxes just after the onset of boiling, where bubbles were captured to nucleate from the channel side walls. Bubbles in the subcooled region shrink after departure, while bubbles continue to grow in size in the saturated region of the channels.

iii. At a given pressure, mass flux and subcooling condition, increasing heat flux activates more nucleation sites and increases the bubble generation activity in the heat sink. The rate of bubble coalescence increases accordingly.

iv. Bubble coalescence and elongation of confined bubbles lead to the development of slug flow in the heat sink.
    a. Flow reversal is triggered in the slug flow regime by the expansion of slugs in the upstream direction toward the inlet plenum of the heat sink.
    b. Nucleation sites were observed in the slug liquid film and were periodically deactivated with liquid film thinning and local wall dryout on the channel walls. Channel rewetting occurs when the incoming subcooled liquid overcomes vapour backflow at the inlet plenum.

v. Churn flow develops with the distortion of slugs at high vapour velocities and annular flow develops when a clear vapour core is established in the channels.
    a. Nucleation sites were also observed in the annular liquid film, which were periodically suppressed with liquid film thinning. Intermittent churn waves

rewet the channel walls and reactivate nucleation sites in the annular liquid film. Dryout cycles were typically shorter in the annular flow regime compared to the slug flow regime.

vi. Increasing system pressure and degree of inlet subcooling at a given mass flux delayed flow regime transitions, while increasing mass flux accelerated flow pattern development in the plain microchannel heat sink.
    a. Delayed flow pattern transition at higher system pressures were attributed to smaller bubble departure diameters at higher saturation pressures, due to higher vapour density of the working fluid at higher pressures.
    b. Bubble shrinkage and lower bubble generation activity at higher degrees of subcooling could have contributed to delayed flow pattern transitions in the heat sink.

vii. Increasing mass flux at a fixed inlet pressure and subcooling condition increased flow inertia in the channels, which increased the rate of bubble coalescence in the heat sink, leading to earlier flow regime transitions in the channels.

viii. Flow pattern data were used to assess several flow pattern maps in literature. None of the flow pattern maps were capable of predicting all flow regime boundaries accurately. This could be because some of the maps evaluated were developed for single channels and may not be appropriate for multichannel configurations due to flow reversal and parallel channel interactions.
    a. The flow pattern maps of Ong and Thome and Revellin and Thome predicted bubbly-slug flow transition relatively well, but underpredicted and overpredicted churn-annular transition respectively. The effect of mass flux, pressure and subcooling on flow patterns were well-captured by the flow maps.
    b. The classifications of flow regimes of the Ong and Thome and Revellin and Thome maps (isolated bubble, coalescing bubble regimes) do not match the general classifications of flow regimes to allow for straight-forward comparison of flow pattern data.

ix. A universal two-phase flow pattern map that captures the appropriate sensitivities of relevant operating parameters employing the primary flow pattern classifications is still required by the community.

10.1.1.1 Effect of Surface Coating

i. Flow patterns generally developed earlier in the coated microchannel heat sink in comparison to the plain microchannel heat sink at a given operating condition, especially between bubbly and slug flow. This is attributed to higher bubble generation frequency in the coated channels due to the availability of more nucleation sites (i.e. 24 times higher) and deeper cavities on the coated surface. The deeper cavities may have encouraged vapour entrapment during bubble departure and reduced waiting time between successive nucleation cycles on the coated surface.

ii. Higher bubble nucleation activity led to longer wall dryout periods in the coated channels in comparison to the plain heat sink in some instances. However, at low heat fluxes, the coating generally mitigated two-phase instabilities, which prevented flow reversal and subsequently channel wall dryout.

iii. Increasing mass flux and inlet subcooling degree at a fixed pressure condition accelerated and delayed flow pattern development in the coated heat sink, which was similarly observed in the plain microchannel heat sink. Furthermore, increasing mass flux and degree of subcooling appeared to prevent dryout in the channels. This may be attributed to the higher flow inertia (improved rewetting capability) and lower bubble generation activity at higher subcooling.

iv. Increasing system pressure for a fixed mass velocity accelerated flow regime transitions in the coated heat sink, which was contrary to the observation in the plain heat sink, as mentioned in Section 10.1.1(vi) above. The earlier transitions are because the effect of higher bubble nucleation activity at higher pressures dominated over the effect of smaller bubble diameter in the coated heat sink.

10.1.2 Two-Phase Flow Instability

Flow boiling instability in the current study was examined using flow visualisation at the inlet and outlet plenum of the heat sink. The pressure drop signal measured across the heat sink was also used to assess two-phase flow oscillations in the microchannels.

i. Two-phase flow instability in the microchannels were found to be most severe when the slug flow regime was dominant in the heat sink, as the expansion of vapour slugs in the upstream direction induced flow reversal at the inlet plenum. The magnitude of flow oscillations typically decreased when churn and annular flow began to dominate in the heat sink.

ii. In the plain microchannel at low wall heat fluxes, increasing the system pressure and degree of subcooling at a fixed mass velocity lowered two-phase flow oscillations related to bubble nucleation and expansion in the channels. This was mainly due to the delay in slug flow development in the heat sink.

10.1.2.1 Effect of Surface Coating

i. At low heat fluxes where slug flow was predominantly observed in the microchannels, two-phase oscillations may be mitigated using the coating, despite the higher bubble nucleation activity from the coated channels. This was attributed to the reduction in wall superheat (lower by ~ 3 K on the coated channels compared to the plain channels) at a given wall heat flux condition in the coated heat sink. The lower wall superheat may have suppressed rapid bubble growth instabilities and flow reversal in the inlet plenum.

ii. There was some evidence to suggest a potential link between two-phase flow oscillations, duration of wall dryout and magnitude of two-phase pressure drop, although, it must be noted that flow boiling instabilities did not appear to affect heat transfer coefficients in the plain and coated microchannel heat sink.

10.1.3 Two-Phase Heat Transfer

i. Local heat transfer coefficients generally increased with increasing vapour quality in the subcooled region. This is due to the change in heat transfer mode from single-phase liquid convection to nucleate boiling in the channels.

ii. Heat transfer coefficients typically reached a maximum at low vapour qualities near the onset of boiling, where bubbly flow was observed. The peak in heat transfer coefficients was attributed to the high heat transfer rates in the nucleate boiling mechanism, which was evidenced by intense bubble nucleation activity in the channels from flow visualisation.

iii. The high heat transfer coefficients evaluated near the onset of boiling was determined to be unaffected by the assumption of a linear pressure drop trend, as opposed to a parabolic trend, in the two-phase region of the channels due to the small values of pressure drop (highest two-phase pressure drop in the channels was only around 11 kPa in both microchannel heat sinks).

iv. After the initial peak, heat transfer coefficients gradually decreased with increasing vapour quality corresponding to flow pattern development to slug, churn and annular flow in the channels. Flow visualisation revealed that this was because of periodic suppression of nucleation sites with liquid film thinning, especially in the slug and annular flow regime. The suppression of nucleation cavities reduced the time-averaged heat transfer coefficient at a given location on the channels.

v. With flow pattern transition towards the annular flow regime in the heat sink, through thin-film evaporation, the contribution of convective boiling to total heat transfer increases. This was ascertained by the stronger mass flux effect on average two-phase heat transfer coefficients in the heat flux region where annular flow dominated in the heat sink. A small increase in heat transfer coefficient near the channel exit was attributed to heat loss to the outlet plenum.

vi. Average two-phase heat transfer coefficients increased with increasing heat flux in the plain microchannels but did not reach the critical heat flux limit in the experimental range investigated in this study. The high wettability of HFE-7200 on the copper channels and the churn wave rewetting mechanism could have prevented the occurrence of premature dryout in the heat sink.

vii. Average flow boiling heat transfer coefficients generally increased with increasing system pressure for a given heat flux. This may be attributed to an increase in bubble generation frequency due to higher vapour density and higher reduced pressure ratio with increasing saturation pressure.

viii. For average two-phase heat transfer, the mass flux effect is negligible at low to medium wall heat fluxes but begins to manifest at heat fluxes where annular flow begins to dominate in the heat sink. This indicates that the contribution of the convective boiling component increases with flow regime transition to annular flow. At heat fluxes where the mass flux effect is insignificant, the nucleate boiling mechanism could dominate two-phase heat transfer.

ix. Increasing the degree of subcooling lowered flow boiling heat transfer coefficients slightly in the heat sink, which may be attributed to lower bubble generation frequency due to the narrower range of active nucleation sites at higher subcooling. This was also supported by delayed flow pattern transitions at higher degrees of subcooling.

x. The effect of mass flux and inlet subcooling on overall heat transfer coefficients (averaged heat transfer coefficient including the subcooled region) is significant at low wall heat fluxes due to the substantial fraction of the subcooled region with respect to total channel length. Local heat transfer coefficients in the subcooled region are generally several times lower than the heat transfer coefficients in the saturated region. With increasing heat flux, the subcooled length decreases and its influence on overall heat transfer coefficient diminishes accordingly.

xi. Two-phase heat transfer results were assessed against 18 two-phase heat transfer correlation in literature. The top three performing correlations were the Sun and Mishima (2009), Kim and Mudawar (2013) and Kandlikar and Balasubramaniam (2010), which are based on the nucleate boiling model, asymptotic model and predominant mechanism model respectively. The abovementioned correlations were based on relatively large database involving several working fluids and considered dimensionless parameters including the Boiling number, liquid-vapour density ratio and fluid-only Weber number.

xii. The local heat transfer trend was closely predicted by the Fang et al. (2017), however, wall temperatures were required as an input parameter in the correlation, which may not be suitable for real-life applications and during design stages where intricate temperature readings are not available.

10.1.3.1 Effect of Surface Coating

i. A similar local heat transfer trend was observed in the coated microchannel heat sink as in the plain microchannel test section. The rise in heat transfer coefficient near the channel exit was less apparent in the coated microchannels, potentially due to the larger magnitudes of heat transfer coefficients in the coated heat sink.

ii. Similar effects of operating parameters were observed in the coated test section for two-phase heat transfer as in the plain channels. Average flow boiling heat transfer coefficients in the coated channels increased with increasing heat flux and saturation pressure, but only exhibited a notable mass flux effect toward high heat fluxes. The effect of inlet subcooling on two-phase heat transfer was also marginal in the coated heat sink.

iii. The critical heat flux was exceeded in the coated microchannel heat sink at a mass flux of 200 kg/m^2 s at a wall heat flux of around 129 kW/m^2 when the system pressure was increased to 1.5 bar and 2 bar. The critical heat flux limit was also reached at a wall heat flux of 174.2 kW/m^2 when the subcooling was 20 K. At similar operating

conditions in the plain microchannels, critical heat flux was not observed. This was attributed to excessive bubble nucleation activity in the channels (owing to the higher density of nucleation sites), which induced persistent wall dryout lasting up to 30 ms observed in the annular flow regime as determined from the corresponding flow visualisation at the critical heat flux condition.

iv. Two-phase heat transfer enhancement, i.e. heat transfer rates compared to the plain microchannels, using the coated heat sink was highly dependent on heat flux level. The peak enhancement effect for a given operating condition was found to be typically at heat fluxes where slug flow was dominant in the heat sink. This could be because the heat transfer mechanism during this flow regime is largely controlled by the nucleate boiling mechanism. Flow boiling heat transfer enhancement depreciated with increasing heat flux, corresponding to the suppression of bubble nucleation with flow pattern development towards annular flow in the heat sink.

v. Prior to reaching critical heat flux, increasing system pressure generally improved two-phase heat transfer enhancement in the coated heat sink. The highest percentage of heat transfer enhancement obtained in the current study was almost 50 % at 2 bar. This was mainly attributed to higher bubble generation activity and shorter waiting time between successive nucleation cycles due to the higher vapour density at higher pressures.

vi. At low wall heat fluxes, increasing mass flux appear to suppress heat transfer enhancement in the slug flow regime in the coated channels. This could be because of accelerated flow pattern transition to slug flow in the heat sink at higher mass fluxes. At higher heat fluxes, the increased flow inertia at higher mass fluxes may prevent channel wall dryout and sustain heat transfer enhancement in the annular flow regime. At the lowest mass flux condition, the percentage of heat transfer enhancement depreciated significantly with increasing heat flux where annular flow was dominant in the heat sink.

vii. The enhancement effect in the coated heat sink was stronger at higher inlet subcooling conditions. The higher enhancement effect at the highest subcooling condition may be due to the comparatively lower bubble nucleation activity at higher subcooling in the

plain microchannel heat sink at a subcooling condition of 20 K. This was supported by the large shift in flow pattern transition between bubbly and slug flow in the plain and coated heat sink.

10.1.4 Two-Phase Pressure Drop

i. Flow boiling pressure drop increased with increasing heat flux and exit vapour quality in the channel. Bubble nucleation activity increases with increasing heat flux, resulting in an overall increase in channel void fraction. The higher void fraction accelerates the flow, directly increasing acceleration pressure loss and also a steeper velocity gradient at the channel wall, thus increasing frictional pressure loss in the channels.

ii. Increasing system pressure generally decreased microchannel flow boiling pressure drop. This was mainly due to a considerable increase in vapour density with pressure increment. This decelerated vapour flow in the channels, resulting in lower interfacial shear and a smaller velocity gradient at the channel wall, decreasing acceleration and frictional pressure drop accordingly. A delay in flow pattern development in the channels at higher pressures because of smaller bubble sizes could also have lowered pressure drop in the two-phase region.

iii. Increasing the channel mass flux increased two-phase pressure drop in the microchannels, mainly because the higher flow inertia accelerates the flow in the channels. Both the frictional and acceleration pressure drop component are proportional to the square of mass flux. Flow regime transitions are also accelerated with increasing mass velocity, which could contribute to higher pressure drop in the channels.

iv. Increasing the degree of inlet subcooling from 5 K to 10 K at a nominal mass flux and pressure condition did not appear to have a notable effect on two-phase pressure drop, however flow boiling pressure drop was significantly lower with further increase in subcooling to 20 K. This may be because of the more substantial delay in flow regime development at 20 K.

v. Amongst the twelve two-phase pressure drop correlations assessed for the pressure drop data obtained in the current study, Chisholm's B-coefficient method for macroscale flows, the Mishima and Hibiki and Qu and Mudawar microscale correlations were the top three performing correlations. The latter two correlations were based on the

classical Lockhart-Martinelli correlation and calculated the C coefficient with the assumption of a laminar liquid and vapour phase in the channels.

vi. Notably, all correlations assessed overpredicted two-phase pressure drop at the subcooling condition of 20 K. The lower flow boiling pressure drop was associated with substantially delayed flow regime development in the heat sink. This indicates that two-phase pressure drop models should incorporate the effect of flow pattern in their correlation.

10.1.4.1 Effect of Surface Coating

i. Two-phase pressure drop in the coated microchannel heat sink was generally larger by comparison to the plain test section. Similar to the observation in the plain channels, two-phase pressure drop increased with heat flux, due to higher bubble generation activity and channel void fraction.

ii. For a given wall heat flux condition, increasing mass velocity increased flow boiling pressure drop because of higher flow acceleration in the microchannels. On the other hand, increasing system pressure and degree of subcooling reduced two-phase pressure loss. The former is attributed to an increase in vapour density while the latter is because of delayed flow pattern transition in the microchannels.

iii. Two-phase pressure drop penalty generally increased with increasing heat flux, corresponding to accelerated flow regime transitions in the coated heat sink in relation to the plain test section. Larger disparity between flow pattern transition boundaries appear to result in larger flow boiling pressure drop penalties. The penalty in flow boiling pressure drop may be lower at low heat fluxes where the subcooled length is a substantial fraction of the total channel length.

iv. Low wall superheat degree at a given wall heat flux in the coated heat sink alleviated bubble growth instabilities related pressure drop oscillations in the channels. This may

also have reduced two-phase pressure drop (thus lower pressure drop penalty in the coated channels).

v. Severe flow oscillations and prolonged wall dryout, where milder in the plain microchannels, could result in a large percentage penalty in two-phase pressure drop in the coated heat sink. However, flow boiling pressure drop penalty do not necessarily spike at critical heat flux condition, where prolonged periods of wall dryout are observed in the coated channels. The relationship between pressure drop oscillations, channel wall dryout and the magnitude of two-phase pressure drop should be clarified in further investigations.

10.1.5 Design of a Small-Scale Two-Phase Cooling System

i. In the present study, a maximum cooling capacity of 800 kW/m^2, i.e. heat dissipation of 320 W on a footprint area of 20 mm x 20 mm, was demonstrated. The maximum wall temperature at the highest base heat flux condition using both the plain and coated microchannels were below the typical allowable junction limits for industrial and military electronics devices. Importantly, a high heat flux capacity was achieved using a low subcooling condition of 10 K, which is realistically attainable in an integrated, small-scale thermal management system.

ii. The surface coating lowered maximum wall temperatures on the heat sink by around 3 K to 4 K at a similar heat flux condition compared to the plain microchannels. Maximum temperature gradient on the heat sink decreased from 2 K in the plain channels to 1 K in the coated test section. This showed that temperature uniformity may be improved using the coating due to lower wall superheat at a given heat flux condition.

iii. Although the pressure drop penalty may be quite high in the coated channels, the increase in pumping power consumption using the coated heat sink was small. Experimental data showed that the majority of pumping losses in the experimental loop was outside of the heat sink assembly. Pump power required to operate the microchannel heat sinks was less than 3 W while the power consumption of the experimental facility reached 24 W.

iv. Flow boiling instabilities did not appear to depreciate heat transfer performance in both microchannel heat sinks, contrary to some studies in literature. Nevertheless, the surface coating appeared to suppress flow instabilities at low heat fluxes, as highlighted in Section 10.1.2.1. Critical heat flux phenomenon was only observed at certain conditions in the coated heat sink, triggered by excessive bubble generation and wall dryout in the coated channels. Efficient cooling may be achieved using two-phase cooling in the current microchannel heat sink configuration, provided that the design range is within the envelope of safe operation, i.e. below the critical heat flux limit.

v. A design for a microchannel flow boiling cooling system was proposed for an electronics device with multiple heat sources. The integrated system contains a small reservoir, pump, the microchannel heat sink plates and a microchannel condenser all within the footprint of the electronics chassis. Based on experimental data, the power consumption of the cooling system was projected to be less than 10 % of the total power input to the device.

vi. Design recommendations of a two-phase cooling system for avionics applications were presented. Special attention should be paid to the size, weight, power and cost of the system. Ultimate heat rejection from the electronics package, through the microchannel condenser, should interface well with the global cooling system, which may be conditioned air or aircraft fuel.

10.2 Summary of Novel Contributions

Novel contributions to the research community from the current study are summarised as follows:

i. New experimental data on the flow boiling of dielectric fluid HFE-7200 in multi-microchannels are presented. To the best of the author's knowledge, there is some data available in pool boiling and micro-pin fin heat sinks but limited data available for this working fluid in parallel microchannel configurations.

ii. The effect of heat flux, system pressure, mass flux and degree of inlet subcooling on microchannel two-phase flow patterns, flow instability, flow boiling heat transfer and pressure drop were investigated independently. Additionally, relatively low mass flux and degrees of inlet subcooling were employed in the current study to best represent feasible thermal design conditions in practical application. Sensitivity analysis on two-phase flow regime maps, heat transfer correlations and pressure drop prediction methods was conducted.

iii. Heat transfer enhancement by means of surface modification using a porous metallic coating was explored. The effect of the surface coating on flow pattern development, heat transfer enhancement, pressure drop penalty and two-phase oscillations in the microchannel heat sink were reported. Extensive work on surface characterisation and analysis of active cavity range on the plain and coated channels were included.

iv. The power consumption of the experimental loop, including the power consumption of the microchannel heat sink was examined. Practical implications of operating conditions on microchannel heat sink performance and the resultant power consumption of the experimental system was reported. To the best of the author's knowledge, the power consumption of a pumped two-phase cooling loop has not been directly measured in literature.

v. A design of a small-scale, integrated thermal management system adopting microchannel flow boiling technology for multiple heat sources within an electronics chassis was proposed. The power consumption of the conceptual two-phase pumped cooling loop was estimated based on experimental data, see Section 9.4.

10.3 Recommendations

The current experimental study has identified several key areas for further research to encourage a wider adoption of two-phase microchannel cooling in order to meet current and future needs in industry. These are summarised as follows:

i. Flow visualisation, heat transfer and pressure drop data should be synchronised to investigate heat transfer deterioration, pressure drop behaviour as well as wall temperature profiles during cyclic wall dryout in the channels. For this purpose, temperature sensors with higher response time should be employed. There was some evidence to suggest that there is a tangible link between two-phase flow oscillations, wall dryout and pressure drop magnitude in the heat sink, which should be a subject for further investigation.

ii. Flow boiling behaviour with dynamic heat loads should be studied. In the present study, heat input to the base of the heat sink (for each heat flux level) was kept constant during experiments. Nonetheless, many devices operate on pulsed modes and thus may have dynamic power dissipation profiles at the heat source. The transient response of the microchannel heat sink with a time-dependent heat load should be explored, with particular attention to hysteresis and flow instabilities in the heat sink.

iii. Flow patterns, two-phase instabilities and temperature uniformity on microchannel heat sinks with hotspots at different locations on the base area should be investigated for applications in chip cooling with non-uniform heat dissipation profiles. The effect of the magnitude of the hotspot, with reference to the background heat flux should also be studied. A small number of studies examining non-uniform heat flux distribution have found significant implications on flow boiling behaviour [307]–[309].

iv. Optimisation of the cavities on the porous coating for applications with different working fluids based on the active cavity range should be explored. The longevity and durability of the coating under prolonged periods of thermal cycling should be tested.

v. A prototype of a small-scale thermal management system for multiple heat sources should be investigated, with particular attention on the size, weight and power

consumption of the system. A compact microchannel condenser, ideally air-cooled as it is most common in industry, should be employed.

vi. Further work on developing reliable thermal design correlations (including the prediction of heat transfer coefficient, pressure drop and critical heat flux) in order to optimise two-phase systems and predict the operational limits of two-phase microchannel heat sinks would benefit the development of design tools of two-phase pumped loops.

Appendix A

Propagated Uncertainty Analysis

Data obtained from the experimental rig is subject to uncertainties caused by systematic errors, usually associated with instrumentation and random errors due to unpredictability during the experimental process. Systemic bias are minimised by calibration of the measuring equipment, detailed in Section 3.2. Random errors are reduced by increasing the sample size of the recording data. In this study, each data point is averaged from a data sample obtained at a frequency of 1 kHz for a duration of 90 s, i.e. 90 000 points. Assuming the distribution of the readings follow a standard Gaussian distribution, the random uncertainties of the experimental variables, U_{random}, may be estimated using statistical analysis method following a 95 % confidence level as proposed by Coleman and Steele [268]:

$$U_{random} = t_{95\%} S_X \tag{A.1}$$

$$S_X = \sqrt{\frac{1}{n-1} \sum_{i=1}^{n} X_i - \bar{X}^2} \tag{A.2}$$

$$\bar{X} = \frac{1}{n} \sum_{i=1}^{n} X_i \tag{A.3}$$

where $t_{95\%}$ is value from the t-distribution table that achieves a 95% confidence level, S_X is the standard deviation of the sample population, X_i is the sample value and $\bar{X}$ is the mean of the sample value.

The systematic uncertainty considers the bias uncertainty, B_x, resulting from element k, typically obtained by referring to technical data of equipment or calibration certificate. The standard deviation of the systematic uncertainty, S_{BX}, is half of the bias uncertainty:

$$B_X = \sqrt{\sum_{k=1}^{M} (B_X)^2_k} \tag{A.4}$$

$$S_{BX} = \frac{B_X}{2} \tag{A.5}$$

The overall uncertainty, U, may be evaluated again based on a 95 % confidence level from u_c, which is the combined uncertainty of the random and systematic errors:

$$u_c = \sqrt{S_{BX}{}^2 + S_X{}^2} \tag{A.6}$$

$$U = t_{95\%}\, u_c \tag{A.7}$$

For an experimental variable r, which is a function of j number of variables, X:

$$r = r(X_1, X_2, X_3 \ldots X_j) \tag{A.8}$$

The absolute and relative propagated uncertainty of the experimental variable, U_r, are respectively as follows:

$$U_r{}^2 = \left(\frac{\partial r}{\partial X_1}\right) U_{X_1}{}^2 + \left(\frac{\partial r}{\partial X_2}\right) U_{X_2}{}^2 + \left(\frac{\partial r}{\partial X_3}\right) U_{X_3}{}^2 + \ldots + \left(\frac{\partial r}{\partial X_j}\right) U_{X_j}{}^2 \tag{A.9}$$

$$\frac{U_r{}^2}{r^2} = \left(\frac{X_1}{r}\frac{\partial r}{\partial X_1}\right)^2 \left(\frac{U_{X_1}}{X_1}\right)^2 + \left(\frac{X_2}{r}\frac{\partial r}{\partial X_2}\right)^2 \left(\frac{U_{X_2}}{X_2}\right)^2 + \ldots + \left(\frac{X_j}{r}\frac{\partial r}{\partial X_j}\right)^2 \left(\frac{U_{X_j}}{X_j}\right)^2 \tag{A.10}$$

Uncertainty analysis for the experimental variables in this study was performed according to the approach outlined above. The uncertainty values of the measured variables are summarised in Table A.1, obtained from technical datasheets and calibration certificates.

The K-type thermocouples employed in the current study were calibrated between 20 °C to 120 °C in 5 °C increments in a water-glycol bath using a precision thermometer (ASL F250 MKII, full range accuracy ± 0.005 K) and the data logger through a LabVIEW software. The temperature readings were recorded at 1 kHz over a window of 90 s and averaged accordingly. The actual and measured values of temperature were plotted on a graph and the line of best fit for each individual thermocouple was implemented as the calibration equation on LabVIEW. The average standard deviation of the measured values to the actual value obtained from the prevision thermometer was calculated to be ± 0.2 K and used as the uncertainty value.

On the other hand, the propagated uncertainties of experimental variables were calculated based on Eq. (A.10). The data reduction procedure are thoroughly presented in Section 3.3.

The relative uncertainty of the channel hydraulic diameter is expressed as follows:

$$\frac{U_{D_h}}{D_h} = \sqrt{\left\{\frac{H_{ch}}{(H_{ch}+W_{ch})}\,\frac{U_{W_{ch}}}{W_{ch}}\right\}^2 + \left\{\frac{W_{ch}}{(H_{ch}+W_{ch})}\,\frac{U_{H_{ch}}}{H_{ch}}\right\}^2} \tag{A.11}$$

where $U_{W_{ch}}$ and $U_{H_{ch}}$ are the absolute uncertainty of the channel width and height respectively, as listed in Table A.1.

The propagated uncertainty of the channel mass flux, U_G, may be calculated using the uncertainty in mass flow rate, $U_{\dot{m}}$, (see Table A.1) and the uncertainty of the channel cross-section area, $U_{A_{ch}}$:

$$\frac{U_G}{G} = \sqrt{\left\{\frac{U_{\dot{m}}}{\dot{m}}\right\}^2 + \left\{\frac{U_{A_{ch}}}{A_{ch}}\right\}^2} \tag{A.12}$$

$$\frac{U_{A_{ch}}}{A_{ch}} = \sqrt{\left\{\frac{U_{W_{ch}}}{W_{ch}}\right\}^2 + \left\{\frac{U_{H_{ch}}}{H_{ch}}\right\}^2} \tag{A.13}$$

The relative uncertainty in base heat flux is calculated based on the uncertainties of the thermocouples, U_T, and vertical distance on the heat sink block, $U_{\Delta y}$. From Table A.1, the values for U_T and $U_{\Delta y}$ are ± 0.2 K and ± 0.01 mm respectively.

$$\frac{U_{q_b''}}{q_b''} = \sqrt{\left\{\frac{U_T}{\Delta T_{tc}}\right\}^2 + \left\{\frac{U_{\Delta y}}{\Delta y}\right\}^2} \tag{A.14}$$

where ΔT_{tc} and Δy are the temperature difference of the vertical thermocouples and the distance between the vertical thermocouples respectively, for thermocouples locations see Section 3.3.

Accordingly, the wall heat flux is calculated based on $U_{q_b''}$, and the heat transfer area, $U_{A_{ht}}$:

$$\frac{U_{q_w''}}{q_w''} = \sqrt{\left\{\frac{U_{q_b''}}{q_b''}\right\}^2 + \left\{\frac{U_{A_{ht}}}{A_{ht}}\right\}^2 + \left\{\frac{U_{W_b}}{W_b}\right\}^2 + \left\{\frac{U_{L_{ch}}}{L_{ch}}\right\}^2} \tag{A.15}$$

$$\frac{U_{A_{ht}}}{A_{ht}} = \sqrt{\left\{\frac{2U_{H_{ch}}}{(2H_{ch} + W_{ch})}\right\}^2 + \left\{\frac{U_{W_{ch}}}{(2H_{ch} + W_{ch})}\right\}^2 + \left\{\frac{U_{L_{ch}}}{L_{ch}}\right\}^2} \tag{A.16}$$

where U_{W_b} and $U_{L_{ch}}$ are the absolute uncertainties of the width of the heat sink base and length of the channel, which are both ± 0.01 mm from Table A.1.

The absolute uncertainty of the local wall temperature, $U_{Tw(z)}$, and the local fluid temperature, $U_{Tf(z)}$ may be expressed as follows:

$$U_{T_{w(z)}} = \sqrt{\{ U_T \}^2 + \left\{ \frac{Y\, U_{q_b''}}{k_{cu}} \right\}^2 + \left\{ \frac{q_b''\, U_Y}{k_{cu}} \right\}^2} \tag{A.17}$$

$$U_{T_{f(z)}} = \sqrt{\begin{aligned} &\{ U_{T_i} \}^2 + \left\{ \frac{W_b\, z\, U_{q_b''}}{\dot{m}\, c_{p,l}} \right\}^2 + \left\{ \frac{q_b''\, z\, U_{W_b}}{\dot{m}\, c_{p,l}} \right\}^2 + \left\{ \frac{q_b''\, W_b\, z\, U_z}{\dot{m}\, c_{p,l}} \right\}^2 \\ &+ \left\{ \frac{q_b''\, W_b\, z\, U_{\dot{m}}}{\dot{m}^2\, c_{p,l}} \right\}^2 \end{aligned}} \tag{A.18}$$

In Eq. (A.17). k_{cu} is the thermal conductivity of the wall, i.e. copper, and Y is the distance between the bottom wall of the channel and the thermocouple, i.e. 1.6 mm. U_Y is the absolute uncertainty in the distance between the channel bottom wall and the thermocouple, U_{Ti} is the absolute uncertainty of the inlet temperature (i.e. ± 0.2 K from Table A.1) and U_z is the absolute uncertainty in axial location along the channel

The relative uncertainty of the local heat transfer coefficient is expressed as:

$$\frac{U_{h_{(z)}}}{h_{(z)}} = \sqrt{\begin{aligned} &\left\{ \frac{U_{q_b''}}{q_b''} \right\}^2 + \left\{ \frac{U_{W_b}}{W_b} \right\}^2 + \left\{ \frac{2U_{H_{ch}}}{(2H_{ch} + W_{ch})} \right\}^2 + \left\{ \frac{U_{W_{ch}}}{(2H_{ch} + W_{ch})} \right\}^2 \\ &+ \left\{ \frac{U_{T_{w(z)}}}{T_{w(z)} - T_{f(z)}} \right\}^2 + \left\{ \frac{U_{T_{f(z)}}}{T_{w(z)} - T_{f(z)}} \right\}^2 \end{aligned}} \tag{A.19}$$

As covered in Section 3.3, $T_{f(z)}$ is calculated from Eq. (3.17) if the corresponding z location is in the subcooled region and evaluated based on Eq. (3.29) if in the two-phase region. The uncertainties in the subcooled length is expressed as:

$$\frac{U_{L_{sub}}}{L_{sub}} = \sqrt{\left\{ \frac{U_{\dot{m}}}{\dot{m}} \right\}^2 + \left\{ \frac{U_{q_b''}}{q_b''} \right\}^2 + \left\{ \frac{U_{W_b}}{W_b} \right\}^2 + \left\{ \frac{U_{T_i}}{T_{sat(z,sub)} - T_i} \right\}^2} \tag{A.20}$$

Assuming a negligible uncertainty in fluid properties, for e.g. the specific heat capacity, c_p, the relative uncertainty in local enthalpy and local vapour quality are obtained using Eq. (A.21) and Eq. (A.22):

$$U_{i_{(z)}} = \sqrt{\left\{ \frac{W_b\, z\, U_{q_b''}}{\dot{m}} \right\}^2 + \left\{ \frac{q_b''\, z\, U_{W_b}}{\dot{m}} \right\}^2 + \left\{ \frac{q_b''\, W_b\, U_z}{\dot{m}} \right\}^2 + \left\{ \frac{q_b''\, W_b\, z\, U_{\dot{m}}}{\dot{m}^2} \right\}^2} \tag{A.21}$$

$$U_{x_{(z)}} = \frac{U_{i_{(z)}}}{i_{fg(z)}} \tag{A.22}$$

Hence the relative uncertainties of the localised liquid and vapour superficial velocities may be found as follows:

$$\frac{U_{J_{l(z)}}}{J_{l(z)}} = \sqrt{\left\{\frac{U_G}{G}\right\}^2 + \left\{\frac{U_{x_{(z)}}}{(1-x_z)}\right\}^2} \tag{A.23}$$

$$\frac{U_{J_{g(z)}}}{J_{g(z)}} = \sqrt{\left\{\frac{U_G}{G}\right\}^2 + \left\{\frac{U_{x_{(z)}}}{x_z}\right\}^2} \tag{A.24}$$

For the single-phase and two-phase pressure drop, the uncertainties $U_{\Delta P_{sp}}$ and $U_{\Delta P_{tp}}$ are:

$$\frac{U_{\Delta P_{sp}}}{\Delta P_{sp}} = \sqrt{\left\{\frac{U_{D_h}}{D_h}\right\}^2 + \left\{\frac{2\,U_G}{G}\right\}^2 + \left\{\frac{U_{L_{sub}}}{L_{sub}}\right\}^2} \tag{A.25}$$

$$U_{\Delta P_{tp}} = \sqrt{\left\{U_{\Delta P_{ch}}\right\}^2 + \left\{U_{\Delta P_{sp}}\right\}^2} \tag{A.26}$$

In Eq. (A.26), $U_{\Delta P_{ch}}$ is the absolute uncertainty in channel pressure drop and may be calculated as follows:

$$U_{\Delta P_{ch}} = \sqrt{\left\{U_{\Delta P_{total}}\right\}^2 + \left\{U_{\Delta P_{loss}}\right\}^2} \tag{A.27}$$

where $U_{\Delta P_{total}}$ is the absolute uncertainty of the measured pressure and is ± 0.08 %, from Table A.1. On the other hand, $U_{\Delta P_{loss}}$ is the absolute uncertainty of the pressure losses in the plenum as well as due to sudden contraction into the channel array and sudden expansion from the channel array. For single-phase experiments, $U_{\Delta P_{loss}}$ is calculated based on the propagated uncertainties of Eq. (3.3) to Eq. (3.6) in Section 3.3:

$$U_{\Delta P_{loss}} = \sqrt{\left\{U_{ip}\right\}^2 + \left\{U_{sc}\right\}^2 + \left\{U_{se}\right\}^2 + \left\{U_{op}\right\}^2} \tag{A.28}$$

When the outlet of the channels is in the two-phase region, $U_{\Delta P_{loss}}$ is calculated based on the propagated uncertainties of Eq. (3.3), Eq. (3.5) and from Eq. (3.8) to Eq. (3.13) in Section 3.3:

The propagated uncertainty in the experimental Fanning friction factor, U_f, is thus:

$$\frac{U_f}{f} = \sqrt{\left\{\frac{U_{\Delta P_{ch}}}{\Delta P_{ch}}\right\}^2 + \left\{\frac{U_{D_h}}{D_h}\right\}^2 + \left\{\frac{2\,U_G}{G}\right\}^2 + \left\{\frac{U_{L_{ch}}}{ch}\right\}^2} \qquad \text{(A.29)}$$

Following the procedure above, the uncertainty range for single-phase and flow boiling experiments are presented in Table 3.4, see Section 3.3.

Table A.1: Uncertainties of measured variables.

Variable	Measurement Instrument	Uncertainty
Channel dimensions	TESA-VISIO 200GL (manufacturer)	± 0.002 mm
Heat sink base dimensions	Digital vernier callipers (manufacturer)	± 0.01 mm
Mass flow rate	OPTIMASS 3000 (manufacturer)	± 0.035 %
Differential pressure	OMEGA PX409-015 (manufacturer)	± 0.08 %
Inlet and outlet pressure transducer	OMEGA PX409-007 (manufacturer)	± 0.08 %
Temperatures	K-type thermocouples (calibrated)	± 0.2 K

Publications

Conference

1. V. Y. S. Lee, A. Al-Zaidi, G. Henderson, and T. G. Karayiannis, "Flow Boiling Results of HFE-7200 in a Multi-Microchannel Evaporator and Comparison with HFE-7100," in 4th International Conference on Multiphase Flow and Heat Transfer, Rome, April 10 – 12, 2019. (Best Paper Award)

2. V. Y. S. Lee, G. Henderson, and T. G. Karayiannis, "Effect of Inlet Subcooling on Flow Boiling Behaviour of HFE-7200 in a Microchannel Heat Sink," in Proceedings of the 16th UK Heat Transfer Conference, September 8 – 10, 2019. (Best Student Paper)

3. V. Y. S. Lee, G. Henderson and T.G. Karayiannis, "Flow Boiling in Plain and Porous Coated Microchannels," in Proceedings of the 6th World Congress on Momentum, Heat and Mass Transfer (MHMT'21), June 17 – 19, 2021.

Journal

1. V. Y. S. Lee and T. G. Karayiannis, "Effect of Inlet Subcooling on Flow Boiling in Microchannels," Applied Thermal Engineering, vol. 181, p. 115966, 2020.

References

[1] K. Rupp, “42 Years of Microprocessor Trend Data,” 2018. [Online]. Available: https://www.karlrupp.net/2018/02/42-years-of-microprocessor-trend-data/. [Accessed: 12-Nov-2019].

[2] “Moore’s Law: Transistors per microprocessor,” *Our World in Data*, 2017. [Online]. Available: https://ourworldindata.org/grapher/transistors-per-microprocessor?time=1971..2017. [Accessed: 12-Nov-2019].

[3] G. E. Moore, “Cramming more components onto integrated circuits,” *Electronics*, vol. 38, no. 8, 1965.

[4] “The story of the Intel 4004: Intel’s first microprocessor.” [Online]. Available: http://www.intel.com/content/www/us/en/history/museum-story-of-intel-4004.html. [Accessed: 13-Nov-2019].

[5] “Nvidia Tesla V100 GPU Architecture: the world’s most advanced data center GPU,” 2017.

[6] I. Mudawar, “Assessment of high-heat-flux thermal management schemes,” *IEEE Trans. Components Packag. Technol.*, vol. 24, no. 2, pp. 122–141, 2001.

[7] T. G. Karayiannis and M. M. Mahmoud, “Flow boiling in microchannels: Fundamentals and applications,” *Appl. Therm. Eng.*, vol. 115, pp. 1372–1397, 2017.

[8] C. Bachmann and A. Bar-Cohen, “Hotspot remediation with anisotropic thermal interface materials,” *2008 11th IEEE Intersoc. Conf. Therm. Thermomechanical Phenom. Electron. Syst. I-THERM*, pp. 238–247, 2008.

[9] B. Allard, C. Buttay, C. Martin, H. Morel, B. Allard, C. Buttay, C. Martin, and H. Morel, “Considerations for High Temperature Power Electronics,” 2015.

[10] A. Jamnia, “Design and reliability considerations in avionics electronics packaging,” *Electronics Cooling*, 1999. [Online]. Available: https://www.electronics-cooling.com/1999/09/design-and-reliability-considerations-in-avionics-electronics-packaging/. [Accessed: 20-Feb-2020].

[11] V. Wong, “Data Sheet Intricacies — Absolute Maximum Ratings and Thermal

Resistances," 2011.

[12] Lytron, "Custom Cold Plates for Mission Critical Power Electronics Cooling," 2019.

[13] P. Zhou, J. Horn, G. Upadhya, K. Goodson, and M. Munch, "Electro-kinetic microchannel cooling system for desktop computers," *Annu. IEEE Semicond. Therm. Meas. Manag. Symp.*, vol. 20, pp. 26–29, 2004.

[14] J. F. Tullius, R. Vajtai, and Y. Bayazitoglu, "A review of cooling in microchannels," *Heat Transf. Eng.*, vol. 32, no. 7–8, pp. 527–541, 2011.

[15] S. Krishnan, S. V. Garimella, G. M. Chrysler, and R. V. Mahajan, "Towards a thermal Moore's law," *IEEE Trans. Adv. Packag.*, vol. 30, no. 3, pp. 462–474, 2007.

[16] S. Krishnan, D. Hernon, M. Hodes, J. Mullins, and A. M. Lyons, "Design of complex structured monolithic heat sinks for enhanced air cooling," *IEEE Trans. Components, Packag. Manuf. Technol.*, vol. 2, no. 2, pp. 266–277, 2012.

[17] C. C. Wang, "A Quick Overview of Compact Air-Cooled Heat Sinks Applicable for Electronic Cooling—Recent Progress," *Inventions*, vol. 2, no. 1, p. 5, 2017.

[18] A. Siricharoenpanich, S. Wiriyasart, A. Srichat, and P. Naphon, "Thermal management system of CPU cooling with a novel short heat pipe cooling system," *Case Stud. Therm. Eng.*, vol. 15, p. 100545, 2019.

[19] S. K. Sahoo, M. K. Das, and P. Rath, "Hybrid Cooling System for Electronics Equipment during Power Surge Operation," *IEEE Trans. Components, Packag. Manuf. Technol.*, vol. 8, no. 3, pp. 416–426, 2018.

[20] R. G. Willoh, "Apollo Experience Report - Lunar Module Landing Gear Subsystem," *Nasa Tech. Note*, 1972.

[21] D. J. Delia *et al.*, "System cooling design for the water-cooled IBM enterprise system/9000 processors," *IBM J. Res. Dev.*, vol. 36, no. 4, pp. 791–803, 1992.

[22] M. Barwick, M. Midkiff, and D. Seals, "Liquid flow-through cooling for avionics applications," *IEEE Proc. Natl. Aerosp. Electron. Conf.*, vol. 1, pp. 227–230, 1991.

[23] R. LeVasseur, "Liquid cooled approaches for high density avionics," *IEEE/AIAA Digit. Avion. Syst. Conf. 10th, Los Angeles, CA, Oct. 14-17, 1991, Proc. (A92-49251 21-06)*, pp. 147–152, 1991.

[24] D. B. Tuckerman and R. F. W. Pease, “High-Performance Heat Sinking for VLSI,” *IEEE Electron Device Lett.*, vol. 2, no. 5, pp. 126–129, 1981.

[25] W. Escher, T. Brunschwiler, B. Michel, and D. Poulikakos, “Experimental investigation of an ultrathin manifold microchannel heat sink for liquid-cooled chips,” *J. Heat Transfer*, vol. 132, no. 8, pp. 1–10, 2010.

[26] A. Mohammadi and A. Koşar, “Review on Heat and Fluid Flow in Micro Pin Fin Heat Sinks under Single-phase and Two-phase Flow Conditions,” *Nanoscale Microscale Thermophys. Eng.*, vol. 22, no. 3, pp. 153–197, 2018.

[27] Z. Wan and Y. Joshi, “Pressure drop and heat transfer characteristics of pin fin enhanced microgaps in single phase microfluidic cooling,” *Int. J. Heat Mass Transf.*, vol. 115, pp. 115–126, 2017.

[28] D. Kong, K. W. Jung, S. Jung, D. Jung, J. Schaadt, M. Iyengar, C. Malone, C. R. Kharangate, M. Asheghi, K. E. Goodson, and H. Lee, “Single-phase thermal and hydraulic performance of embedded silicon micro-pin fin heat sinks using R245fa,” *Int. J. Heat Mass Transf.*, vol. 141, pp. 145–155, 2019.

[29] C. S. Sharma, M. K. Tiwari, S. Zimmermann, T. Brunschwiler, G. Schlottig, B. Michel, and D. Poulikakos, “Energy efficient hotspot-targeted embedded liquid cooling of electronics,” *Appl. Energy*, vol. 138, pp. 414–422, 2015.

[30] D. Ansari and K.-Y. Kim, “Hotspot management using a hybrid heat sink with stepped pin-fins,” *Numer. Heat Transf. Part A Appl.*, vol. 75, no. 6, pp. 359–380, 2019.

[31] Y. Hu, T. Sarvey, M. Bakir, and Y. Joshi, “Single phase liquid cooling of hotspots in a heterogeneous pin-fin-enhanced microgap with non-uniform fin array,” *Proc. 16th Intersoc. Conf. Therm. Thermomechanical Phenom. Electron. Syst. ITherm 2017*, pp. 500–504, 2017.

[32] R. Wu, Y. Fan, T. Hong, H. Zou, R. Hu, and X. Luo, “An immersed jet array impingement cooling device with distributed returns for direct body liquid cooling of high power electronics,” *Appl. Therm. Eng.*, vol. 162, 2019.

[33] T. M. Bandhauer, D. R. Hobby, C. Jacobsen, and D. Sherrer, “Thermal performance of micro-jet impingement device with parallel flow, jet-adjacent fluid removal,” in *ASME 2018 16th International Conference on Nanochannels, Microchannels, and*

Minichannels, ICNMM 2018, 2018.

[34] M. K. Sung and I. Mudawar, "Single-phase and two-phase cooling using hybrid micro-channel/slot-jet module," *Int. J. Heat Mass Transf.*, vol. 51, no. 15–16, pp. 3825–3839, 2008.

[35] T. Brunschwiler, H. Rothuizen, M. Fabbri, U. Kloter, B. Michel, R. J. Bezama, and G. Natarajan, "Direct liquid jet-impingement cooling with micronsized nozzle array and distributed return architecture," *Thermomechanical Phenom. Electron. Syst. - Proceedings Intersoc. Conf.*, pp. 196–203, 2006.

[36] J. Z. Yi, H. X. Hu, Z. B. Wang, and Y. G. Zheng, "On the critical flow velocity for erosion-corrosion in local eroded regions under liquid-solid jet impingement," *Wear*, vol. 422–423, pp. 94–99, 2019.

[37] J. R. Thome and A. Cioncolini, "Flow Boiling in Microchannels," *Adv. Heat Transf.*, vol. 49, no. January 2017, pp. 157–224, 2017.

[38] J. Lee and I. Mudawar, "Fluid flow and heat transfer characteristics of low temperature two-phase micro-channel heat sinks – Part 1: Experimental methods and flow visualization results," *Int. J. Heat Mass Transf.*, vol. 51, no. 17–18, pp. 4315–4326, 2008.

[39] K. P. Drummond, D. Back, M. D. Sinanis, D. B. Janes, D. Peroulis, J. A. Weibel, and S. V. Garimella, "A hierarchical manifold microchannel heat sink array for high-heat-flux two-phase cooling of electronics," *Int. J. Heat Mass Transf.*, vol. 117, pp. 319–330, 2018.

[40] X. Gao and R. Li, "Spray Impingement Cooling: The State of the Art," in *Advanced Cooling Technologies and Applications*, IntechOpen, 2019.

[41] J. R. Barbosa, G. B. Ribeiro, and P. A. De Oliveira, "A state-of-the-art review of compact vapor compression refrigeration systems and their applications," *Heat Transf. Eng.*, vol. 33, no. 4–5, pp. 356–374, 2012.

[42] A. Poachaiyapoom, R. Leardkun, J. Mounkong, and S. Wongwises, "Miniature vapor compression refrigeration system for electronics cooling," *Case Stud. Therm. Eng.*, vol. 13, p. 100365, 2019.

[43] J. Homitz, R. Scaringe, and G. Cole, "Evaluation of a vapor-compression thermal

management system for reliability while operating under thermal transients," *SAE Tech. Pap.*, 2010.

[44] Z. Wu and R. Du, "Design and experimental study of a miniature vapor compression refrigeration system for electronics cooling," *Appl. Therm. Eng.*, vol. 31, no. 2–3, pp. 385–390, 2011.

[45] J. He, Y. Wu, X. Chen, Y. Lu, C. Ma, C. Du, G. Liu, and R. Ma, "Experimental study of a miniature vapor compression refrigeration system with two heat sink evaporators connected in series or in parallel," *Int. J. Refrig.*, vol. 49, pp. 28–35, 2015.

[46] S. Mancin, C. Zilio, G. Righetti, and L. Rossetto, "Mini Vapor Cycle System for high density electronic cooling applications," *Int. J. Refrig.*, vol. 36, no. 4, pp. 1191–1202, 2013.

[47] C.-H. H. Kim, M.-J. J. Lee, and C. Y. Park, "An experimental study on the heat transfer and pressure drop characteristics of electronics cooling heat sinks with FC-72 flow boiling," *J. Mech. Sci. Technol.*, vol. 32, no. 3, pp. 1449–1462, 2018.

[48] C. R. Bradshaw, E. A. Groll, and S. V. Garimella, "A comprehensive model of a miniature-scale linear compressor for electronics cooling," *Int. J. Refrig.*, vol. 34, no. 1, pp. 63–73, 2011.

[49] K. Liang, "A review of linear compressors for refrigeration," *Int. J. Refrig.*, vol. 84, pp. 253–273, 2017.

[50] J. B. Marcinichen, J. A. Olivier, N. Lamaison, and J. R. Thome, "Advances in electronics cooling," *Heat Transf. Eng.*, vol. 34, no. 5–6, pp. 434–446, 2013.

[51] L. Y. Jeng and T. P. Teng, "Performance evaluation of a hybrid cooling system for electronic chips," *Exp. Therm. Fluid Sci.*, 2013.

[52] S. G. Kandlikar, "History, advances, and challenges in liquid flow and flow boiling heat transfer in microchannels: A critical review," *Journal of Heat Transfer*, vol. 134, no. 3. 2012.

[53] L. Cheng and G. Xia, "Fundamental issues, mechanisms and models of flow boiling heat transfer in microscale channels," *Int. J. Heat Mass Transf.*, vol. 108, pp. 97–127, 2017.

[54] V. V. Kuznetsov, "Fundamental Issues Related to Flow Boiling and Two-Phase Flow

Patterns in Microchannels – Experimental Challenges and Opportunities," *Heat Transf. Eng.*, vol. 40, no. 9–10, pp. 711–724, 2019.

[55] T. G. Karayiannis, M. M. Mahmoud, and D. B. R. Kenning, "A study of discrepancies in flow boiling results in small to microdiameter metallic tubes," *Exp. Therm. Fluid Sci.*, vol. 36, pp. 126–142, 2012.

[56] M. M. Mahmoud and T. G. Karayiannis, "Flow Boiling in Mini to Microdiameter Channels," in *Encyclopedia of Two-Phase Heat Transfer and Flow IV*, J. R. Thome, Ed. World Scientific Publishing, 2018, pp. 233–301.

[57] A. H. Al-Zaidi, M. M. Mahmoud, and T. G. Karayiannis, "Flow boiling of HFE-7100 in microchannels: Experimental study and comparison with correlations," *Int. J. Heat Mass Transf.*, vol. 140, pp. 100–128, 2019.

[58] T.-H. H. Yen, N. Kasagi, and Y. Suzuki, "Forced convective boiling heat transfer in microtubes at low mass and heat fluxes," *Int. J. Multiph. Flow*, vol. 29, no. 12, pp. 1771–1792, 2003.

[59] S.-M. Kim and I. Mudawar, "Thermal design and operational limits of two-phase micro-channel heat sinks," *Int. J. Heat Mass Transf.*, vol. 106, pp. 861–876, 2017.

[60] 3M, "3M Thermal Management Fluids: Cool Under Fire - Dielectric heat transfer fluid solutions for military and aerospace applications," vol. Datasheet, 2008.

[61] A. Reeser, A. Bar-Cohen, and G. Hetsroni, "High Vapor Quality Two Phase Heat Transfer in Staggered and Inline Micro Pin Fin Arrays," in *Thermomechanical Phenomena in Electronic Systems -Proceedings of the Intersociety Conference*, 2014, pp. 213–221.

[62] Z. M. Wan, "Transport Characteristics of Pin-Fin Enhanced Microgaps under Single and Two Phase Cooling, Ph.D Thesis," Georgia Institute of Technology, 2016.

[63] D. Lorenzini and Y. Joshi, "Numerical modeling and experimental validation of two-phase microfluidic cooling in silicon devices for vertical integration of microelectronics," *Int. J. Heat Mass Transf.*, vol. 138, pp. 194–207, 2019.

[64] Z. Wu, Z. Cao, and B. Sundén, "Saturated pool boiling heat transfer of acetone and HFE-7200 on modified surfaces by electrophoretic and electrochemical deposition," *Appl. Energy*, vol. 249, pp. 286–299, 2019.

[65] Z. Cao, Z. Wu, A. D. Pham, Y. Yang, S. Abbood, P. Falkman, T. Ruzgas, C. Albèr, and B. Sundén, “Pool boiling of HFE-7200 on nanoparticle-coating surfaces: Experiments and heat transfer analysis,” *Int. J. Heat Mass Transf.*, vol. 133, pp. 548–560, 2019.

[66] A. Sathyanarayana, P. Warrier, Y. Joshi, and A. Teja, “Saturated and subcooled pool boiling of HFE-7200 mixtures on a copper nanowire surface,” *Front. Heat Mass Transf.*, vol. 2, no. 4, pp. 1–7, 2011.

[67] P. Warrier, A. Sathyanarayana, D. V. Patil, S. France, Y. Joshi, and A. S. Teja, “Novel heat transfer fluids for direct immersion phase change cooling of electronic systems,” *Int. J. Heat Mass Transf.*, vol. 55, no. 13–14, pp. 3379–3385, 2012.

[68] S. S. Bertsch, E. A. Groll, and S. V. Garimella, “Refrigerant flow boiling heat transfer in parallel microchannels as a function of local vapor quality,” *Int. J. Heat Mass Transf.*, vol. 51, no. 19–20, pp. 4775–4787, 2008.

[69] S. S. Bertsch, E. A. Groll, and S. V. Garimella, “Effects of heat flux, mass flux, vapor quality, and saturation temperature on flow boiling heat transfer in microchannels,” *Int. J. Multiph. Flow*, vol. 35, no. 2, pp. 142–154, 2009.

[70] E. M. Fayyadh, M. M. Mahmoud, K. Sefiane, and T. G. Karayiannis, “Flow boiling heat transfer of R134a in multi microchannels,” *Int. J. Heat Mass Transf.*, vol. 110, pp. 422–436, 2017.

[71] C. Falsetti, H. Jafarpoorchekab, M. Magnini, N. Borhani, and J. R. Thome, “Two-phase operational maps, pressure drop, and heat transfer for flow boiling of R236fa in a micro-pin fin evaporator,” *Int. J. Heat Mass Transf.*, vol. 107, pp. 805–819, 2017.

[72] A. Reeser, A. Bar-Cohen, and G. Hetsroni, “High quality flow boiling heat transfer and pressure drop in microgap pin fin arrays,” *Int. J. Heat Mass Transf.*, vol. 78, pp. 974–985, 2014.

[73] L. Yin, P. Jiang, R. Xu, H. Hu, and L. Jia, “Heat transfer and pressure drop characteristics of water flow boiling in open microchannels,” *Int. J. Heat Mass Transf.*, vol. 137, pp. 204–215, 2019.

[74] B. Markal, O. Aydin, and M. Avci, “An experimental investigation of saturated flow boiling heat transfer and pressure drop in square microchannels,” *Int. J. Refrig.*, vol. 65, pp. 1–11, 2016.

[75] Y. Li, G. Xia, Y. Jia, Y. Cheng, and J. Wang, “Experimental investigation of flow boiling performance in microchannels with and without triangular cavities – A comparative study,” *Int. J. Heat Mass Transf.*, vol. 108, pp. 1511–1526, 2017.

[76] Y. F. Li, G. D. Xia, D. D. Ma, J. L. Yang, and W. Li, “Experimental investigation of flow boiling characteristics in microchannel with triangular cavities and rectangular fins,” *Int. J. Heat Mass Transf.*, vol. 148, p. 119036, 2020.

[77] J. Zeng, S. Zhang, Y. Tang, Y. Sun, and W. Yuan, “Flow boiling characteristics of micro-grooved channels with reentrant cavity array at different operational conditions,” *Int. J. Heat Mass Transf.*, vol. 114, pp. 1001–1012, 2017.

[78] D. Deng, L. Chen, W. Wan, T. Fu, and X. Huang, “Flow boiling performance in pin fin-interconnected reentrant microchannels heat sink in different operational conditions,” *Appl. Therm. Eng.*, vol. 150, pp. 1260–1272, 2019.

[79] C. T. Lu and C. Pan, “Convective boiling in a parallel microchannel heat sink with a diverging cross section and artificial nucleation sites,” *Exp. Therm. Fluid Sci.*, vol. 35, no. 5, pp. 810–815, 2011.

[80] D. Deng, W. Wan, Y. Qin, J. Zhang, and X. Chu, “Flow boiling enhancement of structured microchannels with micro pin fins,” *Int. J. Heat Mass Transf.*, vol. 105, pp. 338–349, 2017.

[81] P.-S. Lee and S. V. Garimella, “Saturated flow boiling heat transfer and pressure drop in silicon microchannel arrays,” *Int. J. Heat Mass Transf.*, vol. 51, no. 3–4, pp. 789–806, 2008.

[82] B. J. Jones and S. V. Garimella, “Surface roughness effects on flow boiling in microchannels,” *J. Therm. Sci. Eng. Appl.*, vol. 1, no. 4, pp. 1–9, 2009.

[83] E. Costa-Patry, J. Olivier, B. Michel, and J. R. Thome, “Two-phase flow of refrigerants in 85 um-wide multi-microchannels: Part II – Heat transfer with 35 local heaters,” *Int. J. Heat Fluid Flow*, vol. 32, no. 2, pp. 464–476, 2011.

[84] T. Harirchian and S. V Garimella, “Effects of Channel Dimension, Heat Flux, and Mass Flux on Flow Boiling Regimes in Microchannels,” *Int. J. Multiph. Flow*, vol. 35, pp. 249–362, 2009.

[85] T. Harirchian and S. V. Garimella, “Microchannel size effects on local flow boiling heat

transfer to a dielectric fluid," *Int. J. Heat Mass Transf.*, vol. 51, no. 15–16, pp. 3724–3735, 2008.

[86] E. J. Choi, J. Y. Park, and M. S. Kim, "Two-phase cooling using HFE-7100 for polymer electrolyte membrane fuel cell application," *Appl. Therm. Eng.*, vol. 148, pp. 868–877, 2019.

[87] B. Agostini, J. R. Thome, M. Fabbri, B. Michel, D. Calmi, and U. Kloter, "High heat flux flow boiling in silicon multi-microchannels – Part II: Heat transfer characteristics of refrigerant R245fa," *Int. J. Heat Mass Transf.*, vol. 51, no. 21–22, pp. 5415–5425, 2008.

[88] B.-R. Fu, C.-Y. Lee, and C. Pan, "The effect of aspect ratio on flow boiling heat transfer of HFE-7100 in a microchannel heat sink," *Int. J. Heat Mass Transf.*, vol. 58, no. 1–2, pp. 53–61, 2013.

[89] J. Chen, S. Zhang, Y. Tang, H. Chen, W. Yuan, and J. Zeng, "Effect of operational parameters on flow boiling heat transfer performance for porous interconnected microchannel nets," *Appl. Therm. Eng.*, vol. 121, pp. 443–453, 2017.

[90] W. Qu and I. Mudawar, "Transport phenomena in two-phase micro-channel heat sinks," *J. Electron. Packag. Trans. ASME*, vol. 126, no. 2, pp. 213–224, 2004.

[91] K. Balasubramanian, P. S. Lee, L. W. Jin, S. K. Chou, C. J. Teo, and S. Gao, "Experimental investigations of flow boiling heat transfer and pressure drop in straight and expanding microchannels – A comparative study," *Int. J. Therm. Sci.*, vol. 50, no. 12, pp. 2413–2421, 2011.

[92] H. Huang, N. Borhani, and J. R. Thome, "Experimental investigation on flow boiling pressure drop and heat transfer of R1233zd(E) in a multi-microchannel evaporator," *Int. J. Heat Mass Transf.*, vol. 98, pp. 596–610, 2016.

[93] H. Huang and J. R. Thome, "Local measurements and a new flow pattern based model for subcooled and saturated flow boiling heat transfer in multi-microchannel evaporators," *Int. J. Heat Mass Transf.*, vol. 103, pp. 701–714, 2016.

[94] B. Agostini and J. R. Thome, "Comparison of an extented database for flow boiling heat transfer coefficients in multi-microchannels elements with the three-zone model," *ECI Engineering Conferences International Heat Transfer and Fluid Flow in Microscale*.

2005.

[95] J. R. Thome, “State-of-the-Art Overview of Boiling and Two-Phase Flows in Microchannels,” 2007.

[96] E. Costa-Patry, J. Olivier, B. A. Nichita, B. Michel, and J. R. Thome, “Two-phase flow of refrigerants in 85um-wide multi-microchannels: Part I - Pressure drop,” *Int. J. Heat Fluid Flow*, vol. 32, no. 2, pp. 451–463, 2011.

[97] E. R. Dário, J. C. Passos, M. L. Sánchez Simón, and L. Tadrist, “Pressure drop during flow boiling inside parallel microchannels,” *Int. J. Refrig.*, 2016.

[98] V. Y. S. Lee, A. Al-Zaidi, G. Henderson, and T. G. Karayiannis, “Flow Boiling Results of HFE-7200 in a Multi-Microchannel Evaporator and Comparison with HFE-7100,” in *4th International Conference on Multiphase Flow and Heat Transfer, Rome, April 10-12th*, 2019.

[99] Y. Madhour, J. Olivier, E. Costa-Patry, S. Paredes, B. Michel, and J. R. Thome, “Flow boiling of R134a in a multi-microchannel heat sink with hotspot heaters for energy-efficient microelectronic CPU cooling applications,” *IEEE Trans. Components, Packag. Manuf. Technol.*, vol. 1, no. 6, pp. 873–883, 2011.

[100] John G. Collier; John R. Thome, *Convective Boiling and Condensation*, Third. Clarendon Press, 1996.

[101] C.-J. Kuo and Y. Peles, “Pressure effects on flow boiling instabilities in parallel microchannels,” *Int. J. Heat Mass Transf.*, vol. 52, no. 1–2, pp. 271–280, 2009.

[102] S. Saisorn, J. Kaew-On, and S. Wongwises, “Flow pattern and heat transfer characteristics of R-134a refrigerant during flow boiling in a horizontal circular mini-channel,” *Int. J. Heat Mass Transf.*, vol. 53, no. 19–20, pp. 4023–4038, 2010.

[103] D. Euh, B. Ozar, T. Hibiki, M. Ishii, and C.-H. Song, “Characteristics of Bubble Departure Frequency in a Low-Pressure Subcooled Boiling Flow,” *J. Nucl. Sci. Technol.*, vol. 47, no. 7, pp. 608–617, 2010.

[104] D. Yuan, L. Pan, D. Chen, H. Zhang, J. Wei, and Y. Huang, “Bubble behavior of high subcooling flow boiling at different system pressure in vertical narrow channel,” *Appl. Therm. Eng.*, vol. 31, no. 16, pp. 3512–3520, 2011.

[105] S. M. S. Murshed, K. Vereen, D. Strayer, and R. Kumar, “An experimental investigation of bubble nucleation of a refrigerant in pressurized boiling flows,” *Energy*, vol. 35, no. 12, pp. 5143–5150, 2010.

[106] V. Prodanovic, D. Fraser, and M. Salcudean, “Bubble behavior in subcooled flow boiling of water at low pressures and low flow rates,” *Int. J. Multiph. Flow*, vol. 28, no. 1, pp. 1–19, 2002.

[107] R. Situ, M. Ishii, T. Hibiki, J. Y. Y. Tu, G. H. H. Yeoh, and M. Mori, “Bubble departure frequency in forced convective subcooled boiling flow,” *Int. J. Heat Mass Transf.*, vol. 51, no. 25–26, pp. 6268–6282, 2008.

[108] J. F. Klausner, R. Mei, D. M. Bernhard, and L. Z. Zeng, “Vapor bubble departure in forced convection boiling,” *Int. J. Heat Mass Transf.*, vol. 36, no. 3, pp. 651–662, 1993.

[109] Y. Y. Hsu, “On the size range of active nucleation cavities on a heating surface,” *J. Heat Transfer*, vol. 84, no. 3, pp. 207–213, 1962.

[110] C.-J. J. Kuo and Y. Peles, “Flow Boiling Instabilities in Microchannels and Means for Mitigation by Reentrant Cavities,” *J. Heat Transfer*, vol. 130, no. 7, 2008.

[111] I. Mudawar and M. B. Bowers, “Ultra-high critical heat flux (CHF) for subcooled water flow boiling—I: CHF data and parametric effects for small diameter tubes,” *Int. J. Heat Mass Transf.*, vol. 42, no. 8, pp. 1405–1428, 1999.

[112] Z. Y. Bao, D. F. Fletcher, and B. S. Haynes, “Flow boiling heat transfer of Freon R11 and HCFC123 in narrow passages,” *Int. J. Heat Mass Transf.*, vol. 43, no. 18, pp. 3347–3358, 2000.

[113] W. Owhaib, C. Martín-Callizo, and B. Palm, “Evaporative heat transfer in vertical circular microchannels,” *Appl. Therm. Eng.*, vol. 24, no. 8–9, pp. 1241–1253, 2004.

[114] X. Huo, L. Chen, Y. S. Tian, and T. G. Karayiannis, “Flow boiling and flow regimes in small diameter tubes,” *Appl. Therm. Eng.*, vol. 24, no. 8–9, pp. 1225–1239, 2004.

[115] Y. Xu, X. Fang, G. Li, D. Li, and Y. Yuan, “An experimental study of flow boiling heat transfer of R134a and evaluation of existing correlations,” *Int. J. Heat Mass Transf.*, vol. 92, pp. 1143–1157, 2016.

[116] R. Ali, B. Palm, and M. H. Maqbool, “Flow boiling heat transfer characteristics of a

minichannel up to dryout conditiona," *J. Heat Transfer*, vol. 133, no. 8, 2011.

[117] P. Thiangtham, C. Keepaiboon, P. Kiatpachai, L. G. Asirvatham, O. Mahian, A. S. Dalkilic, and S. Wongwises, "An experimental study on two-phase flow patterns and heat transfer characteristics during boiling of R134a flowing through a multi-microchannel heat sink," *Int. J. Heat Mass Transf.*, vol. 98, pp. 390–400, 2016.

[118] S. Basu, S. Ndao, G. J. Michna, Y. Peles, M. K. Jensen, S. Ndao, and G. J. Michna, "Flow Boiling of R134a in Circular Microtubes—Part I: Study of Heat Transfer Characteristics," *J. Heat Transfer*, vol. 133, no. 5, p. 051502, 2011.

[119] T. Wen, H. Zhan, and D. Zhang, "Flow boiling heat transfer in mini channel with serrated fins: Experimental investigation and development of new correlation," *Int. J. Heat Mass Transf.*, vol. 128, no. May 2017, pp. 1081–1094, 2019.

[120] S. In and S. Jeong, "Flow boiling heat transfer characteristics of R123 and R134a in a micro-channel," *Int. J. Multiph. Flow*, vol. 35, no. 11, pp. 987–1000, 2009.

[121] T. Alam, W. Li, F. Yang, W. Chang, J. Li, Z. Wang, J. Khan, and C. Li, "Force analysis and bubble dynamics during flow boiling in silicon nanowire microchannels," *Int. J. Heat Mass Transf.*, vol. 101, pp. 915–926, 2016.

[122] T. Chen and S. V. Garimella, "Measurements and high-speed visualizations of flow boiling of a dielectric fluid in a silicon microchannel heat sink," *Int. J. Multiph. Flow*, vol. 32, no. 8, pp. 957–971, 2006.

[123] X. Li and L. Jia, "The Investigation on Flow Boiling Heat Transfer of R134a in Micro-channels," *J. Therm. Sci.*, vol. 24, no. 5, pp. 452–462, 2015.

[124] D. Deng, W. Wan, H. Shao, Y. Tang, J. Feng, and J. Zeng, "Effects of operation parameters on flow boiling characteristics of heat sink cooling systems with reentrant porous microchannels," *Energy Convers. Manag.*, vol. 96, pp. 340–351, 2015.

[125] T. Chen and S. V. Garimella, "Local heat transfer distribution and effect of instabilities during flow boiling in a silicon microchannel heat sink," *Int. J. Heat Mass Transf.*, vol. 54, no. 15–16, pp. 3179–3190, 2011.

[126] B. Markal, O. Aydin, and M. Avci, "Effect of aspect ratio on saturated flow boiling in microchannels," *Int. J. Heat Mass Transf.*, vol. 93, pp. 130–143, 2016.

[127] S. Krishnamurthy and Y. Peles, “Flow boiling of water in a circular staggered micro-pin fin heat sink,” *Int. J. Heat Mass Transf.*, vol. 51, no. 5–6, pp. 1349–1364, 2008.

[128] G. Hetsroni, A. Mosyak, E. Pogrebnyak, and Z. Segal, “Explosive boiling of water in parallel micro-channels,” *Int. J. Multiph. Flow*, vol. 31, no. 4, pp. 371–392, 2005.

[129] W. Qu and I. Mudawar, “Measurement and correlation of critical heat flux in two-phase micro-channel heat sinks,” *Int. J. Heat Mass Transf.*, vol. 47, no. 10–11, pp. 2045–2059, 2004.

[130] J. Lee and I. Mudawar, “Critical heat flux for subcooled flow boiling in micro-channel heat sinks,” *Int. J. Heat Mass Transf.*, vol. 52, no. 13–14, pp. 3341–3352, 2009.

[131] T. Alam, W. Li, W. Chang, F. Yang, J. Khan, and C. Li, “A comparative study of flow boiling HFE-7100 in silicon nanowire and plainwall microchannels,” *Int. J. Heat Mass Transf.*, 2018.

[132] B. Agostini, R. Revellin, J. R. Thome, M. Fabbri, B. Michel, D. Calmi, and U. Kloter, “High heat flux flow boiling in silicon multi-microchannels – Part III: Saturated critical heat flux of R236fa and two-phase pressure drops,” *Int. J. Heat Mass Transf.*, vol. 51, no. 21–22, pp. 5426–5442, 2008.

[133] B. T. Holcomb, T. Harirchian, and S. V. Garimella, “An experimental investigation of microchannel size effects on flow boiling with de-ionized water,” American Society of Mechanical Engineers Digital Collection, 2009.

[134] S. G. Kandlikar, “Nucleation characteristics and stability considerations during flow boiling in microchannels,” *Exp. Therm. Fluid Sci.*, vol. 30, no. 5, pp. 441–447, 2006.

[135] P. Goel, A. K. Nayak, P. Ghosh, and J. B. Joshi, “Experimental study of bubble departure characteristics in forced convective subcooled nucleate boiling,” *Exp. Heat Transf.*, vol. 31, no. 3, pp. 194–218, 2018.

[136] J. Lee and I. Mudawar, “Fluid flow and heat transfer characteristics of low temperature two-phase micro-channel heat sinks – Part 2. Subcooled boiling pressure drop and heat transfer,” *Int. J. Heat Mass Transf.*, vol. 51, no. 17–18, pp. 4327–4341, 2008.

[137] C. L. Ong and J. R. Thome, “Flow boiling heat transfer of R134a, R236fa and R245fa in a horizontal 1.030 mm circular channel,” *Exp. Therm. Fluid Sci.*, vol. 33, no. 4, pp. 651–663, 2009.

[138] S. Zhang, W. Yuan, Y. Tang, J. Chen, and Z. Li, “Enhanced flow boiling in an interconnected microchannel net at different inlet subcooling,” *Appl. Therm. Eng.*, vol. 104, pp. 659–667, 2016.

[139] Y. K. Prajapati and P. Bhandari, “Flow boiling instabilities in microchannels and their promising solutions – A review,” *Exp. Therm. Fluid Sci.*, vol. 88, pp. 576–593, 2017.

[140] S. Lee, V. S. Devahdhanush, and I. Mudawar, “Frequency analysis of pressure oscillations in large length-to-diameter two-phase micro-channel heat sinks,” *Int. J. Heat Mass Transf.*, vol. 116, pp. 273–291, 2018.

[141] D. Bogojevic, K. Sefiane, A. J. Walton, H. Lin, and G. Cummins, “Two-phase flow instabilities in a silicon microchannels heat sink,” *Int. J. Heat Fluid Flow*, vol. 30, pp. 854–867, 2009.

[142] T. A. Kingston, J. A. Weibel, and S. V. Garimella, “High-frequency thermal-fluidic characterization of dynamic microchannel flow boiling instabilities: Part 2 – Impact of operating conditions on instability type and severity,” *Int. J. Multiph. Flow*, vol. 106, pp. 189–201, 2018.

[143] C. L. Ong and J. R. Thome, “Macro-to-microchannel transition in two-phase flow: Part 2 – Flow boiling heat transfer and critical heat flux,” *Exp. Therm. Fluid Sci.*, vol. 35, no. 6, pp. 873–886, 2011.

[144] R. Revellin and J. R. Thome, “A theoretical model for the prediction of the critical heat flux in heated microchannels,” *Int. J. Heat Mass Transf.*, vol. 51, no. 5–6, pp. 1216–1225, 2008.

[145] C. E. Brennen, “Chapter 7: Flow Patterns,” in *Fundamentals of Multiphase Flow*, Cambridge University Press, 2005.

[146] J. R. Thome and A. Cioncolini, “Two-Phase Flow Pattern Maps for Microchannels,” in *Encyclopedia of Two-Phase Heat Transfer and Flow, Set 1: Fundamentals and Methods, Volume 3: Flow Boiling in Macro and Microchannels*, no. October, World Scientific Publishing, 2015, pp. 47–84.

[147] L. Cheng, G. Ribatski, and J. R. Thome, “Two-phase flow patterns and flow-pattern maps: Fundamentals and applications,” *Appl. Mech. Rev.*, vol. 61, no. 1–6, pp. 0508021–05080228, 2008.

[148] A. Kalani and S. G. Kandlikar, “A photographic study of flow boiling stability on a plain surface with tapered manifold,” in *ASME 2015 13th International Conference on Nanochannels, Microchannels, and Minichannels, ICNMM 2015, collocated with the ASME 2015 International Technical Conference and Exhibition on Packaging and Integration of Electronic and Photonic Microsystems*, 2015.

[149] G. Wang, P. Cheng, and A. E. Bergles, “Effects of inlet/outlet configurations on flow boiling instability in parallel microchannels,” *Int. J. Heat Mass Transf.*, vol. 51, no. 9–10, pp. 2267–2281, 2008.

[150] M. M. Shah, “Unified correlation for heat transfer during boiling in plain mini/micro and conventional channels,” *Int. J. Refrig.*, vol. 74, pp. 606–626, 2017.

[151] J. R. Thome, V. Dupont, and A. M. Jacobi, “Heat transfer model for evaporation in microchannels. Part I: Presentation of the model,” *Int. J. Heat Mass Transf.*, 2004.

[152] E. Costa-Patry and J. R. Thome, “Flow pattern-based flow boiling heat transfer model for microchannels,” *Int. J. Refrig.*, vol. 36, no. 2, pp. 414–420, 2013.

[153] M. Magnini and J. R. Thome, “An updated three-zone heat transfer model for slug flow boiling in microchannels,” *Int. J. Multiph. Flow*, 2017.

[154] W. Qu and I. Mudawar, “Flow boiling heat transfer in two-phase micro-channel heat sinks—II. Annular two-phase flow model,” *Int. J. Heat Mass Transf.*, vol. 46, no. 15, pp. 2773–2784, 2003.

[155] S. M. Kim and I. Mudawar, “Theoretical model for local heat transfer coefficient for annular flow boiling in circular mini/micro-channels,” *Int. J. Heat Mass Transf.*, vol. 73, pp. 731–742, 2014.

[156] J. R. Thome and A. Cioncolini, “Unified Modeling Suite for Two-Phase Flow, Convective Boiling, and Condensation in Macro-and Microchannels,” *Heat Transf. Eng.*, vol. 37, no. 13–14, pp. 1148–1157, 2016.

[157] T. Harirchian and S. V. Garimella, “A comprehensive flow regime map for microchannel flow boiling with quantitative transition criteria,” *Int. J. Heat Mass Transf.*, vol. 53, no. 13–14, pp. 2694–2702, 2010.

[158] T. Harirchian and S. V. Garimella, “Flow regime-based modeling of heat transfer and pressure drop in microchannel flow boiling,” *Int. J. Heat Mass Transf.*, vol. 55, no. 4,

pp. 1246–1260, 2012.

[159] M. G. G. Cooper, “Heat Flow Rates in Saturated Nucleate Pool Boiling-A Wide-Ranging Examination Using Reduced Properties,” *Adv. Heat Transf.*, vol. 16, no. C, pp. 157–239, 1984.

[160] R. Revellin and J. R. R. Thome, “A new type of diabatic flow pattern map for boiling heat transfer in microchannels Related content,” *J. Micromechanics Microengineering*, vol. 17, pp. 788–796, 2007.

[161] C. L. L. Ong and J. R. R. Thome, “Macro-to-microchannel transition in two-phase flow: Part 1 – Two-phase flow patterns and film thickness measurements,” *Exp. Therm. Fluid Sci.*, vol. 35, no. 1, pp. 37–47, 2011.

[162] M. M. Mahmoud and T. G. Karayiannis, “Flow pattern transition models and correlations for flow boiling in mini-tubes,” *Exp. Therm. Fluid Sci.*, vol. 70, pp. 270–282, 2016.

[163] Y.-S. Choi, T. Lim, S.-S. You, and H.-S. Kim, “Two-phase flow boiling heat transfer of FC-72 in parallel micro-channels,” *Exp. Heat Transf.*, vol. 30, no. 4, pp. 284–301, 2017.

[164] H. Li and P. Hrnjak, “Flow visualization of R32 in parallel-port microchannel tube,” *Int. J. Heat Mass Transf.*, vol. 128, pp. 1–11, 2019.

[165] L. Chen, “Flow patterns in upward two-phase flow in small diameter tubes,” Brunel University School of Engineering and Design PhD Theses, 2006.

[166] G. Harirchian and S. V Garimella, “Boiling Heat Transfer and Flow Regimes in Microchannels-A Comprehensive Understanding 1,” *J. Electron. Packag.*, vol. 133, 2011.

[167] G. Ribatski, “A Critical Overview on the Recent Literature Concerning Flow Boiling and Two-Phase Flows Inside Micro-Scale Channels,” *Exp. Heat Transf.*, vol. 26, no. 2–3, pp. 198–246, 2013.

[168] E. Costa-Patry, J. Olivier, and J. R. Thome, “Heat transfer characteristics in a copper micro-evaporator and flow pattern-based prediction method for flow boiling in microchannels,” *Front. Heat Mass Transf.*, vol. 3, p. 13002, 2012.

[169] S. W. Churchill and R. Usagi, “A general expression for the correlation of rates of

transfer and other phenomena," *AIChE J.*, vol. 18, no. 6, pp. 1121–1128, 1972.

[170] J. R. Thome, A. Bar-Cohen, R. Revellin, and I. Zun, "Unified mechanistic multiscale mapping of two-phase flow patterns in microchannels," *Exp. Therm. Fluid Sci.*, vol. 44, pp. 1–22, 2013.

[171] X. Fang, F. Zhuang, C. Chen, Q. Wu, Y. Y. Chen, Y. Y. Chen, and Y. He, "Saturated flow boiling heat transfer: review and assessment of prediction methods," *Heat Mass Transf.*, vol. 55, pp. 197–222, 2019.

[172] G. R. Warrier, V. K. Dhir, and L. A. Momoda, "Heat transfer and pressure drop in narrow rectangular channels," *Exp. Therm. Fluid Sci.*, vol. 26, no. 1, pp. 53–64, 2002.

[173] X. Fang, "International Journal of Heat and Mass Transfer A new correlation of flow boiling heat transfer coefficients based on R134a data," *Int. J. Heat Mass Transf.*, vol. 66, pp. 279–283, 2013.

[174] X. Fang, Q. Wu, and Y. Yuan, "A general correlation for saturated flow boiling heat transfer in channels of various sizes and flow directions," *Int. J. Heat Mass Transf.*, vol. 107, pp. 972–981, 2017.

[175] B. Markal, O. Aydin, M. Avci, B. Markal, O. Aydin, and M. Avci, "Prediction of Heat Transfer Coefficient in Saturated Flow Boiling Heat Transfer in Parallel Rectangular Microchannel Heat Sinks : An Experimental Study Prediction of Heat Transfer Coefficient in Saturated Flow Boiling Heat Transfer in Parallel Rectangular," *Heat Transf. Eng.*, vol. 38, no. 16, pp. 1415–1428, 2017.

[176] L. Sun and K. Mishima, "An evaluation of prediction methods for saturated flow boiling heat transfer in mini-channels," *Int. J. Heat Mass Transf.*, vol. 52, no. 23–24, pp. 5323–5329, 2009.

[177] T. N. Tran, M. W. Wambsganss, and D. M. France, "Small circular- and rectangular-channel boiling with two refrigerants," *Int. J. Multiph. Flow*, vol. 22, no. 3, pp. 485–498, 1996.

[178] W. Yu, D. M. France, M. W. Wambsganss, and J. R. Hull, "Two-phase pressure drop, boiling heat transfer, and critical heat flux to water in a small-diameter horizontal tube," *Int. J. Multiph. Flow*, vol. 28, no. 6, pp. 927–941, 2002.

[179] G. M. Lazarek and S. H. Black, "Evaporative heat transfer, pressure drop and critical

heat flux in a small vertical tube with R-113," *Int. J. Heat Mass Transf.*, vol. 25, no. 7, pp. 945–960, 1982.

[180] J. C. Chen, "Correlation for boiling heat transfer to saturated fluids in convective flow," *Ind. Eng. Chem. Process Des. Dev.*, vol. 5, no. 3, pp. 322–329, 1966.

[181] S. S. Bertsch, E. A. Groll, and S. V. Garimella, "A composite heat transfer correlation for saturated flow boiling in small channels," *Int. J. Heat Mass Transf.*, vol. 52, no. 7–8, pp. 2110–2118, 2009.

[182] M. M. Mahmoud and T. G. Karayiannis, "Heat transfer correlation for flow boiling in small to micro tubes," *Int. J. Heat Mass Transf.*, vol. 66, pp. 553–574, 2013.

[183] Z. Liu and R. H. S. Winterton, "A general correlation for saturated and subcooled flow boiling in tubes and annuli, based on a nucleate pool boiling equation," *Int. J. Heat Mass Transf.*, vol. 34, no. 11, pp. 2759–2766, 1991.

[184] S.-M. Kim and I. Mudawar, "Universal approach to predicting saturated flow boiling heat transfer in mini/micro-channels Part II. Two-phase heat transfer coefficient," *Int. J. Heat Mass Transf.*, vol. 64, pp. 1239–1256, 2013.

[185] M. M. Shah, "Chart correlation for saturated boiling heat transfer: Equations and further study," in *ASHRAE Transactions*, 1982, vol. 88, no. 1, pp. 185–196.

[186] S. G. Kandlikar, "A general correlation for saturated two-phase flow boiling heat transfer inside horizontal and vertical tubes," *J. Heat Transfer*, vol. 112, no. 1, pp. 219–228, 1990.

[187] S. G. Kandlikar and P. Balasubramanian, "An Extension of the Flow Boiling Correlation to Transition, Laminar, and Deep Laminar Flows in Minichannels and Microchannels," *Heat Transf. Eng.*, vol. 25, no. 3, pp. 86–93, 2004.

[188] M. Ducoulombier, S. Colasson, J. Bonjour, and P. Haberschill, "Carbon dioxide flow boiling in a single microchannel - Part II: Heat transfer," *Exp. Therm. Fluid Sci.*, vol. 35, no. 4, pp. 597–611, 2011.

[189] V. V Klimenko, "A generalizes correlation for two-phase forced flow heat transfer," 1988.

[190] J. Lee and I. Mudawar, "Two-phase flow in high-heat-flux micro-channel heat sink for

refrigeration cooling applications: Part II—heat transfer characteristics," *Int. J. Heat Mass Transf.*, vol. 48, no. 5, pp. 941–955, 2005.

[191] W. Li and Z. Wu, "A general criterion for evaporative heat transfer in micro/mini-channels," *Int. J. Heat Mass Transf.*, vol. 53, no. 9–10, pp. 1967–1976, 2010.

[192] S. L. Qi, P. Zhang, R. Z. Wang, and L. X. Xu, "Flow boiling of liquid nitrogen in micro-tubes: Part II – Heat transfer characteristics and critical heat flux," *Int. J. Heat Mass Transf.*, vol. 50, no. 25–26, pp. 5017–5030, 2007.

[193] Y. Qiu, D. Garg, L. Zhou, C. R. Kharangate, S. M. Kim, and I. Mudawar, "An artificial neural network model to predict mini/micro-channels saturated flow boiling heat transfer coefficient based on universal consolidated data," *Int. J. Heat Mass Transf.*, vol. 149, p. 119211, 2020.

[194] M. Eraghubi, P. Di Marco, and A. J. Robinson, "Low mass flux upward vertical forced flow boiling of HFE7000," *Exp. Therm. Fluid Sci.*, vol. 102, no. November 2018, pp. 291–301, 2019.

[195] D. Gorenflo, U. Chandra, S. Kotthoff, and A. Luke, "Influence of thermophysical properties on pool boiling heat transfer of refrigerants," *Int. J. Refrig.*, vol. 27, no. 5, pp. 492–502, 2004.

[196] L. Cheng, G. Ribatski, L. Wojtan, and J. R. Thome, "New flow boiling heat transfer model and flow pattern map for carbon dioxide evaporating inside horizontal tubes," *Int. J. Heat Mass Transf.*, vol. 49, no. 21–22, pp. 4082–4094, 2006.

[197] S. M. Kim and I. Mudawar, "Universal approach to predicting saturated flow boiling heat transfer in mini/micro-channels – Part I. Dryout incipience quality," *Int. J. Heat Mass Transf.*, vol. 64, pp. 1226–1238, 2013.

[198] H. Hausen, "Darstellung des Wärmeüberganges in Rohren durch verallgemeinerte Potenzbeziehungen," *Z. VDF Beih. Verfahrenstecknik*, pp. 91–102, 1943.

[199] X. Li and T. Hibiki, "Frictional pressure drop correlation for two-phase flows in mini and micro multi-channels," *Appl. Therm. Eng.*, vol. 116, pp. 316–328, 2017.

[200] W. H. McAdams, W. K. Woods, and R. L. Bron, "Vaporization inside horizontal tubes - II. Benzene-oil mixtures.," *Trans. ASME1*, pp. 193–200, 1942.

[201] A. Cicchitti, C. Lombardi, M. Silvestri, G. Soldaini, and R. Zavattarelli, “Two-phase cooling experiments: Pressure drop, heat transfer and burnout measurements,” 1959.

[202] S.-M. Kim and I. Mudawar, “Universal approach to predicting two-phase frictional pressure drop for mini/micro-channel saturated flow boiling,” *Int. J. Heat Mass Transf.*, vol. 58, no. 1–2, pp. 718–734, 2013.

[203] R.W., Lockhart, R.C., Martinelli, “Proposed correlation of data for isothermal two-phase, two-component flow in pipes,” *Chem. Engng Prog.*, vol. 45, no. 1, pp. 39–48, 1949.

[204] D. Chisholm, “A theoretical basis for the Lockhart-Martinelli correlation for two-phase flow,” *Int. J. Heat Mass Transf.*, vol. 10, no. 12, pp. 1767–1778, 1967.

[205] K. Mishima and T. Hibiki, “Some characteristics of air-water two-phase flow in small diameter vertical tubes,” *Int. J. Multiph. Flow*, vol. 22, no. 4, pp. 703–712, 1996.

[206] W. Qu and I. Mudawar, “Measurement and prediction of pressure drop in two-phase micro-channel heat sinks,” *Int. J. Heat Mass Transf.*, vol. 46, no. 15, pp. 2737–2753, 2003.

[207] C. Keepaiboon, P. Thiangtham, O. Mahian, A. S. Dalkılıç, and S. Wongwises, “Pressure drop characteristics of R134a during flow boiling in a single rectangular micro-channel,” *Int. Commun. Heat Mass Transf.*, vol. 71, pp. 245–253, 2016.

[208] H. Huang and J. R. Thome, “An experimental study on flow boiling pressure drop in multi-microchannel evaporators with different refrigerants,” *Exp. Therm. Fluid Sci.*, vol. 80, pp. 391–407, 2017.

[209] B. Markal, O. Aydin, and M. Avci, “Prediction of Pressure Drop for Flow Boiling in Rectangular Multi-Microchannel Heat Sinks,” *Heat Transf. Eng.*, pp. 1–13, 2017.

[210] C. J. Baroczy, “A systematic correlation for two-phase pressure drop,” *Chem. Eng. Prog. Symp. Ser.*, vol. 64, pp. 232–249, 1966.

[211] D. Chisholm, “Pressure gradients due to friction during the flow of evaporating two-phase mixtures in smooth tubes and channels,” *Int. J. Heat Mass Transf.*, vol. 16, no. 2, pp. 347–358, 1973.

[212] T. . Tran, M.-C. Chyu, M. . Wambsganss, and D. . France, “Two-phase pressure drop of

refrigerants during flow boiling in small channels: an experimental investigation and correlation development," *Int. J. Multiph. Flow*, vol. 26, no. 11, pp. 1739–1754, 2000.

[213] H. J. Lee, D. Y. Liu, Y. Alyousef, and S. C. Yao, "Generalized two-phase pressure drop and heat transfer correlations in evaporative micro/minichannels," *J. Heat Transfer*, vol. 132, no. 4, pp. 1–9, 2010.

[214] A. Kawahara, P. Y. Chung, and M. Kawaji, "Investigation of two-phase flow pattern, void fraction and pressure drop in a microchannel," *Int. J. Multiph. Flow*, vol. 28, no. 9, pp. 1411–1435, 2002.

[215] T. A. Shedd, "Void fraction and pressure drop measurements for refrigerant R410A flows in small diameter tubes," 2012.

[216] A. Cioncolini and J. R. Thome, "Void fraction prediction in annular two-phase flow," *Int. J. Multiph. Flow*, vol. 43, pp. 72–84, 2012.

[217] K. A. Triplett, S. M. Ghiaasiaan, S. I. Abdel-Khalik, A. LeMouel, and B. N. McCord, "Gas-liquid two-phase flow in microchannels Part II: Void fraction and pressure drop," *Int. J. Multiph. Flow*, vol. 25, no. 3, pp. 395–410, 1999.

[218] S. Saisorn and S. Wongwises, "Flow pattern, void fraction and pressure drop of two-phase air–water flow in a horizontal circular micro-channel," *Exp. Therm. Fluid Sci.*, vol. 32, no. 3, pp. 748–760, 2008.

[219] S. M. Zivi, "Estimation of steady-state steam void-fraction by means of the principle of minimum entropy production," *J. Heat Transfer*, vol. 86, no. 2, pp. 247–251, 1964.

[220] D. Chisholm, "Void Fraction during Two-Phase Flow," *J. Mech. Eng. Sci.*, vol. 15, no. 3, pp. 235–236, 1973.

[221] W. Qu and I. Mudawar, "Flow boiling heat transfer in two-phase micro-channel heat sinks-I. Experimental investigation and assessment of correlation methods," *Int. J. Heat Mass Transf.*, vol. 46, no. 15, pp. 2755–2771, 2003.

[222] S. Z. Rouhani and E. Axelsson, "Calculation of void volume fraction in the subcooled and quality boiling regions," *Int. J. Heat Mass Transf.*, vol. 13, no. 2, pp. 383–393, 1970.

[223] M. Shojaeian and A. Koşar, "Pool boiling and flow boiling on micro- and nanostructured surfaces," *Experimental Thermal and Fluid Science*, vol. 63. Elsevier Inc., pp. 45–73,

2015.

[224] G. Liang and I. Mudawar, “Review of channel flow boiling enhancement by surface modification, and instability suppression schemes,” *Int. J. Heat Mass Transf.*, vol. 146, p. 118864, 2020.

[225] S. A. Khan, M. A. Atieh, and M. Koç, “Micro-nano scale surface coating for nucleate boiling heat transfer: A critical review,” *Energies*, vol. 11, no. 11, pp. 1–30, 2018.

[226] A. Kosar, K. Chih, J. Kuo, and Y. Peles, “Suppression of Boiling Flow Oscillations in Parallel Microchannels by Inlet Restrictors,” 2006.

[227] S. K. Oudah, R. Fang, A. Tikadar, A. S. Salman, and J. A. Khan, “An experimental investigation of the effect of multiple inlet restrictors on the heat transfer and pressure drop in a flow boiling microchannel heat sink,” *Int. J. Heat Mass Transf.*, vol. 153, p. 119582, 2020.

[228] Y. Sun, L. Zhang, H. Xu, and X. Zhong, “Subcooled flow boiling heat transfer from microporous surfaces in a small channel,” *Int. J. Therm. Sci.*, vol. 50, no. 6, pp. 881–889, 2011.

[229] F. Yang, X. Dai, Y. Peles, P. Cheng, and C. Li, “Can multiple flow boiling regimes be reduced into a single one in microchannels?,” *Appl. Phys. Lett.*, vol. 103, no. 043122, 2013.

[230] P. Bai, T. Tang, and B. Tang, “Enhanced flow boiling in parallel microchannels with metallic porous coating,” *Appl. Therm. Eng.*, vol. 58, no. 1–2, pp. 291–297, 2013.

[231] A. K. M. M. Morshed, T. C. Paul, and J. Khan, “Effect of Cu-Al2O3 nanocomposite coating on flow boiling performance of a microchannel,” *Appl. Therm. Eng.*, vol. 51, no. 1–2, pp. 1135–1143, 2013.

[232] S. Wang, H. H. Chen, and C. L. Chen, “Enhanced flow boiling in silicon nanowire-coated manifold microchannels,” *Appl. Therm. Eng.*, vol. 148, pp. 1043–1057, 2019.

[233] D. Li, G. S. Wu, W. Wang, Y. D. Wang, D. Liu, D. C. Zhang, Y. F. Chen, G. P. Peterson, and R. Yang, “Enhancing Flow Boiling Heat Transfer in Microchannels for Thermal Management with Monolithically-Integrated Silicon Nanowires,” 2012.

[234] V. Khanikar, I. Mudawar, and T. S. Fisher, “Flow boiling in a micro-channel coated

with carbon nanotubes," *IEEE Trans. Components Packag. Technol.*, vol. 32, no. 3, pp. 639–649, 2009.

[235] C. S. Sujith Kumar, S. Suresh, L. Yang, Q. Yang, and S. Aravind, "Flow boiling heat transfer enhancement using carbon nanotube coatings," *Appl. Therm. Eng.*, vol. 65, no. 1–2, pp. 166–175, 2014.

[236] A. K. M. M. Morshed, T. C. Paul, and J. A. Khan, "Effect of Al2O3 nanoparticle deposition on flow boiling performance of water in a microchannel," *Exp. Therm. Fluid Sci.*, vol. 47, pp. 6–13, 2013.

[237] Y. J. Choi, D. H. Kam, and Y. H. Jeong, "Analysis of CHF enhancement by magnetite nanoparticle deposition in the subcooled flow boiling region," *Int. J. Heat Mass Transf.*, vol. 109, pp. 1191–1199, 2017.

[238] C. Choi and M. Kim, "Wettability Effects on Heat Transfer," in *Two Phase Flow, Phase Change and Numerical Modeling*, 2011.

[239] C. Choi, J. S. Shin, D. I. Yu, and M. H. Kim, "Flow boiling behaviors in hydrophilic and hydrophobic microchannels," *Exp. Therm. Fluid Sci.*, vol. 35, no. 5, pp. 816–824, 2011.

[240] H. T. Phan, N. Caney, P. Marty, S. Colasson, and J. Gavillet, "How does surface wettability influence nucleate boiling?," *C. R. Mec.*, vol. 337, pp. 251–259, 2009.

[241] A. R. Betz, J. Jenkins, C. J. Kim, and D. Attinger, "Boiling heat transfer on superhydrophilic, superhydrophobic, and superbiphilic surfaces," *Int. J. Heat Mass Transf.*, vol. 57, no. 2, pp. 733–741, 2013.

[242] H. Jo, H. S. Ahn, S. Kang, and M. H. Kim, "A study of nucleate boiling heat transfer on hydrophilic, hydrophobic and heterogeneous wetting surfaces," *Int. J. Heat Mass Transf.*, vol. 54, no. 25–26, pp. 5643–5652, 2011.

[243] J. M. Kim, T. J. Kim, D. I. Yu, H. Noh, M. H. Kim, K. Moriyama, and H. S. Park, "Effect of heterogeneous wetting surface characteristics on flow boiling performance," *Int. J. Heat Fluid Flow*, vol. 70, pp. 141–151, 2018.

[244] E. J. Davis and G. H. Anderson, "The incipience of nucleate boiling in forced convection flow," *AIChE J.*, vol. 12, no. 4, pp. 774–780, 1966.

[245] S. G. Kandlikar, V. Mizo, M. G. Cartwright, and E. Ikenze, “Bubble nucleation and growth characteristics in subcooled flow boiling of water,” *HTD-Vol. 342, ASME Proc. 32nd Natl. Heat Transf. Conf.*, vol. 4, pp. 11–18, 1997.

[246] S. K. Saha, *Microchannel Phase Change Transport Phenomena*. Elsevier Science & Technology, 2015.

[247] D. Liu, P.-S. Lee, and S. V Garimella, “Prediction of the onset of nucleate boiling in microchannel flow,” 2005.

[248] A. E. Bergles and W. M. Rohsenow, “The determination of forced-convection surface-boiling heat transfer,” *J. Heat Transfer*, vol. 86, no. 3, pp. 365–372, 1964.

[249] L. Zhang, E. N. Wang, K. E. Goodson, and T. W. Kenny, “Phase change phenomena in silicon microchannels,” *Int. J. Heat Mass Transf.*, vol. 48, no. 8, pp. 1572–1582, 2005.

[250] F. Yang, W. Li, X. Dai, and C. Li, “Flow boiling heat transfer of HFE-7000 in nanowire-coated microchannels,” *Appl. Therm. Eng.*, vol. 93, pp. 260–268, 2016.

[251] H. T. Phan, N. Caney, P. Marty, S. Colasson, and J. Gavillet, “Flow boiling of water on nanocoated surfaces in a microchannel,” *J. Heat Transfer*, vol. 134, no. 2, 2012.

[252] Y. Sun, L. Zhang, H. Xu, and X. Zhong, “Flow boiling enhancement of FC-72 from microporous surfaces in minichannels,” *Exp. Therm. Fluid Sci.*, vol. 35, no. 7, pp. 1418–1426, 2011.

[253] T. Cubaud, U. Ulmanella, and C. M. Ho, “Two-phase flow in microchannels with surface modifications,” *Fluid Dyn. Res.*, vol. 38, no. 11, pp. 772–786, 2006.

[254] A. K. Kota, G. Kwon, and A. Tuteja, “The design and applications of superomniphobic surfaces,” *NPG Asia Materials*, vol. 6, no. 6. Nature Publishing Group, 2014.

[255] M. Nedaei, A. R. Motezakker, M. C. Zeybek, M. Sezen, G. O. Ince, and A. Kosar, “Subcooled flow boiling heat transfer enhancement using polyperfluorodecylacrylate (pPFDA) coated microtubes with different coating thicknesses,” *Exp. Therm. Fluid Sci.*, vol. 86, pp. 130–140, 2017.

[256] A. Kaya, R. Demiryurek, E. Armagan, G. Ozaydin-Ince, M. Sezen, and A. Kosar, “Boiling heat transfer enhancement in mini/microtubes via polyhydroxyethylmethacrylate (pHEMA) coatings on inner microtube walls at high

mass fluxes," *J. Micromechanics Microengineering*, vol. 23, no. 115017, 2013.

[257] T. Çikim, E. Armağan, G. O. Ince, and A. Koşar, "Flow boiling enhancement in microtubes with crosslinked pHEMA coatings and the effect of coating thickness," *J. Heat Transfer*, vol. 136, no. 8, 2014.

[258] C. S. Sujith Kumar, S. Suresh, C. R. Aneesh, M. C. Santhosh Kumar, A. S. Praveen, and K. Raji, "Flow boiling heat transfer enhancement on copper surface using Fe doped Al 2 O 3 -TiO 2 composite coatings," *Appl. Surf. Sci.*, vol. 334, pp. 102–109, 2015.

[259] M. Nedaei, E. Armagan, M. Sezen, G. Ozaydin Ince, and A. Kosar, "Enhancement of flow boiling heat transfer in pHEMA/pPFDA coated microtubes with longitudinal variations in wettability," *AIP Adv.*, vol. 6, no. 3, p. 035212, 2016.

[260] F. Yang, X. Dai, Y. Peles, P. Cheng, J. Khan, and C. Li, "Flow boiling phenomena in a single annular flow regime in microchannels (I): Characterization of flow boiling heat transfer," *Int. J. Heat Mass Transf.*, vol. 68, pp. 703–715, 2014.

[261] J. Y. Chang and S. M. You, "Boiling heat transfer phenomena from micro-porous and porous surfaces in saturated FC-72," *Int. J. Heat Mass Transf.*, vol. 40, no. 18, pp. 4437–4447, 1997.

[262] R. Remsburg, *Thermal Design of Electronic Equipment*. 2001.

[263] R. J. Phillips, *Forced Convection, Liquid Cooled, Microchannel Heat Sinks*. Massachusetts Institute of Technology, 1987.

[264] D. Chisholm, "Two-phase flow in bends," *Int. J. Multiph. Flow*, vol. 6, no. 4, pp. 363–367, 1980.

[265] D. Chisholm, "Two-phase flow in heat exchangers and pipelines," *Heat Transf. Eng.*, vol. 6, no. 2, pp. 48–57, 1985.

[266] R. K., Shah, A. L., London, *Laminar Flow Forced Convection in Ducts: A Source Book for Compact Heat Exchanger Analytical Data*, 1st ed. Academic Press, 1978.

[267] F. P. Incropera, T. L. Bergman, D. P. DeWitt, and A. S. Lavine, *Fundamentals of Heat and Mass Transfer 7th Edition*. John Wiley & Sons, 2012.

[268] Hugh W., Coleman, W. Glenn, Steele, *Experimentation, Validation, and Uncertainty Analysis for Engineers, 3rd Edition*. John Wiley & Sons, 2009.

[269] X. F. Peng and G. P. Peterson, “Convective heat transfer and flow friction for water flow in microchannel structures,” *Int. J. Heat Mass Transf.*, vol. 39, no. 12, pp. 2599–2608, 1996.

[270] Stephan, K., Preusser, P., “Wärmeűbergang Und Maximale Wärmstromichte Beim Behältersieden Binärer Und Ternärer Flűssigkeitsgemische,” *Chem. Ing. Tech.*, vol. 51, no. 37, 1979.

[271] P. S. Lee, S. V. Garimella, and D. Liu, “Investigation of heat transfer in rectangular microchannels,” *Int. J. Heat Mass Transf.*, vol. 48, no. 9, pp. 1688–1704, 2005.

[272] P. Balasubramanian and S. G. Kandlikar, “Experimental Study of Flow Patterns, Pressure Drop, and Flow Instabilities in Parallel Rectangular Minichannels,” *Heat Transf. Eng.*, vol. 26, no. 3, pp. 20–27, 2005.

[273] N. Borhani and J. R. Thome, “Intermittent dewetting and dryout of annular flows,” *Int. J. Multiph. Flow*, vol. 67, pp. 144–152, 2014.

[274] A. H. Al-Zaidi, M. M. Mahmoud, and T. G. Karayiannis, “Flow Boiling in Microchannels With HFE-7100 : Experimental Results and Comparision With,” in *Proceedings of the 16th International Heat Transfer Conference, August 10-15*, 2018, pp. 1–8.

[275] E. Costa-Patry, S. Nebuloni, J. Olivier, and J. R. Thome, “On-chip two-phase cooling with refrigerant 85 um-wide multi-microchannel evaporator under hot-spot conditions,” *IEEE Trans. Components, Packag. Manuf. Technol.*, vol. 2, no. 2, pp. 311–320, 2012.

[276] S.-M. M. Kim and I. Mudawar, “Review of two-phase critical flow models and investigation of the relationship between choking, premature CHF, and CHF in micro-channel heat sinks,” *Int. J. Heat Mass Transf.*, vol. 87, pp. 497–511, 2015.

[277] M. M. Awad, “Two-Phase Flow,” in *An Overview of Heat Transfer Phenomena*, InTech, 2012.

[278] N. Zuber, “The dynamics of vapor bubbles in nonuniform temperature fields,” *Int. J. Heat Mass Transf.*, vol. 2, no. 1–2, pp. 83–98, 1961.

[279] B. B. Mikic, W. M. Rohsenow, and P. Griffith, “On bubble growth rates,” *Int. J. Heat Mass Transf.*, vol. 13, pp. 657–666, 1970.

[280] P. C. Lee, F. G. Tseng, and C. Pan, “Bubble dynamics in microchannels. Part I: single microchannel,” *Int. J. Heat Mass Transf.*, vol. 47, no. 25, pp. 5575–5589, 2004.

[281] T. A. Kingston, J. A. Weibel, and S. V. Garimella, “Time-resolved characterization of microchannel flow boiling during transient heating: Part 1 – Dynamic response to a single heat flux pulse,” *Int. J. Heat Mass Transf.*, vol. 154, p. 119643, 2020.

[282] TC Ltd., “Mineral Insulated Thermocouples - Type 12,” 2019.

[283] Omega Engineering, “Micro-Machined Silicon Wet/Wet Differential Pressure Transducers.” [Online]. Available: https://www.omega.co.uk/pptst/PX409-WWDIF.html. [Accessed: 20-Apr-2020].

[284] K. Moriyama and A. Inoue, “Thickness of the liquid film formed by a growing bubble in a narrow gap between two horizontal plates,” *J. Heat Transfer*, vol. 118, no. 1, pp. 132–139, 1996.

[285] L. Yin, L. Jia, P. Guan, and D. Liu, “Experimental investigation on bubble confinement and elongation in microchannel flow boiling,” *Exp. Therm. Fluid Sci.*, vol. 54, pp. 290–296, 2014.

[286] A. H. M. Al-Zaidi, “Flow Boiling and Condensation with Refrigerant HFE-7100 for Cooling High Heat Flux Devices, Ph.D Thesis,” Brunel University London, 2019.

[287] S. G. Kandlikar, “Scale effects on flow boiling heat transfer in microchannels: A fundamental perspective,” *Int. J. Therm. Sci.*, vol. 49, no. 7, pp. 1073–1085, 2010.

[288] Y. Liu, D. F. Fletcher, and B. S. Haynes, “On the importance of upstream compressibility in microchannel boiling heat transfer,” *Int. J. Heat Mass Transf.*, vol. 58, no. 1–2, pp. 503–512, 2013.

[289] S. Gedupudi, D. B. R. Kenning, and T. G. Karayiannis, “Flow Boiling in Rectangular Microchannels: 1-D Modeling of the Influence of Inlet Resistance on Flow Reversal,” *Heat Transf. Eng.*, vol. 37, no. 13–14, pp. 1114–1125, 2016.

[290] P. A. Kew and K. Cornwell, “Correlations for the prediction of boiling heat transfer in small-diameter channels,” *Appl. Therm. Eng.*, vol. 17, no. 8–10, pp. 705–715, 1997.

[291] S. M. Kim and I. Mudawar, “Review of databases and predictive methods for pressure drop in adiabatic, condensing and boiling mini/micro-channel flows,” *International*

Journal of Heat and Mass Transfer. 2014.

[292] W. Qu and A. Siu-Ho, "Experimental study of saturated flow boiling heat transfer in an array of staggered micro-pin-fins," *Int. J. Heat Mass Transf.*, vol. 52, no. 7–8, pp. 1853–1863, 2009.

[293] S. G. Singh, R. R. Bhide, S. P. Duttagupta, B. P. Puranik, and A. Agrawal, "Two-phase flow pressure drop characteristics in trapezoidal silicon microchannels," *IEEE Trans. Components Packag. Technol.*, vol. 32, no. 4, pp. 887–900, 2009.

[294] J. Moreno Quibén and J. R. Thome, "Flow pattern based two-phase frictional pressure drop model for horizontal tubes, Part II: New phenomenological model," *Int. J. Heat Fluid Flow*, vol. 28, no. 5, pp. 1060–1072, 2007.

[295] L. Wojtan, T. Ursenbacher, and J. R. Thome, "Investigation of flow boiling in horizontal tubes: Part I - A new diabatic two-phase flow pattern map," *Int. J. Heat Mass Transf.*, vol. 48, no. 14, pp. 2955–2969, 2005.

[296] J. M. Quibén, L. Cheng, R. J. da Silva Lima, and J. R. Thome, "Flow boiling in horizontal flattened tubes: Part I - Two-phase frictional pressure drop results and model," *Int. J. Heat Mass Transf.*, vol. 52, no. 15–16, pp. 3634–3644, 2009.

[297] C. Choi and M. Kim, "Flow pattern based correlations of two-phase pressure drop in rectangular microchannels," *Int. J. Heat Fluid Flow*, vol. 32, no. 6, pp. 1199–1207, 2011.

[298] R. Hino and T. Ueda, "Studies on heat transfer and flow characteristics in subcooled flow boiling-Part 1. Boiling characteristics," *Int. J. Multiph. Flow*, vol. 11, no. 3, pp. 269–281, 1985.

[299] T. A. Kingston, J. A. Weibel, and S. V. Garimella, "High-frequency thermal-fluidic characterization of dynamic microchannel flow boiling instabilities: Part 1 – Rapid-bubble-growth instability at the onset of boiling," *Int. J. Multiph. Flow*, vol. 106, pp. 179–188, 2018.

[300] Micropump, "Series GJ," 2016. [Online]. Available: http://www.micropump.com/support_documents/GJ_EagleDrive.pdf.

[301] I. Mudawar, "Two-phase microchannel heat sinks: Theory, applications, and limitations," *J. Electron. Packag. Trans. ASME*, vol. 133, no. 4, 2011.

[302] TMD Technologies Ltd., “MPMs (Microwave Power Modules),” 2016.

[303] A. H. Al-Zaidi, M. M. Mahmoud, and T. G. Karayiannis, “Condensation flow patterns and heat transfer in horizontal microchannels,” *Exp. Therm. Fluid Sci.*, vol. 90, pp. 153–173, 2018.

[304] Y. Lei, I. Mudawar, and Z. Chen, “Computational and experimental investigation of condensation flow patterns and heat transfer in parallel rectangular micro-channels,” *Int. J. Heat Mass Transf.*, vol. 149, 2020.

[305] C. Konishi and I. Mudawar, “Review of flow boiling and critical heat flux in microgravity,” *Int. J. Heat Mass Transf.*, vol. 80, pp. 469–493, 2015.

[306] D. M. Iceri, G. Zummo, L. Saraceno, and G. Ribatski, “Convective boiling heat transfer under microgravity and hypergravity conditions,” *Int. J. Heat Mass Transf.*, vol. 153, 2020.

[307] D. Bogojevic, K. Sefiane, A. J. Walton, H. Lin, G. Cummins, D. B. R. Kenning, and T. G. Karayiannis, “Experimental investigation of non-uniform heating effect on flow boiling instabilities in a microchannel-based heat sink,” *Int. J. Therm. Sci.*, vol. 50, no. 3, pp. 309–324, 2011.

[308] S. N. Ritchey, J. A. Weibel, S. V Garimella, S. N. Ritchey, J. A. Weibel, and S. V Garimella, “Effects of Non-Uniform Heating on the Location and Magnitude of Critical Heat Flux in a Microchannel Heat Sink,” *Int. J. Micro-Nano Scale Transp.*, vol. 5, no. 3, 2014.

[309] E. S. Cho, J. W. Choi, J. S. Yoon, and M. S. Kim, “Experimental study on microchannel heat sinks considering mass flow distribution with non-uniform heat flux conditions,” *Int. J. Heat Mass Transf.*, vol. 53, no. 9–10, pp. 2159–2168, 2010.